

University of Alberta  
Department of Civil &  
Environmental Engineering



Structural Engineering Report No. 279

**LIMIT STATES DESIGN APPROACH FOR  
ROLLED WIDE FLANGE BEAMS SUBJECT  
TO COMBINED TORSION AND FLEXURE**

by  
Dennis Bremault  
Robert G. Driver  
and  
Gilbert Y. Grondin

January 2008

**Limit States Design Approach for Rolled Wide Flange Beams  
Subject to Combined Torsion and Flexure**

by

Dennis Bremault

Robert G. Driver

and

Gilbert Y. Grondin

**Structural Engineering Report 279**

Department of Civil and Environmental Engineering  
University of Alberta  
Edmonton, Alberta, Canada

January 2008

## **ABSTRACT**

Current design standards have not adopted an ultimate limit state interaction equation for rolled steel wide flange sections subject to combined torsion and flexure due to limited verification of proposed diagrams.

A finite element model capable of accurately predicting the behaviour and ultimate capacity was developed and validated using the experimental results of Driver and Kennedy (1987) and Comeau (1998). The model was used in a broad parametric study to expand the current database of experimental and analytical results. An ULS interaction diagram was developed using this database of results based on the work of Driver and Kennedy (1987) and Pi and Trahair (1994b; Trahair and Pi, 1997) that was shown to be a simple and accurate means of predicting the ULS capacity of beams subject to combined torsional and flexural loads. The serviceability limit states govern over the ultimate limit state in approximately 90% of the beams investigated.

## **ACKNOWLEDGEMENTS**

Funding for this project was provided by the Natural Sciences and Engineering Research Council of Canada.

Thanks are extended to the Rail and Transportation Groups at UMA Engineering Ltd. in Edmonton, Alberta, for their support of the first author in the pursuit of his Master's degree, and especially Lance Pepper who developed a figure for use in this project.

# TABLE OF CONTENTS

1	INTRODUCTION.....	1
1.1	Background and Need for the Research .....	1
1.2	Objectives and Scope.....	2
2	LITERATURE REVIEW .....	4
2.1	General Behaviour and Response.....	4
2.1.1	Torsional Behaviour .....	4
2.1.1.1	Linear Elastic Analysis.....	4
2.1.1.2	Non-Linear Inelastic Analysis .....	6
2.1.1.3	Plastic Collapse Analysis.....	8
2.1.1.4	Strength Design for Torsion.....	9
2.1.2	Flexural Behaviour .....	11
2.1.3	Combined Flexural and Torsional Behaviour .....	12
2.2	Design Models and Standards.....	14
2.2.1	Elastic Design Models.....	14
2.2.2	Inelastic Design Models .....	18
2.2.3	Current Design Standards.....	27
2.3	Unpublished Experimental Research .....	29
2.4	Finite Element Models for Combined Torsional and Flexural Loading.....	31
2.5	Summary .....	36

3	FINITE ELEMENT MODEL DEVELOPMENT USING TESTS OF DRIVER AND KENNEDY (1987).....	41
3.1	Introduction.....	41
3.2	Model Development.....	42
3.2.1	Element Properties and Model Mesh .....	42
3.2.2	Material Model .....	44
3.2.3	Solution Strategy.....	46
3.2.4	Modified Loading Bracket.....	46
3.2.5	Residual Stresses .....	48
3.2.6	Fillets.....	51
3.2.7	Comparison with 3-D Element Model.....	53
3.2.8	Cable Loading.....	54
3.3	Discussion of Finite Element Model Results.....	56
3.4	Summary .....	57
4	FURTHER DEVELOPMENT OF MODEL USING TESTS OF COMEAU (1998).....	75
4.1	Experimental Description.....	75
4.2	Description of Model.....	79
4.3	Test 1 – Uniform Torsion .....	84
4.4	Test 3 – Pure Flexure .....	85
4.4.1	12 m Beams .....	87
4.4.2	6 m Beams .....	88

4.5	Test 4 – Combined Torsion and Biaxial Bending.....	89
4.5.1	12 m Beams.....	90
4.5.2	6 m Beams.....	91
5	PARAMETRIC STUDY METHODOLOGY .....	117
5.1	Parameter Selection.....	117
5.1.1	Global Parameter List .....	117
5.1.2	Parameter Investigation .....	117
5.1.3	Parameter Reductions .....	122
5.2	Methodology.....	124
5.2.1	Beam Cross-section.....	124
5.2.2	Beam Slenderness.....	125
5.2.3	Load Type.....	125
5.2.4	Boundary Conditions.....	125
5.2.5	Moment–Torque Ratio .....	126
5.2.6	Nomenclature.....	126
5.3	Finite Element Model.....	127
5.3.1	Geometric Factors.....	127
5.3.1.1	Discretization of Beam.....	127
5.3.1.2	Boundary Conditions .....	128
5.3.1.2	Boundary Conditions .....	128
5.3.1.3	Initial Imperfections .....	129
5.3.2	Material Properties.....	130
5.3.3	Residual Stresses .....	131
5.3.4	Load Application .....	132

6	PARAMETRIC STUDY RESULTS .....	144
6.1	Parametric Study .....	147
6.1.1	Moment–Torque Ratio .....	147
6.1.1.1	Pure Flexure (E0 beams) .....	147
6.1.1.2	Torsion Only Load Case (E4 beams) .....	148
6.1.1.3	Combined Torsion and Flexure (E1, E2, and E3 beams) .....	150
6.1.2	Effect of Load Eccentricity under Various Boundary Conditions .....	151
6.1.2.1	Simply Supported (B1 beams).....	151
6.1.2.2	Fixed-Fixed (B2 beams) .....	153
6.1.2.3	Fixed End Cantilever (B3 beams).....	155
6.1.3	Cross-sectional Dimensions.....	157
6.1.4	Effect of Beam Length.....	160
6.2	General Discussion .....	160
6.2.1	Proposed Modifications to the Interaction Diagram.....	161
6.2.2	Web Yielding.....	163
6.2.3	Serviceability Limit States (SLS) .....	166
6.2.3.1	Maximum Normal Stress Limit.....	166
6.2.3.2	Elastic Deflection Limits.....	167
6.2.3.3	SLS versus ULS .....	168
6.2.4	Torsional Rotations at the Ultimate Limit State .....	168
6.3	Summary .....	170
7	FURTHER VALIDATION OF PROPOSED DESIGN METHODOLOGY .....	192
7.1	Basic Complementary Cases .....	192
7.1.1	Additional Moment–Torque Ratios.....	193
7.1.2	Additional Beam Lengths .....	195

7.1.3	Additional Cross-Sections .....	197
7.1.4	Additional Load Type .....	199
7.1.5	Additional Boundary Condition.....	201
7.2	Investigation of Built-Up Cross-Sections .....	202
7.2.1	Wide Flange Section with One Flange Reinforced with a Channel Section.....	202
7.2.2	Welded Plate Girders.....	207
7.3	Previous Research .....	209
7.4	Rotations at the Ultimate Limit State .....	210
7.5	Summary .....	211
8	SUMMARY AND CONCLUSIONS .....	237
8.1	Summary of Research Project.....	237
8.2	Recommendations and Conclusions .....	238
9	REFERENCES.....	243
	APPENDIX A – DESCRIPTION OF CALCULATIONS .....	247
	APPENDIX B – RESULTS OF THE PARAMETRIC STUDY .....	252
	APPENDIX C – COMPLEMENTARY CASE RESULTS .....	290

## LIST OF TABLES

	Page
Table 3.1 Modelled Engineering Stress vs. Strain Curves.....	59
Table 3.2 Modelled True Stress vs. Plastic Strain Curve.....	59
Table 3.3 Comparison of Finite Element model with Test Results at the Point at which the Second Phase of Behaviour Starts.....	59
Table 3.4 Comparison of Finite Element model with Test Results of the Maximum Moments and Loads.....	60
Table 3.5 Comparison of Finite Element model with Test Results of the Initial Slopes of the Moment vs. Torque and Torque vs. Rotation Diagrams .....	60
Table 4.1 Nominal and Average Cross-Sectional Dimensions .....	95
Table 4.2 Modelled Engineering Stress vs. Strain Curves.....	95
Table 4.3 Comparison of Finite Element, Theoretical, and Experimental Results for Test 1 .....	95
Table 4.4 Comparison of Lateral Deflections from Lateral Loading .....	96
Table 4.5 Comparison of Finite Element, Theoretical, and Experimental Peak Load Results for Test 4 .....	96
Table 5.1 Distribution of Class of Sections .....	135
Table 5.2 Slenderness Limits from CSA S16-01 .....	135
Table 5.3 Variation of $\frac{b}{2t}$ and $\frac{h}{w}$ for Standard Wide Flange Sections.....	135
Table 5.4 Variation in $\lambda$ Sorted by Section Class .....	136

Table 5.5 Section Choices.....	136
Table 5.6 Length Selection Table .....	137
Table 5.7 Naming and Numbering Convention for Parametric Study .....	137
Table 5.8 Element Lengths, Widths, and Aspect Ratios for Parametric Study .....	138
Table 5.9 Peak Moment, Torque, and Load Values for Imperfection Study .....	138
Table 5.10 Engineering and True Stress vs. Strain Curves for Finite Element Models.....	138
Table 5.11 Method Used to Calculate Required Vertical Load Eccentricity ...	139
Table 5.12 Eccentricities Used in Parametric Study .....	140
Table 6.1 Average FEPR and Coefficients of Variation for Parametric Study Results .....	172
Table 6.2 Von Mises Yield Criterion Checks of Web .....	173
Table 6.3 Complete List of FEPR Values for Basic Factorial Approach using the Modified Interaction Diagram .....	174
Table 6.4 Complete List of FEPR Values for Basic Factorial Approach using the Modified Interaction Diagram with 30 Degree Cut-Off..	175
Table 7.1 Naming and Numbering Convention for Basic Complementary Cases .....	213
Table 7.2 Results at Service and Ultimate Points – Thickened vs. Non-Thickened Web Model .....	213
Table 7.3 Lengths and Eccentricities Used in Beam Length Variation .....	213

Table 7.4 Eccentricities Used with Additional Cross-Sections .....	214
Table 7.5 Eccentricities Used with T2 Beams.....	214
Table 7.6 Method Used to Calculate Required Vertical UDL Eccentricity.....	214
Table 7.7 Comparison of the Results of the T1 and T2 Beams .....	215
Table 7.8 Eccentricities Used for Additional Boundary Conditions .....	215
Table 7.9 Method Used to Calculate Required Vertical Load Eccentricity .....	215
Table 7.10 Eccentricities Used for Wide Flange Beams Reinforced with a Channel Section .....	216
Table 7.11 Total Torsional Resistance Calculated by the Method Proposed in Section 7.2.1.....	216
Table 7.12 Eccentricities Used for the Welded Plate Girder .....	216
Table 7.13 Theoretical Pure Flexure Capacity of Welded Plate Girders.....	217
Table 7.14 Finite-Element-to-Predicted Ratios for Test Results.....	217
Table 7.15 List of Finite-Element-to-Predicted Ratios for Complementary Cases .....	218
Table 7.16 List of Finite-Element-to-Predicted Ratios for Complementary Eccentricity Cases.....	218
Table 7.17 List of Finite-Element-to-Predicted Ratios for Complementary Cases with 30 Degree Cut-Off.....	219
Table 7.18 List of Finite-Element-to-Predicted Ratios for Complementary Eccentricity Cases with 30 Degree Cut-Off .....	219

## LIST OF FIGURES

	Page
Figure 2.1 Combined Bending and Torsional Stresses in Wide Flange Sections.....	38
Figure 2.2 Eccentric Vertical Load Simplified Using the Flexure Analogy.....	38
Figure 2.3 Test Set-up from Driver and Kennedy’s (1987) Experimental Research.....	39
Figure 2.4 Simplified Moment vs. Torque Interaction Diagram .....	39
Figure 2.5 Moment vs. Torque Interaction Diagram for Unbraced Beams compared to Finite Element Results (after Trahair and Pi, 1994a).....	40
Figure 3.1 Mesh 2 for Beam 3 .....	61
Figure 3.2 Moment at Fixed End vs. Torque at Fixed End for Beam 2 – Mesh Refinement Study.....	61
Figure 3.3 Torque at Fixed End vs. Rotation at Free End for Beam 2 – Mesh Refinement Study.....	62
Figure 3.4 Modelled Engineering Stress vs. Strain Curves .....	62
Figure 3.5 Moment at Fixed End vs. Torque at Fixed End for Beam 2 – Effect of Loading Bracket Model .....	63
Figure 3.6 Original Loading Bracket with Mesh 1 for Beam 2.....	63
Figure 3.7 Torque at Fixed End vs. Rotation at Free End for Beam 2 – Effect of Loading Bracket Model .....	64

Figure 3.8 Moment at Fixed End vs. Torque at Fixed End for Beam 4 – Effect of Residual Stresses .....	64
Figure 3.9 Torque at Fixed End vs. Rotation at Free End for Beam 4 – Effect of Residual Stresses .....	65
Figure 3.10 Comparison between the Equilibrated Residual Stresses and the Modelled Residual Stresses .....	65
Figure 3.11 Moment at Fixed End vs. Torque at Fixed End for Beam 3 – Fillets.....	66
Figure 3.12 Torque at Fixed End vs. Rotation at Free End for Beam 3 – Fillets.....	66
Figure 3.13 Moment at Fixed End vs. Torque at Fixed End for Beam 3 – Comparison Between Brick and Shell Element Models.....	67
Figure 3.14 Torque at Fixed End vs. Rotation at Free End for Beam 3 – Comparison Between Brick and Shell Element Models.....	67
Figure 3.15 Top Flange Strain for Beam 3 - Brick and Shell Models .....	68
Figure 3.16 Web Strain for Beam 3 - Brick and Shell Models.....	68
Figure 3.17 Bottom Flange Strain for Beam 3 - Brick and Shell Models.....	69
Figure 3.18 Top Flange Stress for Beam 3 - Brick and Shell Models .....	69
Figure 3.19 Web Stress for Beam 3 - Brick and Shell Models.....	70
Figure 3.20 Bottom Flange Stress for Beam 3 - Brick and Shell Models .....	70
Figure 3.21 Moment at Fixed End vs. Torque at Fixed End for Beam 4 – Model Loaded With Cable.....	71

Figure 3.22 Torque at Fixed End vs. Rotation at Free End for Beam 4 - Model Loaded With Cable.....	71
Figure 3.23 Moment at Fixed End vs. Torque at Fixed End for Beam 2 – Model Loaded With Cable.....	72
Figure 3.24 Torque at Fixed End vs. Rotation at Free End for Beam 2 – Model Loaded With Cable.....	72
Figure 3.25 Moment at Fixed End vs. Torque at Fixed End.....	73
Figure 3.26 Torque at Fixed End vs. Rotation at Free End.....	73
Figure 3.27 Vertical Load vs. Lateral Deflection at Free End.....	74
Figure 3.28 Moment at Fixed End vs. Vertical Deflection at Free End.....	74
Figure 4.1 Test 1 Experimental Set-Up.....	97
Figure 4.2 Test 3 Experimental Set-Ups.....	97
Figure 4.3 Test 4 Experimental Set-Ups.....	98
Figure 4.4 Mesh for Beam P1-A for Test 4 .....	98
Figure 4.5 Comparison of the Measured and Modelled Residual Stress Pattern for Both Beams for the Top Flange of the Wide Flange Section .....	99
Figure 4.6 Comparison of the Measured and Modelled Residual Stress Pattern for Both Beams for the Web of the Wide Flange Section .....	99
Figure 4.7 Comparison of the Measured and Modelled Residual Stress Pattern for Both Beams for the Bottom Flange of the Wide Flange Section .....	100

Figure 4.8 Comparison of the Measured and Modelled Residual Stress Pattern for Both Beams for the Channel Web .....	100
Figure 4.9 Comparison of the Measured and Modelled Residual Stress Pattern for Both Beams for the Channel Left Flange.....	101
Figure 4.10 Comparison of the Measured and Modelled Residual Stress Patterns for Both Beams for the Channel Right Flange.....	101
Figure 4.11 Comparison of the Equilibrated Residual Stresses for Beam P1-A with the Measured and Modelled Distributions for the Top Flange of the Wide Flange Section .....	102
Figure 4.12 Comparison of the Equilibrated Residual Stresses for Beam P1-A versus the Measured and Modelled Distribution for the Web of the Wide Flange Section.....	102
Figure 4.13 Comparison of the Equilibrated Residual Stresses for Beam P1-A with the Measured and Modelled Distribution for the Bottom Flange of the Wide Flange Section.....	103
Figure 4.14 Comparison of the Equilibrated Residual Stresses for Beam P1-A with the Measured and Modelled Distribution for the Channel Web .....	103
Figure 4.15 Comparison of the Equilibrated Residual Stresses for Beam P1-A with the Measured and Modelled Distribution for the Channel Left Flange .....	104
Figure 4.16 Comparison of the Equilibrated Residual Stresses for Beam P1-A vs. the Measured and Modelled Distribution for the Channel Right Flange.....	104
Figure 4.17 Load vs. Rotation for Beam P1 – Test 1 .....	105

Figure 4.18 Load vs. Rotation for Beam P2 – Test 1 .....	105
Figure 4.19 Load vs. Vertical Deflection at Mid-span for Beam P1 – Test 3.....	106
Figure 4.20 Load vs. Lateral Deflection at Mid-span for Beam P1 – Test 3.....	106
Figure 4.21 Load vs. Vertical Deflection at Mid-span for Beam P2 – Test 3.....	107
Figure 4.22 Load vs. Lateral Deflection at Mid-span for Beam P2 – Test 3.....	107
Figure 4.23 Load vs. Average Vertical Deflection at Load Application Points for Beam P1-B – Test 3 .....	108
Figure 4.24 Load vs. Lateral Deflection at Mid-Span for Beam P1-B – Test 3 .....	108
Figure 4.25 Load vs. Average Vertical Deflection at Load Application Points for Beam P2-B – Test 3 .....	109
Figure 4.26 Load vs. Lateral Deflection at Mid-span for Beam P2-B – Test 3 .....	109
Figure 4.27 Vertical Load vs. Vertical Deflection at LVDT Locations at Mid-Span for Beam P1 Load Cycle (LC) 1 – Test 4 .....	110
Figure 4.28 Vertical Load vs. Lateral Deflection for Beam P1 LC 1 – Test 4.....	110
Figure 4.29 Vertical Load vs. Vertical Deflection at LVDT Locations at Mid-Span for Beam P1 LC 2 – Test 4.....	111

Figure 4.30 Vertical Load vs. Lateral Deflection for Beam P1 LC 2 – Test 4 .....	111
Figure 4.31 Vertical Load vs. Vertical Deflection at LVDT Locations at Mid-Span for Beam P2 LC 1 – Test 4.....	112
Figure 4.32 Vertical Load vs. Lateral Deflection for Beam P2 LC 1 – Test 4.....	112
Figure 4.33 Vertical Load vs. Vertical Deflection at LVDT Locations at Mid-Span for Beam P2 LC 2 – Test 4.....	113
Figure 4.34 Vertical Load vs. Lateral Deflection for Beam P2 LC 2 – Test 4.....	113
Figure 4.35 Vertical Load vs. Vertical Deflection at Loading Points for Beam P1-A – Test 4.....	114
Figure 4.36 Vertical Load vs. Vertical Deflection at LVDT Locations at Mid-Span for Beam P1-A – Test 4.....	114
Figure 4.37 Vertical Load vs. Lateral Deflection for Beam P1-A – Test 4.....	115
Figure 4.38 Vertical Load vs. Vertical Deflection at Loading Points for Beam P2-A – Test 4.....	115
Figure 4.39 Vertical Load vs. Vertical Deflection at LVDT Locations at Mid-Span for Beam P2-A – Test 4.....	116
Figure 4.40 Vertical Load vs. Lateral Deflection for Beam P2-A – Test 4.....	116
Figure 5.1 Bending and Torsional Moment Diagrams for UDL and a Point Load at Mid-Span.....	141
Figure 5.2 Typical Finite Element Mesh.....	141

Figure 5.3 Maximum Moment vs. Torque Diagram for Imperfection Study .....	142
Figure 5.4 Stress vs. Strain Curve for Parametric Study .....	142
Figure 5.5 Residual Stress Pattern Modelled .....	143
Figure 6.1 Moment–Torque Interaction Diagram .....	176
Figure 6.2 Moment vs. Torque Diagram for Beam S4L1T1B1E0 .....	176
Figure 6.3 Torque vs. Rotation Diagram for Beam S1L2T1B2E4 .....	177
Figure 6.4 Torque vs. Rotation Diagram for Beam S5L2T1B3E4 .....	177
Figure 6.5 Von Mises Stress Contour Plot for Beam S5L2T1B3E4 at ULS .....	178
Figure 6.6 Torque vs. Rotation Diagram for Beam S2L1T1B1E4 .....	178
Figure 6.7 Von Mises Stress Contour Plot for Beam S2L1T1B1E4 at ULS .....	179
Figure 6.8 Torque vs. Rotation Diagram for Beam S5L1T1B2E4 .....	179
Figure 6.9 Von Mises Stress Contour Plot for Beam S5L1T1B2E4 at ULS .....	180
Figure 6.10 Moment vs. Torque Diagram for Beam S3L1T1B1 .....	180
Figure 6.11 Torque vs. Rotation Diagram for Beam S3L1T1B1 .....	181
Figure 6.12 Von Mises Stress Contour Plot for Beam S4L2T1B1E1 at the Ultimate Limit State .....	181
Figure 6.13 Moment vs. Torque Diagram for Beam S5L2T1B1E2 .....	182

Figure 6.14 Von Mises Stress Contour Plot for Beam S5L2T1B1E1 at ULS .....	182
Figure 6.15 Moment vs. Torque Diagram for Beam S1L2T1B1E3 .....	183
Figure 6.16 Moment vs. Torque Diagram for Beam S1L2T1B2.....	183
Figure 6.17 Torque vs. Rotation Diagram for Beam S1L2T1B2 .....	184
Figure 6.18 Vertical Load vs. Vertical Deflection Diagram for Beam S1L2T1B2E1.....	184
Figure 6.19 Moment vs. Torque Diagram for Beam S2L1T1B2E2 .....	185
Figure 6.20 Moment vs. Torque Diagram for Beam S2L2T1B2.....	185
Figure 6.21 Vertical Load vs. Vertical Deflection Diagram for Beam S2L2T1B2E2.....	186
Figure 6.22 Von Mises Stress Contour Plot for Beam S2L2T1B2E2 at ULS .....	186
Figure 6.23 Moment vs. Torque Diagram for Beam S3L2T1B3.....	187
Figure 6.24 Torque vs. Rotation Diagram for Beam S3L2T1B3 .....	187
Figure 6.25 Moment vs. Torque Diagram for Beam S2L1T1B3.....	188
Figure 6.26 Torque vs. Rotation Diagram for Beam S2L1T1B3 .....	188
Figure 6.27 Von Mises Stress Contour Plot for Beam S2L1T1B3E1 at ULS .....	189
Figure 6.28 Vertical Load vs. Vertical Deflection Diagram for Beam S3L2T1B3E2.....	189

Figure 6.29 Modified Normalized Moment vs. Torque Interaction Diagram for Simply Supported Beams with all Parametric Study Results .....	190
Figure 6.30 Moment vs. Torque Interaction Diagram for Beam S6L1T1B1 (Modified to Class 2 in Flexure).....	190
Figure 6.31 Moment vs. Torque Interaction Diagram for Beam S5L1T1B2 (Modified to Class 1 in Torsion).....	191
Figure 6.32 Moment vs. Torque Interaction Diagram for Beam S6L2T1B3 (Modified to Class 1 in Both Torsion and Flexure) .....	191
Figure 7.1 Moment vs. Torque Diagram - Thickened vs. Non-Thickened Web Models .....	220
Figure 7.2 Torque vs. Rotation Diagram - Thickened vs. Non-Thickened Web Model .....	220
Figure 7.3 Moment vs. Torque Interaction Diagram for Beam S1L2T1B2 .....	221
Figure 7.4 Moment vs. Torque Interaction Diagram for Beam S3L1T1B2 .....	222
Figure 7.5 Moment vs. Torque Interaction Diagram for Beam S4L2T1B3 .....	222
Figure 7.6 Moment vs. Torque Interaction Diagram for Beam S2L3T1B1 .....	223
Figure 7.7 Moment vs. Torque Interaction Diagram for Beam S2L4T1B1 .....	223
Figure 7.8 Moment vs. Torque Interaction Diagram for Beam S4L3T1B2 .....	224
Figure 7.9 Moment vs. Torque Interaction Diagram for Beam S4L4T1B2 .....	224
Figure 7.10 Vertical Load vs. Vertical Deflection Diagram for Beam S4L4T1B2E1 .....	225

Figure 7.11 Moment vs. Torque Interaction Diagram for Beam S9LT1B3 .....	225
Figure 7.12 Moment vs. Torque Interaction Diagram for Beam S10L2T1B2 .....	226
Figure 7.13 Moment vs. Torque Interaction Diagram for Beam S11L1T1B1 .....	226
Figure 7.14 Mesh used for Beam S1L2T2B2.....	227
Figure 7.15 Moment vs. Torque Interaction Diagram for Beam S3L1T2B1 .....	227
Figure 7.16 Moment vs. Torque Interaction Diagram for Beam S1L2T2B2 .....	228
Figure 7.17 Moment vs. Torque Interaction Diagram for Beam S6L1T2B3 .....	228
Figure 7.18 Moment vs. Torque Interaction Diagram for Beam S1L2T1B4 .....	229
Figure 7.19 Torque vs. Rotation Diagram for Beam S1L2T1B4 .....	229
Figure 7.20 Moment vs. Torque Interaction Diagram for Beam S5L1T1B4 .....	230
Figure 7.21 Moment vs. Torque Interaction Diagram for Beam SPL1T1B1 .....	230
Figure 7.22 Moment vs. Torque Interaction Diagram for Beam SPL2T1B1 .....	231
Figure 7.23 Moment vs. Torque Interaction Diagram for Beam SPL1T1B2 .....	231

Figure 7.24 Moment vs. Torque Interaction Diagram for Beam SPL2T1B2 .....	232
Figure 7.25 Moment vs. Torque Interaction Diagram for Beam S7L1T1B1 .....	232
Figure 7.26 Moment vs. Torque Interaction Diagram for Beam S7L3T1B2 .....	233
Figure 7.27 Moment vs. Torque Interaction Diagram for Beam S8L1T1B2 .....	233
Figure 7.28 Moment vs. Torque Interaction Diagram for Beam S8L3T1B1 .....	234
Figure 7.29 Torque vs. Rotation Diagram for Beam S7L1T1B1 .....	234
Figure 7.30 Test Results from Razzaq and Galambos (1979b).....	235
Figure 7.31 Test results from Razzaq and Galambos (1979b) .....	235
Figure 7.32 Driver and Kennedy (1987) Test Results.....	236

## LIST OF SYMBOLS

$A$	cross-sectional area
$B$	bi-moment
$b$	flange or plate width
$B^*$	design or applied bi-moment
$B_p$	plastic flange bi-moment
$B_y$	yield flange bi-moment
$C_w$	warping constant of the cross-section
$d$	depth of section
$e$	eccentricity
$E$	modulus of elasticity
$F_u$	ultimate stress
$F_y$	yield stress
$G$	shear modulus of elasticity
$h$	web height found by $d - 2 \times t$
$I$	moment of inertia
$I_z$	strong axis moment of inertia
$I_y$	weak axis moment of inertia
$J$	torsional constant
$K$	a factor for Class 1 and 2 sections presented by Driver and Kennedy (1987, 1989) to determine the warping torsional resistance
$k$	vertical cross-sectional fillet dimension, measured from the outside of the flange
$K^*$	a factor for Class 3 sections presented by Driver and Kennedy (1987, 1989) to determine the warping torsional resistance
$k_1$	horizontal cross-sectional fillet dimension, measured from the centre of the web
$k_2$	ratio of the flexural to torsional resistance according to Driver and Kennedy (1987)
$k_T$	torsional stiffness
$L$	member length between points of lateral supports

$L_u$	characteristic length (laterally unsupported length below which lateral torsional does not take place)
$L / r_y$	global slenderness ratio
$M$	bending moment
$m$	slope of diagram
$M^*$	design factored applied bending moment
$M/B$	moment to bi-moment ratio
$M/T$	moment–torque ratio
$M_n/T_n$	normalized moment–torque ratio
$M_{bf}$	portion of bending moment carried by flanges
$M_o$	plastic collapse bending moment
$M_p$	plastic bending moment
$M_{pf}$	the plastic moment of the flange alone about the principal axis of bending, usually the strong axis
$M_{pw}$	the plastic moment of the web alone about the principal axis of bending, usually the strong axis
$M_r$	moment resistance of the cross-section
$M_{sa}$	strong axis bending moment
$M_u$	elastic lateral torsional buckling moment
$M_{wa}$	weak axis bending moment
$M_x$	torsional moment about the X-axis
$m_x$	distributed torsional moment about the X-axis
$M_y$	bending moment about the Y-axis or the weak axis bending moment
$M_z$	bending moment about the Z-axis or the strong axis bending moment
$M_{z,MAX}$	maximum bending moment about the Z-axis or the maximum strong axis bending moment
$P$	point load

$Q$	first moment of area of section at cut of section for flexural shear stress calculation
$R_T$	torque ratio of point 2 to point 4 for calculation of FEPR for Driver and Kennedy (1987) interaction diagram
$R_M$	moment ratio of point 3 to point 1 for calculation of FEPR for Driver and Kennedy (1987) interaction diagram
$r_y$	weak axis radius of gyration
$S$	elastic section modulus
$S_w$	warping statical moment
$t$	flange or plate thickness
$T$	torque
$T_o$	plastic collapse torque
$T^*$	design factored applied torque
$T_u^*$	design or applied uniform torque
$t_c$	thickness of material at cut of section for flexural shear stress calculation
$t_m$	maximum wall thickness
$T_r$	torsional resistance of the cross-section
$T_{sv}$	pure or St. Venant torsional resistance
$T_{sv,C}$	pure or St. Venant torsional resistance of channel section
$T_{sv,T}$	total pure or St. Venant torsional resistance of channel and wide flange sections
$T_{sv,W}$	pure or St. Venant torsional resistance of wide flange section
$T_{up}$	uniform or pure torsion plastic torque
$T_{uy}$	first yield uniform torsion (equivalent to the membrane analogy)
$T_w$	warping torsional resistance
$u$	deformation in the direction of the X-axis
$u'$	first derivative of the deformation in the direction of the X-axis
$v$	deformation in the direction of the Y-axis
$V$	total internal shear force in the cross-section

$v''$	second derivative of the deformation in the direction of the Y-axis
$V_y$	the shear in the Y-direction or the strong axis shear for this coordinate system
$W$	Wagner stress resultant
$w$	web thickness, uniformly distributed load, or deformation in the direction of the Z-axis
$w'$	first derivative of the deformation in the direction of the Z-axis
$w''$	second derivative of the deformation in the direction of the Z-axis
$W_n$	normalized unit warping of cross-section
$y$	Y-coordinate
$Z$	plastic section modulus
$z$	Z-coordinate
$\alpha$	torque conversion factor for determining the FEPR
$\beta$	modification factor used by Lin (1977)
$\delta$	a factor from Heins and Seaburg (1963) that is a function of the cross-section, boundary, and loading conditions
$\varepsilon$	engineering normal strain
$\varepsilon_T$	true normal strain
$\phi$	angle of twist or resistance factor
$\phi'$	first derivative of the angle of twist
$\phi''$	second derivative of the angle of twist
$\phi'''$	third derivative of the angle of twist
$\phi^{iv}$	fourth derivative of the angle of twist
$\gamma$	a dimensionless factor used by Chu and Johnson (1974) to account for the interaction of flexure and torque
$\gamma_{cr}$	the critical value of $\gamma$ that causes torsional buckling to be the governing failure mode
$\gamma_x$	exponent on the moment term of the interaction equation proposed by Pi and Trahair (1994a)
$\gamma_z$	exponent on the torsion term of the interaction equation proposed by Pi and Trahair (1994a)
$\lambda$	Lambda

$\lambda_L$	slenderness ratio defined at the $\sqrt{M_p/M_u}$
$\lambda_p$	plastic collapse factor found as the factor multiplied to the applied load to develop a plastic collapse failure mechanism in the beam
$\lambda_{p,b}$	plastic collapse factor for in-plane bending
$\lambda_{p,t}$	total plastic collapse factor for torsion
$\lambda_{p,u}$	uniform torsion plastic collapse factor
$\lambda_{p,w}$	warping torsion plastic collapse factor
$\eta$	moment conversion factor for determining the FEPR
$\nu$	poisson ratio
$\sigma$	engineering normal stress
$\sigma_b$	normal stress due to bending of the cross-section
$\sigma_{b,s}$	normal stress due to strong axis bending of the cross-section
$\sigma_{b,w}$	normal stress due to weak axis bending of the cross-section
$\sigma_p$	plastic stress
$\sigma_T$	true normal stress
$\sigma_w$	normal stress due to warping of the cross-section
$\sigma_i$	the normal stress in direction of the $i$ -axis
$\sigma_x$	normal stress in the direction of the X-axis
$\sigma_y$	normal stress in the direction of the Y-axis
$\sigma_{YP}$	von Mises yield criterion stress
$\sigma_z$	normal stress in the direction of the Z-axis
$\tau_{ij}$	shear stress in the $i - j$ Plane
$\tau_b$	shear stress caused by bending
$\tau_{bx}$	shear stress caused by strong axis bending
$\tau_{sv}$	St. Venant torsion shear stress
$\tau_t$	shear stress caused by torsion in the X-Y Plane

$\tau_w$	warping torsion shear stress
$\tau_{xy}$	shear stress in the X-Y Plane
$\tau_{yz}$	shear stress in the Y-Z Plane
$\tau_{zx}$	shear stress in the Z-X Plane
$\omega_2$	equivalent moment factor and is a function of the bending moment diagram

# 1 INTRODUCTION

## 1.1 *Background and Need for the Research*

Combined torsion and flexure occurs in a beam when vertical or transverse loads are applied eccentrically to the shear centre or when an attached member applies a gravity load and relies upon the primary member for torsional restraint inducing a point torque. Although the influence of torsion on wide flange beams is often minimized intentionally in the design and detailing process, in some cases the effects of combined loading can be critical. This problem has garnered attention for some time and, as such, significant amounts of research on the behaviour of structural members under torsion have been performed. Theory on pure flexure or torsion only loading is well understood in both elastic and inelastic ranges. The combined behaviour and its interaction, however, is highly complex and not as well understood.

Historically, design standards based on allowable stress methods required elastic analyses and the principle of superposition to calculate a combined stress, which was then compared against an allowable proportion of the material yield strength. As a result, the majority of the technical literature available presents theories on elastic behaviour. Many of these elastic theories neglect the interaction between torsion and flexure that occurs under combined loading. Some theories deal with this interaction, but use highly demanding processes including the use of complex differential equations; graphs specific to boundary conditions, sections, and loading; large tables; or approximate equations. These solutions are generally too elaborate for design purposes.

Over the last 30 years, design standards have shifted towards limit states design, a method that requires the assessment of the full capacity of the member for each potential limit state. This type of design compares a factored (reduced) ultimate strength to a factored (increased) load based

on statistical data on both loads and resistances. The purpose of this is to provide more predictable and consistent levels of safety throughout the design. This has led to a more urgent interest in the inelastic and ultimate behavior of beams under combined torsion and flexure. In the hopes of developing a safe and efficient design methodology for limit states design, recent research has focused on this range of behaviour.

Current design standards provide little guidance for beams loaded in combined torsion and flexure. The current edition of the Canadian steel design standard CSA S16-01 (2001) requires that “Beams and girders subjected to torsion shall have sufficient strength and rigidity to resist the torsional moment and forces in addition to other moment or forces.” However, it does not specify how engineers are to satisfy this requirement. A few procedures have been proposed in the literature that appear to be able to effectively and accurately predict the behaviour of beams under combined torsional and flexural loads through elastic behaviour and into the inelastic range. These procedures, however, have not been adopted as part of a design standard due to the limited experimental and analytical verification that has been completed to ensure they are universally safe for design.

## **1.2 Objectives and Scope**

The primary objective of this research was to develop a simple limit states design procedure for beams under combined torsional and flexural loading. A literature review revealed two promising design procedures: one developed by Driver and Kennedy (1987, 1989) and the other developed by Pi and Trahair (1994a, 1994b; Trahair and Pi, 1997). These design procedures have been developed based on the results of limited experimental and analytical work. The first objective of this project was to develop an analytical (finite element) model that is capable of predicting the behaviour of beams under combined loading that have been tested in previous experimental research projects. Through further finite element

analyses in a broad general parametric study, a design procedure is proposed based on the work of Driver and Kennedy (1987) and Pi and Trahair (1994a, 1994b; Trahair and Pi, 1997) that is sufficiently verified and modified such that it can be adopted for use in design standards. No new experimental work was performed in this project.

The methodology developed is complete and shown to be sufficiently conservative for general design cases. This procedure provides both ultimate (ULS) and serviceability (SLS) limit state criteria. The main focus is on the ultimate behaviour and developing an acceptable ULS moment–torque interaction diagram. However, the existing SLS criteria in CSA S16-01, prevention of yielding and maintaining appropriate deflection limits under service loads, are also evaluated. In a practical sense, guidance is provided as to when the ultimate limit state is expected to govern a design. Existing research indicates that the ultimate limit state only governs for very short stocky members. Although not mentioned in standard CSA S16-01, this project also considered the interaction between torsional and flexural loads found to be significant by previous research.

The design procedure developed includes the three primary flexural classifications of beams, Classes 1 through 3. A design procedure for Class 4 sections is not required, as existing elastic methods are sufficient even for ultimate loading; these sections will buckle locally prior to yielding. To be complete, initial imperfections and fabrication tolerances are included in the study. The effect of residual stresses is also considered in this project. The design procedure is limited to wide flange sections and other sections with similar shapes. Various boundary conditions are accounted for in both torsion and flexure, including simple-simple, fixed-fixed, fixed-free, and fixed-simple. The goal was to develop a method that allows practitioners to design members subject to combined torsion and flexure under uniformly distributed or concentrated point loads.

## 2 LITERATURE REVIEW

### 2.1 General Behaviour and Response

#### 2.1.1 Torsional Behaviour

##### 2.1.1.1 Linear Elastic Analysis

Torsion theory for elastic stresses in members with open cross-sections has been well established for several years (Galambos, 1968). Driver and Kennedy (1989) provide a review of both the development of this theory and the existing analysis equations. Pi and Trahair (1994b) and Trahair and Pi (1997) divide this analysis into two parts: a cross-sectional analysis that relates the stress resultants to the deformed shape of the member and a linear analysis that is used to relate the applied loads to the torsional rotations.

St. Venant found that torsion causes non-circular cross-sections to warp. Although generally insignificant in rectangular cross-sections, this warping torsional resistance is important in wide flange (I-shaped) sections (Timoshenko, 1983). The total torsional resistance consists of the sum of the pure, or St. Venant, torsion and the warping torsion components. The maximum St. Venant shear stress,  $\tau_{sv,Max}$ , is obtained as follows (Heins, 1975):

$$\tau_{sv,Max} = Gt_m\phi' \quad [2.1]$$

where  $G$  is the shear modulus of elasticity,  $t_m$  is the maximum wall thickness, and  $\phi'$  is the first derivative of the angle of twist (rotation about the longitudinal axis),  $\phi$ , with respect to the distance along the member. Integration of the shear stresses over the cross-section results in the St. Venant torsional resistance,  $T_{sv}$ , obtained from:

$$T_{sv} = GJ\phi' \quad [2.2]$$

where  $J$  is the torsional constant and can be estimated for any thin-walled open cross-section composed of plates of width,  $b$ , and thickness,  $t$ , by (Salmon and Johnson, 1980):

$$J = \frac{1}{3} \sum (bt^3) \quad [2.3]$$

The shear stress,  $\tau_w$ , and normal stress,  $\sigma_w$ , that develop in the flanges as a result of warping in the section are obtained from (Heins, 1975):

$$\tau_w = -ES_w \phi''' \quad [2.4]$$

$$\sigma_w = -EW_n \phi'' \quad [2.5]$$

where  $E$  is the modulus of elasticity,  $S_w$  is the warping statical moment,  $W_n$  is the normalized unit warping of the cross-section, and  $\phi''$  and  $\phi'''$  are the second and third derivative of the angle of twist with respect to the distance along the length of the member, respectively. Warping of a wide flange cross-section results in the lateral deformation of the two flanges in opposite directions. When the warping deformations are restrained or non-uniform over the length of the member both shear and normal stresses develop in the flanges. Boulton (1962) and Dinno and Merchant (1965) note that no warping torque develops if the flanges are free to warp, that is, where there is no warping restraint in the member. Non-uniform torque creates warping restraint that develops shear stresses that are able to resist torsional loads. The warping torsional resistance,  $T_w$ , develops from the couple created by the flange shear stresses calculated by (Heins, 1975):

$$T_w = -EC_w \phi''' \quad [2.6]$$

where  $C_w$  is the warping constant of the cross-section. The total torsional resistance,  $T_r$ , is found by adding the pure torsion component (Equation [2.2]) to the warping torsion component (Equation [2.6]) as follows:

$$T_r = T_{sv} + T_w \quad [2.7]$$

$$T_r = GJ\phi' - EC_w\phi''' \quad [2.8]$$

The solution of differential Equation [2.8] has been presented for various boundary conditions and applied torque distributions (Heins and Seaburg, 1963; AISC, 1997). Pastor and DeWolf (1979) developed similar differential equations accounting for the interaction between torsion and flexure.

#### 2.1.1.2 Non-Linear Inelastic Analysis

Hodge (1959) developed an approximate lower bound interaction equation between moment and fully-plastic torque with warping restraint using experiments to confirm the theory. Boulton (1962) presented the lower bound approximation developed by Hodge (1959) but accounted for warping restraint. This lower bound estimate was developed for a member with varying levels of uniform strong axis bending moment combined with uniform torsion. Boulton (1962) and Farwell and Galambos (1969) noted that I-shaped beams under torsion only loads are able to carry loads beyond their full plastic torsional capacity. Boulton explains this phenomenon using experimental results that show a development of longitudinal tension in the outer edges of the beam. These axial forces result because of the development of helical curvatures in equal and opposite directions in the top and bottom portions of the cross-section. This phenomenon, referred to as the Wagner effect, was observed with and without warping restraint. These longitudinal forces increase quite significantly as the angle of twist becomes large. Performing experimental tests to verify his theory, Boulton (1962) found that this lower bound approximation estimated the capacity quite well using the Tresca yield criterion for beams with and without warping restraint.

Trahair and Pi (1997) developed an inelastic non-linear relationship between normal strain,  $\varepsilon$ , and angle of twist for wide flange beams as follows:

$$\varepsilon = u' - W_n \phi'' + \frac{1}{2}(y^2 + z^2)\phi'^2 \quad [2.9]$$

where  $u'$  is the uniform axial strain (the first derivative of the longitudinal, X-axis, deflection with respect to the distance along the X-axis),  $u$ , and  $y$  and  $z$  are the vertical and lateral coordinates at a given point in the cross-section relative to its shear centre. The first term on the right hand side of Equation [2.9] is the uniform axial strain, the second is the warping axial strain, and the third is the Wagner axial strain arising from the change in length of a longitudinal element as it undergoes a helical deformation due to twisting of the member. Trahair and Pi (1997) describe the tensile Wagner strains that develop through the cross-section with the maximum being achieved at the flange tips and the minimum, zero, developing at the shear centre. The Wagner stress resultant,  $W$ , is expressed by (Trahair and Pi, 1997):

$$W = \int_A ((y^2 + z^2)\sigma_p) dA \quad [2.10]$$

where  $\sigma_p$  is the plastic stress. For an elasto-plastic material, this plastic stress is assumed to be the yield strength. Trahair and Pi (1997) developed a finite element model that showed good agreement with earlier theoretical models and test results. Their analysis found that as rotations become large, the value of  $W$  increases even after significant yielding takes place causing the member to stiffen torsionally. Trahair and Pi's results supported their conclusion as they found that the flange tips fail in a tensile fracture mode.

### 2.1.1.3 Plastic Collapse Analysis

Pi and Trahair (1994b) and Trahair and Pi (1997) proposed a method to determine the plastic collapse torque. First, the cross-section is analyzed to determine the plastic uniform, or pure, torque,  $T_{sv}$ , using the sand heap analogy and the fully plastic bi-moment,  $B_p$ , capacities:

$$T_{sv} = \frac{1}{6} \left[ 4t^3 + 6(b-t)t^2 + 3(d-t)w^2 + w^3 \right] \left( \frac{F_y}{\sqrt{3}} \right) \quad [2.11]$$

$$B_p = \frac{1}{4} F_y b^2 t (d-t) \quad [2.12]$$

where  $F_y$  is the yield strength,  $d$  is the depth of the cross-section, and  $b$  and  $t$  are the flange width and thickness, respectively. A bi-moment,  $B$ , is defined as the product of the moment in the flanges of the I-section and the distance between the centres of gravity of the flanges,  $d-t$ . It is a measure of the warping torsional resistance of the cross-section. Dinno and Merchant (1965) found that the actual plastic uniform torsional capacity of an I-section is larger than that provided by the sand heap analogy but did not propose a theory or method to account for this additional capacity. Although no rigorously correct theory has been established to determine the plastic collapse of torsion members since the collapse modes for uniform and warping torsion are independent, Trahair and Pi (1997) proposed an approximate method whereby the plastic collapse load factor,  $\lambda_{p,t}$ , is found by finding the plastic collapse load factors in warping,  $\lambda_{p,w}$ , and uniform,  $\lambda_{p,u}$ , torsion independently and then adding them:

$$\lambda_{p,t} = \lambda_{p,u} + \lambda_{p,w} \quad [2.13]$$

where a plastic collapse load factor,  $\lambda_p$ , is the factor multiplied by the applied load to develop a plastic collapse failure mechanism in the beam. In uniform torsion, a failure mechanism develops when  $T_{sv}$  is reached at

the supports. In warping torsion, a failure mechanism results from the formation of three hinges (a hinge can consist of a support condition at the end of a beam that does not restrain warping) in each of the flanges. Trahair and Pi (1997) found this method to be conservative in several experimental and analytical examples, as it neglects Wagner stresses. Additional examples of their method are found in Trahair (1999).

#### 2.1.1.4 Strength Design for Torsion

Trahair and Pi (1997) developed a model for strength design of torsional members based on the class of the section in flexure. Cross-sections were classified according to AS4100-1998 (SAA, 1998) as compact, non-compact, or slender according to the width-to-thickness ratios of the plates that comprise the section. Compact sections are able to develop the smaller value of the plastic moment and 1.5 times the yield moment before local buckling occurs when laterally braced (SAA, 1998). Non-compact sections are able to develop at least the yield moment prior to local buckling when laterally braced (SAA, 1998). Slender sections are unable to develop the yield moment before local buckling (SAA, 1998). Classification of sections in torsion according to the flexural rules was justified as follows (Pi and Trahair, 1994b):

- Classification of sections in torsion must be made in a similar way to account for the reduction in the section capacity due to local buckling;
- There are similarities between the warping normal stress and flexural normal stress distributions;
- The warping shear stresses that develop are relatively small;
- St. Venant shear stresses vary across the thickness of any thin-walled member such that they have no effect on local buckling.

Compact members that meet the requirements for plastic design in Clause 4.5.2 of AS4100-1998 are designed by the plastic design method

using Equation [2.13] and a resistance factor,  $\phi$ , equal to 0.9, where the following must hold true:

$$1 \leq \phi \lambda_{p,t} \quad [2.14]$$

Clause 4.5.2 (SAA, 1998) is similar to Clause 8.6 in CSA S16-01 (CSA, 2001) and states that plastic design may only be used for doubly-symmetric wide flange sections that are compact, hot-rolled, not subject to fatigue or impact loading, as well as having material properties with strain hardening, a yield plateau that extends more than six times the yield strain, meets minimum ductility requirement, and a tensile strength at least 1.2 times the yield strength.

Trahair and Pi (1997) suggest that compact beams that do not meet all of the requirements of Clause 4.5.2 of AS4100-1998 should be designed using the first hinge method, that is, neglecting the strength developed after the formation of the first plastic hinge. This implies that the capacity of the member is limited to the load present when the cross-section becomes fully plastic at a single location. The maximum design loads, the uniform torque,  $T_u^*$ , and bi-moment,  $B^*$ , are found by performing a linear elastic analysis under the ultimate loads. These loads are then compared with the plastic capacities as follows:

$$T_u^* \leq \phi T_{up} \quad [2.15]$$

$$B^* \leq \phi B_p \quad [2.16]$$

For members that just meet the non-compact limit, failure is assumed to occur when the yield stress is first developed at a single location in the member. Using a linear elastic analysis under the ultimate loads, the maximum design uniform torques and bi-moments are checked using the following:

$$T_u^* \leq \phi T_{uy} \quad [2.17]$$

$$B^* \leq \phi B_y \quad [2.18]$$

where  $T_{uy}$  is the first-yield uniform torque found using the membrane analogy and  $B_y$  is the yield bi-moment found by:

$$T_{uy} = \left( \frac{F_y}{\sqrt{3}} \right) \left( \frac{J}{t} \right) \quad [2.19]$$

$$B_y = \frac{1}{6} F_y b^2 t (d - t) \quad [2.20]$$

The following interaction equation must be satisfied at locations where uniform torque and bi-moment are combined:

$$\left( \frac{T_u^*}{T_{uy}} \right)^2 + \left( \frac{B^*}{B_y} \right)^2 \leq \phi^2 \quad [2.21]$$

For non-compact sections between the limit for compact and non-compact members, a linear interpolation is performed between the first yield and first plastic hinge design methods. For slender sections, Trahair and Pi (1997) recommended a local buckling method to reduce the capacity below that of the first yield design method to account for elastic and inelastic post-buckling effects. Slender sections are not considered explicitly in this project.

### 2.1.2 Flexural Behaviour

Flexural theory for steel members is well established and only the basics required to calculate the elastic stresses and plastic moment are presented here. Shear stresses on a cross-section caused by flexural loads,  $\tau_b$ , are obtained from:

$$\tau_b = \frac{VQ}{It_c} \quad [2.22]$$

where  $V$  is the total internal shear force at that section,  $Q$  is the first moment of area of the portion of the cross-section beyond the point of interest (i.e., where the shear stress is being calculated),  $I$  is the moment

of inertia of the entire cross-section, and  $t_c$  is the thickness of the material at the point of interest. For a wide flange section, the maximum shear stress is at the centroid of the cross-section and the stress decreases in a parabolic shape towards the flanges, as shown in Figure 2.1(a).

The elastic normal flexural stresses,  $\sigma_b$ , at the flange tips are obtained from:

$$\sigma_b = \frac{M}{S} \quad [2.23]$$

where  $S$  is the elastic section modulus. The elastic normal stress distribution is depicted in Figure 2.1(b). The elastic normal flexural stresses reach the yield value when the yield moment,  $M_y$ , is developed. For moments greater than the yield moment, the cross-section begins to yield and the stress distribution becomes non-linear at the flanges and expands towards the centroidal axis. When the moment reaches the plastic moment,  $M_p$ , the entire cross-section has effectively yielded. The plastic moment can be obtained from:

$$M_p = F_y Z \quad [2.24]$$

where  $Z$  is the plastic section modulus. According to CSA S16-01, Class 1 and 2 sections can develop the plastic moment before local buckling occurs. Class 3 sections can develop the yield moment before local buckling occurs.

### 2.1.3 Combined Flexural and Torsional Behaviour

Trahair and Pi (1997) classified torsional actions as either primary or secondary. Primary torsion develops when the torsional action is needed to transmit a load. Primary torque can be destabilizing, free, or restrained. A destabilizing torque results when the member applying the torque is not able to restrain the member carrying the torsion from deflecting laterally or twisting. Trahair and Pi (1997) indicated that this action might result in

amplified torsion and out-of-plane bending due to the tendency to buckle laterally. If the member applying the torsional load does not restrain twisting but prevents lateral displacement of the loaded member, the primary torque is considered free torsion. If both the lateral deflection and twist are restrained at the loading point, the torsion is considered to be restrained. Secondary torsion develops when twist rotations are imposed on a member at connection locations for compatibility. Trahair and Pi (1997) compared this secondary torsion to the secondary bending moments that develop in rigidly connected trusses that are often ignored in practice. Similarly, these secondary torques can be ignored if an alternate load path of high stiffness is available.

Using the principle of superposition, the elastic stresses obtained for bending and torsion can be added. Figure 2.1 illustrates the stresses that develop in a wide flange shape as a result of combined flexure and torsion. In general, shear stresses are not considered in the design of such members (Kulak and Grondin, 2005) because the maximum values do not occur at the same location in the cross-section, and often not at the same location along the span length, as the normal stresses resulting from flexure or warping. The importance of the shear stresses depends on the nature of the loads and the cross-section used. In most applications, shear stresses are not found to be critical. If required, shear and normal stresses can be combined using standard stress transformation methods. These combined stresses can be used to assess the yielding condition using an appropriate failure criterion such as the von Mises or Tresca criteria. Typically, a combination of shear and normal stresses does not result in critical stress conditions and designers should only be concerned with the combined normal stresses.

## 2.2 Design Models and Standards

### 2.2.1 Elastic Design Models

In working stress design, elastic analyses are required to analyze laterally unsupported beams under both torsional and flexural loads (Chu and Johnson, 1974). The previous work of Heins and Seaburg (1963) does not consider the effects of interaction between torsion and flexure. Neglecting such interaction was found to be safe only for small moments (Chu and Johnson, 1974). As the moments become large, torsional buckling can occur even if no torsional loads are present. Near the lateral torsional buckling load, the torsional deformations were found to become large. Chu and Johnson (1974) developed a set of curves accounting for these effects that could be used to design wide flange shapes. The authors studied four cases: simply supported and cantilever beams subjected to eccentrically applied concentrated or uniformly distributed loads.

The following equations of equilibrium of a beam were presented by Chu and Johnson (1974):

$$EI_z v'' = M_z \quad [2.25]$$

$$-EI_y w'' - M_y \phi = M_z \quad [2.26]$$

$$EC_w \phi^{iv} - GJ\phi = -M_z w'' = m_x \quad [2.27]$$

where  $I_z$  is the strong axis moment of inertia of the cross-section;  $v''$  is the second derivative of the deflection in the Y-direction (parallel to the web),  $v$ ;  $M_z$  is the moment about the Z-axis (the strong axis);  $I_y$  is the weak axis moment of inertia of the cross-section;  $w''$  is the second derivative of the deflection in the Z-direction,  $w$ , with respect to  $x$ , the distance along the length of the beam;  $M_y$  is the moment about the Y-axis (the weak axis);  $\phi^{iv}$  is the fourth derivative of the angle of twist; and  $m_x$  is a

distributed torsional moment. Substituting Equations [2.25] and [2.26] into [2.27] yields:

$$EC_w\phi^{iv} - GJ\phi'' - \left(\frac{M_z^2}{EI_y}\right)\phi = m_x \quad [2.28]$$

which can be solved if four boundary conditions for the angle of twist are known. The following equation replaces Equation [2.27] when a concentrated torsional moment or moment about the X-axis,  $M_x$ , is applied instead of a distributed torsional moment:

$$EC_w\phi''' - GJ\phi' - M_z w' - V_y w = M_x \quad [2.29]$$

where  $w'$  is the first derivative of the deflection in the Z-direction and  $V_y$  is the shear in the Y-direction or the strong axis shear for this coordinate system.

Chu and Johnson (1974) simplified Equations [2.28] and [2.29] using several non-dimensional factors that include  $\gamma$ , which accounts for the interaction between flexure and torsion, and is defined as:

$$\gamma = \left(\frac{M_{z,MAX}}{GJ}\right) \sqrt{\frac{C_w}{I_y}} \quad [2.30]$$

where  $M_{z,MAX}$  is the maximum strong axis bending moment. They defined  $\gamma_{cr}$  as the critical value of  $\gamma$  when torsional buckling occurs. Their differential equations can be reduced to produce results identical to those of Heins and Seaburg (1963) for torsion alone when  $\gamma$  is set equal to zero.

Chu and Johnson (1974) presented the solution to Equation [2.29] in charts for different values of  $\gamma$  developed from the results of finite element analyses. It was found that as the value of  $\gamma$  increases, the magnitudes of the angle of twist and its derivatives also increase when all other parameters are held constant for a cantilever beam. Beams loaded with

large eccentricities are unable to carry large flexural stresses. Accounting for these interaction effects increases the twist rotations and torsional stresses by 50% for simple supports and by as much as 80% for cantilevers near the allowable stress limits. This difference can become as large as 125% when an allowable stress greater than  $0.5 F_y$  is used and approaches infinity as the allowable stress approaches the yield stress.

Pastor and DeWolf (1979) also investigated this interaction between torsional and flexural loads, making an analogy to flexure and axial compression in beam-columns. Two interaction effects were identified. The first is comparable to the  $P-\delta$  effects in beam-columns; the effective eccentricity of the load is increased as the beam deflects both laterally and torsionally under increasing loads. The second effect is minor axis bending that develops as the member rotates and a component of the applied force acts in the direction of the member's minor axis as per Equation [2.26]. Pastor and DeWolf (1979) indicated that Chu and Johnson (1974) do not include all of the normal stresses that develop as a result of this second type of interaction.

Pastor and DeWolf (1979) developed a set of differential equations and solved them for three I-sections that provide a good range of commonly designed members. They found that interaction between torsion and flexure is small until the bending moment becomes large. They also found the shear stresses to be insignificant under design loads. These authors stated that accounting for these interaction effects in determining the angle of twist is too complicated for design purposes. Since the interaction affected the normal stresses by only a small amount, they suggested that the angle of twist can be found, without significant error, by neglecting the interaction of the two types of loads. To account for these effects approximately, Pastor and DeWolf (1979) suggested using an allowable stress of  $0.57 F_y$  instead of the previously used value of  $0.6 F_y$  (AISC,

1969) when checking combined torsion and flexure. The proposed allowable stress design equation is therefore:

$$\sigma_{b,s} + \sigma_{b,w} + \sigma_w \leq 0.57F_y \quad [2.31]$$

where  $\sigma_{b,s}$  is the normal stress that develops as a result of the strong axis bending and  $\sigma_{b,w}$  is the normal stress that develops as a result of the weak axis bending. They also recommended that the strong axis bending stress be compared against the allowable value for lateral torsional buckling.

Using the elastic analyses proposed by Heins and Seaburg (1963), Johnston (1982) provides several design examples for wide flange shapes. Unlike previous researchers, Johnston accounts for the effects of structural details that are often not considered, such as the torsional restraint provided by attached members. Approaches to address the following situations are presented:

- A beam loaded at mid-span by a column where the column is pinned at the top, but has a full moment connection at the bottom where it connects to the beam;
- A beam loaded with an eccentric masonry wall on the top flange; and
- A beam with other beams framing into it, introducing both vertical and torsional loads while providing torsional restraint to the beam.

Lin (1977) proposed the use of the flexural analogy, which simplifies the torsion problem by transforming it into a biaxial flexural problem, as seen in Figure 2.2. Since the method does not require the angle or twist or its derivatives, it simplifies the calculations of the stresses due to bending and torsion. The applied torsional moment is converted into an equivalent lateral flexural load in the flanges by dividing the applied torsion by the distance between the flange centroids. The flanges are then analyzed separately as if in pure flexure to determine the “warping” stresses that

develop. These flange stresses are then added to the strong or weak axis bending stresses to find the maximum normal stress in the cross-section. Since this method assumes the torsion is carried purely in warping and neglects the St. Venant torsional resistance, this method is generally conservative (Kulak and Grondin, 2006). To correct for this conservatism, Lin (1977) proposed a modification factor  $\beta$  applied to the equivalent warping stresses that reduces the torsion that is carried in warping because of the torsional resistance of the member. The value of  $\beta$  depends upon the support and loading conditions, in addition to the member length and the ratio of pure torsional stiffness to warping torsional stiffness calculated by:

$$\lambda = \sqrt{\frac{GJ}{EC_w}} \quad [2.32]$$

Walker (1975) presented an approximate approach similar to the flexural analogy based on the principle of superposition, which neglects the interaction between torsion and flexure. Walker used a series of diagrams of bi-moments along with rotational correction factors to take into consideration the discrepancy between the exact and approximate solutions. Johnston *et al.* (1980) proposed another design procedure that uses simple formulae for the calculation of the normal stresses only. This solution reverts to the flexural analogy approach for short beams but has some correction factors for intermediate to long beams.

### 2.2.2 Inelastic Design Models

Hodge (1959) presented a circular interaction equation for combined flexure and torsion, one of the first inelastic models. Boulton (1962) presented a method of determining the fully plastic torsional and flexural resistance including the effects of warping restraint similar to Hodge (1959). This method is likely too complex for common design problems. Dinno and Merchant (1965) proposed the use of a similar circular

interaction diagram as a lower bound method to calculate the plastic capacity of an I-shaped section at factored applied torsional and flexural loads,  $T^*$  and  $M^*$ , respectively:

$$\left(\frac{T^*}{T_o}\right)^2 + \left(\frac{M^*}{M_o}\right)^2 = 1 \quad [2.33]$$

where  $M_o$  is the plastic collapse moment and  $T_o$  is the plastic collapse torque. This method accounts for warping using the expression proposed by Boulton (1962). For a cantilever beam, the warping torsional resistance is obtained by dividing the plastic bi-moment, as defined in Equation [2.12], by the length of the beam,  $L$ . The pure torsional component of the resistance,  $T_{sv}$ , is calculated using the sand heap analogy. If there is no warping restraint,  $T_w$  is taken as zero. Dinno and Merchants (1965) test results all lie outside of the proposed interaction diagram, indicating that the method is conservative for the members tested. The experiments used to validate the method were of small-scale and were limited to very stocky beams, which therefore neglects the effect of slenderness and potential lateral torsional buckling. Augusti (1966) has proven the method of Dinno and Merchant (1965) to give an upper bound solution, with the yield stress as the limiting criterion.

Driver and Kennedy (1987) reported on the the work of Kollbrunner *et al.* (1978) and Kollbrunner *et al.* (1979). Kollbrunner *et al.* developed the following interaction equation based on their work on cantilever beams under combined torsional and flexural loads:

$$\frac{(M^* - M_{pw})^2}{M_{pf}^2} + \left(\frac{B^*}{B_p}\right) = 1 \quad [2.34]$$

where,  $M_{pw}$  and  $M_{pf}$  are the plastic moments of the web and flange alone, respectively, about the primary axis of bending. This equation uses bi-moments to describe the torsion and is used to predict the point when

the section is fully plastic. Kollbrunner *et al.* (1978) found a limiting load by assuming that the moment to bi-moment ratio,  $M/B$ , remains constant throughout the loading beyond the elastic region and into the inelastic region, requiring the solution of a cubic and a quadratic equation to obtain the solution. The capacities predicted by Equation [2.34] showed good agreement with the experimental results of Kollbrunner *et al.* (1978, 1979). They indicated that the section is unable to become fully plastic for large load eccentricities because of the large strains that must develop at the flange tips. The limiting load was therefore modified to be consistent with an expected ultimate load that results from a maximum allowable strain in the elasto-plastic region (Driver and Kennedy, 1987).

Razzaq and Galambos (1979) investigated the behaviour of I-sections under combined biaxial bending, with and without torsion. This investigation involved a theoretical derivation of differential equations and solution techniques, as well as the testing of 24 beams to failure, eight for each of three load cases as follows:

- Equal end moments about a non-principal axis;
- Concentrated torque applied first, followed by a moment about a non-principal axis created by an eccentric vertical load at mid-span, and then apply equal end moments about the same non-principal axis; and
- Equal end moments about a non-principal axis, followed by a concentrated torque and moment about the same non-principal axis created by an eccentric vertical load at mid-span.

For each load case, the ratio of strong-to-weak axis bending was varied over the eight specimens by rotating the beam's cross-section from the vertical in the test set-up. A complex set of boundary conditions was used where the ends of the beam were fixed torsionally and pinned flexurally about the axis of bending, and lateral movement was prevented. Rotational springs were applied flexurally perpendicular to the axis of

bending. The stiffness of these springs was determined after the test by calibrating the analytical model to match the test results using an iterative procedure. These boundary conditions proved to be difficult to apply when analyzing the beam as the authors encountered a problem in determining the beam end moments in the out-of-plane direction.

Razzaq and Galambos (1979) developed differential equations for each loading case that include both elastic and inelastic behaviour. Despite the fact that these solutions are limited only to the loading cases presented, they are in good agreement with the test results. Due to their complexity, however, they are not useful for typical design purposes. The authors made these important conclusions:

- Torque dramatically reduces the moment carrying capacity of biaxially loaded beams;
- As the slenderness of a biaxially loaded beam increases, its torsional capacity is reduced;
- The strong axis moment capacity is very sensitive to weak axis moments;
- Warping strains are important in wide flange beams;
- Residual stresses do not have a significant impact on beam capacities;
- Failure of these beams can occur by local instabilities as well as overall member instabilities that usually occur at strain levels below the onset of strain hardening.

Driver and Kennedy (1987, 1989) proposed a simple limit states design procedure based on a set of four experimental tests on cantilever beams in addition to other experimental data in the literature. Fixed-ended cantilever W150x18 sections were tested under combined torsional and flexural loading applied by means of an eccentric vertical load applied at the tip of the cantilever. Four specimens were tested, loaded with eccentricities of 0, 30, 100, and 220 mm, corresponding to Beams 1, 2, 3,

and 4, respectively. Bracing was provided at the supporting column to provide, as closely as possible, full fixity. The small deformations at this “fixed” end were measured and used in the analysis that followed to remove any rigid body motions of the beam caused by deflection of the supporting column. A loading bracket was attached to the free end of the beam to transfer the eccentrically applied load to the web of the beam, thereby permitting free warping of the flanges. Refer to Driver and Kennedy (1987) for a detailed description of the loading bracket. A steel cable connected to the loading clevis of the testing machine was used to apply a tensile (upward) load to the beam. Figure 2.3 presents a diagram of the test set-up.

Driver and Kennedy’s (1987, 1989) proposed method for designing for the effects of combined torsional and flexural loads addresses both serviceability and ultimate limit states. Two serviceability limit states must be satisfied: (1) a limit is set on the deflection and rotation of the member; and (2) the maximum normal stress in the member is limited to the yield stress. Both of these checks are performed under service loads, implying an elastic analysis, and are described in Clause 14.10 of CSA S16-01. There is, however, little guidance in CSA S16-01 for limiting the rotation of a member.

To check the ultimate strength at factored loads, Driver and Kennedy (1987, 1989) recommend a moment–torque interaction diagram of the form shown in Figure 2.4. Any combination of moment and torque that falls below the interaction curve is considered safe. Point 1 on the diagram is the point where there is no torque and the beam can carry its full moment resistance,  $M_r$ , for the class of section, including the effects of lateral torsional buckling. They suggested that there is minimal interaction between the St. Venant torque and the bending moment since the St. Venant torque produces only shear stress. This means that even at the full moment resistance, the cross-section can still carry a torque less

than or equal to the St. Venant torsional resistance, as described by Point 2. The following equations are used to express the nominal pure torsional resistance for Class 1, 2, and 3 (a generally conservative and more expedient approximation for Class 3) sections:

$$\text{Class 1: } T_{sv} = \frac{1}{6} \left[ 4t^3 + 6(b-t)t^2 + 3(d-t)w^2 + w^3 \right] \left( \frac{F_u}{\sqrt{3}} \right) \quad [2.35]$$

$$\text{Class 2: } T_{sv} = \frac{1}{6} \left[ 4t^3 + 6(b-t)t^2 + 3(d-t)w^2 + w^3 \right] \left( \frac{F_y}{\sqrt{3}} \right) \quad [2.36]$$

$$\text{Class 3: } T_{sv} = \left( \frac{F_y}{\sqrt{3}} \right) \left( \frac{J}{t} \right) \quad [2.37]$$

where  $w$  is the web thickness. The maximum pure torsional resistance for Class 1 and 2 sections is based on the sand heap analogy, whereas Class 3 sections use the membrane analogy. Driver and Kennedy (1987, 1989) suggested that Class 1 sections can develop a stress up to the ultimate stress,  $F_u$ , whereas Class 2 and 3 sections are based on the yield strength,  $F_y$ .

Point 4 on the interaction diagram is developed for the case where the member is subjected to torsion only loading. The total torsional resistance consists of the sum of the St. Venant and warping torsional resistances. Driver and Kennedy (1989) proposed the following equations to determine the nominal warping torsional resistance,  $T_w$ , for Class 1, 2, and 3 sections:

$$\text{Class 1: } T_w = \frac{Kb^2t(d-t)F_u}{L} \quad [2.38]$$

$$\text{Class 2: } T_w = \frac{Kb^2t(d-t)F_y}{L} \quad [2.39]$$

$$\text{Class 3: } T_w = \frac{K^*b^2t(d-t)F_y}{L} \quad [2.40]$$

where  $K$  and  $K^*$  are factors that depend on the torsional end support and the loading conditions. Driver and Kennedy (1989) present some values for common combinations of load and boundary conditions. Point 3 was established based on the assumption that the web does not contribute to the warping torque. Therefore, even at the full torsional resistance, the member is still able to carry a bending moment equal to the moment resistance of the web alone,  $M_w$ , given as follows nominally for Class 1, 2 and 3 sections:

$$\text{Class 1: } M_w = \frac{1}{4} F_y w h^2 \quad [2.41]$$

$$\text{Class 2: } M_w = \frac{1}{4} F_y w h^2 \quad [2.42]$$

$$\text{Class 3: } M_w = \frac{1}{6} F_y w h^2 \quad [2.43]$$

where  $h$  is the web height found by  $d - 2t$ . Points 2 and 3 on the interaction diagram are connected with either a straight line or a parabolic equation as follows (Driver and Kennedy, 1989):

$$T_w = -M_{bf}^2 \left[ \frac{K F_u}{t(d-t) L F_y^2} \right] + \frac{K b^2 t (d-t) F_u}{L} \quad [2.44]$$

where  $M_{bf}$  is the portion of the moment carried by the flanges.

Pi and Trahair (1994a) conducted an investigation into the combined action of flexure and torsion on simply supported (both torsionally and flexurally) beams using a finite element approach. Their formulation accounted for large deformations, residual stresses, geometric imperfections, and material inelasticity. They analyzed continuously braced beams (has only displacements in-plane and rotations), centrally braced beams (no lateral displacement at mid-span), and beams unbraced against lateral torsional buckling.

For continuously braced beams, they found that if the eccentricity is small, flexure is dominant and the ultimate load can be determined from the bending moment vs. deflection and torque vs. rotation curves. If the eccentricity is large, torsion is dominant and the ultimate load can be found from the torque vs. rotation curve alone. Pi and Trahair (1994a) observed that, for cases with larger load eccentricity, the torque could reach values larger than the Dinno and Merchant (1965) upper bound results because of the Wagner effect at large torsional rotations. If the beam is braced only at mid-span, its capacity decreases slightly but its general behaviour is the same as for continuously braced members. For unbraced members, the capacity decreases significantly as lateral buckling becomes an issue. Pi and Trahair (1994a) concluded that non-linear geometry and material properties are important in the prediction of the capacity of beams under combined bending and torsion. The interaction of bending and torsion has the effect of developing secondary minor axis bending as per Equation [2.26]. Amplified angles of twist develop as a result of the loss of torsional stiffness due to yielding and the increased possibility of torsional buckling.

Looking at the interaction between flexure and torsion for continuously braced members, Pi and Trahair (1994a) found that the interaction is far more critical for slender beams. Pi and Trahair (1994a) measured slenderness using  $\lambda_L$  calculated by:

$$\lambda_L = \sqrt{\frac{M_p}{M_u}} \quad [2.45]$$

where  $M_u$  is the elastic lateral torsional buckling moment for the specific bracing case. Comparing their results with the interaction equation developed by Hodge (1959) (Equation [2.33]), they found Equation [2.33] to be safe for stocky elements but inadequate for beams with a slenderness  $\lambda_L$  greater than 1.41. This decrease in strength results from

a lower torsional stiffness that leads to significant secondary minor axis bending. The same observations were made for beams braced at mid-span, although their capacity was found to be slightly lower than continuously braced members. For unbraced members, Pi and Trahair (1994a) found that the lower bound was unsatisfactory for any of the beams investigated in their analysis. The calculated capacities were found to be much lower than the lower bound equation proposed by Hodge.

Using their finite element analysis results, Pi and Trahair (1994a) proposed the following interaction equation:

$$\left(\frac{M^*}{M_r}\right)^{\gamma_x} + \left(\frac{T^*}{T_r}\right)^{\gamma_z} = 1 \quad [2.46]$$

where  $\gamma_x$  and  $\gamma_z$  are the exponents on the moment and torque terms, respectively. The value of  $\gamma_x$  is 2 for continuously braced beams and 1 for centrally braced and unbraced beams. The value of  $\gamma_z$  is taken as 1 for all bracing conditions. Figure 2.5 illustrates how this proposed interaction equation provides a good lower bound for the finite element results of Trahair and Pi (1994a).

Pi and Trahair (1994a) concluded that the circular interaction equation suggested by Hodge (1959) and Dinno and Merchant (1965) is not acceptable for design purposes. It overestimates the strength of members when secondary minor axis bending and lateral torsional buckling effects become important. For slender beams subject to destabilizing torsion, these effects are significant. At high rotations, interaction develops between lateral torsional buckling and torsion due to the Wagner effect. This interaction is favourable and increases the strength of the member. In practice however, serviceability limit states are likely to govern the design of these slender members.

Pi and Trahair (1994b) and Trahair and Pi (1997) present a more formal model that works with the Australian Steel Design Standard AS4100-1998 based on the above work. The class of the section is determined based on flexure alone as presented for torsional strength design in Section 2.1.1.4. Depending on the class of the section, a plastic or elastic analysis is performed on the member according to the rules provided in Section 2.1.1.4 for torsion alone by Pi and Trahair (1994a, 1994b; Trahair and Pi, 1997). If a plastic analysis is performed, the plastic section capacities are found:  $M_p$ ,  $T_{up}$ , and  $B_p$ . The plastic collapse load factors for flexure and torsion respectively,  $\lambda_{p,b}$  and  $\lambda_{p,t}$ , are then found and checked using the following circular interaction equation:

$$\frac{1}{\lambda_{p,b}^2} + \frac{1}{\lambda_{p,t}^2} \leq \phi^2 \quad [2.47]$$

For cases of elastic analysis, distributions of factored in-plane moment  $M^*$  as well as distributions of torque  $T_u^*$  and bi-moment  $B^*$  are found.  $T_r$  is found as presented in Section 2.1.1.4. The maximum applied moments and torques are then checked using the interaction Equation [2.46] where the values of  $\gamma_x$  and  $\gamma_z$  are taken as 1.0 for all bracing conditions.

### 2.2.3 Current Design Standards

In limit states design, both serviceability and ultimate limit states must be considered. Elastic analysis and design methods used in the allowable stress design context are no longer sufficient for the design of members subject to combined torsion and flexure. There is a general consensus that existing design standards provide little guidance for the design of members subject to these types of loads. Trahair and Pi (1997) provided a few possible reasons for this apparent neglect, including the belief that torsion is seldom developed in members and even if it does occur, it has a negligible effect on the member capacity. This is being challenged, as

recent analyses are bringing attention to the effect of torsion on the flexural capacity of beams.

In Canada, the current steel design standard CSA S16-01 provides some guidance in Clause 14.10 for the design of members under combined flexure and torsion. However, it does not provide any detailed design method. Rather, it presents very general requirements but lacks direction as to how to apply them. Clause 14.10.1 states:

Beams and girders subjected to torsion shall have sufficient strength and rigidity to resist the torsional moment and forces in addition to other moments or forces. The connections and bracing of such members shall be adequate to transfer the reactions to the supports.

There is no direct guidance as to how this clause is to be accomplished.

Clause 14.10.2 states:

The factored resistance of I-shaped members subject to combined flexure and torsion may be determined from moment-torque interaction diagrams that take into account the normal stress distribution due to flexure and warping torsion and the St. Venant torsion. Assumed normal stress distributions shall be consistent with the class of section.

This clause is a little more helpful in that it describes a method to determine the ultimate resistance of a member. It still lacks specific direction in establishing an appropriate moment–torque interaction diagram, although references to the relevant torsion literature are provided in the commentary. As shown previously, some interaction diagrams are inappropriate in certain situations as they do not provide a safe design.

Clause 14.10.3 states:

Members subject to torsional deformations required to maintain compatibility of the structure need not be designed to resist the associated torsional moments, provided that the structure satisfies the requirements of equilibrium.

This clause allows a designer to neglect the torsional moments that develop as a result of torsional deformations imposed by adjacent

members as long as they are required only to maintain compatibility.

Clause 14.10.4 states:

For all members subject to loads causing torsion, the torsional deformations under specified loads shall be limited in accordance with the requirements of Clause 6.2.1. For members subject to torsion or to combined flexure and torsion, the maximum combined normal stress, as determined by an elastic analysis, arising from warping torsion and bending due to the specified loads shall not exceed  $F_y$ .

Clause 6.2.1 pertains to meeting acceptable deflection limits, but none are provided explicitly for torsion. Kulak and Grondin (2006) refer to these requirements and refer to the interaction diagram proposed by Driver and Kennedy (1989). It has, however, limited experimental or analytical verification. Driver and Kennedy (1989) tested four beams experimentally and then used the experimental data from other authors to help verify their relationship, all of which satisfied their proposed moment–torque interaction diagram. Further verification of this method is highly desirable.

### **2.3 Unpublished Experimental Research**

Comeau (1998) performed an experimental investigation into the behaviour of mono-symmetric rolled crane runway beams, each made up of a wide flange section topped by a rolled channel with the flanges pointing downward. These beams were exposed to combined bending and torsion considered typical of crane loads. The main variable investigated was the effect of a discontinuous weld between the two elements of the built-up section on the beam behaviour. Two beams with simply supported boundary conditions were put through several tests, including combined torsional and flexural loading. The beams were composed of a C310x31 channel welded to the top flange of a W460x74 section made of 350W steel. The channel provides additional lateral support and strength to the compression flange, which otherwise would be vulnerable to lateral torsional buckling due to large spans that are typical

of crane beams because of difficulties in providing lateral supports. Beam P1 had a continuous 6 mm fillet weld connecting the channel to the top flange of the wide flange section at both flange tips, and Beam P2 had 40 mm long intermittent 8 mm fillet welds spaced at 300 mm (centre-to-centre). Tests were performed to determine the residual stresses and material properties of both beams individually.

Four tests were performed on each of these two beams. Several tests remained elastic so that no permanent strains developed in the beam to allow them to be reused in other tests. These elastic tests were performed first on 12.7 m long beams. Then, the two beams were each cut into two approximately 6 m long beams, creating two of each weld type and these tested into the inelastic range of behaviour to their ultimate capacity.

Test 1 was an elastic uniform torsion test to calculate the torsion constant. Test 2 was an elastic test of non-uniform torsion that allowed for the determination of the warping coefficient. Test 3 was conducted to determine the elastic buckling load in pure flexure and the ultimate moment resistance of the cross-section. Test 4 loaded the beam in combined biaxial bending and torsion. Separate elastic and inelastic experiments were performed as part of Test 4. The elastic tests were used to determine the service longitudinal stresses and the elastic buckling load. The inelastic tests were used to determine the ultimate resistance under combined loading.

Comeau (1998) used the results of the experiments to compare to the theoretical values of the above mentioned variables. The author found good strong agreement between the experimental and theoretical values of the torsion constant for Beam P1 (-5.9%) but the values for Beam P2 (17.5%) were not as good. The differences between the experimental and theoretical values of the warping coefficient were very poor with average percent errors greater than 80% for both beams. The experimental results

agreed well with the theoretical ultimate pure bending moment capacities (average percent error of 3.4 for both beams). Looking at the results of Test 4, the average percent error for both beams for both the yield and ultimate loads is -13.6% indicating that the theory over-estimates the capacity of the beams. Overall, the experimental results of Comeau (1998) had poor agreement with the theoretical results providing indication that more research is required for these types of built-up members under combined torsion and flexure.

#### **2.4 Finite Element Models for Combined Torsional and Flexural Loading**

Bathe and Wiener (1983) investigated several models used to predict the combined flexural and torsional behaviour of fixed end cantilever I-shaped beams including warping. These beams had two load cases applied: a transverse load at the free end causing a bending moment about the strong axis and a torsional moment at the free end. Their work included linear and non-linear material effects on a very small and stocky beam with  $b$ ,  $t$ ,  $d$ , and  $w$  of 25.4 mm, 2.54 mm, 25.4 mm, and 2.54 mm respectively. The beam was 254 mm long. The authors used two different types of elements:

- 9-node iso-parametric shell elements
- Hermitian 2 and 4-node iso-parametric beam elements of rectangular cross-section

For linear elastic behaviour, the more detailed shell element model predicted the normal and shear stresses from the torsion load case best because the warping restraint at the fixed end can be modeled (Bathe and Wiener, 1983). For non-linear inelastic behaviour, the shell model was found to predict an ultimate torsional load 10% larger than the beam models, although both results lied between the sand-heap analogy and Merchant's upper bound. The authors concluded that the shell elements

predict the stress distributions more accurately based on comparisons with theoretical capacities and differences between the results of the models.

Kanok-Nukulchai and Sivakumar (1988) used the direct degeneration concept for finite element idealizations of thin-walled structural members under combined torsion and flexure. Two different types of elements were considered, both assuming that no cross-sectional distortion occurs:

- 10-node brick elements: Although this element requires high computational effort, the lateral motion in the plane of the cross-section is assumed to be rigid and there are three translational degrees of freedom (D.O.F.) and the rotation about the longitudinal axis per node.
- 6-node thin-walled elements: This element assumes that the variation of warping displacements across the wall thickness is linear. It has three translational and two rotational D.O.F per node.

In the degeneration process (the process of creating finite elements from 3D equations), the authors assumed that distortion of the cross-section was negligible, warping was allowed, the thickness of the elements was small such that straight normals remain straight after deformation, and the transverse normal stress across the wall is negligible. Investigating several different numerical examples the authors found that their simplified shell elements were very effective in modelling restrained warping. Some of these examples include: a cantilever I, C, or Z-shape under concentrated end torque; a cantilever I-shape under combined loading; and a simply supported I-shape under either concentrated or distributed torque.

El-Khenas and Nethercot (1989) derived a general set of equilibrium equations starting from the principle of virtual work for an arbitrary open section. These equations were used to develop the stiffness matrices for

the complete non-linear response. The following describes the model used:

- Transverse displacements are much larger than longitudinal displacements;
- Beam length is much larger than cross-sectional dimensions;
- No cross-sectional distortion;
- Shearing strain in middle surface and in planes normal to the individual plate elements are neglected;
- Yielding is governed by normal stresses;
- Warping stresses are neglected;
- A piecewise linear curve is used to approximate the true stress vs. true strain curve;
- Reasonable residual stress distribution is used; and
- Order of polynomial interpolation functions must be high enough to approximate true solution.

These equations were used in a finite element procedure the authors tested against experimental results and found good agreement with the out-of-plane displacements. In-plane deflections increased faster in the test than in the finite element model because of cross-sectional deformations. For non-linear behaviour, the model reduces the ultimate load by about 8% since yielding spreads more rapidly in the finite element model than in the test.

Bild *et al.* (1992) developed a finite element formulation that compared well with the finite element formulation of Hancock and Trahair (1978) for simply supported beams with an eccentric point load at mid-span. This model was also shown to be effective in modelling beams and beam-columns. The model accounted for non-linear material effects, yielding, instability, initial imperfections, residual stresses, large transverse displacements, but neglected large rotations, cross-sectional distortion, and shear strains at the mid-thickness surface of the beam. An

elastic-yielded strain-hardened diagram assuming tangent modulus unloading is used for the stress vs. strain curve.

Driver (2000) developed an analytical model using a mesh of 20-node, 3D brick elements with the non-linear finite element program ABAQUS. The goal of this project was to expand the applicability of the proposed design method by Driver and Kennedy (1987) using an analytical model that predicts their experimental results well. The fillets were modelled because Driver and Kennedy (1989) found that the St. Venant Torsional resistance is 16% greater including the additional thickness of the fillets compared to the resistance found when the cross-section is assumed to consist of rectangular elements only. The web had a single layer of elements, whereas the flanges each had two layers of elements. The mesh of elements became denser near the fixed end where the nodes were fully restrained in all six D.O.F due to the large strain gradients and material inelasticity in this region. The loading bracket was modelled explicitly. Non-linear geometric effects were included. The brick element used for the models was the C3D20R, 20-node 3-Dimensional quadratic brick element with reduced integration and large strain capability. Each node had three translational D.O.F. The material was modelled as initially isotropic using an elasto-plastic constitutive model including strain hardening and used the von Mises yield criterion. The different properties of the flange and web were modelled using measured stress versus strain curves, both idealized as elastic-plastic-strain-hardening with a bilinear curve in the strain-hardening range to the ultimate stress. Residual stresses were not measured in the test. Therefore, one model was developed with no residual stresses and two others used different residual stress distributions in the flanges while neglecting any residual stresses in the web, anticipating their effect to be negligible.

The finite element and experimental results were in good agreement with the moment vs. torque and torque vs. rotation diagrams. To provide

further verification, an investigation of the normal stresses over the section was performed. The normal stresses provided a means of assessing the interaction of flexural and warping behaviour. The expected pattern of stress reversal between flange tips was found in the model. As expected, the web appeared to develop only flexural stresses and was unaffected by the presence of torsion. As found by Driver and Kennedy (1987), very little of the cross-section remained elastic and stresses over a large portion of the cross-section were higher than yield and indeed approached the ultimate stress. The benefit of including residual stresses was determined to be marginal as it had little influence on the results. Overall, the model was effective at predicting the stress distribution in the cross-section.

Mohareb and Nowzartash (2003) presented a finite element derivation for non-uniform torsion of thin-walled open sections that accounted for both uniform and warping torsion. It was based on the assumptions that the material remains elastic, the beam carries only torsional loads, the cross-section is prismatic and neglects shear deformations along the middle surface of the cross-section, web distortions, and local buckling. The beam elements have two end nodes each having two D.O.F. and continuity by the angle of twist and its first derivative. The solution was derived using the principle of virtual work for a given torsional moment, end twisting moments, and end bi-moments.

Hermitian interpolation functions were reasonably accurate when the warping torsion is much larger than the pure torsion (short deep I-sections with thin walls) and a large number of elements are used. For slender beams, linear shape functions can be used accurately (long shallow I-sections with thick walls). Although complex, their solution was in excellent agreement with the closed-form solution, but yielded larger errors if the Hermitian functions were used.

## 2.5 Summary

The majority of the research performed in the area of combined torsion and flexure of steel I-sections has focused on the elastic behaviour and developing elastic design procedures. Many of these elastic design methods do not account for the interaction between torsion and flexure or are much too elaborate for use in general design. Other simpler approaches such as the flexural analogy require the use of a modification factor to prevent excessive conservatism. This modification factor is limited to tables that have been derived for specific boundary and loading conditions.

There is no method that provides a complete ultimate limit states design approach that has been sufficiently proven for use in a steel design standard. The researchers who have proposed inelastic design procedures have all found good agreement with their own test results, but few considered other sets of test results. The work of Hodge (1959) and Dinno and Merchant (1965) has been shown to be unsafe for large beam slenderness ratios. Kollbrunner *et al.* (1978, 1979) required the use of rather involved equations, while limiting strain rather than a stress. Razzaq and Galambos (1979) developed design equations and graphs for use for highly limited loading and boundary conditions. Although the majority of the work has been performed on I-shaped sections, recent work by Comeau (1998), sheds light onto the torsional behaviour of crane runway girders composed of a channel welded to the top flange of a rolled wide flange section.

The most promising models have been proposed by two groups of researchers: Driver and Kennedy (1987, 1989) and Pi and Trahair (1994a, 1994b; Trahair and Pi, 1997). These models appear to provide sound ultimate limit states design procedures. However, the amount of experimental or analytical verification of their models is quite limited.

Existing design standards provide little guidance in designing members under such combined loading. Before a model can be adopted by a steel design standard, further work must be done to validate the proposed design models.

Recent research has illustrated the ability of finite element models to predict accurately the behaviour of beams subject to combined torsion and flexure using various types of elements including beam, brick, and shell elements. Thus, there is potential to use finite element analysis to provide the validation required for these procedures without requiring extensive and expensive additional experimental research.

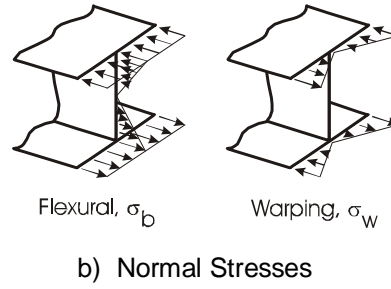
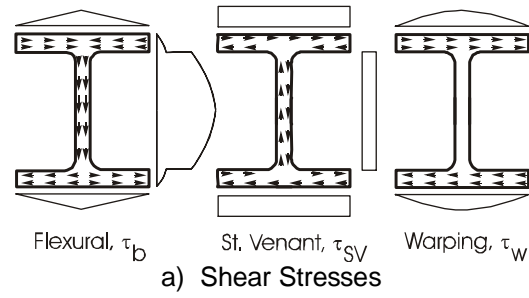
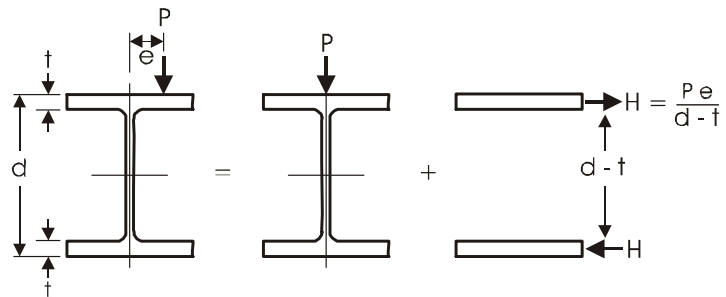


Figure 2.1 Combined Bending and Torsional Stresses in Wide Flange Sections



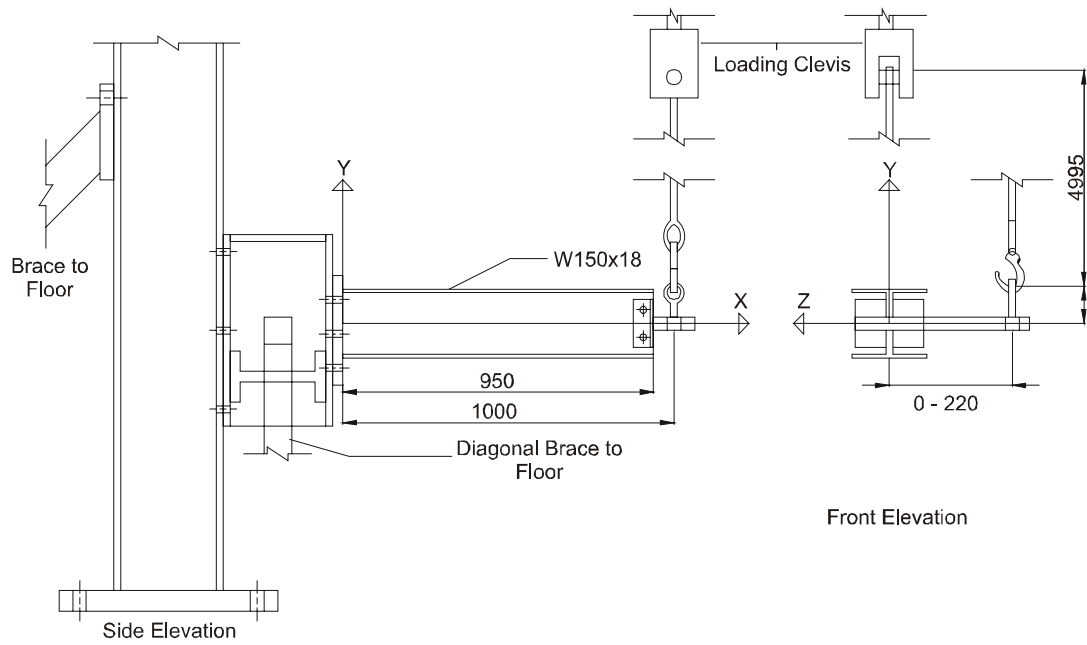


Figure 2.3 Test Set-up from Driver and Kennedy's (1987) Experimental Research

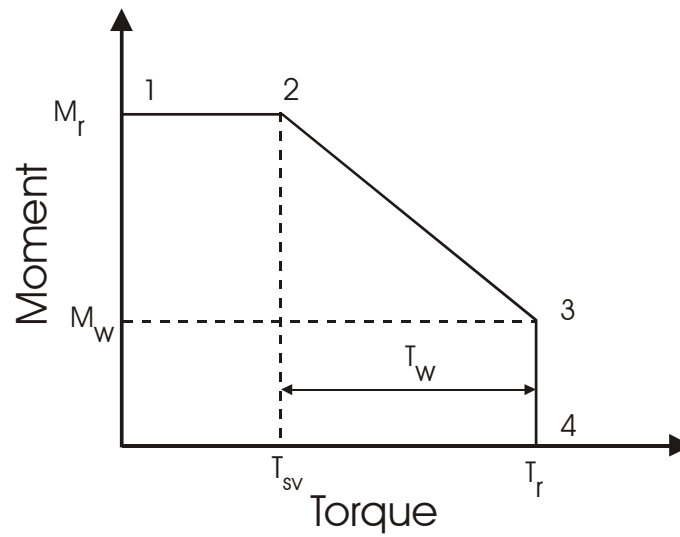


Figure 2.4 Simplified Moment vs. Torque Interaction Diagram (Driver and Kennedy 1987)

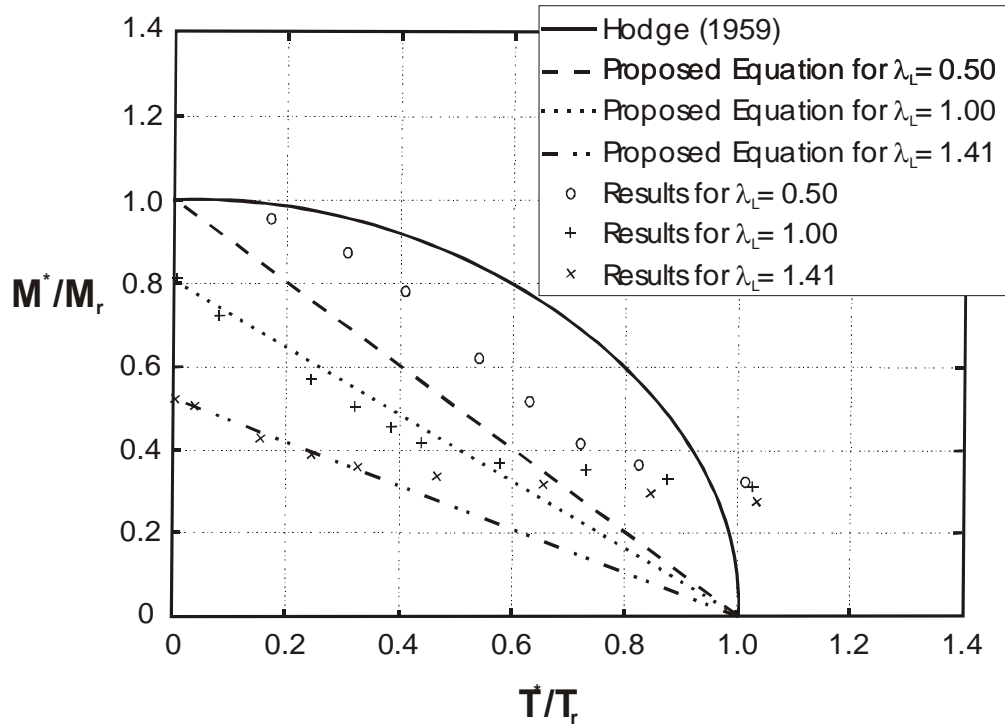


Figure 2.5 Moment vs. Torque Interaction Diagram for Unbraced Beams compared to Finite Element Results (after Trahair and Pi, 1994a)

### **3 FINITE ELEMENT MODEL DEVELOPMENT USING TESTS OF DRIVER AND KENNEDY (1987)**

#### **3.1 Introduction**

This project uses the non-linear general-purpose finite element program ABAQUS (Hibbitt *et al.*, 2002) for all numerical simulations. The finite element model presented in this chapter is constructed based primarily on the experimental research performed by Driver and Kennedy (1987) on combined torsion and flexure. The two response relationships seen as being most representative of the overall behaviour of the tested cantilever beams, and thus used as the primary focus for validation of the model, are the moment at the fixed end vs. torque at the fixed end and the torque at the fixed end vs. rotation at the free end diagrams. The cross-sectional stress and strain distributions are the secondary means of comparison. The tertiary means are the moment at the fixed end vs. vertical deflection at the free end and the vertical load vs. lateral deflection at the free end. The goal is to develop a model that accurately predicts the entire range of behaviour, although special attention is placed on the first phase (described in the next paragraph), which is believed to be the usable portion for design (Driver and Kennedy, 1987). A finite element model of the beams tested by Driver and Kennedy was developed using large displacement and finite strain shell elements and material properties and boundary conditions as reported in their work.

The test set-up and experimental procedures of Driver and Kennedy (1987) are summarized in Chapter 2. Results presented in this chapter are limited to those considered to be the most important for characterizing the combined torsional and flexural behaviour of the beams. Therefore, the results are used for comparison throughout the development of the finite element model. Driver and Kennedy (1987) observed two distinct phases of behaviour during their tests, the second being characterized largely by weak axis bending. The first phase was

dominated by twisting and strong-axis bending behaviour where no significant lateral deflections occurred, and the only source of torsion was the eccentrically applied load. (Beam 1 had no applied torque in this phase.) In the second phase, the beams developed more significant lateral and vertical deformations at the free end, as well as larger rotations. The lateral deflections at the free end caused the torque at the cantilever root to increase further by increasing the effective eccentricity. The cross-sectional rotation caused the beam behaviour to become dominated by weak axis bending in the second phase.

There is a distinct point where the second phase of behaviour begins for each of the beams. The cross-sectional strain and stress distributions at the start of the second phase of behaviour were presented by Driver and Kennedy (1987) for Beams 3 and 4 based on strain measurements at a location 30 mm from the support. The stress distribution was calculated from the measured strain values using the appropriate experimental stress vs. strain material curve. The strain and stress distribution curves are used for validation of the model described in this chapter.

## ***3.2 Model Development***

### **3.2.1 Element Properties and Model Mesh**

This project develops a finite element model using the S4R shell element. This element has four nodes and uses the Mindlin thick shell theory to account for transverse shear deformations. It is a stress/displacement, quadrilateral shell element with reduced integration and the default number of integration points through the shell thickness is five points, which was used in this work. The S4R shell element is a finite-strain and large displacement element that can be used in large strain analyses and has all six degrees of freedom—three rotational and three translational—active at each node. The shell element S4R is particularly well suited for

this analysis because the beams tested by Driver and Kennedy (1987) showed large strains and large displacement.

A Microsoft® Office Excel spreadsheet was used to develop finite element mesh and the input files for the models to allow for easy adjustment of variables as required. The measured cross-sectional dimensions are used for the model beam geometry. The average measured values for the cross-section depth,  $d$ , the flange width,  $b$ , the flange thickness,  $t$ , and the web thickness,  $w$ , are 154, 99.5, 6.67, and 5.97 mm, respectively. The first model consisted of eight elements across each flange and ten over the height of the web, with 50 elements over the beam length for a total of 1 300 elements. The elements are defined based on centreline thickness locations and then given the appropriate material thickness. A meshing bias was used, reducing the length of the elements near the support to capture the local buckling and yielding phenomena of the beam (where the strains are largest). The bias created a variation in the aspect ratio (length:width) over the length of the beam that ranged from 1:1.88 at the fixed end to 3.31:1 at the free end for the flange and from 1:2.23 at the fixed end to 2.78:1 at the free end for the web. The practical limit for the aspect ratio of shell elements is approximately 3.5, although the ideal value, according to Hibbitt *et al.* (2002), is below 2.0. As the aspect ratio becomes too large, the results become less accurate as the shell elements behave artificially stiffly.

Two additional meshes were developed as part of a mesh refinement study performed to ensure convergence of the solution and to help minimize mesh dependencies. Mesh 2 was developed with 16 elements across each flange and 20 across the web height with 100 elements over the beam length for a total of 5 200 elements. A typical Mesh 2 is shown in Figure 3.1. Mesh 3 was developed with 24 elements across each flange and 30 across the web height with 150 elements over the beam length for a total of 11 700 elements. The aspect ratio was maintained at the same

approximate values by making small adjustments to the bias used to vary the element length. For Mesh 2, the aspect ratio (length:width) ranged from 1:1.75 to 3.19:1 for the flanges and from 1:2.07 to 2.69:1 for the web. For Mesh 3, the aspect ratio ranged from 1:1.81 to 3.26:1 for the flanges and from 1:2.15 to 2.74:1 for the web.

Although the refined meshes had no significant effect on the Beam 1 results, they caused a marked difference in the results for the other three beams. As the mesh is refined, the beam becomes torsionally softer. In addition, it is found to increase the slope and peak moment achieved in the moment vs. torque diagram slightly, although the effect on the peak moment is not significant. Mesh 2 was selected as the final mesh to be used in the model because the differences between the original mesh and Mesh 2 were significant, but the discrepancies between Meshes 2 and 3 were considered negligible for all beams and Mesh 2 was considerably more efficient. The effects of the mesh refinement study can be seen in Figure 3.2 and Figure 3.3 for Beam 2.

### **3.2.2 Material Model**

The material properties are based on an average engineering stress vs. strain curve for each of the flange and the web material developed by Driver (2000) from material properties reported by Driver and Kennedy (1987). The flange curve was developed based on the average test results of eight flange coupons taken across the width of the two flanges and the web curve was developed based on the average results of five web coupons taken across the height of the web. Average values of the modulus of elasticity used for the web and flanges are 204 900 MPa and 201 900 MPa, respectively. These average curves, shown in Figure 3.4, are broken down into five-part piecewise linear representations of the actual curves for use in the model. At strains beyond the ultimate stress, it is assumed that the ultimate stress can be maintained to an infinite strain. The end points selected for the individual line segments for the

engineering stress vs. strain curve are shown in Table 3.1. ABAQUS requires the appropriate input material curve to be the plastic components of the true stress,  $\sigma_T$ , vs. true strain,  $\varepsilon_T$ , and thus requires the engineering stress,  $\sigma$ , vs. strain,  $\varepsilon$ , curve to be transformed by (e.g., Lay, 1982):

$$\sigma_T = \sigma \times (1 + \varepsilon) \quad [3.1]$$

$$\varepsilon_T = \ln(1 + \varepsilon) \quad [3.2]$$

These values are found in

Table 3.2. The model initially did not include any attempt to model the residual stresses, the initial imperfections, the fillets at the web-to-flange junction, or the cable through which the load was delivered to the test specimen, and only included a basic loading bracket model. Due to the absence of imperfections in the model, a small lateral load of 10 N (0.02% of the maximum vertical force applied at the cantilever tip during testing) was applied to Beam 1 (in the negative Z-direction as seen in Figure 2.3, the direction of the beam deflection in the test) to ensure that the beam deflected in the desired direction in the numerical model.

The original loading bracket consisted of a vertical plate perpendicular to the web simulating the extensions of the angles attached to the web with a horizontal plate at the shear centre level to model the horizontal plate used in the test (see Figure 2.3). The angle legs bolted to the beam web were modelled as a thickened web section. This assumes that the end plate has slipped to place the bolts into bearing to avoid the need for modelling a contact surface. This region corresponded to the middle eight web elements in the first two rows of elements at the free end of the beam. The dimensions of the modelled angle legs are within 1 mm of the actual values. The load is applied vertically at the node corresponding to the appropriate eccentricity and moment arm on the horizontal plate. This corresponds to the point on the actual loading bracket where the eyebolt connected to the plate. The bracket is composed of S4R shell elements

assumed to remain elastic using the same elastic modulus as the flange material. No significant deformation of the loading bracket was detected in the analysis.

### **3.2.3 Solution Strategy**

All four beams tested by Driver and Kennedy (1987) underwent large deformations and extensive material plastification. Thus, non-linear behaviour was expected in the model, not only because of material plasticity but also because of second order geometric effects. To account for the material plasticity, the model uses the idealized uniaxial stress vs. strain curves described in Table 3.1 and Table 3.2 as well as the von Mises yield criterion. To account for the second order geometric effects, the non-linear geometry option in ABAQUS is used.

The modified arc length method proposed by Riks (Hibbitt *et al.*, 2002) was used as the solution strategy, the analysis was able to proceed with good convergence characteristics and no numerical problems throughout the load response. This method allowed the solution to progress beyond buckling and/or material yielding. The applied load is varied during the step by means of a single load factor (Hibbitt *et al.*, 2002). This assumes that all loading is proportional. The basic premise is that there is a single solution path along the load displacement curve that is unique for the beam. The solution process follows the path until it reaches a certain deflection or load limit set in the input file or until the analysis no longer converges. The Newton-Raphson method is the base iterative method, however, this method treats both load and displacement as unknowns.

### **3.2.4 Modified Loading Bracket**

As shown in Figure 3.5, the analysis results using the original loading bracket (refer to Figure 3.6 for a diagram of the original loading bracket with Mesh 1 for Beam 2) do not capture the second phase of behaviour observed by Driver and Kennedy (1987). Rather, they seem to indicate

that the first phase continues indefinitely. Also, the moment versus torque behaviour is quite different as the slope is much more gradual and does not increase as the test progresses, resulting in a significantly lower peak moment. Although several simplified bracket models were investigated, to achieve accurate finite element results for the beam itself it was found that the loading bracket had to be modelled explicitly using the actual bracket dimensions and adding vertical extensions to model the eyebolts used in the test. The purpose of looking at these simple models of the loading bracket was to investigate the unique behaviour of the test results caused by the loading bracket used by Driver and Kennedy (1987). On the final loading bracket, these extensions (representing the eyebolts), shown in Figure 3.1, were initially parallel to the beam web and were modelled with S4R shell elements located at each of the loading point eccentricities. The height of the vertical extensions is 96.8 mm (the measured value from the centreline of the horizontal plate) with an assumed thickness of 30 mm. Figure 3.5 and Figure 3.7 illustrate the improved agreement of the final version of the loading bracket for Beam 2 compared to the original version. Unlike the original version of the bracket, the final version is able to predict both phases of behaviour well. To match the analysis performed by Driver and Kennedy (1987) on the experimental results, the torque is calculated by multiplying the effective eccentricity (with respect to the cantilever root) of the loading point as it moves in space, by the applied load. The moment is calculated by multiplying the vertical load by the instantaneous value of the moment arm measured from the load application point to the fixed support parallel to the X-axis that changes as the test progresses (see Figure 2.3).

The differences in behaviour between the finite element analysis results for the original and the final versions of the loading bracket indicate that the bracket used in the Driver and Kennedy (1987) tests affects uniquely the behaviour of the test specimen resulting from the eyebolts. As the loading progresses, the free end deflects vertically in the positive

Y-direction and laterally in the negative Z-direction. It also rotates about the positive X-axis. The lateral deflection has the effect of increasing the eccentricity but the rotation reduces this effective eccentricity. The vertical extensions (eyebolts) have the effect of amplifying this decrease in effective eccentricity caused by the rotation of the beam. As the effective eccentricity decreases, the applied torque is also reduced. For Beams 1 and 2, the rotations that develop in the second phase of behaviour are rather small but the lateral deflections are larger. This has the effect of increasing the effective eccentricity with only small reductions due to the rotation. Beams 3 and 4, however, have smaller lateral deflections and much larger rotations in the second phase resulting in a more significant reduction to the effective eccentricity. Thus, it was expected that the amplified rotational reduction to the effective eccentricity caused by the eyebolts would be largest for the larger rotations and the greatest initial eccentricities.

### **3.2.5 Residual Stresses**

In hot-rolled steel, residual stresses are caused by the rolling process and differential cooling rates that cause local yielding of some regions of the cross-section at stresses below the nominal yield value. Although indicated by previous research to be insignificant to the overall behaviour of members subject to combined flexure and torsion (Razzaq and Galambos, 1979a and 1979b; Driver, 2000), most research considers their effect in finite element approximations to provide a comparison with and to expand the database of test results. To account for the residual stresses in the model, an initial stress condition is applied to the centroid of each shell element in the analysis. An initial equilibrium step is performed in the analysis to ensure that the residual stresses are in equilibrium.

Driver and Kennedy (1987) did not measure the actual residual stress pattern of the beam, so a reasonable pattern has been used in the model. The distribution of the residual stresses across the flanges is assumed to

follow a parabolic representation with a maximum compressive stress of 160 MPa at each flange tip and a maximum tensile stress of 80 MPa at the flange-to-web junction as seen in Figure 3.10. No residual stresses are modelled in the web because they are not expected to have a significant effect on the overall behaviour of beams under combined torsion and flexure (Driver, 2000). This reasonable distribution is the same as the RS1 pattern used by Driver (2000) that was selected in part to provide a better means of comparison against the brick element model. The averaged stress values for each shell element, determined by integrating the assumed parabolic function over the element width and then dividing by the width, are used as the input centroidal element stresses.

To determine how the magnitude of the residual stress pattern influences the results, another residual stress pattern from Driver (2000), RS2, was modelled. This pattern is equivalent to the first pattern except that the magnitudes are doubled. Thus, RS2 has compressive residual stresses at the flange tips equal to 320 MPa and tensile residual stresses at the flange-to-web junction equal to 160 MPa. Once again, no residual stresses are modelled in the beam web. In this pattern, the maximum residual stresses are nearing the measured yield strength of the material.

Comparing the results of models with the two residual stress patterns described above with a model without any residual stresses, it was found that the residual stresses had a very small effect on the beam behaviour. As the magnitude of the residual stresses increases, the beam becomes softer torsionally. The moment also increases more rapidly compared to the torque (increases the slope of the moment vs. torque diagram), although the maximum moment achieved does not change. This effect is greater as moment becomes more dominant in the beam behaviour, that is, as the initial eccentricity decreases. This difference is negligible in the first phase of behaviour, as seen in Figure 3.8 and Figure 3.9 in the Beam 4 (largest load eccentricity) results. As the second phase of

behaviour is considered less important, as discussed previously, the precise residual stress pattern used has little effect on the outcome of this investigation.

Through the equilibrium step, the residual stresses dissipate from the fixed end towards the free end due to the decrease in effective longitudinal restraint. The equilibrated residual stresses range from a smoothed representation of the modelled distribution near the fixed end to nearly zero at the free end of the beam. This is acceptable since yielding occurs at the fixed end where the applied loads are the largest and, in any case, a reduction of residual stress magnitudes toward the free end of the beam is expected. Figure 3.10 presents the modelled residual stress pattern (RS1) and the equilibrated values at the flange nodes at both the fixed and free ends.

Since widely varying magnitudes of the same residual stress pattern have a similar effect on the results, as long as the assumed distribution is reasonable the predicted behaviour should be accurate. The work performed by Pi and Trahair (1994a, 1994b; Trahair and Pi, 1997) made use of a residual stress pattern that varies linearly instead of parabolically. Their flange residual stress pattern varies from  $0.35 F_y$  in compression at the flange tips to  $0.5 F_y$  in tension at the flange-to-web junction. Pattern RS1 ranges from  $0.47 F_y$  at the flanges tips to  $0.24 F_y$  at the flange-to-web junction, where  $F_y$  is the measured yield stress. Pattern RS1 places more emphasis on the flange tips that are likely to be the first part of the cross-section to yield due to the combination of normal stresses from warping and bending. Essa and Kennedy (2000) recommend a residual stress distribution for wide flange section flanges ranging from  $0.33 F_y$  at both the flange tips in tension and at the flange-to-web junction in compression that is close to parabolic in shape, which is likely somewhat less severe than pattern RS1 used here.

Neglecting the residual stresses in the web seems practical for beams subject to combined torsion and flexure as the largest normal stresses develop in the flanges first, making them more likely to yield first unless the interaction between normal and shear stresses becomes important.

### 3.2.6 Fillets

According to Driver & Kennedy (1987), including the fillet area in the calculation of the sand heap or fully plastic St. Venant torque increases the resulting value of that component of the total torsional capacity by 16% compared to the value found assuming only rectangular elements. Thus, it is important to consider the effects of fillets in the finite element analysis. In addition to improving the torsional resistance, fillets provide additional area far from the centroidal strong axis, which should improve the pure flexural resistance and should increase the flexural stiffness of the member. Including fillets in the model provides additional area to the cross-section, increasing the torsional constant and thus the torsional stiffness and the slope of the torque vs. rotation diagram, while reducing the slope of the moment vs. torque diagram (by increasing the torque that develops at the same moment).

An approximate method was developed to model the fillets with shell elements. This method adds the fillet area to the cross-section at the appropriate location with respect to the centroidal axes. Due to the construction of the shell model, the flange and web are connected at a single point at the web-to-flange junction rather than over a distributed region, limiting the transfer of shear stresses between the flanges and the web. Using Mesh 2, the fillet region of the beam is modelled using the top and bottom two elements of the web. The method involves thickening these two elements in the fillet region to provide the additional fillet area. By varying the thickness between the two elements, the centroid of the fillet area can be adjusted to match the theoretical or nominal value. Mesh 2 has a  $k$  value ( $k$  is the vertical dimension from the bottom of the

fillet to the outside surface of the top flange) of 18.1 mm, only 4.7% different from the nominal value of 19 mm (CISC, 2007).

As part of Driver and Kennedy's (1987) experiment, the fillet area was measured to be 17.9 mm<sup>2</sup>. The theoretical centroid was then calculated using this fillet area and decreasing the nominal values of  $k$  and  $k_1$  such that the elliptical complement area provided the correct fillet area. The appropriate  $k$  and  $k_1$  values were found to be 16.6 mm and 11.4 mm, respectively, which are lower than the nominal values found in the Handbook of 19 mm and 13 mm, which are upper bounds to be used for detailing purposes. The centroid of the fillet area was then found to be 67.0 mm from the section centroid. Matching the fillet area and centroid of 17.9 mm<sup>2</sup> and 67.0 mm, respectively, the two fillet elements require thicknesses of 7.19 mm and 9.60 mm each having a height of 7.39 mm, where the thicker element is nearest to the flange as expected.

It is seen in Figure 3.11 and Figure 3.12 that the effect of modelling the fillets is to stiffen the beam torsionally and cause a slight reduction in the slope of the moment vs. torque diagram. These effects are negligible in the first part of the curves, but become more prominent at higher load levels where the curves for the model that includes the fillets are significantly closer to the test response. The fillets caused the peak moment (for this beam, the peak moment corresponds to the ultimate limit state or failure point selected by Driver and Kennedy (1987)) to decrease as more torque is attracted at the same rotation reducing the ability of the beam to carry the same moment. As the area of the fillets increases, these effects are greater. As the eccentricity decreases, the stiffening effect of the beam torsionally decreases but the decreased moment capacity effect becomes more pronounced as the flexural loads become more important to the behaviour as compared to the torsional loads. The proposed model using shell elements at the flange-to-web junction to

model the fillets provides an excellent prediction of the experimental results.

### **3.2.7 Comparison with 3-D Element Model**

It was found that the model developed using S4R shell elements is capable of producing results as good as, or in some cases better than, the brick elements used by Driver (2000), while considerably saving modelling and computational effort. Figure 3.13 through Figure 3.20 show comparisons between the shell and brick models for Beam 3, along with the test results. In the model, the cross-section used to obtain the stress and strain values is within 0.16 mm of the location of the centre of the strain gauges used in the test, which had a gauge length of 5 mm. In order to compare the finite element results with the test results, the output from ABAQUS is taken at the integration points and on the surfaces of the elements where strain gauges were mounted on the test specimens, namely, at the top of the top flange, the left side of the web in the positive Z-direction opposite to the eccentricity, and the bottom of the bottom flange. ABAQUS presents the results in true stress and true strain. The true stress results were converted to engineering stress using Equation [3.1]. The true strain results were not converted to engineering strain because there is very little difference between the two until well past strain hardening.

The flange stress distributions indicated that significant inelastic behaviour develops in the finite element models and test specimen due to the warping bi-moments and bending moments (see Figure 3.18 and Figure 3.20). These bi-moments are sufficient to cause a stepped stress distribution across the flanges. Some discrepancy may result from the idealized stress vs. strain curve used in the model, the subjectivity in selecting the point when the second phase of behaviour begins (the point in the loading when the stress and strain are presented), and the method of calculating the finite element stress results. The finite element stress

results are presented as the component of the 3D state of stress in the longitudinal direction. The test stress results were obtained in an analogous manner at the strain rosette locations and by direct conversion of the longitudinal test strains at the strain gauge locations using the average stress vs. strain curves for each of the flange and web, as obtained from the tension coupon tests.

### **3.2.8 Cable Loading**

Thus far, the load has been applied vertically at the point on the top of the vertical extensions of the loading bracket that corresponds with the underside of the top part of the eyebolt at the appropriate eccentricity. The actual experimental set-up loaded the beam by means of a cable that hooked into the eyebolt. The cable was then attached to the clevis of the testing machine at a point 4 995 mm from the eyebolt directly above the undeformed beam's web (see Figure 2.3). To apply the load to the beam, the machine imposed a vertical displacement at the end of the cable attached to the clevis. When the eccentricity is zero (Beam 1, initially), the cable applies the load vertically.

For the cases where the load is applied eccentrically, the cable forms a small angle with the vertical Y-axis. Although the load is applied vertically at the top of the cable, the angle in the cable causes a small transverse load to be applied to the loading bracket in the positive Z-direction (see Figure 2.3) in addition to the vertical load. This transverse load has two effects. It causes biaxial bending in the beam and applies an additional torque at the free end of the beam due to the eccentricity of this transverse load relative to the shear centre. Moreover, this effect is amplified by the deformation of the beam. As the free end of the beam rotates and deflects both laterally and vertically, the angle the cable makes with the vertical changes. At the same time, the extra torsional load from the cable increases as the eccentricity of the transverse load and the angle of the cable increases. In addition, the beam develops curvature as a result of

the applied moment, reducing the moment arm of the cantilever beam and causing the cable to rotate in the negative direction about the Z-axis. The cable then applies a small tensile axial load to the free end of the beam at the loading bracket. This tensile axial load is eccentric, resulting in a moment at the free end of the beam, effectively reducing the strong axis bending moment slightly.

Driver and Kennedy (1987) considered all of these effects in their analysis. To provide a more consistent means of comparison, the cable was thus included in the finite element model. This cable element connected the previously used eyebolt loading point on the loading bracket to the actual loading point in the testing machine. A vertical load was then applied using displacement control at the actual loading point that was restrained from any lateral deflection. Prior to loading, the cable is vertical for Beam 1. For Beams 2, 3, and 4, the only angle the cable makes with the vertical initially is in the Y-Z plane as a result of the initial eccentricity.

The cable was modeled using a T3D2 truss element from the ABAQUS element library. This element is a 3-dimensional, 2-node straight truss element that uses linear interpolation for position and displacement, thus resulting in a constant strain over the length of the element. The cable was modeled as a 7/8" diameter steel cable having a net area of 388 mm<sup>2</sup>. It is assumed to remain elastic and used an effective elastic modulus equal to 67 300 MPa, considered to be typical of the wound steel wire rope used in the test. An ancillary investigation found that the results were insensitive to the value of the modulus selected.

Figure 3.21 and Figure 3.22 show the effect the cable has on the moment vs. torque and torque vs. rotation diagrams for Beam 4, the beam with the largest load eccentricity. The cable softens the beam response torsionally because the lateral load applied by the cable creates an additional torsional load. The maximum moment achieved is also increased slightly.

The greater the eccentricity of the load, the larger the angle the cable makes with the vertical, and thus the larger the effect of including the cable in the model. In the first phase of behaviour the effect of the presence of the cable is greatest for Beams 3 and 4. In the second phase of behaviour, however, the effect is the largest in Beams 1 and 2. Figure 3.23 and Figure 3.24 present the moment vs. torque and torque vs. rotation diagrams from Beam 2 comparing the finite element results with and without the cable. Although Beams 1 and 2 have small load eccentricities in the first phase, these beams undergo large lateral deflections with only small rotations, causing large effective loading eccentricities in the second phase. This causes the effect of cable loading to be large in the second phase for these beams. For Beams 3 and 4, the initial eccentricities are large but the smaller lateral deformations and large free end rotations (nearing 65 degrees in Beam 4) reduce the effective eccentricity and thus reduce the effect in the second phase.

### **3.3 Discussion of Finite Element Model Results**

The finite element analysis results from the final model are presented in Figure 3.15 through Figure 3.20 and Figure 3.25 through Figure 3.28. The results of the torque vs. rotation diagram for Beam 1 (Figure 3.26) presents only the second phase of behaviour because torsion develops only after the cross-section rotates and deflects laterally near the ultimate load after the beam buckles. The model provides very good results throughout the loading history for all the test specimens. It can be seen in Table 3.3 that the points at which the second phase of behaviour begins in the model response match well with the test results. The discrepancies between the finite element analysis and the test results for Beams 1 and 2 are amplified due to the small magnitudes of the torque. Similar accuracy is demonstrated in Table 3.4, where the average difference between the finite element and test results for the peak moments and loads is 0.7% and 2.0%, respectively. In the first phase of behaviour, the model predicts the

initial slope for the moment vs. torque and torque vs. rotation diagrams very well, as seen in Table 3.5. The slope of the torque vs. rotation diagram represents the torsional stiffness of the beam.

In the Beam 1 test, the bolted connection between the loading bracket and the beam web slipped such that the bolts came into bearing with the web. For the remaining three tests, shims were added between the legs of the loading bracket angles adjacent to the beam web and the flanges to avoid this slippage without interfering with the warping of the flanges at the free end. Although the bracket slippage was accounted for in the test data reduction, the fact that it was not present in the finite element simulation may help to explain some of the discrepancy in the Beam 1 results in the second phase of behaviour.

Another possible source of error is the assumption in the model that the hook does not slip at its bearing point in the eyebolt. Any slip that may have occurred in the test, changing the torsional moment arm, is neglected. Table 3.3 shows that the finite element torque at the end of the first phase of behaviour is below the test capacities, as selected by Driver and Kennedy (1987), for all beams except Beam 4 and that the rotation that develops in the finite element model is always larger than in the experiment.

### **3.4 Summary**

The finite element model developed in this chapter and validated using the test results of Driver and Kennedy (1987) provides the basis of the model to be used in this project and the parametric study presented in Chapters 5 and 6. The model accounts for the effects of residual stresses and the actual geometry of the cross-section, including the presence of the fillets. The models presented in this chapter included the the loading bracket and the loading cable used in these tests. (The loading bracket and cable will not be used in further finite element modelling since they are unique to

Driver and Kennedy's (1987) experimental set-up.) By using shell elements, the model provides accuracy equivalent to or better than the brick elements used by Driver (2000), but greatly reduces the required modelling and computational effort. The model accounts for non-linearity in the material properties and geometry. The solution is able to progress beyond yielding and beyond the ultimate capacity of the beams. Overall, the finite element model illustrates excellent agreement with the experimental results of Driver and Kennedy (1987).

*Table 3.1 Modelled Engineering Stress vs. Strain Curves*

Point	Web		Flange	
	Stress (MPa)	Strain	Stress (MPa)	Strain
First Yield	340	0.0017	339	0.0017
Onset of Strain Hardening	340	0.0152	339	0.0148
Intermediate Strain Hardening	420	0.0336	420	0.0273
Ultimate	473	0.1490	470	0.1510

*Table 3.2 Modelled True Stress vs. Plastic Strain Curve*

Point	Web		Flange	
	Stress (MPa)	Plastic Strain	Stress (MPa)	Plastic Strain
First Yield	341	0.0000	339	0.0000
Strain Hardening	346	0.0134	344	0.0130
Intermediate Strain Hardening	434	0.0309	431	0.0248
Ultimate	544	0.1370	541	0.1370

*Table 3.3 Comparison of Finite Element model with Test Results at the Point at which the Second Phase of Behaviour Starts*

Beam	Moment (kNm)			Torque (kNm)			Rotation (deg)		
	Test	Model	% Diff.	Test	Model	% Diff.	Test	Model	% Diff.
1	47.0	47.5	1.1	0.016	0.012	-25.0	0.0	0.0	0.0
2	49.3	47.1	-4.5	0.98	0.81	-17.3	9.1	9.2	1.1
3	43.0	43.8	1.9	2.56	2.50	-0.2	29.2	32.2	10.3
4	36.0	35.8	-0.6	3.39	3.43	1.2	53.2	57.1	7.3

*Table 3.4 Comparison of Finite Element model with Test Results of the Maximum Moments and Loads*

<b>Beam</b>	<b>Maximum Moment (kNm)</b>			<b>Maximum Load (kN)</b>		
	<b>Test</b>	<b>Model</b>	<b>% Diff.</b>	<b>Test</b>	<b>Model</b>	<b>% Diff.</b>
<b>1</b>	58.2	59.0	1.4	59.7	60.0	0.5
<b>2</b>	52.9	52.7	-0.4	55.9	53.4	-4.5
<b>3</b>	44.8	44.6	-0.4	46.6	45.3	-2.8
<b>4</b>	37.7	36.4	-3.4	39.2	38.7	-1.3

*Table 3.5 Comparison of Finite Element model with Test Results of the Initial Slopes of the Moment vs. Torque and Torque vs. Rotation Diagrams*

<b>Beam</b>	<b>Moment vs. Torque</b>			<b>Torque vs. Rotation (kNm/deg)</b>		
	<b>Test</b>	<b>Model</b>	<b>% Diff.</b>	<b>Test</b>	<b>Model</b>	<b>% Diff.</b>
<b>1</b>	∞	∞	—	—	—	—
<b>2</b>	33.4	33.4	0.00	0.150	0.150	0.00
<b>3</b>	10.5	10.5	0.00	0.150	0.150	0.00
<b>4</b>	4.97	4.89	-1.52	0.192	0.192	0.00

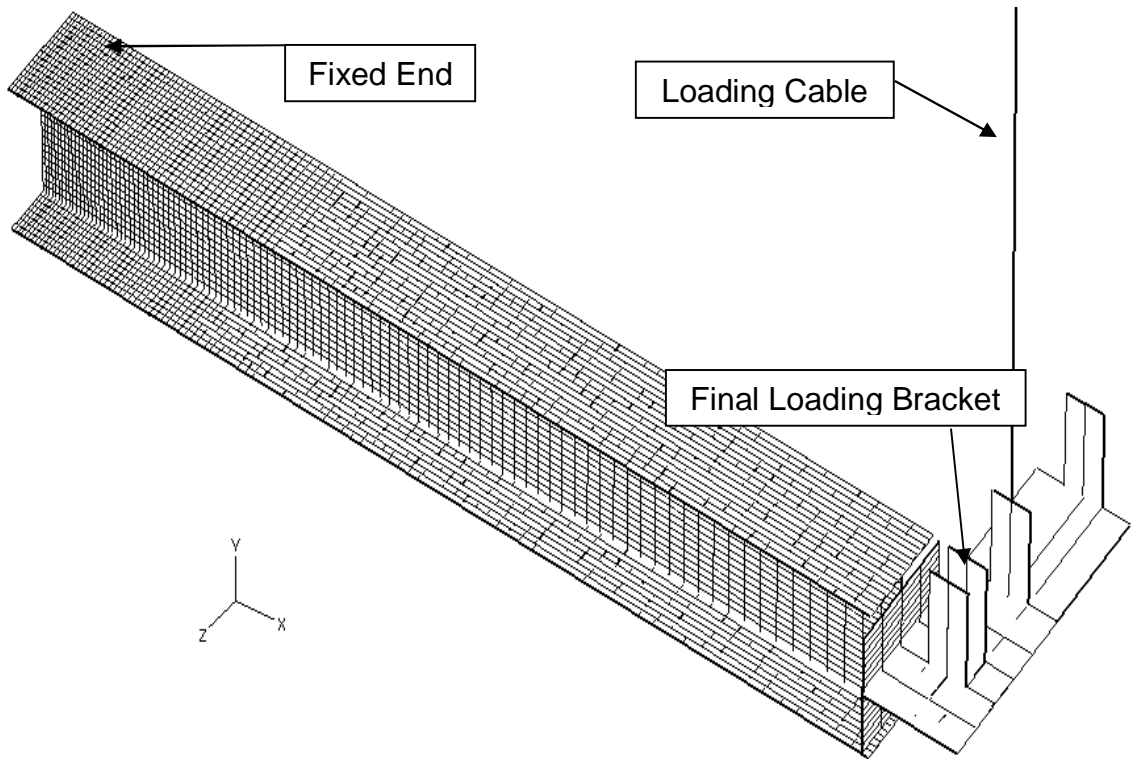


Figure 3.1 Mesh 2 for Beam 3

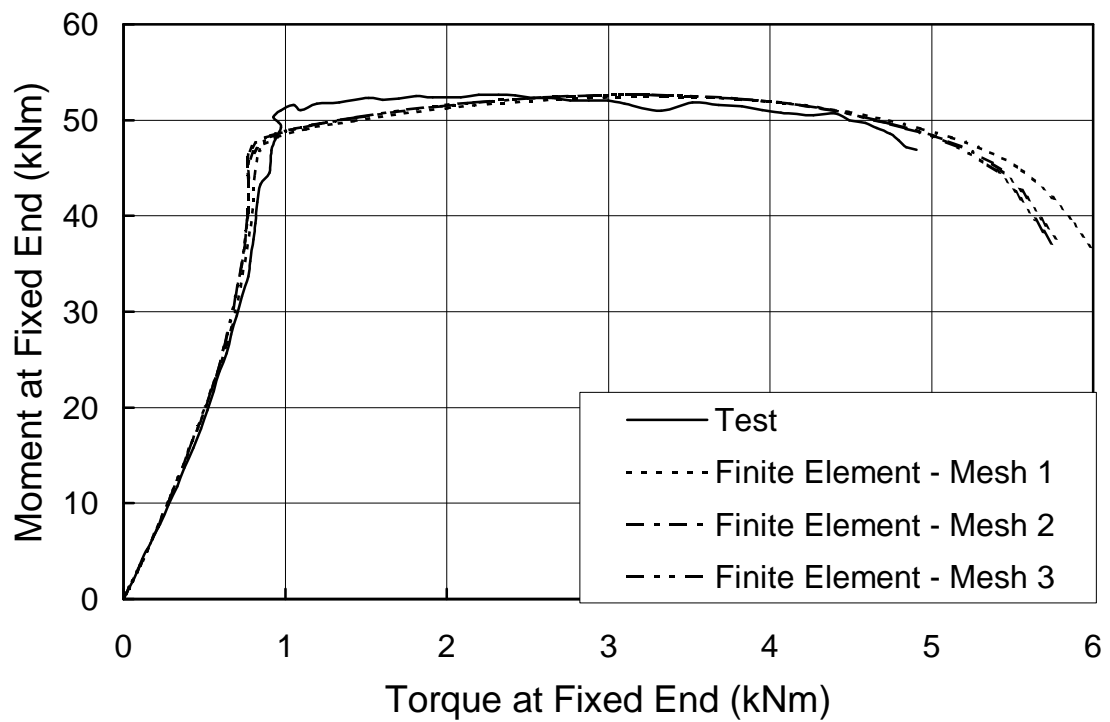


Figure 3.2 Moment at Fixed End vs. Torque at Fixed End for Beam 2 – Mesh Refinement Study

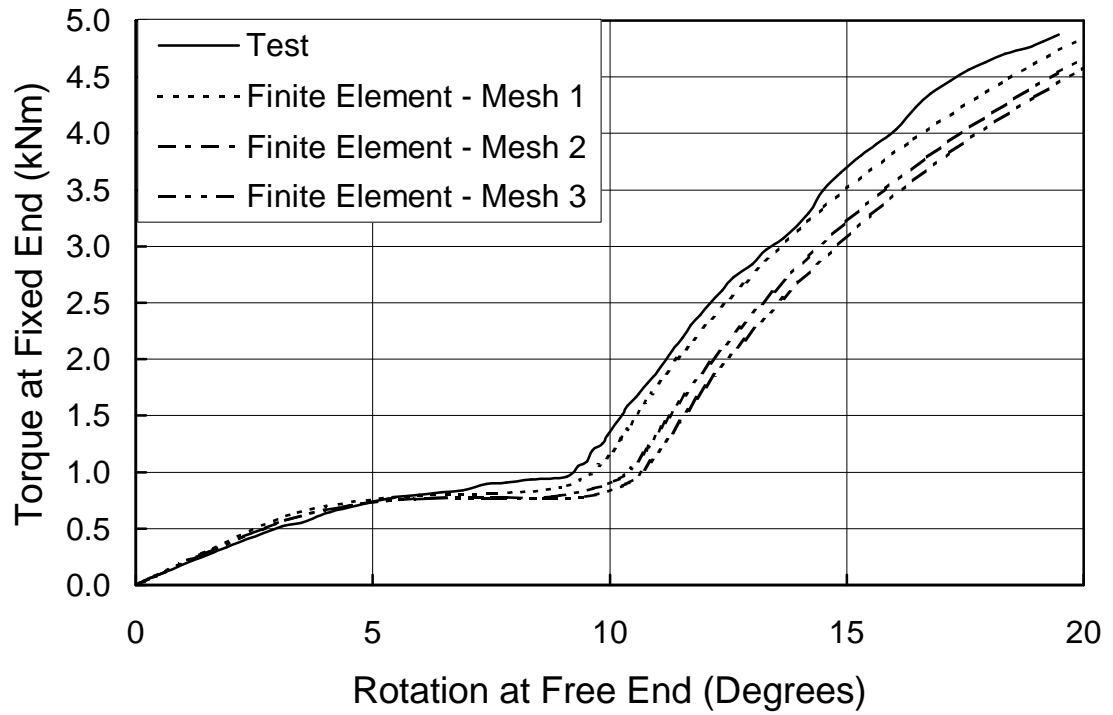


Figure 3.3 Torque at Fixed End vs. Rotation at Free End for Beam 2 – Mesh Refinement Study

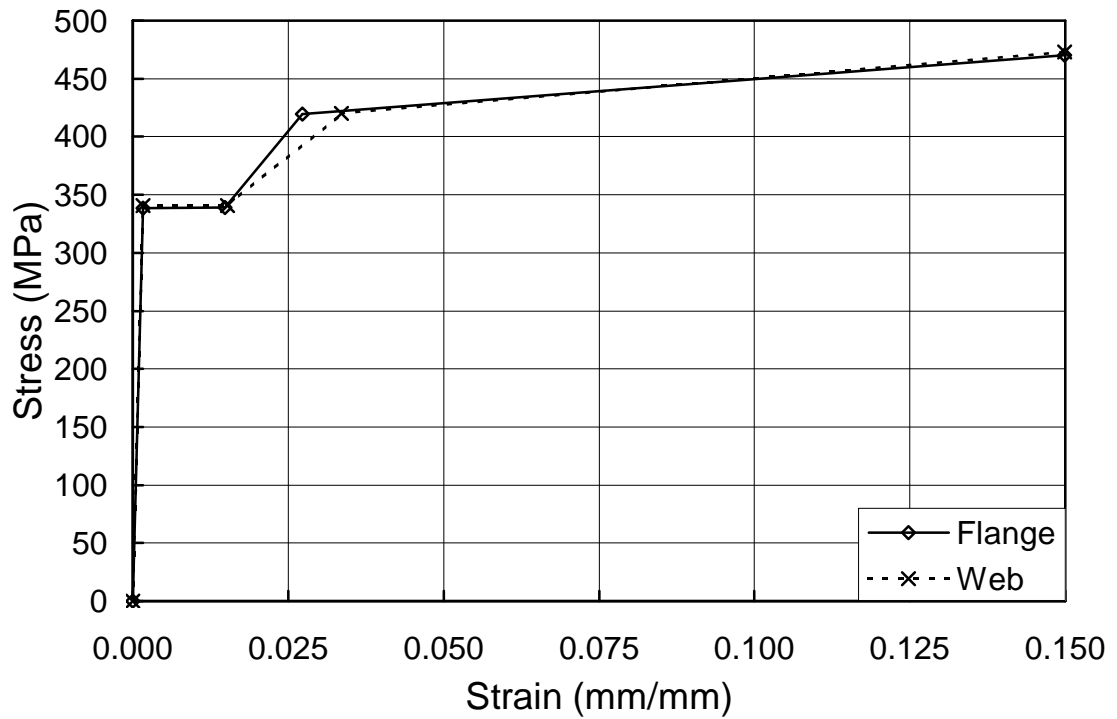


Figure 3.4 Modelled Engineering Stress vs. Strain Curves

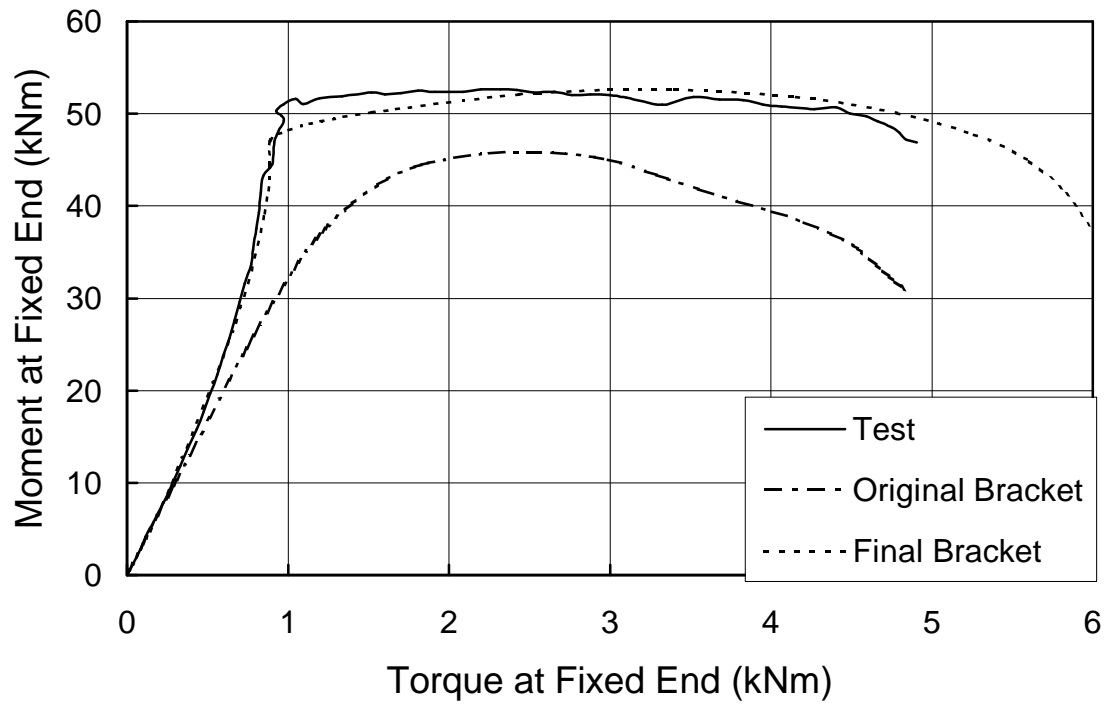


Figure 3.5 Moment at Fixed End vs. Torque at Fixed End for Beam 2 – Effect of Loading Bracket Model

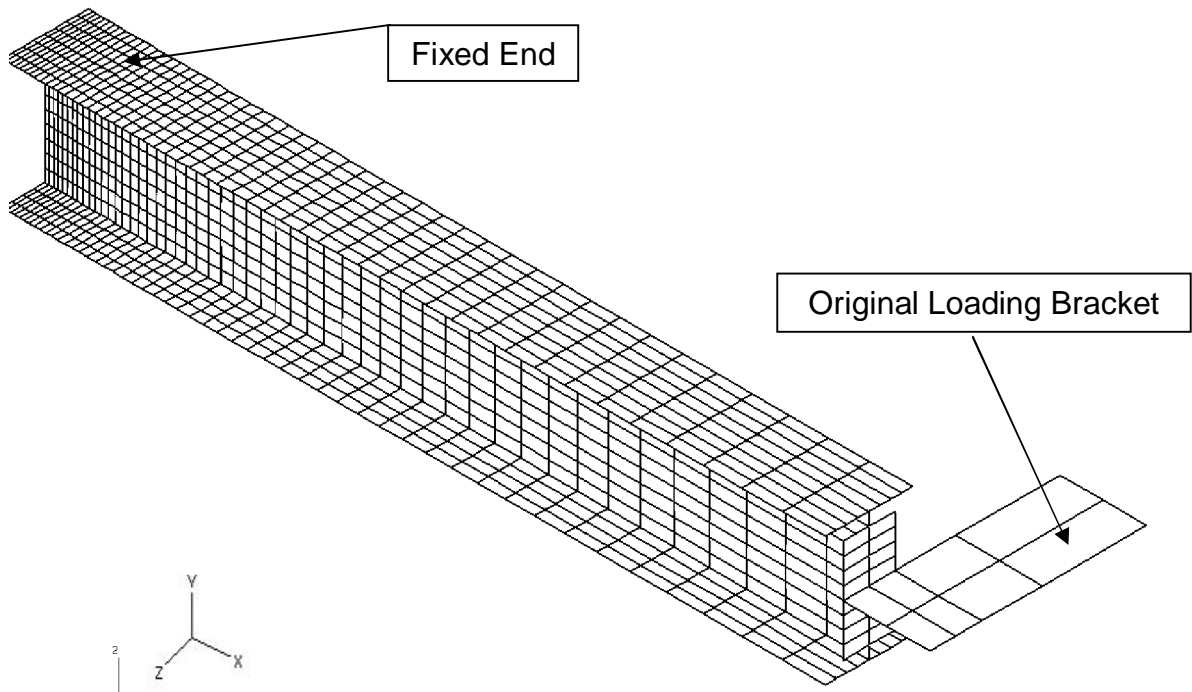


Figure 3.6 Original Loading Bracket with Mesh 1 for Beam 2

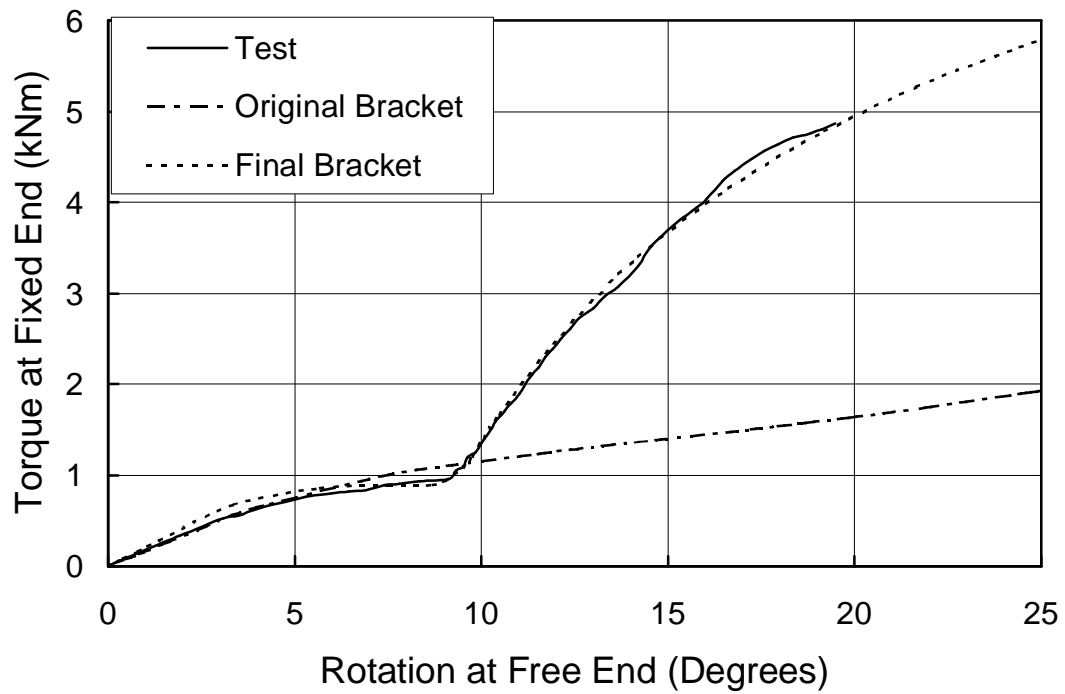


Figure 3.7 Torque at Fixed End vs. Rotation at Free End for Beam 2 – Effect of Loading Bracket Model

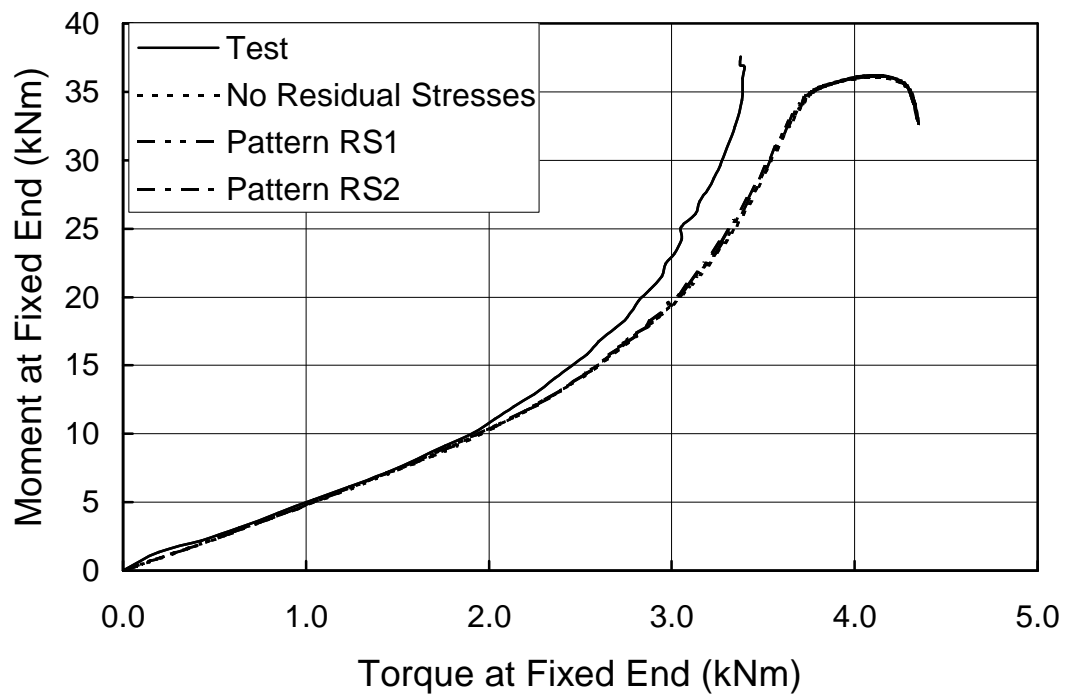


Figure 3.8 Moment at Fixed End vs. Torque at Fixed End for Beam 4 – Effect of Residual Stresses

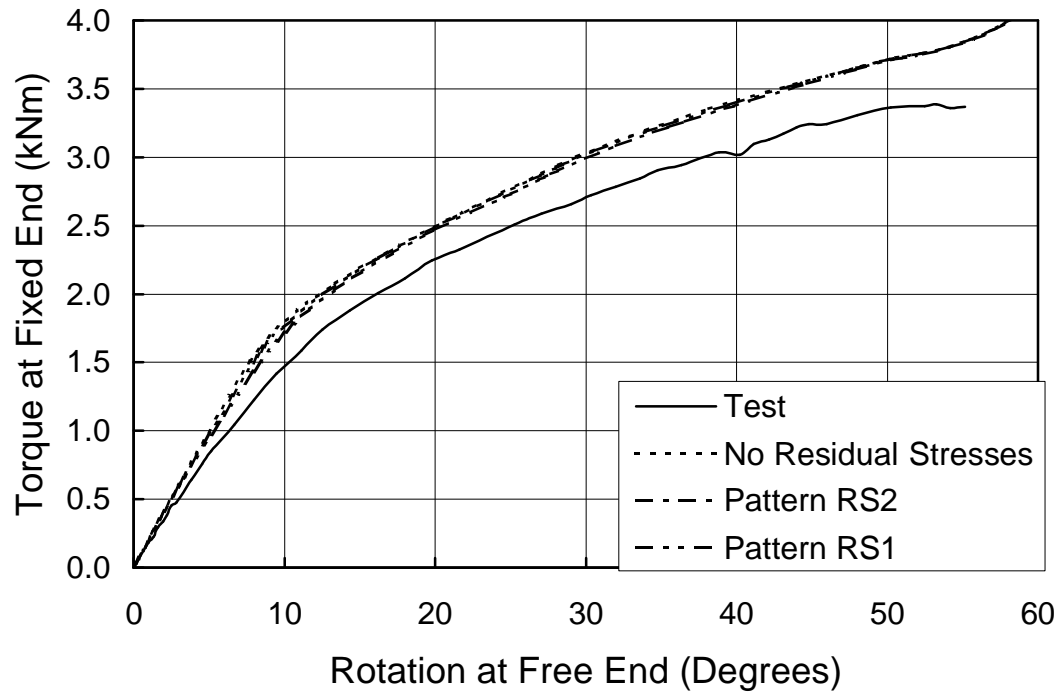


Figure 3.9 Torque at Fixed End vs. Rotation at Free End for Beam 4 – Effect of Residual Stresses

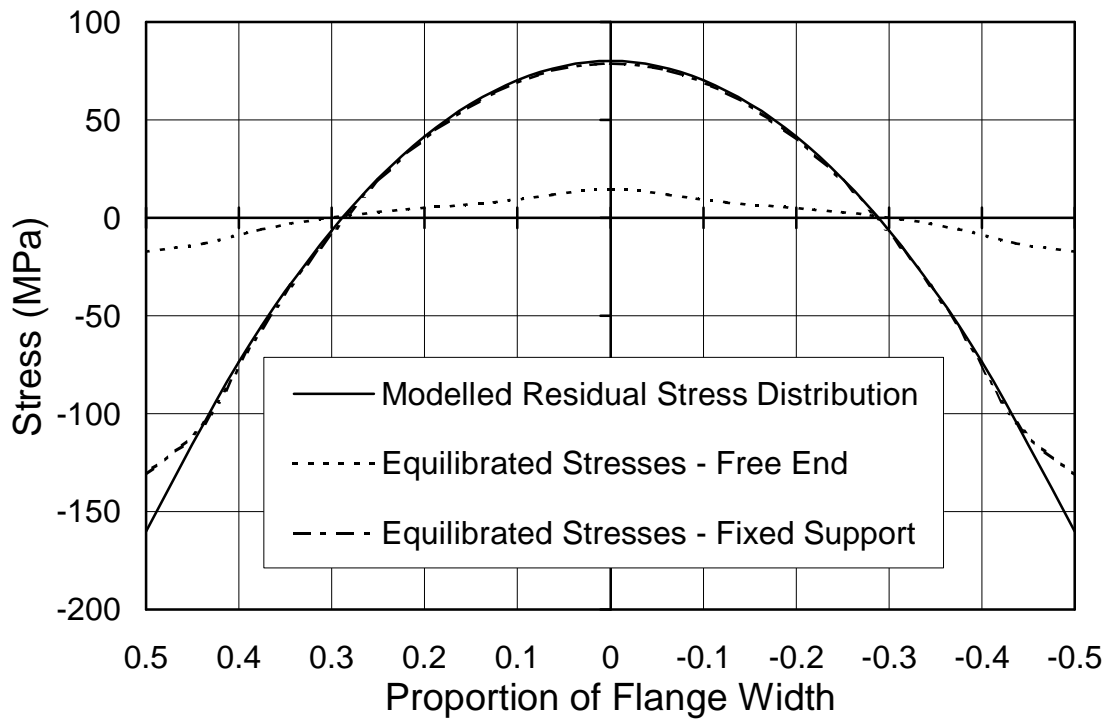


Figure 3.10 Comparison between the Equilibrated Residual Stresses and the Modelled Residual Stresses

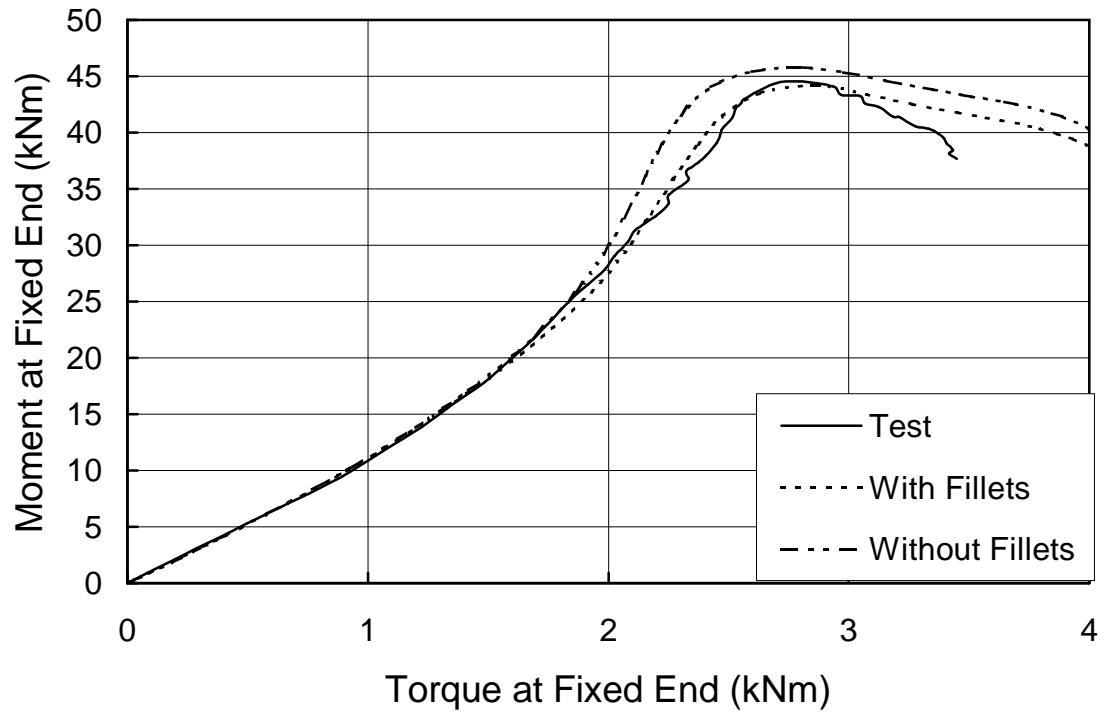


Figure 3.11 Moment at Fixed End vs. Torque at Fixed End for Beam 3 – Fillets

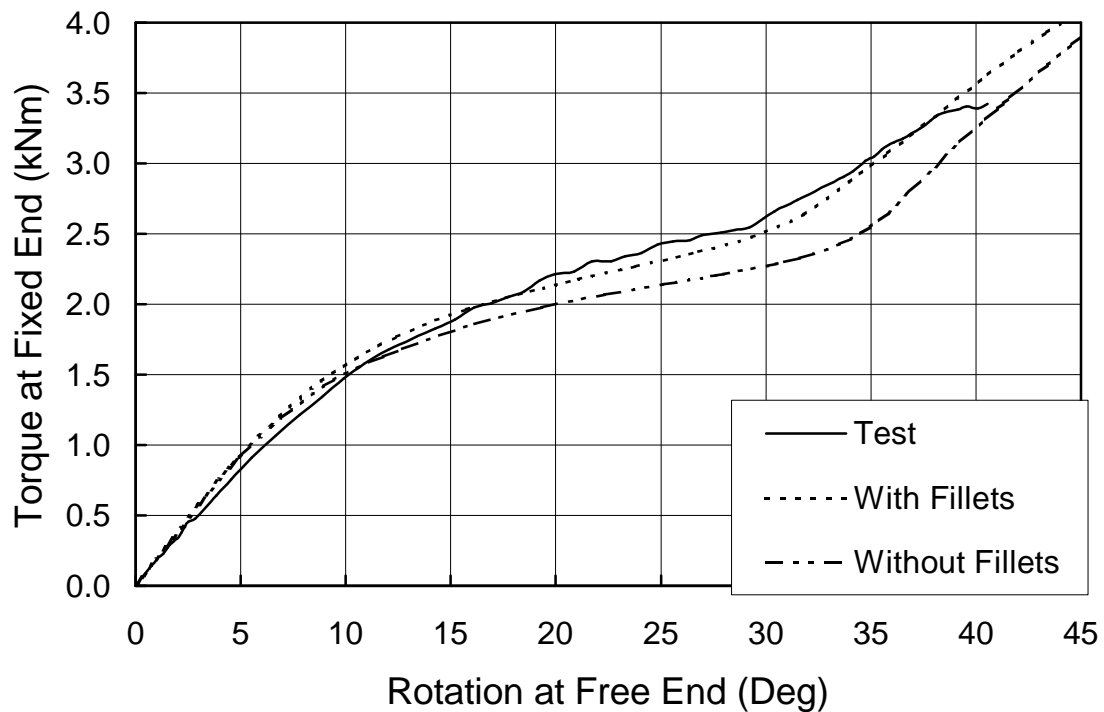


Figure 3.12 Torque at Fixed End vs. Rotation at Free End for Beam 3 – Fillets

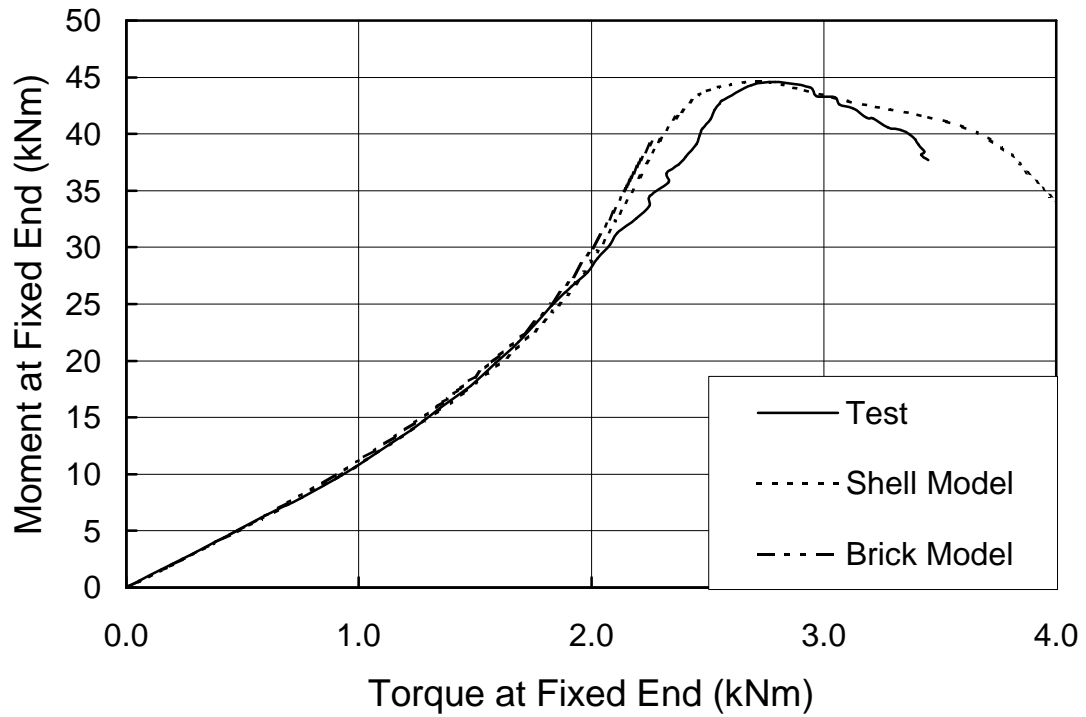


Figure 3.13 Moment at Fixed End vs. Torque at Fixed End for Beam 3 – Comparison Between Brick and Shell Element Models

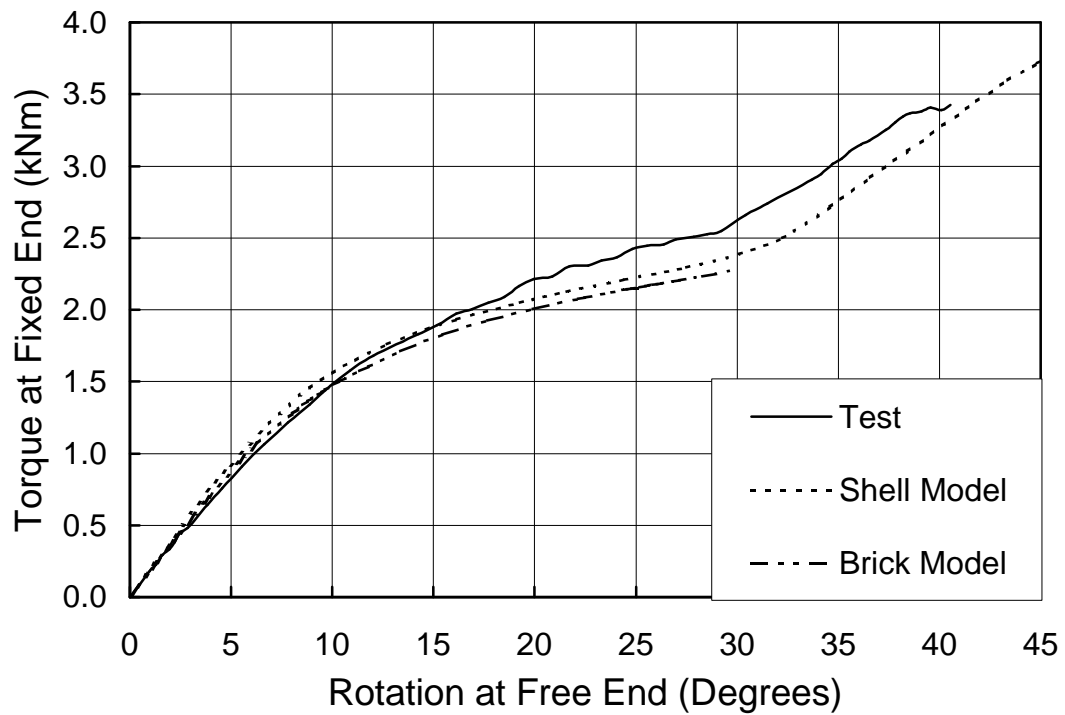


Figure 3.14 Torque at Fixed End vs. Rotation at Free End for Beam 3 – Comparison Between Brick and Shell Element Models

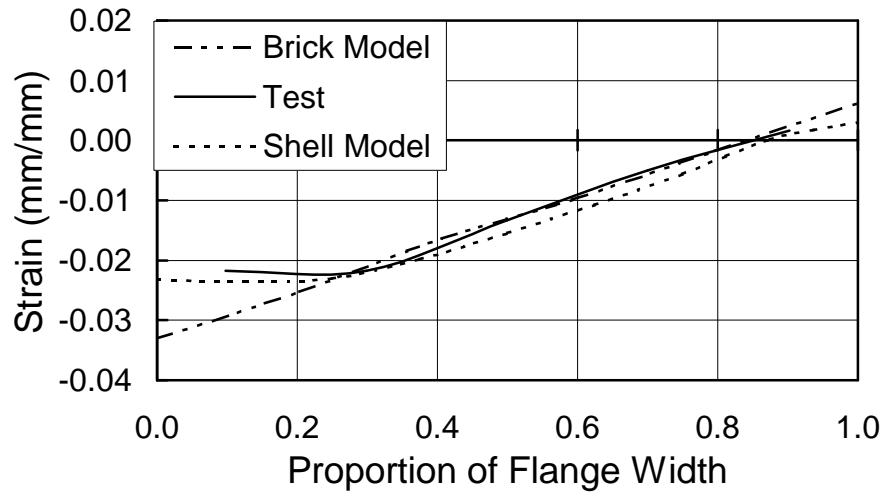


Figure 3.15 Top Flange Strain for Beam 3 - Brick and Shell Models

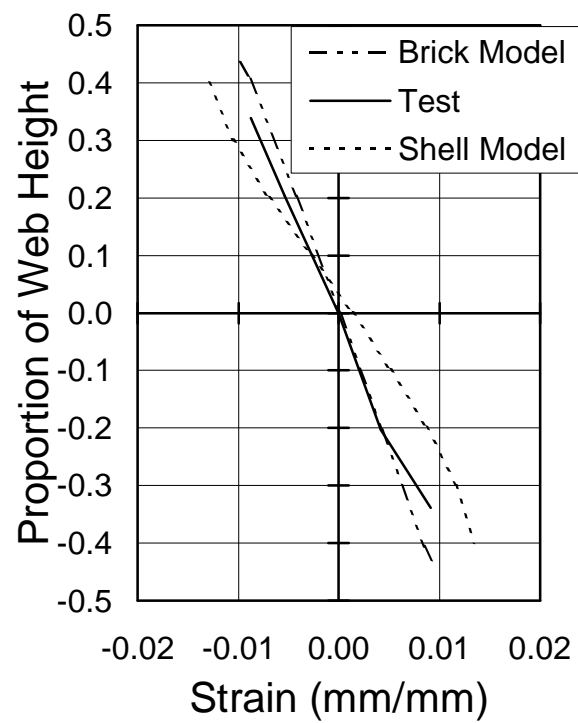


Figure 3.16 Web Strain for Beam 3 - Brick and Shell Models

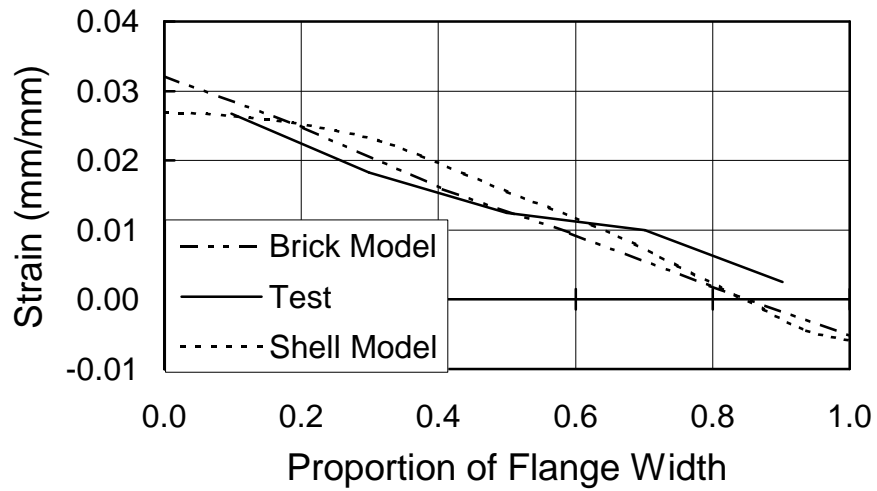


Figure 3.17 Bottom Flange Strain for Beam 3 - Brick and Shell Models

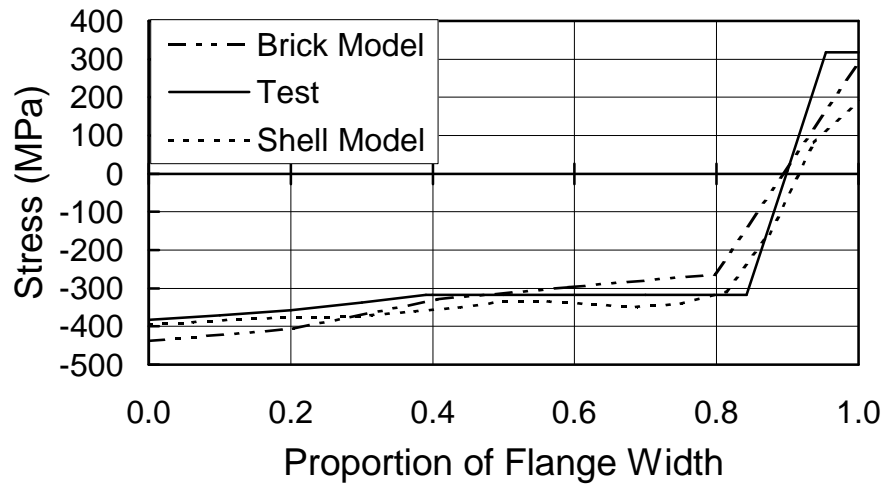


Figure 3.18 Top Flange Stress for Beam 3 - Brick and Shell Models

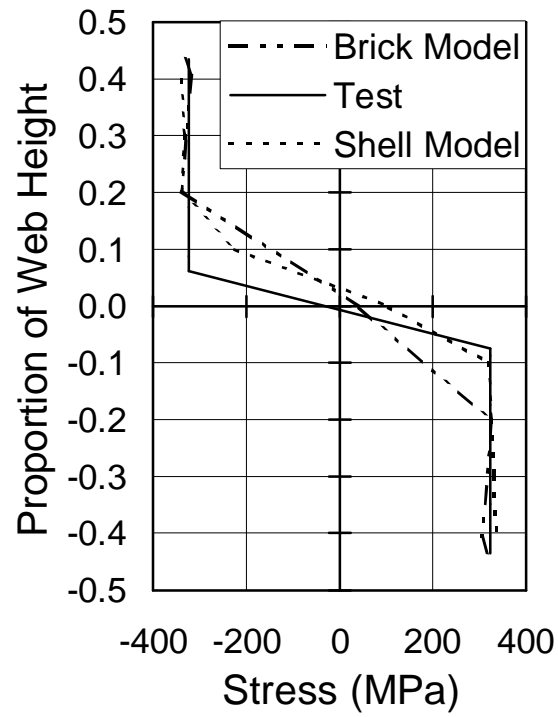


Figure 3.19 Web Stress for Beam 3 - Brick and Shell Models

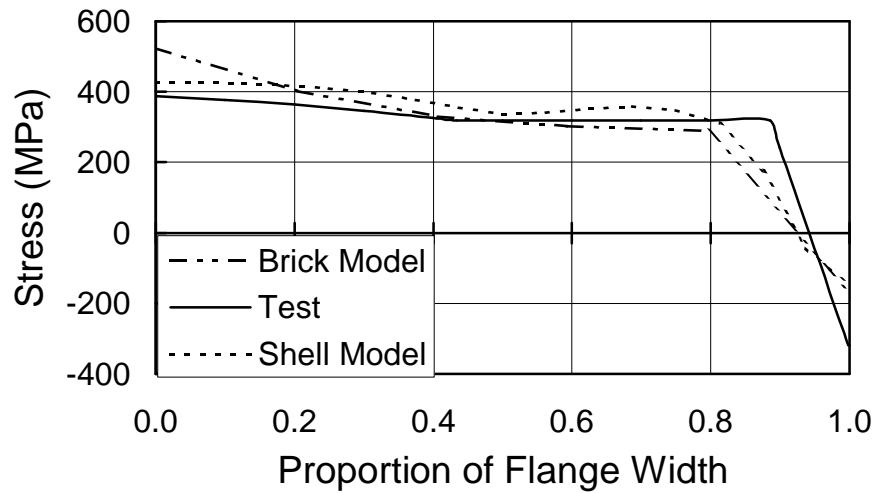


Figure 3.20 Bottom Flange Stress for Beam 3 - Brick and Shell Models

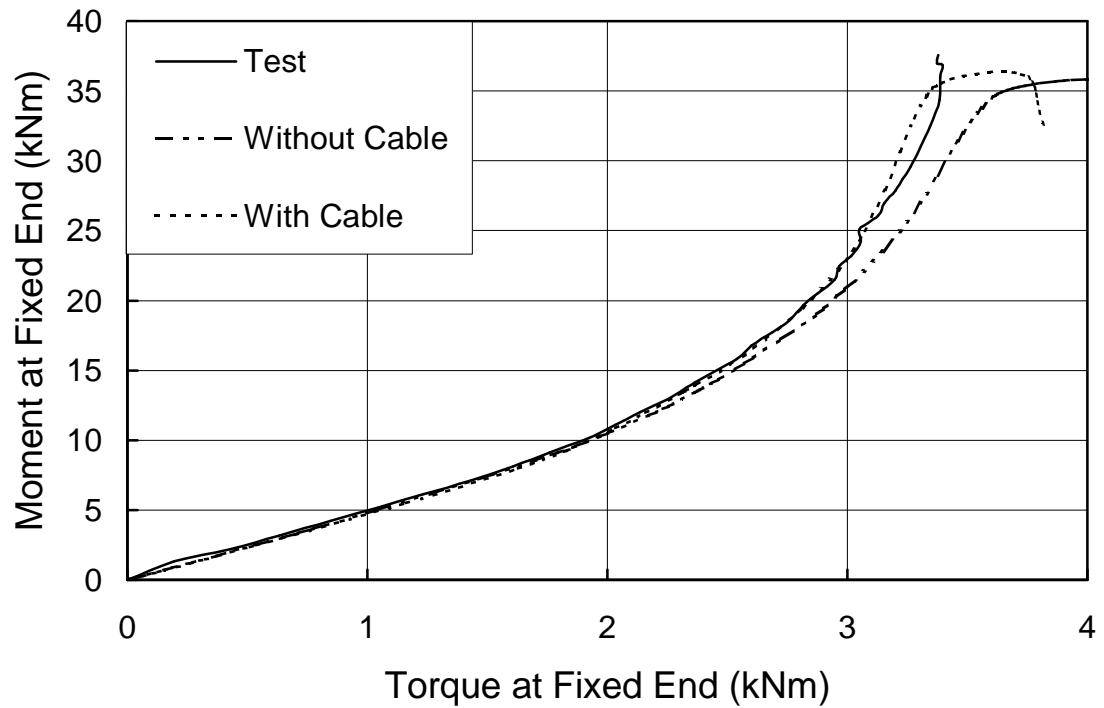


Figure 3.21 Moment at Fixed End vs. Torque at Fixed End for Beam 4 – Model Loaded With Cable

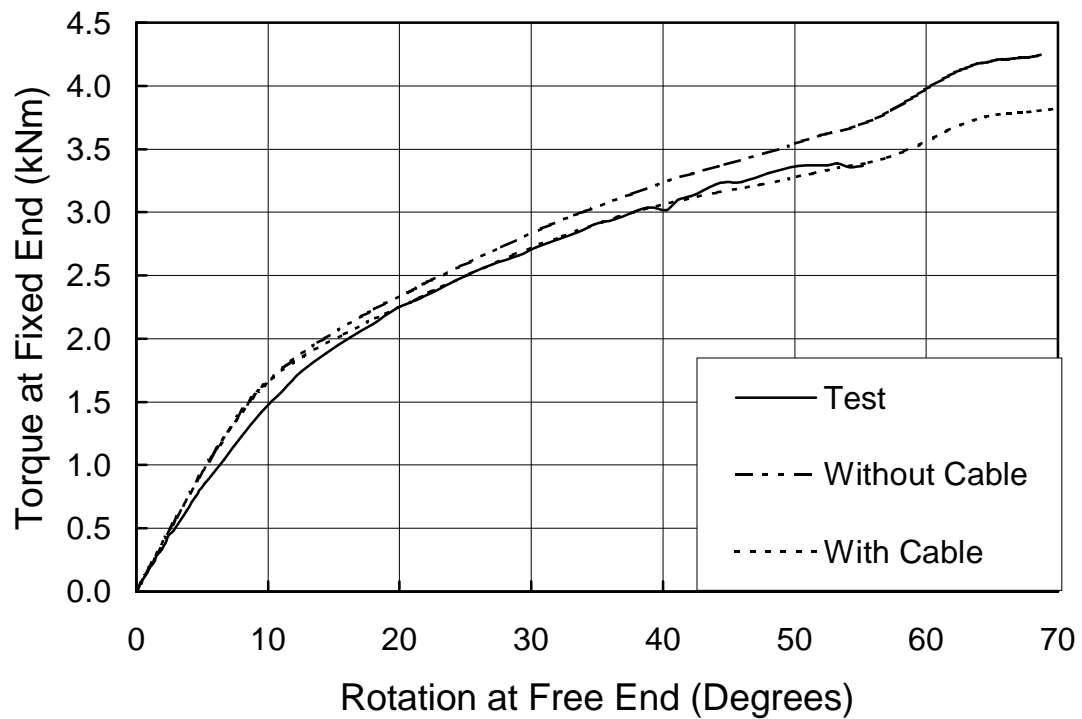


Figure 3.22 Torque at Fixed End vs. Rotation at Free End for Beam 4 - Model Loaded With Cable

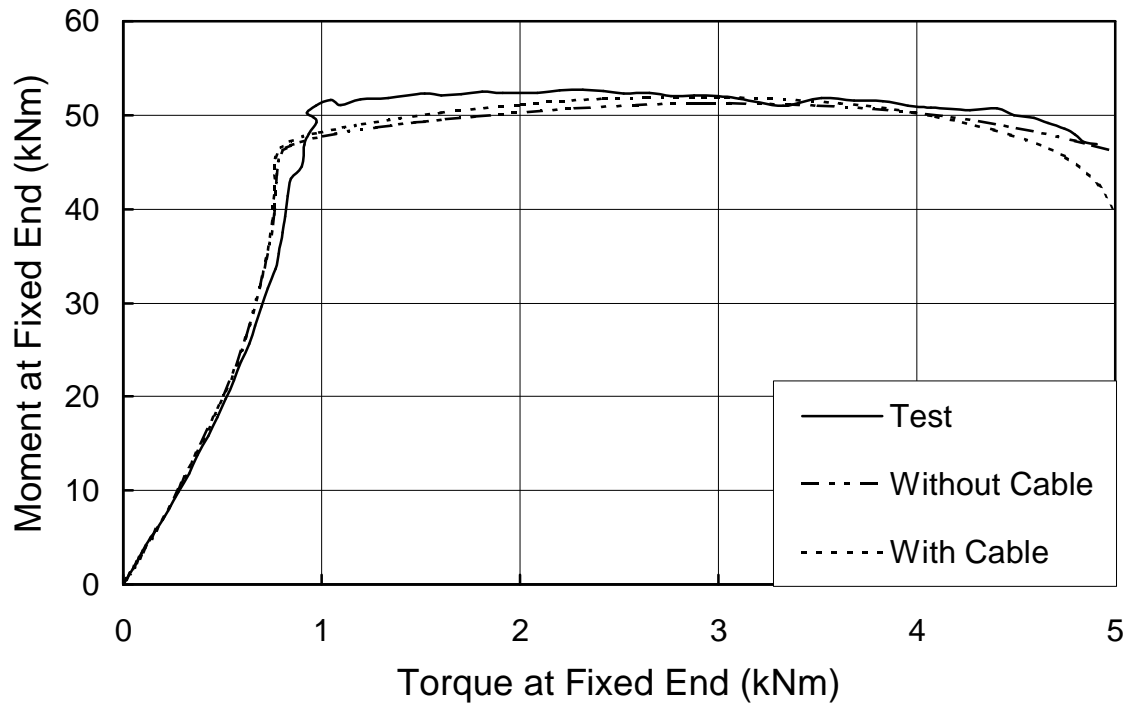


Figure 3.23 Moment at Fixed End vs. Torque at Fixed End for Beam 2 – Model Loaded With Cable

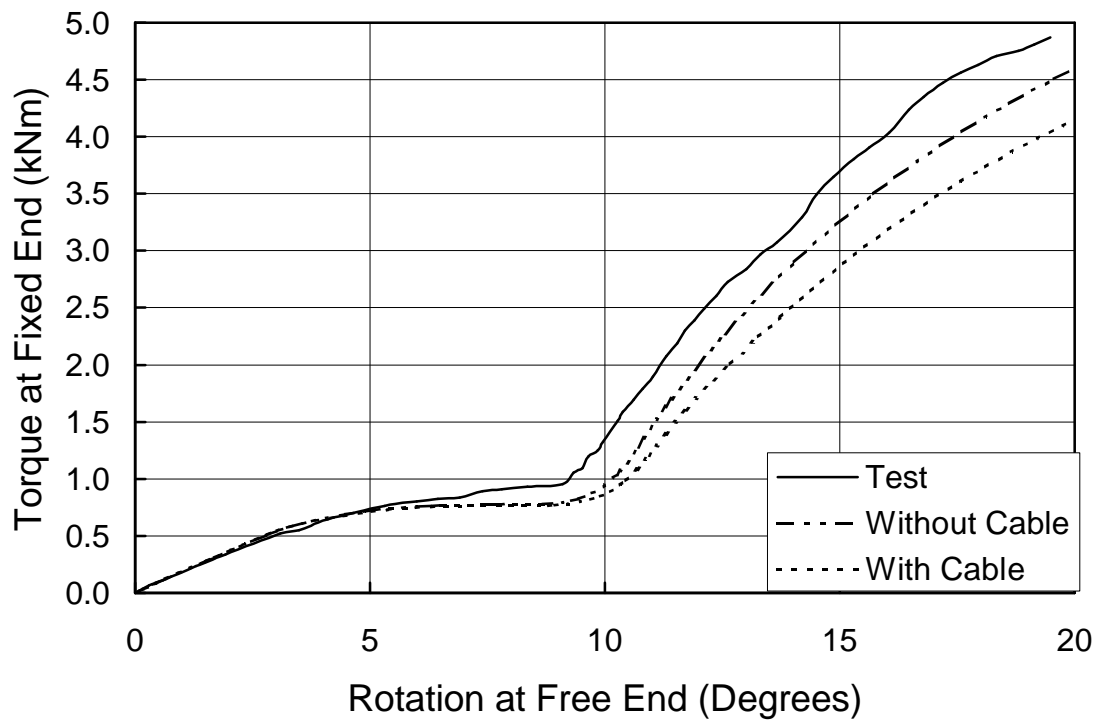


Figure 3.24 Torque at Fixed End vs. Rotation at Free End for Beam 2 – Model Loaded With Cable

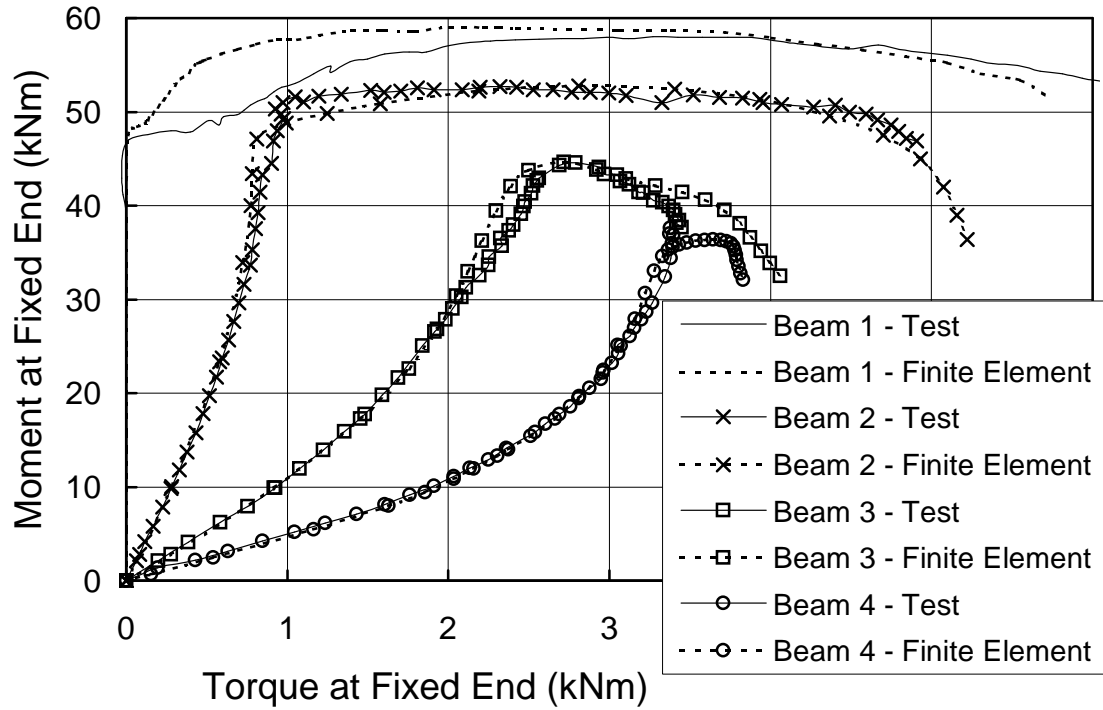


Figure 3.25 Moment at Fixed End vs. Torque at Fixed End

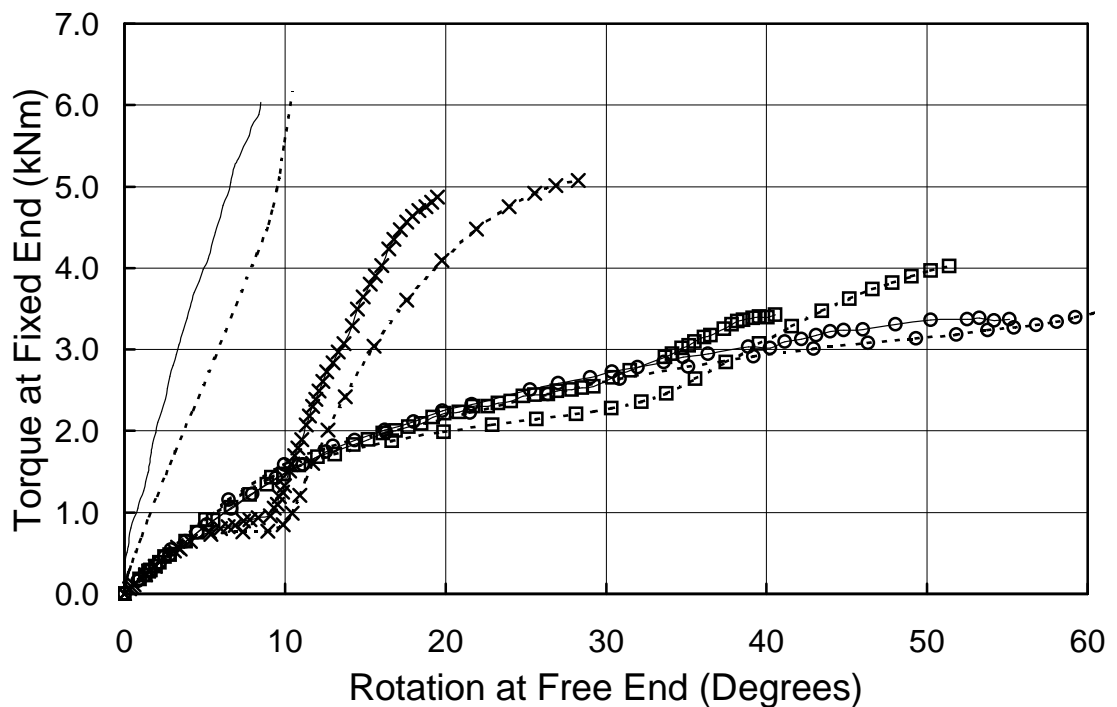
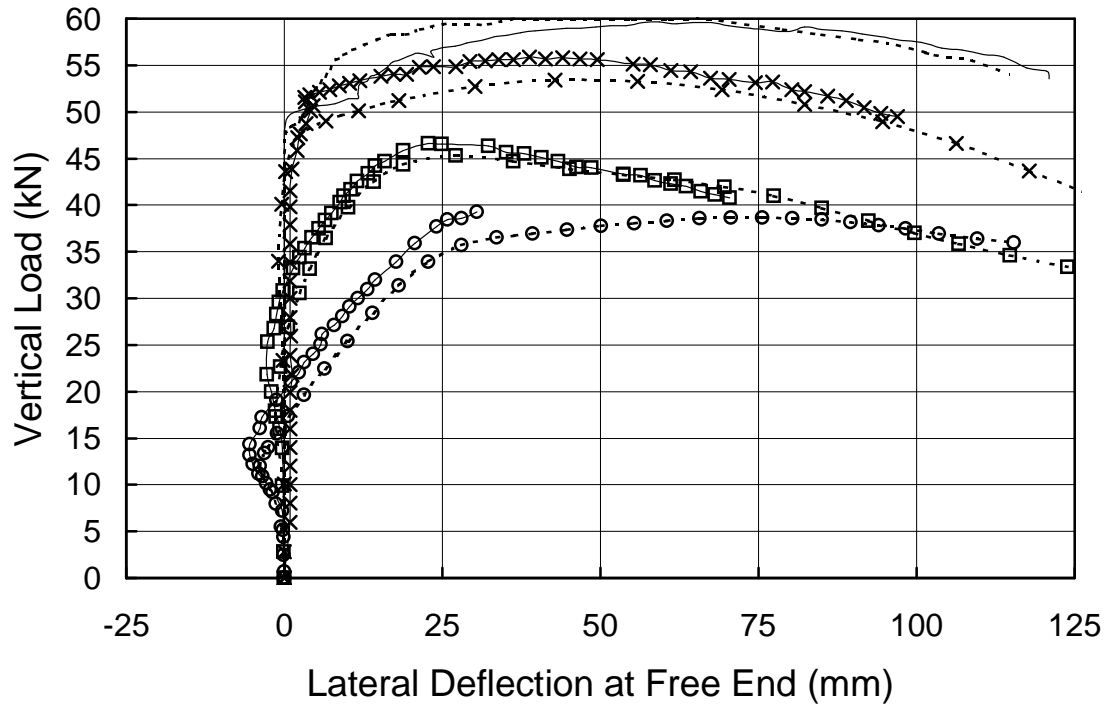
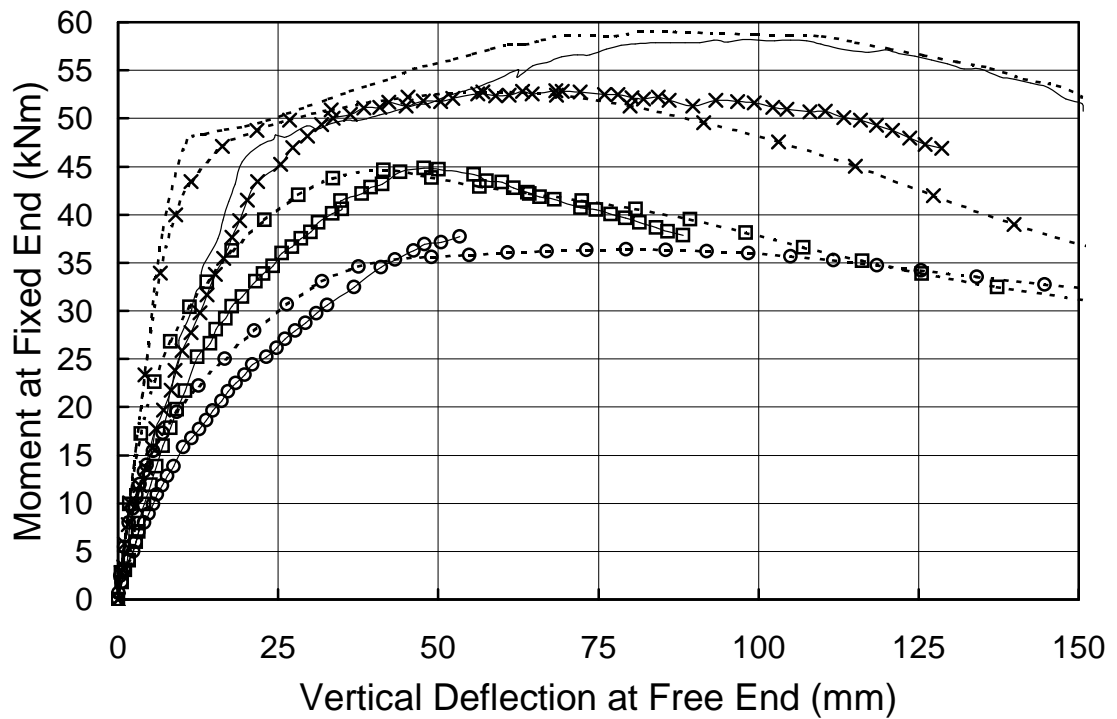


Figure 3.26 Torque at Fixed End vs. Rotation at Free End

Note: The Legend for Figure 3.26 is the same legend used in Figure 3.25.



*Figure 3.27 Vertical Load vs. Lateral Deflection at Free End*  
 Note: The Legend for Figure 3.27 is the same legend used in Figure 3.25.



*Figure 3.28 Moment at Fixed End vs. Vertical Deflection at Free End*  
 Note: The Legend for Figure 3.28 is the same legend used in Figure 3.25.

## **4 FURTHER DEVELOPMENT OF MODEL USING TESTS OF COMEAU (1998)**

The finite element model developed in the previous chapter is applied in this chapter to the experimental work of Comeau (1998), discussed in Section 4.1, to verify further that the model can predict beam behaviour accurately and to expand the model for use with built-up cross-sections made up of a channel (with toes down) welded to the top flange of a wide flange shape, as is often used for crane runway beams. Several features had to be added to the previously developed model to account for the varying thickness of the channel flanges, the built-up section, the welds between the two sections, and the boundary conditions (now simply supported). The generalized model is first compared to the experimental results of Tests 1 (uniform torsion) and 3 (pure flexure) to ensure that it can accurately predict the beam behaviour at both ends of the loading spectrum: torsion only and pure flexure. The finite element model is then evaluated against the results of Test 4, which included combined torsional and flexural loading. Test 2 (an elastic investigation for the purpose of determining the warping constant of the built-up section) was not used to verify the model because the experimental values of the warping constant were found to be different from the theoretical values determined by the original researchers by as much as 235%. It had no influence on the model.

### ***4.1 Experimental Description***

Comeau (1998) performed an experimental investigation into the behaviour of mono-symmetric rolled crane runway beams, each made up of a wide flange section topped by a rolled channel with the flanges pointing downward. These beams were exposed to combined bending and torsion considered typical of crane loads. The main variable investigated was the effect of a discontinuous weld between the two elements of the built-up section on the beam behaviour. Two beams with

simply supported boundary conditions were put through several tests, including combined torsional and flexural loading. The beams were composed of a C310x31 channel welded to the top flange of a W460x74 section made of 350W steel. The channel provides additional lateral support and strength to the compression flange, which otherwise would be vulnerable to lateral torsional buckling due to large spans that are typical of crane beams because of difficulties in providing lateral supports. Beam P1 had a continuous 6 mm fillet weld connecting the channel to the top flange of the wide flange section at both flange tips, and Beam P2 had 40 mm long intermittent 8 mm fillet welds spaced at 300 mm (centre-to-centre). The average weld length and spacing for Beam P2 was measured as 59 mm and 302 mm, respectively. This additional length of weld was a result of the 10 mm development length on each end of the discontinuous welds.

The two beams were each fabricated with a length of 14.9 m. A section 2.20 m long was cut from these two beams to determine the residual stresses and material properties. Residual stresses were determined for the individual beam cross-sections, including the channel and its web, using the method of sectioning. The residual strains were measured and then converted into residual stresses using the material properties of the beam. The residual stresses were reported by Comeau (1998) to have an estimated error of  $\pm 2$  MPa. The material properties were found using standard tension coupon tests. Based on three samples for each, stress vs. strain curves were developed for the channel web, I-section web, and I-section top flange. The top flange yield strength was found to be lower than the nominal value. The section geometry was measured and used to calculate the section properties using Part 7 of the CISC Handbook of Steel Construction (CISC, 2007) for the torsional properties.

Four tests were performed on each of these two beams. Several tests remained elastic so that no permanent strains developed in the beam to

allow them to be reused in other tests. These elastic tests were performed first on the 12.7 m long beams. Then, the two beams were each cut into two approximately 6 m long beams, creating two of each weld type (P1-A, P1-B, P2-A, and P2-B) and tested into the inelastic range of behaviour to their ultimate capacity.

Test 1 was an elastic uniform torsion test to calculate the torsion constant. Figure 4.1 shows a diagram of the experimental set-up for Test 1. The 12.2 m span beam was tested upside down so that the channel was on the bottom. The support at the left end was simply supported in flexure and torsion; that is, the end was prevented from rotating by supports at the two corners of the cross-section required to prevent rotation of the cross-section but warping was permitted. At the right end, the supports were simply supported in flexure about both the strong and weak axis and the section was free to rotate and warp. The flexure supports were applied at a single point on the bottom flange to ensure that free warping is allowed. At the right support, a channel was welded to the beam web near the top flange as a loading bracket. A gravity load composed of attached masses was connected to the loading bracket at an eccentricity of 400 mm to apply the torsional load without applying any flexural loads.

Test 3 was conducted to determine the elastic buckling load in pure flexure and the ultimate moment resistance of the cross-section. Figure 4.2 shows a diagram of the experimental set-ups for Test 3. The member was tested right side up with the channel on top. For the elastic tests, the vertical load was applied at the mid-span of a 12.2 m span selected to ensure that elastic lateral torsional buckling governed. Both ends were simply supported in flexure and torsion. Each end was supported on a small block to model a vertical support at a single point on the bottom flange while allowing free warping. The ends were prevented from rotating along the longitudinal axis by supports at the top two corners of the cross-section. Three elastic load cycles were performed for Beam P1 and

two for Beam P2. For the inelastic tests on Beams beams P1-B and P2-B (after cutting the beams, as described previously), the load was applied at two points 1.6 m apart centred on the beam spanning 5.94 m using a set of transfer beams to apply the load evenly. The boundary conditions were identical to the elastic test components except that all four corners of the cross-section were braced at both supports using HSS sections to prevent rotation.

In Test 4 the beam was loaded in combined biaxial bending and torsion. Figure 4.3 shows a diagram of the experimental set-ups for Test 4. Both the 5.94 m and 12 m beams were tested right side up with the channel on top and the beam. Initially, a small vertical load of 10 kN was applied downwards on top of the channel to ensure that the loading device was in contact with the beam prior to applying the lateral load. The lateral load was then applied to create torsion and weak axis bending, followed by a vertical load inducing strong axis bending. Test 4 had four separate elastic tests and two inelastic tests. For each 12 m beam (Beam P1 and P2), two elastic tests were run each with different lateral loads to determine the service longitudinal stresses and the elastic buckling load. The beams were then cut into the 5.94 m beams and then two beams, Beams P1-A and P1-B, were tested into the inelastic range by first applying a lateral load and then applying a vertical load until failure. The purpose of the inelastic tests was to determine the ultimate resistance in combined loading.

The end supports and beam span for the elastic experimental components of Test 4 were identical to those used in the elastic test component of Test 3. The vertical load was applied at mid-span and the two lateral loads were applied at a distance of 215 mm on each side of mid-span. The lateral loads were applied by cables attached to lateral load application brackets composed of HSS 89x89x6.4 sections welded to top

of the channel web. The two loads were applied at a height of 102 mm above the channel web.

Both end supports were simply supported in flexure and torsion in the inelastic tests as well. The ends were prevented from rotating by having supports at the two corners of the cross-section required to prevent rotation of the cross-section. The flexural pin supports were applied at a single point to allow free warping. Two vertical loads were applied at 800 mm on each side of mid-span in the same manner as for the inelastic component of Test 3. The lateral loads were applied using the same HSS sections as used in the elastic component, but welded to the top of the channel web at a distance of 918 mm on either side of mid-span.

#### **4.2 Description of Model**

The finite element model used here is based upon the model developed for the Driver and Kennedy (1987) tests, as described in Chapter 3. Rather than modelling the beam dimensions separately for Beams P1 and P2, since their cross-sections were nominally identical and the measured differences were small, the base model uses the average measured dimensions of the beams. Table 4.1 presents the nominal values, the individual measured values, and the average measured values, with the latter being used in the finite element model. The percent difference presented in this table represents the maximum difference between the actual and average measured values. The two fillet elements at each of the top and bottom of the web were modelled as 8.41 mm and 10.58 mm (closest to the flanges) thick. This provides the theoretical fillet area at the appropriate centroid, as described in Chapter 3.

The channel flange thickness varies over its width and the flange thickness  $t$  value presented in the Handbook of Steel Construction (CISC, 2007) represents the average thickness. It was found that modelling the channel flange thickness as an average value instead of directly modelling the

thickness variation influences the torsion results. Therefore, to model the cross-section accurately, the varying channel flange thickness is accounted for by using the average value at the centre of the flange width and an assumed slope of 1:6 to extrapolate the flange thickness to the various nodes over the flange width. Linear interpolation was used internally to determine the shell thickness between the nodes. This method neglects a small portion of fillet at the connection with the channel web (based on nominal dimensions, each of the two fillets have an area of  $13.1 \text{ mm}^2$ , which corresponds to 0.3% of the total cross-sectional area and 1.4% of the flange area) that is considered to be insignificant.

The cross-section was meshed in a similar manner to Mesh 2 described in Chapter 3. For the wide flange section, the flanges were divided into 16 elements and the web into 24 elements. The channel section was divided into 24 elements across the web and five elements over each flange. A typical mesh used in the model for Test 4 for Beam P1-A is shown in Figure 4.4. The node spacing of the middle 16 elements of the channel web was identical to that used in the adjacent wide flange section flange. This allows the flange tip nodes to align precisely with a line of nodes in the channel web to facilitate modelling the welds. The element lengths were selected to maintain an aspect ratio similar to that used in the model of the Driver and Kennedy (1987) specimens. Unlike the previous model, no bias was used to define the element length because the most critical section was not known *a priori*.

Selecting the element lengths proved challenging, as it was difficult to match the nodal locations with important locations along the beam such as boundary conditions, weld regions, and loading locations. By using an average element length of 30 mm with some smaller elements 15 mm long, nodes were defined at all required locations along the beam length. In the wide flange section, the flange element width is 12.0 mm, resulting in aspect ratios of these elements ranging from 1.25 to 2.50. For the web

elements of the wide flange section, the element width is 20.1 mm, resulting in aspect ratios ranging from 1.36 to 1.47. In the channel section, the flange element width is 13.4 mm, making the aspect ratio range from 1.12 to 2.25. Likewise, for the web elements of the channel section, the aspect ratio ranges from 1.18 to 2.35 for an element width of 12.8 mm. Due to the beam lengths, the number of elements increased substantially from the model of the previous chapter, nearing 20 000 for the 6 m beam and 37 000 for the 12 m beam. To ensure that web crippling or buckling did not occur at the supports due to the concentrated reactions, the ends of the beam were extended 150 mm—or five elements—beyond the support locations.

Since the maximum moments achieved in the tests for the two welding patterns are not significantly different, the cross-sectional area of the welds connecting the channel and wide flange section was deemed to not be critical to the flexural capacity of the beam. It is far more critical to model the connection properly so that the two members behave compositely. Because the weld area between the channel section and the wide flange section represents only a small portion of the area of the flange section (1.1% for an 8 mm fillet weld compared to 2.7% for the portion of the fillets in the models presented in Chapter 3), the welds were not directly incorporated into the finite element model. The wide flange and channel sections were attached together using Rigid Beam Multi-Point Constraints (MPC), which create a fictitious rigid beam between any two nodes by constraining the displacement and rotation about all axes (Hibbitt *et al.*, 2002). The welds for Beam P1 were provided over the entire length of the beam. The welds for Beam P2 were modelled as 60 mm in length with a centre-to-centre spacing of 300 mm. Instead of using the prescribed (nominal) weld length of 40 mm, a weld length of 60 mm was used because the average measured weld length is 59 mm. The welds for Beam P2 were centred about the mid-span of the beams to ensure symmetry along the beam length. Using MPC proved to be an effective

means of modelling the welds, while ensuring numeric stability and convergence.

The material properties are based on the experimental engineering stress vs. strain curves reported by Comeau (1998). Similar to the material properties used in modelling the Driver and Kennedy's (1987) tests, six-part linear piecewise representations of each of the two average curves, one for the P1 beam and one for the P2 beam, are used in the model. It is assumed that beyond ultimate, the ultimate stress can be carried for an infinite strain, so material rupture is a failure mode not included in the model. The six points used are the origin, first yield, onset of strain hardening, two points along the strain hardening curve, and ultimate stress, as presented in Table 4.2.

Three different material curves are developed, one for each of the wide flange section flange and web and the channel web. Each curve is based on the average of three uniaxial tension coupon tests. The material properties for the channel flange, although not measured, are modelled using the same curve as for the channel web. The engineering stress and strain values are then converted into true stress and strain for use in the finite element model. From the experimental data, the values of  $E$  were found to be unrealistic and highly variable, ranging from 80 000 to 160 000 MPa, considerably different from the expected value of approximately 200 000 MPa. In the finite element model, an assumed value of 200 000 MPa is used and the yield strain is adjusted to correspond with the appropriate measured yield stress.

The residual stresses were determined using the method of sectioning (Galambos, 1998). These are input into the model using the method described in Chapter 3. After the equilibrium step, the equilibrated residual stresses agreed well with the experimental values at the mid-span and at the support locations, despite some minor dissipation near each

support. The measured and modelled residual stress distributions for both beams post-welding are shown in Figure 4.5 through Figure 4.10. Figure 4.11 through Figure 4.16 show the measured, modelled, and equilibrated residual stresses from Beam P1-A analysis. The residual stresses are measured at the supports that are located 150 mm from the free edge of the beam. It can be seen from these figures that the modelled residual stresses become quite large at the flange tips of the wide flange section, nearing the yield value. These large values are a result of the welding process where the residual stresses would be expected to approach the yield stress. As seen in Figure 4.16, the equilibrated residual stresses for the channel flanges do not agree as well with the test or modelled results. The slope of the equilibrated mid-span results matches well although the magnitudes are reduced. The lack of agreement results from the modelled residual stresses not being in equilibrium. This initial equilibrium step in the analysis allows these residual stresses to equilibrate prior to applying any loads to the beam.

Although initial out-of-straightness was not directly accounted for in the model, the method of inputting residual stresses has the effect of introducing some initial imperfections in the model. Since the input stress distribution is unbalanced from left to right, in the initial stage of the analysis, which allows the residual stresses to equilibrate, the beam deflects laterally as the stresses redistribute. The larger initial imperfections in the finite element model compared to the actual measured values in the test (these are quantified in coming sections) may lead to some error in the finite element results. To ensure that no uncontrolled imperfections arise in the parametric study due to this method of introducing residual stresses, a balanced residual stress pattern must be used with the initial imperfections in the form of lateral and vertical deflections input separately to provide worst-case scenarios at the permissible limits.

### 4.3 Test 1 – Uniform Torsion

A detailed description of the test can be found in Section 4.1. Figure 4.1 presents a diagram of the test set-up. The loading bracket, a C200x17 channel, is modelled using shell elements assumed to remain elastic, with a modulus of elasticity,  $E$ , of 200 000 MPa. The dimensions of this channel,  $d$ ,  $b$ ,  $w$ , and  $t$ , are 200.5, 62.8, 5.60, and 9.90 mm, respectively, and are selected to match existing node locations on the beam web at the section where the two members are connected. Their respective differences, as compared to the nominal values, are  $-1.3\%$ ,  $10.2\%$ ,  $0.0\%$ , and  $0.0\%$ . As shown in figure 4.14, the test beam was inverted in the test set-up and the position of the load point was at 400 mm from the centroid of the wide flange section and 89 mm from the bottom of the channel web. Since the beam rotation at the end of the test was only five degrees, it was assumed during the analysis of both the experimental and finite element data that the load eccentricity remained constant constant, i.e., neglecting the effect the rotation has on reducing the effective eccentricity (moment arm) in calculating the applied torque. To prevent one end from rotating, the two corners of the built-up cross-section (one flange of channel and the opposite tip of the bottom flange) required to prevent rotation of the cross-section were restrained laterally in the Z-direction. At the end where the section is free to rotate, the point of support on the bottom of the channel web is free to rotate in all directions but restrained from translation in the X-(longitudinal) and Y-(vertical) directions.

The load vs. rotation diagrams are used to calculate the effective torsional constant,  $J$ , to compare the finite element and test results. The rotation presented is the relative rotation between mid-span and a section 1 000 mm from the left support. Both the finite element and test results were linear, as the behaviour was elastic and the second order effects

were negligible. The values of  $J$  are calculated using the slope,  $m$ , of the load vs. rotation diagram according to the following equation:

$$J = \frac{mL_{BC}e}{G} \quad [4.1]$$

where  $L_{BC} = 5\,100$  mm is the length between the two sections where the relative rotation is being measured and  $e$  is the load eccentricity, equal to 400 mm. The shear modulus of elasticity is assumed to be 77 000 MPa. Figure 4.17 and Figure 4.18 present the load vs. rotation diagrams for Beams P1 and P2, respectively, comparing the finite element to the test results. The finite element results are slightly stiffer than the test results for both beams, but the agreement is excellent, as seen in Table 4.3. The theoretical results were calculated based on Part 7 from the CISC Handbook of Steel Construction (CISC, 2007). For Beam P2, the theoretical results are based upon an effective weld length of 59 mm.

#### **4.4 Test 3 – Pure Flexure**

In the pure flexure test, the load was applied directly to the top of the channel at the loading points, as described in Section 4.1. Figure 4.2 shows a diagram of the test set-up used for the 12 m beam and the 6 m beam. In the finite element model, all four corners of the cross-section were restrained from deflection in the Z-direction at the simple supports to prevent rotation. These lateral restraints were provided over the entire height of the channel flanges and flanges of the wide flange section. The flexural supports were applied to the bottom flange of the wide flange section at a single point at each end. The left support was modelled as a pin (fixed in all three directions against translation, but free to rotate about the Y and Z-axes) and the right support (a roller) was free to rotate in all directions but fixed in the Y and Z-directions against translation.

It was found that during loading the channel web deflected and protruded through the top flange of the wide flange section. A bearing/contact

surface was then defined over the entire length of the beam between the bottom of the channel web and the top of the top flange so that only compressive stresses could be transmitted. The surfaces were defined as element-type surfaces so that the outer faces of the shell elements act as the surface so that the surfaces are initially in contact.

In analyzing the modified model (with contact), ABAQUS had difficulties establishing the correct surface due to small numerical imperfections that caused the surfaces to be initially overlapping slightly. These imperfections were corrected by adding a gap initially between the two surfaces that is closed during the analysis, although modelling a contact surface required large computational effort. To reduce the demand on the finite element model, the contact surface was removed and the load is applied to the top flange of the wide flange section instead of the top of the channel web. This lowers the point of load application approximately 11 mm along the Y-axis. As the section rotates, the load is applied at a slightly different eccentricity with respect to the shear centre. Since the beam does not develop significant rotations until after buckling, this effect is considered negligible since post-buckling behaviour is not important for the pure flexure validation of the model. Nevertheless, even at a rotation of 90 degrees, this error is less than 5% for a W460x74 beam. The test results from Comeau (1998) used for comparison with the finite element model are the load vs. vertical deflection at loading points and the load vs. lateral deflection at mid-span diagrams. For the 6 m beams, the load was applied at two points and the load was reported as the total of the two loads applied to the beam. For the 12 m beams, the load was applied at single point. For both the 12 m and 6 m beams, this simplified method is effective in modelling the behaviour of the beam without increasing the computational effort required. Thus, it is used in the finite element model from this point forward.

#### 4.4.1 12 m Beams

For the 12 m beam elastic tests, only the third load cycle for Beam P1 and the first load cycle for Beam P2 are considered here. For this load cycle for Beam P1, an initial lateral sweep of 6.54 mm was introduced in the experiment to help force lateral torsional buckling, since previous cycles did not show indications of this phenomenon. This initial lateral sweep was not introduced in the finite element analysis. It appeared that buckling was just beginning at the end of the test for Beam P2. The finite element and test results are compared in Figure 4.19 through Figure 4.22, which present the load vs. vertical deflection at mid-span and the load vs. lateral deflection at mid-span diagrams for both beams.

Significant discrepancies between the test results and the finite element analysis results are observed. In the load vs. vertical deflection diagrams (Figure 4.19 and Figure 4.21), the model has a reduced slope, especially for Beam P1. This might be influenced by lateral displacements and rotations that tend to soften the beam for vertical deflections, although there is likely another unknown underlying cause to this discrepancy. Also, the neglected area of the weld material as a result of the conclusions of Comeau (1998) may be partially responsible for the disagreement, even though this difference is expected to be negligible. Figure 4.20 and Figure 4.22, the load vs. lateral deflection diagrams, indicate that the model is undergoing significant lateral displacement, as expected by theory, however, the presence of initial imperfections prevents classical bifurcation buckling from being observed. In the experiment, the beams do not appear to buckle laterally, even with an additional forced lateral imperfection of 6.54 mm for Beam P1.

Although the measured maximum lateral sweep for the 12 m beams is up to 9 mm ( $L/1350$ ) for Beam P1 and only 2 mm ( $L/6100$ ) for Beam P2, the maximum lateral sweep in the model is about 16 mm ( $L/750$ ) for Beam P1 and 10 mm ( $L/1200$ ) for Beam P2. These imperfections were

not removed from the model. The imperfections arising from the application of the residual stresses are significantly different than the actual measured imperfections. These increased initial imperfections may explain some of the discrepancy between the test results and the finite element analysis results. The model imperfections are at or beyond the fabrication allowances for this beam for lateral sweep of  $L/1000$  from ASTM A6 / A6M (ASTM, 2001), as presented in the Handbook of Steel Construction (CISC, 2007). The severe initial imperfections used in the finite element model soften the beam's behaviour and accelerate the lateral deflection, as seen in the analysis results.

#### **4.4.2 6 m Beams**

A comparison between the test results and the results from the finite element analysis for Beam P1-B are found in Figure 4.23 and Figure 4.24 and for Beam P2-B in Figure 4.25 and Figure 4.26. Good agreement is observed between the test results and the analysis results. For Beam P1-B, the maximum capacity predicted from the finite element analysis is 674 kN at a vertical deflection of 134 mm, a difference of -3.6% and -5.0%, respectively, as compared to the test results. For Beam P2-B, the predicted maximum load is 668 kN at a vertical deflection of 118 mm, a difference of -4.3% and 9.2%, respectively, as compared to the test results. Both beams fail as the plastic moment develops and the beam buckles laterally. In both beams, the peak load predicted by the finite element analysis is slightly lower than observed in the test. The finite element results are in very good agreement with the theoretical capacity, the plastic moment of the combined section, of 676 kN for both beams with differences of only -0.4% and -1.2% for Beams P1-B and P2-B, respectively. The differences between the test and finite element results may be caused by the differences in initial imperfections or from neglecting the weld material in the finite element model. As for the lateral deflection diagrams, the model predicts the load at which the beam buckles laterally

relatively well. Beam P2-B has greater lateral deflections in the finite element results than in the experimental results. Some of the discrepancy may be a result of the initial imperfections induced by the residual stresses not corresponding to those measured on the test specimen.

The effect of initial imperfections is not as critical for the 6 m beams since the beam fails by the formation of a plastic hinge. Here, the measured maximum lateral sweep is 3 mm ( $L/2000$ ) for Beam P1-B and 2 mm ( $L/3000$ ) for Beam P2-B, compared to the finite element lateral sweep (induced by the residual stresses) results indicating a maximum for Beam P1-B of 3.8 mm ( $L/1550$ ) and 2.5 mm ( $L/2400$ ) for Beam P2-B. Overall, the model and test results for the 6 m beams are in excellent agreement. Unlike the results of the previous section where some of the discrepancy between the finite element analysis and the test results for the 12 m beams results from the severe initial sweep used in the finite element model, the imperfections of the 6 m beams are in good agreement with the measured values. The better agreement for the shorter beams may be due to the fact that the finite element analysis model is not able to predict the failure mode for the long beams. However, the 6 m beams are a more important measure of the ability of the model to predict the behaviour of the test results, as it better represents the actual test conditions (i.e. the lateral imperfections) and predicts the entire range of behaviour including the inelastic range.

#### **4.5 Test 4 – Combined Torsion and Biaxial Bending**

To tie the loading brackets directly to the finite element mesh of the beam, the HSS 89x89x6.4 section loading brackets are modelled with S4R shell elements with outside dimensions of 90 mm by 96 mm and a thickness of 4.95 mm to maintain the appropriate section modulus. The elements are assumed to remain elastic, with an elastic modulus of 200 000 MPa. The finite element model for this test uses the previous modifications, including applying the load to the top flange of the wide flange section. For both the

6 m and 12 m beam finite element models, the boundary conditions matched the restraint provided in the tests, restraining the two corners of the cross-section required to prevent rotation at the supports. For the channel, this restraint is applied over the entire height of the channel flange. The flexural supports are identical to those used in Test 3. A more detailed description of the test can be found in Section 4.1. Figure 4.3 presents a diagram of both test set-ups.

#### **4.5.1 12 m Beams**

The vertical load versus vertical deflection at mid-span and vertical load versus lateral deflection at mid-span curves for the test and finite element results for the 12 m elastic tests are shown in Figure 4.27 through Figure 4.34. The vertical deflection at mid-span was measured by two Linear Variable Displacement Transducers (LVDTs), LVDT1 and LVDT2, at two points 400 mm apart on a transverse bar connected to the bottom flange of the cross-section. The average of the two LVDTs represent the vertical deflection whereas the difference between these two vertical deflections indicates a torsional rotation at mid-span. The vertical load vs. lateral deflection diagrams (Figure 4.28, Figure 4.30, Figure 4.32, and Figure 4.34) show good agreement between the model and the test results for both stages of loading, lateral and vertical, applied in that order. The lateral load develops a torque and a weak axis bending moment. The good agreement in the lateral load step is shown in Table 4.4, where the average difference between the lateral deflections at the end of this step is only 2.0%. Looking at the vertical load vs. vertical deflection diagrams for both beams (Figure 4.27, Figure 4.29, Figure 4.31, and Figure 4.33), it can be seen that the finite element model captures the effect of the initial lateral load on the beam. The differences in the LVDT 1 and 2 readings indicate a rotation of the cross-section that develops from the torsion induced by the lateral load. The test beam did not deflect vertically as much as the finite element model. In the vertical load step, the finite

element model rotates slightly less than the test beams. Despite this difference, the finite element model predicts the behaviour of these complex tests well.

To avoid modelling the bar to which the LVDTs are attached, which was wider than the bottom flange, the vertical deflection values are found at the edges of the bottom flange and then extrapolated using similar triangles based on the rotation of the cross-section. This may introduce some discrepancy into the finite element values if there is any cross-sectional distortion. Another possible source of discrepancy is the difference of torsional support stiffness between the test and the numerical model. Although the test support stiffness had a finite stiffness, the supports used in the finite element model were infinitely stiff. This difference in stiffness may explain why the beam rotates more in the tests. The greatest source of error is likely the larger initial imperfections in the model due to the residual stress input. The increased initial imperfections may soften the beam response. Also, the lateral load is applied by means of a cable, which would tend to restrain the section from deflecting downwards during vertical loading. This effect was not included in the model.

#### **4.5.2 6 m Beams**

The important diagrams for comparison purposes are the vertical load vs. vertical deflection at the vertical load application points (LVDT 4 and LVDT 5), the vertical load vs. vertical deflection of LVDT 1 and LVDT 2 at mid-span (as per the 12 m beams), and the vertical load vs. lateral deflection at mid-span. The LVDT set-up at mid-span is the same as for the experiments in combined torsion and flexure on the 12 m beams. The initial lateral and final vertical load steps are modelled explicitly. The modelled beams for P1 and P2, although predicting the slope of the initial linear elastic behaviour well, fail at a load about 40% higher than the peak test loads. The theoretical capacities presented in Comeau (1998) are significantly larger than the test results and significantly below the finite

element results, as seen in Table 4.5. The discrepancy is clear in the model results for both beams seen in Figure 4.35 to Figure 4.40. The finite element models do not deflect or rotate as observed in the tests during the initial lateral loading step, which, in turn, affects the vertical load step results.

It is possible to speculate that there was a problem with the test and its results since the finite element model developed here has shown good agreement with all other experimental results. However, the report by Comeau (1998) does not discuss or record any experimental problems making it impossible to confirm any hypothesis made. Prior to the lateral load, a small vertical load was applied in the experiment to ensure proper contact is maintained between the vertical load application apparatus and the beams. It is possible that this initial vertical load was not effective in forcing and maintaining contact between the vertical loading device and the beam allowing the surfaces to slip during the lateral loading phase. If this slip occurred, the beam would undergo a sudden rotation and lateral deflection as the same 10 kN load (applied in the test to develop contact between the beam and the vertical load application apparatus) is applied to the suddenly rotated section causing a “second order” effect. This effect would amplify the rotation and deflection of the cross-section possibly explaining the discrepancy of the model results. This would apply a larger weak axis moment due to the larger rotation and reduce the beam capacity. Including this initial vertical loading had very little effect on the results.

Because of the many uncertainties existing for this test, further investigation is carried out. A lateral load of 9 kN is applied at an eccentricity of 231 mm, creating a torque of 2.07 kNm. As a result of the torsional boundary conditions, the torque is constant between the points of lateral load application and the supports while there is no torque between these two loading points. According to Driver and Kennedy (1989), a

W460x74 section has a pure (St. Venant) torsion resistance of 14.8 kNm calculated using the sand heap analogy. Furthermore, the beam should be able to carry its full moment capacity at the applied torque of 2.07 kNm. However, the test results indicate that the beam loses about 35% of its flexural capacity for Beam P1 and 40% for Beam P2.

These beams were loaded in biaxial bending as the lateral load develops a weak axis bending moment of 17.9 kNm. This represents only 18.8% of the wide flange section's weak axis bending resistance of 94.9 kNm (determined as the plastic moment about the weak axis for the Class 1 wide flange section only). Looking at the built-up section, considered to be Class 3 because of the channel section, the weak axis bending moment resistance based on the measured dimensions is 164 kNm (determined as the yield moment about the weak axis of the built-up section). The applied weak axis moment was approximately 11.9% of its capacity. The pure torsion resistance of the section is also increased by the presence of the channel. According to the finite element model, the strong axis bending capacity is reduced by 10.2% for Beam P1 and 10.7% for Beam P2. It is not practical that such small torques and weak axis moments would reduce the strong axis bending capacity of the section by such a significant amount as indicated by the test results.

The test results show an irregularity for both Beams P1 and P2 at a vertical load of 200 kN and 150 kN, respectively. For Beam P1, there is a sudden drop in the vertical deflection at the loading points and mid-span as well as a small drop in the lateral deflection. This sudden drop in vertical and lateral deformation at mid-span is larger for Beam P2, although the abrupt change in vertical deflection at the loading points is barely noticeable. Comeau (1998) did not discuss this anomaly in his results although it was not very noticeable since his data points were not connected using lines. These results seem to indicate that a problem occurred during the tests.

It is possible that the beam slipped at one of the supports in the test set-up. There was a problem with the supports for Beam P2-B in Test 3 that required all four corners of the cross-section at the supports to be restrained laterally instead of just the top two corners. In Test 4, only two corner restraints were required to prevent rotation instead of four corner restraints used for Test 3, creating a potential problem similar to what occurred in Test 3.

Without any experimental evidence to confirm what, if anything, actually occurred, it is very difficult to determine the effect any possible problems may have on the results. The model has had strong agreement with the test results for twelve different experimental tests up to and including the 12 m beams subject to combined flexure and torsion. The two 6 m beams investigated in Test 4 are the first test results that the model appears to have serious agreement problems. Possible explanations are available for this discrepancy leading to a belief that the finite element model is predicting the appropriate behaviour and there may be problems with the experimental results for the 6 m beams subject to combined loading.

Table 4.1 Nominal and Average Cross-Sectional Dimensions

Member	Property	Nominal Value (mm)	P1 Beam (mm)	P2 Beam (mm)	Average Value (mm)	% Difference
<b>W460x74</b>	<i>w</i>	9	8.1	8.6	8.4	-3.6
	<i>b</i>	190	192.9	191.8	192.4	-3.1
	<i>t</i>	14.5	14.6	14.9	14.8	-1.4
	<i>d</i>	457	456.0	456.0	456.0	0.0
<b>C310x31</b>	<i>w</i>	7.2	7.2	7.2	7.2	0.0
	<i>b</i>	74	74.0	73.6	73.8	±0.3
	<i>t</i>	12.7	13.3	13.3	13.3	0.0
	<i>d</i>	305	307.0	308.0	307.5	±0.2

Table 4.2 Modelled Engineering Stress vs. Strain Curves

Point	Wide Flange Section Web		Wide Flange Section Flange		Channel Web	
	Strain	Stress (MPa)	Strain	Stress (MPa)	Strain	Stress (MPa)
<b>First Yield</b>	0.0019	389	0.0017	335	0.0019	375
<b>Onset of Strain Hardening</b>	0.0298	393	0.0175	335	0.0215	388
<b>Point 1</b>	0.0631	441	0.0479	395	0.0398	445
<b>Point 2</b>	0.0881	459	0.0754	423	0.0916	495
<b>Ultimate</b>	0.1610	468	0.1420	442	0.1630	507

Table 4.3 Comparison of Finite Element, Theoretical, and Experimental Results for Test 1

Beam	<i>J</i> (mm <sup>4</sup> )			% Difference	
	Theoretical	Test	Finite Element	Finite Element to Theory	Finite Element to Test
<b>P1</b>	1 120 000	1 050 000	1 130 000	0.8	6.6
<b>P2</b>	810 000	915 000	959 000	15.5	4.6

*Table 4.4 Comparison of Lateral Deflections from Lateral Loading*

<b>Beam</b>	<b>Load Cycle</b>	<b>Test (mm)</b>	<b>Model (mm)</b>	<b>% Difference</b>
<b>P1</b>	1	20.7	21.3	2.9
	2	30.9	31.2	1.0
<b>P2</b>	1	21.2	21.2	0
	2	29.8	31.0	4.0

*Table 4.5 Comparison of Finite Element, Theoretical, and Experimental Peak Load Results for Test 4*

<b>Results</b>		<b>Peak Load (kN)</b>	
		<b>P1-A</b>	<b>P2-A</b>
<b>Test</b>		455	422
<b>Theory</b>		520	515
<b>Finite Element</b>		628	623
<b>% Diff.</b>	<b>Test to Theory</b>	-12.5	-18.1
	<b>Finite Element to Theory</b>	20.8	21.0

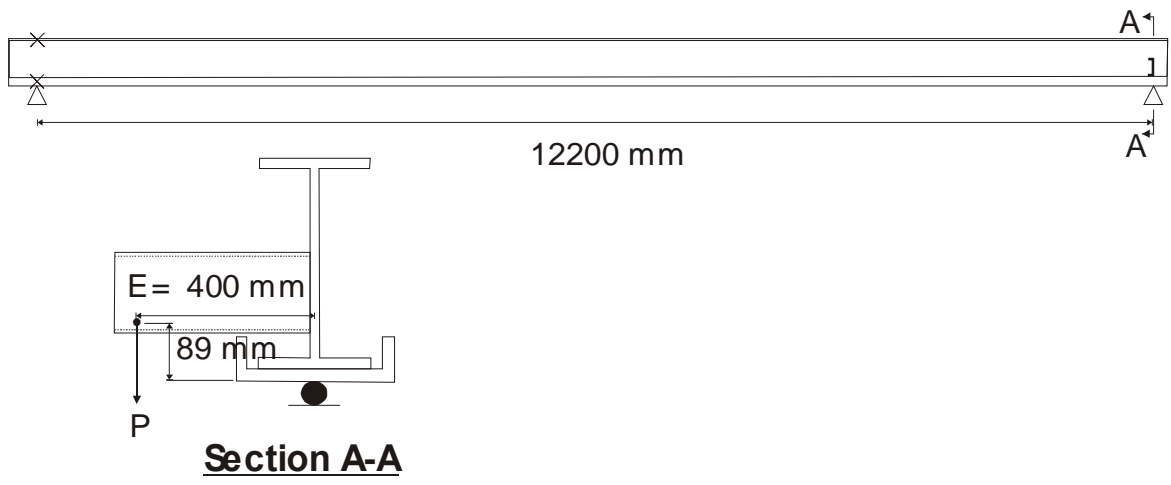
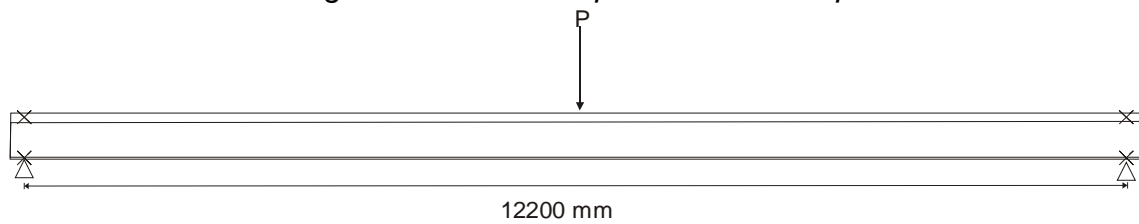
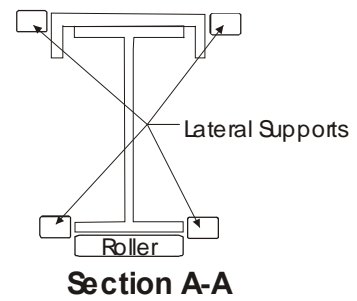
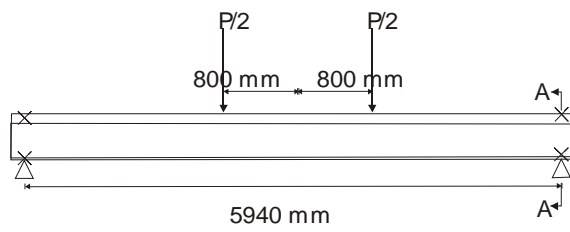


Figure 4.1 Test 1 Experimental Set-Up

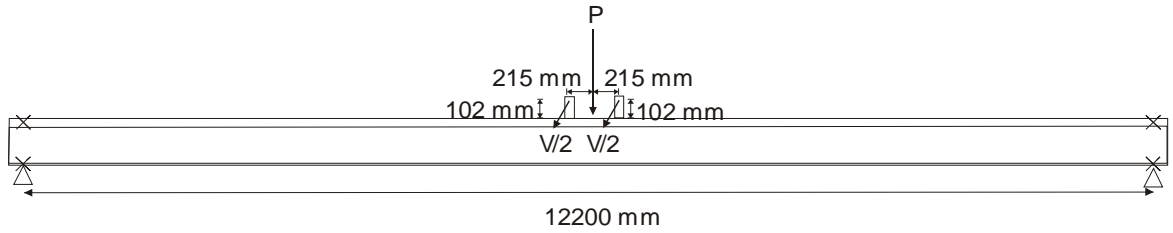


**A) 12 m Beam**

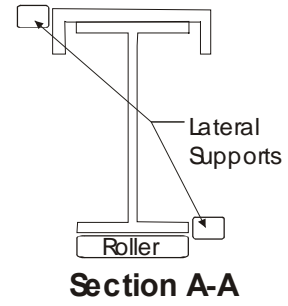
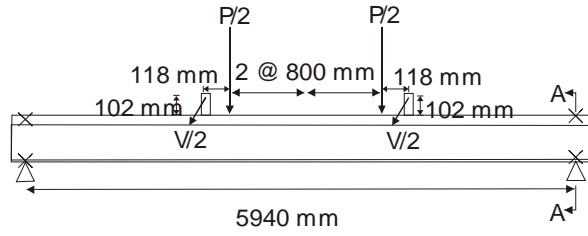


**B) 6 m Beam**

Figure 4.2 Test 3 Experimental Set-Ups



**A) 12 m Beam**



**B) 6 m Beam**

Figure 4.3 Test 4 Experimental Set-Ups

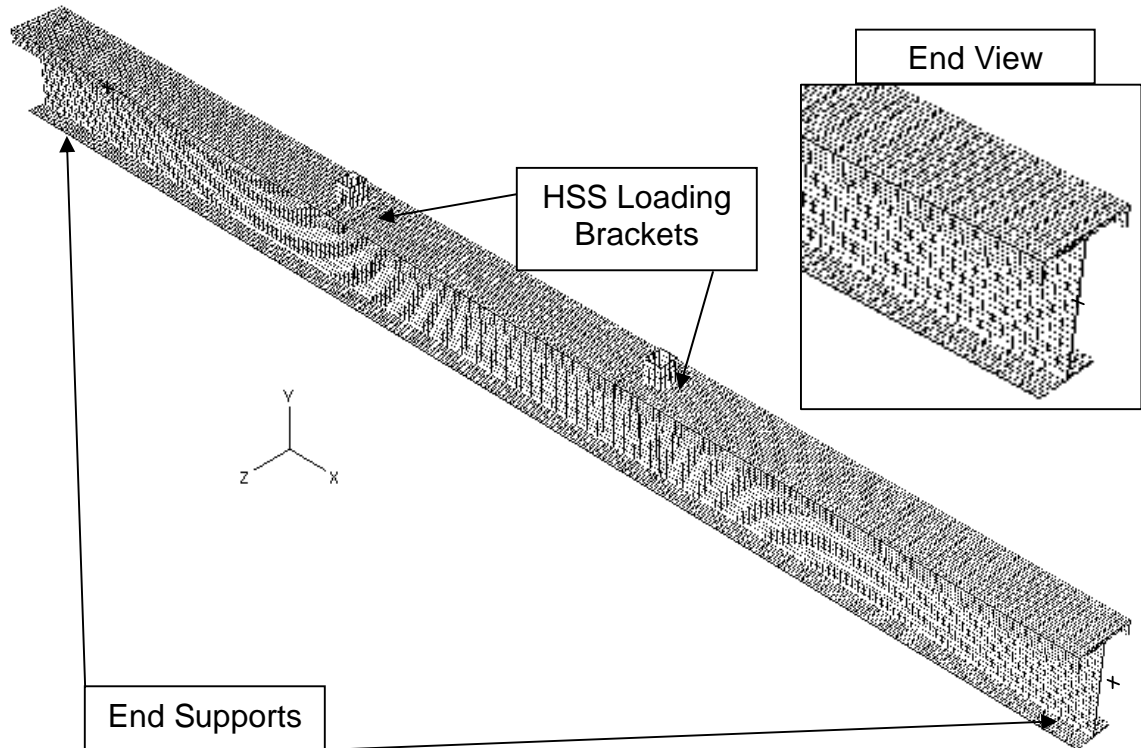


Figure 4.4 Mesh for Beam P1-A for Test 4

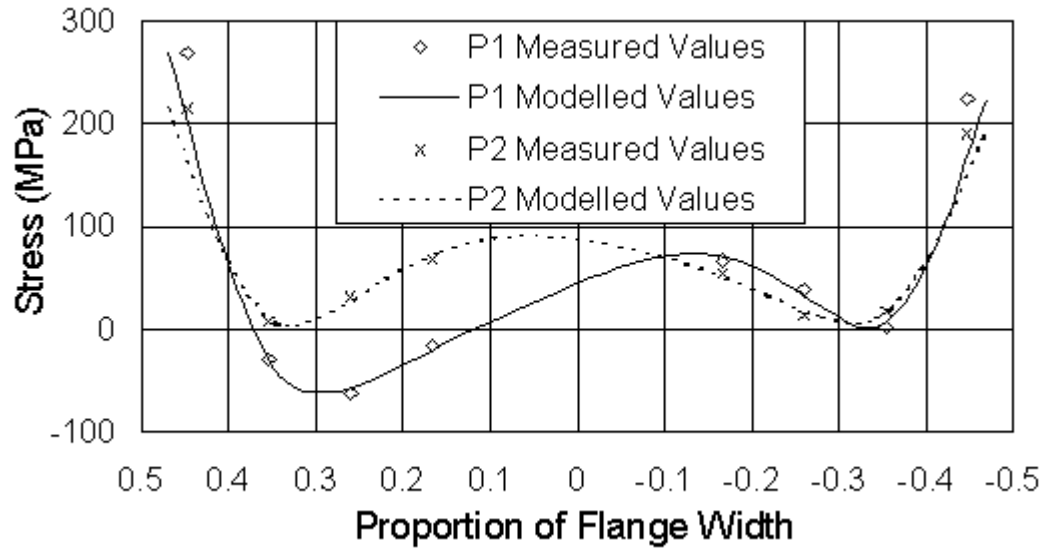


Figure 4.5 Comparison of the Measured and Modelled Residual Stress Pattern for Both Beams for the Top Flange of the Wide Flange Section

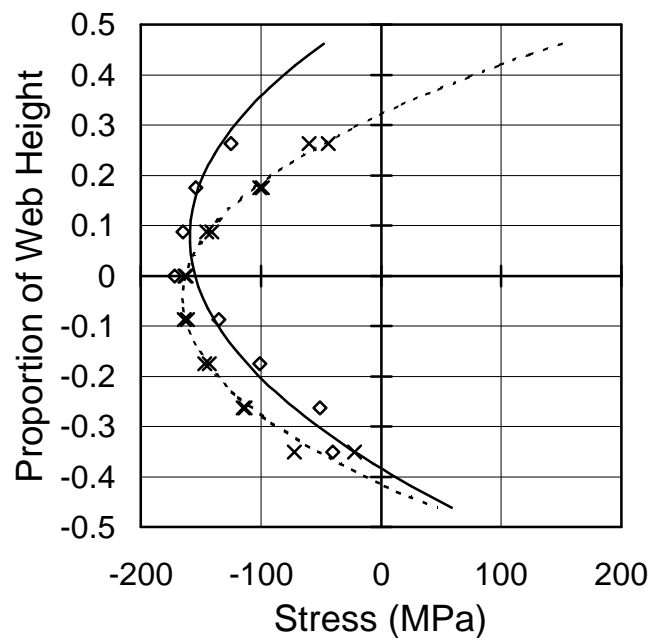
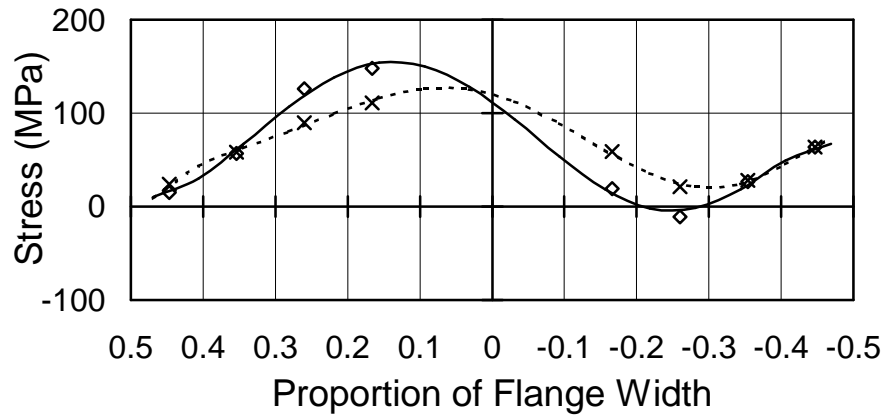


Figure 4.6 Comparison of the Measured and Modelled Residual Stress Pattern for Both Beams for the Web of the Wide Flange Section

Note: The Legend for Figure 4.6 is the same legend used in Figure 4.5.



*Figure 4.7 Comparison of the Measured and Modelled Residual Stress Pattern for Both Beams for the Bottom Flange of the Wide Flange Section*

Note: The Legend for Figure 4.7 is the same legend used in Figure 4.5.

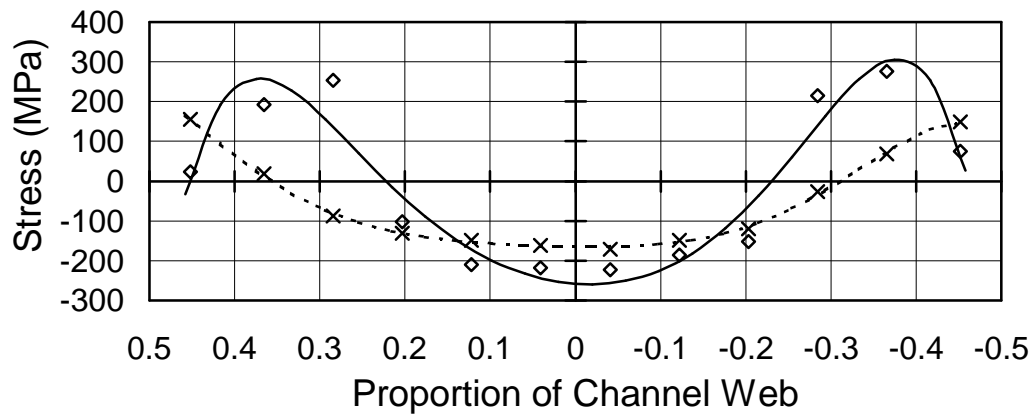


*Figure 4.8 Comparison of the Measured and Modelled Residual Stress Pattern for Both Beams for the Channel Web*

Note: The Legend for Figure 4.8 is the same legend used in Figure 4.5.

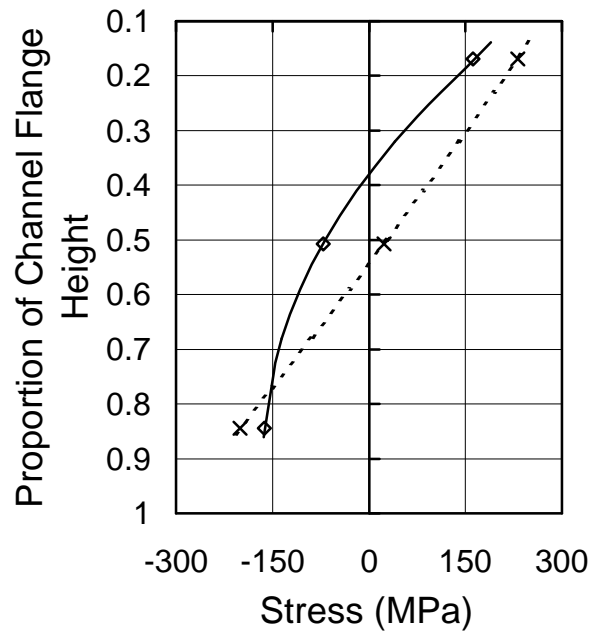


Figure 4.9 Comparison of the Measured and Modelled Residual Stress Pattern for Both Beams for the Channel Left Flange

Note: The Legend for Figure 4.9 is the same legend used in Figure 4.5.

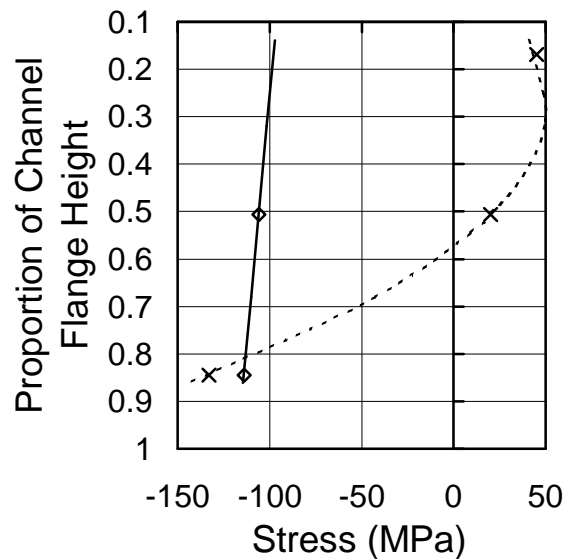


Figure 4.10 Comparison of the Measured and Modelled Residual Stress Patterns for Both Beams for the Channel Right Flange

Note: The Legend for Figure 4.10 is the same legend used in Figure 4.5.

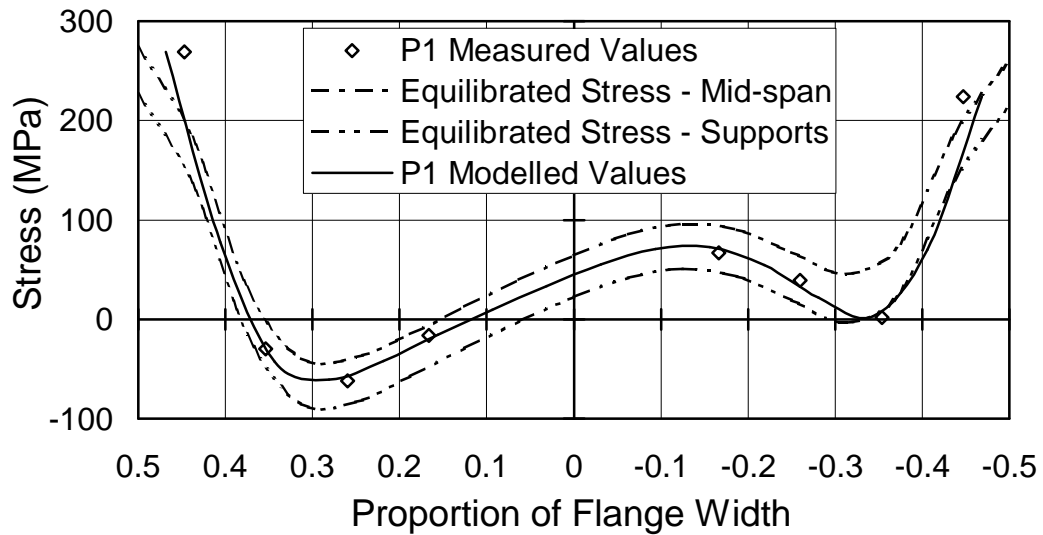


Figure 4.11 Comparison of the Equilibrated Residual Stresses for Beam P1-A with the Measured and Modelled Distributions for the Top Flange of the Wide Flange Section

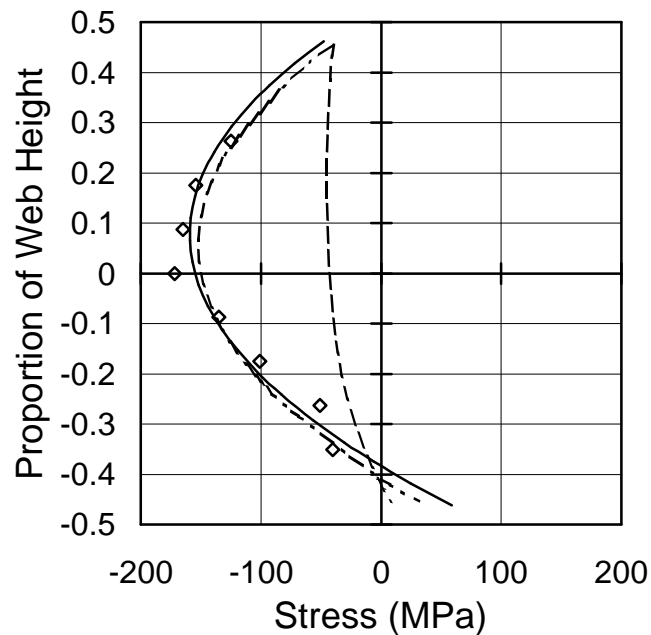
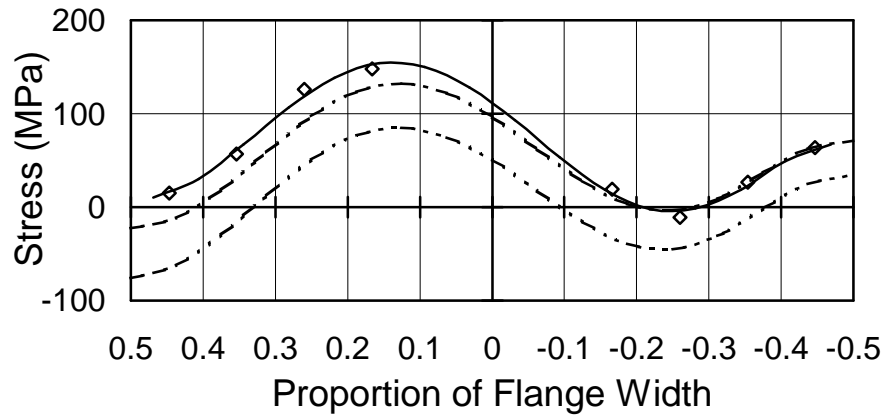


Figure 4.12 Comparison of the Equilibrated Residual Stresses for Beam P1-A versus the Measured and Modelled Distribution for the Web of the Wide Flange Section

Note: The Legend for Figure 4.12 is the same legend used in Figure 4.11.



*Figure 4.13 Comparison of the Equilibrated Residual Stresses for Beam P1-A with the Measured and Modelled Distribution for the Bottom Flange of the Wide Flange Section*

Note: The Legend for Figure 4.13 is the same legend used in Figure 4.11.

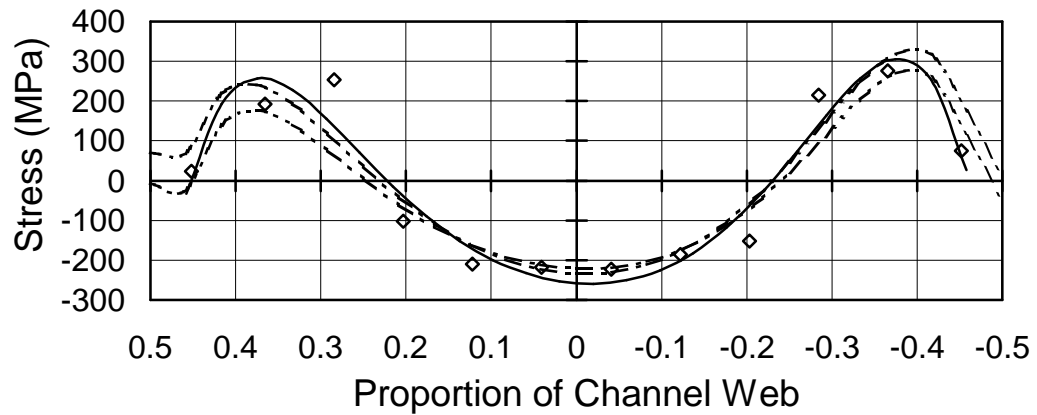


*Figure 4.14 Comparison of the Equilibrated Residual Stresses for Beam P1-A with the Measured and Modelled Distribution for the Channel Web*

Note: The Legend for Figure 4.14 is the same legend used in Figure 4.11.

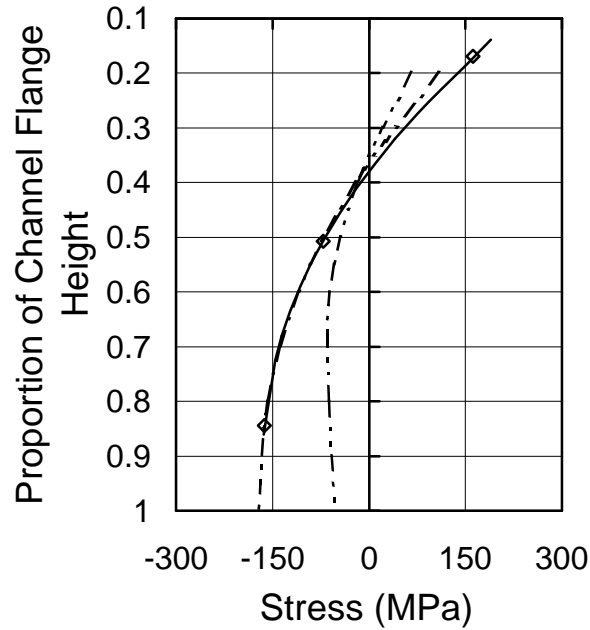


*Figure 4.15 Comparison of the Equilibrated Residual Stresses for Beam P1-A with the Measured and Modelled Distribution for the Channel Left Flange*

Note: The Legend for Figure 4.15 is the same legend used in Figure 4.11.

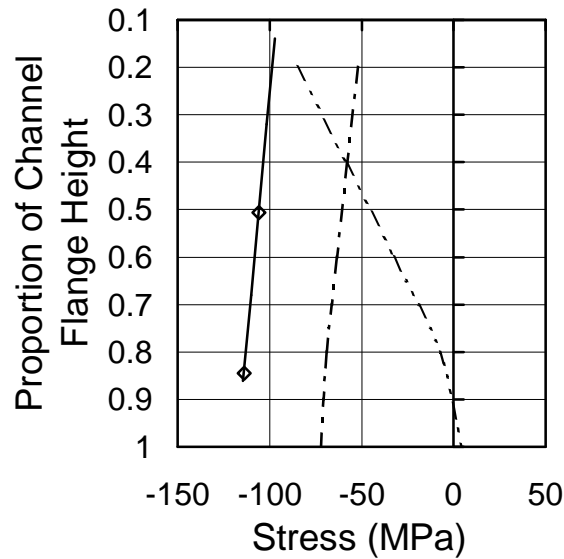


*Figure 4.16 Comparison of the Equilibrated Residual Stresses for Beam P1-A vs. the Measured and Modelled Distribution for the Channel Right Flange*

Note: The Legend for Figure 4.16 is the same legend used in Figure 4.11.

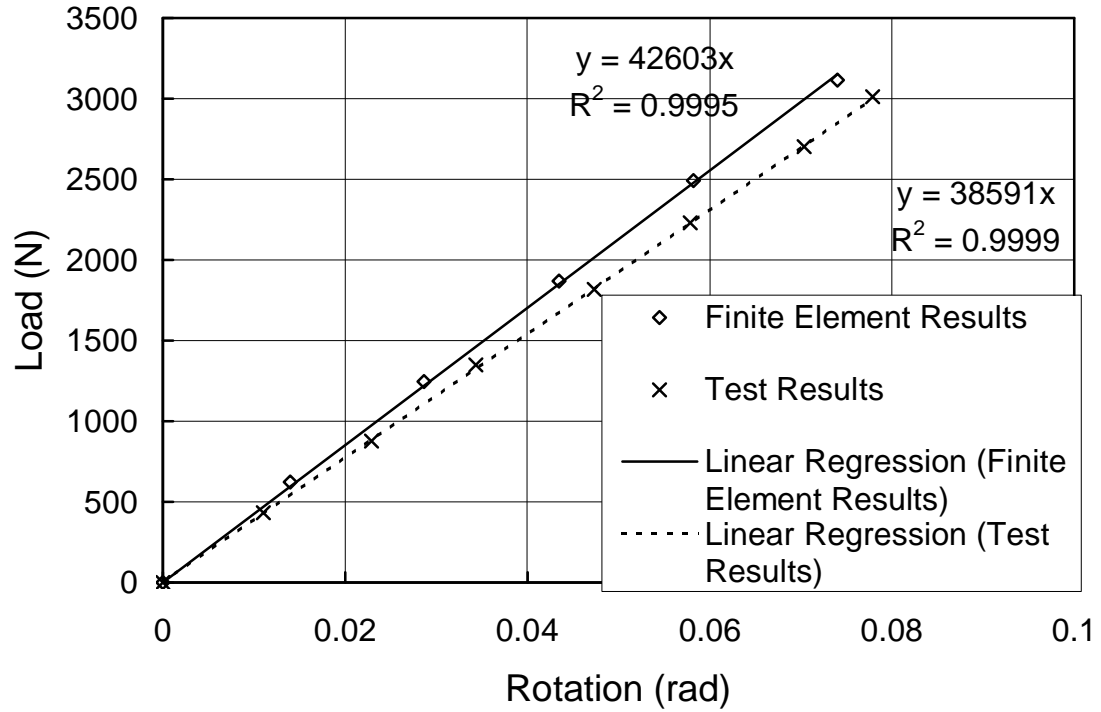


Figure 4.17 Load vs. Rotation for Beam P1 – Test 1

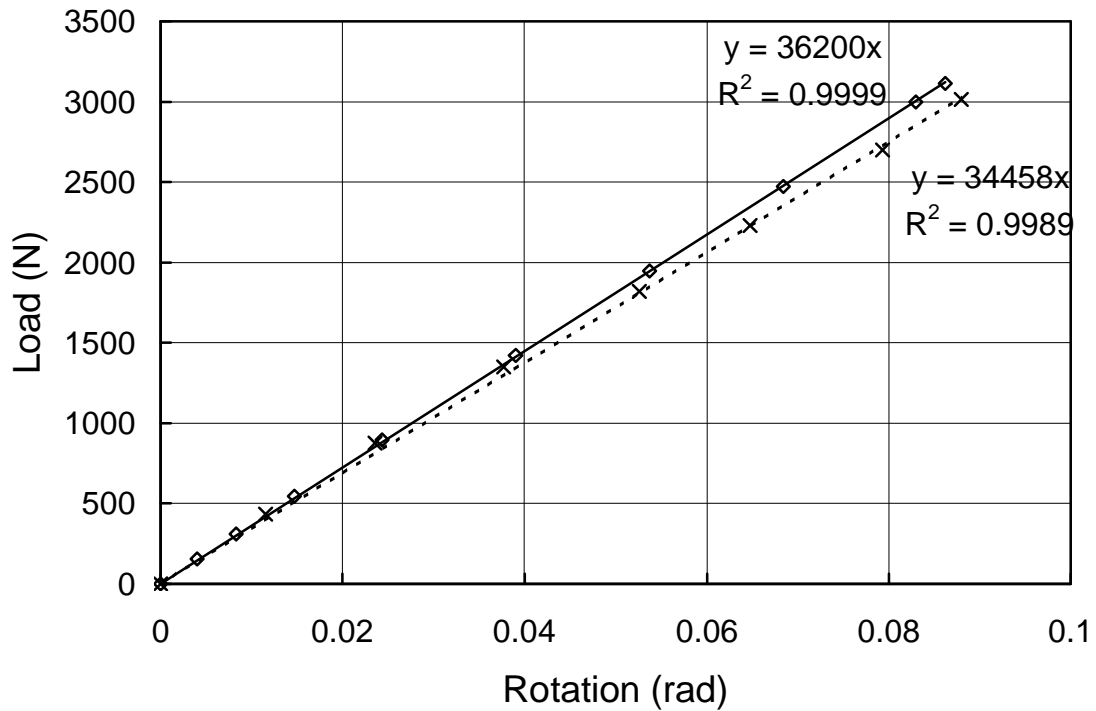


Figure 4.18 Load vs. Rotation for Beam P2 – Test 1

Note: The Legend for Figure 4.18 is the same legend used in Figure 4.17.

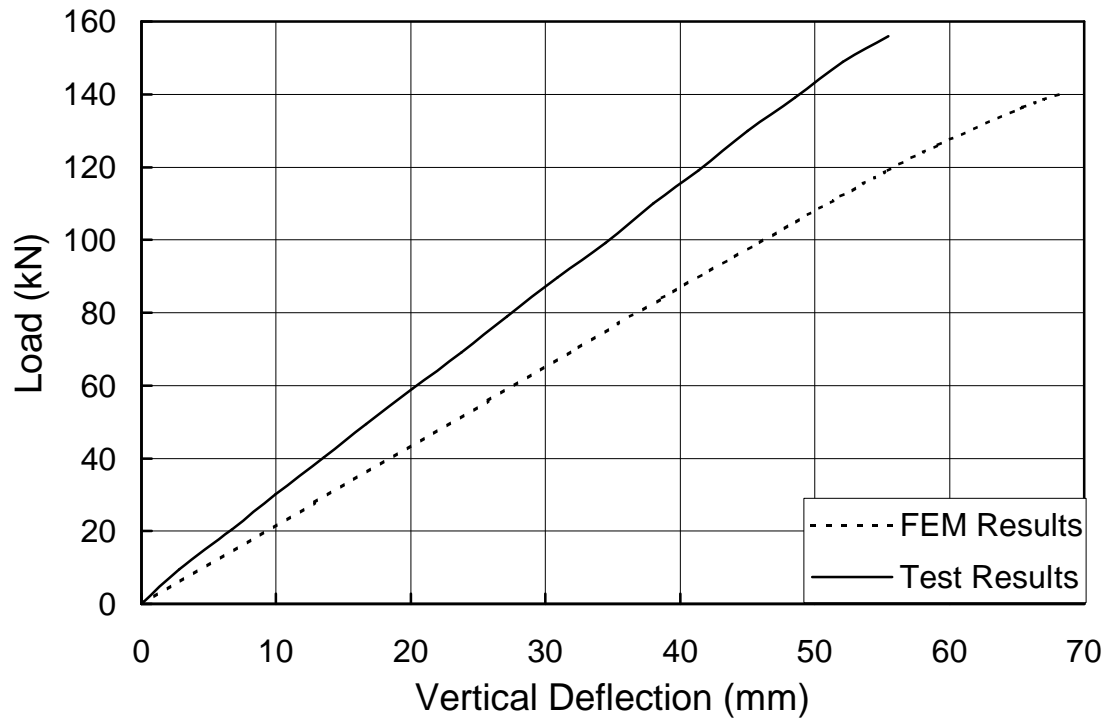


Figure 4.19 Load vs. Vertical Deflection at Mid-span for Beam P1 – Test 3

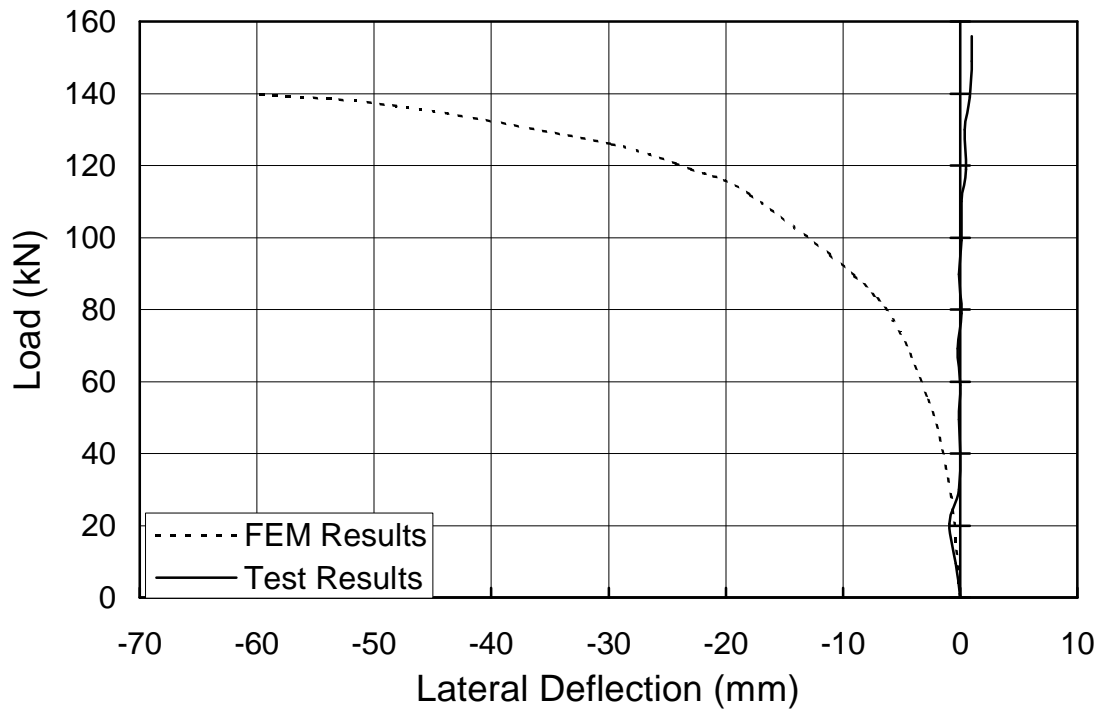


Figure 4.20 Load vs. Lateral Deflection at Mid-span for Beam P1 – Test 3

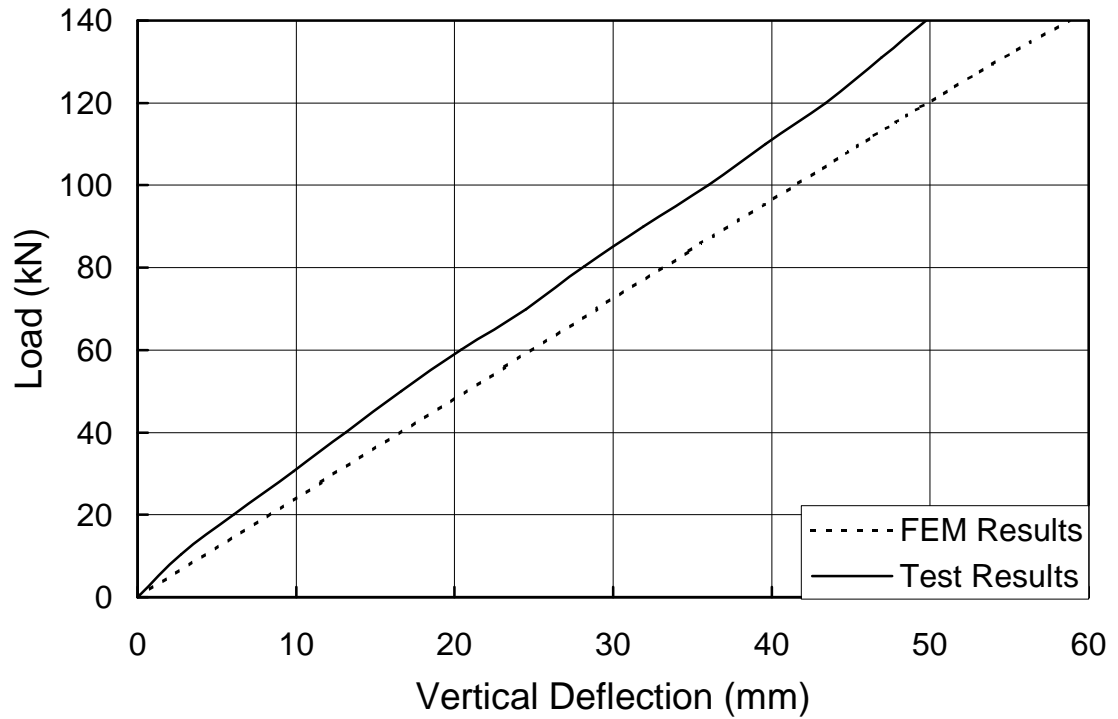


Figure 4.21 Load vs. Vertical Deflection at Mid-span for Beam P2 – Test 3

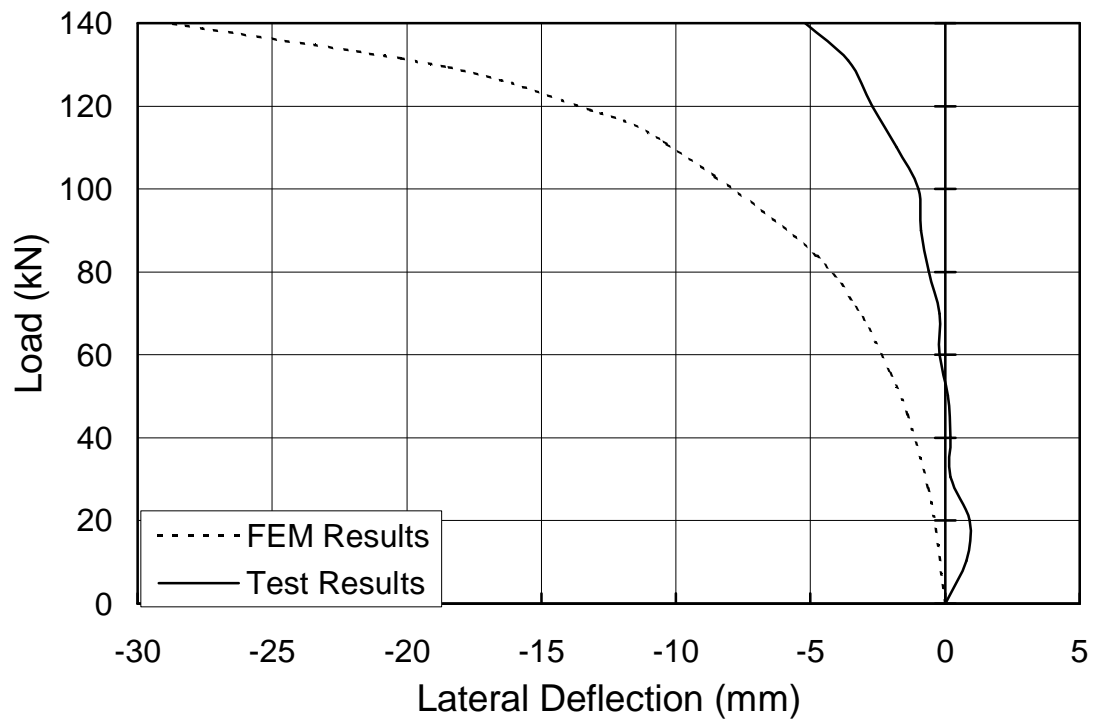


Figure 4.22 Load vs. Lateral Deflection at Mid-span for Beam P2 – Test 3

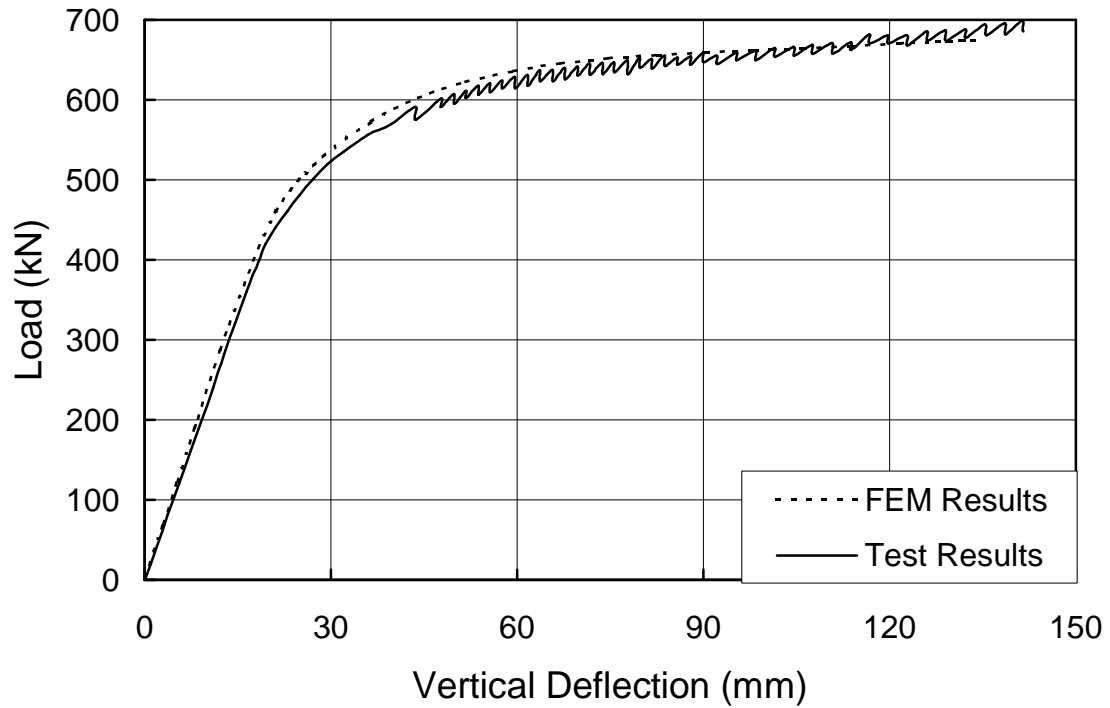


Figure 4.23 Load vs. Average Vertical Deflection at Load Application Points for Beam P1-B – Test 3

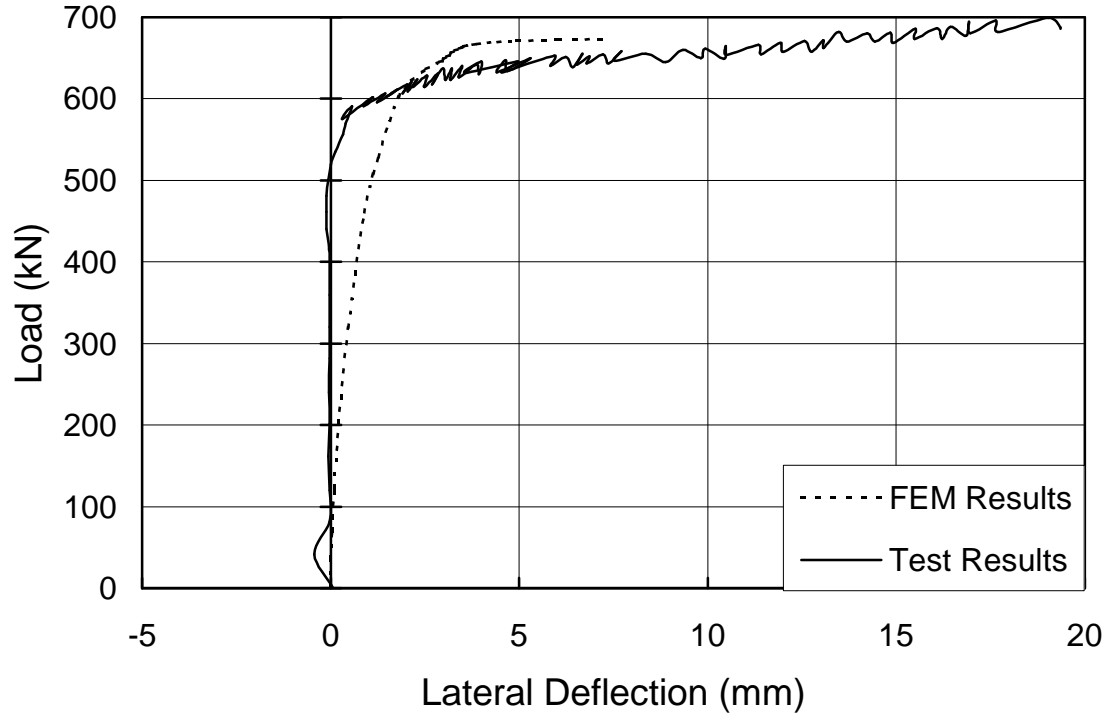


Figure 4.24 Load vs. Lateral Deflection at Mid-Span for Beam P1-B – Test 3

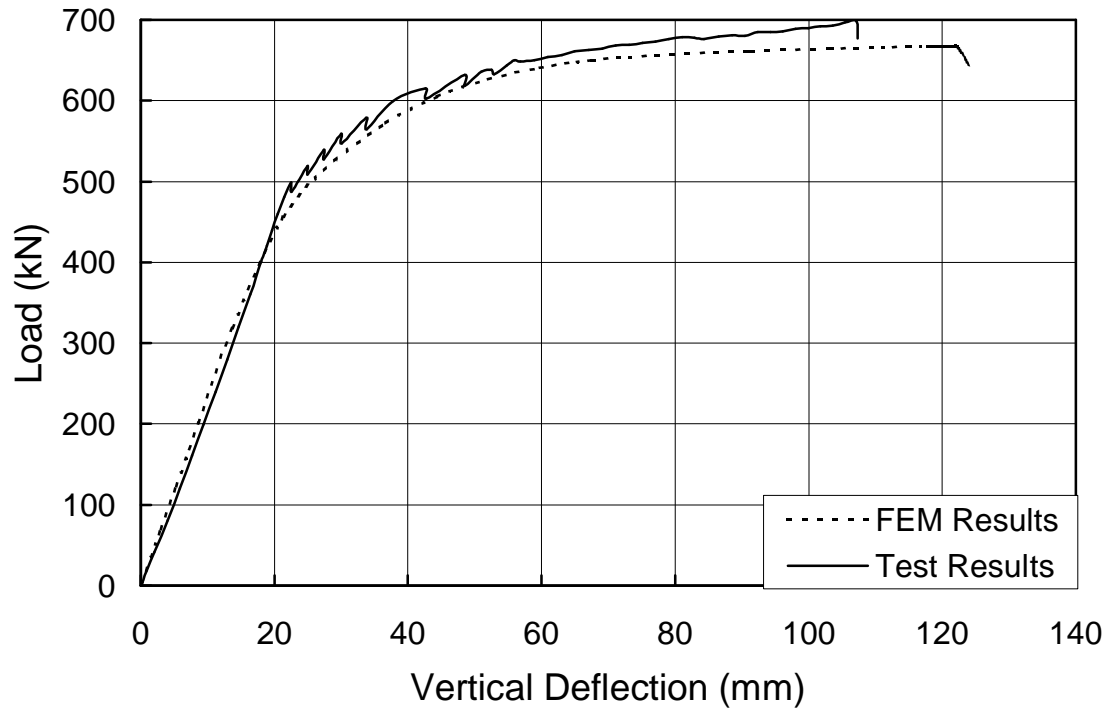


Figure 4.25 Load vs. Average Vertical Deflection at Load Application Points for Beam P2-B – Test 3

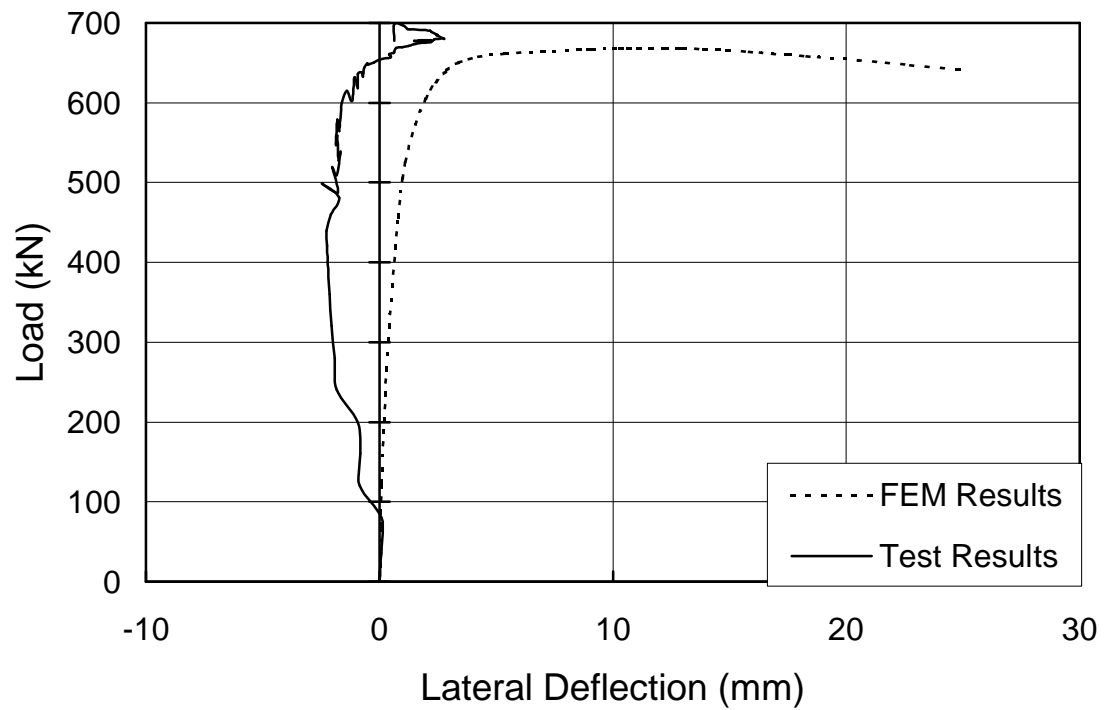


Figure 4.26 Load vs. Lateral Deflection at Mid-span for Beam P2-B – Test 3

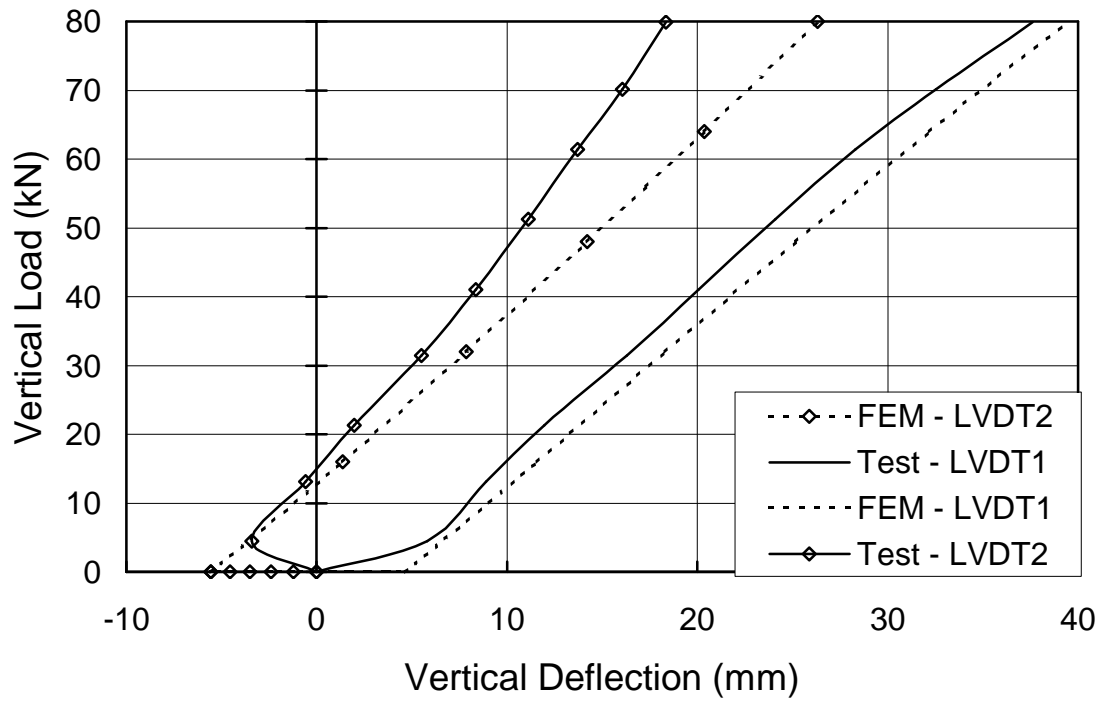


Figure 4.27 Vertical Load vs. Vertical Deflection at LVDT Locations at Mid-Span for Beam P1 Load Cycle (LC) 1 – Test 4

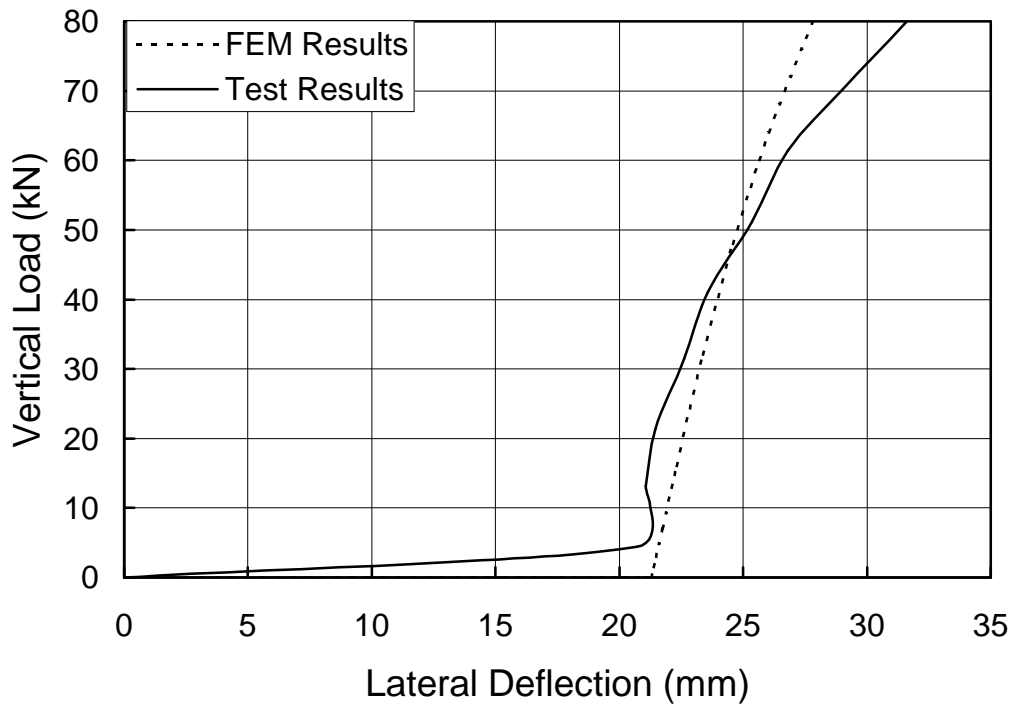


Figure 4.28 Vertical Load vs. Lateral Deflection for Beam P1 LC 1 – Test 4

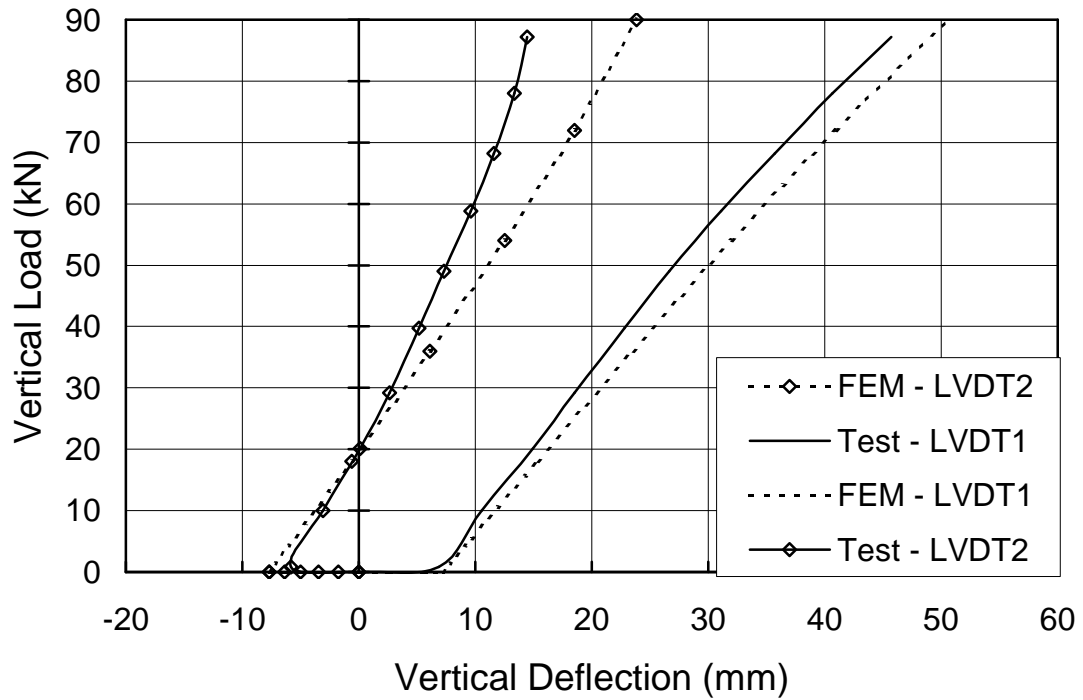


Figure 4.29 Vertical Load vs. Vertical Deflection at LVDT Locations at Mid-Span for Beam P1 LC 2 – Test 4

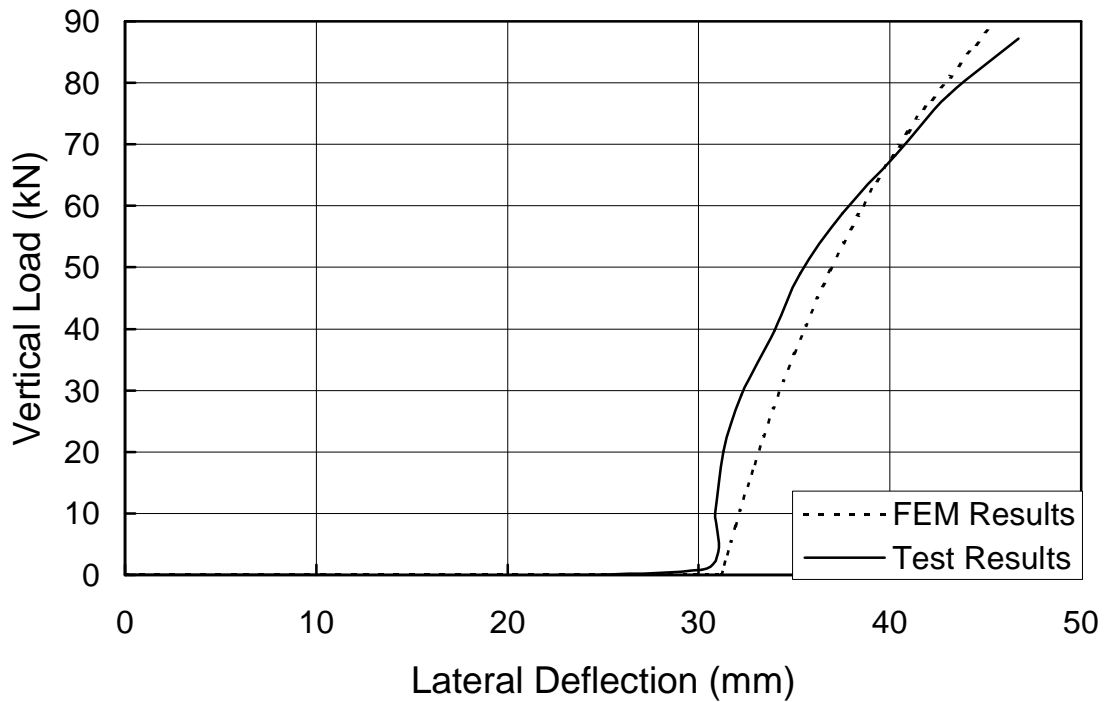


Figure 4.30 Vertical Load vs. Lateral Deflection for Beam P1 LC 2 – Test 4

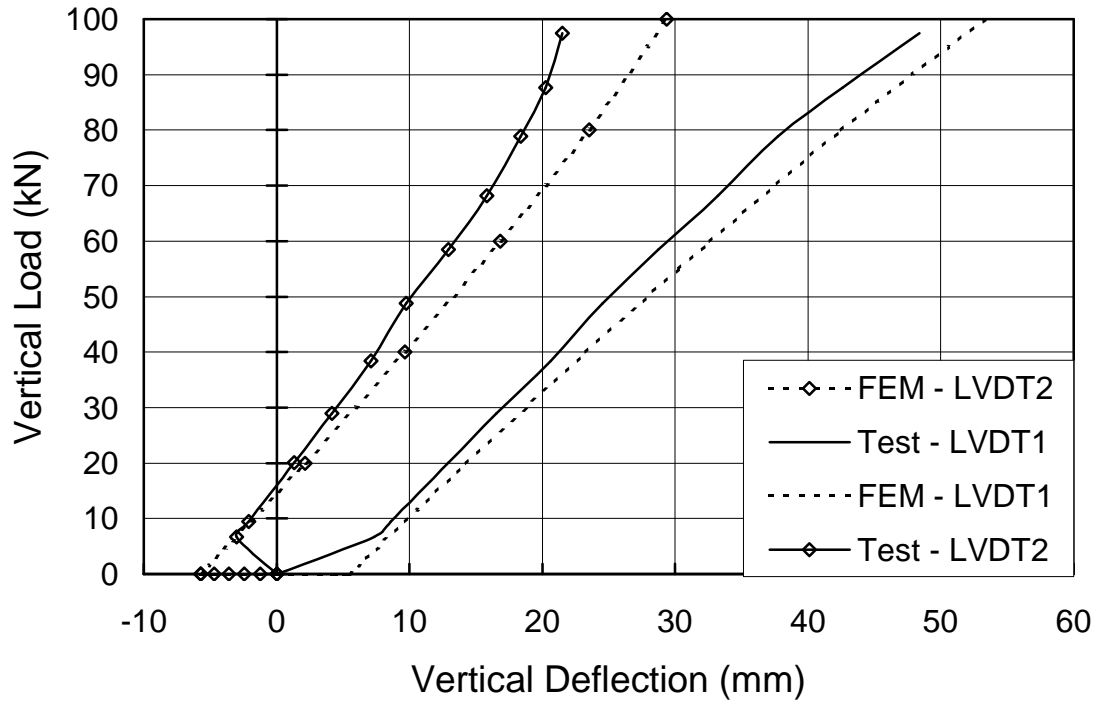


Figure 4.31 Vertical Load vs. Vertical Deflection at LVDT Locations at Mid-Span for Beam P2 LC 1 – Test 4

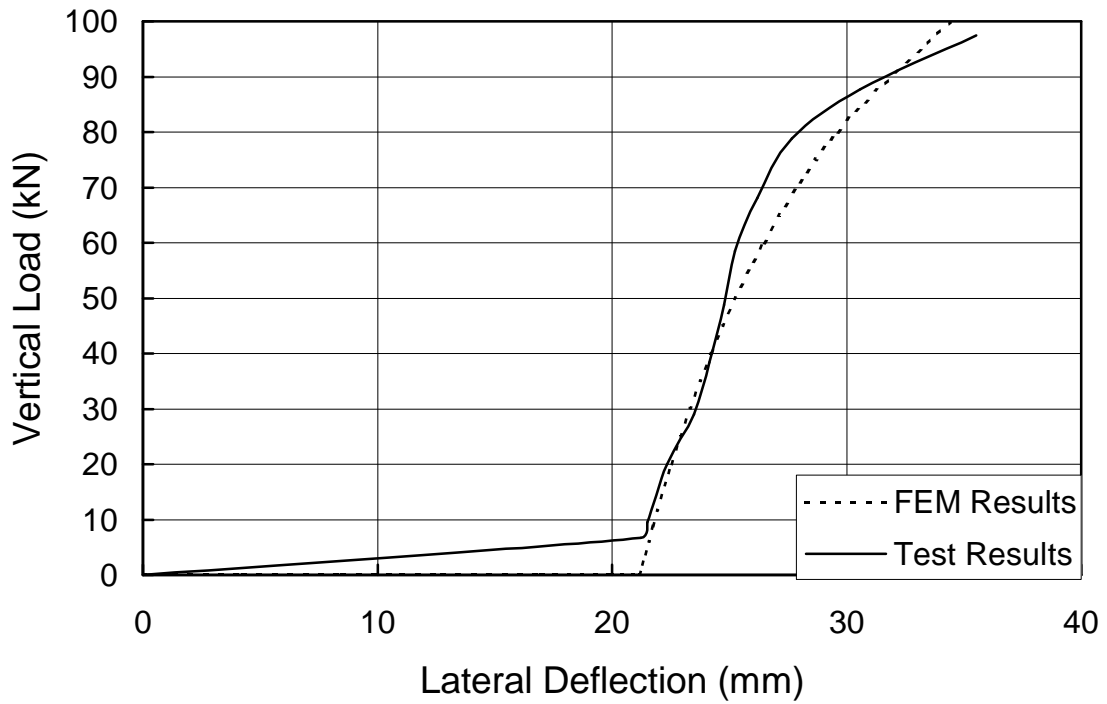


Figure 4.32 Vertical Load vs. Lateral Deflection for Beam P2 LC 1 – Test 4

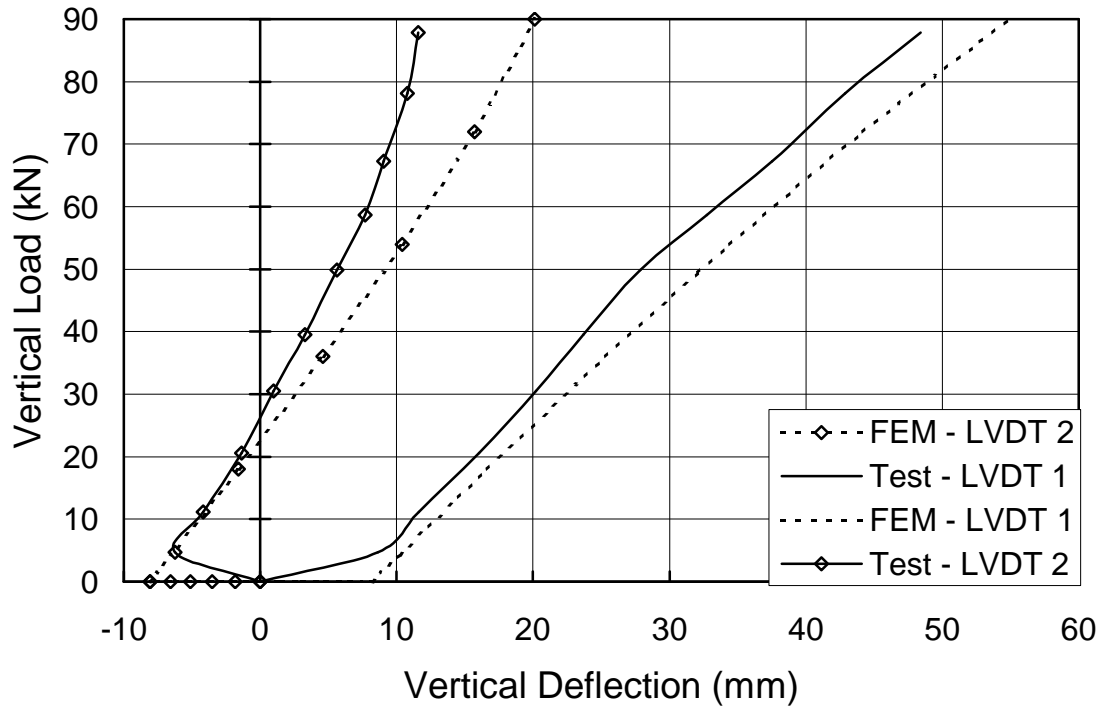


Figure 4.33 Vertical Load vs. Vertical Deflection at LVDT Locations at Mid-Span for Beam P2 LC 2 – Test 4

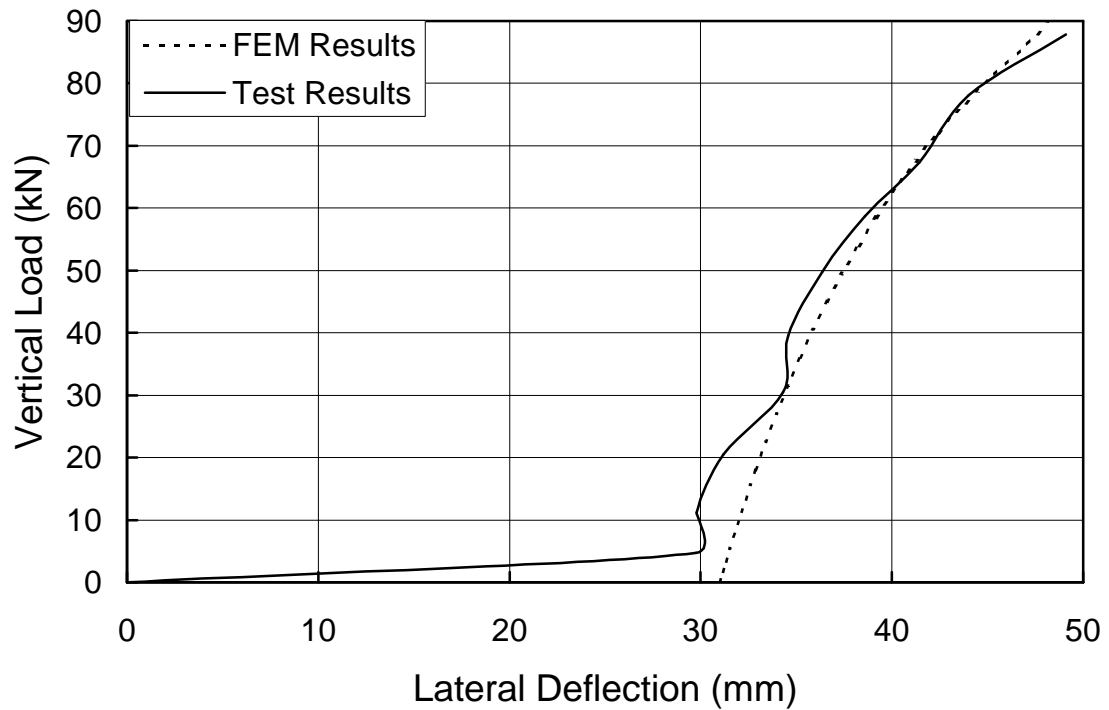


Figure 4.34 Vertical Load vs. Lateral Deflection for Beam P2 LC 2 – Test 4

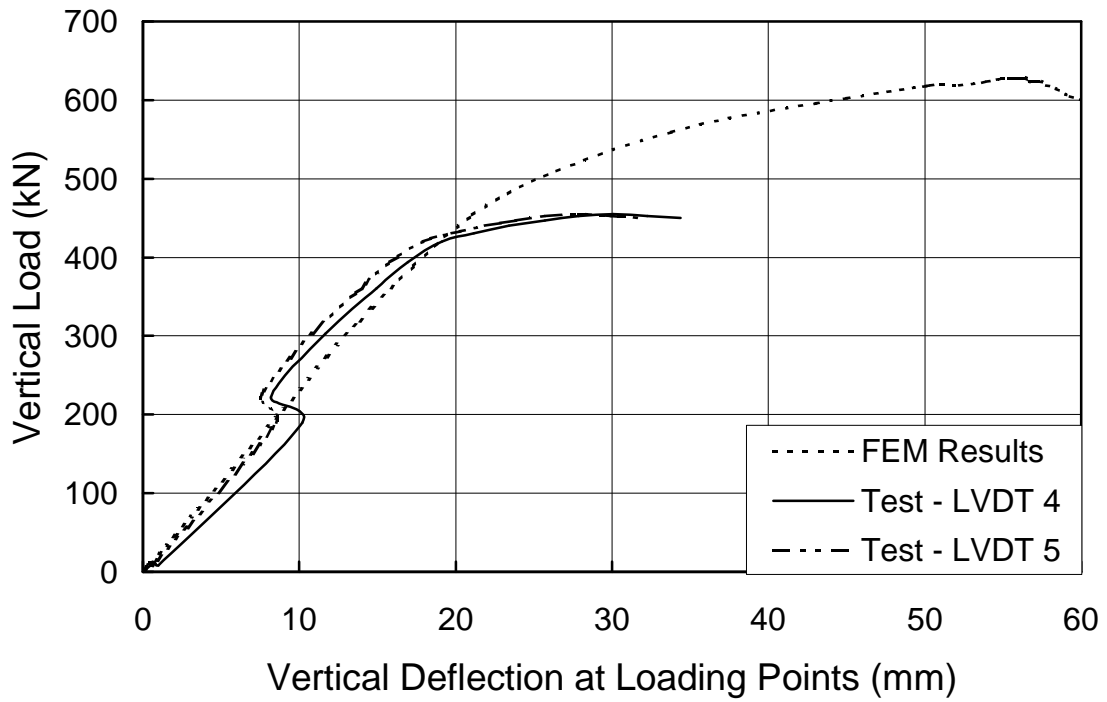


Figure 4.35 Vertical Load vs. Vertical Deflection at Loading Points for Beam P1-A – Test 4

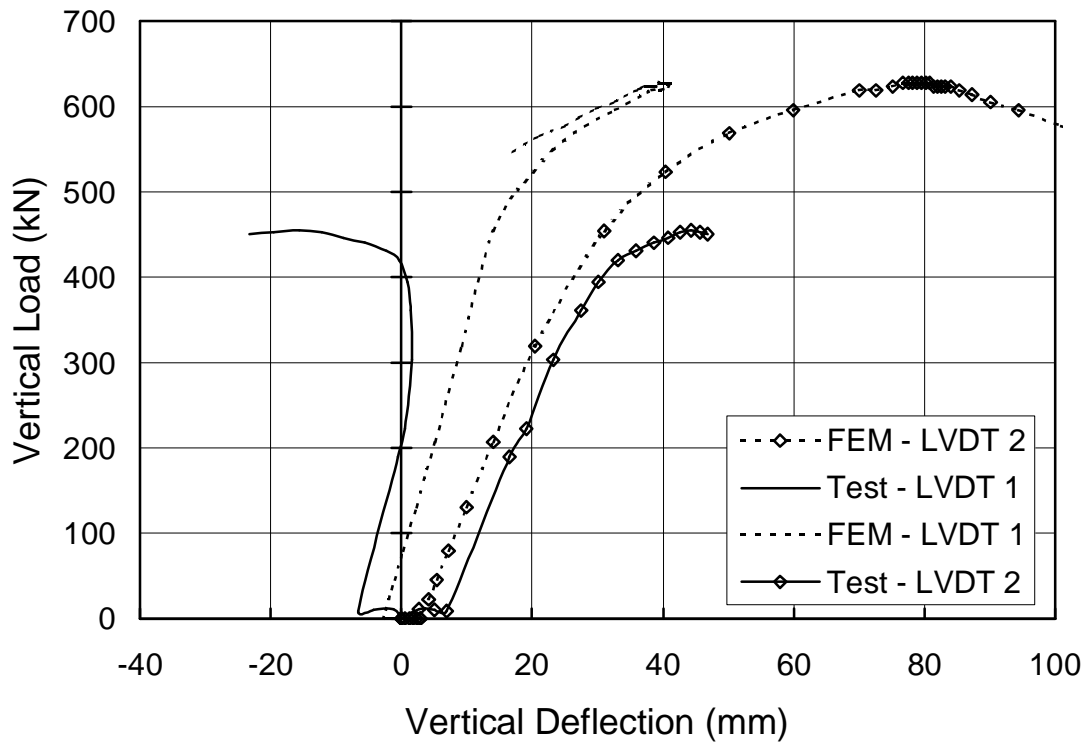


Figure 4.36 Vertical Load vs. Vertical Deflection at LVDT Locations at Mid-Span for Beam P1-A – Test 4

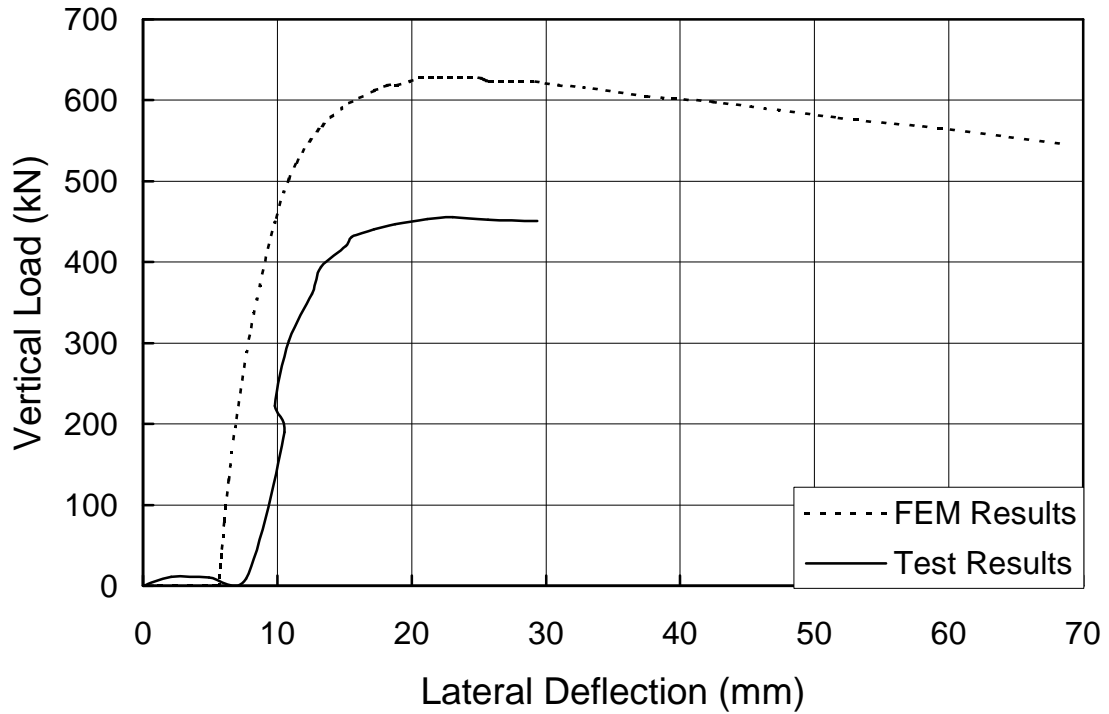


Figure 4.37 Vertical Load vs. Lateral Deflection for Beam P1-A – Test 4

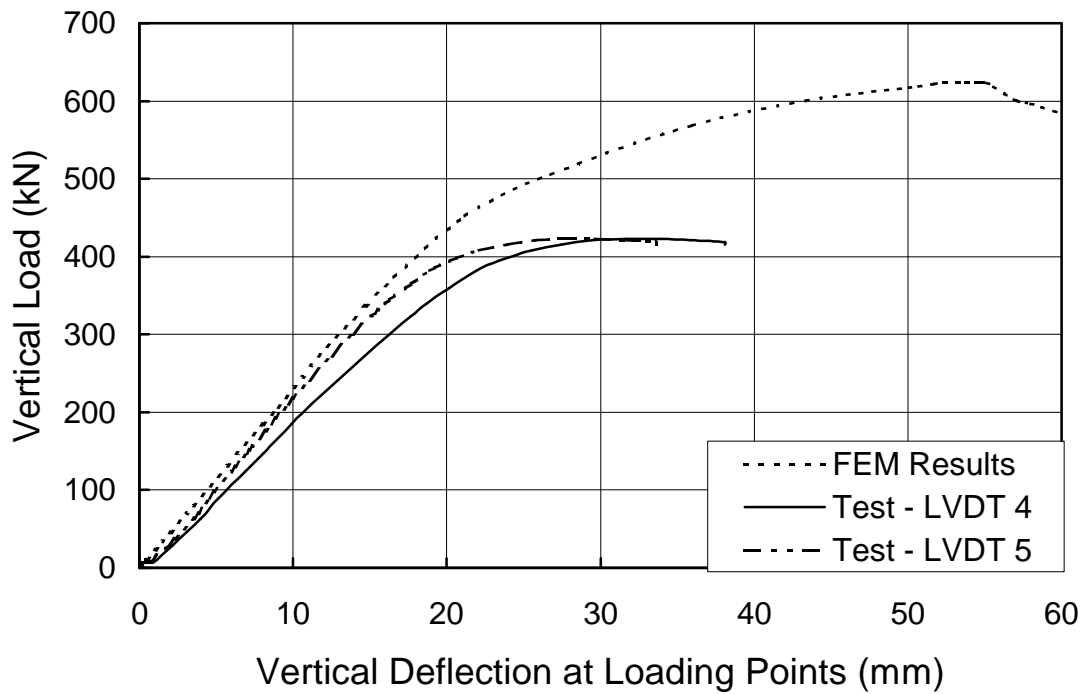


Figure 4.38 Vertical Load vs. Vertical Deflection at Loading Points for Beam P2-A – Test 4

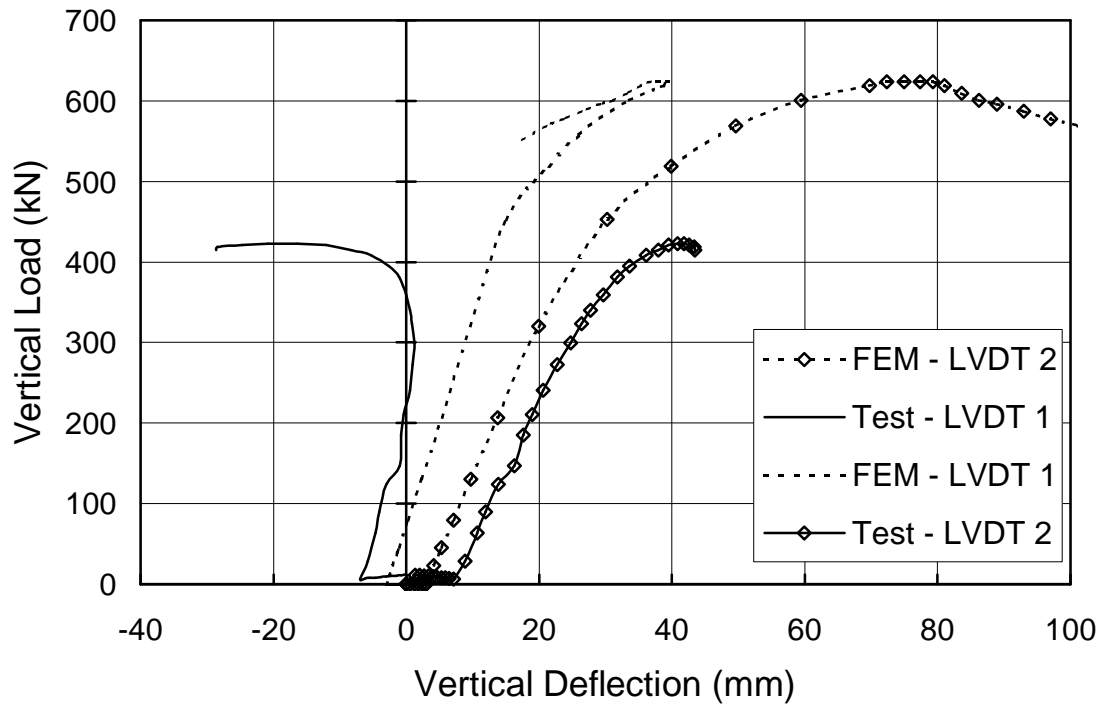


Figure 4.39 Vertical Load vs. Vertical Deflection at LVDT Locations at Mid-Span for Beam P2-A – Test 4

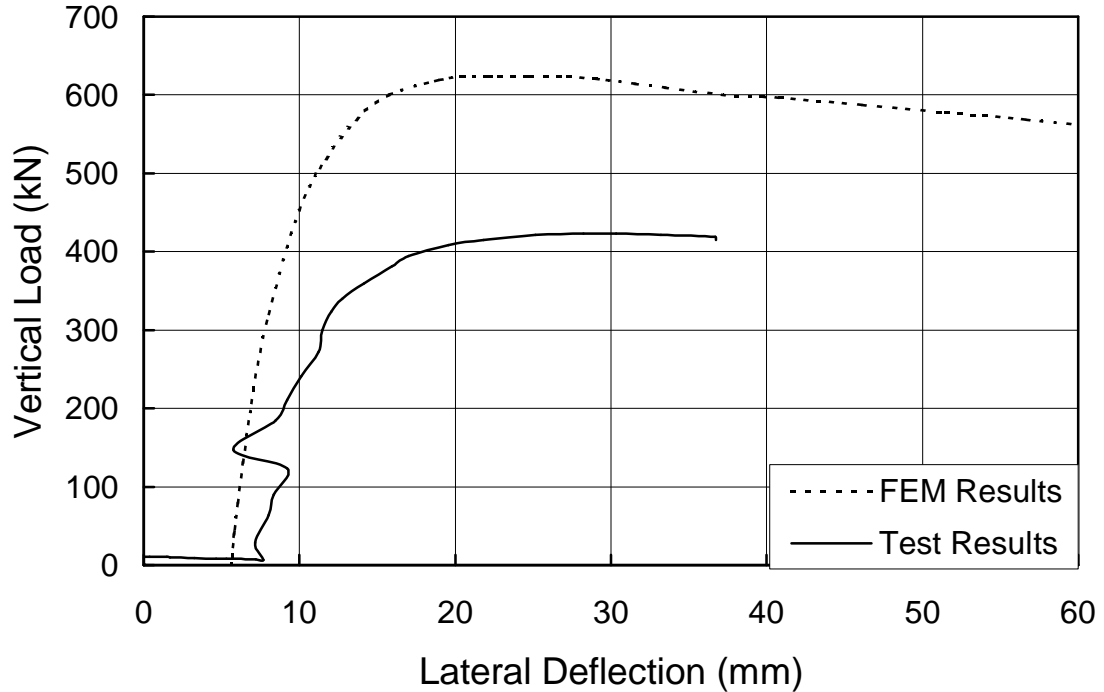


Figure 4.40 Vertical Load vs. Lateral Deflection for Beam P2-A – Test 4

## **5 PARAMETRIC STUDY METHODOLOGY**

### **5.1 *Parameter Selection***

#### **5.1.1 Global Parameter List**

Driver and Kennedy (1987) proposed a list of parameters important to the behaviour of wide flange sections subject to combined torsion and flexure. The list below includes these factors and other factors that influence the beam behaviour:

- Beam length;
- Material properties (i.e., stress vs. strain curve);
- Beam continuity;
- Loading conditions
  - Load application location relative to the shear centre;
  - Load distribution (point load at mid-span, uniformly distributed load, etc.);
  - Load history;
  - Moment–torque ratio for eccentric loading;
- Boundary conditions;
- Class of cross-section in flexure according to CSA S16-01;
- Cross-sectional dimensions;
- Lateral–torsional buckling;
- Braced vs. unbraced beams;
- Ratio of pure torsional stiffness to warping torsional stiffness;
- Ratio of pure torsional to warping torsional resistance;
- Beam slenderness;
- Residual stress pattern and magnitude;
- Magnitude and shape of initial imperfections.

#### **5.1.2 Parameter Investigation**

Some of the factors presented in the previous section are outside the scope of this project. The residual stress pattern, magnitude of initial

imperfections, and grade of steel are to be discussed later in the description of the finite element model. Parameters outside the scope of this investigation include cross-sectional shapes other than I-shapes, beam continuity, member bracing, and location of load application relative to the shear centre. Continuity and bracing are partially considered through the boundary conditions and the length of the beam. Since Pi and Trahair (1994a, 1994b; Trahair and Pi, 1997) found that beams that are unbraced between supports are the most critical, the beams in this study will be unbraced between supports.

In pure flexure, the point of application of the load to the cross-section has a significant effect on the lateral-torsional buckling capacity. In positive moment regions, it is generally conservative to consider only top flange loading. Under combined torsion and flexure, the gravity load applied to the top flange creates a destabilizing torque and bending of the cross-section about its weak axis. For this study, only shear centre loading, which represents an idealized loading condition, is considered to be consistent with earlier research (Pastor and DeWolf, 1979; Pi and Trahair, 1994a; Trahair and Pi, 1997).

For this parametric study, a vertical load is applied at an eccentricity to the shear centre, causing the moment–torque ratio to remain approximately constant in the elastic region. Comparing the results of past research (Driver and Kennedy, 1987; Comeau, 1998; Razzaq and Galambos, 1979a, 1979b) on the moment vs. torque interaction diagram proposed by Driver and Kennedy (1987) indicates that load history (order of application of torsional and flexural loads) has no significant effect on the behaviour, as all of the capacity results lie outside of the proposed diagram.

Five variables are investigated in the parametric study, namely, wide flange section geometric properties, beam slenderness, loading condition, boundary conditions and the moment–torque ratio.

## I. Wide Flange Section Geometric Properties

Wide flanges sections were selected from the CISC Handbook of Steel Construction (CISC, 2007). The cross-sections were selected to allow the following parameters to be investigated:

### A. Class of cross-section (flexural classification according to CSA S16-01):

The behaviour of beams subjected to combined bending and torsion at the ultimate limit state is governed by the class of the cross-section. Although Table 5.1 illustrates that the vast majority of wide flange sections in the Handbook of Steel Construction are Class 1, sections are selected to provide information for all section classes. Class 1 sections (plastic design sections), Class 2 sections (compact sections) and Class 3 sections (non-compact sections) were selected for this investigation.

Table 5.2 presents the flange and web slenderness limits for Classes 1 to 3 sections, as defined in CSA S16-01. Since these limits and classes are a function of the strains at which local buckling occurs in the cross-section, cross-sections are to be selected based upon the strain at which local buckling occurs in the flange and web by varying the local slenderness ratios  $h/w$  and  $b/2t$ .

### B. Ratio of Pure Torsional Stiffness to Warping Torsional Stiffness and Resistance

The ratio of pure torsional stiffness to warping torsional stiffness is a measure of the ratio of torque that is carried by pure and warping torsion in the elastic range. This ratio is expressed by the variable  $\lambda$  calculated by Equation [2.32]. This torsional

stiffness ratio is varied by selecting sections with varying ratios of  $J$  and  $C_w$ , since the values of  $G$  and  $E$  are considered constant for structural steel. In the inelastic range, the ratio of torsional resistance is more critical, as it determines how the torsion is carried. Cross-sections are selected to provide a range of  $\lambda$ .

## II. Beam Slenderness

The slenderness of a beam affects its susceptibility to lateral torsional buckling. Different methods have been proposed in the existing literature to quantify the slenderness of a beam (Pi and Trahair, 1994a; CSA, 2001), but it is most commonly defined as  $L/r_y$ , where  $L$  is the beam length measured between points of lateral support and  $r_y$  is the radius of gyration about the weak axis. In pure flexure, lateral torsional buckling of I-shaped sections occurs because the sections have a small torsional resistance as well as a lower bending stiffness about their weak axis than about their strong axis, the primary axis of bending. Under torsional moments larger than the pure torsional resistance of the beam, Driver and Kennedy (1987) indicated that the beam will twist rather than fail by lateral torsional buckling. To investigate lateral torsional buckling behaviour of beams under combined bending and torsion, beam lengths larger and smaller than the characteristic length of selected the cross-section (laterally unsupported length below which lateral torsional does not take place) were selected.

## III. Loading Condition

Different loading conditions provide different combinations of moment and torque at various sections of the beam. This influences the beam behaviour as well as the failure mechanism. Two loading conditions are considered in this project, namely, an eccentric uniformly distributed load and an eccentric point load at mid-span. The general

shapes of the bending moment and total torque diagrams for these two load distributions are shown in Figure 5.1 for simply supported end conditions. For the same total load,  $P$  or  $wL$ , the point load,  $P$ , at mid-span is more critical as the maximum moment is twice as large and the peak total torque is more uniform over the beam length. The goal of investigating different loading scenarios is to determine how these load cases influence the beam behaviour and the interaction diagram for beams subjected to combined bending and torsion.

#### IV. Boundary Conditions

Considering a single span beam, there are many possible combinations of simple, free and fixed torsional and flexural boundary conditions (BC) of which eight are shown below. These combinations are presented in the format “Left End Flexural BC/Left End Torsional BC – Right End Flexural BC/Right End Torsional BC”.

- i. Simple/Simple – Simple/Simple
- ii. Simple/Simple – Simple/Fixed
- iii. Simple/Fixed – Simple/Fixed
- iv. Fixed/Fixed – Fixed/Fixed
- v. Fixed/Fixed – Simple/Simple
- vi. Fixed/Fixed – Free/Free (Fixed End Cantilever)
- vii. Fixed/Fixed – Free/Simple (Fixed End Cantilever)
- viii. Fixed/Fixed – Simple/Fixed

A simple flexural boundary condition prevents the beam from translating in all directions, but allows bending about the weak and strong axes (referred to as a pin). For lateral torsional buckling, it is usually assumed that rotation about the beam longitudinal X-axis is restrained, but warping is free at both ends. The longitudinal translation is typically released at one of the ends (referred to as a roller) if both ends of the beam are simply supported in flexure. This model was also used in this project. A fixed flexural boundary

condition completely restrains the end of the beam in all six degrees of freedom except the rotation about the axis of the member. A free boundary condition restrains none of these six degrees of freedom. A simple torsional boundary condition prevents the end of the beam from rotating about its longitudinal axis but does not prevent warping of the cross-section. A fixed boundary condition in torsion prevents the end of the beam from rotating about its longitudinal axis and prevents warping. Free boundary conditions in torsion prevent neither rotation nor warping at the end of the beam.

Different boundary conditions result in different torque and moment distributions. It is important that the design method's applicability to a variety of boundary conditions can be verified.

## V. Moment–Torque Ratio

The moment,  $M$ , to torque,  $T$ , ratio,  $M/T$ , is varied by changing the eccentricity of the applied vertical load. Several values of moment–torque ratios are investigated to establish a moment versus torque interaction diagram. When the load is applied with no eccentricity ( $M/T = \infty$ ), the beam behaves in pure flexure. When the load is applied at an infinite eccentricity ( $M/T = 0$ ), the beam behaves in torsion only. To create a torsion only load case, a torsional couple is applied by means of two equal and opposite eccentric follower loads at the shear centre.

### 5.1.3 Parameter Reductions

Although both dimensional analysis (Langhaar, 1951; Taylor, 1974) and effective length approaches were considered in detail, neither was found to be an effective means of reducing the number of influential parameters significantly. It is found by re-arranging the elastic lateral torsional

buckling equation presented in CSA S16-01 that  $M_u$  is inversely proportional to the slenderness ratio  $L/r_y$ , expressed in the following form:

$$M_u = \frac{\omega_2 \pi}{\left(\frac{L}{r_y}\right)} \sqrt{EAGJ + \left(\frac{\pi E}{L}\right)^2 AC_w} \quad [5.1]$$

where  $\omega_2$  is the equivalent moment factor and is a function of the shape of the bending moment diagram and  $A$  is the cross-sectional area. A similar result is found when re-arranging Equation [2.32] for the calculation of  $\lambda$ . Following the work of Lin (1977),  $\lambda$  is non-dimensionalized with respect to  $L$  as follows:

$$\lambda L = L \sqrt{\frac{GJ}{EC_w}} = \sqrt{\frac{G}{E}} \sqrt{\frac{JL^2}{C_w}} \quad [5.2]$$

Substituting the approximate expressions given in Equations [5.3] and [5.4] for  $J$  and  $C_w$ , respectively, for a wide flange section in the second radical, the following form of  $\lambda L$  is obtained that is linearly proportional to the slenderness ratio  $L/r_y$ :

$$J \cong \frac{1}{3}(2bt^3 + (d-t)w^3) \quad [5.3]$$

$$C_w \cong \frac{1}{4}(d-t)^2 I_y \quad [5.4]$$

$$\frac{JL^2}{C_w} = \left(\frac{4}{3}\right) \left(\frac{L}{r_y}\right)^2 \left(\frac{2bt^3 + (d-t)w^3}{A(d-t)^2}\right) \quad [5.5]$$

$$\lambda L = \left(\frac{L}{r_y}\right) \sqrt{\frac{G}{E}} \sqrt{\left(\frac{4}{3}\right) \left(\frac{2bt^3 + (d-t)w^3}{A(d-t)^2}\right)} \quad [5.6]$$

The slenderness ratio,  $L/r_y$ , is found to be important in determining the distribution of torsional loads as well in determining the lateral torsional buckling strength of a beam in flexure.

## 5.2 Methodology

Since no simplifications from dimensional analysis or an effective length approach helped to reduce the size of the study, a partial factorial approach was used to investigate the effect of the main parameters influencing the capacity of beams subjected to combined bending and torsion. The range of the parameters presented below was selected so that design methods could be verified and modified if required. Then, additional complementary cases are used to expand the applicability of the design method and to verify its use for other cases not directly modelled in the basic factorial study approach.

### 5.2.1 Beam Cross-section

Wide flange sections are selected from the tables of section properties presented in the Handbook of Steel Construction (CISC, 2007). The selection of standard wide flange sections is based primarily on the value of  $h/w$  and  $b/2t$ . In addition, an attempt was made to vary section size and values of  $\lambda$  as much as possible. The maximum, minimum, average, and range of  $b/2t$  and  $h/w$  ratios for standard wide flange sections are presented in Table 5.3. The variation in  $\lambda$  values, organized by flexural class for 350W steel sections, is shown in Table 5.4. Since 350W steel is the most commonly available grade of steel for rolled wide flange sections, it is the only grade considered in the parametric study. Only four cross-sections from the list of standard wide flange sections in the Handbook of Steel Construction (CISC, 2007) have a web that does not meet the Class 1 section requirement. The flange slenderness ratio  $b/2t$  is always the governing limit that controls the class of section.

To minimize the number of cases to include in the parametric study, three values of  $b/2t$  and two values of  $h/w$  are included in the study, resulting in a total of six cross-sections. This provides a greater variation in the more critical local slenderness ratio,  $b/2t$ , which has a greater effect on

the local buckling stress for the standard wide flange sections. Table 5.5 displays the six sections selected for the parametric study, as well as the three sections that are used in the additional complementary cases. To provide a good range of  $b/2t$  ratios, values approximately equal to 5.0, 8.1, and 9.7 are used. Values of  $h/w$  approximately equal to 23.0 and 40.0 are used to provide some variation.

### **5.2.2 Beam Slenderness**

To limit the number of cases incorporated in the parametric study, only two values of beam slenderness are used. For the wide flange sections selected for this investigation, the average slenderness ratio at which lateral torsional buckling governs for the sections investigated is 63.5. In the parametric study, two slenderness ratios are selected, namely, 50 and 100. Inelastic lateral torsional buckling governs the behaviour of the beam with the larger slenderness ratio. Additional complementary cases are then performed to investigate additional slenderness ratios, including very stocky (25) and slender (125) beams. Table 5.6 presents the lengths modelled for each of the wide flange sections for the two slenderness ratios. This variation provides a wide range of  $\lambda L$  values, although this variable is a linear function of the slenderness ratio.

### **5.2.3 Load Type**

Only one load case is considered in the parametric study, namely, a point load at mid-span. This load case was selected because it represents one of the most severe loading conditions for a transversely loaded beam, as discussed in Section 5.1.2. The case of a uniformly distributed load will be considered in the complementary case study.

### **5.2.4 Boundary Conditions**

Modelling of all eight possible boundary condition combinations for single span beams subject to combined torsion and flexure is beyond the scope

of this study. The goal is to model the conditions most commonly encountered in practice. Of the previously stated possibilities, the following three combinations of boundary conditions are included in the parametric study: i) simple support in bending and torsion at both ends, iv) fixed support in bending and torsion at both ends, and vi) fixed support in bending and torsion at one end and free boundary condition in bending and torsion at the other end. One other combination, namely, v) fixed support in bending and torsion at one end and simple support in bending and torsion at the other end, is included as an additional complementary case only.

### 5.2.5 Moment–Torque Ratio

Five different moment–torque ratios are used for each beam by varying the load eccentricity, providing behaviours ranging from torsion only to bending only. The normalized moment–torque ratios, where both quantities are normalized with respect to their respective ultimate capacities,  $M_n/T_n$ , used are 0.0, 0.4, 1.0, 2.4, and infinity. These values provide a broad range of behaviour on the normalized moment versus normalized torque interaction diagram and the respective nominal interaction diagram. These moment–torque ratios are the initial elastic values and are expected to change as the beam twists and yields based on the work of Driver and Kennedy (1987). The finite element model is further verified by determining the pure flexural resistance in the model and comparing the results to classical flexural theory.

### 5.2.6 Nomenclature

The parametric study includes six different beam cross-sections, two slenderness ratios, one load type, and three boundary conditions, resulting in 36 different beams. For each beam, five different  $M/T$  values are modelled, creating a total of 180 finite element models. The basic format for each model name is “S#L#T#B#E#”. This name consists of ten digits,

two corresponding to each of the five variables. For each variable, two digits are used, the first to represent the name of the variable (S for section, L for slenderness ratio, T for load type, B for boundary condition, and E for eccentricity) and the second, a number used to identify the section type, slenderness ratio, etc., modelled. The naming and numbering convention used for the parametric study is presented in Table 5.7. A certain model or group of models are referred to by using all or part of this naming convention. For example, all B1 models are all beams simply supported at both ends.

### **5.3 Finite Element Model**

The finite element model used for the parametric study was similar to the ones developed and validated in Chapters 3 and 4. The differences between the finite element model used in the parametric study and the one developed earlier are presented in the following.

#### **5.3.1 Geometric Factors**

##### **5.3.1.1 Discretization of Beam**

The nominal cross-sectional dimensions, as presented in the Handbook of Steel Construction (CISC, 2007), are used for each wide flange section. A typical finite element model of a beam is shown in Figure 5.2 (Beam S3L2T1B1E3 is shown). The node coordinates are specified at the flanges and web mid-thickness. The shell element S4R is used to discretize the beams cross-section since it was shown to provide excellent prediction of test results. The flanges are sub-divided into 16 equal size elements across the width and the web is sub-divided into 24 elements over the height and the nominal thickness of the flanges and web is used in the model definition. As for the models presented in Chapters 3 and 4, the top and bottom two web elements are used to model the fillet area. The area of a fillet is calculated from the nominal dimensions as the total area of the cross-section,  $A$ , minus the two flanges,  $2bt$ , and the web,

$hw$ , areas, and dividing by four. Using this fillet area, the centroid of the fillet relative to the centroid of the cross-section and fillet dimensions are calculated, assuming the complement of an elliptical shape. The fillet dimensions are then used to determine the height of the two fillet elements comprising the fillet region. The thicknesses of these two elements are adjusted to provide the correct additional fillet area at the correct fillet centroidal location. The other 20 web elements are of equal height. The element lengths are selected to maintain a constant aspect ratio of approximately 2.0. For each section, the same element length and aspect ratios are used for both beam lengths. The element lengths, widths, and aspect ratios for the six wide flange sections are presented in Table 5.8.

#### 5.3.1.2 Boundary Conditions

For the simply supported boundary condition, each end is prevented from rotating about the axis of the member by restraining the web-to-flange junctions from deflecting laterally. At one end of the beam the node located at the centroid of the cross-section is restrained against translation in all three directions, but rotation is allowed about all three axes at this point. This also creates torsionally simple supports. At the other end of the beam the node at the centroid of the cross-section is restrained against translation in the Y-(vertical) and Z-(transverse) directions but translation is free in the X-(longitudinal) direction. As for the other end of the beam, all rotational degrees of freedom are free. An additional five elements are added beyond the end supports to provide sufficient bearing capacity at these locations to prevent local distortion of the web at the end supports.

The fixed boundary condition is created by restraining all six degrees of freedom at each node of the end cross-sections.

### 5.3.1.3 Initial Imperfections

Although not directly accounted for in the validation of the finite element model, initial imperfections are included in the parametric study. The Imperfection command from ABAQUS was used to create a nodal displacement imperfection in any of the six nodal degrees of freedom. Two different types of imperfections, camber and sweep, common to rolled wide flange members, were included in the parametric study. Other types of imperfections, such as cross-sectional distortion, were considered beyond the scope of this investigation.

According to ASTM A6/A6M (2001), the fabrication tolerance limits for both vertical camber and lateral sweep is  $L/500$  when the flange width is less than 150 mm and  $L/1000$  when the flange width is greater. These imperfections were oriented in the direction that led to the smallest capacity of the beam. The shape of the imperfections was approximated using a parabola similar to the deflected shape. The difference between the buckled shape and simplified deflected shape is small.

For boundary conditions consisting of pinned or fixed end supports, B1 and B2, the imperfection shape consisted of a parabola with the maximum imperfection at mid-span. For boundary condition B3 (fixed end cantilever), the shape of the initial imperfection consisted of a half parabola with the maximum imperfection at the free end. To verify the worst-case orientation of these shapes, a small study is performed comparing the results of models without imperfections with the results for various orientations of imperfections for Beam S1L1T1B1E2. Four different conditions are analysed:

- Base – No Imperfections
- Test 1 – Lateral sweep in the direction of the eccentricity only
- Test 2 – Lateral sweep in the direction of the eccentricity and vertical camber opposite to the vertical loading

- Test 3 – Lateral sweep in the direction of the eccentricity and vertical camber in the direction of vertical loading

The results of this investigation are presented in Figure 5.3 and Table 5.9 where a comparison of the peak moment, as well as the torque and loads at this moment, for the various imperfection orientation models are presented. In Chapter 3, it was found that the most critical imperfection orientation (that produces the lowest torsional and flexural capacities) was a lateral sweep in the direction of the eccentricity and a vertical sweep opposite to the loading direction, although the differences between these orientations and other directions were very small. Figure 5.3 shows that the effect is greatest near the peak loads and that the lateral sweep appears to have the most influence on the results although the effect appears to be very small. The results of this study resulted in the selection of the imperfections modelled in Test 2 for use in the parametric study.

### 5.3.2 Material Properties

In the parametric study, only Grade 350W steel has been included because it is the most common grade currently used in Canada for wide flange sections. The grade of steel has two major effects on the results: the beam capacity, as determined by the yield and tensile strengths, and the beam behaviour, as a result of the shape of the stress vs. strain curve.

The stress vs. strain curve used in the parametric study is based on nominal values. Past finite element analyses of steel beams under combined bending and torsion have used a tri-linear stress vs. strain curve composed of a straight line to yield, a yield plateau, and a linear strain-hardening section to infinity (Pi and Trahair, 1994a, 1994b; Trahair and Pi, 1997; Bild *et. al.*, 1992; El-Khenfas and Nethercot, 1989). These authors conclude that modelling the strain-hardening region accurately is not necessary, as this region is rarely entered into for beams subject to these combined loads. To improve the material model used in this finite

element analysis, a four-part piecewise linear model is used to define the engineering stress vs. strain curve. This is composed of the following straight-line segments:

- The elastic region up to yield is defined by the modulus of elasticity,  $E$ , and Poisson's ratio,  $\nu$ , which are assumed to be 200 000 MPa and 0.3, respectively. The yield stress and strain are 350 MPa and 1750  $\mu\epsilon$ , respectively.
- The yield plateau extends horizontally to a strain of 11 times the yield strain (Pi and Trahair, 1994a; Bild *et al.*, 1992), or 19 250  $\mu\epsilon$ .
- A strain-hardening modulus of 6 000 MPa (Pi and Trahair, 1994a; Bild *et al.*, 1992) is used. This region stretches from the end of the yield plateau to the point where the ultimate tensile stress of 450 MPa is reached at 44 250  $\mu\epsilon$ .
- At a stress equal to the tensile strength, the stress vs. strain curve is a horizontal line assumed to extend to infinity. Typically, the strain at the ultimate stress is in the order of 15% to 20% for mild steel. The ultimate stress of 450 MPa was very rarely reached in any of the analyses in the parametric study.

Although the material properties are described in terms of engineering stress and strain, ABAQUS requires material properties to be in terms of true stress and true strain. The engineering values are converted to the true values using Equations [3.1] and [3.2]. Figure 5.4 presents the engineering and the corresponding true stress vs. strain curves used in the finite element model and Table 5.10 specifies the points from which the two curves are constructed.

### 5.3.3 Residual Stresses

The work presented in Chapter 3 indicated that modelling the exact residual stress pattern is not critical as long as the representation used is reasonable. This finite element approximation uses the linear residual

stress pattern used by Pi and Trahair (1994a) as seen in Figure 5.5. The flanges have a maximum tensile residual stress of  $0.5F_y$  at the flange-to-web junctions and a maximum compressive residual stress of  $0.35F_y$  at the flange tips. The web has a maximum compressive residual stress of  $0.35F_y$  over the middle half of the web, with a maximum tensile residual stress of  $0.5F_y$  at the flange-to-web junctions. Residual stresses were incorporated into the models using the method of average element stress as an initial stress condition as described in Chapter 3. An initial equilibrium step allows the residual stresses to equilibrate. Since this residual stress pattern is balanced left to right and top to bottom (equilibrium of moments), no uncontrolled initial imperfections develop from the method of inputting the residual stresses. Although the proposed residual stress pattern does not satisfy force equilibrium, equilibrium is achieved during the equilibrium step.

#### 5.3.4 Load Application

After the equilibrium step, a second load step applies an eccentric vertical load at the height of the shear centre. This force remains vertical throughout the analysis. The modified RIKS algorithm is used as the solution strategy, which was shown to be effective in previous chapters. A loading bracket was modelled with S4R shell elements as a vertical plate at the loading location (mid-span for B1 and B2 and at the free end for B3) as shown in Figure 5.2. The plate extends over most of the web height, i.e., over the middle 22 web elements, to avoid significant cross-sectional distortion. This loading bracket extends laterally in the positive Z-direction to the maximum eccentricity used in the E3 model (corresponding to  $M_n/T_n = 0.4$ ), and in the negative Z-direction to the eccentricity of the E1 model (corresponding to  $M_n/T_n = 2.4$ ), the latter being required for applying the couple for the torsion only load case.

The eccentricity is determined to provide the required ratio of maximum moment to maximum torque. For a point load at mid-span for boundary conditions B1 and B2 and at the free end for boundary condition B3 considered in the parametric study, the maximum moment and maximum torque occur at the same location, although the values are dependent upon the support condition. For wide flange sections, the total torsional resistance is often approximately ten times smaller than the flexural resistance, as was observed in the tests of Driver and Kennedy (1987). Since the moment–torque ratios selected for the parametric study were based on the normalised values,  $M_n/T_n$ , the actual moment–torque ratio,  $M/T$ , is obtained as follows:

$$\frac{M}{T} = k_2 \left( \frac{M_n}{T_n} \right) \quad [5.7]$$

where the constant  $k_2$  is the ratio of the flexural resistance (including lateral torsional buckling) according to CSA S16-01 to the total torsional resistance according to the method proposed by Driver and Kennedy (1987). Table 5.11 presents the maximum moment and torque values in beams with different boundary conditions and a point load  $P$  at mid-span as well as the equations used to calculate the required eccentricities from the ratio  $M/T$ . Table 5.12 presents the resulting eccentricities used in the finite element modelling for the parametric study. The load is applied at the shear centre of the beam web with no eccentricity for all E0 beams. The torsional couple for the E4 beams is introduced by applying equal and opposite follower loads to the loading bracket at the shear centre level on each side of the beam web at an eccentricity equal to the E1 eccentricity on each side of the web.

The thickness of the loading bracket is determined to minimize the vertical deflection of the bracket at the tip of the loading bracket relative to the beam web, assuming the bracket behaves as a fixed end cantilever. As a

minimum, the thickness of this loading bracket is 50 mm and it was thickened as required to maintain a relative vertical elastic deformation less than 0.25 mm over the length of the loading bracket to avoid influencing the results. For all of the B2 and B3 E4 beams, the web had to be thickened to 50 mm in the vicinity of the loading bracket to avoid distortion of the cross-section. This thickening is required for five elements on each side of the bracket for B2 beams and for the last five elements in the beam web for the B3 E4 beams. To ensure that this thickening does not have a significant effect on the results, a few models were run where the loading bracket connects to the flanges to avoid cross-sectional distortion and no web thickening was used. No significant differences were found. A benefit of not connecting the flanges to the loading bracket is that neither local buckling nor warping of the flanges at this location is artificially prevented.

Table 5.1 Distribution of Class of Sections

Steel Grade	Class 1	Class 2	Class 3	Class 4
<b>300W</b>	90.7%	6.8%	2.5%	0.0%
<b>350W</b>	84.7%	10.0%	4.3%	1.1%

Table 5.2 Slenderness Limits from CSA S16-01

$\frac{b}{2t}$			$\frac{h}{w}$		
Class	350W Steel $F_y = 350$ MPa	300W Steel $F_y = 300$ MPa	Class	350W Steel $F_y = 350$ MPa	300W Steel $F_y = 300$ MPa
1	7.75	8.37	1	58.80	63.51
2	9.09	9.81	2	90.87	98.15
3	10.69	11.55	3	101.56	109.70

Table 5.3 Variation of  $\frac{b}{2t}$  and  $\frac{h}{w}$  for Standard Wide Flange Sections

	$\frac{b}{2t}$	$\frac{h}{w}$
<b>Maximum</b>	11.52	63.62
<b>Minimum</b>	1.82	4.09
<b>Average</b>	5.69	32.74
<b>Range</b>	9.70	59.53

Table 5.4 Variation in  $\lambda$  Sorted by Section Class

	$\lambda$ ( $\times 10^{-6}$ )		
	Class 1	Class 2	Class 3
<b>Maximum</b>	2542	1144	1172
<b>Minimum</b>	207	256	290
<b>Average</b>	640	565	675
<b>Range</b>	2335	888	882

Table 5.5 Section Choices

Section	$\lambda$ ( $\times 10^{-6}$ )	Local Slenderness Ratios				Class of Section (350W Steel)		
		$\frac{b}{2t}$	$\frac{h}{w}$	$\frac{b}{d}$	$\frac{t}{w}$	Flange	Web	Overall
W150x24	1875	4.95	21.12	0.64	1.56	1	1	1
W530x123	548	5.00	38.29	0.39	1.62	1	1	1
W460x113	380	8.09	39.67	0.60	1.60	2	1	2
W200x52	863	8.10	22.89	0.99	1.59	2	1	2
W200x15	907	9.62	44.09	0.50	1.21	3	1	3
W310x97	474	9.90	28.00	0.99	1.56	3	1	3
W920x381*	433	3.53	35.38	0.33	1.80	1	1	1
W460x260*	779	3.58	18.95	0.57	1.79	1	1	1
W610x84*	290	9.66	63.62	0.38	1.30	3	2	3

\* Sections to be used for additional complementary cases of the parametric study described in the next chapter.



Table 5.8 Element Lengths, Widths, and Aspect Ratios for Parametric Study

Section	Element Length (mm)	Flange		Fillet		Web	
		Width (mm)	Aspect Ratio	Width (mm)	Aspect Ratio	Width (mm)	Aspect Ratio
S1	12.2	6.38	1.92	5.63	2.17	6.36	1.92
S2	23.2	13.3	1.75	11.4	2.03	23.9	1.03
S3	20.7	17.5	1.18	9.18	2.26	20.4	1.01
S4	17.2	12.8	1.35	7.80	2.21	8.11	2.12
S5	10.7	6.25	1.71	4.60	2.33	8.82	1.21
S6	24.1	19.1	1.26	10.5	2.30	12.5	1.92

Table 5.9 Peak Moment, Torque, and Load Values for Imperfection Study

Model	Moment (kNm)		Torque (kNm)		Load (kN)	
	Value	% Diff. w/Base	Value	% Diff. w/Base	Value	% Diff. w/Base
Base	27.9	N/A	3.79	N/A	91.5	N/A
Test 1	27.7	-0.8	3.63	-4.2	90.9	-0.7
Test 2	27.6	-1.1	3.63	-4.2	90.4	-1.2
Test 3	27.8	-0.4	3.54	-6.6	91.1	-0.4

Table 5.10 Engineering and True Stress vs. Strain Curves for Finite Element Models

Point	Engineering Stress vs. Strain		True Stress vs. Strain	
	Strain (mm/mm)	Stress (MPa)	Strain (mm/mm)	Stress (MPa)
1	0.0000	0	0.0000	0
2	0.0018	350	0.0017	351
3	0.0193	350	0.0191	357
4	0.0359	450	0.0353	466
5	0.1500	450	0.1398	518

Table 5.11 Method Used to Calculate Required Vertical Load Eccentricity

Boundary Condition	Maximum Moment	Maximum Torque	$\left(\frac{M_n}{T_n}\right)$	Eccentricity
1	$\frac{PL}{4}$	$\frac{Pe}{2}$	$\frac{L}{2e}$	$\frac{L}{2\left(\frac{M}{T}\right)}$
2	$\frac{PL}{8}$	$\frac{Pe}{2}$	$\frac{L}{4e}$	$\frac{L}{4\left(\frac{M}{T}\right)}$
3	$PL$	$Pe$	$\frac{L}{e}$	$\frac{L}{\left(\frac{M}{T}\right)}$

Table 5.12 Eccentricities Used in Parametric Study

Section (S#)	Length (L#)	Boundary Condition (B#)	$k_2$	Eccentricities (mm)		
				E1	E2	E3
S1	L1	B1	10.4	25	59	147
		B2	7.14	18	43	107
		B3	13.5	49	118	294
	L2	B1	11.8	38	91	227
		B2	10.4	25	59	147
		B3	15.7	76	182	454
S2	L1	B1	13.5	36	86	216
		B2	8.52	28	68	170
		B3	18.9	72	172	431
	L2	B1	15.2	51	123	306
		B2	13.5	36	86	216
		B3	22.6	102	245	613
S3	L1	B1	17.4	51	122	306
		B2	8.49	41	98	244
		B3	24.8	102	245	612
	L2	B1	19.3	72	172	430
		B2	17.4	51	122	306
		B3	29.5	143	344	859
S4	L1	B1	13.8	50	120	300
		B2	9.37	37	89	222
		B3	18.1	100	240	601
	L2	B1	15.6	76	183	458
		B2	13.8	50	120	301
		B3	21.2	153	360	916
S5	L1	B1	24.8	14	35	86
		B2	11.1	12	29	71
		B3	29.4	29	69	173
	L2	B1	29.4	19	47	117
		B2	19.0	14	35	86
		B3	38.8	39	93	233
S6	L1	B1	20.4	67	161	402
		B2	10.1	51	123	307
		B3	23.4	134	322	805
	L2	B1	24.9	99	237	593
		B2	16.2	67	161	402
		B3	29.5	198	474	1186

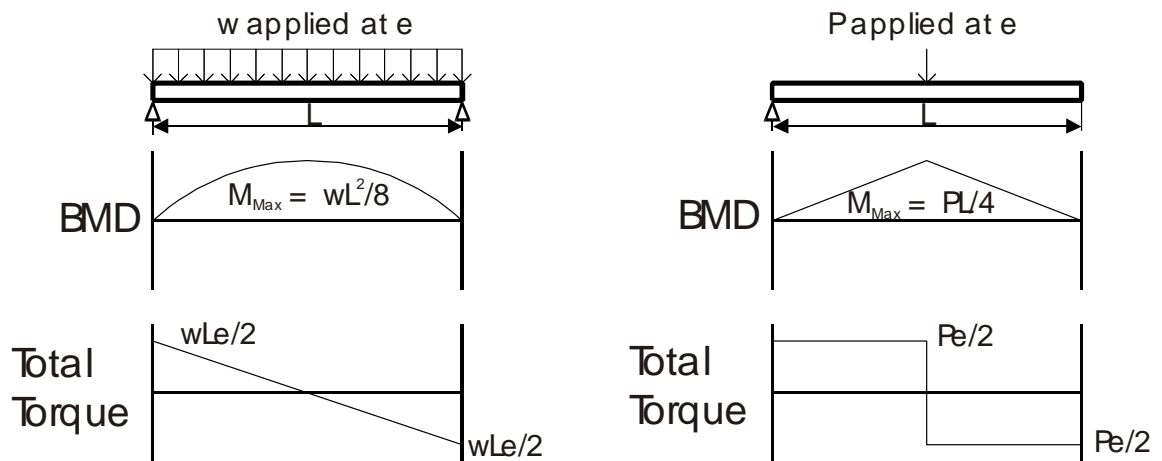


Figure 5.1 Bending and Torsional Moment Diagrams for UDL and a Point Load at Mid-Span

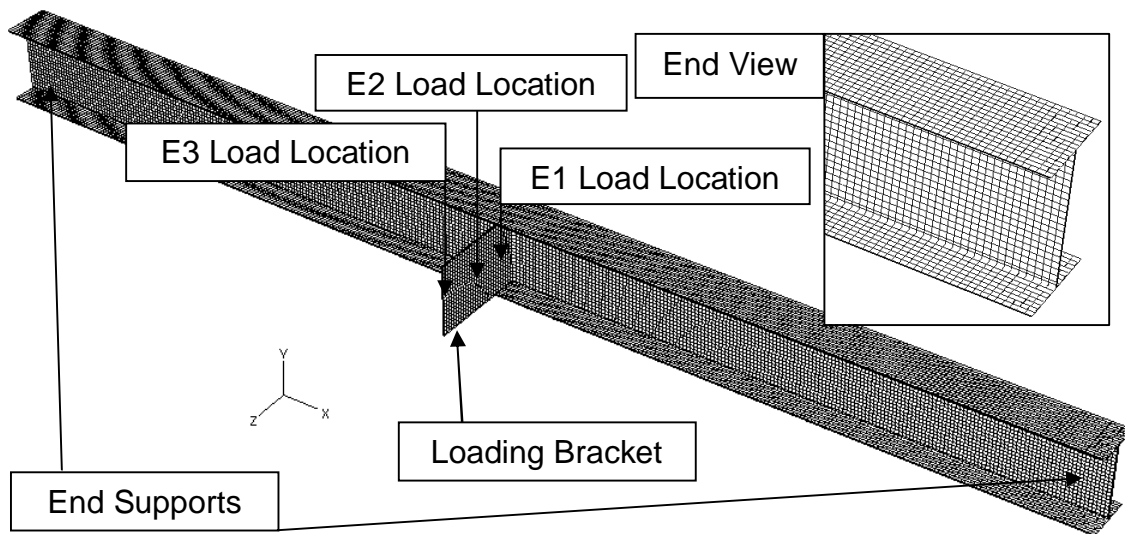


Figure 5.2 Typical Finite Element Mesh

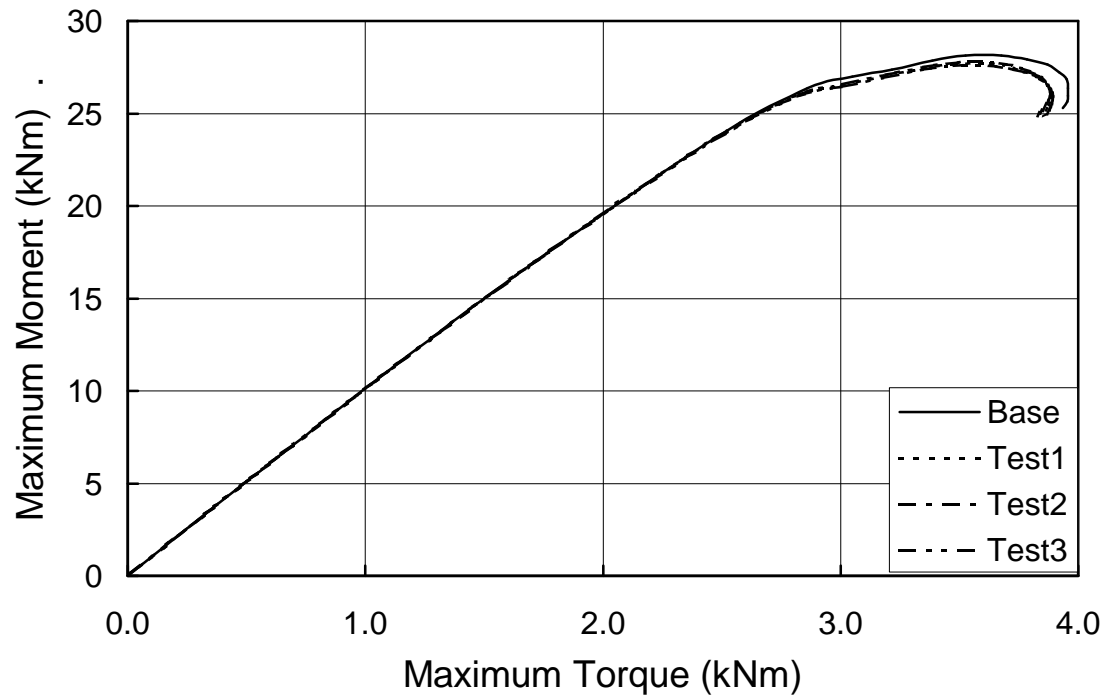


Figure 5.3 Maximum Moment vs. Torque Diagram for Imperfection Study

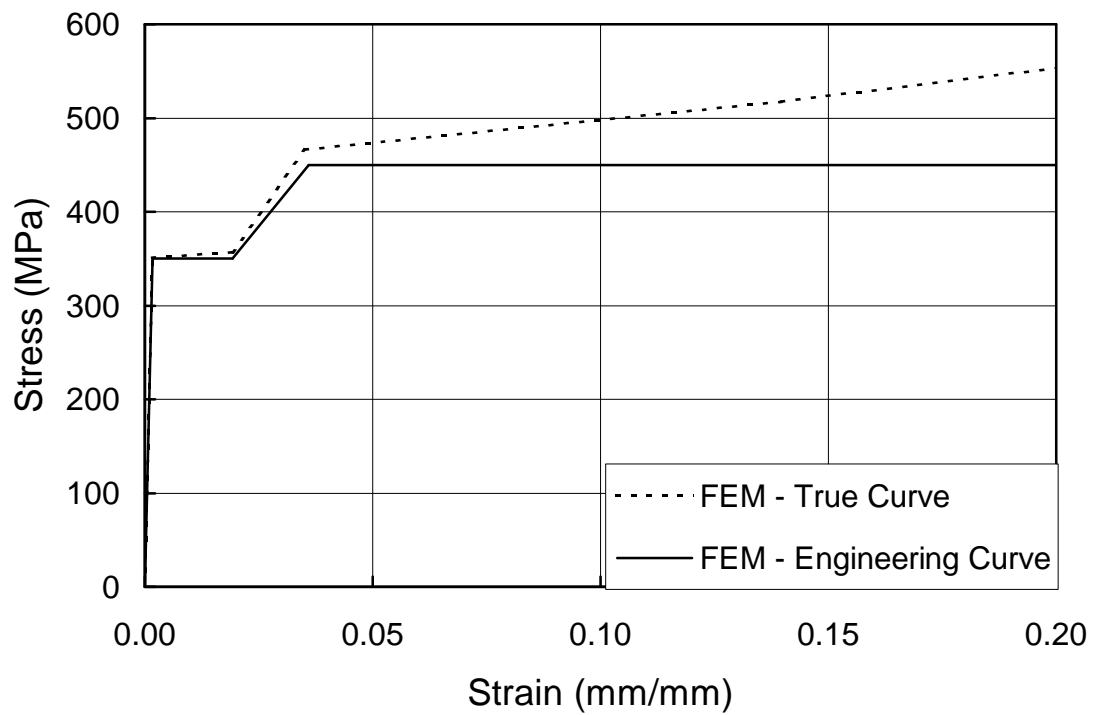
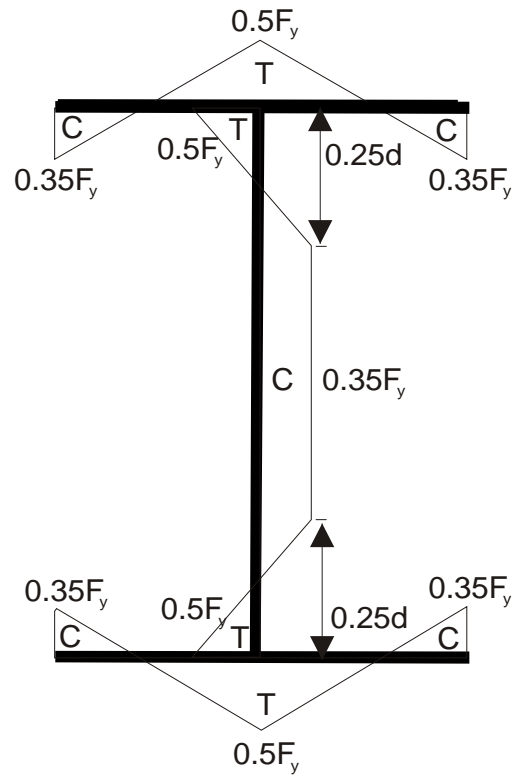


Figure 5.4 Stress vs. Strain Curve for Parametric Study



*Figure 5.5 Residual Stress Pattern Modelled*

## 6 PARAMETRIC STUDY RESULTS

The results of a parametric study using 180 different combinations of beam cross-section, span length, boundary conditions, and loading conditions including both load type and load eccentricity are used to develop a simple and versatile method for designing beams subject to combined flexure and torsion. One of the goals of this parametric study is to verify or modify design methods reviewed in Chapter 2.

For each of the finite element results the point where the ultimate limit state is reached on the moment–torque diagram is determined. To be consistent with limit states design practice, the first hinge concept is used to determine the ultimate limit state for these beams. A diamond is used from this point forward in the various diagrams to indicate the point selected as the ultimate limit state. Since this is an ultimate limit state assessment, no limits on the rotation or deflections are imposed. However, because the torsional rotations in some cases are large when the ultimate limit state is reached, the impact on the conclusions of including a practical rotation limit is discussed in Section 6.2.4.

The ultimate limit state points are compared against the interaction diagram proposed by Driver and Kennedy (1989) by means of the finite element to theoretically predicted ratio, or FEPR. The moment–torque interaction diagram can be normalized separately by the theoretical ultimate moment and torque capacities, respectively. Additional information, including the cross-sectional rotation and the maximum stress and strain, are also recorded at these ultimate points. The FEPR values are determined by three equations following the tri-linear interaction diagram presented in Figure 2.4 and Figure 6.1 (this diagram is not normalized). The coordinates of Point 1 are denoted by  $(T_1, M_1)$  where  $T_1$  equals zero. The line segment between points 1 and 2 represents the portion of the diagram where the section can carry the full moment

capacity ( $M_1 = M_2 = M_r$ ), including the effects of lateral-torsional buckling. The FEPR for this segment of the diagram is determined by the following when the torque,  $T$ , and moment,  $M$ , both taken as the moment and torsional resistances as determined from the finite element analysis that is consistent with reaching the ultimate limit state, is less than  $T_2$ :

$$(FEPR)_{1-2} = \frac{M}{M_1} \quad [5.8]$$

The value of FEPR along the line between points 2 and 3 is defined as:

$$(FEPR)_{2-3} = \frac{M}{M_5} + \frac{T}{T_6} \quad [5.9]$$

where  $M_5$  and  $T_6$  are as shown in Figure 6.1 and obtained by extrapolation of line 2-3.

$$M_5 = \frac{M_1}{\eta} \quad [5.10]$$

$$T_6 = \frac{T_4}{\alpha} \quad [5.11]$$

where  $\eta$  and  $\alpha$  are factors to convert points 1 and 4 on the interaction diagram to the fictitious points 5 and 6:

$$\eta = \frac{1 - \frac{1}{R_T}}{R_M - \frac{1}{R_T}} \quad [5.12]$$

$$\alpha = \frac{1 - R_M}{1 - R_M R_T} \quad [5.13]$$

where  $R_T$  and  $R_M$  are torque and moment ratios calculated by:

$$R_T = \frac{T_2}{T_4} \quad [5.14]$$

$$R_M = \frac{M_3}{M_1} \quad [5.15]$$

For the interaction diagram between points 3 and 4 the FEPR value,  $(FEPR)_{3-4}$ , is calculated by:

$$(FEPR)_{3-4} = \frac{T}{T_4} \quad [5.16]$$

To investigate serviceability limit states, representative service load points, denoted from this point forward by a large “X” in the diagrams, are found by dividing the applied load at the ULS by a load factor of 1.4 that approximates the combined load factor from dead, live, and other load types. To determine whether the ultimate or serviceability limit state governs, the maximum cross-sectional stress and strain (i.e., the stress or strain normal to a cross-section), moment, torque, and rotation are determined for both the ultimate and service load levels, as well as the vertical deflection at the service load. In addition to determining the ultimate and service points for each beam, the following full-history diagrams are found to help describe the beam behaviour:

- maximum moment vs. maximum torque
- maximum moment vs. maximum torque non-dimensionalized or normalized by dividing by the pure moment and pure torque capacities, respectively
- maximum torque vs. maximum rotation
- maximum moment vs. maximum vertical deflection
- vertical load vs. maximum vertical deflection
- vertical load vs. maximum lateral deflection
- maximum weak axis moment vs. maximum lateral deflection
- maximum strong axis moment vs. maximum vertical deflection

Note that the maximum rotation, vertical deflection, and lateral deflection all occur at the concentrated load point.

The remainder of this chapter presents an analysis of the data described above. Appendix A describes how each of these values is calculated.

Refer to Appendix B for a more complete presentation of the data describing the ultimate and service points, as well as the resulting ultimate moment–torque interaction diagrams.

## **6.1 Parametric Study**

### **6.1.1 Moment–Torque Ratio**

#### 6.1.1.1 Pure Flexure (E0 beams)

The failure mechanisms associated with the ultimate limit state under pure flexure, or E0, are clearly identifiable from the finite element analyses. In the L1 and B2 L2 beams (L1 beams are all beams with a slenderness ratio of 50 and B2 L2 beams are all beams with completely fixed boundary conditions at both ends with a slenderness ratio of 100), a flexural plastic hinge forms at mid-span, whereas in all of the B1 L2 and B3 L2 beams (B1 L2 beams are all simply supported beams with a slenderness ratio of 100 and B3 L2 beams are all cantilever beams with a slenderness ratio of 100), the phenomenon of lateral torsional buckling occurs. The flexural resistance is calculated using the guidance of CSA S16-01. The effects of the boundary conditions on the flexural resistance are accounted for by means of  $\omega_2$ , the equivalent moment factor.

In the B2, or fixed-fixed boundary condition, case, the beams have reserve capacity above this initial hinge formation, where two additional hinges are required at the support locations to create a plastic collapse mechanism, resulting in global instability. To take advantage of this reserve capacity, the requirements of Clause 8.6 of CSA S16-01 must be met. This clause limits this design procedure to Class 1 sections with steel having  $F_y \leq 0.85F_u$  where  $F_u$  is the ultimate stress, members are laterally braced as per Clause 13.7, web stiffeners are supplied at points of load application where hinges can form, structure is not subject to fatigue, inelastic deformations are accounted for, and splices are designed for the greater of 1.1 times the maximum moment or one-quarter of the plastic

moment and is thus limited in use. The finite element results had very good agreement with the proposed interaction diagram when the ultimate flexural limit state is determined according to CSA S16-01 including lateral torsional buckling and the equivalent moment factor  $\omega_2$ , as seen in row 1 of Table 6.1 for all boundary conditions, cross-sections, and lengths.

The ultimate limit state for the E0 beams correspond to either a peak in the moment vs. torque diagram or the point in the behaviour where torque starts to develop and become significant as the beam buckles laterally and begins to rotate torsionally. This method is similar to that used by Driver and Kennedy (1987) to select the ULS for Beam 1 where the beginning of the second phase begins. For Beam S4L1T1B1E0, which exhibits typical behaviour for the pure flexure case, the ultimate limit state corresponds to the peak moment that occurs at a very small torque, as denoted in Figure 6.2. As seen in the figure, the typical pure flexural response involves a vertical ascension to a peak moment followed by a long, drawn out yield plateau that is followed by a sharp drop.

#### 6.1.1.2 Torsion Only Load Case (E4 beams)

The torsion only load cases, the E4 beams, have similar behaviour for all boundary conditions. A sample torque vs. rotation behaviour is shown in Figure 6.3 for Beam S1L2T1B2E4. An “initial yield region” characterized by a significant reduction in slope as yielding of the cross-section due to warping reduces the torsional stiffness follows the initial elastic region. In this case, this yielding region of decreasing stiffness starts at a torque of 3.5 kNm and ends at a torque 6.6 kNm. After this “initial yield region”, the slope either remains constant or increases slightly up to, for some beams, a peak in the curve. Typical of the results, the torque for Beam S1L2T1B2E4 increases much beyond the predicted torsional resistance of 6.5 kNm. In general, the beam ultimate limit state capacities determined from the finite element model exceed the predicted capacities determined according to the method proposed by Driver and

Kennedy (1987, 1989). At these ultimate limit states, the beam rotations are often near, or even beyond,  $90^\circ$ , making the situation highly impractical. Some of this additional capacity beyond the predicted capacities develops as a result of the Wagner stresses and strains that develop due to the helical curvatures that arise under these large rotations (Trahair and Pi, 1997).

To be consistent with ultimate limit states design philosophy used also in Section 6.1.1.1, the first plastic hinge concept is used as the ultimate limit state for torsion only loading as well. The development of the first plastic hinge coincides with the end of the “initial yield region”, denoted here by a diamond for the ultimate limit state, where sufficient yielding has occurred from the applied bi-moments to develop a plastic hinge in the flanges referred to hereon as a warping hinge. This observation is supported by the work of Trahair and Pi (1997), who found a similar torsional behaviour to that found in Figure 6.3 and make a similar conclusion in regards to the torsional capacity of a beam. In cases where the torque vs. rotation diagram does not clearly indicate the ULS, the stress plots are used to help determine the ultimate limit state by confirming the development of the plastic hinge. An example of a beam that does not have a clear “initial yield region” is Beam S5L2T1B3E4. The torque vs. rotation and von Mises stress contour plots are shown in Figure 6.4 and Figure 6.5, respectively. The von Mises stress accounts for yielding in a 3D state of stress. The yielded portions are shown in light grey. At the end of the “initial yield region” at the ultimate limit state, the top and bottom flanges have clearly developed warping hinges at the support as a result of the warping normal stresses.

The responses of some of the E4 beams show several apparent “yield regions”. An example of this is shown in Figure 6.6 for Beam S2L1T1B1E4. The ultimate limit state is selected at the end of the second “yield region” because of the von Mises stress contour shown in

Figure 6.7, where plastic warping hinges form in both the top and bottom flanges at mid-span. Some of the E4 beams have a step in the torque vs. rotation behaviour immediately after this “initial yield region”, as seen in Figure 6.8 for Beam S5L1T1B2E4. For all of the beams showing this irregular response, the yielding process is not complete until after this step. Figure 6.9 illustrates the warping hinges that develop in the top and bottom flange at the ultimate limit state selected after this step for Beam S5L1T1B2E4. To be consistent with the first hinge method, the ultimate limit state is selected at the end of this step where warping hinges have developed, and in this case, local buckling has begun in the top flange at mid-span.

Using the first hinge concept to determine the ultimate limit states, the average FEPR and coefficient of variation values for all of the E4 beams are found in row 2 of Table 6.1 (formed from the results found in Appendix B). Only the S1L1T1B1E4 Beam has a FEPR value (0.88) less than 0.95. All of the beams had significant reserve capacity beyond the selected ultimate limit state as well as the torsional resistances predicted using the method proposed by Driver and Kennedy (1989) due in part to the Wagner stresses ranging from a minimum of approximately 20% up to 253% for Beam S1L2T1B3E4. Although there is significant variation in the FEPR values, these beams have sufficient reserve capacity beyond the ULS points and indicate that the theory is generally conservative.

#### 6.1.1.3 Combined Torsion and Flexure (E1, E2, and E3 beams)

A change in the  $M/T$  ratio has a significant effect on how the beam carries the applied load although it is highly difficult to definitively describe or qualify the behaviour. In general, the response for larger eccentricity (E3) beams is commonly characterized by aspects of torsional behaviour such as plastic warping hinges in the flanges. Conversely, for small eccentricities (E1 beams), the beam response is usually dominated by flexural behaviour and develops flexural plastic hinges. These rules are

not definite and there are exceptions. The behaviour of these eccentric load cases will be discussed further in the next sections. Unlike the pure loading responses (i.e. pure moment or pure torque) described in the previous two sections, the beam response under combined loading is dependent upon the boundary conditions and will therefore be discussed in Section 6.1.2.

### **6.1.2 Effect of Load Eccentricity under Various Boundary Conditions**

For each boundary condition considered, twelve different beams are investigated (six sections and two slenderness ratios), each with five moment–torque ratios.

#### **6.1.2.1 Simply Supported (B1 beams)**

Simple support conditions represent the most critical case in that the formation of a single plastic hinge along the beam length creates a collapse mechanism and it is the most critical case for lateral–torsional buckling. Figure 6.10 and Figure 6.11 present typical moment vs. torque and torque vs. rotation diagrams, respectively, for Beam S3L1T1B1 with load eccentricities varying from zero (E0) to larger values (E3) corresponding to a normalized moment–torque ratio of 0.4. As seen in Figure 6.10, a peak moment is achieved for all eccentricities. Beyond the peak load, the moment drops off quickly and eventually the torque begins to decrease as well, as a result of the large rotations making weak axis bending more prominent. Typical of simply supported beams, the torque vs. rotation diagram in Figure 6.11 reaches a peak with three “yield regions” along the curve. As the cross-sectional rotation becomes sufficiently large beyond the peak load and weak axis bending becomes prominent, the torque that develops begins to decrease as the load eccentricity and applied load decrease.

The ultimate limit state is selected as the point of peak moment, as shown in Figure 6.10, which corresponds with the formation of a plastic hinge at

mid-span. For reference, the points of peak moment are also shown on the curves of Figure 6.11. The von Mises stress contour plots reveal that the top and bottom flanges at mid-span have almost completely yielded at the ultimate limit state (see Figure 6.12). At the point of maximum moment, the web is not fully plastic. Also, a plastic hinge has formed in both top and bottom flanges under the combined action of warping bi-moments and flexural normal stresses. This causes the stiffness of the rotated cross-section to suddenly decrease. Beyond this point, the beam undergoes rapid vertical deflection. Figure 6.12 illustrates a plastic warping hinge developed in the flanges at mid-span for Beam S4L2T1B1E1.

A few exceptions to these patterns are noted as for Beam S5L2T1B1E2, where multiple peaks are found in the moment vs. torque diagram presented in Figure 6.13. The first peak is taken as the ultimate limit state because the stress plot at this point represents the formation of a warping hinge in the top flange, as shown in Figure 6.14. Several E3 beams, due to their relatively large load eccentricity, behave differently and reach a peak torque instead of a peak moment, as shown in Figure 6.15 for Beam S1L2T1B1E3. For these beams, the ultimate limit state corresponds to instability of the beam due to the formation of a warping plastic hinge in the top flange at mid-span.

The moment–torque Interaction diagram proposed by Driver and Kennedy (1989) tends to over-predict the capacity of a significant number of the simply supported beams, as several of the selected ultimate limit state points lie well below the proposed diagram, as seen in row 3 of Table 6.1 (refer to Appendix B). In particular, the interaction diagram does not agree well with the finite element results for sections 1, 2, and 3, as shown in row 4 of the table. However, the results for sections 4, 5, and 6 fit the interaction equation proposed by Driver and Kennedy (1987, 1989) well, as shown in row 5 of Table 6.1 (refer to Appendix B) with an average

FEPR value of 1.03. Sections 4 and 6 have  $b/d$  ratios near 1.0, typical of wide flange sections used for columns, whereas Section 5 has a  $b/d$  ratio of 0.5, which is lower than most of the modelled wide flange sections. Section 5 does, however, have a low  $t/w$  value of 1.2 as compared to the other sections selected for the parametric study and all wide flange sections in general. It is possible that for large  $b/d$  ratios or small  $t/w$  ratios, sections are able to develop a capacity that can be predicted by the interaction diagram of Driver and Kennedy (1987, 1989). This hypothesis is further verified when the W610x84 ( $t/w=1.30$ ) section is further investigated in Chapter 7.

#### 6.1.2.2 Fixed-Fixed (B2 beams)

Unlike simply supported beams, the B2 beams (fixed at both ends) have increased capacity beyond the formation of a single plastic hinge. Two phases of behaviour are observed, separated by the point where the first plastic hinge forms. At the end of the first phase of behaviour, warping plastic hinges form at mid-span and at both support locations in the top flange creating a warping failure mechanism. These warping hinges form at the same time due to symmetry caused by the loading conditions. The same warping hinges do not develop in the bottom flange at the same time possibly because of second order effects where the load has a greater effect on the rotated cross-section. At this point, the beam behaves as if a flexural plastic hinge about the strong axis of the beam forms at mid-span. The warping failure mechanism in the top flange allows the rotated and deflected cross-section at mid-span to behave like a flexural plastic hinge. Further loading in the second phase of behaviour causes the development of flexural plastic hinges at the support locations creating a global failure mechanism. Figure 6.16 and Figure 6.17 for S1L2T1B2 illustrates this typical behaviour of fixed ended beams. To be consistent with the limit state design philosophy, the ultimate limit state is selected as the point where the first plastic hinges form.

The beams loaded in combined bending and torsion (E1, E2, and E3) clearly show the two phases of behaviour described above. The beam response captured from the finite element analysis showed the formation of this effective flexural hinge at mid-span as the vertical stiffness of the beam suddenly decreases at the selected ultimate limit state point. This is visible on the vertical load vs. vertical deflection diagram shown in Figure 6.18 for Beam S1L2T1B2E1. The initial stiffness for all B2 beams is high, followed by a region characterized by the initial yielding of the cross-section and the creation of the first plastic hinge referred to here as the “initial yield region”. After this region, the stiffness of the beam decreases significantly due to the plastic hinge at mid-span. The torque decreases through this second phase as the large rotations decrease the eccentricity of the load as weak axis bending becomes more prevalent. The selected ultimate limit state corresponds to the point at the end of this “initial yield region” where the first plastic hinges form.

The only irregularity that occurs for the B2 beams is that for some eccentrically loaded (E1, E2, or E3) cases, a peak moment is reached in the first phase of behaviour. This behaviour was observed in only 25% of the beams investigated (S2L1T1B2E1, S2L1T1B2E2, S2L2T1B2E1, S3L1T1B2E1, S3L1T1B2E2, S3L2T1B2E1, S5L1T1B2E1, S5L1T1B2E2, and S5L2T1B2E1). An example of this moment–torque behaviour is shown in Figure 6.19 for Beam S2L1T1B2E2. For these beams, the hinges that form at mid-span are flexural plastic hinges rather than warping hinges. This result is found typically in beams with smaller global slenderness ratios ( $L/r_y$ ), small  $b/d$  ratios (sections typical of flexural applications), and large  $h/w$  ratios. The ultimate limit state for these beams is selected at the peak moment, which corresponds to the formation of the first plastic hinge.

The ultimate limit state points for the B2 beams are selected when the first plastic hinges are formed in the top flange at mid-span. This point has several key characteristics:

- It is the point where the second phase of behaviour begins in the moment vs. torque diagram corresponding to the end of the first “initial yield region” or inflection point (point where the curvature of the diagram changes from a decreasing slope to an increasing slope). For the beams where a peak moment is developed, the end of the first phase of behaviour is described by the point of peak moment.
- It is the point at the end of the “initial yield region” on the vertical load vs. vertical deflection diagram.
- It is the point where the von Mises stress contour plot first indicates that the cross-section is sufficiently plastified to create either a warping hinge (a stepped stress distribution across the flange) or a flexural hinge (a stepped distribution vertically on the cross-section).

A typical example of each of these three criteria being used to determine the ultimate limit state is shown in Figure 6.20 through Figure 6.22 for Beam S2L2T1B2E2.

The average FEPR and coefficient of variation values can be found in row 6 of Table 6.1 (refer to Appendix B) for all of the B2 beams. Only ten of the 60 B2 Beams have a FEPR less than 1.00. The FEPR values for the five beams with a FEPR less than 0.95 are listed in rows 7 through 11 of Table 6.1. The average FEPR and coefficient of variation values for the E0, E1, E2, E3, and E4 B2 beams are presented in rows 12 to 16 of Table 6.1, respectively.

#### 6.1.2.3 Fixed End Cantilever (B3 beams)

Forty-five of the 60 B3 beams (nine physical beams each with five different eccentricities) have a response that has distinct similarities to the test

results of Driver and Kennedy (1987). A typical beam response for these 45 beams is presented in Figure 6.23 and Figure 6.24 for Beam S3L2T1B3 loaded with different load eccentricities. The point where the second phase of behaviour begins is not well defined in the torque vs. rotation diagram for all eccentricities investigated. Instead, the change is marked by a gradual increase to the slope of the diagram, making this point difficult to determine. The slope of the diagram in the first phase is relatively constant, unlike the results of the finite element model developed in Chapter 3 based on the experimental work of Driver and Kennedy (1987) who found the slope to decrease gradually in the first phase. In the moment vs. torque diagram, the finite element model behaviour is similar to the B1 beams in that a peak moment is achieved.

A typical response for the other 15 beams (three physical beams each with five different eccentricities) is illustrated in Figure 6.25 and Figure 6.26 for Beam S2L1T1B3. Unlike the 45 beams mentioned previously, the torque approaches a constant value as the rotations become large in the torque vs. rotation diagram. In the moment vs. torque diagram, there is a sudden drop in moment capacity until the rotation becomes large enough, in the order of 30 degrees, that weak axis bending becomes prominent. The other ten beams (two physical beams each with five different eccentricities) that demonstrate this behaviour are S3L1T1B3 and S5L1T1B3. These beams, where no second phase of behaviour appears to be present, are all L1 beams (lateral torsional buckling does not govern), with a large  $h/w$  ratio of approximately 40.

Since the two phases of behaviour are not consistent, the points of peak load and thus moment are used as the ultimate limit state whenever a peak is present in the response for several reasons. First, the point where the second phase of behaviour begins is not clearly defined, as for the three beams mentioned above. Second, using the peak load is more consistent with the ultimate limit state used for the other boundary

conditions. Third, this point corresponds to the formation of warping hinges in the top and bottom flanges at the fixed support and is consistent with the first plastic hinge approach used thus far. A sample von Mises stress contour plot shown in Figure 6.27 illustrates the formation of a plastic hinge in the flanges at the ultimate limit state. It also is indicative of the significant plastification of the beam. Last, as seen in Figure 6.28, representative of the three beams without two distinct phases of behaviour, this approach selects the point after the “initial yield region” on the vertical load vs. vertical deflection curves as used to determine the ULS for the fixed-fixed boundary conditions.

Using this approach, the average FEPR and coefficient of variation values for all of the B3 beams is found in row 17 of Table 6.1 (refer to Appendix B). Eight out of the 60 beams have a FEPR less than 1.00. Only one of these eight beams has a FEPR less than 0.95, S1L2T1B3E1, at 0.88. The average FEPR and coefficient of variation values for the E0, E1, E2, E3, and E4 B3 beams are presented in rows 19 to 23 of Table 6.1, respectively. The finite element results indicate that there is a large degree of conservatism and variation of the proposed interaction equation. The finite element results for the S5L2T1B3 beams have very high FEPR values (an average value of 1.79). This extreme degree of conservatism cannot be explained and indicates that further research may be required to reduce the conservatism and variation of this approach for cantilever beams.

### **6.1.3 Cross-sectional Dimensions**

Of the six wide flange sections, theory indicates that two behave as each of Class 1, 2, and 3 sections for 350W steel using the limits in CSA S16-01 for pure flexure, allowing the construction of the interaction equation for each section class to be investigated. The finite element results indicate that 25% of the 180 beams behave as a higher class of section in flexure than predicted by the limits established in CSA S16-01. That is, some

beams that are classified as Class 3 sections in flexure developed the plastic moment capacity prior to local buckling. A similar result is found looking only at the torsional resistances. The finite element results of 75 out of the 180 beams indicate that the beam behaves as a higher class of section in torsion and develops a larger torsional resistance than predicted by the recommended procedure using the previously established flexural limits to select the class of section.

None of the 180 beams behave as a lower class of section, making the results generally conservative. Only 30 beams behave as a higher class of section in both torsion and flexure. To investigate these sections, another interaction diagram labelled “modified classes” is constructed as done previously except that now it is based on a modified class of section. This modified class of section is determined arbitrarily by selecting the class of section that the finite element results can develop the torsional and flexural resistances of treating torsional and flexural behaviour separately. Examples of this behaviour are found in Figure 6.30 through Figure 6.32.

With the beams classified according to the flexural guidelines of CSA S16-01, the average FEPR and coefficient of variation values are presented in row 24 of Table 6.1. The FEPR values improve when the class of section is determined using these modified classes based upon the finite element results instead of the guidelines provided in CSA S16-01. If the beams are reclassified according to these modified classes in flexure only, the average FEPR and coefficient of variation do not significantly improve becoming 1.24 and 21.6%, respectively. If the beams are reclassified according to these modified classes in torsion only, the average FEPR and coefficient of variation significantly improve becoming 1.15 and 15.5%, respectively. If the beams are reclassified according to these modified classes in both flexure and torsion, the

average FEPR and coefficient of variation significantly improve becoming 1.15 and 15.5%, respectively.

Similar to Driver and Kennedy (1987), Pi and Trahair (1994a, 1994b; Trahair and Pi, 1997) suggest that a section loading under combined torsion and flexure should be classified by the flexural limits of their respective design codes. The finite element results indicate that the torsional local slenderness limits might not be the same as for flexure. Several beams appear to behave as a higher class of section in torsion and accounting for this effect arbitrarily as done above using the modified classes has a significant improvement on the FEPR values. Although using the flexural guidelines to classify a cross-section in torsion appears to be conservative in all cases investigated thusfar, further research should be performed to investigate the classification of sections in torsion.

The governing failure mechanisms and ultimate limit states suggested in Section 6.1.2 for both the B2 and the B3 beams are dependent upon the overall behaviour of the section. Wide flange sections with large  $h/w$  ratios and small  $b/d$  ratios behave primarily in a flexural manner (formation of flexural hinges) and the torsional response (formation of warping hinges) is less dominant compared to other cross-sections. That is, the first hinge that tends to form in these cross-sections is a flexural hinge and not a warping hinge. Three important results for beams with large  $h/w$  and/or small  $b/d$  ratios are noted below and in Section 6.1.2:

- The two phases of behaviour typically found for the B3 beams (cantilever beams) are not found when the global slenderness ratio is small.
- The first plastic hinges that form for the B2 beams (fixed at both ends) are flexural hinges compared to warping hinges, which were more common for the beams in this investigation that did not fail by lateral torsional buckling.

- These cross-sections can develop capacities close to the prediction of the proposed interaction equation even for simply supported beams.

Beams with smaller  $h/w$  ratios and larger  $b/d$  ratios are stocky sections used primarily for columns and behave in a primarily torsional manner and the flexural response is less dominant for eccentrically loaded beams.

#### **6.1.4 Effect of Beam Length**

Although true lateral torsional buckling is a phenomenon related to pure flexure, similar effects that reduce the flexural capacity of a member are clearly observed for the beams with smaller eccentrically applied vertical loads. As the eccentricity of the applied vertical load increases, however, the signs of lateral torsional buckling become less apparent. These beams deform (deflect laterally and vertically as well as twisting) gradually and do not exhibit signs of buckling. The moment capacity used to determine the interaction diagram must include the effects of lateral torsional buckling.

The phenomenon of lateral torsional buckling and its effects on capacity are observed in all of the beams where CSA S16-01 and the use of  $\omega_2$  predicts lateral torsional buckling would occur. The average FEPR for the L2 E0 beams is 1.06, with a coefficient of variation of 5.5%.

## **6.2 General Discussion**

The literature review found in Chapter 2 revealed two promising ultimate limit state design approaches. The results of the parametric study have been thus far compared to the method proposed by Driver and Kennedy (1987). The other method proposed by Pi and Trahair (1994b; Trahair and Pi, 1997) has been shown to be accurate for simply supported beams with varying degrees of bracing. For beams braced laterally at the supports only, they propose the use of a straight-line interaction diagram.

Comparing the beams of the parametric study to the tri-linear interaction diagram proposed by Driver and Kennedy (1987) for simply supported beams in Section 6.1.2.1, the results indicate that this interaction diagram tends to give significantly non-conservative predictions of the beams capacity.

The interaction diagram of Figure 6.1 is based on the assumption that a wide flange section can carry a torque up to its full St. Venant torsional resistance, determined according to the class of section, without a reduction in flexural strength (including the effects of lateral torsional buckling). Since St. Venant torsion introduces only shear stresses in the cross-section, it does not increase the normal stresses created by the flexural loads, which could reduce the flexural capacity of the member. However, several E1 beams for both the B2 and B3 boundary conditions lie significantly (as much as 18%) below the ideal FEPR of 1.00. This behaviour is more prominent for the stockier Class 1 or 2 sections, whose pure torsional resistance is larger and calculated using the sand heap analogy compared to the membrane analogy used for Class 3 sections.

As the torque increases along the line segment between Points 1 and 2 of the interaction diagram, the shear stresses that develop as a result of the torque become more important for Classes 1 and 2 sections. The wide flange section's flexural capacity is reduced by the interaction of these shear stresses with the flexural normal stresses causing premature yielding to occur in the cross-section. The introduction of torsion into the beam develops warping torsion in addition to pure torsion in proportion to their respective rigidities. The warping torsion also introduces normal stresses into the flanges that results in premature yielding.

### **6.2.1 Proposed Modifications to the Interaction Diagram**

It is proposed here that two modifications be implemented to the interaction diagram illustrated in Figure 6.1. To account for the first

shortcoming of the interaction diagram of Figure 6.1 outlined above, modification one recommends that a straight-line interaction equation be used to predict the ultimate limit state for all simply supported beams. All other boundary conditions are to use the tri-linear interaction diagram shown in Figure 6.1 as proposed by Driver and Kennedy (1987, 1989). This straight-line interaction diagram connects Points 1 and 4 of Figure 6.1. This proposed approach is supported by the work of Pi and Trahair (1994a, 1994b; Trahair and Pi, 1997) who found a straight-line interaction diagram, identical to that proposed here, to be the best method for predicting the ultimate resistance of an unbraced simply supported beam subject to combined torsion and flexure.

To check the impact of this modification, the FEPR values for B1 beams are recalculated using Equation [6.2], where  $\alpha$  and  $\eta$  are taken as 1.0, causing Points 5 and 6 to coincide with Points 1 and 4, respectively. As shown in row 3 of Table 6.1, the resulting average value of FEPR increases to a more conservative value of 1.13, compared to the original value of 0.95, and the coefficient of variation shows a slight decrease from 19.2% to 16.6%. The new modified normalized moment vs. torque interaction diagram (normalized to compare all beams) for simply supported beams is compared against all 60 beams investigated in this parametric study in Figure 6.29. A total of 14 of the 60 B1 beams have a FEPR less than 1.00 and only five of these have a FEPR value less than 0.95, with a minimum of 0.88 (S1L1T1B1E4). The average FEPR (and coefficient of variation) values, accounting for this modification for the simply supported boundary condition, for E0, E1, E2, E3, and E4 beams are 1.01 (5.2%), 1.18 (14.5%), 1.16 (14.4%), 1.27 (18.9%), and 1.05 (7.9%), respectively. As discussed in Section 6.1.2.1, more research is required to investigate if certain types of cross-sections (large  $h/w$  and small  $b/d$  ratios) for simply supported beams are able to develop beyond

the straight-line proposed here and up to the tri-linear interaction diagram for B1 beams.

To account for the interaction between the torsional shear stresses and the flexural normal stresses at Point 2, the second proposed modification to the tri-linear interaction diagram (used for all boundary conditions except simply supported beams), reduces the torque that can be carried with the full flexural capacity. For all section classes, it is proposed that the torque value for Point 2 on the interaction diagram of Figure 6.1 be taken as the elastic St. Venant torque for the section, calculated using the membrane analogy, typical for Class 3 sections, as per Equation [2.37]. (There is no change to the X-coordinates of Points 3 and 4.) Although this has no effect on the interaction diagram for Class 3 sections, this modification assumes that only a portion of the St. Venant torque for Class 1 and 2 sections (using the sand heap analogy) can be carried in addition to the full flexural resistance.

The interaction diagram of Figure 6.1, but incorporating the two modifications described above, is referred to hereafter as the “modified” interaction diagram. This is to be considered the proposed diagram from this point forward. The last two columns of Table 6.1 (refer to Appendix B) present the resulting average FEPR and coefficient of variation values for this modified interaction diagram. These modifications make the design procedure generally more conservative and they tend to improve the results for the beams that fall well below the original interaction equation.

### **6.2.2 Web Yielding**

As seen in Figure 6.22, Beam S2L2T1B2E2 (and several others, especially B2 beams) shows significant yielding in the web at the ULS in the von Mises stress contour plots. Yielding begins in the top flange at the supports and mid-span at approximately the same time. The centre of the web then yields at approximately the quarter points (occurs at mid-span

when the web is not locally thickened to prevent cross-sectional distortion at the load point) and spreads to the flanges. Since only five elements on either side of mid-span were thickened to prevent local distortion at the load point, the location of web yielding cannot be attributed to this thickening effect. As yielding progresses into the flanges, plastic warping hinges form in the top flange and the beam reaches its ultimate limit state. Although it was expected that yielding would occur first in the flanges and spread to the web, the significant shear stresses in the web cause shear yielding at these locations.

Five fixed-ended (B2) beams are investigated to ensure that yielding occurs in the web at the correct load step, theoretically, using the von Mises yield criterion. The normal and shear stresses are calculated based upon the applied moments and torques. In a general 3D state of stress, the von Mises yield criterion is expressed as (Ugural and Fenster, 1995):

$$2\sigma_{YP}^2 = (\sigma_x - \sigma_y)^2 + (\sigma_y - \sigma_z)^2 + (\sigma_z - \sigma_x)^2 + 6(\tau_{xy}^2 + \tau_{yz}^2 + \tau_{zx}^2) \quad [5.17]$$

where  $\sigma_{YP}$  is an equivalent stress, commonly referred to as the von Mises stress;  $\sigma_x$ ,  $\sigma_y$ , and  $\sigma_z$  are the normal stresses in the direction of the X, Y, and Z axes, respectively;  $\tau_{xy}$  is the shear stress in the X-Y plane;  $\tau_{yz}$  is the shear stress in the Y-Z plane; and  $\tau_{xz}$  is the shear stress in the X-Z plane. Under combined bending and torsion of thin-walled members, the equation simplifies as only two of these six stress terms,  $\sigma_x$  and  $\tau_{xy}$  develop, allowing the equivalent stress,  $\sigma_{YP}$ , to be found by:

$$\sigma_{YP}^2 = \sigma_x^2 + 3\tau_{xy}^2 \quad [5.18]$$

To account for residual stresses in the yielding phenomenon, the residual stress is added to the equivalent stress,  $\sigma_{YP}$ , as calculated by Equation [6.11]. Yielding occurs when this summed value reaches the

uniaxial yield strength, 350 MPa. At the mid-height of the cross-section on the outer surface of the web, the normal stresses are caused only by the weak axis bending moment,  $M_{wa}$ , approximately calculated by multiplying the strong axis bending moment,  $M_{sa}$ , by the sine of the rotation angle of the cross section (this assumes that the section remains close to vertical such that  $\cos \phi \cong 1$  and  $M_{sa} \times \cos \phi \cong M_{sa}$ ):

$$M_{wa} = M_{sa} \sin \phi = \left( \frac{PL}{8} \right) \sin \phi \quad [5.19]$$

The normal stress,  $\sigma_x$ , at the surface of the web is then calculated as:

$$\sigma_x = \frac{M_{wa} W}{2I_y} \quad [5.20]$$

The total shear stress  $\tau_{xy}$  is found by adding the shear stresses that develop as a result of torsion,  $\tau_t$ , and strong axis bending,  $\tau_{bz}$ , found by:

$$\tau_t = \frac{\psi T W}{J} = \frac{\psi P e w}{J} \quad [5.21]$$

$$\tau_{bz} = \frac{V_{sa} Q}{I_z W} \quad [5.22]$$

$$V_{sa} = V_z \cos \phi \quad [5.23]$$

where  $V_{sa}$  is the strong axis shear and  $\psi$  is a factor obtained from charts provided by Heins and Seaburg (1963) used to predict elastic torsional response values (including both rotations and stresses) that is a function of the cross-section, length of member, boundary conditions, and loading conditions. Table 6.2 presents the results for five beams that indicate that the finite element results are predicting the appropriate web yielding behaviour. For each beam, the table presents in the second column the load step where yielding first appears in the von Mises stress plots of the finite element results. For all of the beams, the residual stress at the mid-height of the web is 123 MPa. The table also presents the normal,

shear, and effective uniaxial stress as calculated for the load step in column two as well as the load step before in an attempt to bracket when yielding occurs. The shear stresses, in combination with the residual stresses, become large enough to cause yielding according to the von Mises yield criterion. The load steps at which the classical theory predicts that web yielding should begin correspond well with the results of the model. For two of the beams, S2L2T1B2E1 and S4L2T1B2E2, the theory indicates that web yielding should begin about two load steps earlier than occurs in the finite element results.

### **6.2.3 Serviceability Limit States (SLS)**

Two well accepted SLS are (1) a practical limit on the maximum normal stress of the yield stress and (2) a limit on the vertical and rotational deflections.

#### **6.2.3.1 Maximum Normal Stress Limit**

The first accepted SLS limits the maximum normal stress limit to the uniaxial yield stress of the material. The intent of this limit is to ensure that the cross-section remains elastic under service loads. Since yielding has already occurred at the service load level in the vast majority of the beams as seen in Appendix B (the service load level is determined based on the ultimate limit using an assumed effective load factor of 1.4), the parametric study indicates that the SLS usually governs. The only beams where the ULS governs are those in pure flexure (E0 beams) for the B2 and B3 boundary conditions (22 of the 24 beams). The SLS governs for the other 158 beams in the basic factorial approach. As observed by Driver and Kennedy (1987), the peak surface stresses, local buckling, and plastic hinges do not form exactly at the fixed end, but rather at a distance away from the support. The same result is found in the B3 beams, as seen in Figure 6.27, where the first few elements beyond the fixed support have not yielded although yielding occurs close to the support. The reader is

reminded that the fixed end support was located at the end of the fifth row of elements.

#### 6.2.3.2 Elastic Deflection Limits

Elastic deformations are a function of the boundary and loading conditions. Although the flexural limits can be used for the vertical deflection criteria, there is no specific guidance on the torsional rotational limits in CSA S16-01. Since these limits are highly specific to the design, selecting appropriate criteria is left up to the designer. Different rotational requirements are required depending on the function of the beam and the elements it supports (e.g., cladding). The serviceability criteria are intended to prevent the loss of function of the structure.

The vertical deflection criteria are dependent upon the building type and type of load. A limiting deflection of  $L/360$  is a representative value for pure flexure and is assumed as the limit for all comparisons in this project. Looking at the vertical deflection results of the parametric study found in Appendix B, this SLS governs for the vast majority of the B3 and 20% of the B1 beams (mostly E0 beams and beams with smaller eccentricities). The average vertical deflection at the service load for all of the B3 beams (except the torsion only beams) is  $L/99$ , more than three times the limit. Very few of the other beams exceed the vertical deflection limit of  $L/360$ , unlike the maximum normal stress SLS where the vast majority of the beams exceed the yield stress. This serviceability limit governs in only 63 out of the 180 beams investigated here.

To investigate the torsional rotation SLS, an arbitrary rotational limit of 5 degrees is chosen. Using this limit at the service load level, it is found that this SLS governs over the ULS in 108 out of the 180 beams investigated in this basic factorial approach. This SLS governs for more slender cross-sections and for boundary conditions that provide less torsional restraint (B3 is the worst, then B1, and then B2). The torsional rotations

that develop at the SLS are larger and thus more likely to exceed the 5 degree limit for beams with larger eccentricities. None of the flexure only loading beams exceed this limit where as all of the torsion only loading beams exceed this torsional rotation limit. All of the eccentrically loaded cantilever beams exceed the 5 degree limit at the SLS. If this arbitrary limit is reduced to 2.5 degrees, this SLS governs over the ULS in 129 out of the 180 beams investigated in this chapter.

#### 6.2.3.3 SLS versus ULS

Appendix B presents all of the deflection and stress values for all of the beams at the service load level. Section 6.2.3.1 indicates that the maximum normal stress exceeds the yield stress at the service load level and thus the SLS governs over the ULS in the vast majority of the beams in the parametric study (158 out of the 180 beams). Section 6.2.3.2 indicates that the SLS vertical deflection limit of  $L/360$  in pure flexure is exceeded and thus governs over the ULS for 63 out of the 180 beams. All of these beams that exceed the vertical deflection serviceability limit state also exceed the maximum normal stress limit. Section 6.2.3.2 indicates that the arbitrary SLS torsional rotation limit of 5 degrees is exceeded and thus governs over the ULS for 108 out of the 180 beams. Thus, in 87.8% or 158 of the beams investigated in the parametric study the SLS governs over the ULS.

#### 6.2.4 Torsional Rotations at the Ultimate Limit State

For many of the beams, the torsional rotations at the ultimate limit state were large. Although rotation is usually associated with a serviceability limit state, 74 of the 180 beams analyzed beams had rotations in excess of 30 degrees at the ultimate limit state—with some significantly greater. Rotations larger than 30 degrees call the basic loading assumptions into question as it becomes impractical to load a wide flange beam under such large rotations as gravity loads would become difficult to maintain without

sliding off. For beams with such large rotations, the serviceability limit state governs as seen in Appendix B and Section 6.2.3.

For this investigation, the ultimate limit states are selected by the method used previously, but limiting the maximum rotation at the ULS to 30 degrees. Even though this 30 degree limit is selected arbitrarily, it provides a reasonable basis for an ultimate limit state analysis. Using the modified ultimate limit state, the average FEPR and coefficient of variation are 1.03 and 25.3%, respectively. Of the 180 beams, 32 (or 17.8%) have a FEPR less than 0.85 and of these, 17 (or 9.4% of all of the beams) have a FEPR less than 0.7 with some as low as 0.39. Of the 32 beams with a FEPR less than 0.85, 19 of them are L2 B3 beams and five of these are E4 beams (torsion only loading is a theoretical concept and difficult to develop in practice). Table 6.3 and Table 6.4 provide a list of all of the FEPR values for the ULS as selected without and with the 30 degree cut-off, respectively.

Due to the large number of L2 B3 beams that have FEPR values less than 0.7, it is recommended that cantilever beams with slenderness ratios greater than 50 not be used in design for beams subject to combined torsion and flexure. These beams undergo large rotations under relatively small loads, making them ineffective for carrying eccentric loads. Removing these beams from the analysis, the average FEPR and the corresponding coefficient of variation become 1.10 and 19.1%, respectively. Only one beam, S1L1T1B3E4 (also a cantilever under torsion only loading), has a FEPR less than 0.7 (0.69). Looking at the same reduced set of beams for the ultimate limit states without using the 30 degree cut-off, the average FEPR and coefficient of variation values are 1.21 and 20.0%, respectively. Although using the 30 degree rotation limit slightly improves the average FEPR and coefficient of variation values, a large amount of variation remains. Further research is required to investigate specific cases where FEPR values are obtained that are

significantly less than 1.0. Despite these results, no changes to the modified interaction diagram or to the recommended ultimate limit state selection criteria are recommended in this section. That is, no torsional rotational criteria should be used to select the ULS.

### **6.3 Summary**

The results of the parametric study indicate that the modified interaction diagram provides a simple and generally conservative ultimate limit state for wide flange sections subject to combined torsion and flexure. The overall average FEPR for the ultimate limit state is 1.24 with a coefficient of variation of 21.5%. The complete list of these FEPR values for all 180 beams is presented in Table 6.3. Although the coefficient of variation is large, the vast majority of the beams lie above the predicted modified interaction equation. Only 25 of the 180 beams have a FEPR value less than 1.0, only five have a FEPR value less than 0.95, and only two have a FEPR value less than 0.9. The two beams that have a FEPR value less than 0.9 are S1L1T1B1E4 (0.88) and S2L1T1B2E1 (0.89). The S1L1T1B1E4 model has reserve capacity that develops due in part to the secondary axial stresses and strains (Wagner stresses), allowing the beam to develop a torque close to double the predicted capacity. The S2L1T1B2E1 beam also has reserve capacity in that a global failure mechanism is not created until the loading increases well above 1.5 times the predicted capacity and additional flexural plastic hinges form at the end supports. Thus, even for both of these beams, significant reserve capacity remains such that no global or catastrophic failure will occur.

Section 6.2.3 indicates that cross-sections exposed to combined torsional and flexural loads are governed by the maximum normal stress reaching the yield stress value at the service load level and that the ULS rarely governs. Also, an assessment of the torsional rotations at the ultimate limit state indicates that slender cantilevers are a special case where very large rotations may develop before the ultimate limit state is reached. As

such, even though for these types of beams the SLS will govern over the ULS, they are not recommended for use with the proposed design interaction diagram and for combined loading in general.

*Table 6.1 Average FEPR and Coefficients of Variation for Parametric Study Results*

Row	Description	Driver and Kennedy (1989) Interaction Diagram		Proposed Modified Interaction Diagram	
		Average FEPR	Coefficient of Variation (%)	Average FEPR	Coefficient of Variation (%)
1	All E0 Beams	1.03	5.3	1.03	5.3
2	All E4 Beams	1.20	22.0	1.20	22.0
3	All B1 Beams	0.95	19.2	1.13	16.6
4	All B1 Beams for Sections 1 to 3	0.85	17.7	1.03	8.0
5	All B1 Beams for Sections 4 to 6	1.04	15.7	1.24	16.7
6	All B2 Beams	1.18	20.1	1.21	19.1
7	S2L1T1B2E1	0.82	-	0.89	-
8	S2L2T1B2E1	0.82	-	0.93	-
9	S3L1T1B2E1	0.93	-	1.01	-
10	S3L2T1B2E1	0.92	-	1.00	-
11	S2L1T1B2E2	0.95	-	1.00	-
12	All E0 B2 Beams	1.05	5.6	1.05	5.6
13	All E1 B2 Beams	1.08	18.7	1.15	15.7
14	All E2 B2 Beams	1.26	17.4	1.31	15.7
15	All E3 B2 Beams	1.27	18.6	1.29	17.5
16	All E4 B2 Beams	1.22	26.9	1.22	26.9
17	All B3 Beams	1.32	24.0	1.39	21.9
18	S1L2T1B3E1	0.88	-	1.17	-
19	All E0 B3 Beams	1.04	4.6	1.04	4.6
20	All E1 B3 Beams	1.32	23.6	1.46	15.2
21	All E2 B3 Beams	1.42	22.7	1.53	17.0
22	All E3 B3 Beams	1.51	24.2	1.59	20.2
23	All E4 B3 Beams	1.34	18.9	1.34	18.9
24	All Beams	1.15	25.7	1.24	21.5

Table 6.2 Von Mises Yield Criterion Checks of Web

Beam	Finite Element Load Step at which Yielding in the Web Occurs	Load Step	Stresses (MPa)			Equivalent von Mises Stress (MPa) $\sigma_{YP}$
			$\sigma_x$	$\tau_t$	$\tau_{bx}$	
S1L1T1B2E3	13	12	3.34	63.5	63.7	343
		13	4.24	66.7	66.2	353
S2L2T1B2E1	12	11	13.3	38.8	108	377
		12	19.0	43.3	108	385
S2L2T1B2E2	12	11	16.0	56.1	70.7	343
		12	18.5	59.8	72.7	353
S4L2T1B2E2	12	11	6.81	87.7	47.2	356
		12	7.56	91.3	48.1	364
S4L2T1B2E3	18	17	4.14	105.0	23.5	345
		18	4.80	107.7	24.0	351

Table 6.3 Complete List of FEPR Values for Basic Factorial Approach using the Modified Interaction Diagram

Beam	FEPR				
	E0	E1	E2	E3	E4
S1L1T1B1	1.00	1.15	1.10	1.04	0.88
S1L2T1B1	0.99	1.07	1.09	1.07	1.06
S2L1T1B1	0.96	1.01	0.94	1.04	1.00
S2L2T1B1	0.96	0.92	1.04	1.15	1.20
S3L1T1B1	0.98	1.09	1.01	1.22	0.98
S3L2T1B1	0.97	1.02	0.91	1.02	1.00
S4L1T1B1	1.00	1.22	1.22	1.26	1.10
S4L2T1B1	1.04	1.26	1.36	1.27	1.04
S5L1T1B1	1.09	1.41	1.35	1.69	1.12
S5L2T1B1	0.95	1.17	1.09	1.75	1.12
S6L1T1B1	1.09	1.38	1.43	1.65	1.05
S6L2T1B1	1.02	1.46	1.25	1.25	1.09
S1L1T1B2	1.09	1.20	1.32	1.20	0.97
S1L2T1B2	1.05	1.26	1.36	1.02	1.02
S2L1T1B2	0.96	0.89	1.00	1.24	0.98
S2L2T1B2	1.01	0.93	1.14	1.14	1.03
S3L1T1B2	1.02	1.01	1.10	1.09	1.08
S3L2T1B2	1.01	1.00	1.64	1.67	1.37
S4L1T1B2	1.04	1.31	1.39	1.20	1.05
S4L2T1B2	1.03	1.20	1.08	1.06	0.95
S5L1T1B2	1.03	1.18	1.30	1.50	1.81
S5L2T1B2	1.14	1.11	1.64	1.68	1.91
S6L1T1B2	1.14	1.55	1.43	1.38	1.30
S6L2T1B2	1.13	1.21	1.34	1.28	1.11
S1L1T1B3	1.03	1.37	1.46	1.49	1.00
S1L2T1B3	1.04	1.17	1.23	1.29	0.98
S2L1T1B3	1.00	1.13	1.06	0.99	1.16
S2L2T1B3	0.95	1.24	1.31	1.38	1.34
S3L1T1B3	1.03	1.56	1.51	1.59	1.44
S3L2T1B3	1.01	1.54	1.58	1.68	1.43
S4L1T1B3	1.06	1.50	1.60	1.64	1.11
S4L2T1B3	1.02	1.29	1.39	1.41	1.23
S5L1T1B3	1.14	1.61	1.71	1.79	1.48
S5L2T1B3	1.01	1.86	2.01	2.26	1.82
S6L1T1B3	1.09	1.68	1.79	1.91	1.43
S6L2T1B3	1.05	1.53	1.66	1.70	1.62

Table 6.4 Complete List of FEPR Values for Basic Factorial Approach using the Modified Interaction Diagram with 30 Degree Cut-Off

Beam	FEPR				
	E0	E1	E2	E3	E4
S1L1T1B1	1.00	1.15	1.10	1.04	0.88
S1L2T1B1	0.99	1.07	0.83	0.75	0.71
S2L1T1B1	0.96	1.01	0.94	1.04	1.00
S2L2T1B1	0.96	0.92	1.04	0.83	0.98
S3L1T1B1	0.98	1.09	1.01	1.22	0.98
S3L2T1B1	0.97	1.02	0.91	1.02	0.88
S4L1T1B1	1.00	1.22	1.22	1.03	1.00
S4L2T1B1	1.04	0.87	0.82	0.75	0.70
S5L1T1B1	1.09	1.41	1.35	1.69	1.12
S5L2T1B1	0.95	1.17	1.09	1.31	1.12
S6L1T1B1	1.09	1.38	1.43	1.42	1.05
S6L2T1B1	1.02	0.92	1.25	0.95	0.97
S1L1T1B2	1.09	1.20	1.32	1.20	0.97
S1L2T1B2	1.05	1.26	1.19	0.99	0.84
S2L1T1B2	0.96	0.89	1.00	1.24	0.98
S2L2T1B2	1.01	0.93	1.14	1.14	1.03
S3L1T1B2	1.02	1.01	1.10	1.09	1.08
S3L2T1B2	1.01	1.00	1.40	1.23	1.10
S4L1T1B2	1.04	1.31	1.39	1.20	1.05
S4L2T1B2	1.03	1.20	1.08	0.98	0.88
S5L1T1B2	1.03	1.18	1.30	1.50	1.81
S5L2T1B2	1.14	1.11	1.64	1.61	1.62
S6L1T1B2	1.14	1.55	1.43	1.38	1.30
S6L2T1B2	1.13	1.21	1.24	1.14	1.01
S1L1T1B3	1.03	1.18	0.99	0.79	0.69
S1L2T1B3	1.04	0.90	0.63	0.49	0.44
S2L1T1B3	1.00	1.13	1.06	0.94	0.93
S2L2T1B3	0.95	1.22	0.88	0.62	0.59
S3L1T1B3	1.03	1.23	1.10	0.92	1.12
S3L2T1B3	1.01	0.72	0.59	0.45	0.52
S4L1T1B3	1.06	0.99	0.86	0.73	0.83
S4L2T1B3	1.02	0.57	0.44	0.35	0.43
S5L1T1B3	1.14	1.61	1.61	1.38	1.48
S5L2T1B3	1.01	1.17	0.85	0.73	0.94
S6L1T1B3	1.09	1.05	0.93	0.84	0.93
S6L2T1B3	1.05	0.54	0.44	0.39	0.41

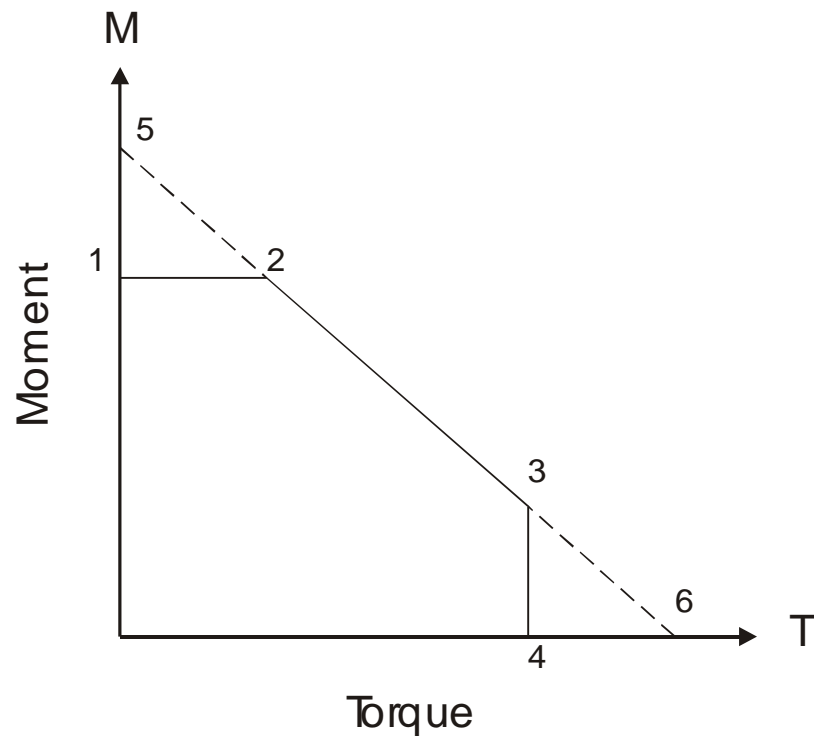


Figure 6.1 Moment-Torque Interaction Diagram

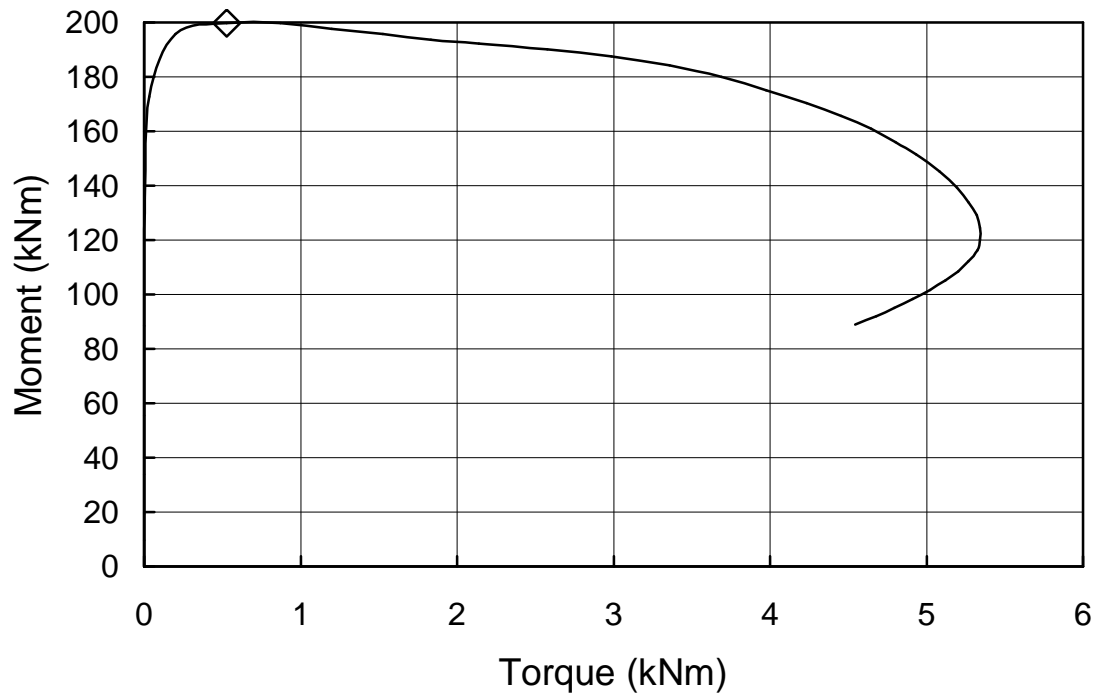


Figure 6.2 Moment vs. Torque Diagram for Beam S4L1T1B1E0

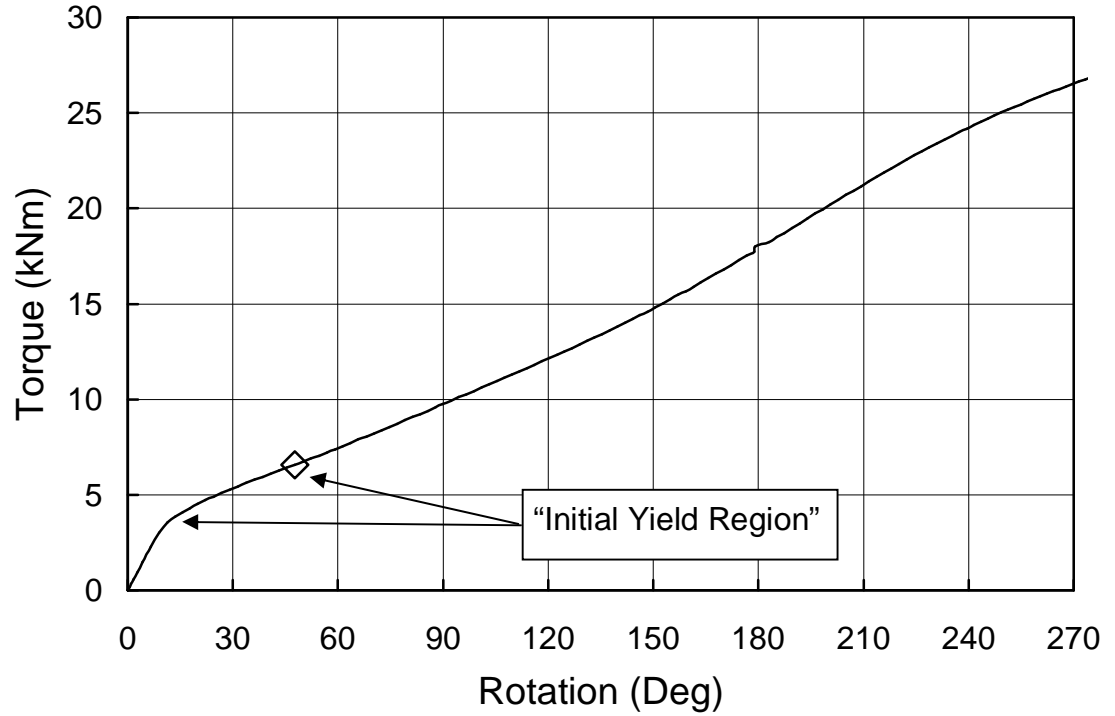


Figure 6.3 Torque vs. Rotation Diagram for Beam S1L2T1B2E4

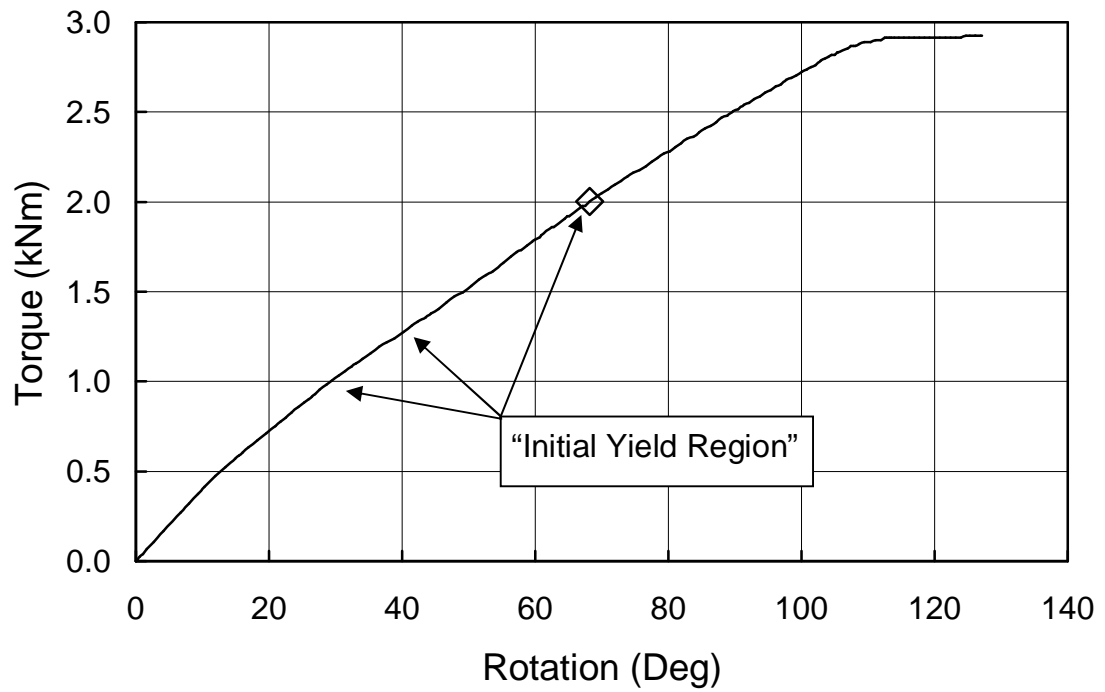


Figure 6.4 Torque vs. Rotation Diagram for Beam S5L2T1B3E4

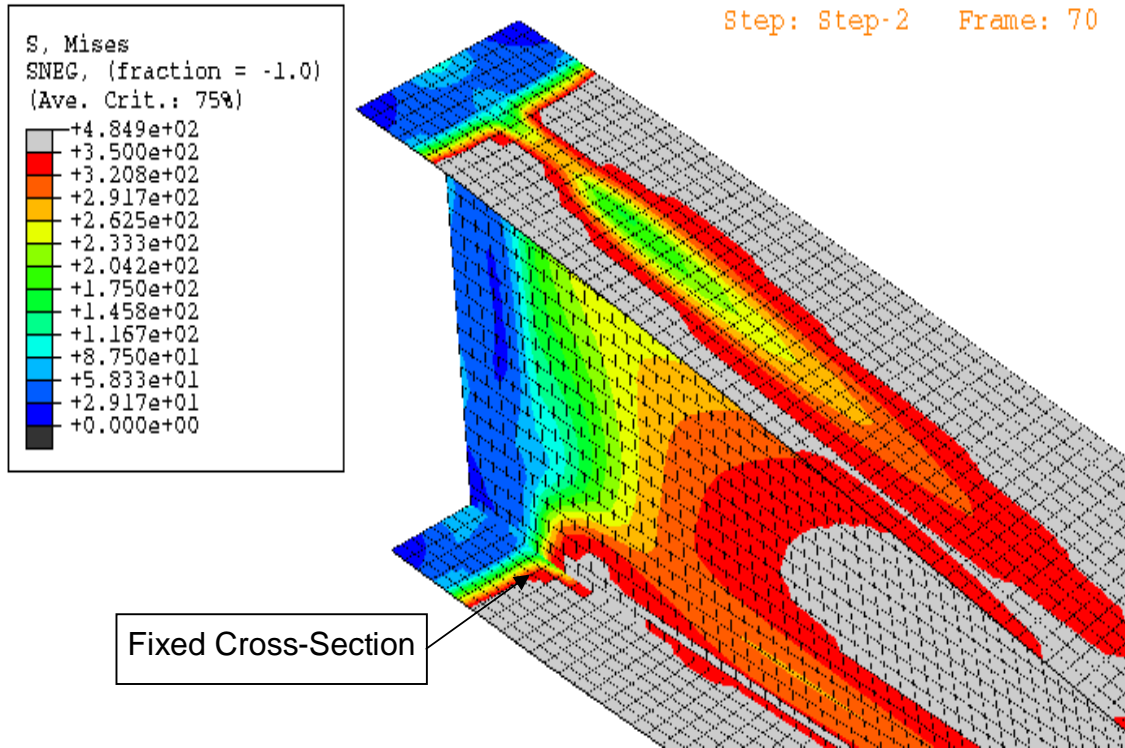


Figure 6.5 Von Mises Stress Contour Plot for Beam S5L2T1B3E4 at ULS

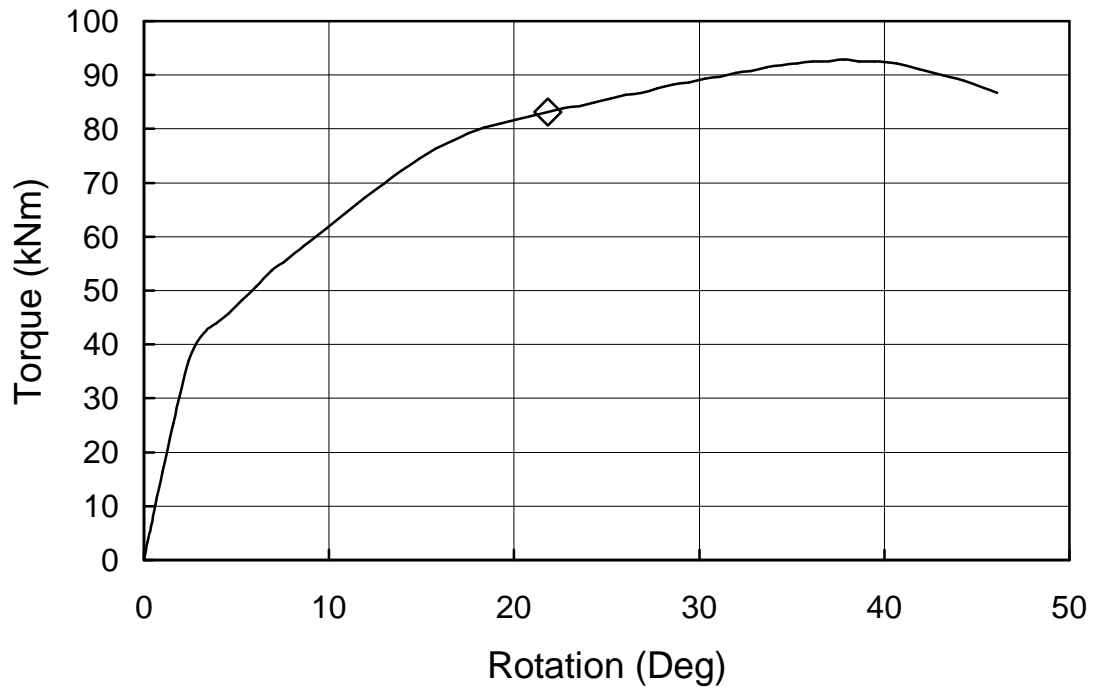


Figure 6.6 Torque vs. Rotation Diagram for Beam S2L1T1B1E4

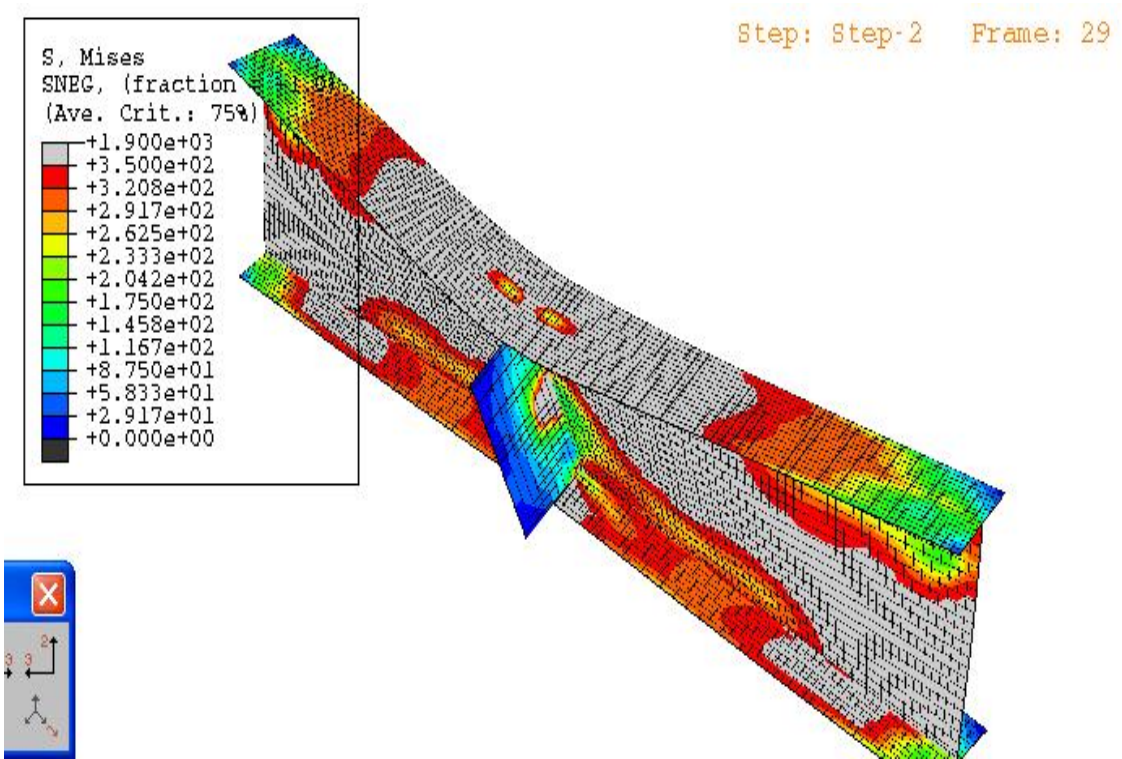


Figure 6.7 Von Mises Stress Contour Plot for Beam S2L1T1B1E4 at ULS

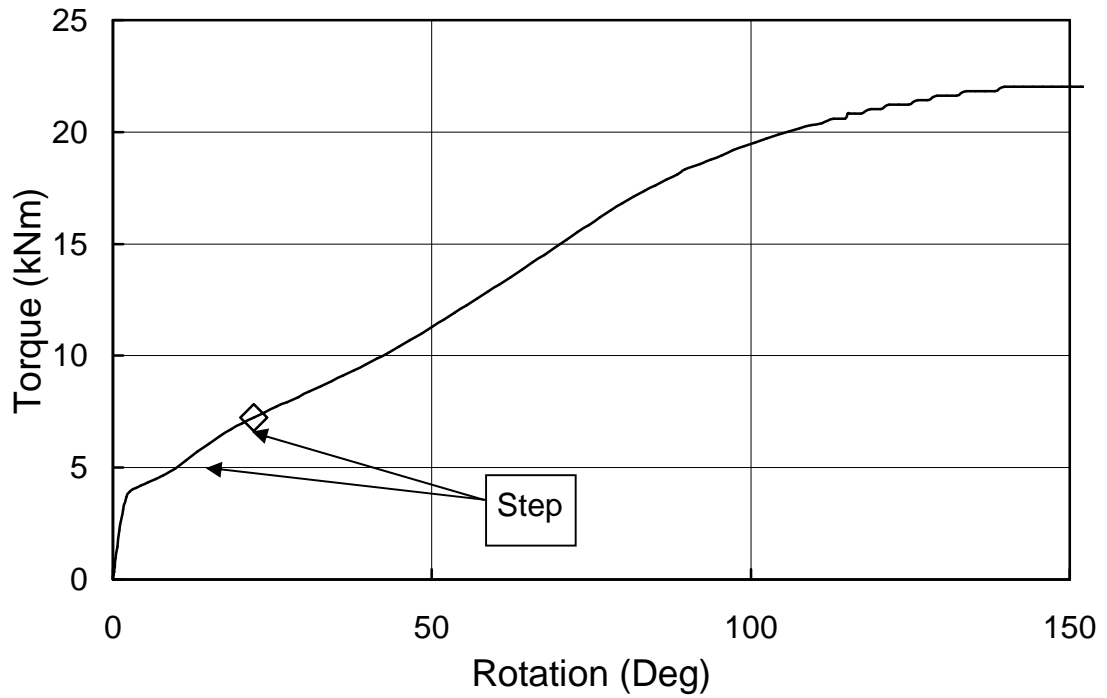


Figure 6.8 Torque vs. Rotation Diagram for Beam S5L1T1B2E4

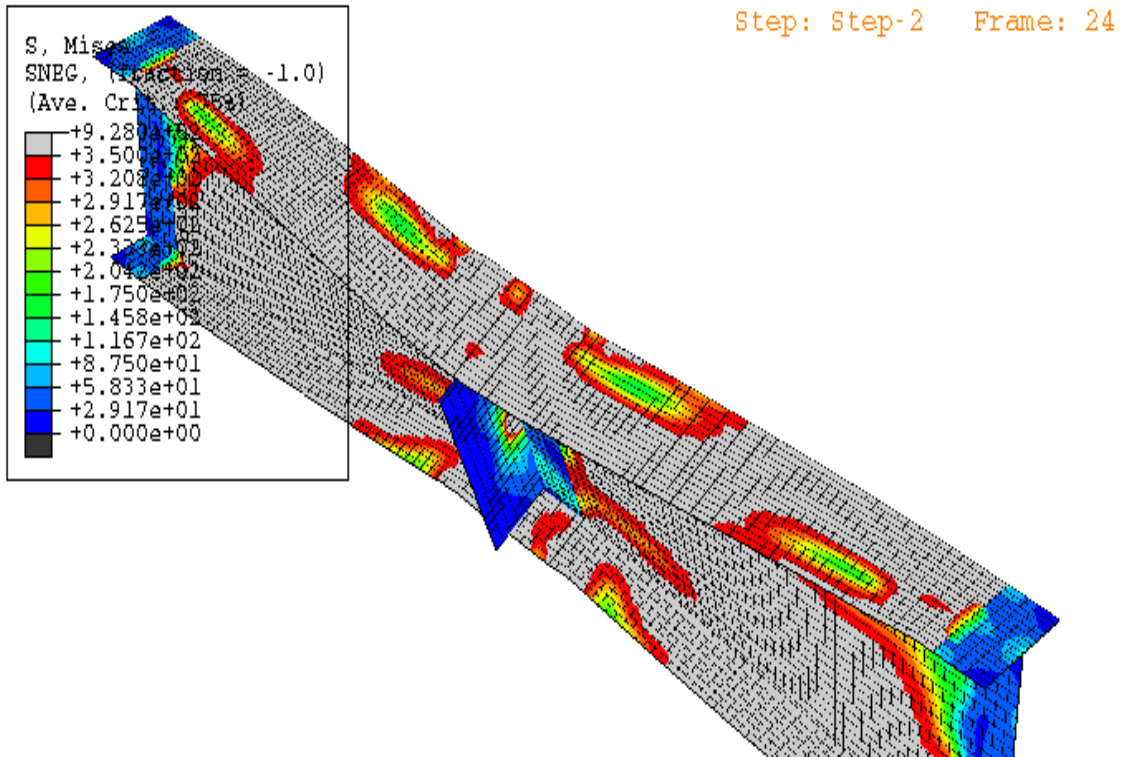


Figure 6.9 Von Mises Stress Contour Plot for Beam S5L1T1B2E4 at ULS

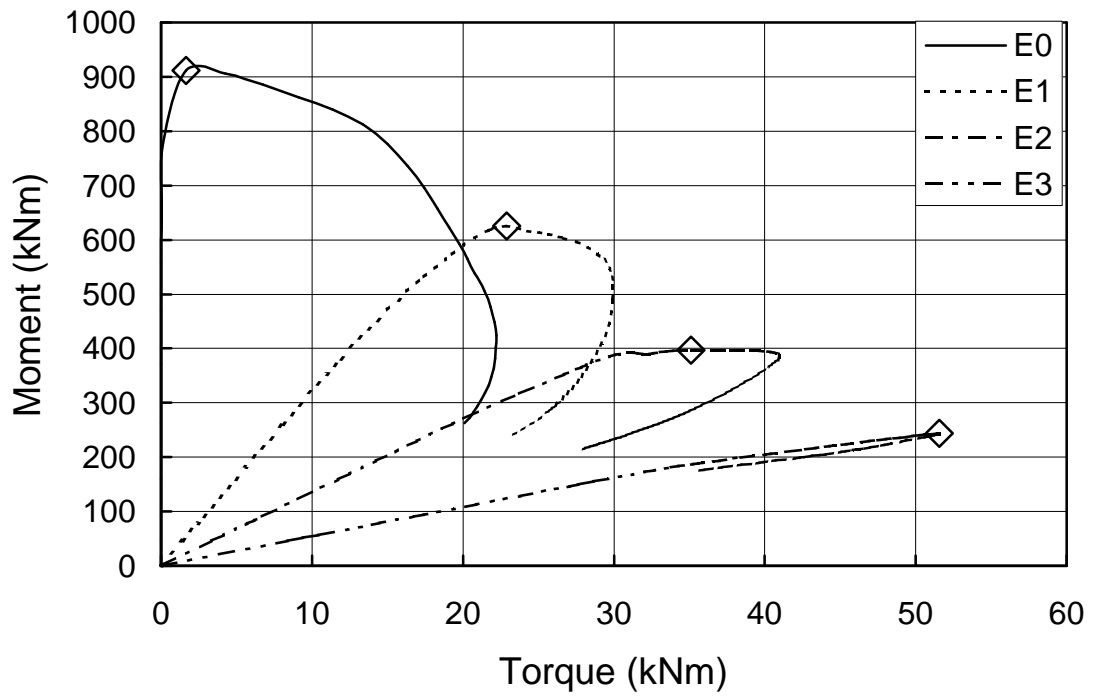


Figure 6.10 Moment vs. Torque Diagram for Beam S3L1T1B1

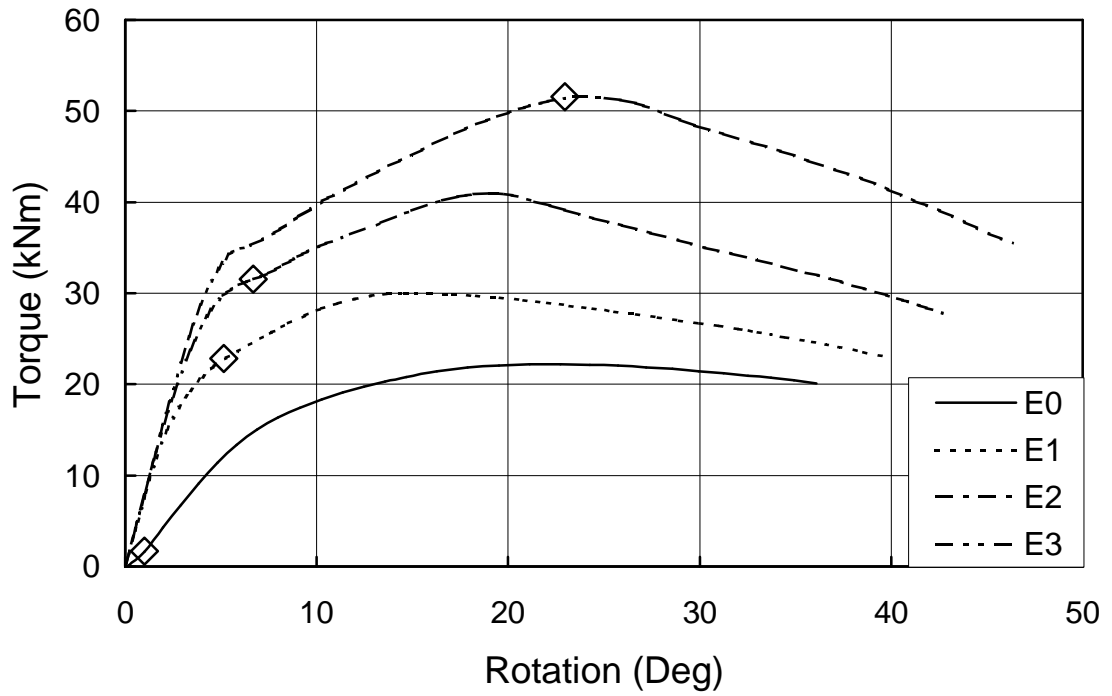


Figure 6.11 Torque vs. Rotation Diagram for Beam S3L1T1B1

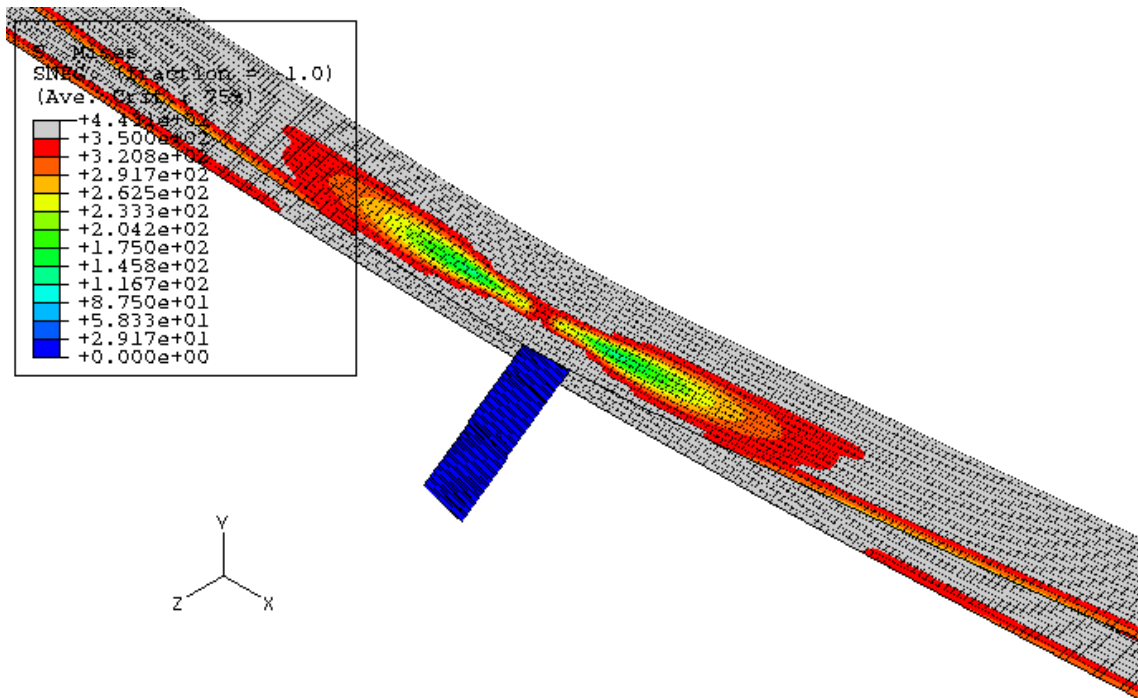


Figure 6.12 Von Mises Stress Contour Plot for Beam S4L2T1B1E1 at the Ultimate Limit State

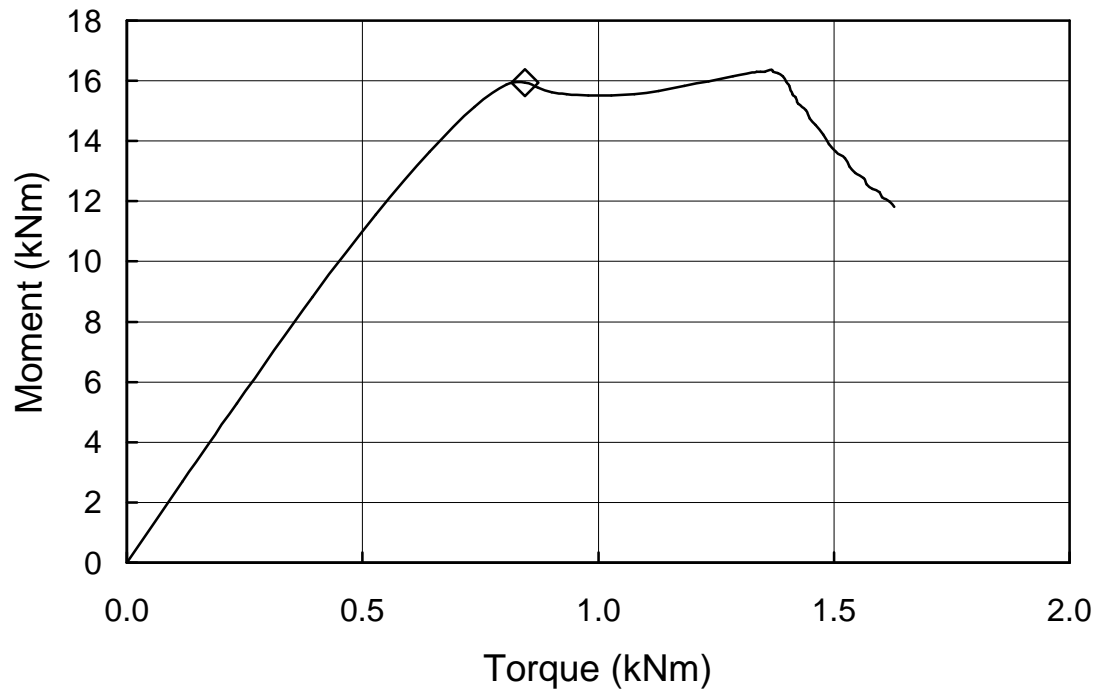


Figure 6.13 Moment vs. Torque Diagram for Beam S5L2T1B1E2

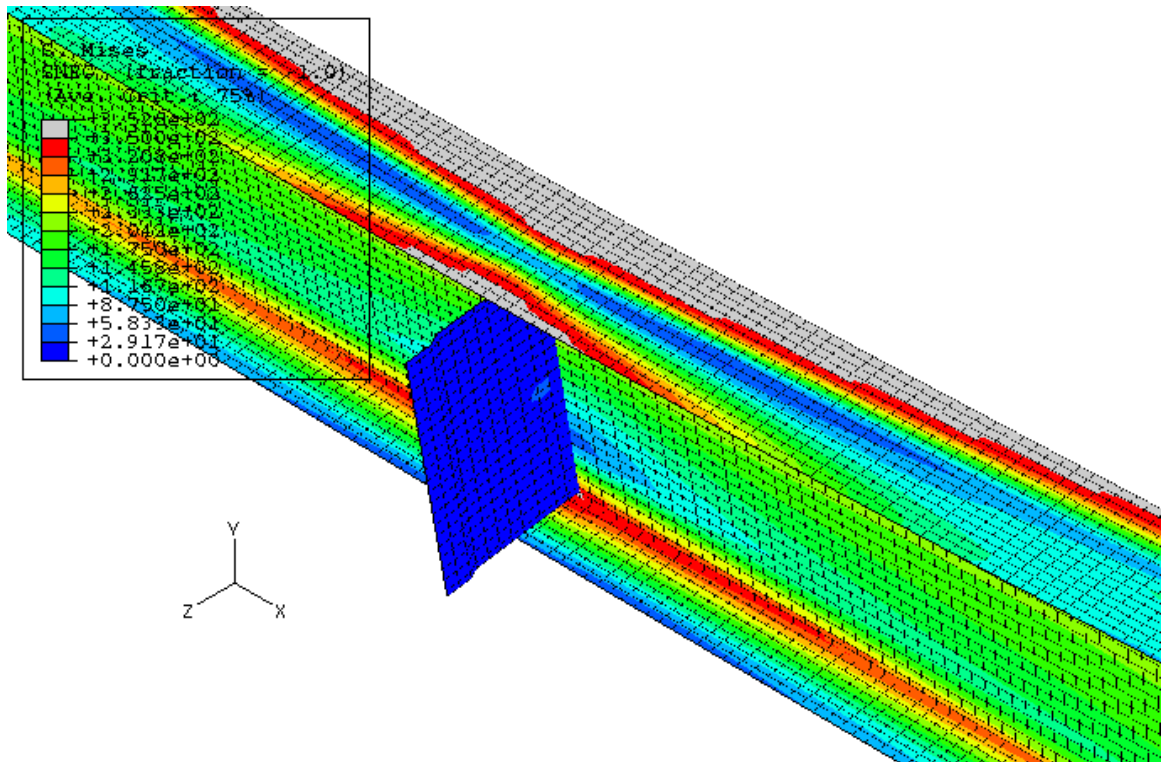


Figure 6.14 Von Mises Stress Contour Plot for Beam S5L2T1B1E1 at ULS

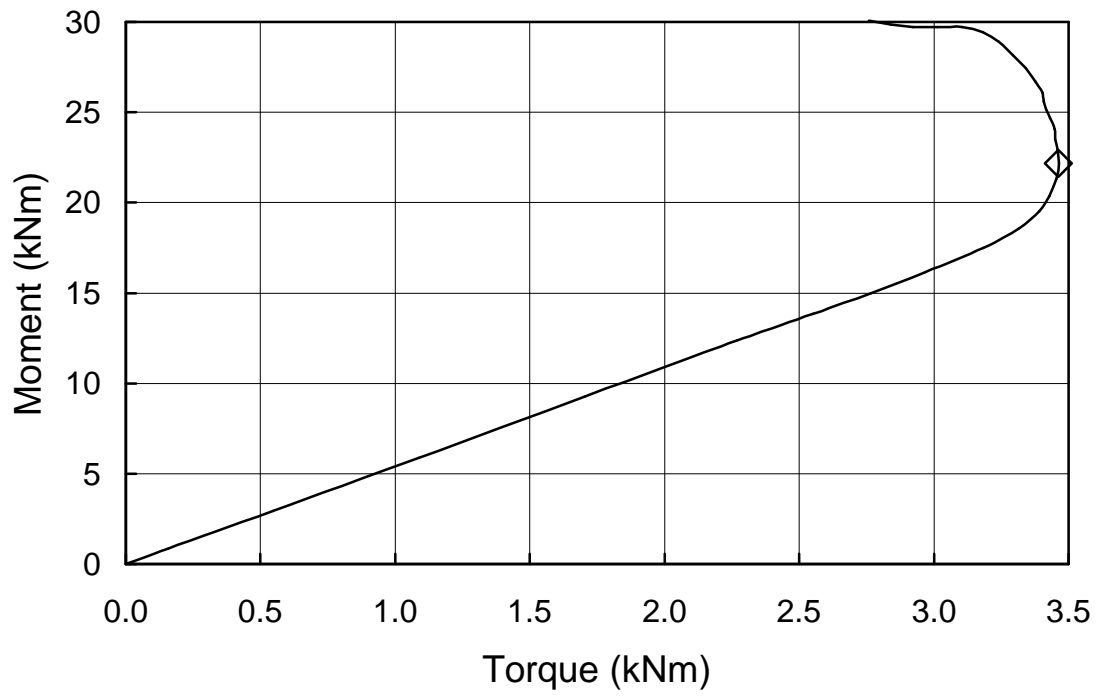


Figure 6.15 Moment vs. Torque Diagram for Beam S1L2T1B1E3

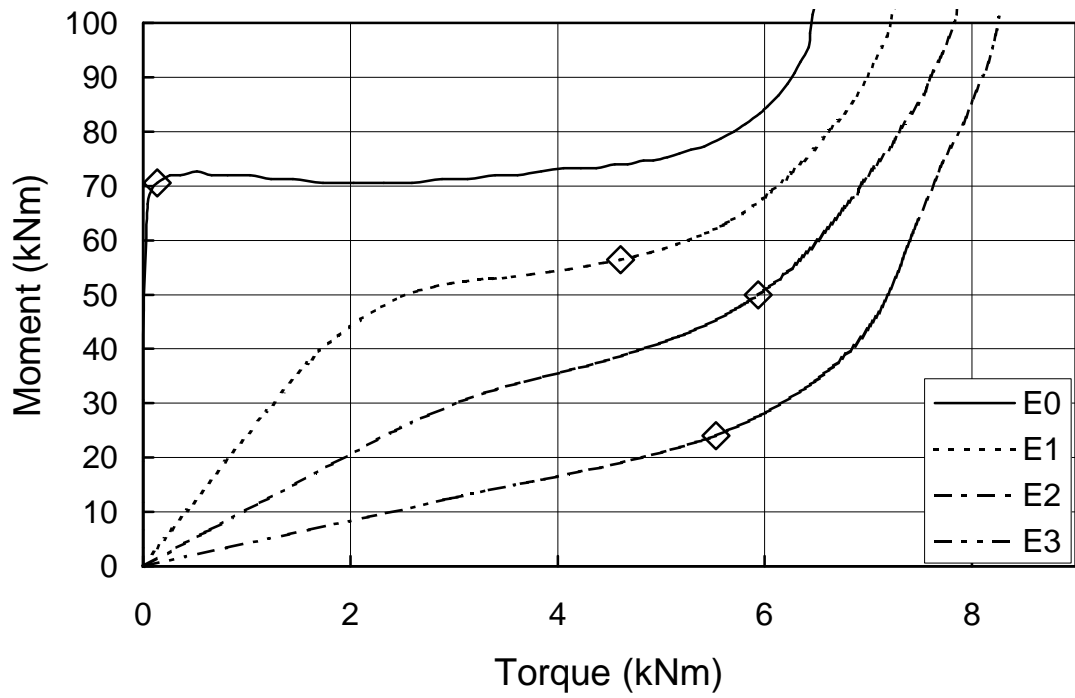


Figure 6.16 Moment vs. Torque Diagram for Beam S1L2T1B2

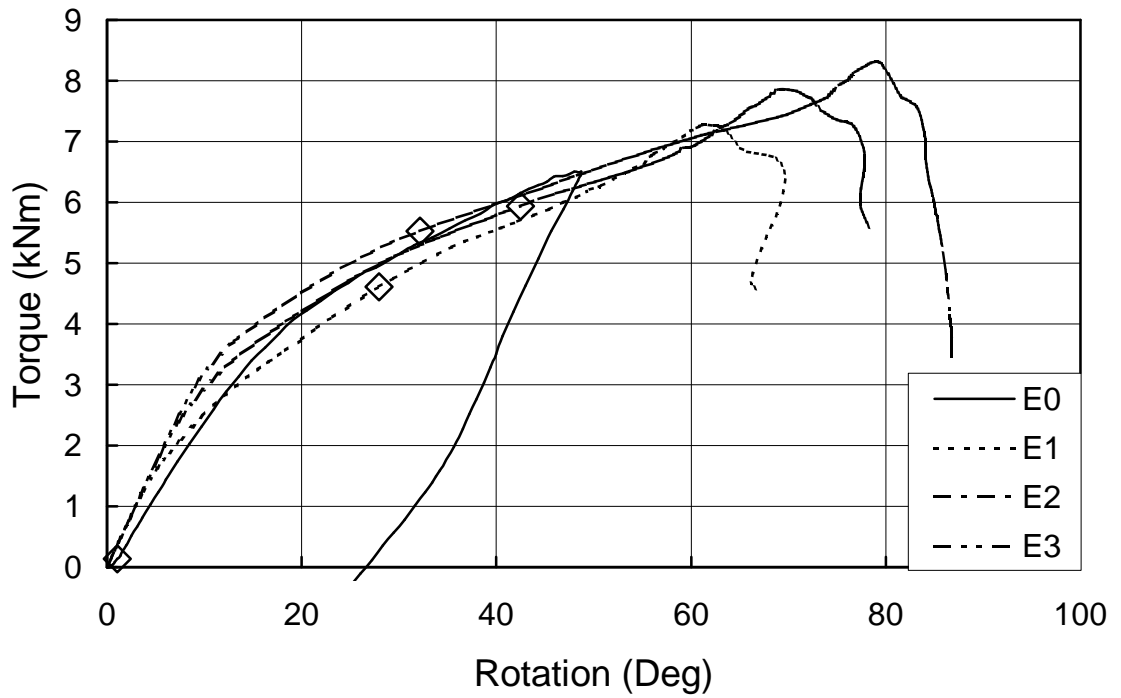


Figure 6.17 Torque vs. Rotation Diagram for Beam S1L2T1B2

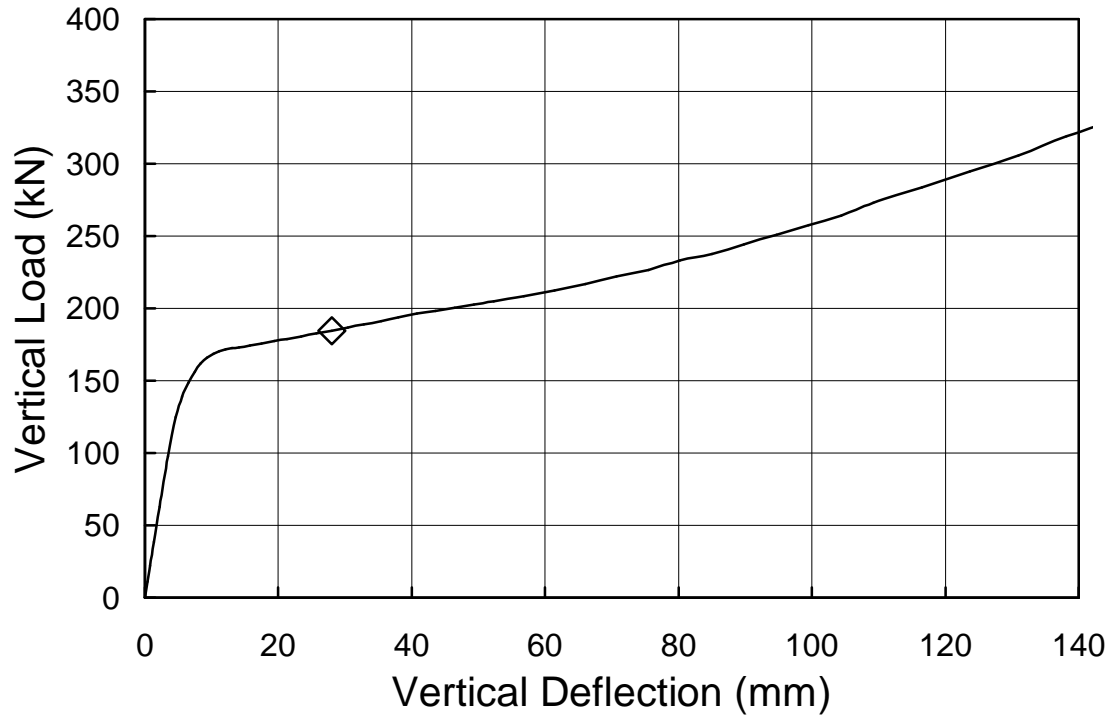


Figure 6.18 Vertical Load vs. Vertical Deflection Diagram for Beam S1L2T1B2E1

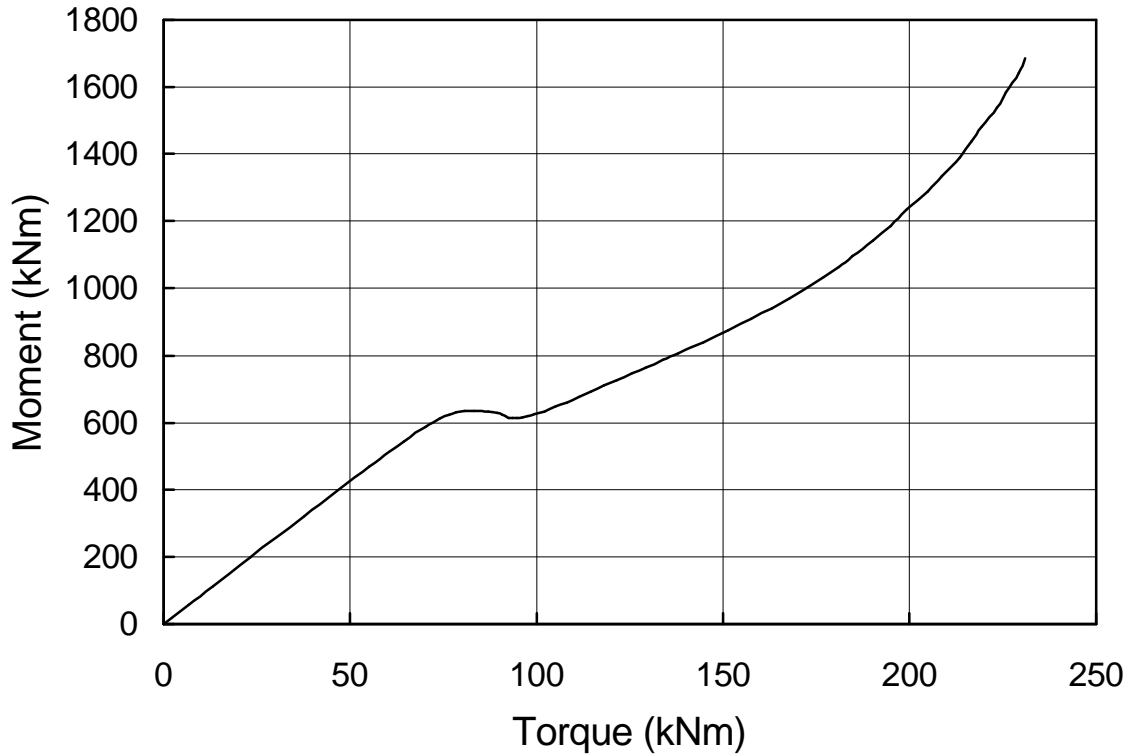


Figure 6.19 Moment vs. Torque Diagram for Beam S2L1T1B2E2

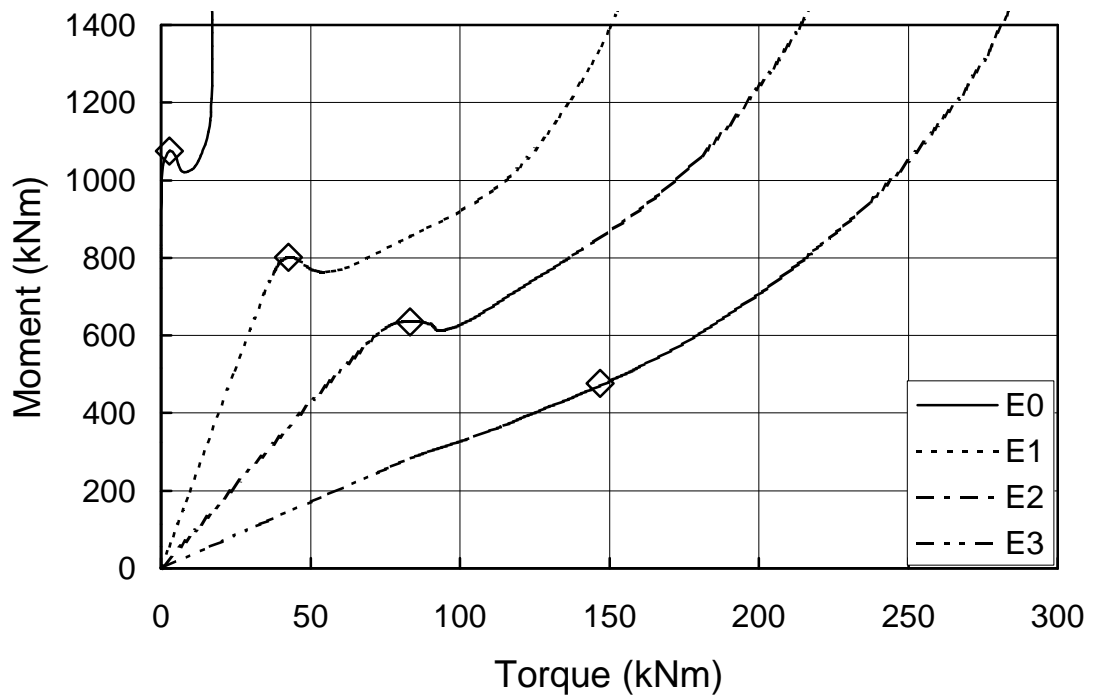


Figure 6.20 Moment vs. Torque Diagram for Beam S2L2T1B2

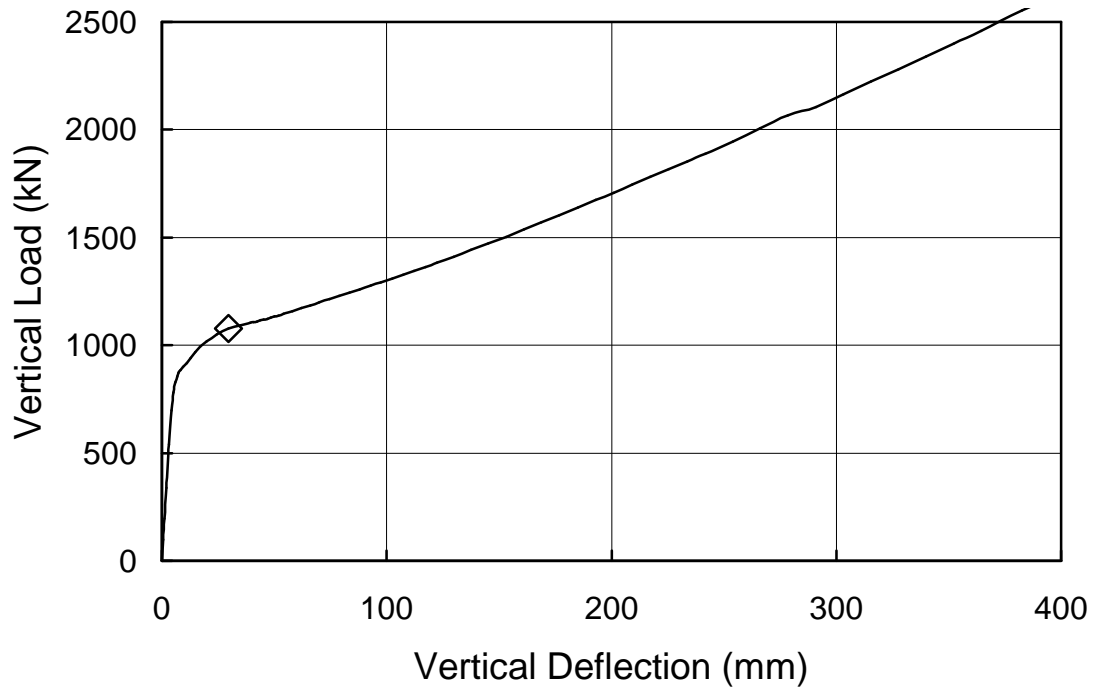


Figure 6.21 Vertical Load vs. Vertical Deflection Diagram for Beam S2L2T1B2E2

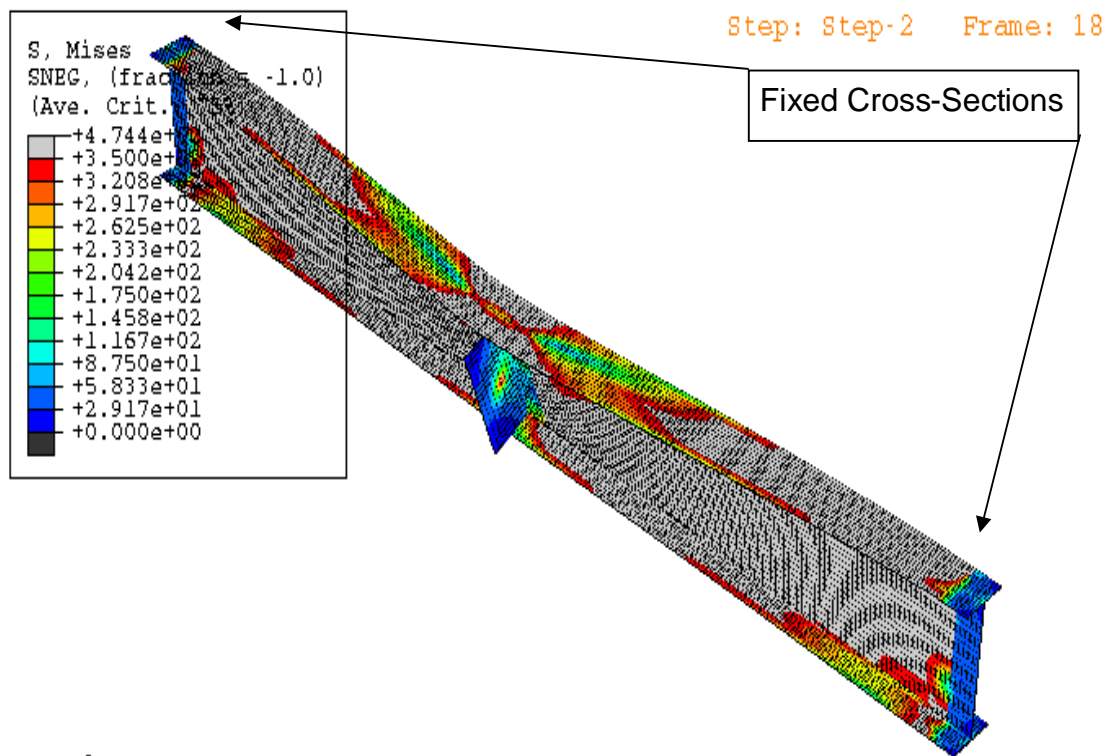


Figure 6.22 Von Mises Stress Contour Plot for Beam S2L2T1B2E2 at ULS

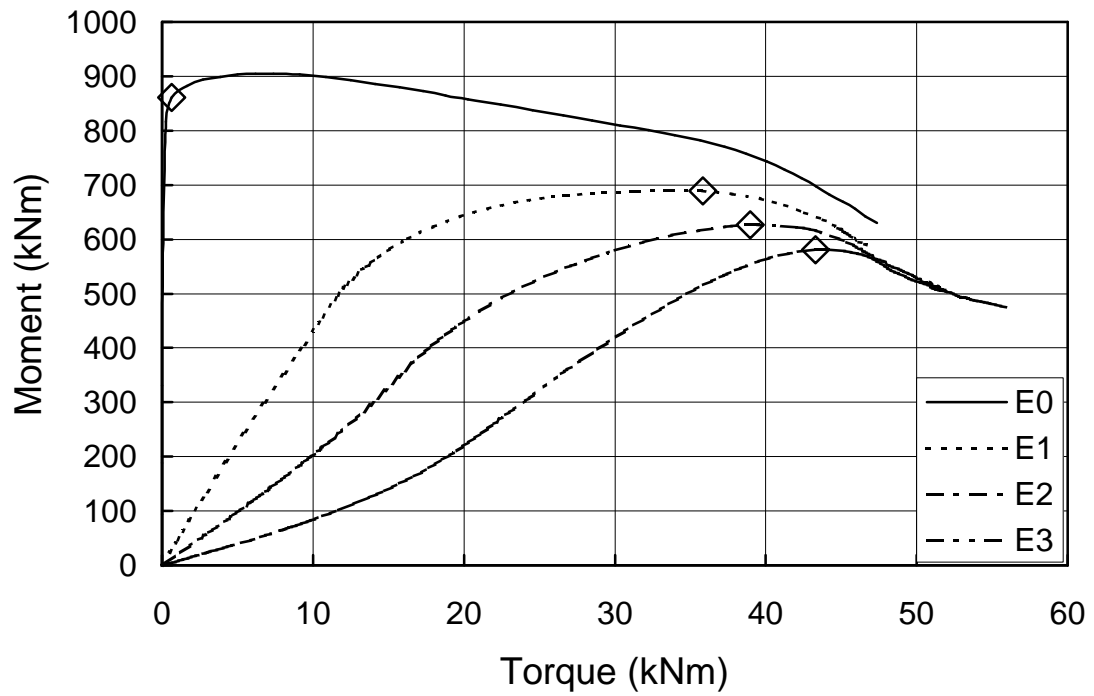


Figure 6.23 Moment vs. Torque Diagram for Beam S3L2T1B3

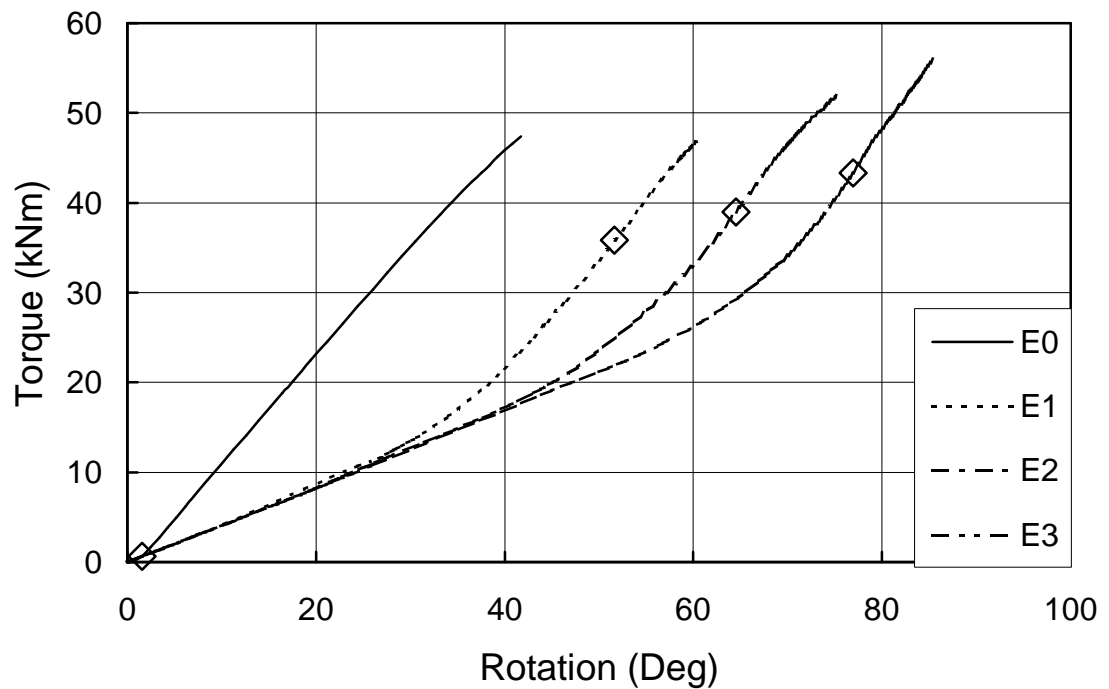


Figure 6.24 Torque vs. Rotation Diagram for Beam S3L2T1B3

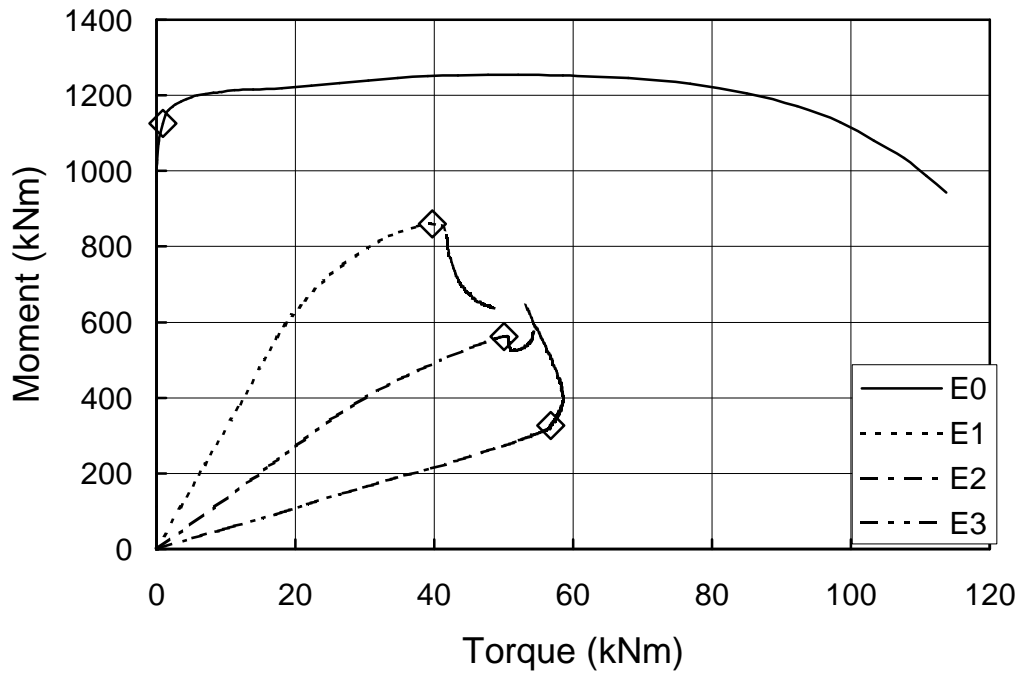


Figure 6.25 Moment vs. Torque Diagram for Beam S2L1T1B3

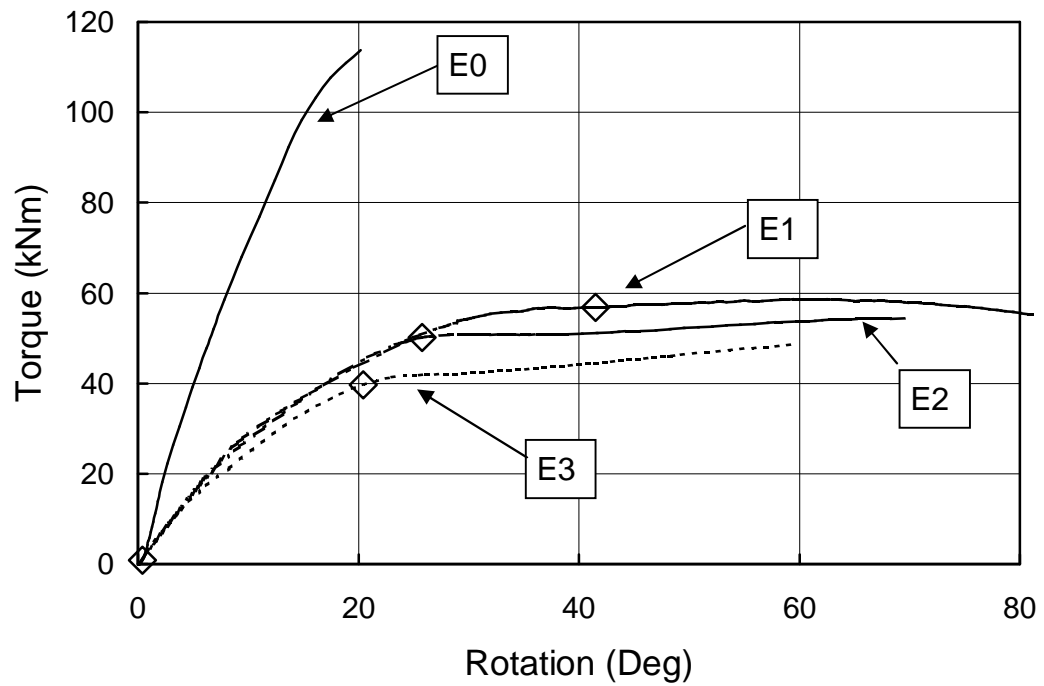


Figure 6.26 Torque vs. Rotation Diagram for Beam S2L1T1B3

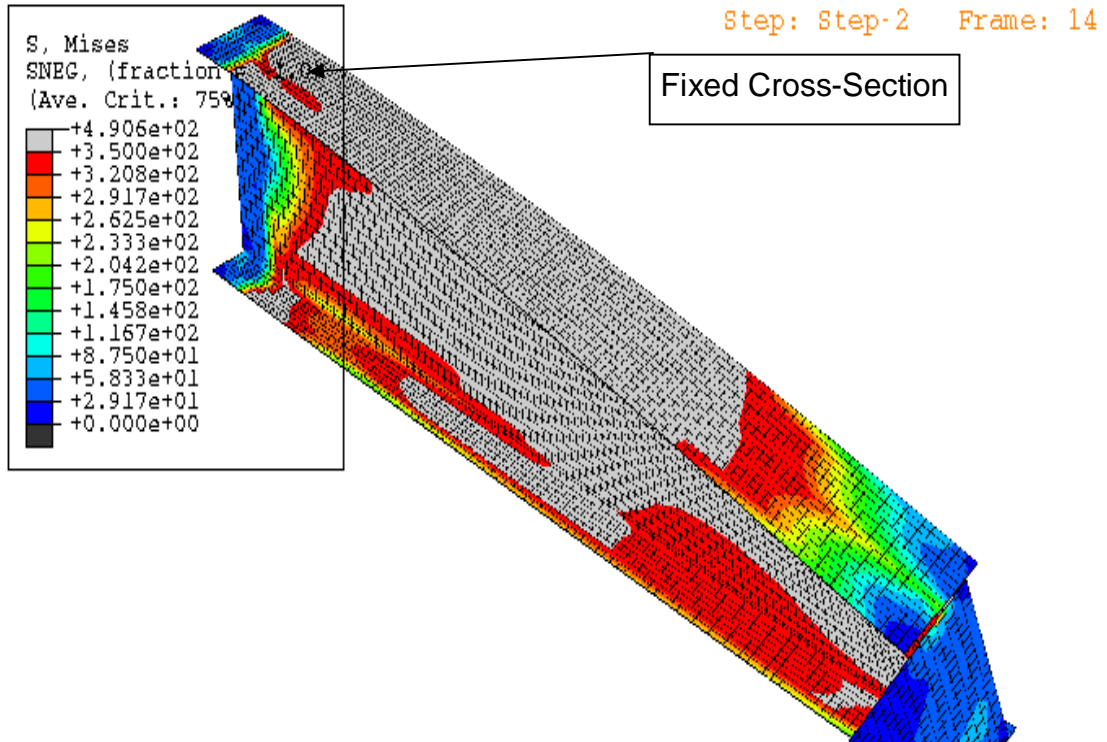


Figure 6.27 Von Mises Stress Contour Plot for Beam S2L1T1B3E1 at ULS

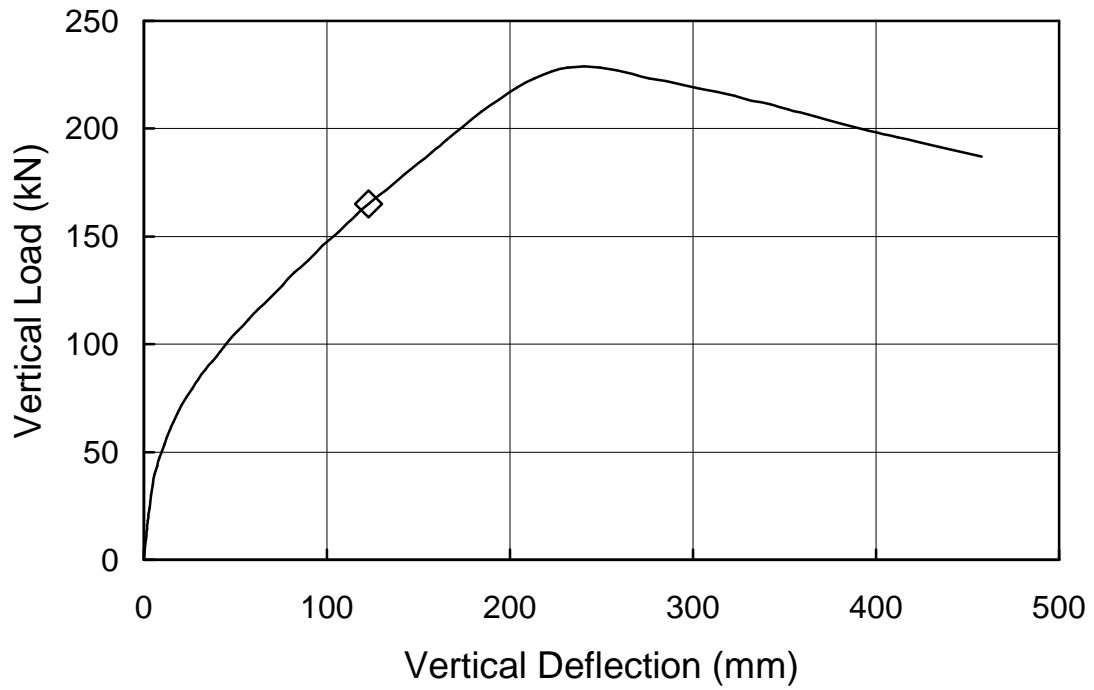


Figure 6.28 Vertical Load vs. Vertical Deflection Diagram for Beam S3L2T1B3E2

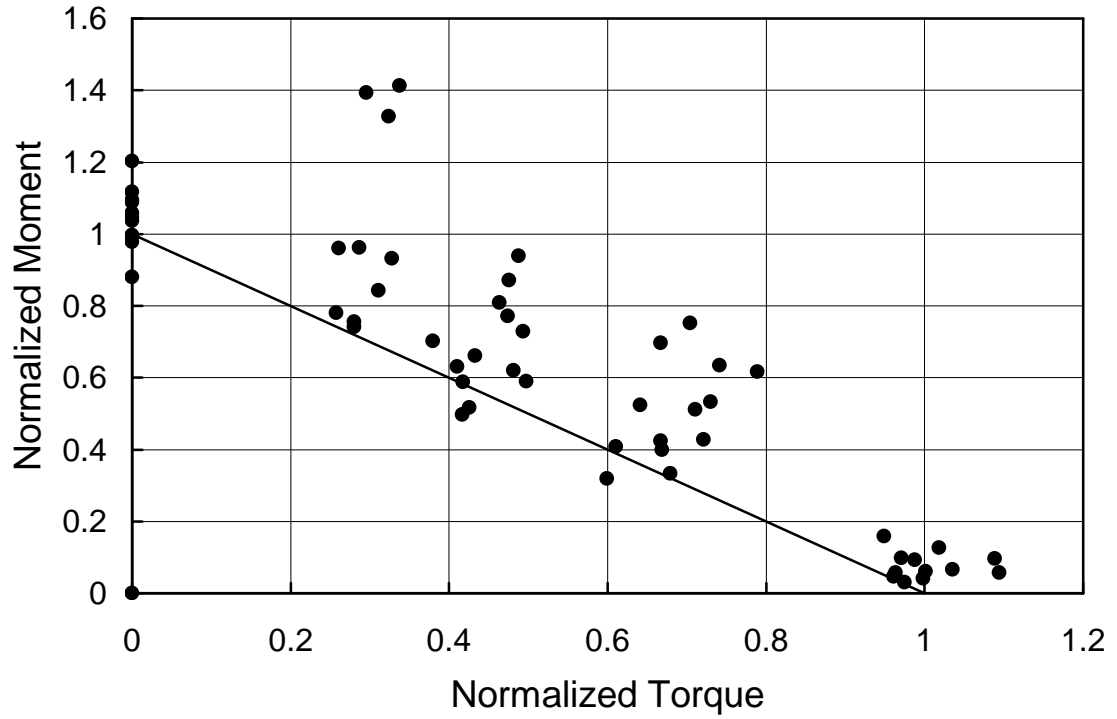


Figure 6.29 Modified Normalized Moment vs. Torque Interaction Diagram for Simply Supported Beams with all Parametric Study Results

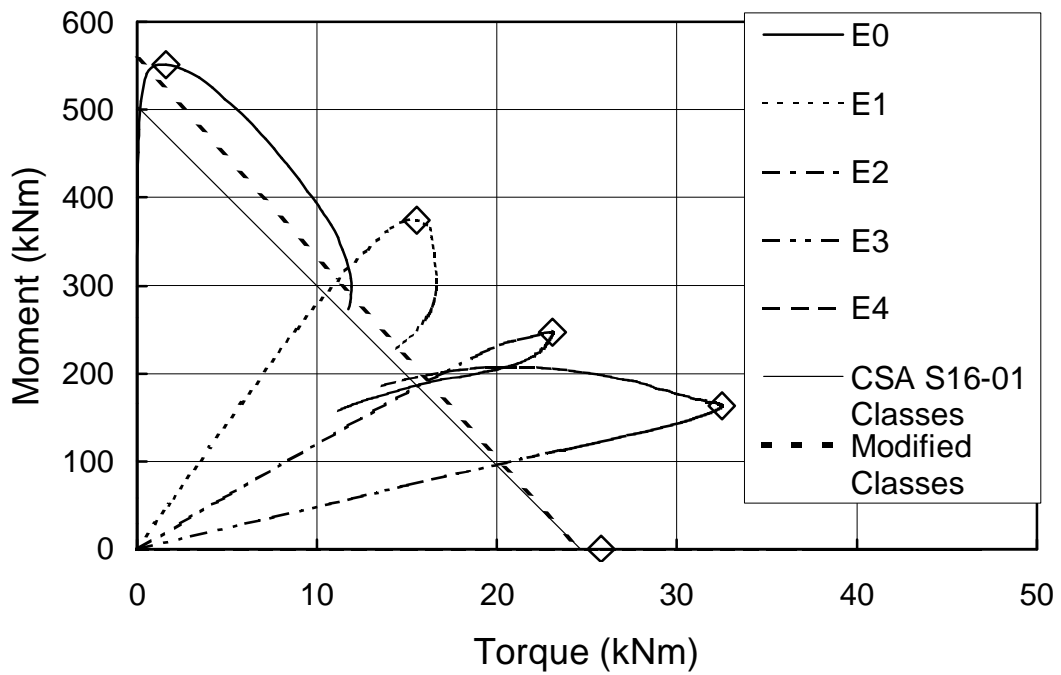


Figure 6.30 Moment vs. Torque Interaction Diagram for Beam S6L1T1B1 (Modified to Class 2 in Flexure)

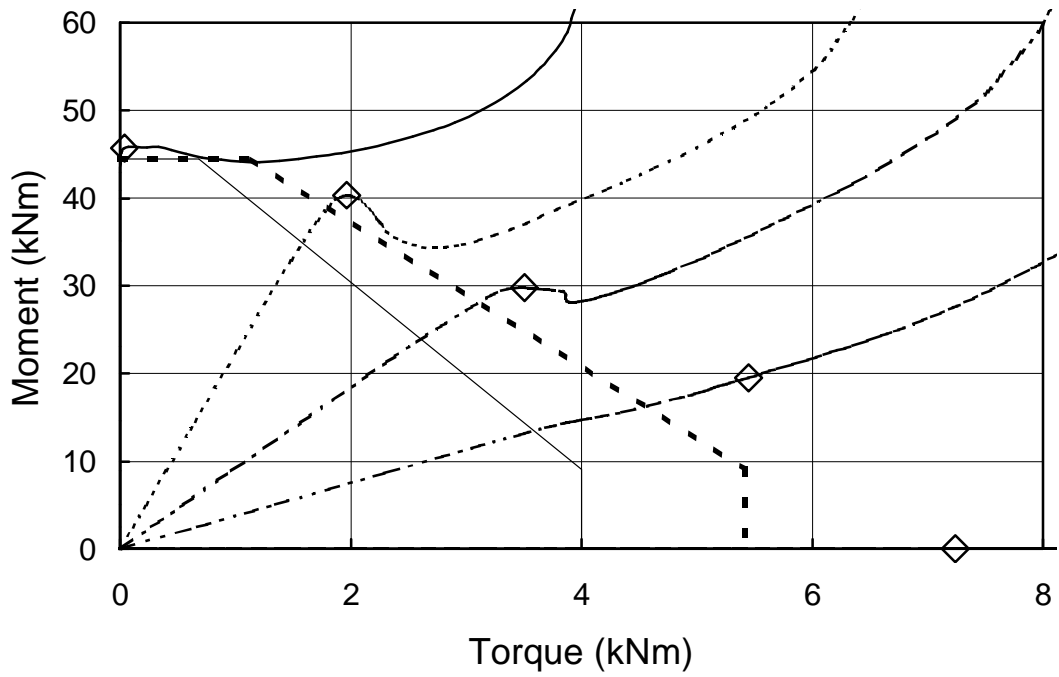


Figure 6.31 Moment vs. Torque Interaction Diagram for Beam S5L1T1B2  
(Modified to Class 1 in Torsion)

Note: The Legend for Figure 6.31 is the same legend used in Figure 6.30.

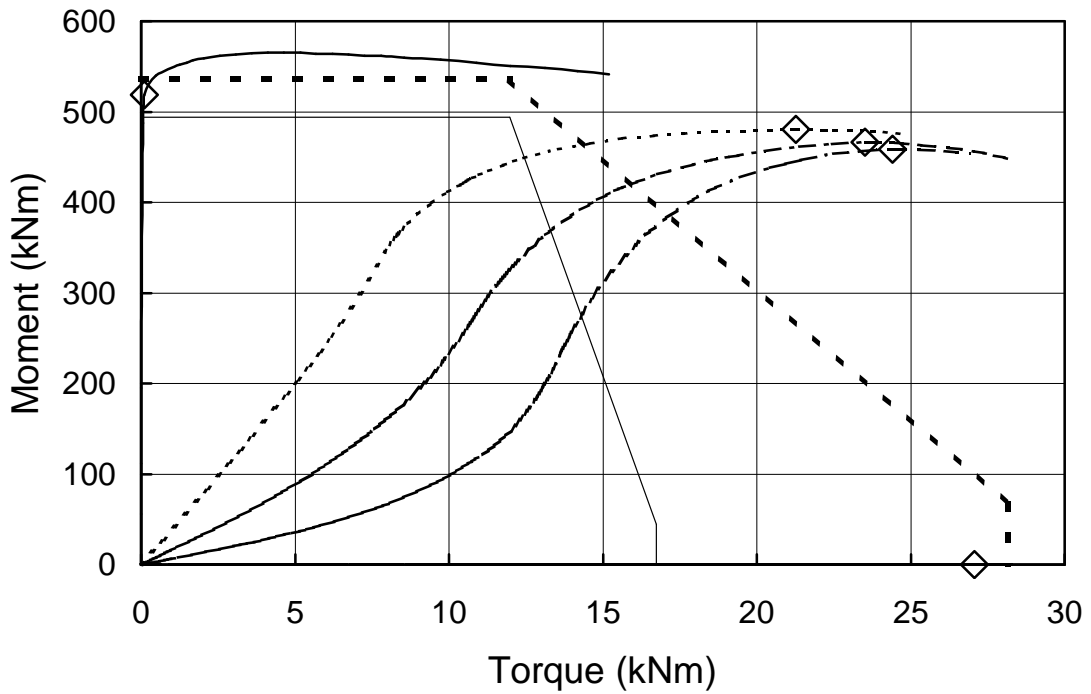


Figure 6.32 Moment vs. Torque Interaction Diagram for Beam S6L2T1B3  
(Modified to Class 1 in Both Torsion and Flexure)

Note: The Legend for Figure 6.32 is the same legend used in Figure 6.30.

## 7 FURTHER VALIDATION OF PROPOSED DESIGN METHODOLOGY

To expand the applicability of the method proposed in the previous chapter, a total of 64 beams are analysed to expand the basic factorial approach described in Chapter 6 to include additional load types, boundary conditions, cross-sections, types of cross-sections (i.e. built-up sections), lengths, and eccentricities. The complete presentation of the results obtained from these additional analyses including individual FEPR, moments, torques, etc. is presented in Appendix C. They are compared against the modified interaction equation described in Section 6.2.1.1. Instead of running five different  $M_n/T_n$  ratios for each beam, only three values are used, namely, E1, E3, and E4, corresponding to the same normalized  $M_n/T_n$  values used in Chapter 6 and defined in Table 5.8. Helping to minimize the number of beams to analyse, the E0 and E2 beams were not included in this process because they behaved well with few irregularities in the basic factorial approach presented in Chapter 6. Additional beams were added to the process, as required, if the behaviour did not fit the expected pattern. The majority of the additional analyses were performed for boundary conditions B1 and B2 because the ULS results of the B3 beams presented earlier were typically very conservative and the SLS would govern over the ULS in the majority of the cases as large rotations developed at the SLS load level.

### 7.1 *Basic Complementary Cases*

A total of 46 basic complementary cases were run to expand the five choice variables used in the basic factorial approach used for the parametric study. For each variable, additional cases are run to spot-check the behaviour of additional cases. These spot-checks or complementary cases did not directly investigate the behaviour of the variables but acted rather to check if the proposed modified interaction diagram was effective in predicting the ultimate limit state for these

additional cases for each variable to expand its applicability without requiring a more extensive factorial approach. The additional cases investigated in this chapter are described in Table 7.1.

Only one beam, S3L1T1B2E2NT (No Thickening), was not a variation of the five choice variables and was included to investigate the effect of thickening the web in the vicinity of the loading bracket to prevent cross-sectional distortion of B2 and B3 E4 beams. Instead of thickening the web around the loading bracket, the loading bracket was connected to the top and bottom flanges using S3R triangular shell elements. Other than for its different shape, the S3R element has similar properties to the quadrilateral shell element S4R described in Chapter 3. Since the Z-coordinate of the nodes on the loading bracket and flanges do not coincide, S3R elements are used instead of the S4R elements to avoid redefining the nodal locations. By connecting the loading bracket to the flanges, local buckling of the flanges at this location is artificially prevented, even though this was found to occur in some of the basic factorial approach results.

The differences between the ultimate and service load points for the thickened and non-thickened beams are small, as seen in Table 7.2. As expected, thickening the web strengthens the beam, as the results of the S3L1T1B2E2 Beam show slightly higher torques and moments. The differences in the moment vs. torque and torque vs. rotation diagrams, illustrated in Figure 7.1 and Figure 7.2, are not significant. Due to the negligible differences between the two models, the effect of web thickening around the loading bracket is considered negligible.

### **7.1.1 Additional Moment–Torque Ratios**

The wide range of moment–torque behaviours investigated in Chapter 6 can be predicted by the modified interaction equation. For beams with supports other than simple, a modification was incorporated into the

interaction diagram of Figure 6.1 at Point 2 to account for shear contributing to yielding of the cross-section. To further investigate this area of the moment vs. torque diagram for support conditions B2 (fixed at both ends) and B3 (cantilever), an additional  $M_n/T_n$  ratio,  $M_n/T_n = 0.5$  (E0.5), is modelled for three different beams: S1L2T1B2, S3L1T1B2, and S4L2T1B3. These three beams are selected because the Finite-Element-to-Predicted Ratios (FEPR) for the E1 beams are below 1.0 for the original interaction diagram and this will ensure that the modified interaction diagram captures the true beam response. The eccentricity for the E0.5 beams is taken as one-half of the E1 values presented in Table 5.13.

The moment versus torque interaction diagrams for E0.5 beams are presented in Figure 7.3 through Figure 7.5. The responses of these three beams are identical to the E1 beams except that their initial  $M/T$  ratio results in a steeper slope, equal to approximately 5.0 on the dimensionless moment–torque diagram, compared to 2.4 for the E1 beams. The FEPR values for beams S1L2T1B2, S3L1T1B2, and S4L2T1B3 are 1.04, 0.94, and 1.13, respectively, with an average value of 1.04. The behaviour of these beams supports the modification to the interaction diagram, which is effective in predicting the beam capacity for the E0.5 beams.

Looking at the deformations and maximum normal stress at service load levels (refer to Appendix C for these results), the SLS governs over the ULS only for Beam S4L2T1B3E0.5 where both the vertical deflection limit of  $L/360$  and a torsional rotation limit of 5 degrees are exceeded. The ULS governs for the other two beams although the maximum normal stress at the service load level is very close to the 350 MPa limit at approximately 348 MPa.

### 7.1.2 Additional Beam Lengths

To investigate further the effect of beam slenderness on its behaviour, two additional slenderness values (obtained by changing the length of the member) are modelled. L3 is modelled with a slenderness ratio equal to 125 to determine the effect of very high slenderness ratios. L4 is modelled with a slenderness ratio of 25 to see how very short, stocky beams behave. It is expected that the ULS will govern in these short beams. Two cross-sections, S2 (W530x123) with boundary condition B1 (simple supports) and S4 (W200x52) with boundary condition B2 (fixed supports), are modelled. For each of these cross-section and boundary condition combinations, both L3 and L4 conditions are applied for eccentricities E1, E3, and E4 creating a total of 12 additional beams. Cross-section S2 is modelled with the B1 support conditions because the behaviour for this cross-section had lower FEPR values for this boundary condition in the basic factorial approach presented in Chapter 6. Elastic lateral torsional buckling governs the flexural resistance for the S2 L3 beams. The selected lengths and load eccentricities, calculated as described in Chapter 5, are presented in Table 7.3.

The average FEPR for the six S2 beams defined above is 1.03 with a coefficient of variation of 11.9%, similar to the average FEPR and coefficient of variation values for the S2L1T1B1 and S2L2T1B1 beams (defined in Chapter 6) of 1.02 and 8.7%, respectively. For the S2L3T1E1 and S2L4T1E1 beams defined in this section, the ultimate limit state points lie below the interaction curve (FEPR values of 0.93 and 0.92 for lengths L3 and L4, respectively), similar to the results of the S2L2T1B1 beam having a FEPR value of 0.92. The moment–torque interaction diagrams for the S2L3T1B1 and S2L4T1B1 beams are shown in Figure 7.6 and Figure 7.7 and illustrate similar responses as the S2L1T1B1 and S2L2T1B1 beams defined in Chapter 6.

The average FEPR and coefficient of variation for the six S4 beams defined above is 1.11 and 14.7%, respectively. The average FEPR and coefficient of variation values for the six S4L1T1B2 and S4L2T1B2 beams defined in Chapter 6 were 1.17 and 9.9%, respectively. Although the six new cases with section S4 with lengths L3 and L4 show a lower mean FEPR and a larger coefficient of variation than for beams S4L1T1B2 and S4L2T1B2, Figure 7.8 and Figure 7.9 show the moment–torque behaviour to be similar to typical B2 (fixed end beams) results presented in Figures 6.16 and 6.17. For Beam S4L4T1B2E1 especially, the ultimate limit state (illustrated by the diamond) does not correspond to the inflection point on the moment vs. torque diagram. The inflection point is found beyond the selected ULS. Looking at Figure 7.10, the “initial yield region” for this beam is different when compared to the “initial yield region” typically found in fixed end beams described in Chapter 6. The point corresponding to the inflection point in the moment vs. torque diagram is highlighted in Figure 7.10. The ULS point is selected at the point after the “initial yield region” at the end of the step found in the vertical load vs. vertical deflection (the slope is approximately equal to the post-“initial yield region” slope) and the bottom flange is completely yielded in tension. This step is similar to the step found in the torque vs. rotation results of the torsion only beams described in Section 6.1.1.2. This ULS point is an exception to the rules used previously stating that the ULS corresponds with the inflection point and is selected differently because the first plastic hinge forms at this load level instead. The selected ULS is conservative when compared to the inflection point as it predicts a lower capacity, although the FEPR value for this beam is 1.00. From these twelve beams, the average FEPR is 1.07 and the coefficient of variation is 13.3%, indicating the ability of the proposed interaction equation to account for the effects of varying slenderness ratios sufficiently accurately.

Looking at the deformations and maximum normal stress at service load levels (refer to Appendix C for these results), the SLS governs over the

ULS in all but one of the 12 beams defined in this section. For the beams with length L4, the maximum normal stress exceeds the yield stress in all but one case and sections do not typically develop deformations larger than the vertical deflection limit of  $L/360$  and the torsional rotation limit of 5 degrees. As expected based on the results of Chapter 6, the torsional rotation limit of 5 degrees is exceeded in all but one of the L3 beams due to the large beam slenderness. For all of these beams with the B1 and B2 boundary conditions, the maximum normal stress is very close to or above the yield value at the service load level.

### 7.1.3 Additional Cross-Sections

Three additional cross-sections have been selected to complement the basic factorial approach. The W920x381 (S9) and W460x260 (S10) cross-sections are selected to provide a greater range of stocky flanges with  $b/(2t)$  values around 3.55. The W610x84 (S11) cross-section is selected because of its large  $h/w$  ratio where the web behaves as Class 2 in flexure. These wide flange sections also provide a greater range of beams with larger cross-sections to provide a better range of cross-section depths in case scale effects are involved. These three wide flange cross-sections are modelled, each with one of the three boundary conditions included in the basic factorial approach and three eccentricities, E1, E3, and E4 defined in Table 7.4, creating a total of nine beams. The boundary conditions are varied as such to spot-check the range of possible boundary condition combinations for the given sections. The W610x84 cross-section is modelled with the B1 boundary condition to investigate the irregularity found amongst the B1 beams of the basic factorial approach for the parametric study. The W920x381 and W460x260 cross-sections are modelled with B3 and B2 support conditions, respectively.

Similar to the results of Chapter 6, the average FEPR is 1.21 and the coefficient of variation is 15.3% for the nine beams defined in this section when compared to the proposed modified interaction diagram. None of these three wide flange cross-sections behaves as a different class of section in either torsion or flexure than as classified by the flexural limits of CSA S16-01. The moment vs. torque diagrams for these beams are presented in Figure 7.11 through Figure 7.13. The behaviour illustrated in these figures is identical to that found in the basic factorial approach results. Only one beam (S10L2T1B2E3) has a FEPR less than 1.0 (0.92). Figure 7.13 (S11L1T1B1 beams) indicates that simply supported beams appear to be able to develop capacities near those predicted by the modified tri-linear interaction equation only for wide flange cross-sections with large  $b/d$  or small  $t/w$  ratios (close to 1). The modified tri-linear interaction diagram, the same as the original interaction diagram proposed by Driver and Kennedy (1987) since the section is Class 3, is also included in Figure 7.13 (dashed) to provide a better understanding of this reserve capacity above the proposed straight-line representation.

Although it appears that for some simply supported wide flange cross-sections a larger capacity can be developed, the straight-line interaction equation is recommended for design as the modified tri-linear interaction equation is highly non-conservative for some wide flange cross-sections as discussed in Section 6.1.2.1 and in Table 6.1. This conclusion is supported by the work of Pi and Trahair (1994a, 1994b) who proposed the use of the same straight-line interaction diagram proposed here for simply supported beams assuming that the beams are either braced only at mid-span or completely unbraced. Pi and Trahair found through an analytical investigation that the circular interaction diagram proposed by Dinno and Merchant (1965) is only adequate for beams that are well-braced (braced laterally at quarter points and at each end).

Looking at the deformations and maximum normal stress at service load levels (refer to Appendix C for these results), the SLS governs over the ULS in all nine of the beams defined in this section using the SLS defined in Section 7.1.1. The deformation serviceability limit states govern over the ULS for all of the cantilever beams with a slenderness ratio of 50. The torsional rotation limit is exceeded for the E3 and E4 eccentricities for both section S9 and S10. For all of these beams with the B1 and B2 boundary conditions, the maximum normal stress is above the yield value at the service load level.

#### **7.1.4 Additional Load Type**

An eccentrically applied vertical Uniformly Distributed Load or UDL, denoted as T2, was added to complement the basic factorial approach. Three different beams, S1L2T2B2, S3L1T2B1, and S6L1T2B3, are selected for this loading condition each with three different load eccentricities creating a total of nine additional beams. To model a UDL, the load is distributed over the length of the beam using multiple loading brackets spaced at every five nodes instead of just a single bracket. Each individual loading bracket is modelled as was done for the point load at mid-span, except that the loading bracket is constructed out of the middle eight web elements instead of the 22 elements used previously. Smaller loading brackets were used to minimize any change to the physical characteristics of the beams as well as the beams response. Since the load on each individual loading bracket is considerably smaller for a UDL, a smaller loading bracket is required to apply the load without causing distortion to the web. By minimizing the depth of the loading brackets, any stiffening effect that these brackets have on the web is reduced to a minimum. For S3L1T2B1 beams, these UDL loading brackets had to be modelled as 16 elements tall to prevent cross sectional distortion. Figure 7.14 presents a typical mesh. The first and last loading brackets are placed at the end supports, which were described in Chapters 5 and 6.

The eccentricities, presented in Table 7.5, are calculated as per Chapter 5 except now in terms of a uniformly distributed load, as shown in Table 7.6. The thickness of the loading brackets is equal to the web thickness except for the S6L1T2B3 beams, where the thickness is taken as 70 mm. This thickness was selected to prevent the loading bracket from developing a vertical deflection at the peak load greater than 0.25 mm relative to the point at which it attaches to the web of the beam.

The moment–torque interaction curves for the nine beams described in above are presented in Figure 7.15 through Figure 7.17. None of these beams have a FEPR value less than 1.0, with an average value of 1.32 and a coefficient of variation of 15.0%. The finite element results illustrate the ability of the modified interaction diagram to safely predict the behaviour and capacity of beams loading with an eccentric uniformly distributed load. The corresponding T1 beams have an average FEPR value of 1.38 with a coefficient of variation of 24.1%. The FEPR values for the corresponding T1 and T2 beams are presented in Table 7.7.

Looking at the deformations and maximum normal stress at service load levels (refer to Appendix C for these results), the SLS governs over the ULS in all but one of the nine beams defined in this section using the SLS defined in Section 7.1.1. As found previously, the deformation serviceability limit states govern over the ULS for all of the cantilever beams even with a slenderness ratio of 50. Similar to the results of the previous section, both the yield stress and the torsional rotation limits are exceeded for the S1L2T2B2E3 and S1L2T2B2E4 beams (slender fixed end beams). For all of these beams with the B1 and B2 boundary conditions, the maximum normal stress is very close to or above the yield value at the service load level.

### 7.1.5 Additional Boundary Condition

One additional boundary condition was added to the investigation: B4 (fixed in bending and torsion at one end and simply supported in bending and torsion at the other end). Refer to Section 5.3.1.2 for a description of how simply supported and fixed end boundary conditions are modelled. For this support condition, six additional beams are modelled, one section with length L1 (S5L1T1B4) and another section with length L2 (S1L2T1B4), each with eccentricities E1, E3, and E4. The modelled eccentricities presented in Table 7.8 are calculated using the method discussed in Chapter 5, modified for the different boundary conditions as shown in Table 7.9.

For the six S5L1T1B4 and S1L2T1B4 beams, the overall model behaviour is similar to the response presented in Chapter 6 for the B1 boundary condition, especially in the moment vs. torque and torque vs. rotation diagrams (the diamonds represent the ULS), as seen in Figure 7.18 and Figure 7.19 for beams S1L2T1B4. The moment–torque interaction diagram for beams S5L1T1B4 is presented in Figure 7.20. For this boundary condition, the beam results indicate that simple-fixed beams can develop moment and torque capacities beyond the straight-line interaction equation proposed for beams simply supported at both ends. The modified tri-linear interaction equation seems to be suitable for all six beams with the B4 boundary condition defined in this section. The average FEPR value for all six B4 beams based on the modified tri-linear interaction diagram is 1.07, with a coefficient of variation of 10.5%. The only beam with a FEPR less than 1.0 is S1L2T1B4E3 (0.93). The fixed support causes the increased resistance, as more than one plastic hinge is required to cause global instability.

Looking at the deformations and maximum normal stress at service load levels (refer to Appendix C for these results), the SLS governs over the ULS in all six of the beams defined in this section using the SLS defined in

Section 7.1.1. For the slender beams S1L2T1B4, the torsional rotation SLS limit of 5 degrees is exceeded for all three beam eccentricities. For all of these beams, the maximum normal stress is above the yield value at the service load level.

## **7.2 Investigation of Built-Up Cross-Sections**

Thus far, the study has been limited to standard rolled wide flange cross-sections. Many cases of combined torsion and flexure occur in stocky industrial beams. These beams are often built-up cross-sections and may not be represented by the selection of wide flange cross-sections. The wide flange cross-sections selected previously provide a wide range of  $b/(2t)$  and  $h/w$  ratios, including very stocky cross-sections. It is impossible to investigate all types of cross-sections that may be exposed to combined torsion and flexure in this project. The goal of this study is to provide a design procedure primarily for wide flange cross-sections. From a limited number of beam models, the design procedure for two types of built-up cross-sections will be assessed: wide flange sections with the top flange reinforced with a channel section as used in the work of Comeau (1998), and custom welded I-shape steel plate girders.

### **7.2.1 Wide Flange Section with One Flange Reinforced with a Channel Section**

The model used to predict the test results of Comeau (1998), as described in Chapter 4, is used to further check the applicability of the proposed interaction diagrams presented in Section 6.2.1. Two lengths are included in this study, L1 and L2, where L1 is the beam 5.94 m long and L2 is the beam 12.2 m long. Only Beam P1 with continuous welds connecting the two sections, as defined in Chapter 4, is considered for this investigation. These two beam lengths are each modelled with two different boundary conditions, B1 and B2, creating a total of four beams (SPL1T1B1,

SPL2T1B1, SPL1T1B2, and SPL2T1B2), where SP (Section Polytechnique) indicates the cross-section tested by Comeau (1998) and described in Chapter 4. The B3 boundary condition is not investigated since either of these lengths of cantilevers are impractical in design. No initial imperfections are introduced in these models since the residual stresses used lead to imperfections near or beyond fabrication tolerances. These imperfections, especially the lateral sweep, are orientated to provide the minimum resistance by mirroring the modelled residual stress pattern about the vertical Y-axis.

The only changes to the finite element mesh used in Chapter 4 is the loading bracket that now resembles the plate at mid-span used thus far in the parametric study. The eccentricities, presented in Table 7.10, are taken as approximately two-thirds of the values found by the previous method for the W460x74 wide flange cross-section alone. This was done because the actual torsional resistance of these crane runway girders required to determine the eccentricity was initially unknown. The load is applied at the shear centre of the wide flange cross-section and neglects the shift of the built-up section's shear centre caused by the addition of the channel section. For the B1 beams, the boundary conditions are applied to the wide flange component of the cross-section in the same manner as for the wide flange cross-sections studied previously. For the B2 beams, the entire cross-section (including the channel) is completely fixed at the supports.

The expressions proposed by Driver and Kennedy (1987, 1989) to determine the theoretical capacities is limited to wide flange cross-sections and plate girders. These beams do not fit into the assumptions of these expressions and require new methods of determining the resistances. The nominal geometric values for the cross-section are used as presented in the Handbook of Steel Construction (CISC, 2007). The cross-section behaves as a Class 1 cross-section. Using the nominal plastic section

modulus of the built-up section and a yield strength of 350 MPa, the nominal plastic moment is 730 kNm. Considering the effects of lateral torsional buckling on a mono-symmetric cross-section, the maximum unsupported length that will result in the plastic moment being reached is 6.15 m. L1 is below the maximum unsupported length, so lateral–torsional buckling is not expected and the moment resistance is equal to the nominal plastic moment. For the L2 beams, the moment resistance is 464 kNm and 692 kNm for support conditions B1 and B2, respectively. The moment capacity of the web is calculated the same as for wide flange cross-sections assuming that the neutral axis is at the mid-height of the wide flange web.

The torsional resistances are more complicated due to the two components of torsion: pure torsion and warping torsion. For Class 3 cross-sections, a simple equation based on the membrane analogy, Equation [2.37], can be used which is a linear function of the torsion constant. The nominal torsion constant for the built-up cross-section is  $669 \times 10^3 \text{ m}^3$ , equal to the sum of the individual  $J$  values for the W460x74 and C310x31 cross-sections. For Class 3 cross-sections, the total pure torsional resistance,  $T_{sv,T}$ , can be found conservatively by summing up the individual pure torsional resistances for the channel,  $T_{sv,C}$ , and the wide flange cross-section,  $T_{sv,W}$ , as follows:

$$T_{sv,T} = T_{sv,C} + T_{sv,W} \quad [7.1]$$

It follows that the same can be done for Class 1 and 2 cross-sections using the sand heap analogy. For a crane runway girder built-up of a W460x74 and a C310x31 cross-section (Class 1 behaviour), the total pure torsional resistance is 19.5 kNm. For the modified interaction equation, the total pure torsional resistance according to the membrane analogy is 9.62 kNm.

The warping torque definitions developed by Driver and Kennedy (1987, 1989) are based on the development of a plastic warping hinge in the flange. There are two different effective flanges in these mono-symmetric built-up cross-sections. The bottom flange consists of only the bottom flange of the wide flange section and has the same warping torque resistance definition. The top flange consists of the channel and top flange of the wide flange cross-section welded together. The warping torsional resistance of the built-up cross-section is determined based on the bottom flange warping resistance.

For crane runway girders composed of a channel welded to the top flange of a wide flange cross-section, the warping torsion resistance should be calculated by considering the wide flange cross-section alone. Using this approach, Table 7.11 illustrates the good agreement between the finite element and theoretical capacities for the simply supported beams (B1 beams). However, the theoretical capacities are very conservative for the B2 beams.

Unlike many of the results for the simply supported beams (B1) from the parametric study on wide flange beams, these simply supported beams are able to develop the straight-line capacities predicted by the modified interaction diagram up to the modified tri-linear interaction diagram proposed for all other boundary conditions. The average FEPR for all twelve beams, compared to the proposed straight-line interaction diagram, is 1.26 with a coefficient of variation of 16.2%. For the six B1 beams presented in Table 7.10, the average FEPR is 1.27 with a coefficient of variation of 17.0%. Only one of these six beams has a FEPR less than 1.0, namely, SPL1T1B1E4 (0.92). For this built-up cross-section, the  $b/d$  ratio is 0.42 when only considering the bottom flange, but is 0.67 when considering the top flange. The  $t/w$  ratio is 1.61 when considering only the bottom flange, but 2.41 when considering the total thickness of the built-up top flange. Unlike the results of the basic factorial approach, these

crane runway girders can develop this additional capacity even for small  $b/d$  and large  $t/w$  ratios. The moment–torque diagrams for the B1 beams are presented in Figure 7.21 and Figure 7.22. The load and support conditions are applied at a nominal distance of 195 mm below the actual shear centre. This causes a slight stabilizing effect as compared to shear centre loading, leading to the development of additional flexural strength if the beam length exceeds the characteristic length for the cross-section used in this investigation.

The behaviour itself is typical of other simply supported beams in this study and the ULS points are selected using the straight-line interaction diagram proposed for this boundary condition in Chapter 6. Even though the bottom flange is the weaker flange in warping, the top flange is still the critical flange for stability of the rotated cross-section and its failure governs for combined torsional and flexural behaviour. The beam capacity is reached when a warping bi-moment causes a plastic warping hinge to form in the top flange, leading to general beam instability and the loss of load carrying capacity.

Looking at only the six B2 beams, the average FEPR is 1.26 with a coefficient of variation of 17.0%. All beams lie above the proposed modified interaction diagram. The response of the beams matched well with the moment–torque behaviour expected for wide flange cross-sections, especially for the L2 beams, as seen in Figure 7.23 and Figure 7.24. An irregularity is found for the SPL1T1B1E1 Beam, where instead of having an “initial yield region” where the slope of the moment–torque diagram decreases, the slope for the beam continues to increase beyond vertical such that the torque begins to decrease as yielding causes the development of a plastic hinge at the ULS. The torque reaches a peak and decreases because large lateral deflections develop in the negative Z-direction, reducing the effective load eccentricity.

Looking at the deformations and maximum normal stress at service load levels (refer to Appendix C for these results), the SLS governs over the ULS in all 12 of the beams defined in this section using the SLS defined in Section 7.1.1. The vertical deflection limit of  $L/360$  is exceeded in only three of the beams. The torsional rotation SLS limit of 5 degrees is exceeded in all 12 of the beams due to the large beam slenderness modelled. For all of these beams, the maximum normal stress is very close to or above (11 of the 12 beams) the yield value at the service load level.

### 7.2.2 Welded Plate Girders

The selection of wide flange cross-sections provides a range of cross-sections with small local slenderness ratios. The differences between very stocky wide flange cross-sections and very stocky welded plate girders are expected to be negligible. To investigate the other end of the spectrum, additional complementary cases are developed on two deep, slender welded plate girders typical of bridges. Cross-section S7 is composed of three welded Grade 350W steel plates resulting in  $d$ ,  $b$ ,  $t$ , and  $w$  values of 1 000 mm, 300 mm, 22.2 mm, and 12.7 mm, respectively. According to CSA S16-01, this cross-section has Class 1 flanges and a Class 2 web. Cross-section S8 is composed of three welded Grade 350W steel plates resulting in  $d$ ,  $b$ ,  $t$ , and  $w$  values of 1 500 mm, 500 mm, 25.4 mm, and 15.9 mm respectively. According to CSA S16-01, this cross-section has Class 3 flanges and web. A difference between these beams and a typical wide flange cross-section is the absence of fillets at the flange-to-web junctions and contributions by the welds are neglected. Although typically used in design, no web stiffeners are provided in the model.

For these cross-sections, two different lengths are modelled. These two lengths, L1 and L3, are selected to provide slenderness ratios of 50 and 125, respectively. This corresponds with lengths of 3.14 m and 7.84 m for

S7 and lengths of 5.23 m and 13.1 m for S8. The L1 beams have lengths less than the maximum unsupported length so that lateral torsional buckling will not govern. Rather than investigating several boundary conditions for each of the resulting four beams, the support conditions B1 and B2 are alternately selected. The four beams are S7L1T1B1, S7L3T1B2, S8L1T1B2, and S8L3T1B1, creating a total of twelve cases. The eccentricity of the vertical load presented in Table 7.12 is calculated as done previously. The theoretical nominal torsional and flexural resistances are calculated using the same approach as was used for wide flange cross-sections.

The finite element results do not have strong agreement with the expected behaviour for the B1 and B2 support conditions as seen in Figure 7.25 through Figure 7.28. The average FEPR and coefficient of variation values for the 12 beams are 1.06 and 20.5%, respectively. Despite the average value being relatively close to 1.0, the large coefficient of variation indicates the large dispersion within the results. In the model results, the failure mode for the E1 L1 and E3 L1 beams is shear buckling of the web and not the mode described previously in Chapter 6. The torque vs. rotation diagram presented in Figure 7.29 indicates how the behaviour of the L1 E1 beams is different because of this failure mode. The shear resistances of the beams, calculated using CSA S16-01, are presented in Table 7.13.

To account for shear failure of the L1 beams, the flexural resistance is taken as the applied moment that develops at the load causing the shear resistance in the member. This changes the average FEPR and coefficient of variation values for all 12 beams to 1.08 and 18.6%, respectively, but there are still areas of concern. First, one of the B1 E4 beams is well below the ideal FEPR value of 1.0, with a value of 0.74 for the S7 beam (Figure 7.25). The other E4 beams are all above 1.0 at 1.17 (S7L3T1B2E4; Figure 7.26), 1.03 (S8L1T1B2E4; Figure 7.27), and

1.22 (S8L3T1B1E4; Figure 7.28). There may be a factor that reduces the ability of some B1 beams to carry the full torsional resistance that is unaccounted for in the modified interaction equation. From the results of the complementary cases, it is recommended that further research is required for tall, slender welded plate girders.

Looking at the deformations and maximum normal stress at service load levels (refer to Appendix C for these results), the SLS governs over the ULS in 10 out of the 12 beams defined in this section using the SLS defined in Section 7.1.1. The vertical deflection limit of  $L/360$  is exceeded in only one of the beams. The torsional rotation SLS limit of 5 degrees is exceeded in the E3 and E4 eccentricities for beams S7L3T1B2 and S8L3T1B1 due to the large beam slenderness. For all of these beams, the maximum normal stress is very close to or above (10 of the 12 beams) the yield value at the service load level.

### **7.3 Previous Research**

Driver and Kennedy (1987) checked their proposed method against several experimental results besides their own to provide further verification. The authors found it impossible to compare the method to the work of Dinno and Merchant (1965), Kollbrunner *et al.* (1978), and Kollbrunner *et al.* (1979) due to limitations in reported information and testing that was terminated prior to failure of the beam. Driver and Kennedy (1987) compared the test results of Razzaq and Galambos (1979b) to the theoretical interaction diagram based on measured dimensions and yield stress. In this project, the experimental results are compared with the modified and original (dashed line) interaction diagrams constructed based on the nominal values. The ultimate limit state points used to compare the work of Razzaq and Galambos (1979b) to the proposed modified interaction diagram are the same dimensionless X and Y-coordinates used in the work of Driver and Kennedy (1987). Figure 7.30, Figure 7.31, and Figure 7.32 present the

moment–torque interaction diagrams for the two sets of test results from Razzaq and Galambos (1979b) and Driver and Kennedy (1987). Table 7.14 presents the FEPR values for these two sets of experimental results. Although the original interaction diagram appears to model the test results well, the modified diagram is clearly conservative.

#### **7.4 Rotations at the Ultimate Limit State**

Similar to the study described in the previous chapter, torsional rotations were not considered in determining the ultimate limit state. However, the torsional rotations that developed at the selected ULS were much larger than 30 degrees in some cases, as found in Chapter 6. Using the same arbitrary 30 degree rotation cut-off as used in Chapter 6 to compare the finite element results to the modified interaction diagram produces an average FEPR and coefficient of variation of 1.05 and 25.9%, respectively, for the 63 beams introduced in this chapter. Of these 63 beams, 15 beams have a FEPR value less than 0.85 and six beams have a FEPR value less than 0.7. Five of the six beams with a FEPR value less than 0.7 are sections built-up of a wide flange and channel section that have values as low as 0.29 (SPL2T1B2E4) with an average FEPR value of 0.44. The other beam with a FEPR value less than 0.7 is a beam under torsion only loading (idealized situation), S1L2T1B4E4, with a value of 0.68. Table 7.15, Table 7.16, Table 7.17, and Table 7.18 present a list of all of the FEPR values for the complementary beam ULS points as selected without (Table 7.15 and Table 7.16, refer to Appendix C) and with (Table 7.17 and Table 7.18) the 30 degree cut-off, respectively.

Due to the large number of crane runway girders that have FEPR values less than 0.5, it is recommended that crane runway girders composed of wide flange cross-sections and rolled channels without torsional bracing over the length of the member not be designed using this design procedure. These beams undergo large rotations under relatively small loads rendering them ineffective in carrying such loads without effective

bracing, likely a result of the large slenderness ratios ( $L/r_y$ ) modelled in this study (82.1 for L1 and 169 for L2). Removing these beams from the analysis, the average FEPR and coefficient of variation values become 1.10 and 19.7%, respectively. Looking at the same reduced set of beams for the ULS points selected without using the 30 degree cut-off, the average FEPR and coefficient of variation values are 1.13 and 16.2%, respectively. Based on the analysis results presented in this chapter and Chapter 6, the modified interaction diagram described in Section 6.2.1 is proposed without any ULS limits on rotation.

## **7.5 Summary**

The complementary beams described in this chapter support the use of the modified interaction diagram for assessing the capacity of rolled wide flange sections under combined flexure and torsion. The modified diagram includes the use of a straight-line interaction equation for simply supported beams only. Beams with all other boundary conditions are capable of developing the capacities defined according to the interaction diagram of Driver and Kennedy (1987, 1989), but with torsional capacity that can be resisted in combination with the full moment capacity modified to the elastic St. Venant torsional capacity for all classes of section. The moment resistance is calculated as per CSA S16-01 and is determined as the flexural resistance including the effects of lateral-torsional buckling. The torsional resistance is calculated using Equations [2.35] through [2.40] as per Driver and Kennedy (1987, 1989).

The list of the FEPR values for the 63 beams investigated in this chapter is presented in Table 7.15 and Table 7.16 (refer to Appendix C). The average FEPR for these beams is 1.15 with a coefficient of variation of 16.6%. The coefficient of variation is large, although not as large as in the basic factorial approach. Of these 63 beams, only 12 have a FEPR value less than 1.0, only three have a value less than 0.85; S7L1T1B1E1 (0.84),

S7L1T1B1E4 (0.74), and S7L3T1B2E1 (0.84). All of the beams with a FEPR value less than 0.85 are built-up cross-sections and it is thus recommended that more research be done to confirm the behaviour of this type of cross-section. The modified ULS interaction diagram appears to provide a means of designing rolled wide flange shapes with a broad variety of parameters for combined flexure and torsion.

Comparing the vertical deflections, torsional rotations, and maximum normal stresses at the service load level presented in Appendix C to the SLS limits defined in Chapter 6, it is found that the SLS governs over the ULS in 90.5% of the 63 beams investigated in this chapter. Only seven of the 63 complementary cases investigated in this chapter exceed the vertical deflection limit at the SLS. A much larger proportion of these 63 beams exceed the torsional rotation limit of 5 degrees and the maximum normal stress of yield, 29 and 36, respectively.

Table 7.1 Naming and Numbering Convention for Basic Complementary Cases

Variable									
#1		#2		#3		#4		#5	
S#	Section	L#	Slenderness Ratio	T#	Load Type	B#	Boundary Condition Number	E#	Normalized $\frac{M_n}{T_n}$ Ratio
9	W920x381	3	125	2	Uniformly Distributed Load	4	Simple Support in Flexure and Torsion at One End and Fixed at the Other End	0.5	5.0
10	W460x260	4	25						
11	W610x84								

Table 7.2 Results at Service and Ultimate Points – Thickened vs. Non-Thickened Web Model

	S3L1T1B2E3	S3L1T1B2E2NT	% Difference
<b>Service Load Level (ULS Divided by Effective Load Factor of 1.4)</b>			
Moment (kNm)	381.6	377.6	-1.0
Torque (kNm)	45.25	44.79	-1.0
Rotation (deg)	1.8	1.8	-0.5
Vertical Deflection (mm)	3.7	3.8	3.8
<b>Ultimate Limit State</b>			
Moment (kNm)	534.2	528.6	-1.0
Torque (kNm)	78.18	76.36	-2.3
Rotation (deg)	12.8	12.9	0.9
FEPR	1.10	1.08	-1.7

Table 7.3 Lengths and Eccentricities Used in Beam Length Variation

Beam	Length (mm)	$k_2$ Values	Load Eccentricity (mm)		
			E1	E2	E3
S2L3T1B1	5800	13.6	58.6	140.8	351.9
S2L4T1B1	1160	8.52	28.4	68.1	170.1
S4L3T1B2	6462	11.7	56.6	136.0	339.9
S4L4T1B2	1292	5.69	30.4	73.0	182.4

Table 7.4 Eccentricities Used with Additional Cross-Sections

Beam	$k_2$ Values	Load Eccentricity (mm)		
		E1	E2	E3
S9L1T1B3	17.3	110.9	266.2	665.4
S10L2T1B2	8.41	79.1	189.9	474.8
S11L1T1B1	28.1	28.1	67.3	168.3

Table 7.5 Eccentricities Used with T2 Beams

Beam	$k_2$ Values	Load Eccentricity (mm)		
		E1	E2	E3
S1L2T2B2	8.46	16.4	39.2	98.1
S3L1T2B1	10.9	25.5	61.2	153.0
S6L1T2B3	16.2	67.1	161.0	402.4

Table 7.6 Method Used to Calculate Required Vertical UDL Eccentricity

Boundary Condition	Maximum Moment	Maximum Torque	$\left(\frac{M_n}{T_n}\right)$	Eccentricity
B1	$\frac{wL^2}{8}$	$\frac{weL}{2}$	$\frac{L}{4e}$	$\frac{L}{4\left(\frac{M}{T}\right)}$
B2	$\frac{wL^2}{12}$	$\frac{weL}{2}$	$\frac{L}{6e}$	$\frac{L}{6\left(\frac{M}{T}\right)}$
B3	$\frac{wL^2}{2}$	$weL$	$\frac{L}{2e}$	$\frac{L}{2\left(\frac{M}{T}\right)}$

Table 7.7 Comparison of the Results of the T1 and T2 Beams

Beam	FEPR		
	T1 Beams	T2 Beams	% Difference
S3L1B1E1	1.10	1.16	5.4
S3L1B1E3	1.08	1.14	5.5
S3L1B1E4	1.22	1.12	-8.3
S1L2B2E1	1.26	1.63	29.9
S1L2B2E3	1.36	1.47	8.3
S1L2B2E4	1.02	1.26	23.5
S6L1B3E1	1.68	1.49	-11.5
S6L1B3E3	1.79	1.46	-18.3
S6L1B3E4	1.91	1.12	-41.6

Table 7.8 Eccentricities Used for Additional Boundary Conditions

Beam	$k_2$ Values	Load Eccentricity (mm)		
		E1	E2	E3
S1L2T1B4	10.8	35.39	89.94	212.34
S5L1T1B4	11.9	16.65	39.95	99.88

Table 7.9 Method Used to Calculate Required Vertical Load Eccentricity

Boundary Condition	Maximum Moment	Maximum Torque	$\left(\frac{M_n}{T_n}\right)$	Eccentricity
B4	$\frac{3PL}{16}$	$\frac{Pe}{2}$	$\frac{3L}{8e}$	$\frac{3L}{8\left(\frac{M}{T}\right)}$

Table 7.10 Eccentricities Used for Wide Flange Beams Reinforced with a Channel Section

Beam	Load Eccentricity (mm)		
	E1	E2	E3
SPL1T1B1	70	200	500
SPL1T1B2	30	80	200
SPL2T1B1	200	600	1 500
SPL2T1B2	75	220	600

Table 7.11 Total Torsional Resistance Calculated by the Method Proposed in Section 7.2.1

Beam	Total Torsional Resistance, $T_r$ (kNm)		
	Theoretical Capacity	Finite Element Capacity	% Difference
SPL1T1B1	28.58	26.20	-8.3
SPL2T1B1	23.91	24.36	1.9
SPL1T1B2	37.69	54.10	43.5
SPL2T1B2	28.02	36.23	29.3

Table 7.12 Eccentricities Used for the Welded Plate Girder

Beam	$k_2$ Values	Load Eccentricity (mm)		
		E1	E2	E3
S7L1T1B1	21.4	30.52	73.24	183.1
S7L3T1B2	22.7	59.05	141.7	354.3
S8L1T1B2	12.1	44.49	107.7	269.2
S8L3T1B1	34.3	77.76	186.2	465.5

*Table 7.13 Theoretical Pure Flexure Capacity of Welded Plate Girders*

<b>Beam</b>	<b>Moment Resistance (kNm)</b>	<b>Shear Resistance (kN)</b>	<b>Applied Moment at Shear Resistance (kNm)</b>	<b>Governing Failure Mode in Pure Flexure</b>
<b>S7L1T1B1</b>	3 296	2 091	3 279	Shear
<b>S7L3T1B2</b>	3 006	2 033	3 985	Flexure
<b>S8L1T1B2</b>	8 323	2 806	5 499	Shear
<b>S8L3T1B1</b>	4 878	2 678	17 507	Flexure

*Table 7.14 Finite-Element-to-Predicted Ratios for Test Results*

<b>Experimental Tests</b>	<b>Beam</b>	<b>Interaction Diagram</b>	
		<b>Original</b>	<b>Modified</b>
<b>Razzaq and Galambos (1979b)</b>	<b>BB-1</b>	1.31	1.31
	<b>TB-1</b>	0.94	0.99
	<b>BB-5</b>	1.04	1.04
	<b>TB-5</b>	1.00	1.07
<b>Driver and Kennedy (1987)</b>	<b>Beam 1</b>	1.04	1.04
	<b>Beam 2</b>	1.09	1.09
	<b>Beam 3</b>	1.13	1.34
	<b>Beam 4</b>	1.30	1.46

Table 7.15 List of Finite-Element-to-Predicted Ratios for Complementary Cases

Beam	Finite-Element-to-Predicted Ratio		
	E1	E3	E4
SPL1T1B1	1.26	1.42	0.92
SPL1T1B2	1.12	1.45	1.44
SPL2T1B1	1.45	1.56	1.02
SPL2T1B2	1.06	1.20	1.28
S9L1T1B3	1.36	1.27	1.25
S10L2T1B2	1.08	0.92	1.00
S11L1T1B1	1.47	1.40	1.18
S2L3T1B1	0.93	1.20	0.94
S2L4T1B1	0.92	1.09	1.14
S4L3T1B2	1.10	0.93	1.01
S4L4T1B2	1.00	1.34	1.26
S5L1T1B4	1.24	1.17	1.01
S1L2T1B4	1.05	0.93	1.02
S3L1T2B1	1.16	1.14	1.12
S1L2T2B2	1.63	1.47	1.26
S6L1T2B3	1.49	1.46	1.12
S7L1T1B1	0.84	1.03	0.74
S7L3T1B2	0.84	1.18	1.17
S8L1T1B2	1.01	1.39	1.03
S8L3T1B1	1.26	1.26	1.22

Table 7.16 List of Finite-Element-to-Predicted Ratios for Complementary Eccentricity Cases

Beam	FEPR					
	E0	E0.5	E1	E2	E3	E4
S1L2T1B2	1.05	1.04	1.26	1.36	1.02	1.02
S3L1T1B2	1.02	0.94	1.01	1.10	1.09	1.08
S4L2T1B3	1.02	1.13	1.29	1.39	1.41	1.23

Table 7.17 List of Finite-Element-to-Predicted Ratios for Complementary Cases with 30 Degree Cut-Off

Beam	Finite-Element-to-Predicted Ratio		
	E1	E3	E4
SPL1T1B1	1.26	0.83	0.57
SPL1T1B2	1.12	1.19	1.12
SPL2T1B1	1.02	0.36	0.29
SPL2T1B2	0.99	0.49	0.48
S9L1T1B3	1.36	1.27	1.25
S10L2T1B2	1.08	0.92	0.82
S11L1T1B1	1.47	1.40	1.18
S2L3T1B1	0.93	1.04	0.85
S2L4T1B1	0.92	1.09	1.14
S4L3T1B2	1.10	0.88	0.74
S4L4T1B2	1.00	1.34	1.26
S5L1T1B4	1.24	1.17	1.01
S1L2T1B4	1.05	0.83	0.68
S3L1T2B1	1.16	1.14	1.12
S1L2T2B2	1.63	1.47	1.26
S6L1T2B3	1.49	1.26	1.12
S7L1T1B1	0.84	1.03	0.74
S7L3T1B2	0.84	1.18	1.17
S8L1T1B2	1.01	1.39	1.03
S8L3T1B1	1.26	1.26	1.22

Table 7.18 List of Finite-Element-to-Predicted Ratios for Complementary Eccentricity Cases with 30 Degree Cut-Off

Beam	Finite-Element-to-Predicted Ratio					
	E0	E0.5	E1	E2	E3	E4
S1L2T1B2	1.05	1.04	1.26	1.19	0.99	0.84
S3L1T1B2	1.02	0.94	1.01	1.10	1.09	1.08
S4L2T1B3	1.02	0.76	0.57	0.44	0.35	0.43

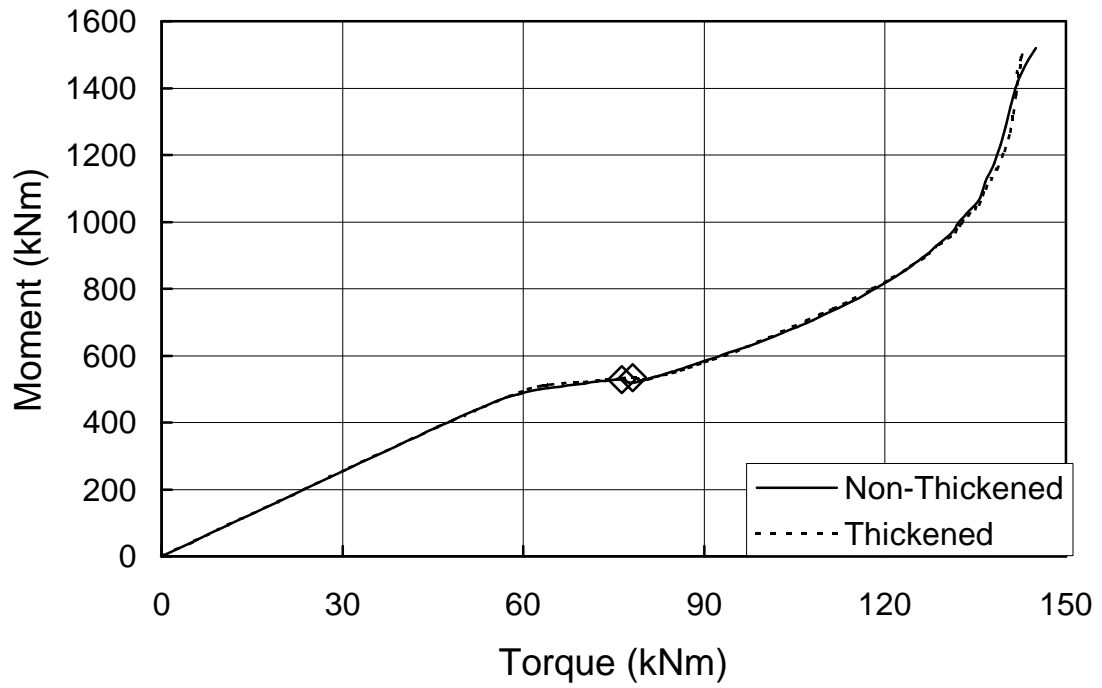


Figure 7.1 Moment vs. Torque Diagram - Thickened vs. Non-Thickened Web Models

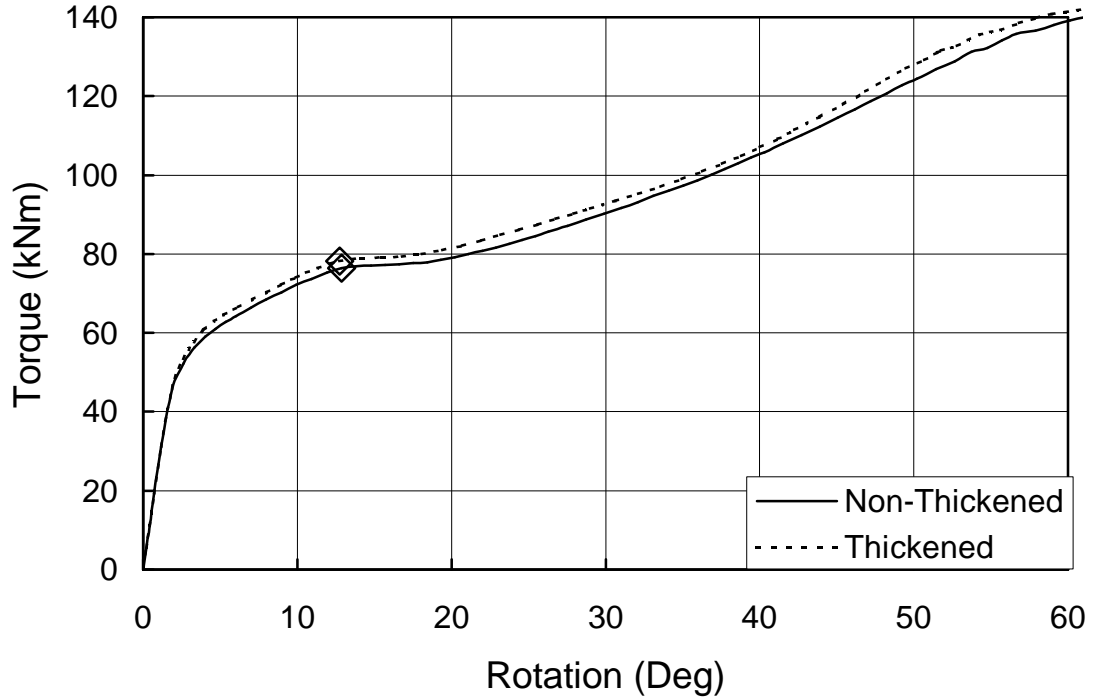


Figure 7.2 Torque vs. Rotation Diagram - Thickened vs. Non-Thickened Web Model

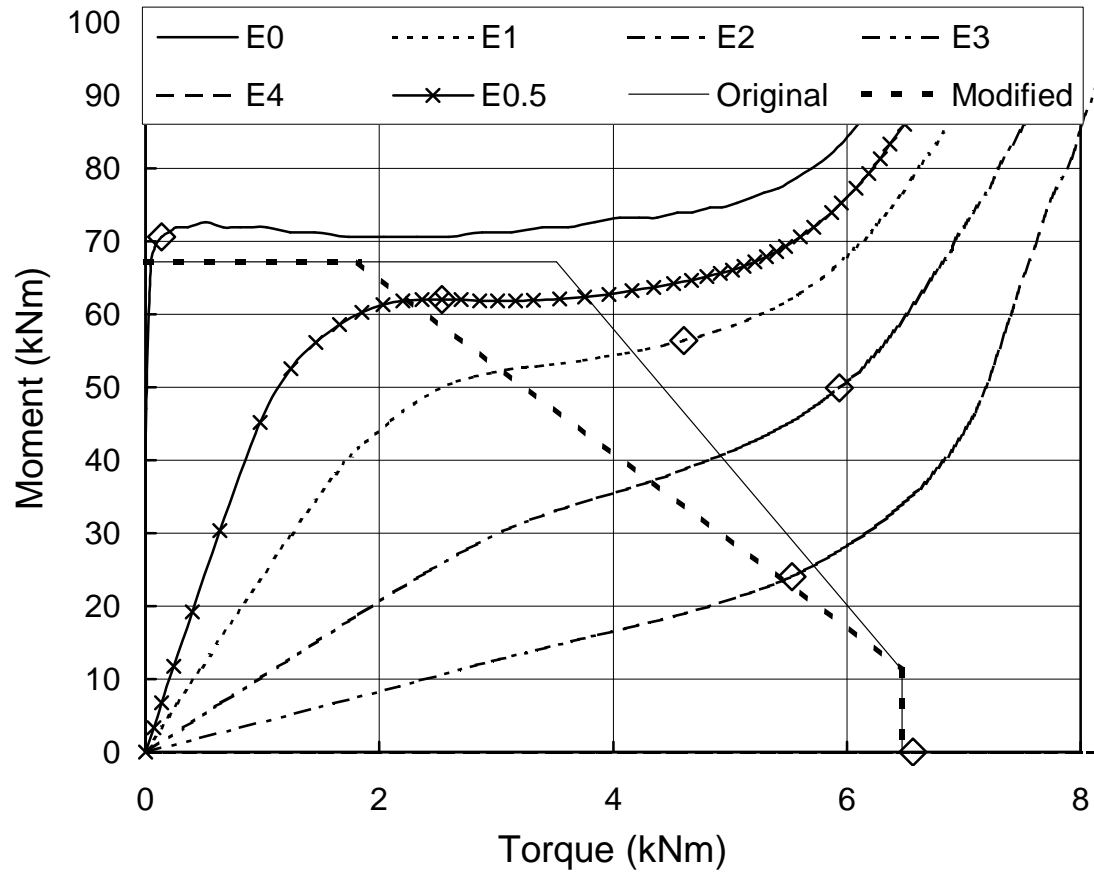


Figure 7.3 Moment vs. Torque Interaction Diagram for Beam S1L2T1B2

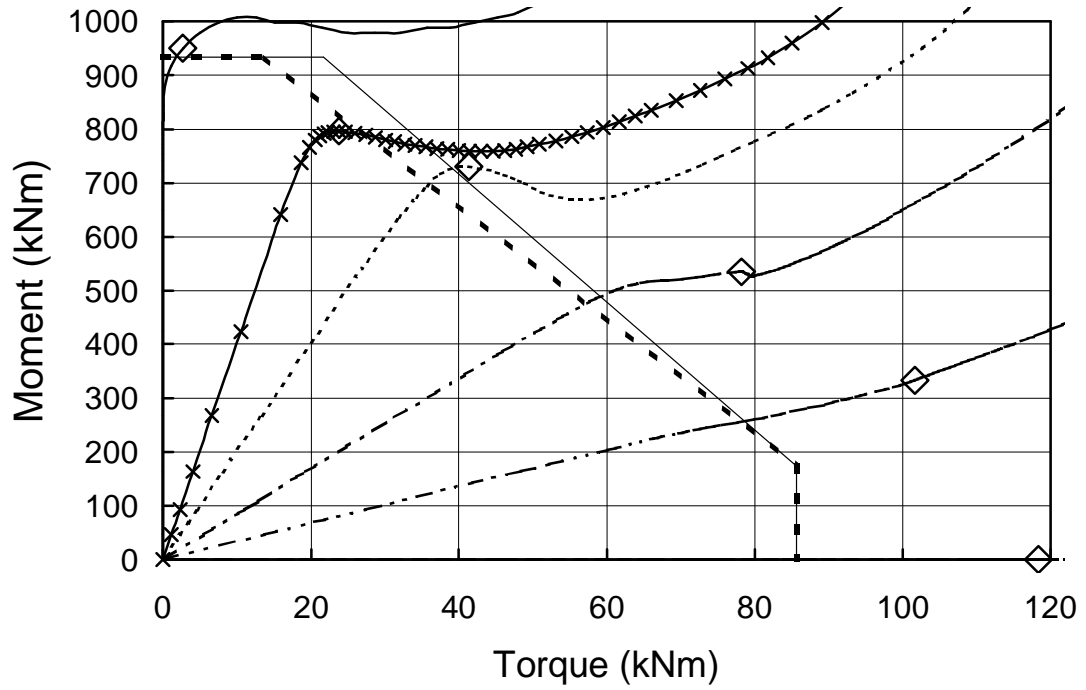


Figure 7.4 Moment vs. Torque Interaction Diagram for Beam S3L1T1B2  
 Note: The legend for Figure 7.4 is the same legend used in Figure 7.3.

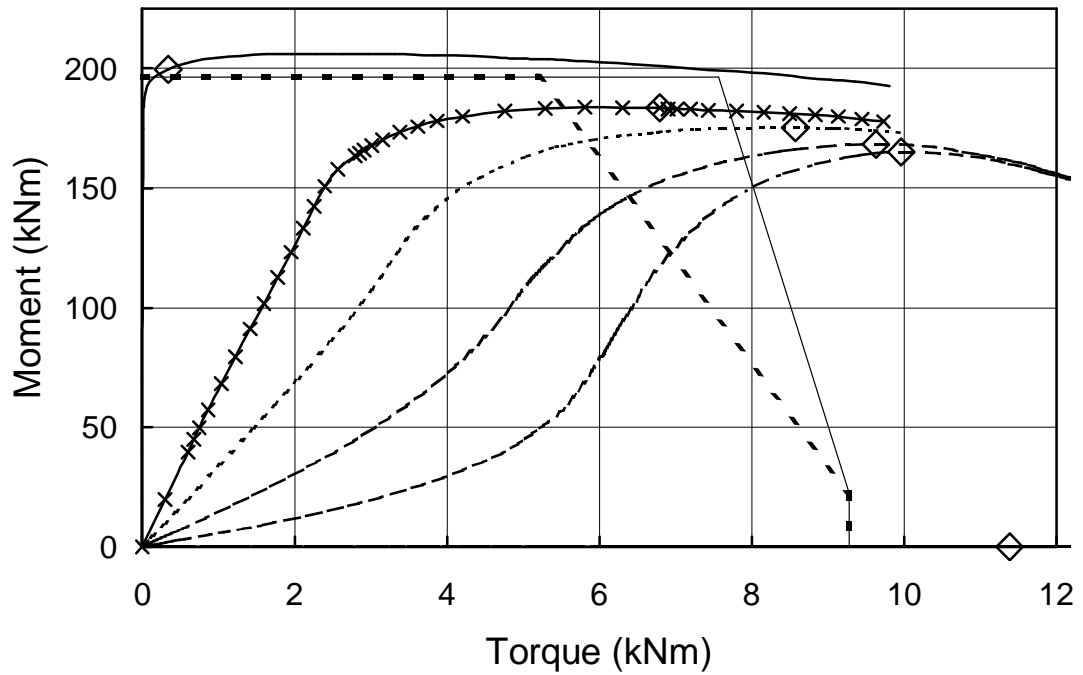


Figure 7.5 Moment vs. Torque Interaction Diagram for Beam S4L2T1B3  
 Note: The legend for Figure 7.5 is the same legend used in Figure 7.3.

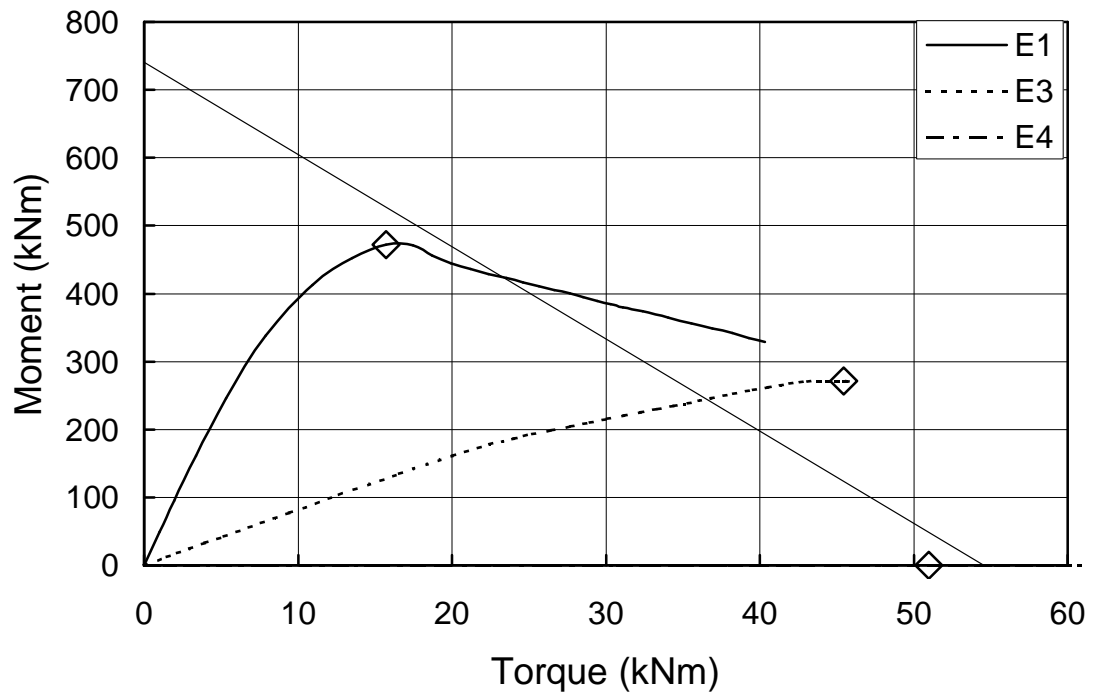


Figure 7.6 Moment vs. Torque Interaction Diagram for Beam S2L3T1B1

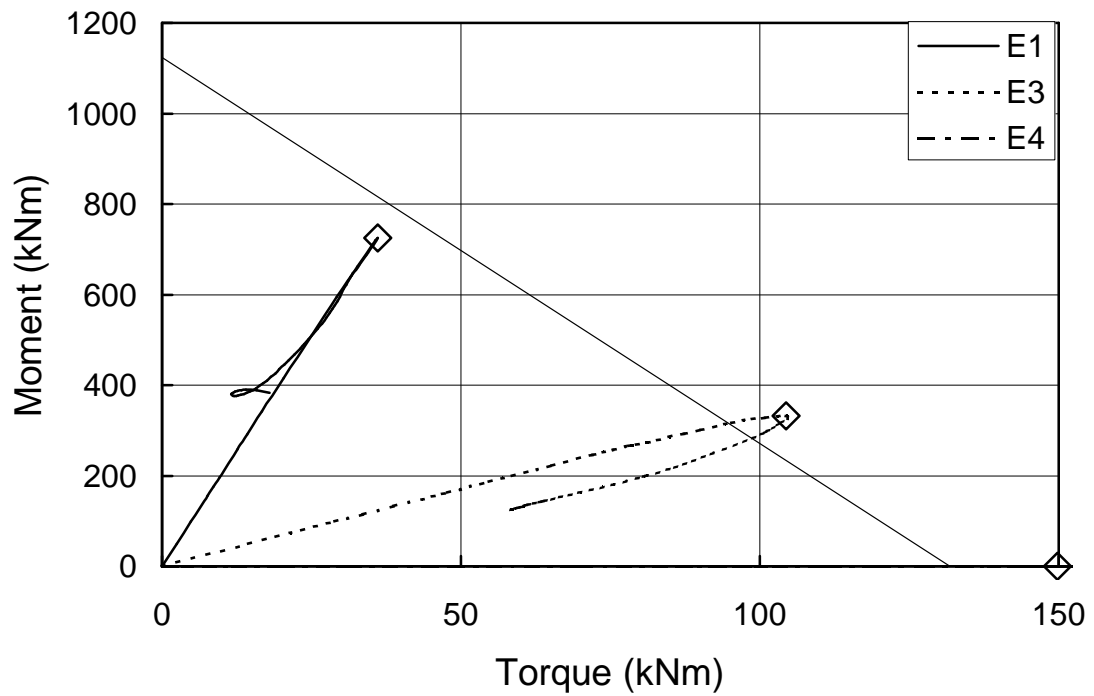


Figure 7.7 Moment vs. Torque Interaction Diagram for Beam S2L4T1B1

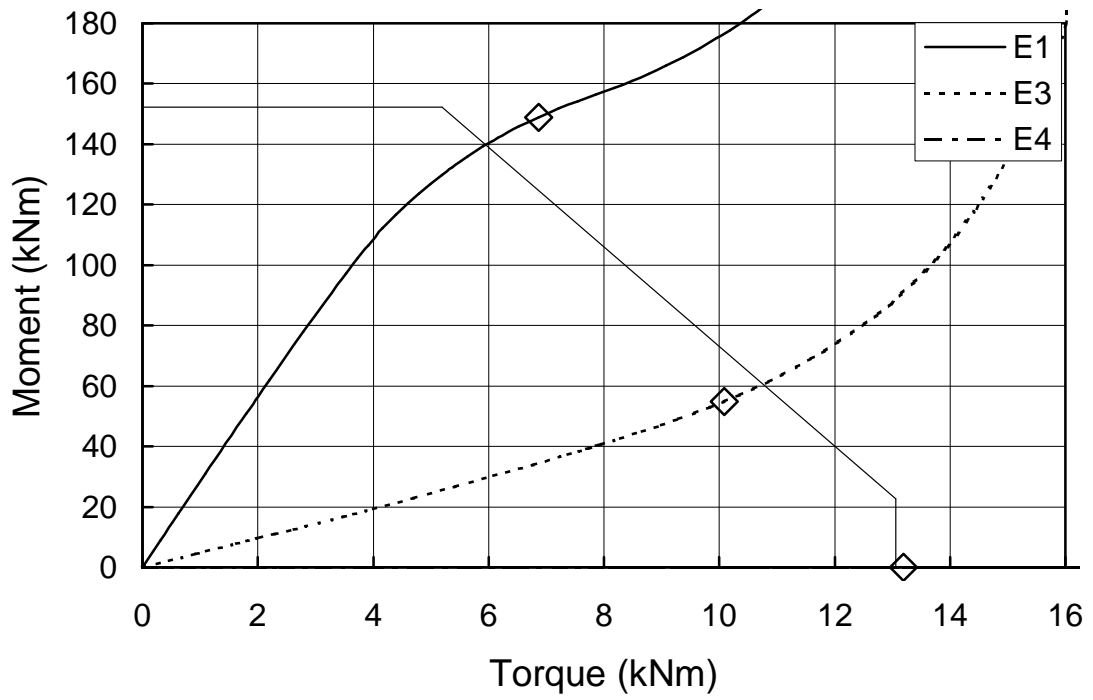


Figure 7.8 Moment vs. Torque Interaction Diagram for Beam S4L3T1B2

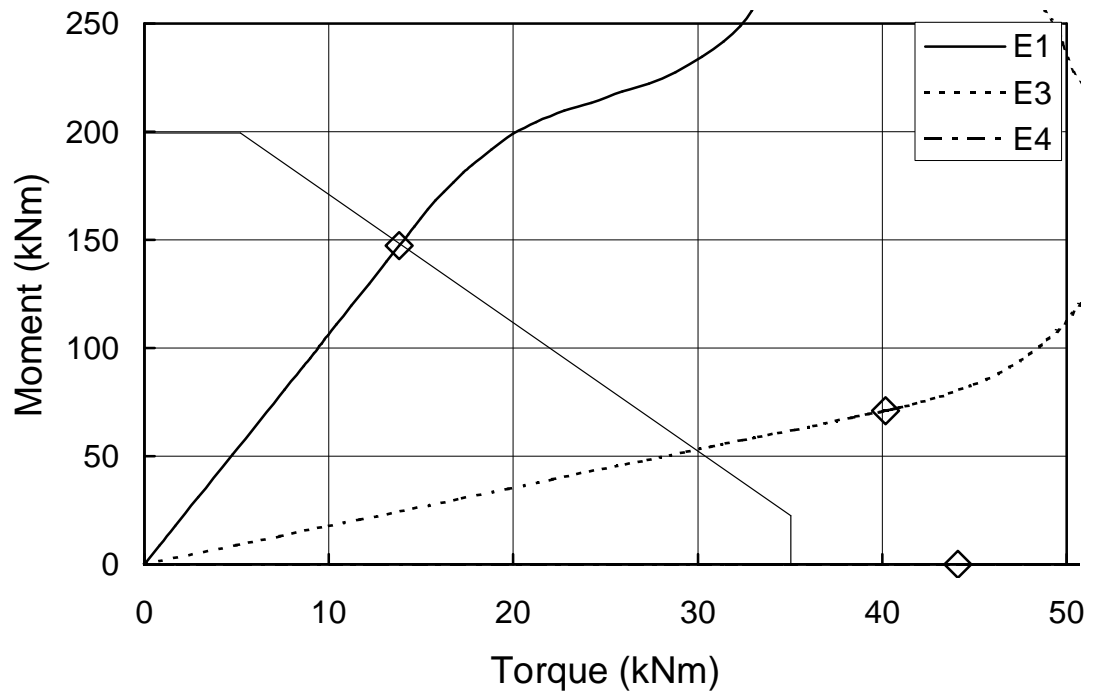


Figure 7.9 Moment vs. Torque Interaction Diagram for Beam S4L4T1B2

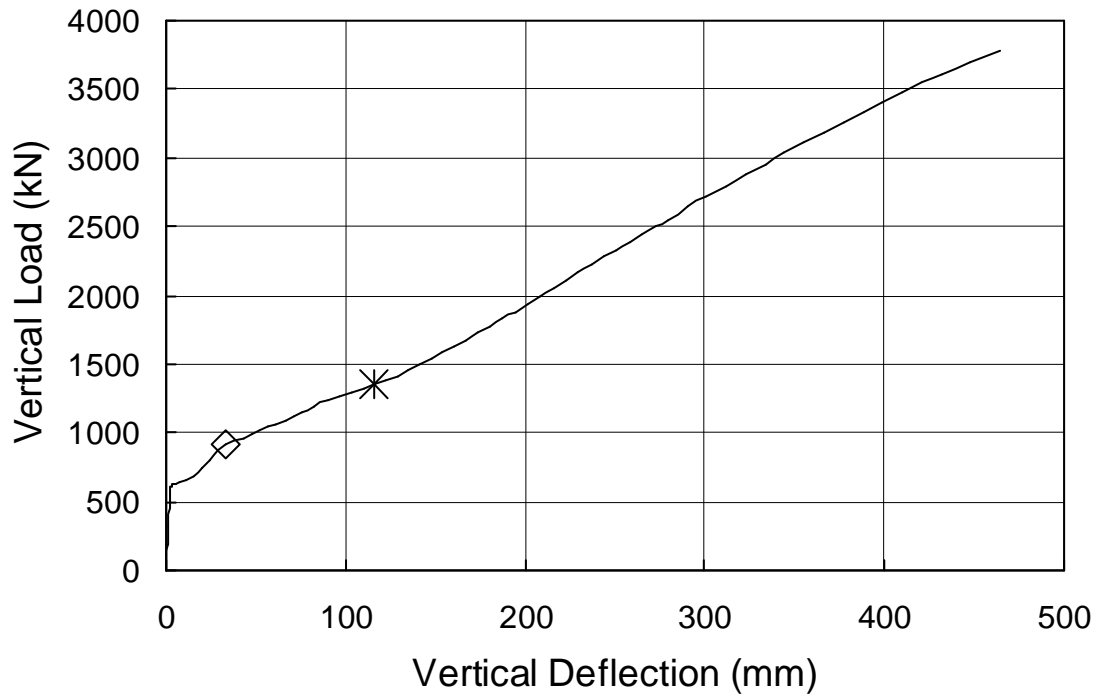


Figure 7.10 Vertical Load vs. Vertical Deflection Diagram for Beam S4L4T1B2E1

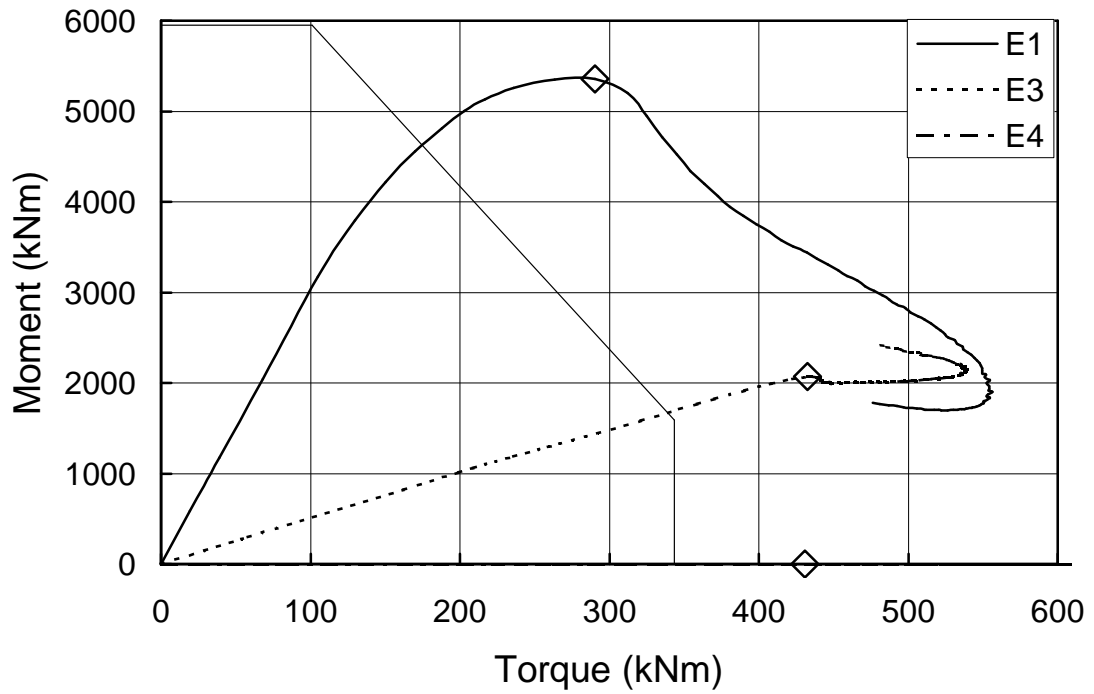


Figure 7.11 Moment vs. Torque Interaction Diagram for Beam S9LT1B3

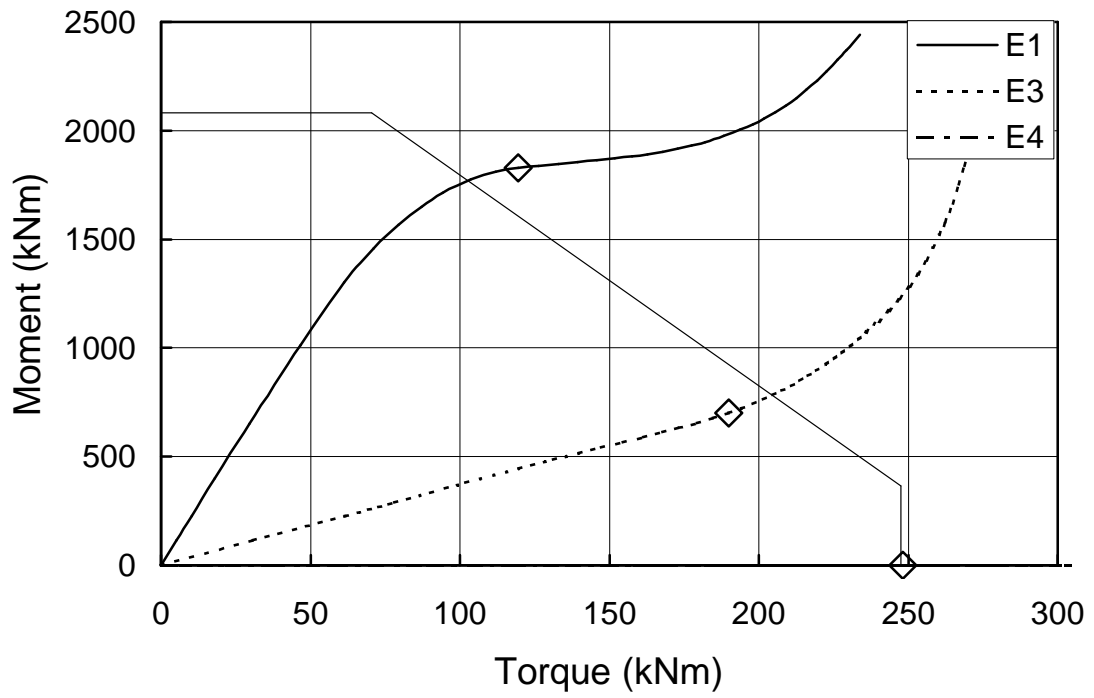


Figure 7.12 Moment vs. Torque Interaction Diagram for Beam S10L2T1B2

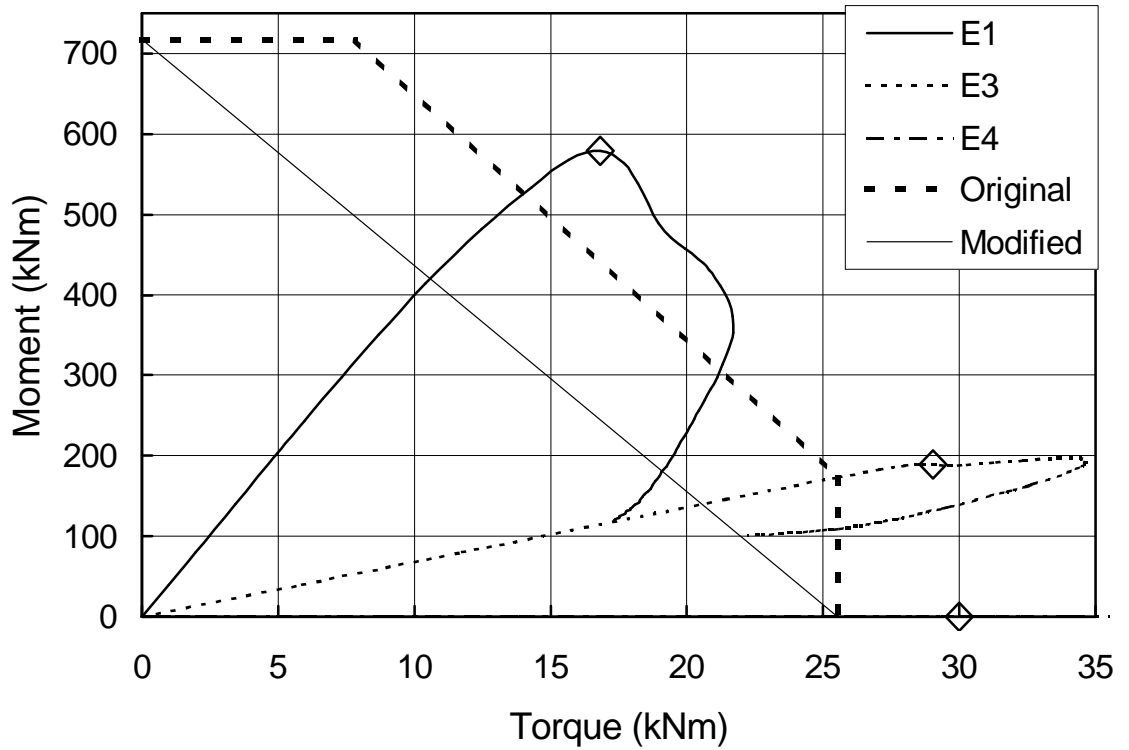


Figure 7.13 Moment vs. Torque Interaction Diagram for Beam S11L1T1B1

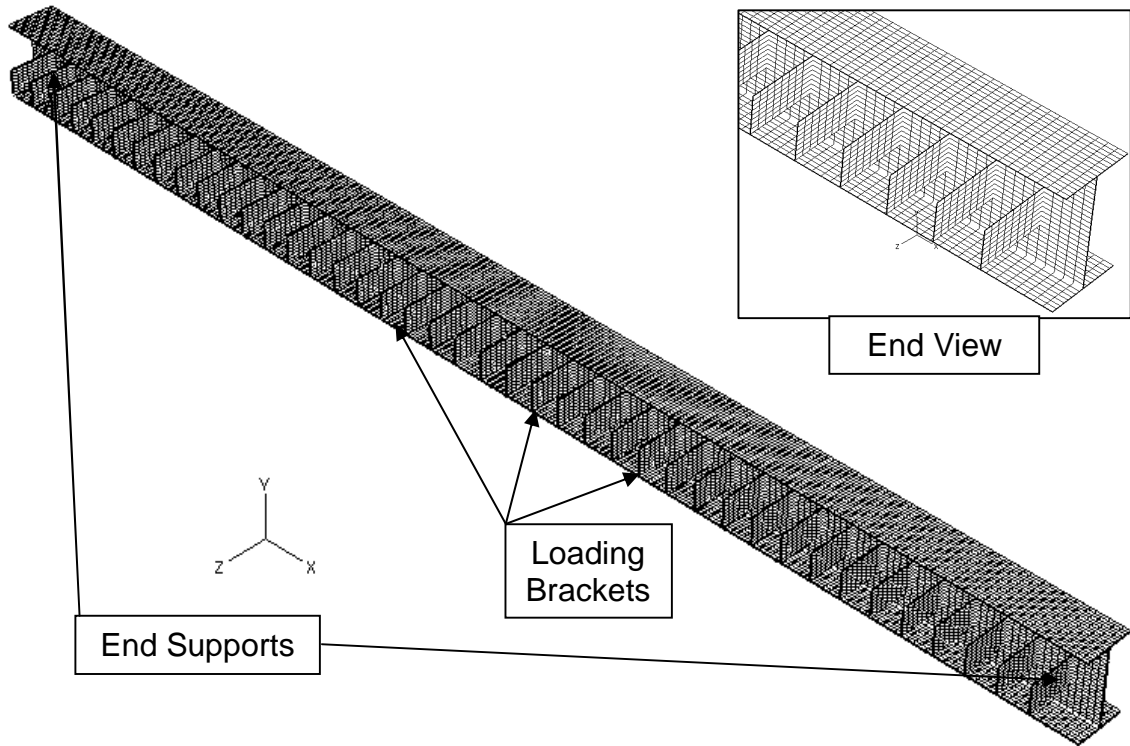


Figure 7.14 Mesh used for Beam S1L2T2B2

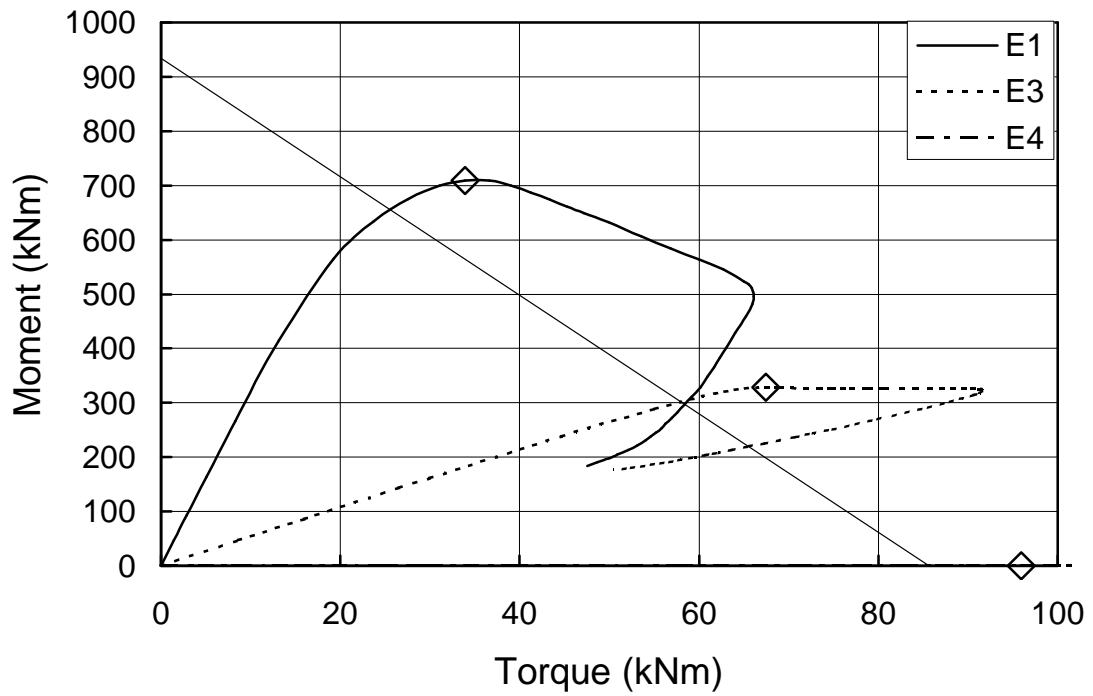


Figure 7.15 Moment vs. Torque Interaction Diagram for Beam S3L1T2B1

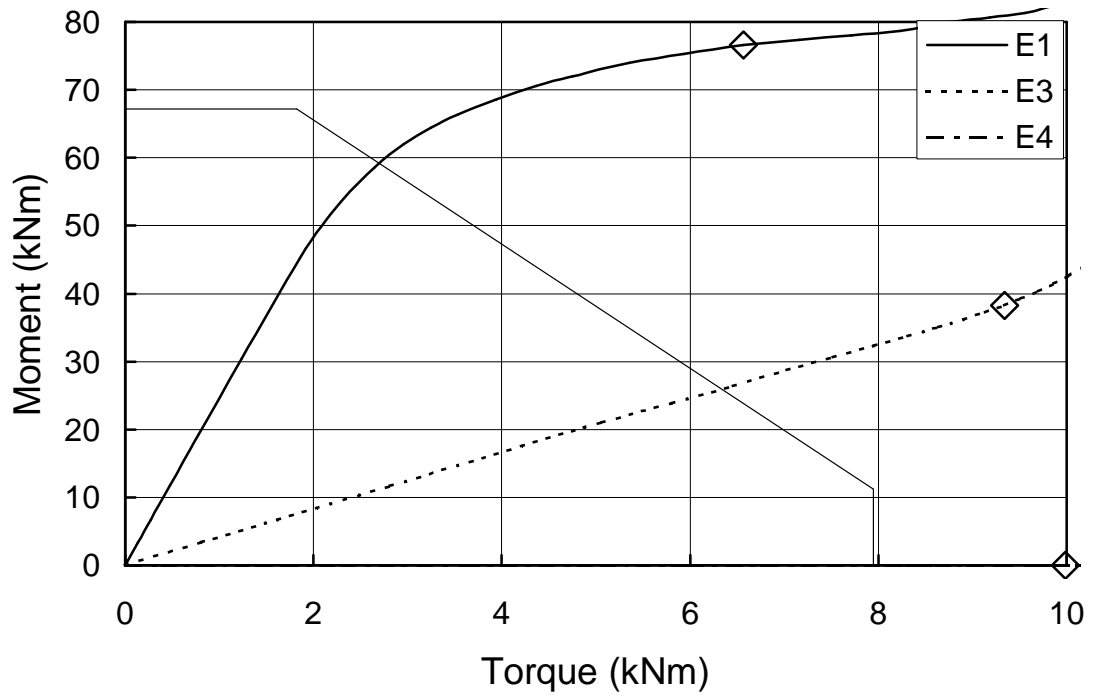


Figure 7.16 Moment vs. Torque Interaction Diagram for Beam S1L2T2B2

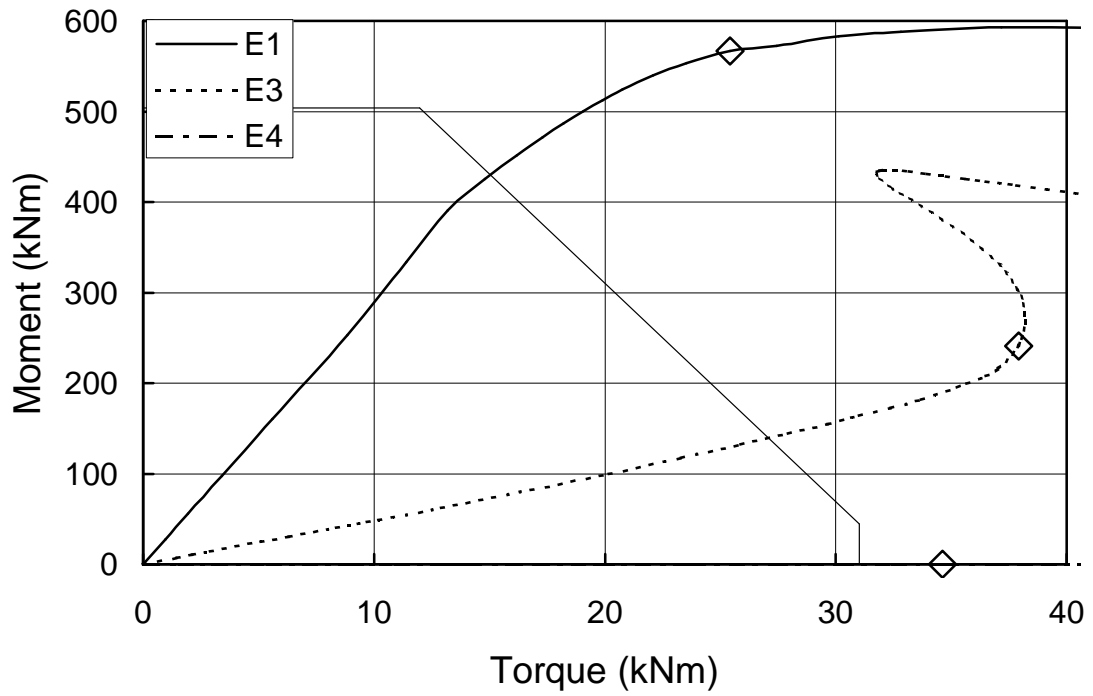


Figure 7.17 Moment vs. Torque Interaction Diagram for Beam S6L1T2B3

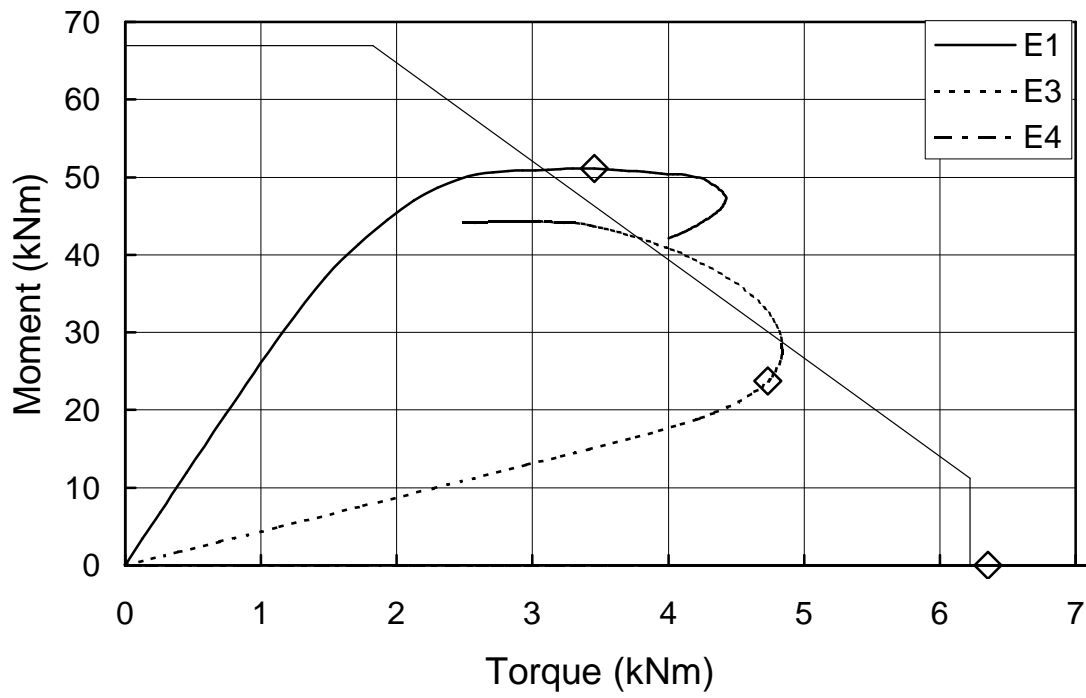


Figure 7.18 Moment vs. Torque Interaction Diagram for Beam S1L2T1B4

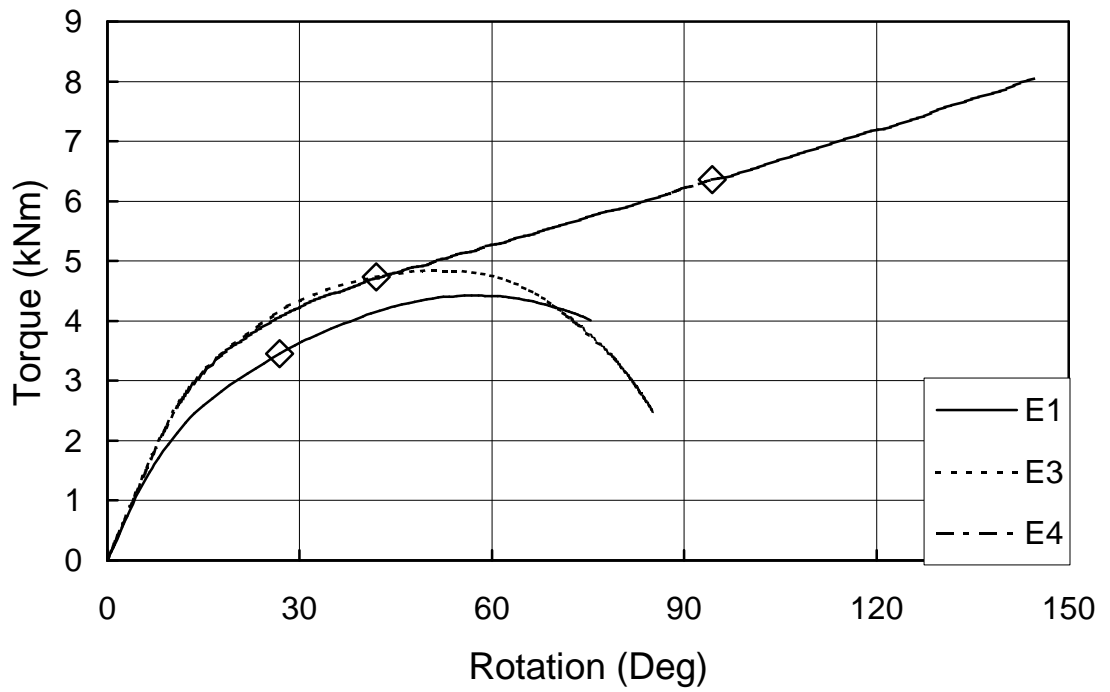


Figure 7.19 Torque vs. Rotation Diagram for Beam S1L2T1B4

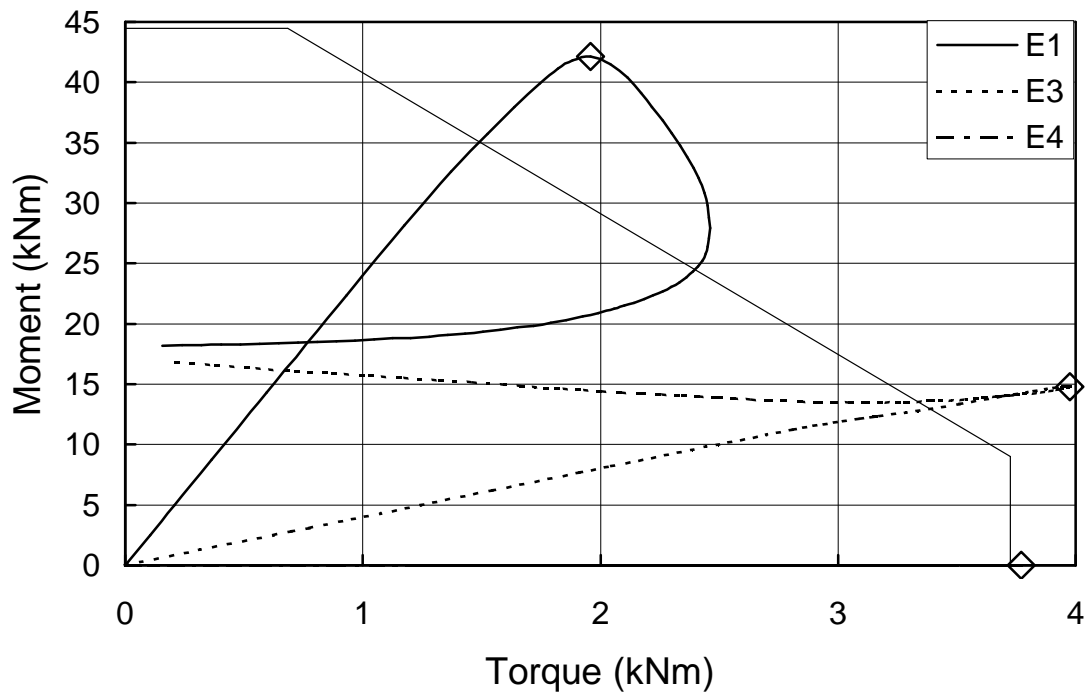


Figure 7.20 Moment vs. Torque Interaction Diagram for Beam S5L1T1B4

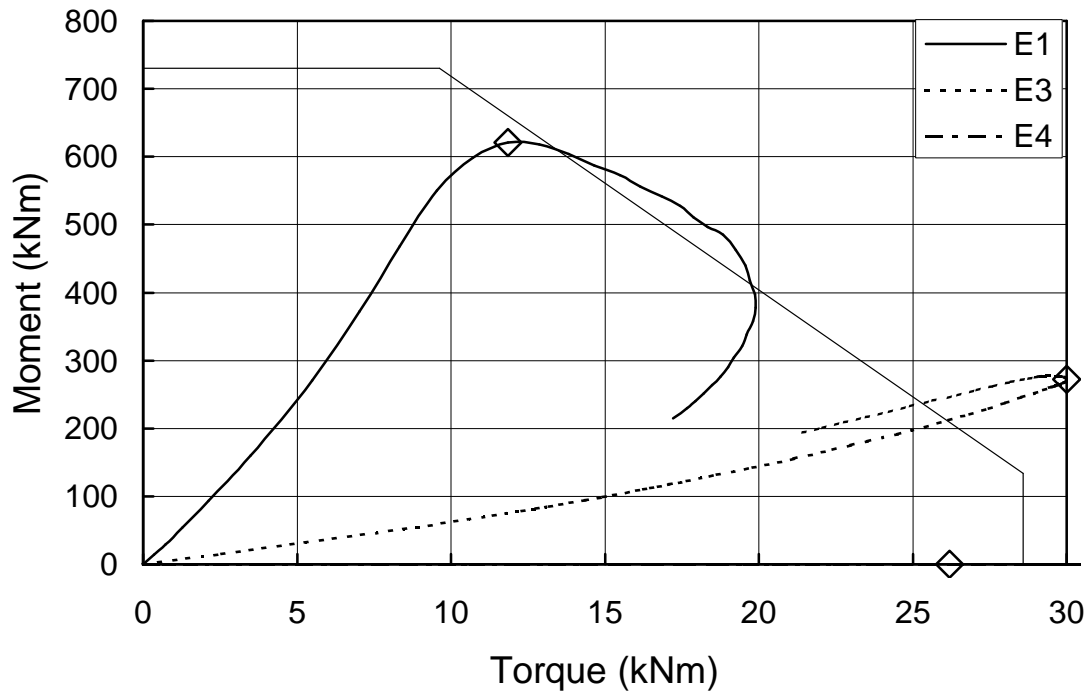


Figure 7.21 Moment vs. Torque Interaction Diagram for Beam SPL1T1B1

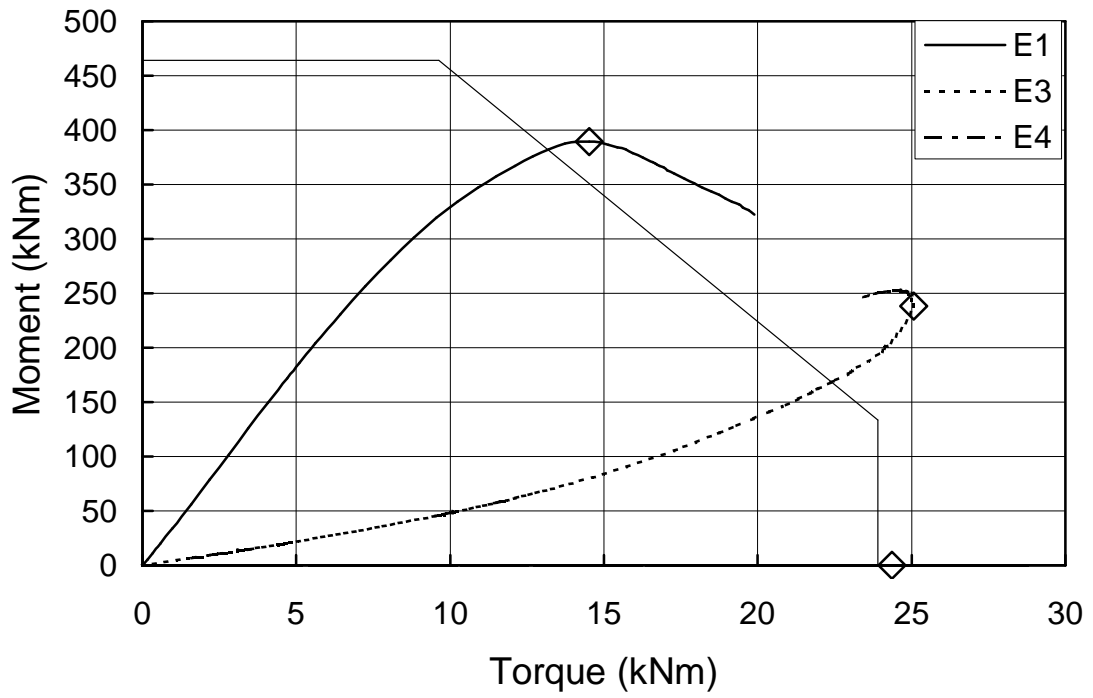


Figure 7.22 Moment vs. Torque Interaction Diagram for Beam SPL2T1B1

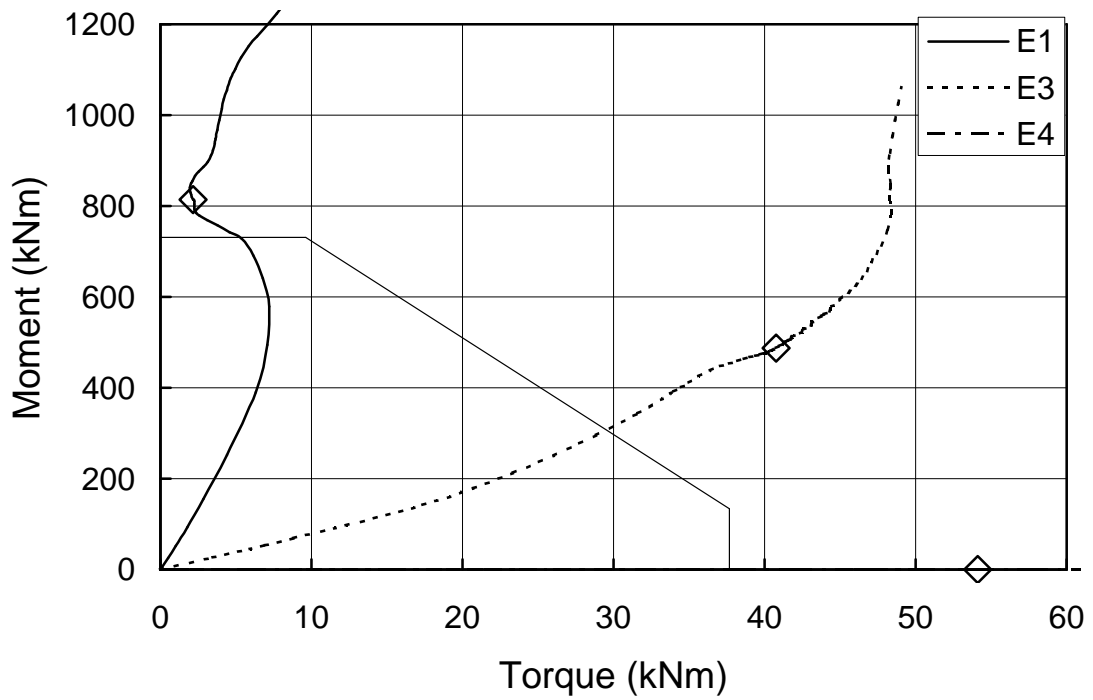


Figure 7.23 Moment vs. Torque Interaction Diagram for Beam SPL1T1B2

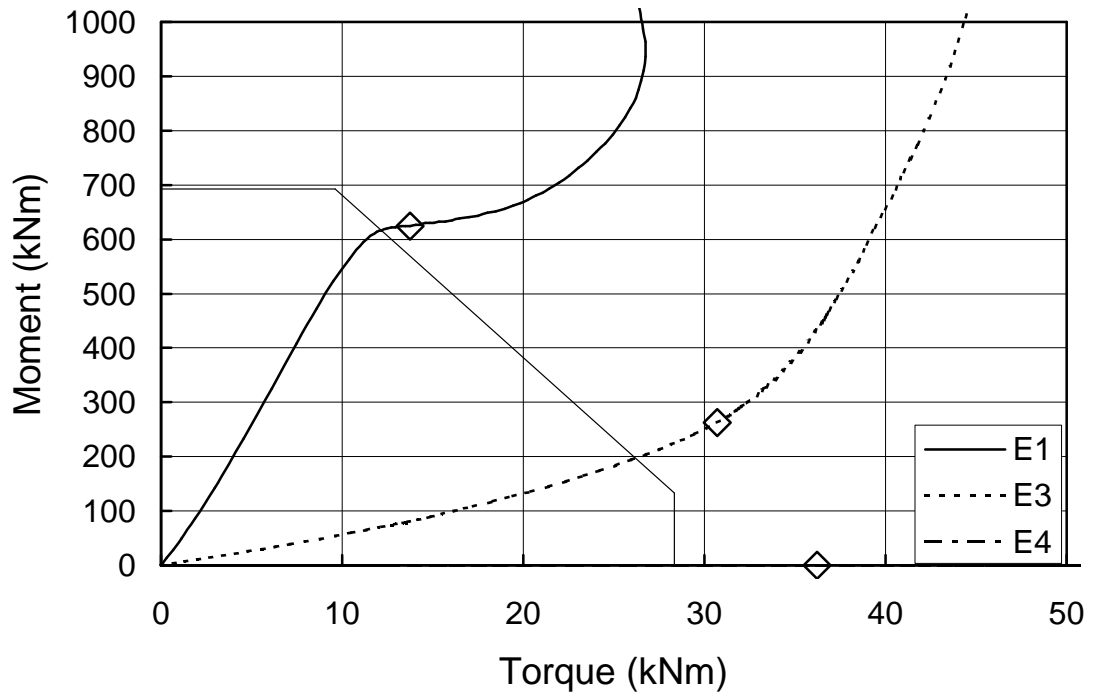


Figure 7.24 Moment vs. Torque Interaction Diagram for Beam SPL2T1B2

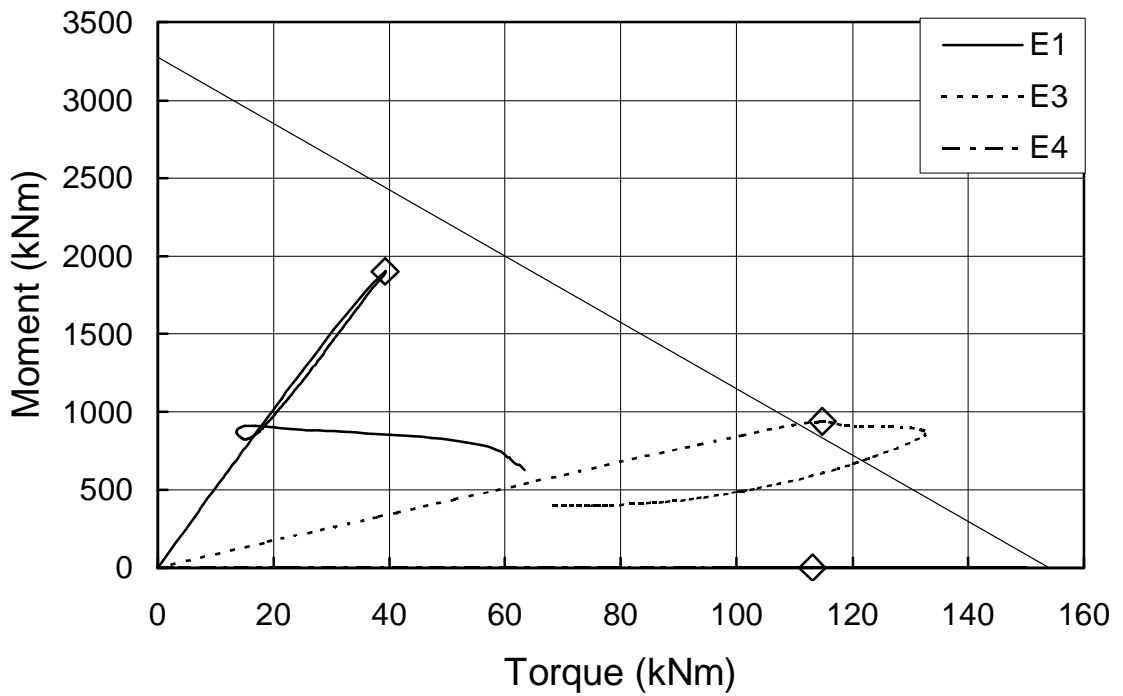


Figure 7.25 Moment vs. Torque Interaction Diagram for Beam S7L1T1B1

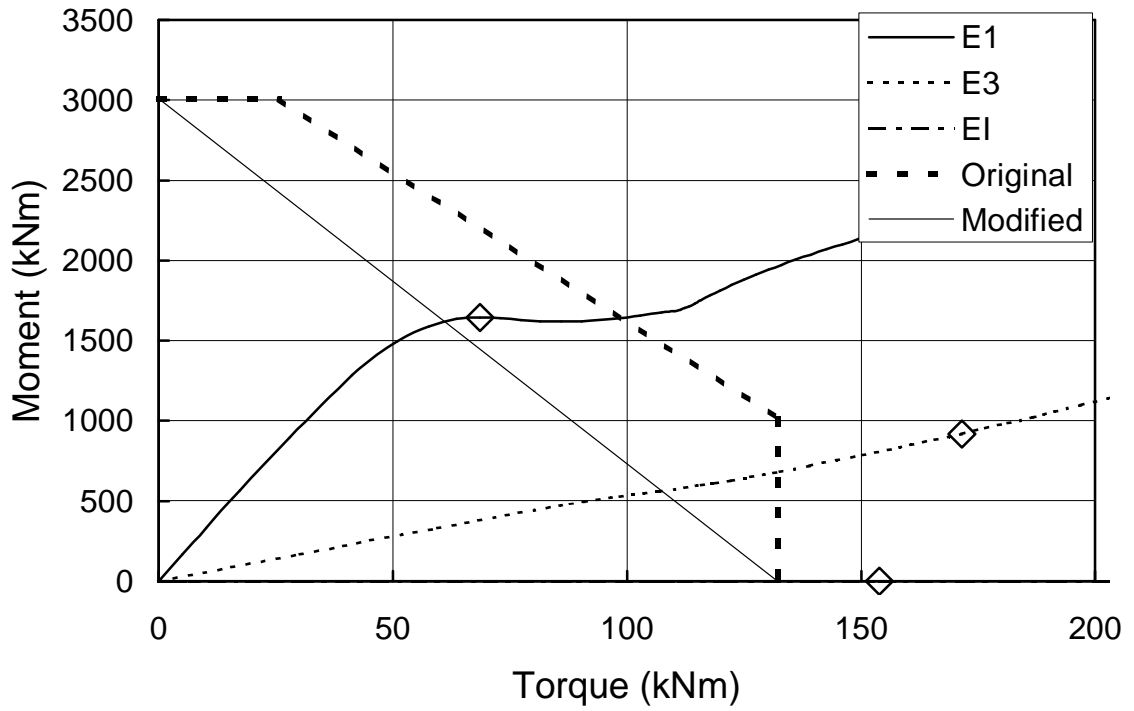


Figure 7.26 Moment vs. Torque Interaction Diagram for Beam S7L3T1B2

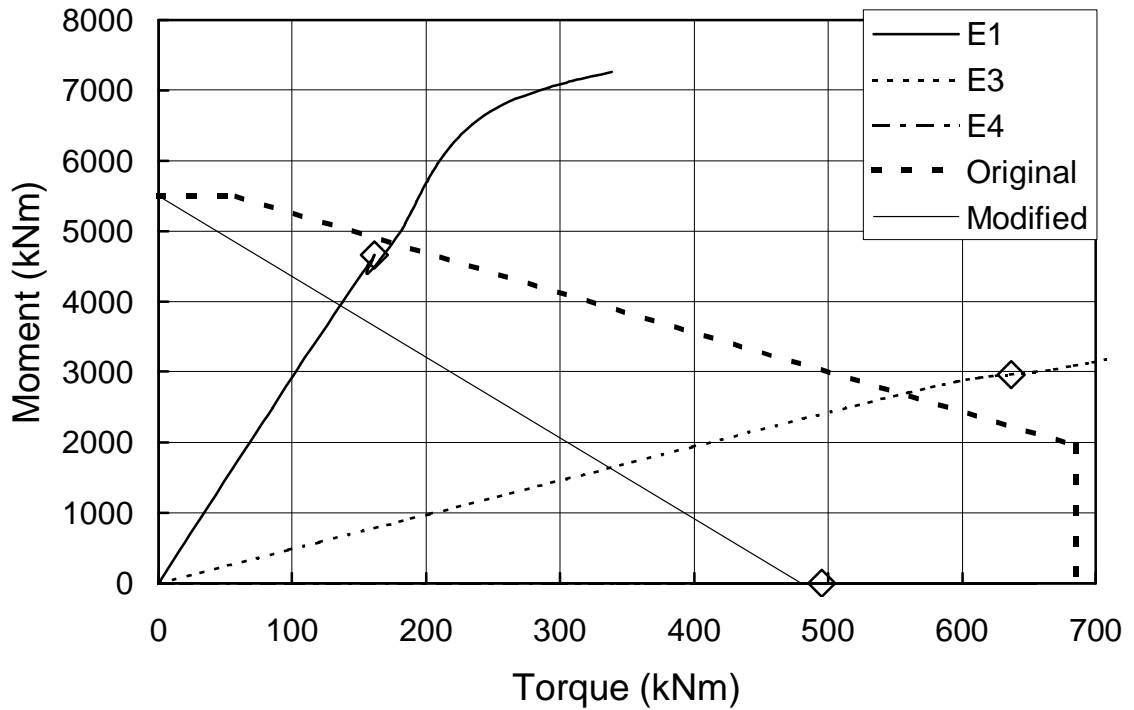


Figure 7.27 Moment vs. Torque Interaction Diagram for Beam S8L1T1B2

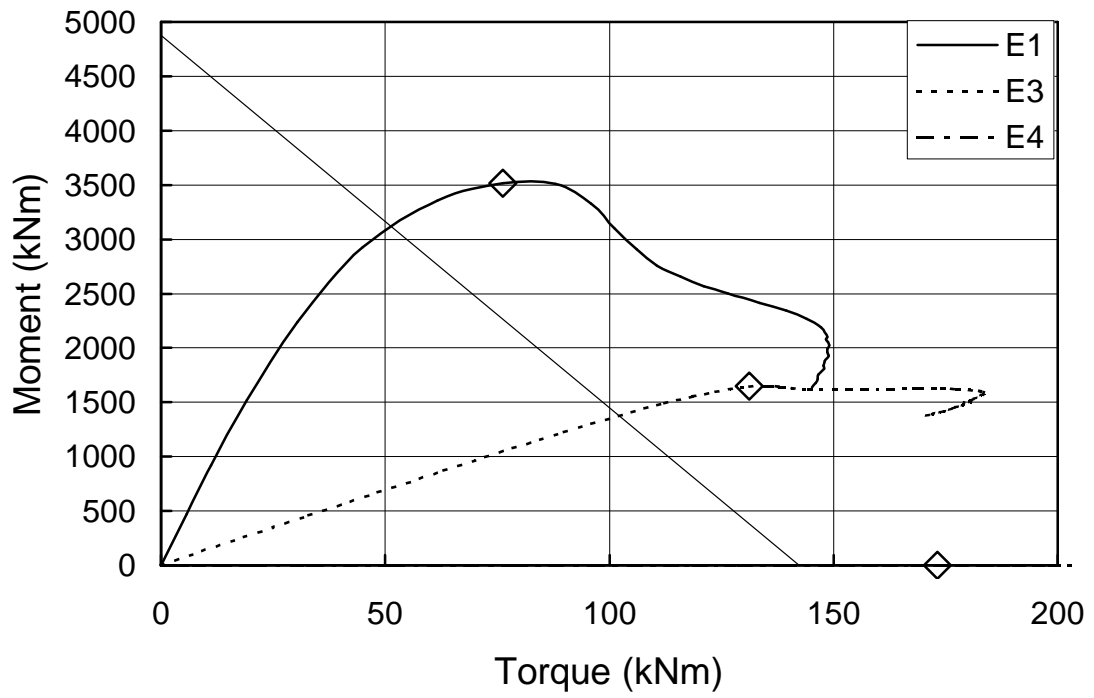


Figure 7.28 Moment vs. Torque Interaction Diagram for Beam S8L3T1B1

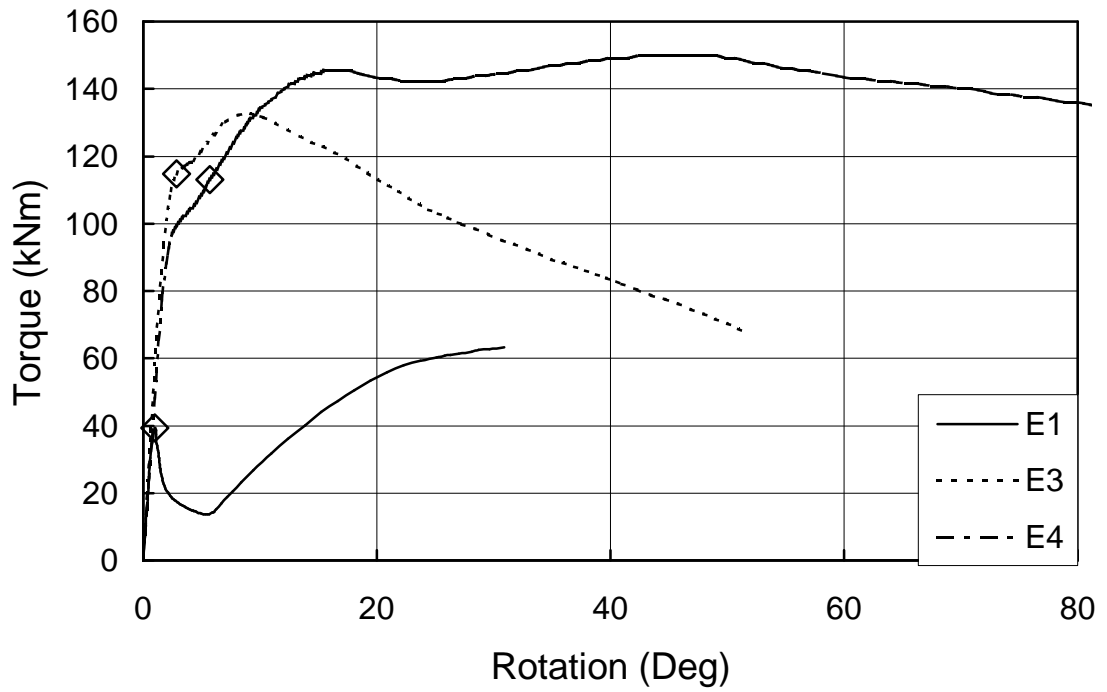


Figure 7.29 Torque vs. Rotation Diagram for Beam S7L1T1B1

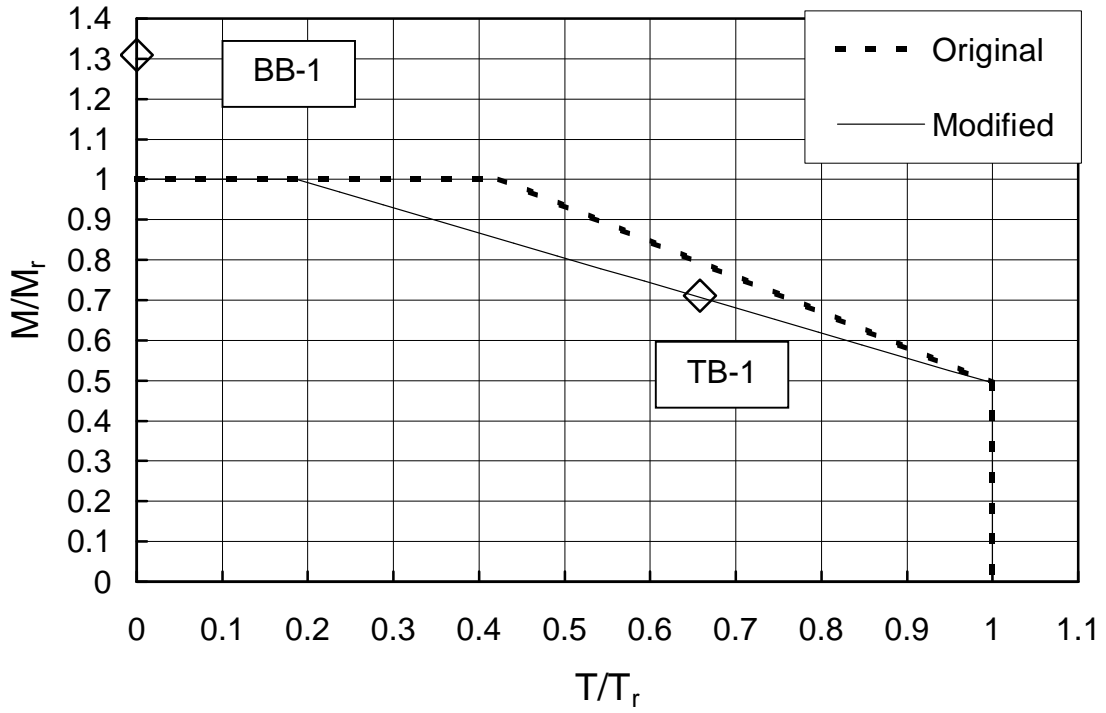


Figure 7.30 Test Results from Razzaq and Galambos (1979b)

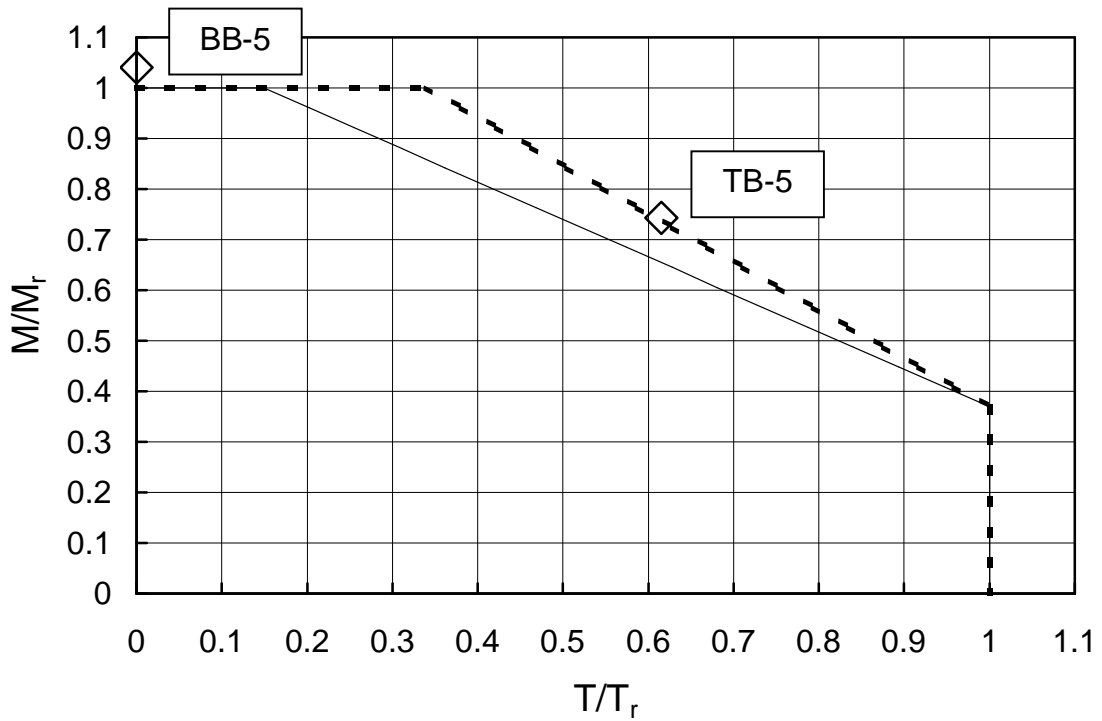
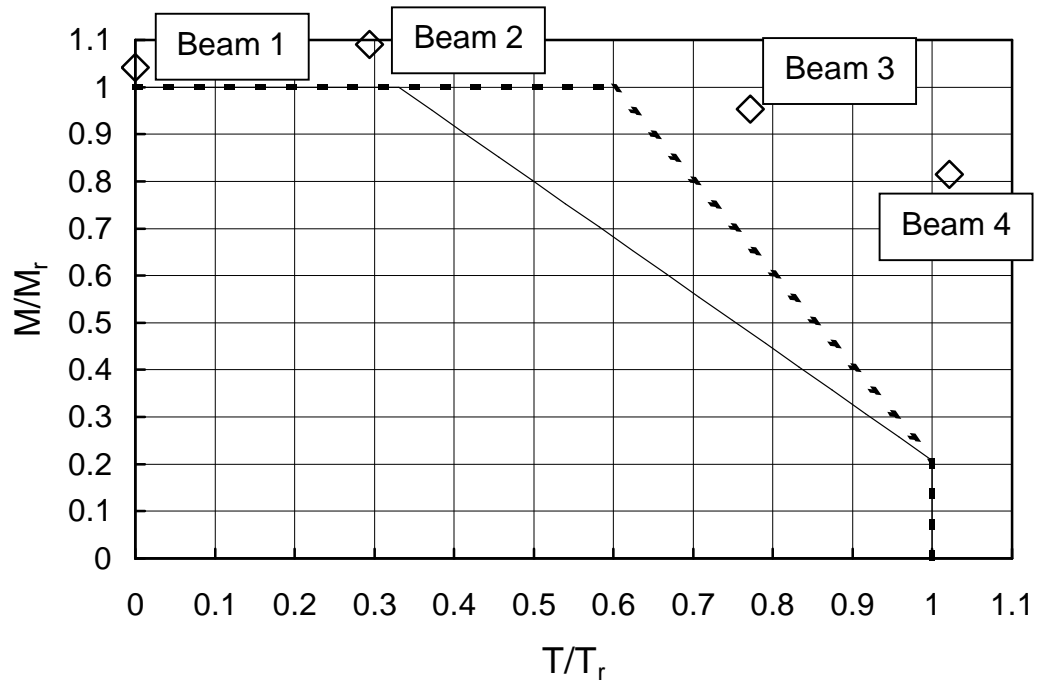


Figure 7.31 Test results from Razzaq and Galambos (1979b)  
 Note: The legend for Figure 7.31 is the same legend used in Figure 7.30.



*Figure 7.32 Driver and Kennedy (1987) Test Results*

Note: The legend for Figure 7.32 is the same legend used in Figure 7.30.

## 8 SUMMARY AND CONCLUSIONS

### 8.1 *Summary of Research Project*

A finite element model was developed to investigate the behaviour and design of beams subject to combined torsion and flexure. The model was validated with test results and is capable of accurately predicting their behaviour. The model was developed to complement the current database of experimental test results with an extensive parametric study. A total of 243 beams of different cross-section, length, load type, boundary conditions, and load eccentricities were added to the database of test results. The ultimate limit state was taken as the formation of the first plastic hinge that coincides with the end of the “initial yield region” typically. Several diagrams, including moment vs. torque, torque vs. rotation, vertical load vs. vertical deflection, and the cross-section stress distributions were used together to determine the ultimate limit state and the end of this “initial yield region”. Using the finite element analysis and experimental results, an appropriate limit states design procedure was developed, verified, and recommended for use for the design of steel beams subject to combined torsion and flexure. The procedure includes serviceability and ultimate limit states. This project focused on the moment–torque interaction diagram to be used for the ultimate limit state verification.

The finite element model was developed with the commercial software ABAQUS and used shell elements formulated using the Mindlin thick plate theory. The model included the effects of flange to web fillets, residual stresses, non-linear geometry, non-linear material properties, and initial imperfections. The Riks arc length analysis method was used that makes use of the Newton-Raphson iterative solution approach. Shell aspect ratios were maintained at values less than 2.0 to avoid artificial element stiffening. This accuracy of the model was verified using the experimental results from two previous researchers: Driver and Kennedy (1987) and

Comeau (1998). The model showed excellent agreement with the test results of Driver and Kennedy (1987) on rolled wide flange sections as well as strong agreement with the experimental work of Comeau (1998) on built-up crane runway girders.

## **8.2 Recommendations and Conclusions**

The following are the most important recommendations and conclusions made as a result of this research program:

1. The tri-linear design interaction curve shown in Figures 2.4 and 6.1, based upon the work of Driver and Kennedy (1987, 1989), is adequate for design at the ultimate limits state provided the following changes be adopted.

For simply supported beams:

- a. The interaction diagram consists of a straight line between Points 1 and 4 of the diagram shown in Figure 2.4.

For beams with other support conditions:

- b. Point 1, remains the same as defined in Figure 2.4. It corresponds to the full moment capacity consistent with the class of section, including the effects of lateral torsional buckling.
- c. The Y-coordinate of Point 2 is the same as that for Point 1. The X-coordinate is taken as the elastic pure (St. Venant) torsional resistance, as obtained using the membrane analogy, for all classes of section.
- d. The Y-coordinate of Point 3 is taken as the moment resistance of the web only neglecting lateral torsional buckling, consistent with the class of the whole section. The

X-coordinate is taken as the full torsional capacity consistent with the class of section calculated as the sum of the pure and warping torsional resistances using Equations 2.35 through 2.40 proposed by Driver and Kennedy (1989).

- e. Point 4 is as shown in Figure 2.4 where the torque capacity is as described above.
2. The two serviceability limit states recommended by Driver and Kennedy (1987, 1989) and also described in CSA S16-01 (CSA, 2001), maximum normal stress limit of the material yield strength as well as rotation and deflection limitations both at the service load level, are valid serviceability limit states and are recommended for this design procedure. An investigation was performed to determine when the SLS and ULS governed. The following conclusions are made:
- a. The serviceability limit states govern over the ultimate limit state in 215 out of the 243 beams, or approximately 90% of the finite element beams analyzed in this project. This is based on an arbitrary torsional rotation limit of 5 degrees and a vertical deflection limit of  $L/360$ . The few remaining beams that are governed by the ULS and not the SLS are primarily pure moment or small loading eccentricity, small slenderness ratio, or fixed ended beams.
  - b. The vertical deflection limit of  $L/360$  is only exceeded in 28.8% of the 243 beams. The majority of these beams are cross-sections with larger slenderness ratios and large eccentricities.
  - c. The arbitrary torsional rotational limit of 5 degrees is exceeded in 56.4% of the 243 beams investigated here.

Similar to the vertical deflection limit, the majority of these beams that exceed the SLS limit of 5 degrees have large slenderness ratios with large eccentricities and are primarily cantilever or simply supported beams.

- d. The maximum normal stress exceeds the yield stress in 79.8% of the 243 beams investigated in this project. For the remaining simply supported and fixed ended beams, the maximum normal stress is typically less than 5% below the yield stress.
3. The design approach proposed here has been verified for rolled wide flange sections using the finite element results obtained in this project as well as previously performed experimental results. Finite element results for two common types of built-up cross-sections, welded steel plate girders and built-up crane runway girders composed of a channel welded to the top flange of a rolled wide flange section, have shown this design approach to be reasonably accurate as well. Further research is recommended for welded steel plate girders and crane runaway girders composed of a channel welded to the top flange of a wide flange section.
  4. The design approach proposed here has been shown explicitly to be accurate for two different load types: uniformly distributed load and single point loading at the critical location for flexure. Based on these results, it is also recommended for typical general loading cases.
  5. The proposed design approach was found to be accurate for several common boundary conditions: simply supported beams in both flexure and torsion, completely fixed at both ends, fixed end cantilevers, and fixed at one end and simply supported at the other.

6. Simply supported beams with small  $t/w$  and large  $b/d$  ratios appear to be able to develop capacities beyond the straight-line interaction diagram proposed here for simply supported beams up to the tri-linear interaction diagram proposed for all other boundary conditions.
7. The finite element results indicate that some beams behave as a higher class of section than determined using the slenderness limits defined for classifying sections for flexure in CSA S16-01 (CSA, 2001). These beams behave as a higher class of section in either flexure or torsion or both. None of the beams modelled in the finite element research were found to behave as a lower class of section, making the method and the results conservative. It is possible that beams need to be classified separately for torsional and flexural capacity calculations. Further research is required to investigate classification of cross-sections for torsion.
8. The combination of normal stresses (due to bending) and shear stresses (due to bending and torsion only loading) cause significant yielding to occur at the mid-height of the web at mid-span at the ultimate limit state for some beams.
9. Large torsional rotations, greater than 30 degrees, developed for many of the beams before the selected ultimate limit state or failure point was reached. This was observed especially in slender cantilevers and beams loaded under large eccentricities (small moment–torque ratios for which the behaviour is predominantly torsional). To assess the impact of these large rotations, capacities were also arbitrarily determined for an ultimate limit state rotation limit of 30 degrees and the proposed design method was still found to give good results. No torsional rotation limit at the ULS is proposed here. For these beams the serviceability limit states,

including torsional rotation and vertical deflection criteria, are likely to govern.

10. Cantilevers with slenderness ratios  $L/r_y$  greater than 50 are not recommended for use for combined torsional and flexural loading as they develop very large rotations under small loads, making them impractical for use in design.

## 9 REFERENCES

- ASTM, 2001. *A6 / A6M Standard Specification for General Requirements for Rolled Structural Steel Bars, Plates, Shapes, and Sheet Piling*, ASTM International, West Conshohocken, PN.
- American Institute of Steel Construction (AISC), 1969. *Specification for the Design, Fabrication and Erection of Structural Steel for Buildings*, American Institute of Steel Construction, New York, NY.
- American Institute of Steel Construction (AISC), 1997. *Steel Design Guide 9 "Torsional Analysis of Structure Steel Members"*, Seaburg, P. A. and Carter, C.J., American Institute of Steel Construction, New York, NY.
- Augusti, G. 1966. Full plastic torque of I-beams. *International Journal of Mechanical Sciences*, **8**: 641-649.
- Bathe, K. J., and Wiener, P. M. 1983. On elastic-plastic analysis of I-beams in bending and torsion. *Computers & Structures*, **17**(5-6): 711-718.
- Bild, S., Chen, G., and Trahair, N. S. 1992. Out-of-plane strengths of steel beams. *Journal of Structural Engineering*, ASCE, **118**(8): 1987-2003.
- Boulton, N. S. 1962. Plastic twisting and bending of an I-beam in which the warp is restricted. *International Journal of Mechanical Sciences*, **4**: 491-502.
- CISC. 2007. *Handbook of Steel Construction – 9<sup>th</sup> Edition*, Canadian Institute of Steel Construction, Toronto, ON.
- Cheng, J. J. R., Kulak, G. L., and Khoo, H. A. 1998. Strength of slotted tubular tension members. *Canadian Journal of Civil Engineering*, **25**(6): 982-991.
- Chu, K., and Johnson, R. B. 1974. Torsion in beams with open sections. *Journal of the Structural Division*, ASCE, **100**(ST7): 1397-1419.
- Comeau, E. 1998. Étude expérimentale du comportement de poutres de roulement unisymétriques pour pont roulants. *Rapport No. EPM/GCS-1998-10*, Département de Génie Civil, École Polytechnique de Montréal, Montreal, QC. (Unpublished)
- CSA, 2001. *Steel structures for buildings – limit states design*, CAN/CSA-S16-01. National Standard of Canada, Canadian Standards Association, Rexdale, ON.
- Dinno, K. S., and Merchant, W. 1965. A procedure for calculating the plastic collapse of I-sections under bending and torsion. *The Structural Engineer*, **43**(7): 219-221.

- Driver, R. G. and Kennedy, D. J. L. 1987. Combined flexure and torsion of I-shaped steel beams. *Structural Engineering Report 144*, Department of Civil Engineering, University of Alberta, Edmonton, AB.
- Driver, R. G., and Kennedy, D.J.L. 1989. Combined flexure and torsion of I-shaped steel beams. *Canadian Journal of Civil Engineering*, **16**(2): 124-139.
- Driver, R. G. 2000. Ultimate strength modeling of wide flange beams subjected to torsion. Proceedings - 2000 Annual Technical Session, Structural Stability Research Council, 24-26 July 2000, Memphis, TN.
- El-Khenfas, M. A., and Nethercot, D. A. 1989. Ultimate strength analysis of steel-beam columns subject to biaxial bending and torsion. *Res Mechanica* **28**: 307-369.
- Essa, H. S. and Kennedy, D. J. L., 2000. Proposed provisions for the design of steel beam-columns in S16-2001, *Canadian Journal of Civil Engineering*, **27**: 610-619.
- Farwell, C. R. and Galambos, T. V., 1969. Non-uniform torsion of steel beams in inelastic range, *Journal of the Structural Division*, ASCE, **95**(ST12): 2813-2829.
- Galambos, T. V. 1968. *Structural Members and Frames*, Prentice-Hall, Inc., Englewood Cliffs, NJ.
- Galambos, T. V. 1998. *Guide to Stability Design Criteria for Metal Structures*. John Wiley & Sons, Inc., Toronto, ON.
- Hancock, G. J. and Trahair, N. S., 1978. Finite element analysis of the lateral buckling of continuously restrained beam-columns, *Transactions of the Institution of Engineers, Australia: Civil Engineering*, **CE20**(2): 120-127.
- Heins, C. P. and Seaburg, P. A., 1963. Torsional Analysis of Rolled Steel Sections, *Bethlehem Steel Company Design Data Handbook 1963-B*, Bethlehem Steel Company, Bethlehem, PA.
- Heins, C. P. 1975. *Bending and torsional design in structural members*. Lexington Books, Lexington, MA.
- Hibbeler, R. C., 2004. *Mechanics of Materials*, Prentice Hall Pearson Education South Asia Pte Ltd., Singapore.
- Hibbitt, Karlsson, and Sorenson, 2002. ABAQUS. Hibbitt, Karlson, & Sorenson, Inc., Pawtucket, RI.
- Hodge, P. G., 1959. *Plastic Analysis of Structures*, McGraw Hill, New York, NY.

- Kanok-Nukulchai, W., and Sivakumar, M. 1988. Degenerate elements for combined flexural and torsional analysis of thin-walled structures. *Journal of Structural Engineering*, ASCE, **114**(3): 657-674.
- Kollbrunner, C. F., Hajdin, N., and Corić 1978. Elastic-plastic thin-walled I-section beam subject to bending and warping torsion. *Institut fur Bauwissenschaftliche Forschung Publikations*, **43**(Dec): 1-51.
- Kollbrunner, C. F., Hajdin, N., and Obradović 1979. Elastic-plastic fixed ended beam of I-section subjected to bending and warping torsion. *Institut fur Bauwissenschaftliche Forschung Publikations*, **46**(May): 1-40.
- Kulak, G. L., and Grondin, G. Y. 2005. *Limit States Design in Structural Steel*, Canadian Institute of Steel Construction, Toronto, ON.
- Johnston, B. G., Lin, F., and Galambos, T. V. 1980. *Basic Steel Design*, Prentice-Hall, Englewood Cliffs, NJ.
- Johnston, B. G. 1982. Design of W-shapes for combined bending and torsion. *Engineering Journal*, AISC, **19**(2): 65-85.
- Langhaar, H. L. 1951. *Dimensional Analysis and Theory of Models*, John Wiley & Sons Inc., New York, NY.
- Lay, M. G., 1982. *Structural Steel Fundamentals: An Engineering and Metallurgical Primer*, Australian Road Research Board, Victoria, Australia.
- Lin, P. H. 1977. Simplified design for torsional loading of rolled steel members. *Engineering Journal*, AISC, **14**(3): 98-107.
- Mohareb, M., and Nowzartash, F. 2003. Exact finite element for nonuniform torsion of open sections. *Journal of Structural Engineering*, ASCE, **129**(2): 215-223.
- Pastor, T. P., and DeWolf, J. T., 1979. Beams with torsional and flexural loads. *Journal of the Structural Division*, ASCE, **105**(ST3): 527-538.
- Pi, Y. L., and Trahair, N. S. 1994a. Inelastic bending and torsion of steel I-beams. *Journal of the Structural Division*, ASCE, **120**(12): 3397-3417.
- Pi, Y. L., and Trahair, N. S. 1994b. Steel member design for combined torsion and bending. *Australian Civil Engineering Transactions*, **CE36**(4): 325-330.
- Razzaq Z., and Galambos, T. V. 1979a. Biaxial bending of beams with or without torsion. *Journal of the Structural Division*, ASCE, **105**(ST11): 2145-2162.
- Razzaq Z., and Galambos, T. V. 1979b. Biaxial bending tests with or without torsion. *Journal of the Structural Division*, ASCE, **105**(ST11): 2163-2185.

- Salmon, C. G., and Johnson, J. E. 1980. *Steel Structures – Design and Behavior*. 2<sup>nd</sup> ed. Harper and Row, Publishers, New York, NY.
- SAA, 1998. *Australian Standard – Steel Structures AS4100-1998*, Standards Association of Australia, 1 The Crescent, Homebush, NSW, Australia.
- Taylor, E. S. 1974. *Dimensional Analysis for Engineers*, Oxford University Press, Ely House, London, UK.
- Timoshenko, S. P. 1983. *History of Strength of Materials*, Dover Publications, Inc., New York, NY.
- Trahair, N. S. 1999. Plastic torsion analysis on monosymmetric and point-symmetric beams. *Journal of Structural Engineering*, ASCE, **125**(2): 175-182.
- Trahair, N. S., and Pi, Y. L. 1997. Torsion, bending and buckling of steel beams. *Engineering Structures*, **19**(5): 372-377.
- Tremblay, R. and LeGault, P. 1997. *Torsional properties of built-up crane runway girders*, Département de génie civil, Ecole Polytechnique de Montréal, Montreal, QB.
- Ugural, A. C. and Fenster, S. K. 1995. *Advanced Strength and Applied Elasticity*. Prentice-Hall Inc., Upper Saddle River, NJ.
- Walker, A. C. 1975. *Design and Analysis of Cold-Formed Sections*. International Textbook Co. Ltd., London.

## **APPENDIX A**

### Description of Calculations

## APPENDIX A – DESCRIPTION OF CALCULATIONS

The nomenclature presented in this appendix is presented with respect to the global reference axes. The global X-axis is taken as the axis parallel to the member and going through the shear centre of the section. The Y-axis is parallel to the web of the wide flange section and also goes through the shear centre of the section. It represents the weak axis of the cross-section. The Z-axis corresponds to the strong axis of the cross-section.

### i. **Eccentricity**

The eccentricity,  $e$ , is the distance from the point where the vertical load is applied to the shear centre of the undeformed beam, measured along the Z-axis. A positive eccentricity is measured in the positive Z-direction.

### ii. **Bending Moment**

The bending moment presented here is the maximum value of bending moment on the beam about the Z-axis. The maximum moment is a function of the applied load and the span length of the beam. Table A.1 presents the maximum moment, and its location in brackets, for each boundary and loading condition investigated in this research. The length of the beam,  $L$ , used in the calculation of the bending moments is assumed to remain constant for all boundary conditions except for cantilevers where the moment arm is calculated based on the beam deflection.

### iii. **Torque**

The torque presented here is the maximum value of torque on the beam. The maximum torque is a function of the applied load and its eccentricity. Table A.2 presents the maximum torque, and its

location in brackets, for each boundary and loading condition. The eccentricity is calculated as described above.

#### iv. Torsional Rotation

The rotation presented here is the maximum rotation angle of the cross-section about the X-axis. The location of maximum rotation is at the shear centre of the beam at the section at the mid-span of the beam (in the X-direction). This rotation is measured relative to the undeformed shape. A positive rotation is measured by a positive rotation about the X-axis.

To calculate this rotation, the two web nodes directly above and below the shear centre are used. The translations of these two points in the Y- and Z-directions are used to calculate the updated coordinates of these nodes. The updated Y- and Z-coordinates are then used to determine the rotation of the cross-section at this location using the following equation:

$$\phi = \arctan\left(\frac{z_a - z_b}{y_a - y_b}\right) \quad [A.1]$$

where  $y_a$  and  $z_a$  are the updated Y- and Z-coordinates of the node above the shear centre and  $y_b$  and  $z_b$  are the updated Y- and Z-coordinates of the node below the shear centre. This formula has to be corrected when rotations are greater than 90 degrees. For angles between 90 and 180 degrees, the actual rotation is found by adding the (negative) rotation found from Equation [A.1] to 180 degrees. For angles between 180 and 270 degrees, the actual rotation is found by adding 180 degrees to the rotation calculated above. For angles between 270 and 360 degrees, the actual rotation is found by adding the (negative) rotation found from Equation [A.1] to 360 degrees.

**v. Strong Axis Bending Moment**

The strong axis bending moment presented here is the maximum strong axis moment determined by multiplying the moment about the Z-axis by the cosine of the torsional rotation.

**vi. Weak Axis Moment**

The weak axis moment presented here is the maximum weak axis moment determined by multiplying the moment about the Z-axis by the sine of the torsional rotation.

**vii. Vertical Deflection**

The vertical deflection (parallel to the Y-axis) presented here is the maximum vertical deflection. It is measured at the same location as the maximum rotation, namely, at the shear centre. This deflection is measured relative to the undeformed shape. A positive deflection is measured in the negative Y-direction.

**viii. Lateral Deflection**

The lateral deflection (parallel to the Z-axis) presented here is the maximum lateral deflection. It is measured at the same location as the maximum vertical deflection and rotation. This deflection is measured relative to the undeformed shape. A positive deflection is measured in the positive Z-direction.

Table A.1 Maximum Bending Moment for the Boundary and Loading Conditions.

Loading Condition	Boundary Condition			
	B1	B2	B3	B4
T1	$\frac{PL}{4}$ (mid-span)	$\frac{PL}{8}$ (mid-span or fixed ends)	$\frac{PL}{2}$ (fixed end)	$\frac{3PL}{16}$ (fixed end)
T2	$\frac{wL^2}{8}$ (mid-span)	$\frac{wL^2}{12}$ (fixed ends)	$\frac{wL^2}{2}$ (fixed end)	$\frac{wL^2}{8}$ (fixed end)

Table A.2 Maximum Torque for the Boundary and Loading Conditions

Loading Condition	Boundary Condition			
	B1	B2	B3	B4
T1	$\frac{Pe}{2}$ (uniform over each half of beam)	$\frac{Pe}{2}$ (uniform over each half of beam)	$\frac{Pe}{2}$ (uniform over beam length)	$\frac{Pe}{2}$ (uniform over each half of beam)
T2	$\frac{weL}{2}$ (support locations)	$\frac{weL}{2}$ (fixed ends)	$\frac{weL}{2}$ (fixed end)	$\frac{weL}{2}$ (support locations)

NOTE: T1 – Point load at mid-span

T2 – Uniformly distributed load

B1 – Simply supported at both ends

B2 – Completely fixed at both ends

B3 – Cantilever

B4 – Completely fixed at one end and simply supported at the other

## **APPENDIX B**

### Results of the Parametric Study

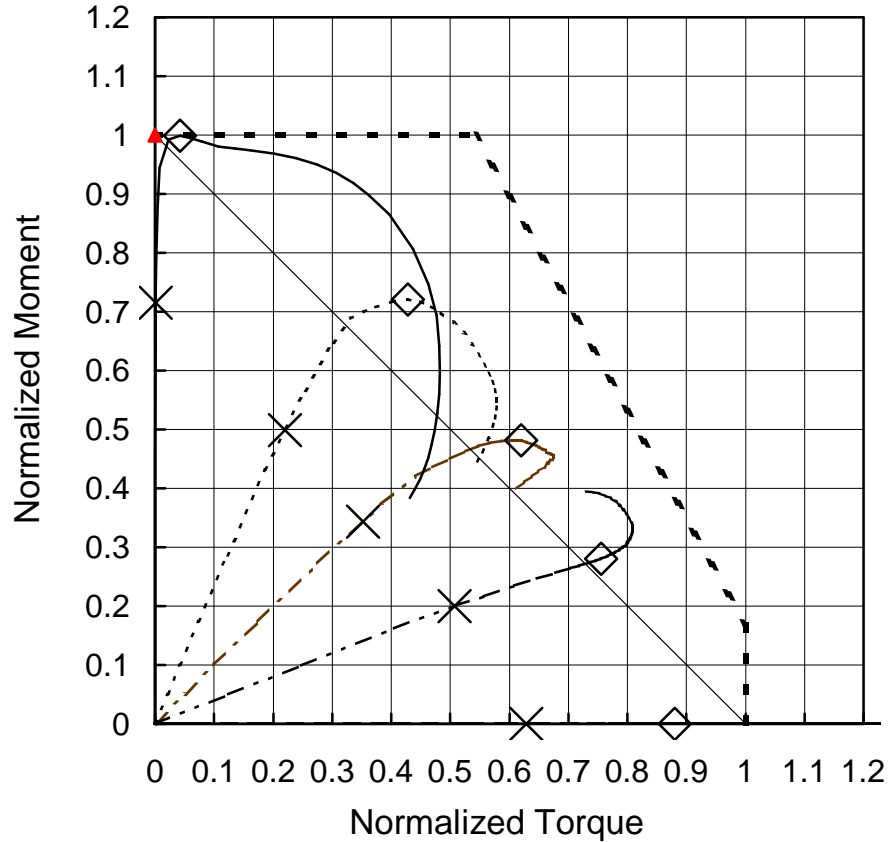
## APPENDIX B – RESULTS OF THE PARAMETRIC STUDY

This appendix contains a complete presentation of the data describing the ultimate and service points (including moment, normalized moment, torque, normalized torque, deflection, rotation, maximum cross-sectional strain and stress, and the Finite Element to Predicted Ratio (FEPR) values for both the original and modified interaction diagrams) as well as the resulting ultimate moment–torque interaction diagrams. The moment and torque values are normalized by dividing the moment and torque values by their respective resistances. This appendix includes the results of all of the beams analyzed as part of the parametric study.

### Legend:

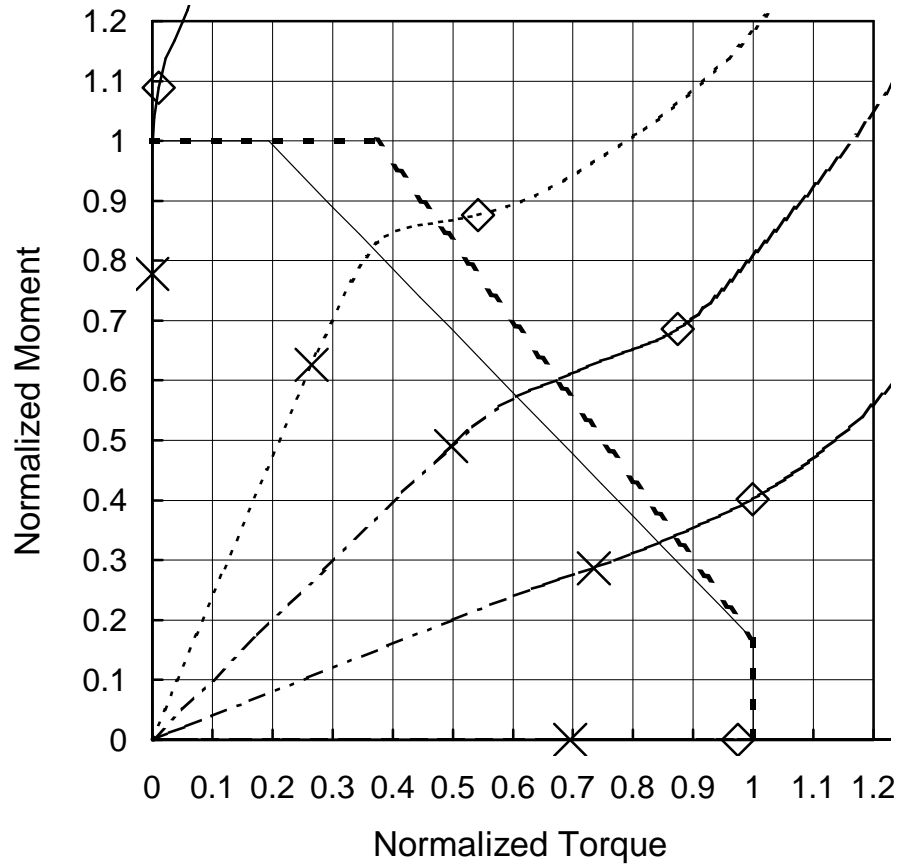
- E0 Beam (Pure moment case)
- E1 Beam (Minimum eccentricity case)
- E2 Beam (Medium eccentricity case)
- E3 Beam (Maximum eccentricity case)
- E4 Beam (Torsion only loading case)
- Modified Interaction Equation
- - - - Original Interaction Equation

## Interaction Diagrams - Beam S1L1T1B1



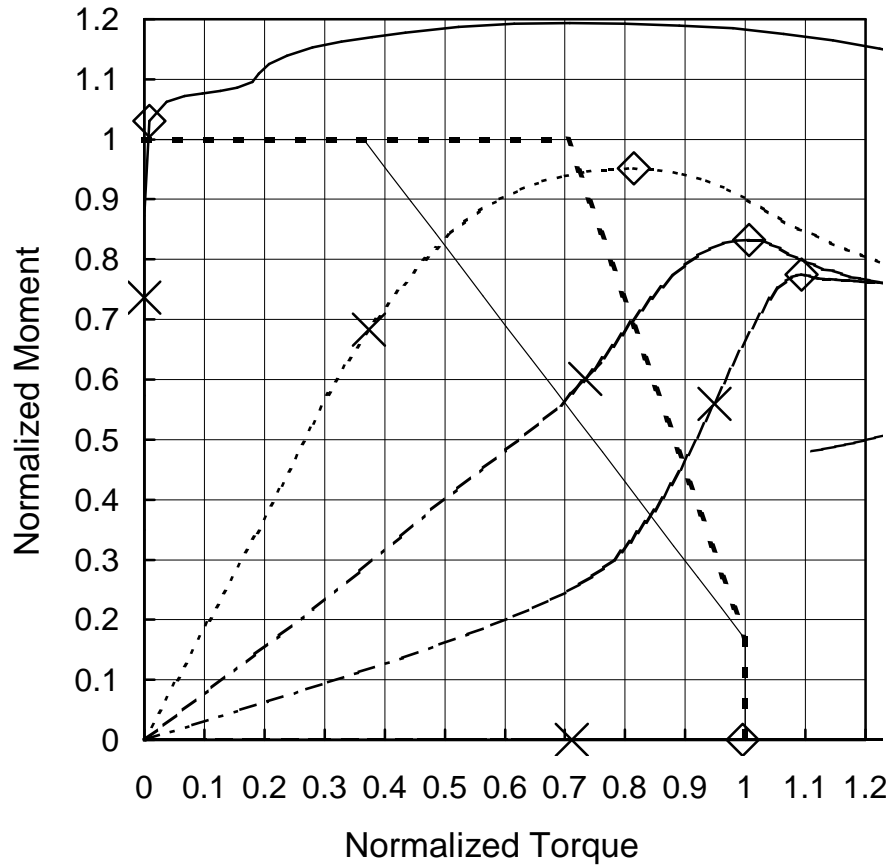
		E0	E1	E2	E3	E4
Service Load Point	Moment (kNm)	48.0	33.5	23.1	13.5	0.0
	Normalized Moment	0.72	0.50	0.34	0.20	0.00
	Torque (kNm)	0.01	1.43	2.28	3.29	4.07
	Normalized Torque	0.00	0.22	0.35	0.51	0.63
	Rotation (Deg)	0.3	2.6	4.0	6.7	10.8
	Maximum Deflection (mm)	3.23	2.32	1.80	1.62	0.47
	L / Deflection	379	528	678	754	2600
	Maximum Strain	0.0025	0.0040	0.0051	0.0008	0.0193
	Maximum Stress (MPa)	366	363	352	305	358
Ultimate Load Point	Moment (kNm)	67.1	48.5	32.3	18.9	0.0
	Normalized Moment	1.00	0.72	0.48	0.28	0.00
	Torque (kNm)	0.27	2.78	4.02	4.90	5.70
	Normalized Torque	0.04	0.43	0.62	0.76	0.88
	Rotation (Deg)	1.4	10.2	18.1	25.0	29.7
	Maximum Strain	0.0118	0.0366	0.0513	0.0118	0.0398
	Maximum Stress (MPa)	385	453	458	384	453
	FEPR Original	1.00	0.92	0.91	0.87	0.88
	FEPR Modified	1.00	1.15	1.10	1.04	0.88

### Interaction Diagrams - Beam S1L1T1B2



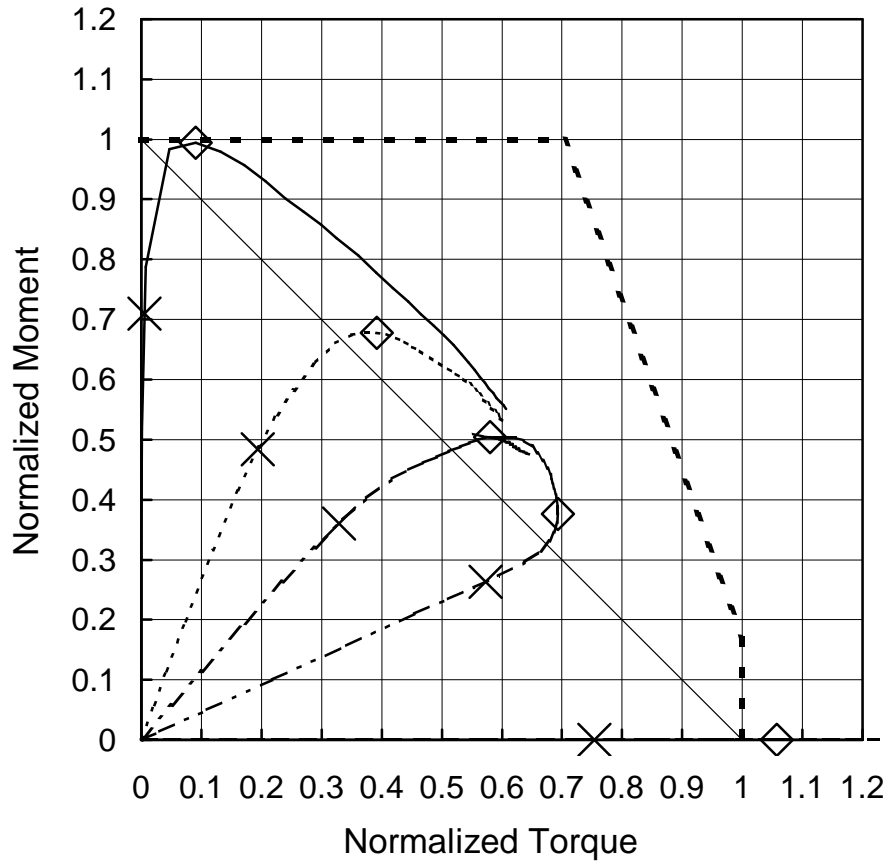
		E0	E1	E2	E3	E4
Service Load Point	Moment (kNm)	52.3	42.1	32.9	19.3	0.0
	Normalized Moment	0.78	0.63	0.49	0.29	0.00
	Torque (kNm)	0.00	2.50	4.69	6.92	6.56
	Normalized Torque	0.00	0.26	0.50	0.73	0.70
	Rotation (Deg)	0.1	1.5	3.1	8.4	6.1
	Maximum Deflection (mm)	2.65	1.99	1.82	1.89	0.08
	$L / \text{Deflection}$	462	616	671	646	15700
	Maximum Strain	0.0013	0.0020	0.0135	0.0029	0.0025
	Maximum Stress (MPa)	340	350	387	360	350
Ultimate Load Point	Moment (kNm)	73.1	58.9	46.1	27.0	0.0
	Normalized Moment	1.09	0.88	0.69	0.40	0.00
	Torque (kNm)	0.10	5.11	8.24	9.42	9.18
	Normalized Torque	0.01	0.54	0.87	1.00	0.97
	Rotation (Deg)	0.7	14.6	25.0	25.5	21.1
	Maximum Strain	0.0022	0.0102	0.1465	0.0087	0.0029
	Maximum Stress (MPa)	384	388	478	398	375
	FEPR Original	1.09	1.07	1.24	1.16	0.97
	FEPR Modified	1.09	1.20	1.32	1.20	0.97

### Interaction Diagrams - Beam S1L1T1B3



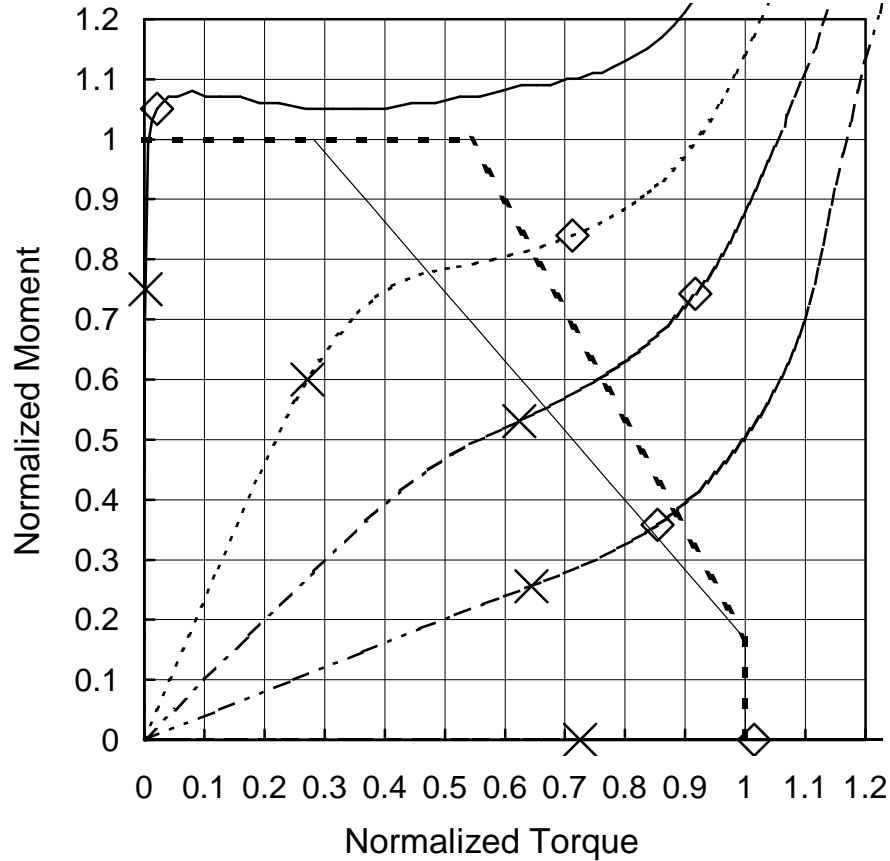
		E0	E1	E2	E3	E4
Service Load Point	Moment (kNm)	49.5	45.9	40.4	37.6	0.0
	Normalized Moment	0.74	0.68	0.60	0.56	0.00
	Torque (kNm)	0.00	1.87	3.66	4.74	3.55
	Normalized Torque	0.00	0.37	0.73	0.95	0.71
	Rotation (Deg)	0.2	13.7	37.2	66.9	32.8
	Maximum Deflection (mm)	9.84	11.43	20.83	35.73	0.42
	$L / \text{Deflection}$	124	107	59	34	2910
	Maximum Strain	0.0011	0.0040	0.0118	0.0168	0.0057
	Maximum Stress (MPa)	242	245	249	266	238
Ultimate Load Point	Moment (kNm)	69.3	63.9	56.0	52.0	0.0
	Normalized Moment	1.03	0.95	0.83	0.77	0.00
	Torque (kNm)	0.05	4.07	5.03	5.46	4.97
	Normalized Torque	0.01	0.81	1.01	1.09	1.00
	Rotation (Deg)	0.5	41.1	64.5	79.3	90.0
	Maximum Strain	0.0034	0.0207	0.0239	0.0243	0.0135
	Maximum Stress (MPa)	245	298	299	298	274
	FEPR Original	1.03	1.09	1.23	1.29	1.00
FEPR Modified	1.03	1.37	1.46	1.49	1.00	

### Interaction Diagrams - Beam S1L2T1B1



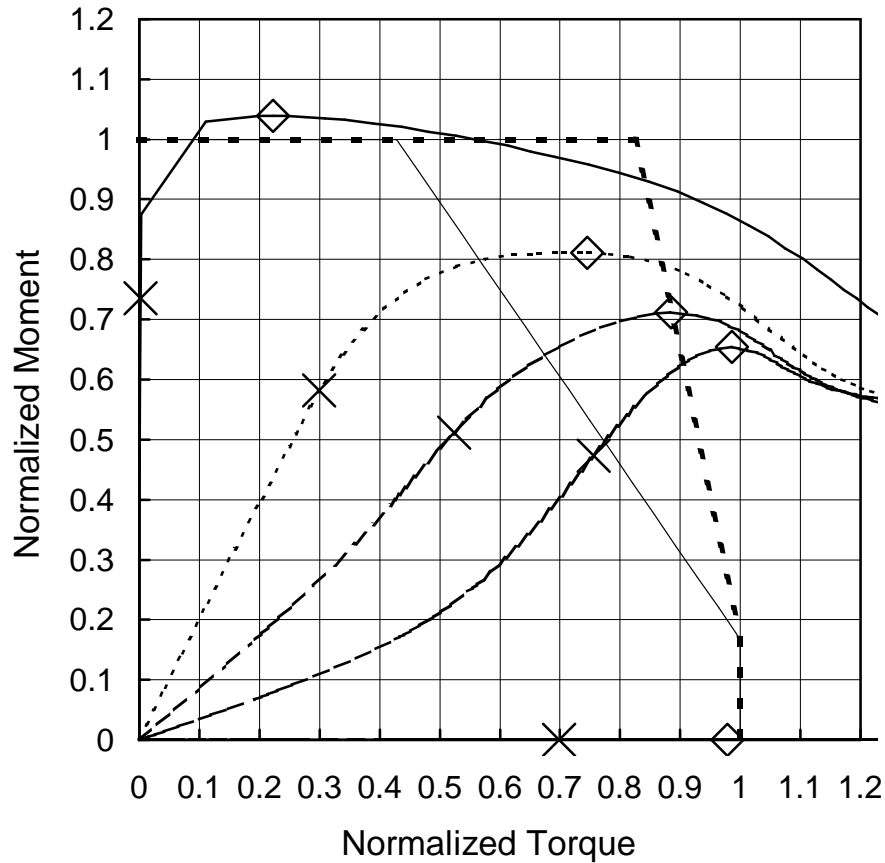
		E0	E1	E2	E3	E4
Service Load Point	Moment (kNm)	41.9	28.6	21.3	15.5	0.0
	Normalized Moment	0.71	0.48	0.36	0.26	0.00
	Torque (kNm)	0.03	0.97	1.64	2.86	3.76
	Normalized Torque	0.01	0.19	0.33	0.57	0.75
	Rotation (Deg)	1.0	6.5	10.7	23.8	35.1
	Maximum Deflection (mm)	8.31	6.58	6.22	14.62	2.12
	$L / \text{Deflection}$	294	372	393	167	1160
	Maximum Strain	0.0017	0.0031	0.0045	0.0276	0.0236
	Maximum Stress (MPa)	361	350	350	414	380
Ultimate Load Point	Moment (kNm)	58.0	40.0	29.8	22.2	0.0
	Normalized Moment	0.99	0.68	0.50	0.38	0.00
	Torque (kNm)	0.45	1.96	2.90	3.46	5.28
	Normalized Torque	0.09	0.39	0.58	0.69	1.06
	Rotation (Deg)	1.6	17.2	33.3	51.1	89.3
	Maximum Strain	0.0062	0.0233	0.0370	0.0495	0.0395
	Maximum Stress (MPa)	383	394	452	460	454
	FEPR Original	0.99	0.80	0.85	0.86	1.06
	FEPR Modified	0.99	1.07	1.09	1.07	1.06

Interaction Diagrams - Beam S1L2T1B2



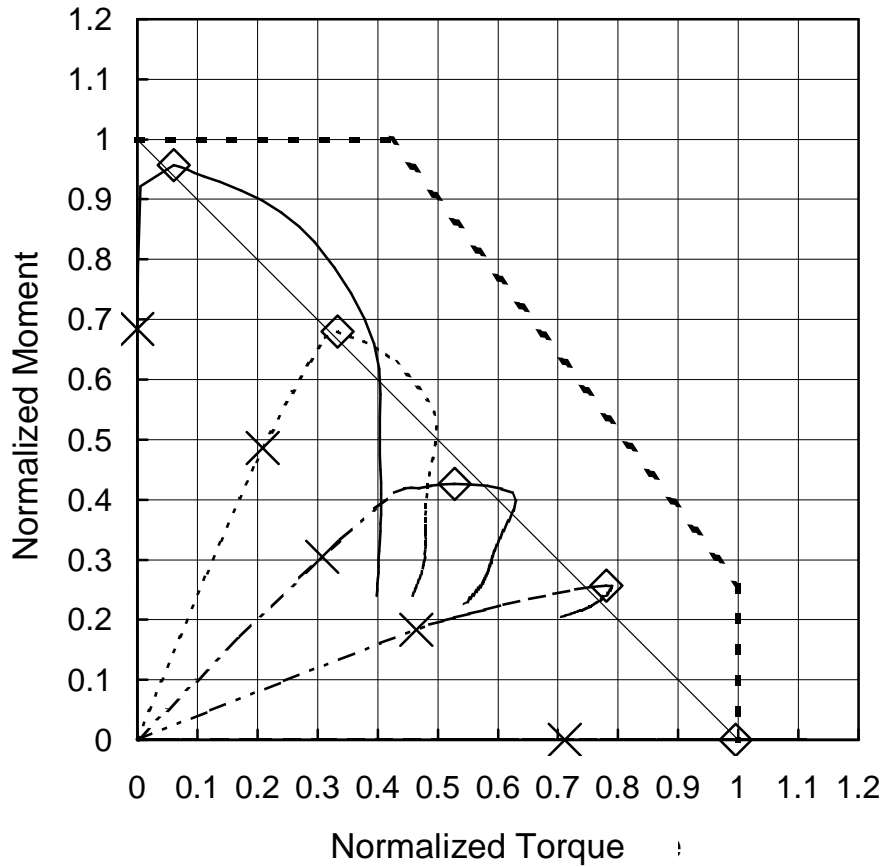
		E0	E1	E2	E3	E4
Service Load Point	Moment (kNm)	50.4	40.3	35.6	17.2	0.0
	Normalized Moment	0.75	0.60	0.53	0.26	0.00
	Torque (kNm)	0.01	1.76	4.04	4.17	4.69
	Normalized Torque	0.00	0.27	0.62	0.64	0.72
	Rotation (Deg)	0.3	5.8	18.4	16.8	21.9
	Maximum Deflection (mm)	5.82	5.11	9.85	4.56	-0.04
	$L / \text{Deflection}$	420	478	248	536	66100
	Maximum Strain	0.0013	0.0022	0.0027	0.0025	0.0155
	Maximum Stress (MPa)	336	350	360	353	349
Ultimate Load Point	Moment (kNm)	70.6	56.4	49.9	24.1	0.0
	Normalized Moment	1.05	0.84	0.74	0.36	0.00
	Torque (kNm)	0.14	4.61	5.93	5.53	6.57
	Normalized Torque	0.02	0.71	0.92	0.85	1.01
	Rotation (Deg)	1.1	27.9	42.4	32.2	47.7
	Maximum Strain	0.0020	0.0042	0.0050	0.0029	0.0299
	Maximum Stress (MPa)	350	377	385	372	417
	FEPR Original	1.05	1.07	1.21	0.96	1.02
	FEPR Modified	1.05	1.26	1.36	1.02	1.02

Interaction Diagrams - Beam S1L2T1B3



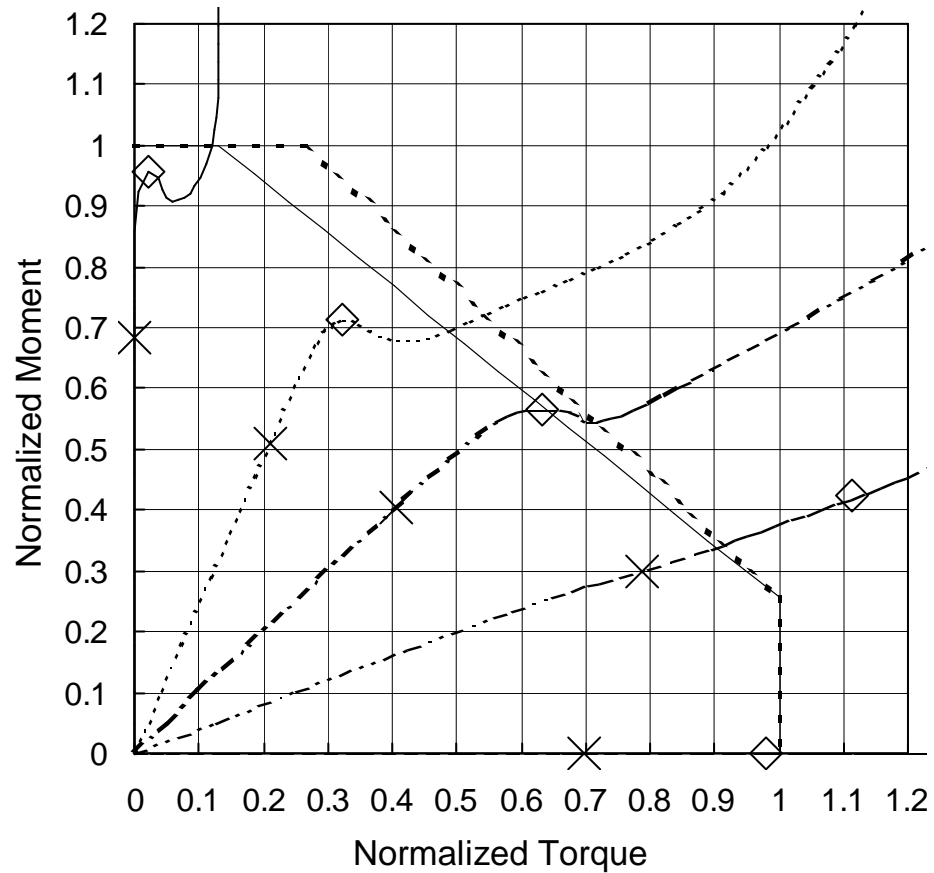
		E0	E1	E2	E3	E4
Service Load Point	Moment (kNm)	49.2	38.9	34.2	31.7	0.00
	Normalized Moment	0.74	0.58	0.51	0.47	0.00
	Torque (kNm)	0.01	1.27	2.23	3.22	2.97
	Normalized Torque	0.00	0.30	0.52	0.76	0.70
	Rotation (Deg)	0.5	20.5	38.5	62.6	60.7
	Maximum Deflection (mm)	37.05	31.26	34.07	47.23	1.50
	$L / \text{Deflection}$	66	78	72	52	1630
	Maximum Strain	0.0011	0.0019	0.0030	0.0073	0.0026
	Maximum Stress (MPa)	241	241	242	245	235
Ultimate Load Point	Moment (kNm)	69.5	54.2	47.6	43.7	0.0
	Normalized Moment	1.04	0.81	0.71	0.65	0.00
	Torque (kNm)	0.95	3.17	3.76	4.20	4.16
	Normalized Torque	0.22	0.75	0.88	0.99	0.98
	Rotation (Deg)	4.9	39.8	58.3	76.0	141
	Maximum Strain	0.0064	0.0106	0.0120	0.0138	0.0095
	Maximum Stress (MPa)	247	250	250	253	245
	FEPR Original	1.04	0.88	1.00	1.08	0.98
FEPR Modified	1.04	1.17	1.23	1.29	0.98	

### Interaction Diagrams - Beam S2L1T1B1



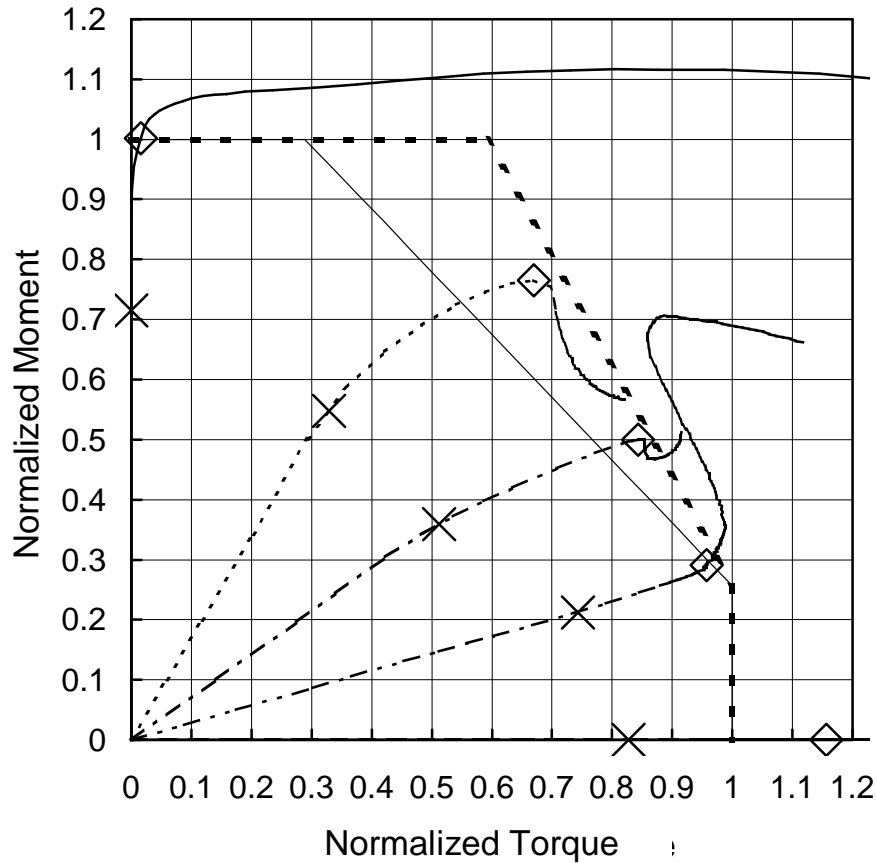
		E0	E1	E2	E3	E4
Service Load Point	Moment (kNm)	768.2	545.5	342.4	206.2	0.0
	Normalized Moment	0.68	0.49	0.30	0.18	0.00
	Torque (kNm)	0.04	17.43	25.71	38.76	59.40
	Normalized Torque	0.00	0.21	0.31	0.46	0.71
	Rotation (Deg)	0.1	1.2	1.7	2.8	9.0
	Maximum Deflection (mm)	8.99	4.65	2.32	1.46	2.33
	$L / \text{Deflection}$	258	499	999	1590	997
	Maximum Strain	0.0027	0.0033	0.0035	0.0070	0.0341
	Maximum Stress (MPa)	367	366	352	353	444
Ultimate Load Point	Moment (kNm)	1075.6	763.7	479.4	288.7	0.0
	Normalized Moment	0.96	0.68	0.43	0.26	0.00
	Torque (kNm)	5.05	27.81	44.14	65.17	83.15
	Normalized Torque	0.06	0.33	0.53	0.78	1.00
	Rotation (Deg)	1.2	3.2	6.6	14.1	21.8
	Maximum Strain	0.0177	0.0140	0.0356	0.0730	0.0871
	Maximum Stress (MPa)	384	396	451	464	469
	FEPR Original	0.96	0.83	0.77	0.83	1.00
	FEPR Modified	0.96	1.01	0.96	1.04	1.00

Interaction Diagrams - Beam S2L1T1B2



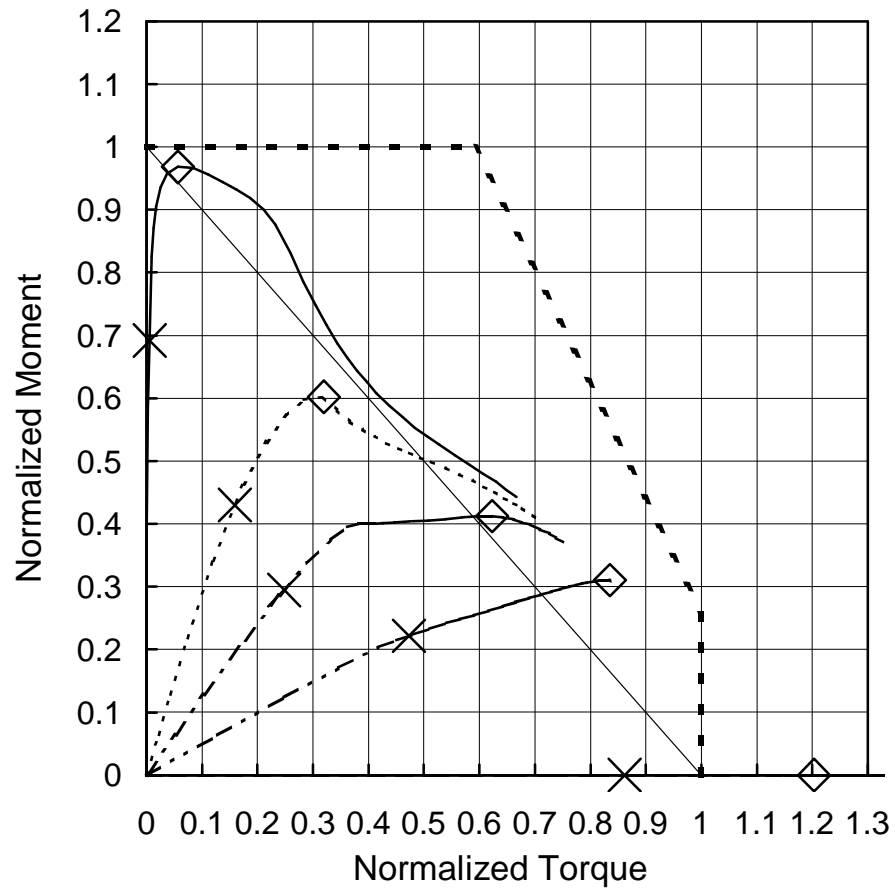
		E0	E1	E2	E3	E4
Service Load Point	Moment (kNm)	767.5	572.8	454.0	336.1	0.0
	Normalized Moment	0.68	0.51	0.40	0.30	0.00
	Torque (kNm)	0.04	27.81	53.40	103.76	92.13
	Normalized Torque	0.00	0.21	0.41	0.79	0.70
	Rotation (Deg)	0.0	0.6	1.0	5.7	3.4
	Maximum Deflection (mm)	5.53	2.91	2.30	3.25	0.20
	$L / \text{Deflection}$	419	796	1010	713	11400
	Maximum Strain	0.0015	0.0024	0.0031	0.0114	0.0079
	Maximum Stress (MPa)	352	350	350	387	389
Ultimate Load Point	Moment (kNm)	1074.5	801.9	635.6	476.5	0.0
	Normalized Moment	0.96	0.71	0.57	0.42	0.00
	Torque (kNm)	2.75	42.67	83.37	146.89	128.99
	Normalized Torque	0.02	0.32	0.63	1.11	0.98
	Rotation (Deg)	0.8	2.2	4.3	22.6	11.2
	Maximum Strain	0.0055	0.0059	0.0115	0.0488	0.0223
	Maximum Stress (MPa)	401	381	375	455	392
	FEPR Original	0.96	0.82	0.95	1.22	0.98
	FEPR Modified	0.96	0.89	1.00	1.24	0.98

**Interaction Diagrams - Beam S2L1T1B3**



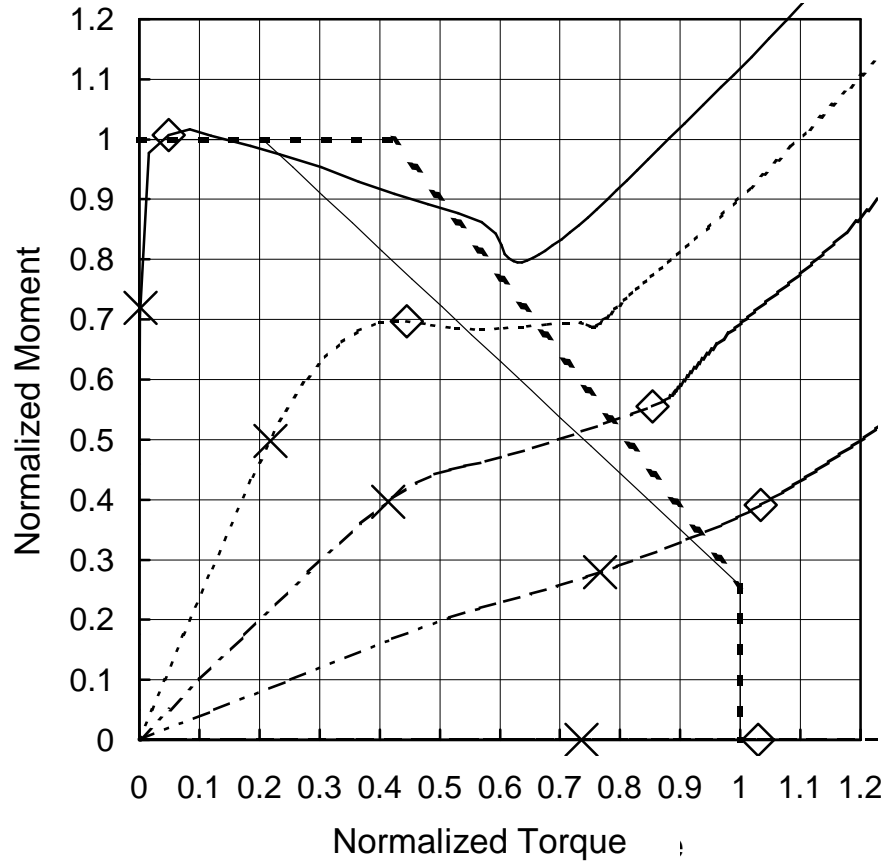
		E0	E1	E2	E3	E4
Service Load Point	Moment (kNm)	803.9	615.5	403.7	238.6	0.0
	Normalized Moment	0.72	0.55	0.36	0.21	0.00
	Torque (kNm)	0.00	19.55	30.38	44.10	49.09
	Normalized Torque	0.00	0.33	0.51	0.74	0.83
	Rotation (Deg)	0.1	7.3	11.5	20.1	24.9
	Maximum Deflection (mm)	11.14	9.94	7.83	7.29	0.63
	<i>L</i> / Deflection	208	233	296	318	3680
	Maximum Strain	0.0011	0.0030	0.0047	0.0103	0.0104
	Maximum Stress (MPa)	234	236	236	239	247
Ultimate Load Point	Moment (kNm)	1125.4	859.8	561.6	327.3	0.0
	Normalized Moment	1.00	0.77	0.50	0.29	0.00
	Torque (kNm)	0.92	39.74	50.08	56.82	68.67
	Normalized Torque	0.02	0.67	0.84	0.96	1.16
	Rotation (Deg)	0.4	20.4	25.8	41.5	50.1
	Maximum Strain	0.0036	0.0134	0.0134	0.0148	0.0181
	Maximum Stress (MPa)	237	262	244	266	302
	FEPR Original	1.00	0.95	0.98	0.98	1.16
FEPR Modified	1.00	1.13	1.06	0.99	1.16	

Interaction Diagrams - Beam S2L2T1B1



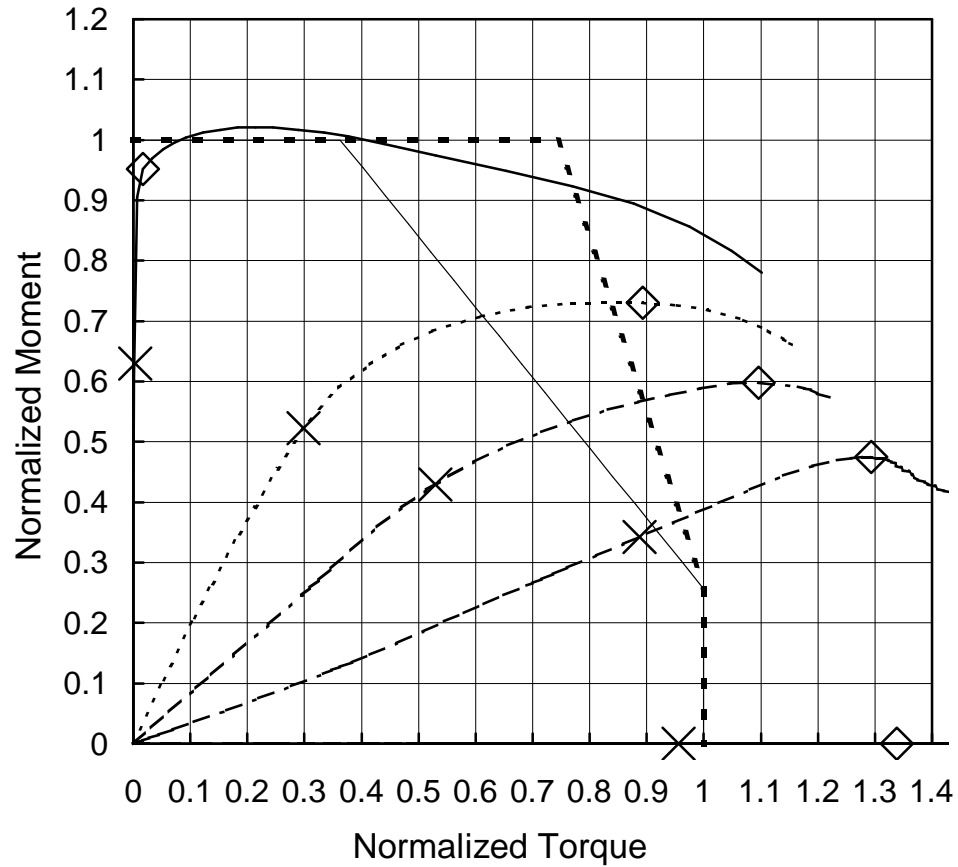
		E0	E1	E2	E3	E4
Service Load Point	Moment (kNm)	623.9	387.7	266.0	199.7	0.0
	Normalized Moment	0.69	0.43	0.29	0.22	0.00
	Torque (kNm)	0.31	9.47	14.73	28.07	51.12
	Normalized Torque	0.01	0.16	0.25	0.47	0.86
	Rotation (Deg)	0.4	3.3	5.0	11.5	25.5
	Maximum Deflection (mm)	8.95	5.94	4.60	9.28	12.28
	$L / \text{Deflection}$	519	782	1010	500	378
	Maximum Strain	0.0016	0.0023	0.0027	0.0191	0.0313
	Maximum Stress (MPa)	361	350	350	361	424
Ultimate Load Point	Moment (kNm)	873.5	542.9	372.4	279.6	0.0
	Normalized Moment	0.97	0.60	0.41	0.31	0.00
	Torque (kNm)	3.33	18.99	36.96	49.60	71.40
	Normalized Torque	0.06	0.32	0.62	0.84	1.20
	Rotation (Deg)	1.9	8.2	24.6	42.1	48.4
	Maximum Strain	0.0036	0.0114	0.0436	0.0879	0.0538
	Maximum Stress (MPa)	369	383	453	462	460
	FEPR Original	0.97	0.71	0.79	0.87	1.20
	FEPR Modified	0.97	0.92	1.04	1.15	1.20

Interaction Diagrams - Beam S2L2T1B2



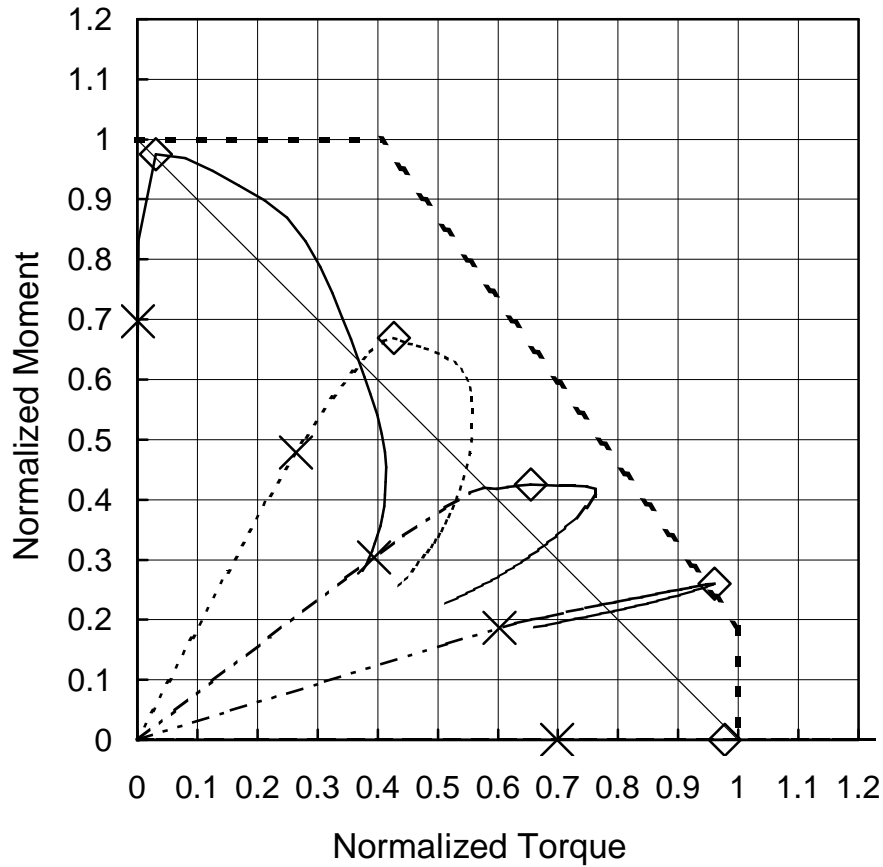
		E0	E1	E2	E3	E4
Service Load Point	Moment (kNm)	807.8	559.0	445.9	313.5	0.0
	Normalized Moment	0.72	0.50	0.40	0.28	0.00
	Torque (kNm)	0.15	18.20	34.58	64.01	61.41
	Normalized Torque	0.00	0.22	0.41	0.77	0.74
	Rotation (Deg)	0.1	2.3	4.6	13.9	13.4
	Maximum Deflection (mm)	7.72	5.42	5.10	9.74	1.40
	$L / \text{Deflection}$	601	856	910	476	3330
	Maximum Strain	0.0014	0.0024	0.0040	0.0073	0.0055
	Maximum Stress (MPa)	351	350	350	380	384
Ultimate Load Point	Moment (kNm)	1131.0	782.7	624.3	438.8	0.0
	Normalized Moment	1.01	0.70	0.56	0.39	0.00
	Torque (kNm)	4.08	37.16	71.30	86.34	85.97
	Normalized Torque	0.05	0.44	0.85	1.03	1.03
	Rotation (Deg)	1.1	7.2	19.9	28.0	24.2
	Maximum Strain	0.0032	0.0070	0.0188	0.0252	0.0092
	Maximum Stress (MPa)	367	358	384	392	391
	FEPR Original	1.01	0.82	1.07	1.12	1.03
FEPR Modified	1.01	0.93	1.14	1.14	1.03	

### Interaction Diagrams - Beam S2L2T1B3



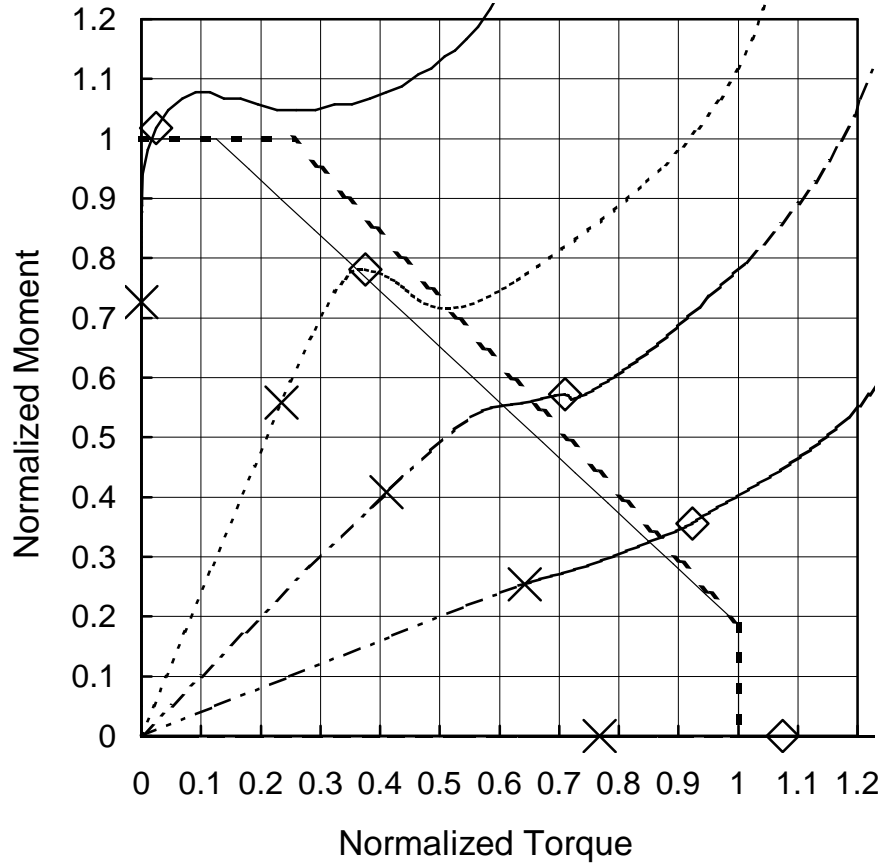
		E0	E1	E2	E3	E4
Service Load Point	Moment (kNm)	672.7	559.2	459.1	366.0	0.0
	Normalized Moment	0.63	0.52	0.43	0.34	0.00
	Torque (kNm)	0.13	14.12	25.02	41.98	45.20
	Normalized Torque	0.00	0.30	0.53	0.89	0.96
	Rotation (Deg)	0.3	14.8	26.5	45.0	57.0
	Maximum Deflection (mm)	35.46	30.12	32.10	46.17	2.17
	$L / \text{Deflection}$	131	154	145	100	2140
	Maximum Strain	0.0009	0.0018	0.0033	0.0099	0.0095
	Maximum Stress (MPa)	234	235	236	238	240
Ultimate Load Point	Moment (kNm)	1017.2	780.8	639.5	507.3	0.0
	Normalized Moment	0.95	0.73	0.60	0.47	0.00
	Torque (kNm)	0.81	42.23	51.80	61.18	63.26
	Normalized Torque	0.02	0.89	1.10	1.29	1.34
	Rotation (Deg)	0.8	31.6	45.1	62.1	99.5
	Maximum Strain	0.0021	0.0106	0.0128	0.0150	0.0143
	Maximum Stress (MPa)	236	239	239	253	280
	FEPR Original	0.95	1.05	1.19	1.33	1.34
	FEPR Modified	0.95	1.24	1.31	1.38	1.34

### Interaction Diagrams - Beam S3L1T1B1



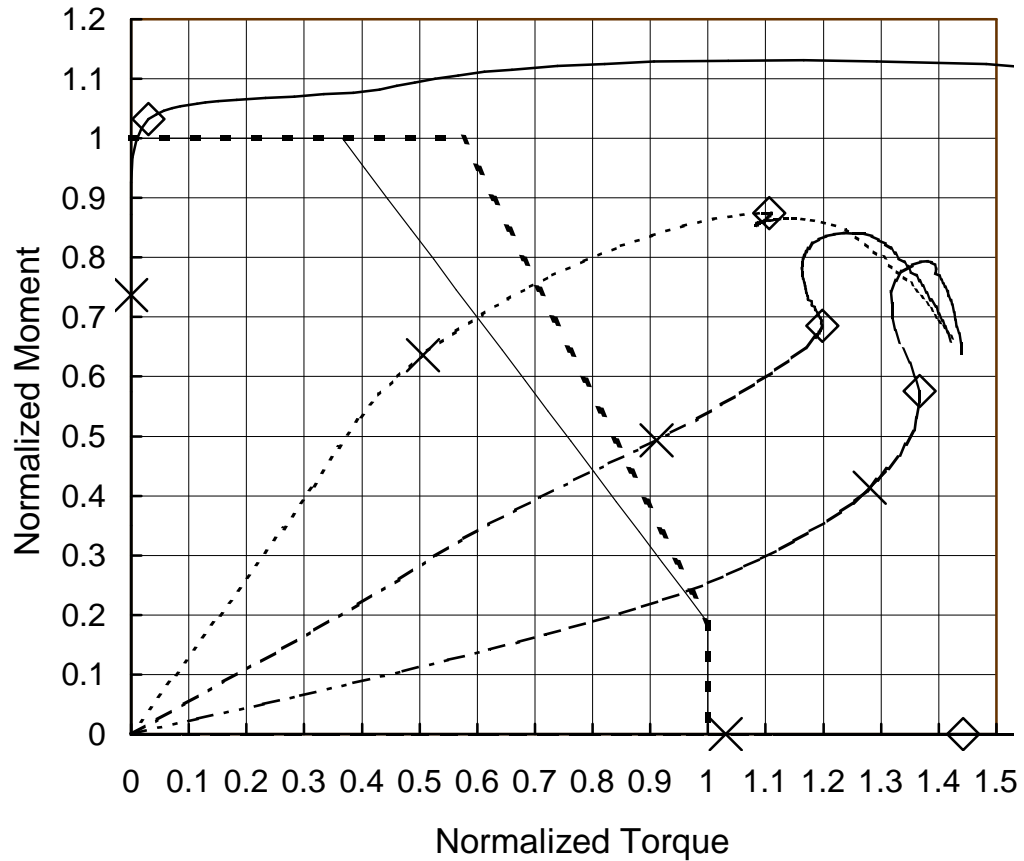
		E0	E1	E2	E3	E4
Service Load Point	Moment (kNm)	651.1	446.7	283.9	173.9	0.0
	Normalized Moment	0.70	0.48	0.30	0.19	0.00
	Torque (kNm)	0.04	14.16	21.16	32.34	37.49
	Normalized Torque	0.00	0.26	0.39	0.60	0.70
	Rotation (Deg)	0.1	2.1	3.0	4.9	6.7
	Maximum Deflection (mm)	10.07	6.12	3.65	2.95	0.60
	$L / \text{Deflection}$	329	542	908	1120	5540
	Maximum Strain	0.0026	0.0031	0.0035	0.0069	0.0119
	Maximum Stress (MPa)	369	367	352	353	361
Ultimate Load Point	Moment (kNm)	911.6	625.4	397.5	243.4	0.0
	Normalized Moment	0.98	0.67	0.43	0.26	0.00
	Torque (kNm)	1.65	22.91	35.12	51.57	52.48
	Normalized Torque	0.03	0.43	0.65	0.96	0.98
	Rotation (Deg)	1.0	5.3	10.1	23.4	17.5
	Maximum Strain	0.0092	0.0145	0.0353	0.0863	0.0326
	Maximum Stress (MPa)	380	399	454	495	434
	FEPR Original	0.98	0.89	0.89	1.02	0.98
FEPR Modified	0.98	1.10	1.08	1.22	0.98	

### Interaction Diagrams - Beam S3L1T1B2



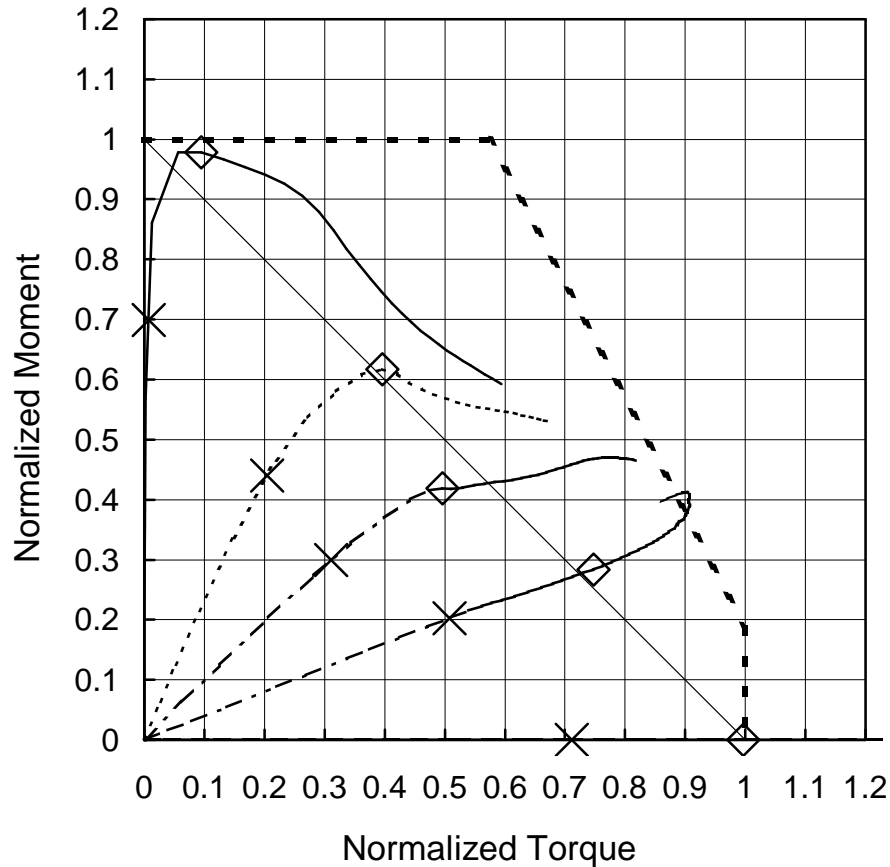
		E0	E1	E2	E3	E4
Service Load Point	Moment (kNm)	679.3	521.4	381.6	237.8	0.0
	Normalized Moment	0.73	0.56	0.41	0.25	0.00
	Torque (kNm)	0.01	25.91	45.25	70.74	84.56
	Normalized Torque	0.00	0.24	0.41	0.64	0.77
	Rotation (Deg)	0.0	1.0	1.8	4.2	9.8
	Maximum Deflection (mm)	6.63	4.92	3.70	3.12	1.01
	$L / \text{Deflection}$	500	674	897	1060	3300
	Maximum Strain	0.0014	0.0024	0.0034	0.0085	0.0221
	Maximum Stress (MPa)	351	350	350	348	391
Ultimate Load Point	Moment (kNm)	951.0	730.0	534.2	332.9	0.0
	Normalized Moment	1.02	0.78	0.57	0.36	0.00
	Torque (kNm)	2.70	41.36	78.18	101.69	118.39
	Normalized Torque	0.02	0.38	0.71	0.92	1.07
	Rotation (Deg)	1.1	5.2	12.8	20.8	24.1
	Maximum Strain	0.0207	0.0173	0.0330	0.0445	0.0424
	Maximum Stress (MPa)	404	396	433	448	447
	FEPR Original	1.02	0.93	1.05	1.07	1.08
	FEPR Modified	1.02	1.01	1.10	1.09	1.08

### Interaction Diagrams - Beam S3L1T1B3



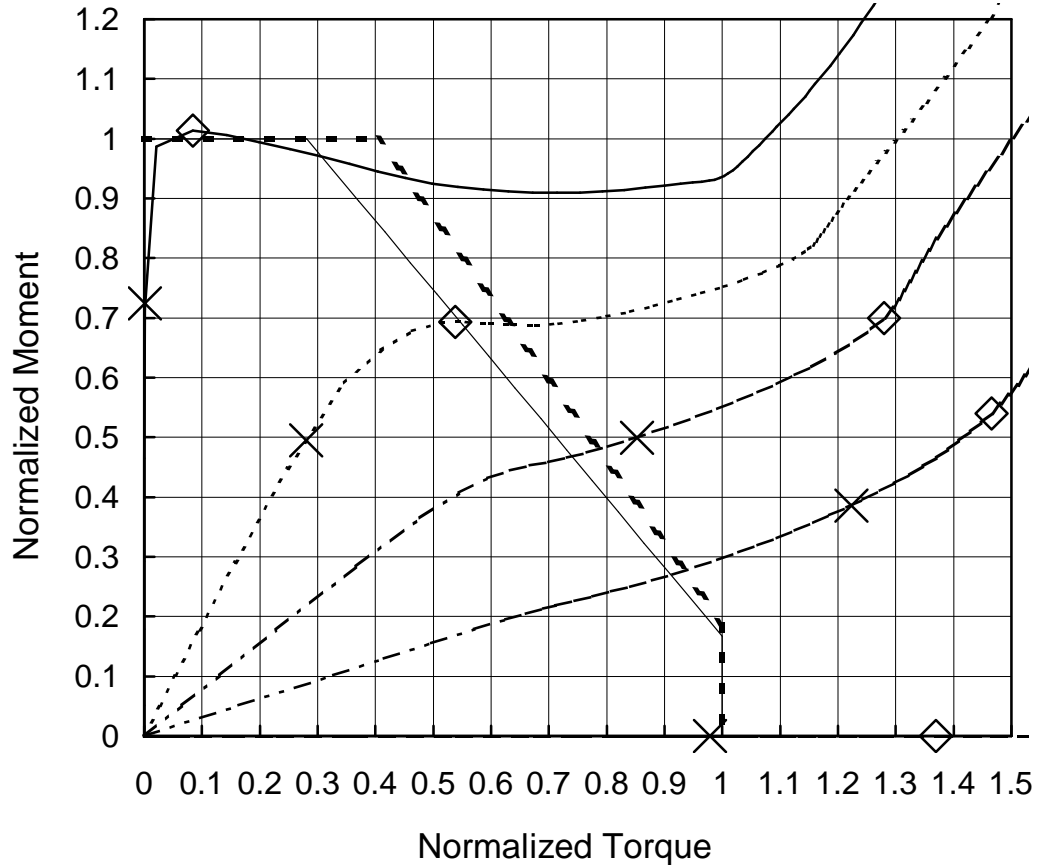
		E0	E1	E2	E3	E4
Service Load Point	Moment (kNm)	688.9	594.8	460.3	386.6	0.0
	Normalized Moment	0.74	0.64	0.49	0.41	0.00
	Torque (kNm)	0.01	19.06	34.30	48.24	38.82
	Normalized Torque	0.00	0.51	0.91	1.28	1.03
	Rotation (Deg)	0.1	16.5	31.8	57.7	26.4
	Maximum Deflection (mm)	24.91	29.56	36.91	64.46	0.64
	$L / \text{Deflection}$	133	112	90	51	5210
	Maximum Strain	0.0011	0.0054	0.0111	0.0163	0.0084
	Maximum Stress (MPa)	219	221	221	262	221
Ultimate Load Point	Moment (kNm)	964.6	817.37	640.1	537.8	0.0
	Normalized Moment	1.03	0.87	0.68	0.58	0.00
	Torque (kNm)	1.14	41.68	45.15	51.51	54.34
	Normalized Torque	0.03	1.11	1.20	1.37	1.44
	Rotation (Deg)	0.9	50.4	57.6	71.4	49.2
	Maximum Strain	0.0044	0.0226	0.0197	0.0200	0.0151
	Maximum Stress (MPa)	224	285	278	278	273
	FEPR Original	1.03	1.42	1.42	1.52	1.44
FEPR Modified	1.03	1.56	1.51	1.59	1.44	

### Interaction Diagrams - Beam S3L2T1B1



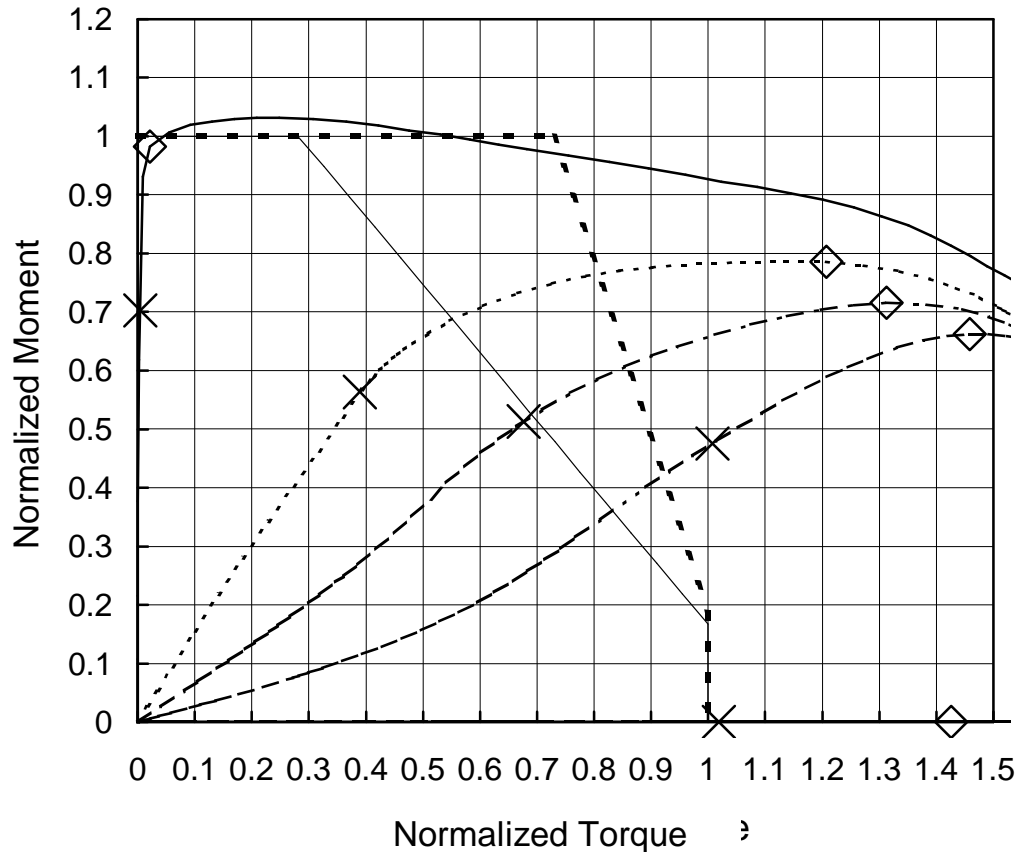
		E0	E1	E2	E3	E4
Service Load Point	Moment (kNm)	509.2	321.0	218.2	147.8	0.0
	Normalized Moment	0.70	0.44	0.30	0.20	0.00
	Torque (kNm)	0.28	7.71	11.73	19.12	26.82
	Normalized Torque	0.01	0.20	0.31	0.51	0.71
	Rotation (Deg)	0.8	5.8	8.5	14.0	21.0
	Maximum Deflection (mm)	18.26	12.90	10.05	10.51	3.27
	$L / \text{Deflection}$	363	514	660	631	2030
	Maximum Strain	0.0014	0.0022	0.0026	0.0046	0.0094
	Maximum Stress (MPa)	361	350	350	350	350
Ultimate Load Point	Moment (kNm)	712.9	449.4	305.4	206.9	0.0
	Normalized Moment	0.98	0.62	0.42	0.28	0.00
	Torque (kNm)	3.59	14.92	18.68	28.16	37.55
	Normalized Torque	0.10	0.40	0.50	0.75	1.00
	Rotation (Deg)	4.1	13.7	16.6	31.7	37.7
	Maximum Strain	0.0041	0.0096	0.0140	0.0307	0.0273
	Maximum Stress (MPa)	373	381	356	428	397
	FEPR Original	0.98	0.76	0.71	0.82	1.00
	FEPR Modified	0.98	1.01	0.92	1.03	1.00

Interaction Diagrams - Beam S3L2T1B2



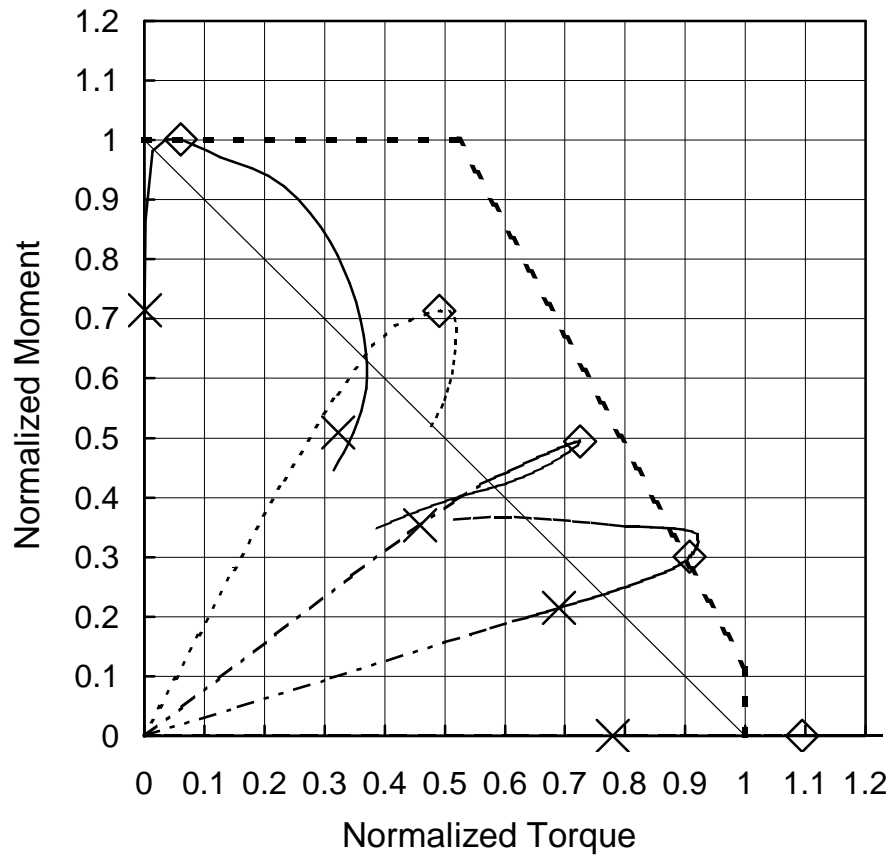
		E0	E1	E2	E3	E4
Service Load Point	Moment (kNm)	676.8	462.9	467.0	360.8	0.0
	Normalized Moment	0.72	0.50	0.50	0.39	0.00
	Torque (kNm)	0.08	15.04	45.76	65.66	52.52
	Normalized Torque	0.00	0.28	0.85	1.22	0.98
	Rotation (Deg)	0.2	4.0	20.6	35.3	24.8
	Maximum Deflection (mm)	14.74	10.53	30.42	47.98	0.61
	$L / \text{Deflection}$	450	629	218	138	10800
	Maximum Strain	0.0014	0.0026	0.0213	0.0327	0.0144
	Maximum Stress (MPa)	351	350	396	428	382
Ultimate Load Point	Moment (kNm)	947.3	648.1	653.8	505.1	0.0
	Normalized Moment	1.01	0.69	0.70	0.54	0.00
	Torque (kNm)	4.49	28.88	68.68	78.66	73.52
	Normalized Torque	0.08	0.54	1.28	1.47	1.37
	Rotation (Deg)	2.3	12.0	41.6	49.9	41.6
	Maximum Strain	0.0047	0.0120	0.0432	0.0485	0.0265
	Maximum Stress (MPa)	350	352	448	448	397
	FEPR Original	1.01	0.92	1.58	1.64	1.37
FEPR Modified	1.01	1.00	1.64	1.67	1.37	

### Interaction Diagrams - Beam S3L2T1B3



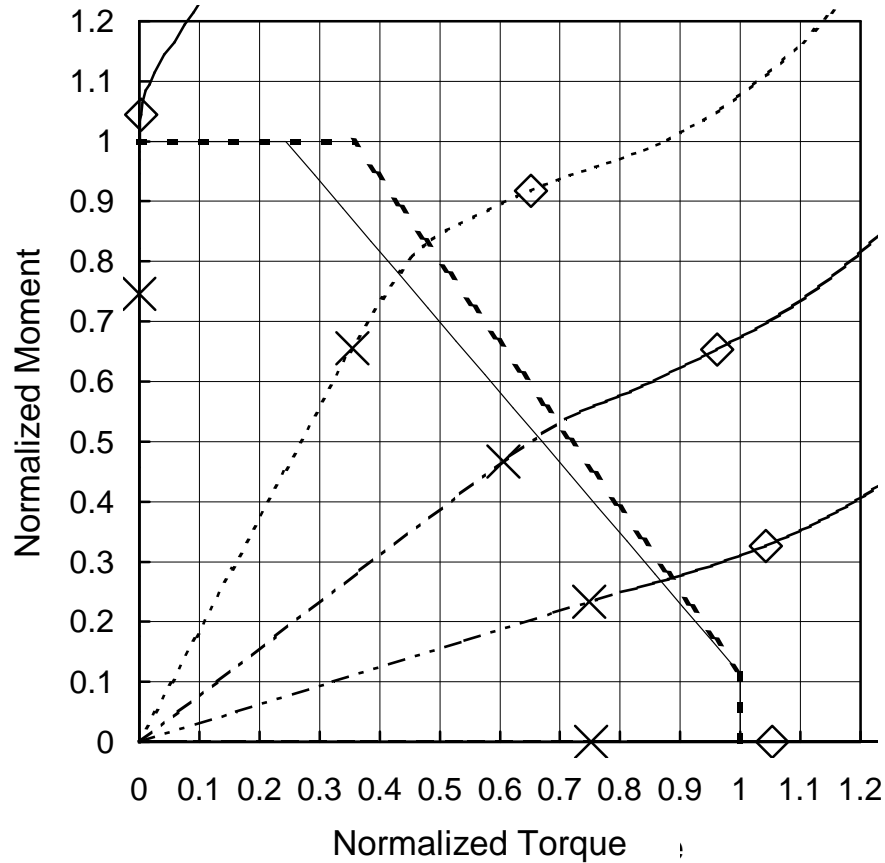
		E0	E1	E2	E3	E4
Service Load Point	Moment (kNm)	615.4	493.7	450.0	417.6	0.0
	Normalized Moment	0.70	0.56	0.51	0.48	0.00
	Torque (kNm)	0.12	11.57	20.09	29.90	30.24
	Normalized Torque	0.00	0.39	0.68	1.01	1.02
	Rotation (Deg)	0.5	26.7	45.2	65.3	68.5
	Maximum Deflection (mm)	82.83	74.55	88.39	119.11	2.73
	$L$ / Deflection	80	89	75	56	2430
	Maximum Strain	0.0010	0.0020	0.0039	0.0086	0.0059
	Maximum Stress (MPa)	217	215	216	217	219
Ultimate Load Point	Moment (kNm)	861.5	688.7	626.9	580.7	0.0
	Normalized Moment	0.98	0.79	0.71	0.66	0.00
	Torque (kNm)	0.65	35.84	38.97	43.30	42.34
	Normalized Torque	0.02	1.21	1.31	1.46	1.43
	Rotation (Deg)	1.6	51.6	64.5	76.9	111
	Maximum Strain	0.0022	0.0126	0.0133	0.0149	0.0121
	Maximum Stress (MPa)	221	234	236	245	249
	FEPR Original	0.98	1.38	1.46	1.58	1.43
	FEPR Modified	0.98	1.53	1.58	1.68	1.43

### Interaction Diagrams - Beam S4L1T1B1



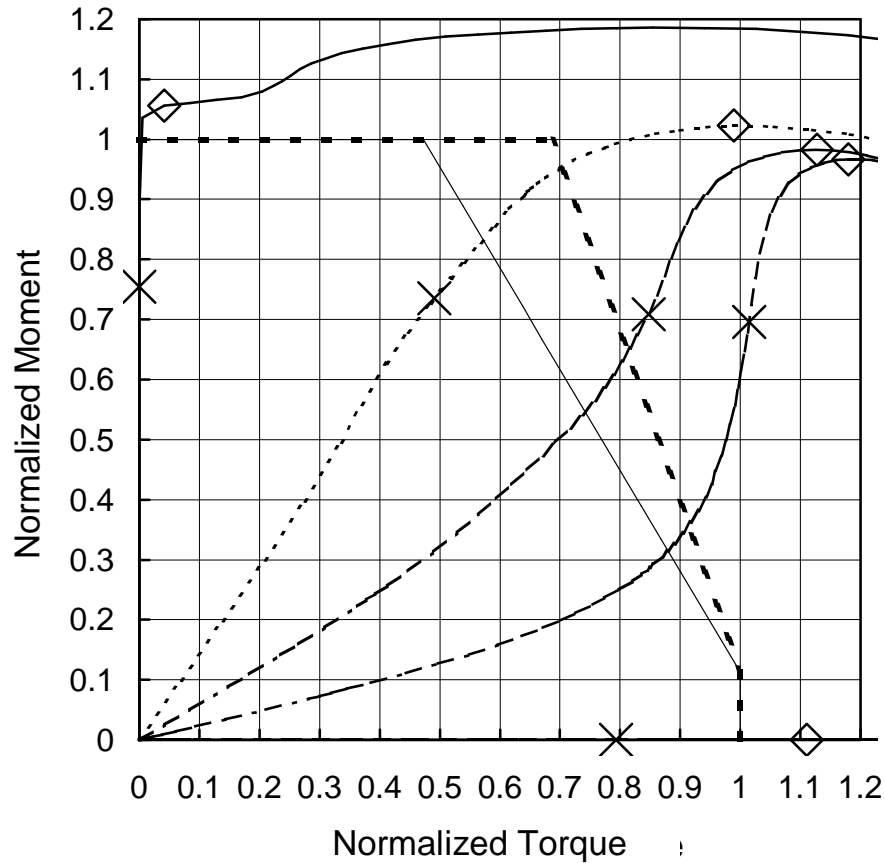
		E0	E1	E2	E3	E4
Service Load Point	Moment (kNm)	142.6	101.7	70.5	42.8	0.0
	Normalized Moment	0.71	0.51	0.35	0.21	0.00
	Torque (kNm)	0.01	4.66	6.62	9.96	11.24
	Normalized Torque	0.00	0.32	0.46	0.69	0.78
	Rotation (Deg)	0.2	4.3	6.9	13.7	16.8
	Maximum Deflection (mm)	9.08	7.02	5.55	6.63	0.79
	$L / \text{Deflection}$	285	368	466	390	3270
	Maximum Strain	0.0024	0.0040	0.0053	0.0217	0.0180
	Maximum Stress (MPa)	368	362	353	371	350
Ultimate Load Point	Moment (kNm)	199.7	142.3	98.7	59.9	0.0
	Normalized Moment	1.00	0.71	0.49	0.30	0.00
	Torque (kNm)	0.87	7.08	10.47	13.10	15.80
	Normalized Torque	0.06	0.49	0.73	0.91	1.09
	Rotation (Deg)	2.2	14.0	24.9	34.7	48.1
	Maximum Strain	0.0139	0.0409	0.0705	0.0547	0.0367
	Maximum Stress (MPa)	383	477	492	484	453
	FEPR Original	1.00	0.93	1.00	1.04	1.10
	FEPR Modified	1.00	1.20	1.22	1.21	1.10

Interaction Diagrams - Beam S4L1T1B2



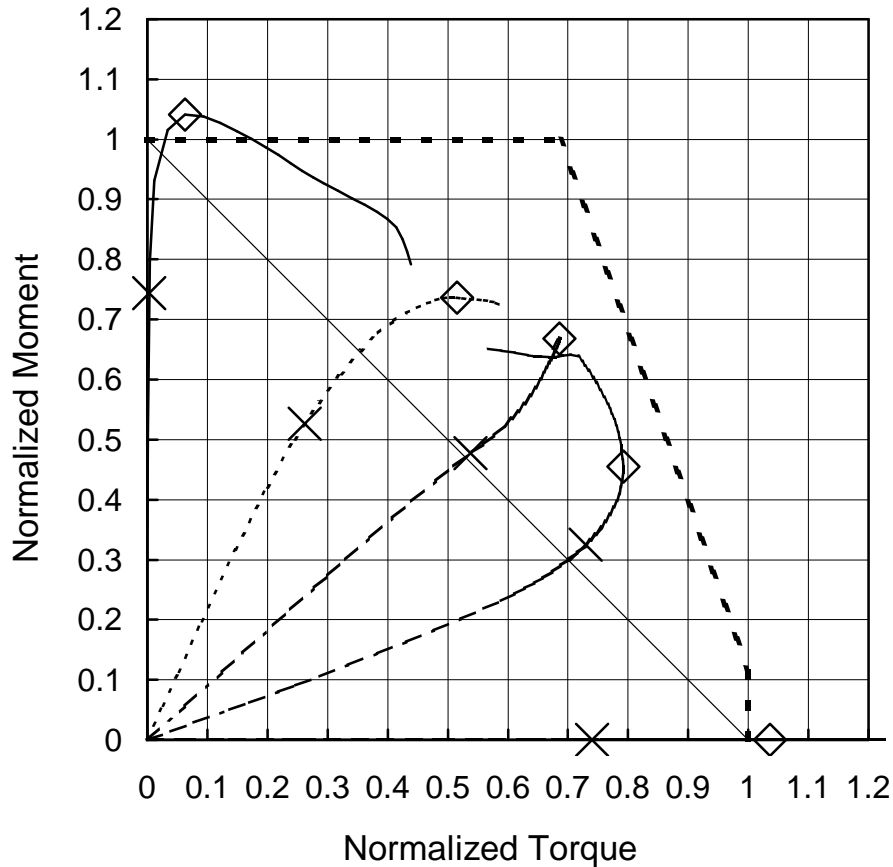
		E0	E1	E2	E3	E4
Service Load Point	Moment (kNm)	148.8	130.8	93.2	46.5	0.0
	Normalized Moment	0.75	0.66	0.47	0.23	0.00
	Torque (kNm)	0.00	7.54	12.90	15.95	16.02
	Normalized Torque	0.00	0.35	0.61	0.75	0.75
	Rotation (Deg)	0.0	2.6	4.9	6.2	5.7
	Maximum Deflection (mm)	6.37	5.85	4.79	2.68	0.07
	$L / \text{Deflection}$	406	442	539	964	35900
	Maximum Strain	0.0013	0.0027	0.0037	0.0040	0.0029
	Maximum Stress (MPa)	341	349	349	349	349
Ultimate Load Point	Moment (kNm)	208.4	183.1	130.4	65.1	0.0
	Normalized Moment	1.04	0.92	0.65	0.33	0.00
	Torque (kNm)	0.06	13.87	20.48	22.20	22.42
	Normalized Torque	0.00	0.65	0.96	1.04	1.05
	Rotation (Deg)	0.3	17.4	23.8	21.7	22.3
	Maximum Strain	0.0051	0.0227	0.0279	0.0188	0.0102
	Maximum Stress (MPa)	396	399	409	401	384
	FEPR Original	1.04	1.22	1.33	1.18	1.05
	FEPR Modified	1.04	1.31	1.39	1.20	1.05

Interaction Diagrams - Beam S4L1T1B3



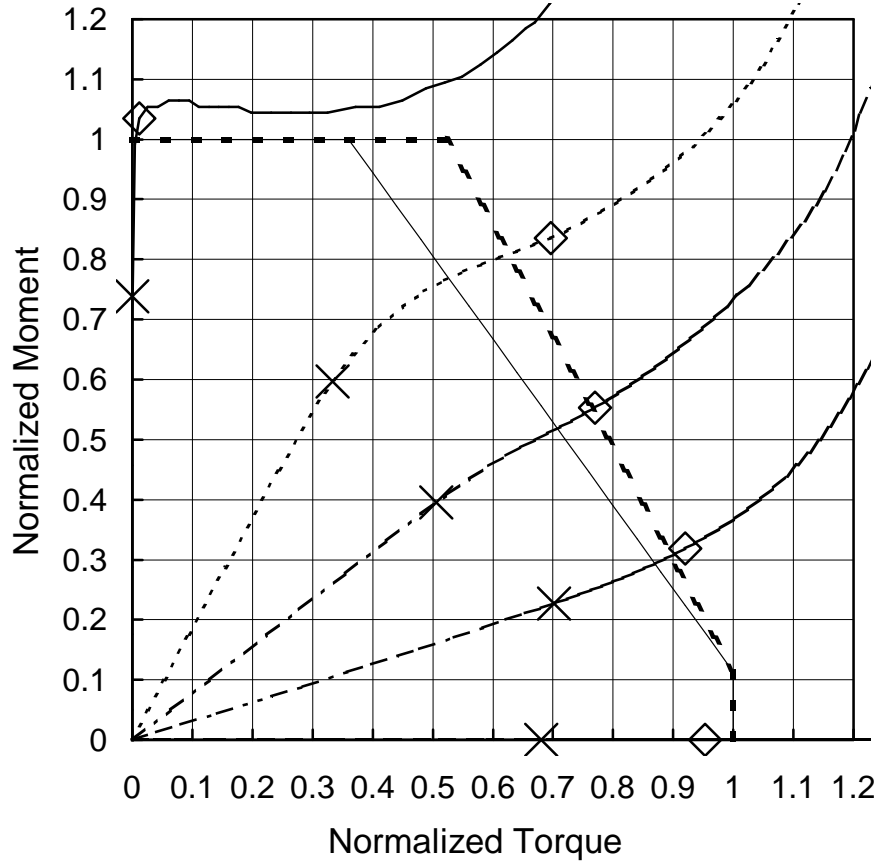
		E0	E1	E2	E3	E4
Service Load Point	Moment (kNm)	150.6	146.7	141.4	138.9	0.0
	Normalized Moment	0.75	0.74	0.71	0.70	0.00
	Torque (kNm)	0.00	5.40	9.32	11.16	8.72
	Normalized Torque	0.00	0.49	0.85	1.01	0.79
	Rotation (Deg)	0.2	24.7	53.2	74.6	30.4
	Maximum Deflection (mm)	33.44	42.91	73.18	92.96	0.38
	$L / \text{Deflection}$	77	60	35	28	6790
	Maximum Strain	0.0010	0.0054	0.0128	0.0163	0.0024
	Maximum Stress (MPa)	236	239	244	256	220
Ultimate Load Point	Moment (kNm)	210.7	204.0	195.9	192.9	0.0
	Normalized Moment	1.06	1.02	0.98	0.97	0.00
	Torque (kNm)	0.46	10.88	12.41	12.97	12.21
	Normalized Torque	0.04	0.99	1.13	1.18	1.11
	Rotation (Deg)	0.7	53.9	73.6	83.5	63.4
	Maximum Strain	0.0070	0.0230	0.0258	0.0256	0.0095
	Maximum Stress (MPa)	243	287	290	290	233
	FEPR Original	1.06	1.30	1.42	1.46	1.11
	FEPR Modified	1.06	1.50	1.60	1.64	1.11

### Interaction Diagrams - Beam S4L2T1B1



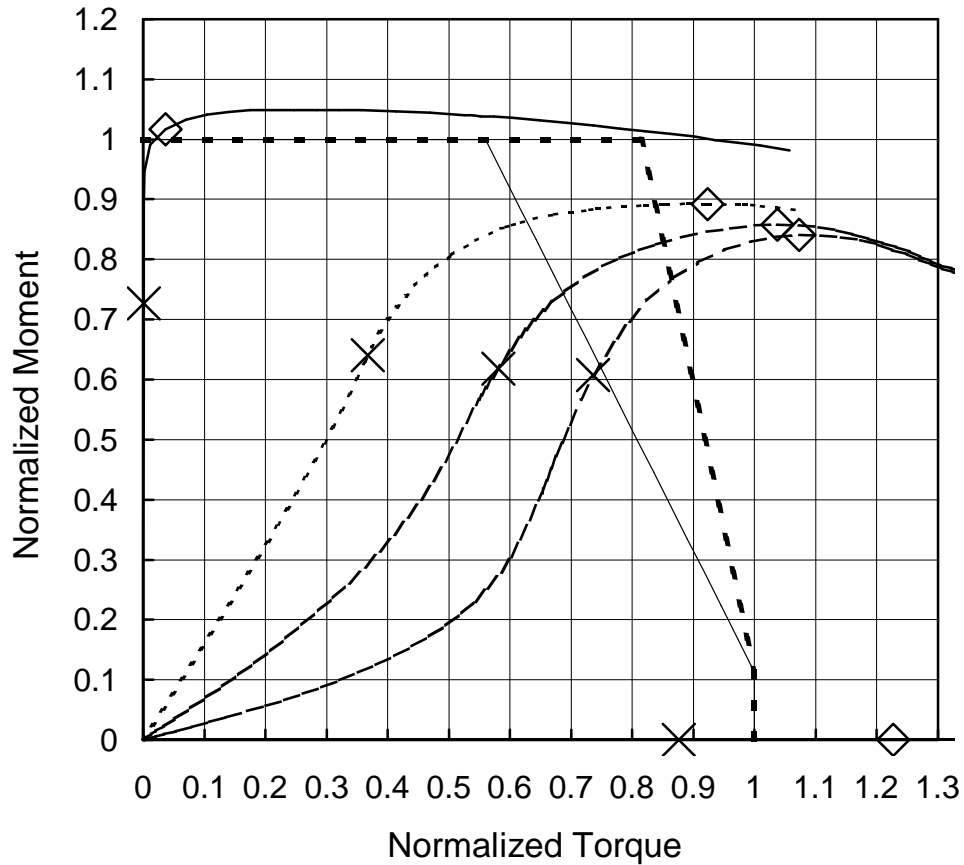
		E0	E1	E2	E3	E4
Service Load Point	Moment (kNm)	127.6	90.3	81.8	55.8	0.0
	Normalized Moment	0.74	0.53	0.48	0.33	0.00
	Torque (kNm)	0.04	2.88	5.92	8.03	8.14
	Normalized Torque	0.00	0.26	0.54	0.73	0.74
	Rotation (Deg)	0.9	11.7	26.6	42.3	34.0
	Maximum Deflection (mm)	27.92	23.15	37.07	51.05	2.93
	$L / \text{Deflection}$	185	223	139	101	1760
	Maximum Strain	0.0016	0.0035	0.0139	0.0059	0.0065
	Maximum Stress (MPa)	361	351	375	350	349
Ultimate Load Point	Moment (kNm)	178.6	126.4	114.6	78.1	0.0
	Normalized Moment	1.04	0.74	0.67	0.46	0.00
	Torque (kNm)	0.69	5.67	7.55	8.71	11.40
	Normalized Torque	0.06	0.52	0.69	0.79	1.04
	Rotation (Deg)	4.5	33.6	64.7	58.4	71.2
	Maximum Strain	0.0016	0.0347	0.0876	0.0173	0.0267
	Maximum Stress (MPa)	373	454	496	349	394
	FEPR Original	1.04	0.89	1.01	0.99	1.04
	FEPR Modified	1.04	1.25	1.35	1.25	1.04

Interaction Diagrams - Beam S4L2T1B2



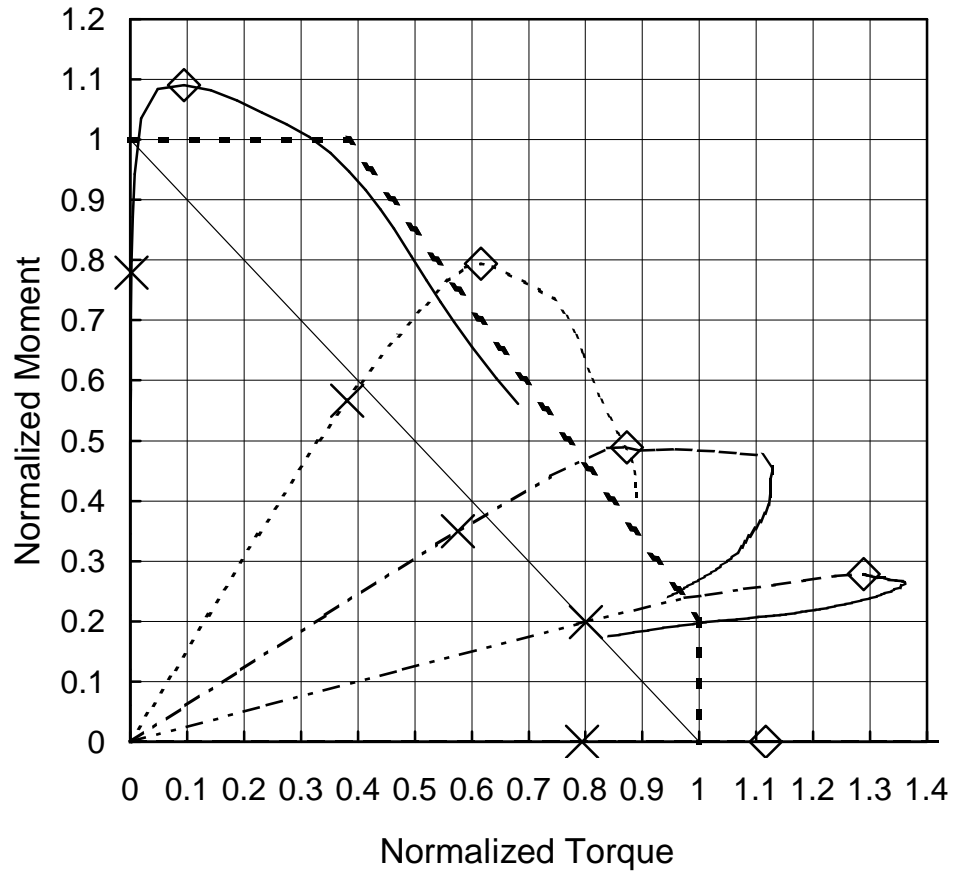
		E0	E1	E2	E3	E4
Service Load Point	Moment (kNm)	147.4	119.1	78.9	45.4	0.0
	Normalized Moment	0.74	0.60	0.40	0.23	0.00
	Torque (kNm)	0.01	4.81	7.30	10.13	9.83
	Normalized Torque	0.00	0.33	0.51	0.70	0.68
	Rotation (Deg)	0.2	9.2	13.6	20.1	17.9
	Maximum Deflection (mm)	17.84	15.64	11.30	8.87	0.34
	$L / \text{Deflection}$	290	330	457	583	15400
	Maximum Strain	0.0014	0.0023	0.0024	0.0027	0.0022
	Maximum Stress (MPa)	337	350	350	351	350
Ultimate Load Point	Moment (kNm)	206.4	166.7	110.4	63.5	0.0
	Normalized Moment	1.03	0.84	0.55	0.32	0.00
	Torque (kNm)	0.16	10.05	11.11	13.28	13.76
	Normalized Torque	0.01	0.70	0.77	0.92	0.95
	Rotation (Deg)	0.9	29.9	29.6	35.3	37.1
	Maximum Strain	0.0024	0.0136	0.0074	0.0059	0.0042
	Maximum Stress (MPa)	351	381	373	386	364
	FEPR Original	1.03	1.08	1.01	1.03	0.95
	FEPR Modified	1.03	1.20	1.08	1.06	0.95

## Interaction Diagrams - Beam S4L2T1B3



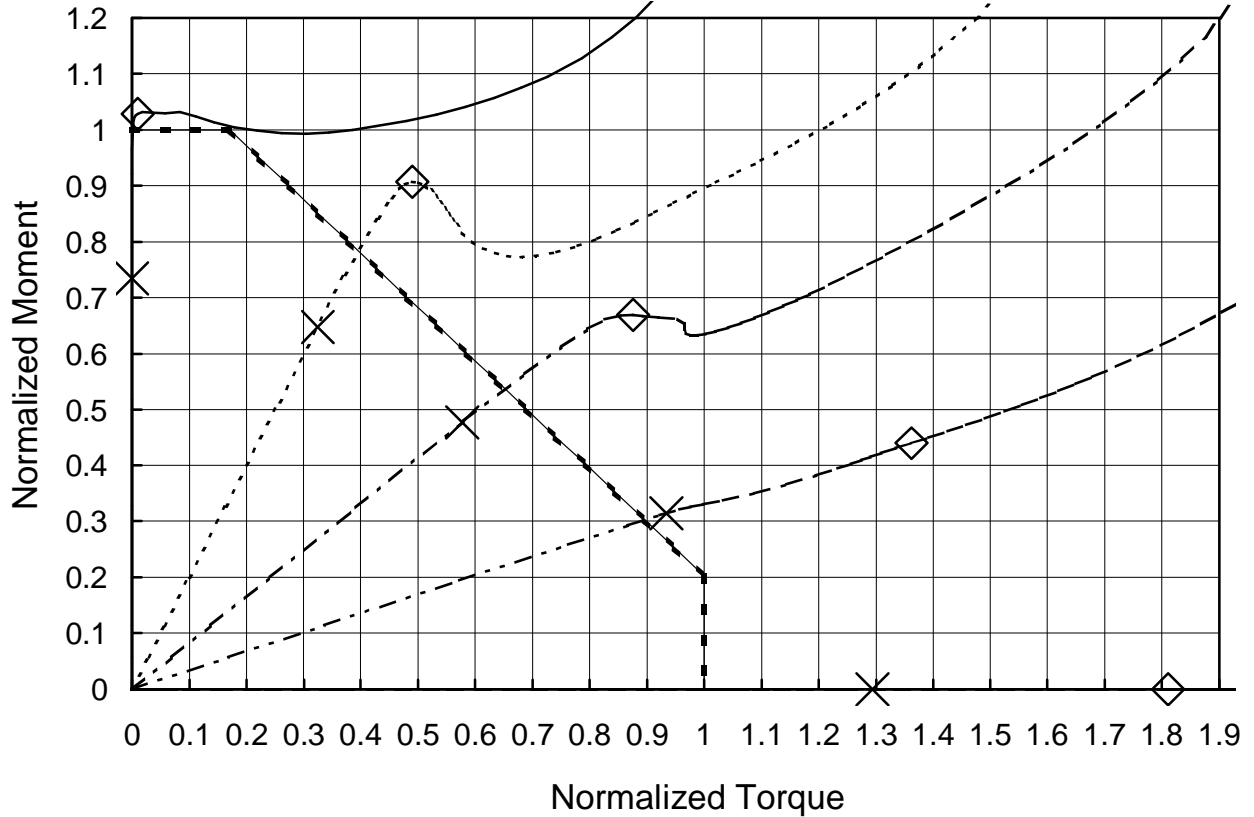
		E0	E1	E2	E3	E4
Service Load Point	Moment (kNm)	142.7	125.8	121.4	119.2	0.0
	Normalized Moment	0.73	0.64	0.62	0.61	0.00
	Torque (kNm)	0.01	3.41	5.39	6.83	8.13
	Normalized Torque	0.00	0.37	0.58	0.74	0.88
	Rotation (Deg)	0.5	34.4	55.4	73.8	73.8
	Maximum Deflection (mm)	122.33	114.53	126.93	145.82	2.29
	$L$ / Deflection	42	45	41	35	2260
	Maximum Strain	0.0010	0.0033	0.0033	0.0051	0.0023
	Maximum Stress (MPa)	235	236	234	237	220
Ultimate Load Point	Moment (kNm)	199.7	175.2	168.4	165.1	0.0
	Normalized Moment	1.02	0.89	0.86	0.84	0.00
	Torque (kNm)	0.34	8.57	9.63	9.96	11.38
	Normalized Torque	0.04	0.92	1.04	1.07	1.23
	Rotation (Deg)	1.7	57.9	72.7	82.5	142
	Maximum Strain	0.0030	0.0128	0.0139	0.0143	0.0093
	Maximum Stress (MPa)	238	243	246	249	232
	FEPR Original	1.02	1.08	1.19	1.22	1.23
FEPR Modified	1.02	1.29	1.39	1.41	1.23	

## Interaction Diagrams - Beam S5L1T1B1



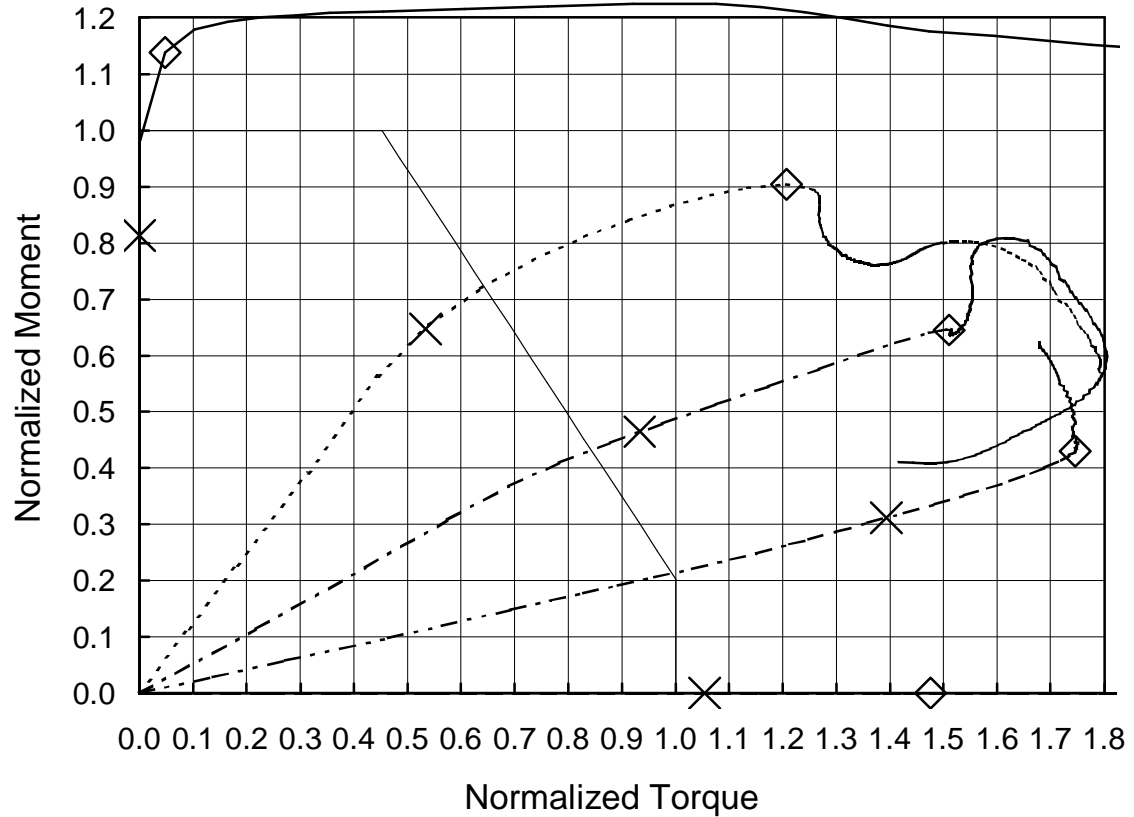
		E0	E1	E2	E3	E4
Service Load Point	Moment (kNm)	34.6	25.2	15.5	8.9	0.0
	Normalized Moment	0.78	0.57	0.35	0.20	0.00
	Torque (kNm)	0.00	0.68	1.03	1.43	1.42
	Normalized Torque	0.00	0.38	0.58	0.80	0.79
	Rotation (Deg)	0.2	1.4	2.0	2.7	2.5
	Maximum Deflection (mm)	2.73	1.75	0.99	0.65	0.07
	$L / \text{Deflection}$	391	610	1090	1650	15300
	Maximum Strain	0.0028	0.0032	0.0032	0.0042	0.0025
	Maximum Stress (MPa)	366	364	351	351	251
Ultimate Load Point	Moment (kNm)	48.5	35.3	21.8	12.4	0.0
	Normalized Moment	1.09	0.79	0.49	0.28	0.00
	Torque (kNm)	0.17	1.10	1.56	2.31	2.00
	Normalized Torque	0.10	0.62	0.87	1.29	1.12
	Rotation (Deg)	1.6	3.8	4.5	11.9	5.9
	Maximum Strain	0.0123	0.0138	0.0175	0.0468	0.0167
	Maximum Stress (MPa)	388	399	399	449	385
	FEPR Original	1.09	1.06	1.08	1.30	1.12
	FEPR Modified	1.09	1.41	1.36	1.57	1.12

## Interaction Diagrams - Beam S5L1T1B2



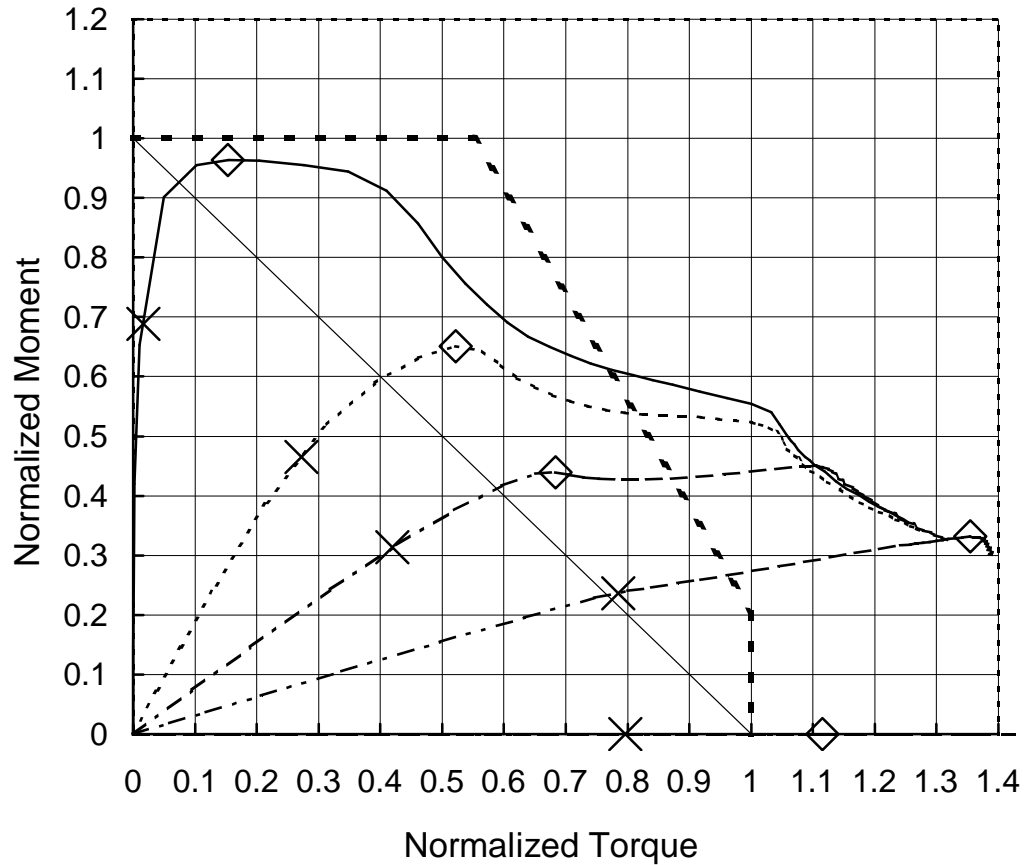
		E0	E1	E2	E3	E4
Service Load Point	Moment (kNm)	32.7	28.8	21.3	14.0	0.0
	Normalized Moment	0.73	0.65	0.48	0.31	0.00
	Torque (kNm)	0.00	1.30	2.31	3.74	5.17
	Normalized Torque	0.00	0.32	0.58	0.93	1.29
	Rotation (Deg)	0.0	0.7	1.2	2.6	10.7
	Maximum Deflection (mm)	1.53	1.34	1.00	0.81	0.09
	$L / \text{Deflection}$	701	800	1070	1320	12400
	Maximum Strain	0.0010	0.0016	0.0018	0.0024	0.0029
	Maximum Stress (MPa)	299	350	350	351	390
Ultimate Load Point	Moment (kNm)	45.7	40.3	29.8	19.6	0.0
	Normalized Moment	1.03	0.91	0.67	0.44	0.00
	Torque (kNm)	0.04	1.96	3.50	5.45	7.24
	Normalized Torque	0.01	0.49	0.88	1.36	1.81
	Rotation (Deg)	0.4	2.8	4.1	18.9	22.1
	Maximum Strain	0.0023	0.0023	0.0025	0.0174	0.0146
	Maximum Stress (MPa)	351	351	357	394	395
	FEPR Original	1.03	1.18	1.30	1.50	1.81
	FEPR Modified	1.03	1.18	1.30	1.50	1.81

### Interaction Diagrams - Beam S5L1T1B3



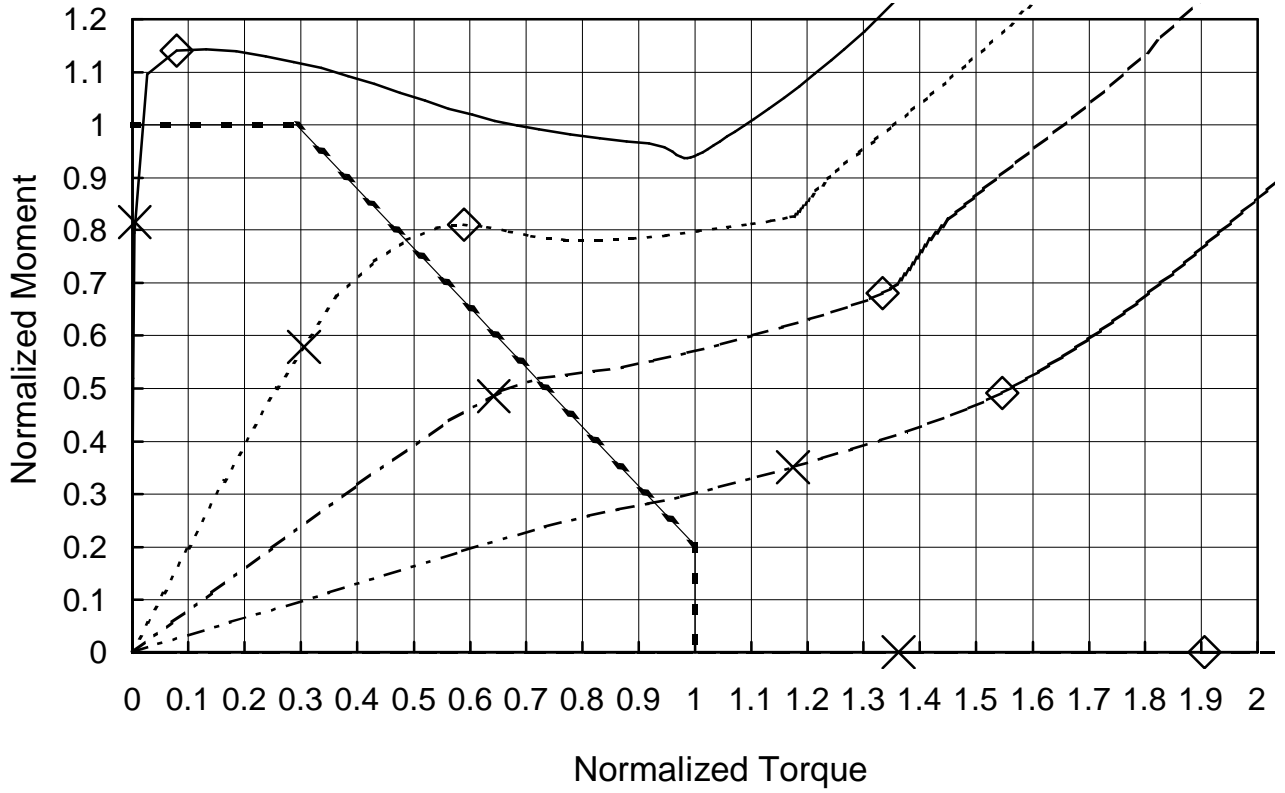
		E0	E1	E2	E3	E4
Service Load Point	Moment (kNm)	36.1	28.8	20.6	13.8	0.0
	Normalized Moment	0.81	0.65	0.46	0.31	0.00
	Torque (kNm)	0.00	0.81	1.41	2.11	1.60
	Normalized Torque	0.00	0.53	0.93	1.39	1.05
	Rotation (Deg)	0.2	9.9	18.1	31.8	7.2
	Maximum Deflection (mm)	6.09	5.98	5.99	7.01	0.08
	$L / \text{Deflection}$	176	179	178	152	12700
	Maximum Strain	0.0011	0.0037	0.0082	0.0134	0.0018
	Maximum Stress (MPa)	232	234	236	263	233
Ultimate Load Point	Moment (kNm)	50.6	40.2	28.7	19.1	0.0
	Normalized Moment	1.14	0.90	0.65	0.43	0.00
	Torque (kNm)	0.07	1.83	2.28	2.64	2.23
	Normalized Torque	0.05	1.21	1.51	1.74	1.48
	Rotation (Deg)	1.4	30.2	39.2	50.5	18.5
	Maximum Strain	0.0045	0.0171	0.0171	0.0179	0.0105
	Maximum Stress (MPa)	237	295	282	298	249
	FEPR Original	1.14	1.61	1.71	1.79	1.48
	FEPR Modified	1.14	1.61	1.71	1.79	1.48

## Interaction Diagrams - Beam S5L2T1B1



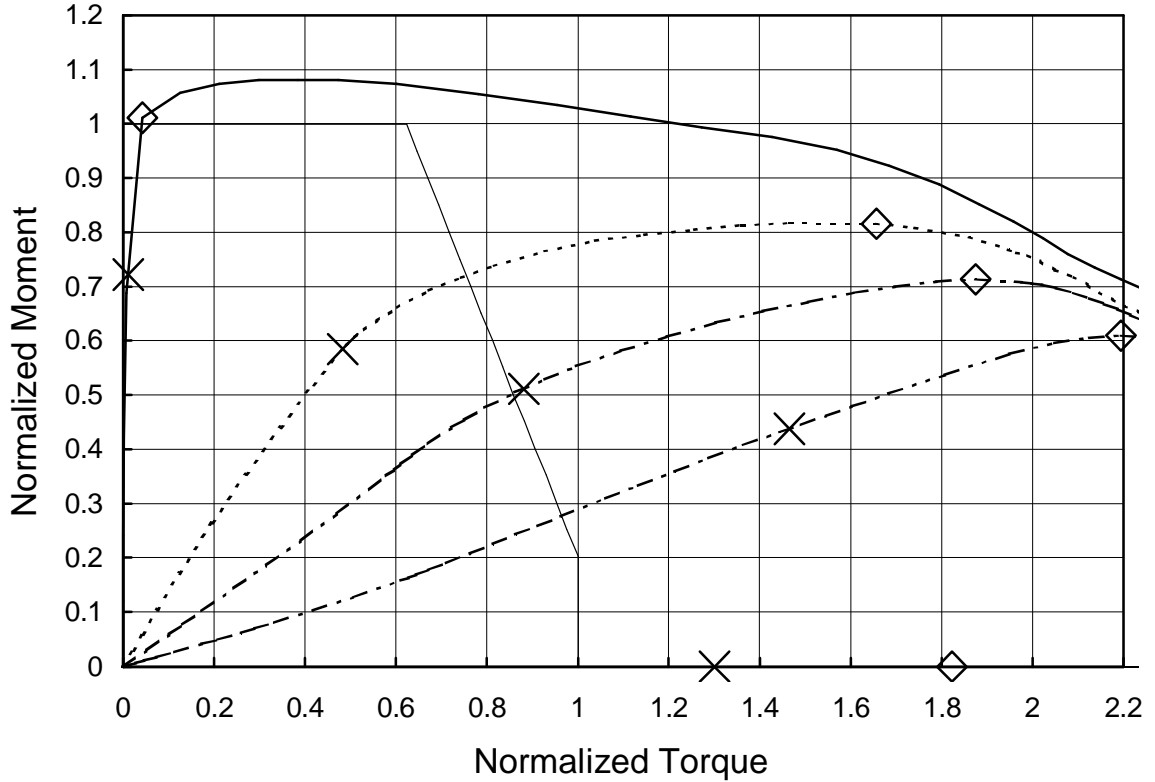
		E0	E1	E2	E3	E4
Service Load Point	Moment (kNm)	25.0	16.9	11.4	8.6	0.0
	Normalized Moment	0.69	0.47	0.31	0.24	0.00
	Torque (kNm)	0.02	0.34	0.52	0.97	0.99
	Normalized Torque	0.02	0.27	0.42	0.79	0.80
	Rotation (Deg)	1.0	4.6	5.7	11.5	10.1
	Maximum Deflection (mm)	4.22	3.25	2.48	3.69	0.55
	<i>L</i> / Deflection	507	658	863	580	3920
	Maximum Strain	0.0013	0.0021	0.0024	0.0089	0.0027
	Maximum Stress (MPa)	360	350	350	350	350
Ultimate Load Point	Moment (kNm)	35.0	23.6	15.9	12.0	0.0
	Normalized Moment	0.96	0.65	0.44	0.33	0.00
	Torque (kNm)	0.19	0.65	0.85	1.68	1.38
	Normalized Torque	0.15	0.52	0.68	1.35	1.12
	Rotation (Deg)	3.8	9.0	11.3	39.1	17.8
	Maximum Strain	0.0042	0.0074	0.0115	0.0903	0.0168
	Maximum Stress (MPa)	370	372	350	536	389
	FEPR Original	0.96	0.79	0.82	1.35	1.12
	FEPR Modified	0.96	1.17	1.12	1.69	1.12

Interaction Diagrams - Beam S5L2T1B2



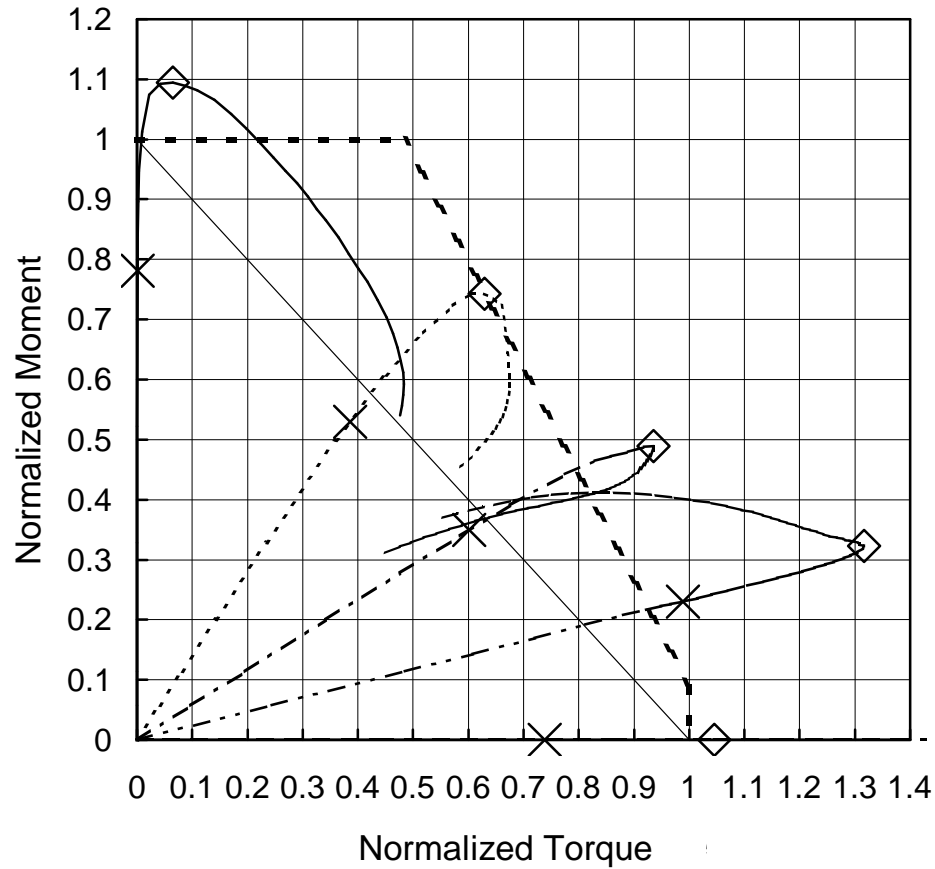
		E0	E1	E2	E3	E4
Service Load Point	Moment (kNm)	36.2	25.7	21.6	15.6	0.0
	Normalized Moment	0.81	0.58	0.49	0.35	0.00
	Torque (kNm)	0.01	0.71	1.50	2.75	3.19
	Normalized Torque	0.00	0.30	0.64	1.17	1.36
	Rotation (Deg)	0.3	2.7	6.1	18.4	24.3
	Maximum Deflection (mm)	3.72	2.73	2.84	6.24	-0.08
	<i>L</i> / Deflection	575	783	753	343	-25800
	Maximum Strain	0.0012	0.0017	0.0022	0.0015	0.0024
	Maximum Stress (MPa)	335	350	350	379	377
Ultimate Load Point	Moment (kNm)	50.7	36.0	30.2	21.9	0.0
	Normalized Moment	1.14	0.81	0.68	0.49	0.00
	Torque (kNm)	0.19	1.38	3.12	3.62	4.46
	Normalized Torque	0.08	0.59	1.33	1.55	1.91
	Rotation (Deg)	1.7	7.6	27.3	33.1	37.9
	Maximum Strain	0.0021	0.0022	0.0096	0.0113	0.0040
	Maximum Stress (MPa)	350	352	398	395	392
	FEPR Original	1.14	1.11	1.64	1.68	1.91
	FEPR Modified	1.14	1.11	1.64	1.68	1.91

Interaction Diagrams - Beam S5L2T1B3



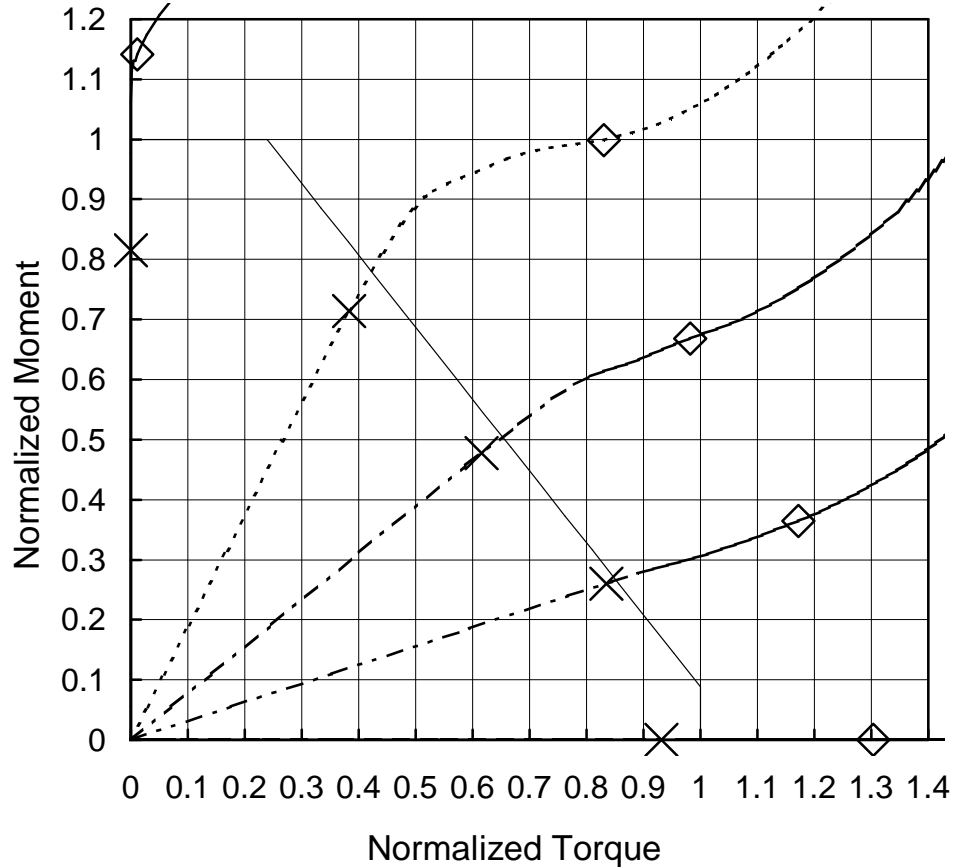
		E0	E1	E2	E3	E4
Service Load Point	Moment (kNm)	30.8	24.9	21.8	18.7	0.0
	Normalized Moment	0.72	0.58	0.51	0.44	0.00
	Torque (kNm)	0.01	0.53	0.97	1.61	1.43
	Normalized Torque	0.01	0.48	0.88	1.47	1.30
	Rotation (Deg)	0.8	20.2	35.0	53.7	46.3
	Maximum Deflection (mm)	18.89	17.53	20.55	20.27	1.20
	<i>L</i> / Deflection	113	122	104	106	1780
	Maximum Strain	0.0009	0.0020	0.0040	0.0102	0.0064
	Maximum Stress (MPa)	231	233	234	237	238
Ultimate Load Point	Moment (kNm)	43.1	34.8	30.4	26.0	0.0
	Normalized Moment	1.01	0.82	0.71	0.61	0.00
	Torque (kNm)	0.05	1.82	2.06	2.41	2.00
	Normalized Torque	0.04	1.66	1.87	2.20	1.82
	Rotation (Deg)	2.0	43.0	54.1	68.0	68.1
	Maximum Strain	0.0019	0.0121	0.0134	0.0156	0.0124
	Maximum Stress (MPa)	234	245	248	262	267
	FEPR Original	1.01	1.86	2.01	2.26	1.82
	FEPR Modified	1.01	1.86	2.01	2.26	1.82

## Interaction Diagrams - Beam S6L1T1B1



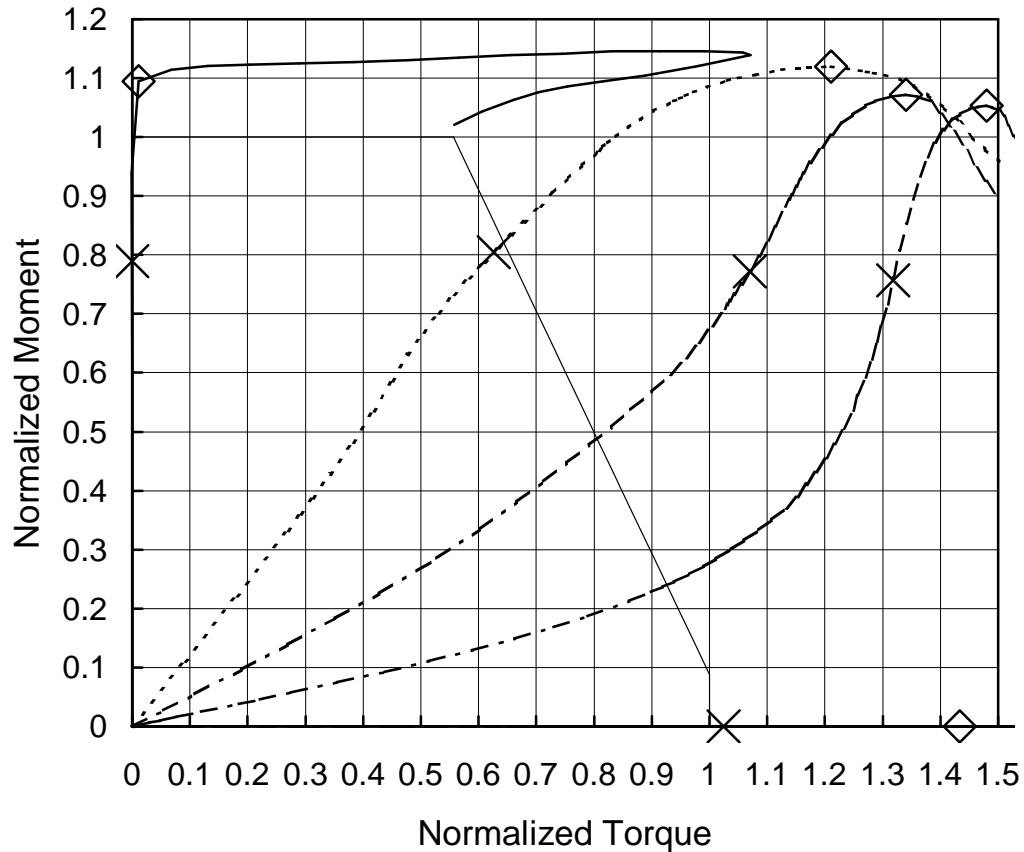
		E0	E1	E2	E3	E4
Service Load Point	Moment (kNm)	393.9	267.2	176.1	116.1	0.0
	Normalized Moment	0.78	0.53	0.35	0.23	0.00
	Torque (kNm)	0.02	9.53	14.84	24.39	18.20
	Normalized Torque	0.00	0.39	0.60	0.99	0.74
	Rotation (Deg)	0.2	3.9	5.8	13.1	6.9
	Maximum Deflection (mm)	13.27	9.44	6.80	9.15	0.35
	$L / \text{Deflection}$	290	408	566	421	10900
	Maximum Strain	0.0023	0.0033	0.0040	0.0206	0.0026
	Maximum Stress (MPa)	368	363	352	364	350
Ultimate Load Point	Moment (kNm)	551.4	374.1	246.5	162.8	0.0
	Normalized Moment	1.09	0.74	0.49	0.32	0.00
	Torque (kNm)	1.59	15.53	23.07	32.50	25.80
	Normalized Torque	0.06	0.63	0.93	1.32	1.05
	Rotation (Deg)	1.9	10.0	16.8	35.7	12.8
	Maximum Strain	0.0023	0.0235	0.0516	0.0619	0.0111
	Maximum Stress (MPa)	382	400	495	514	350
	FEPR Original	1.09	1.00	1.15	1.43	1.05
	FEPR Modified	1.09	1.37	1.42	1.64	1.05

Interaction Diagrams - Beam S6L1T1B2



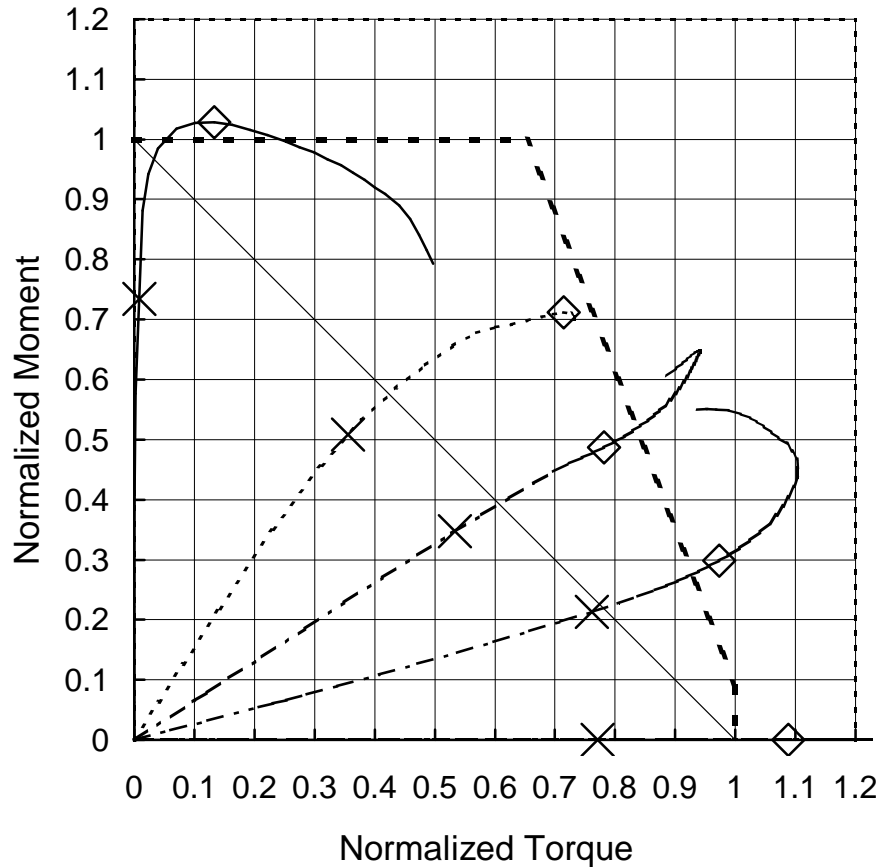
		E0	E1	E2	E3	E4
Service Load Point	Moment (kNm)	411.1	359.7	240.7	131.2	0.0
	Normalized Moment	0.82	0.71	0.48	0.26	0.00
	Torque (kNm)	0.00	19.17	30.85	41.82	46.63
	Normalized Torque	0.00	0.38	0.62	0.84	0.93
	Rotation (Deg)	0.0	2.4	3.9	6.0	7.9
	Maximum Deflection (mm)	9.39	8.39	5.99	3.92	0.19
	$L / \text{Deflection}$	410	459	643	982	20400
	Maximum Strain	0.0014	0.0027	0.0032	0.0041	0.0048
	Maximum Stress (MPa)	336	350	350	349	350
Ultimate Load Point	Moment (kNm)	575.4	503.5	337.0	183.7	0.0
	Normalized Moment	1.14	1.00	0.67	0.36	0.00
	Torque (kNm)	0.56	41.60	49.17	58.68	65.28
	Normalized Torque	0.01	0.83	0.98	1.17	1.30
	Rotation (Deg)	0.6	23.5	18.6	22.8	30.0
	Maximum Strain	0.0067	0.0119	0.0200	0.0228	0.0230
	Maximum Stress (MPa)	376	477	375	362	362
	FEPR Original	1.14	1.55	1.43	1.38	1.30
	FEPR Modified	1.14	1.55	1.43	1.38	1.30

## Interaction Diagrams - Beam S6L1T1B3



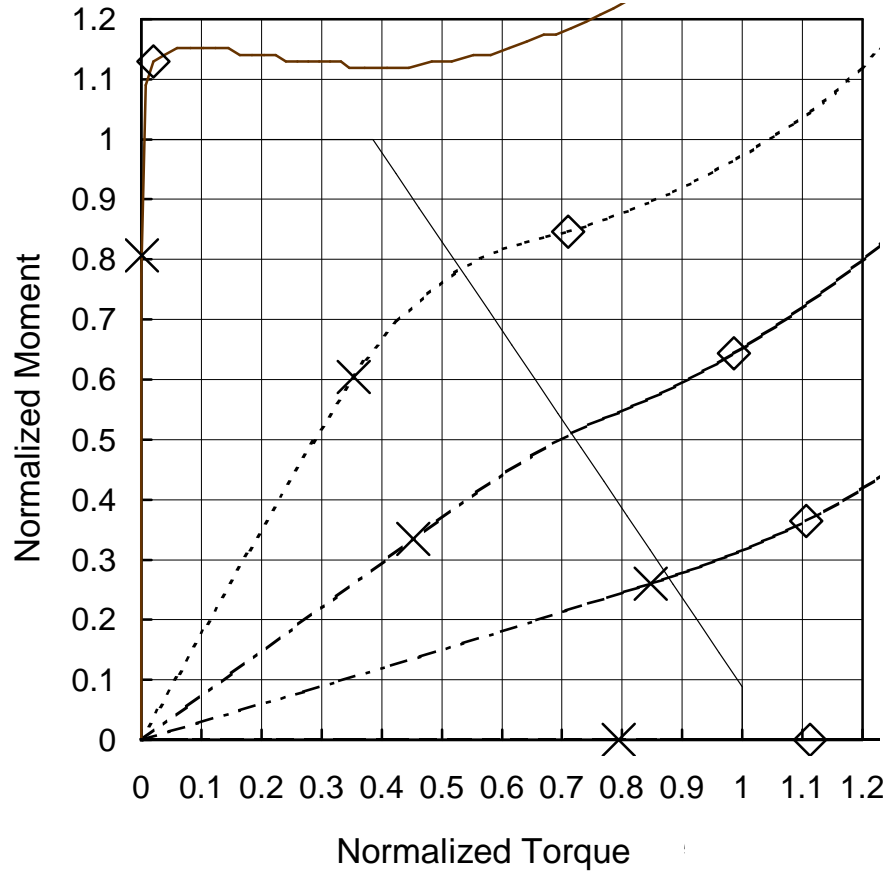
		E0	E1	E2	E3	E4
Service Load Point	Moment (kNm)	398.0	405.5	389.2	381.7	0.0
	Normalized Moment	0.79	0.80	0.77	0.76	0.00
	Torque (kNm)	-0.01	13.47	23.00	28.33	22.02
	Normalized Torque	0.00	0.63	1.07	1.32	1.02
	Rotation (Deg)	0.2	28.0	55.1	74.8	36.6
	Maximum Deflection (mm)	47.94	66.76	109.90	135.33	0.70
	$L / \text{Deflection}$	80	58	35	28	5490
	Maximum Strain	0.0010	0.0064	0.0136	0.0172	0.0036
	Maximum Stress (MPa)	233	237	240	266	219
Ultimate Load Point	Moment (kNm)	551.5	564.1	540.5	530.8	0.0
	Normalized Moment	1.09	1.12	1.07	1.05	0.00
	Torque (kNm)	0.23	26.03	28.80	31.82	30.83
	Normalized Torque	0.01	1.21	1.34	1.48	1.43
	Rotation (Deg)	0.7	58.3	74.5	83.8	73.0
	Maximum Strain	0.0038	0.0229	0.0240	0.0168	0.0120
	Maximum Stress (MPa)	236	284	285	268	251
	FEPR Original	1.09	1.68	1.79	1.91	1.43
	FEPR Modified	1.09	1.68	1.79	1.91	1.43

### Interaction Diagrams - Beam S6L2T1B1



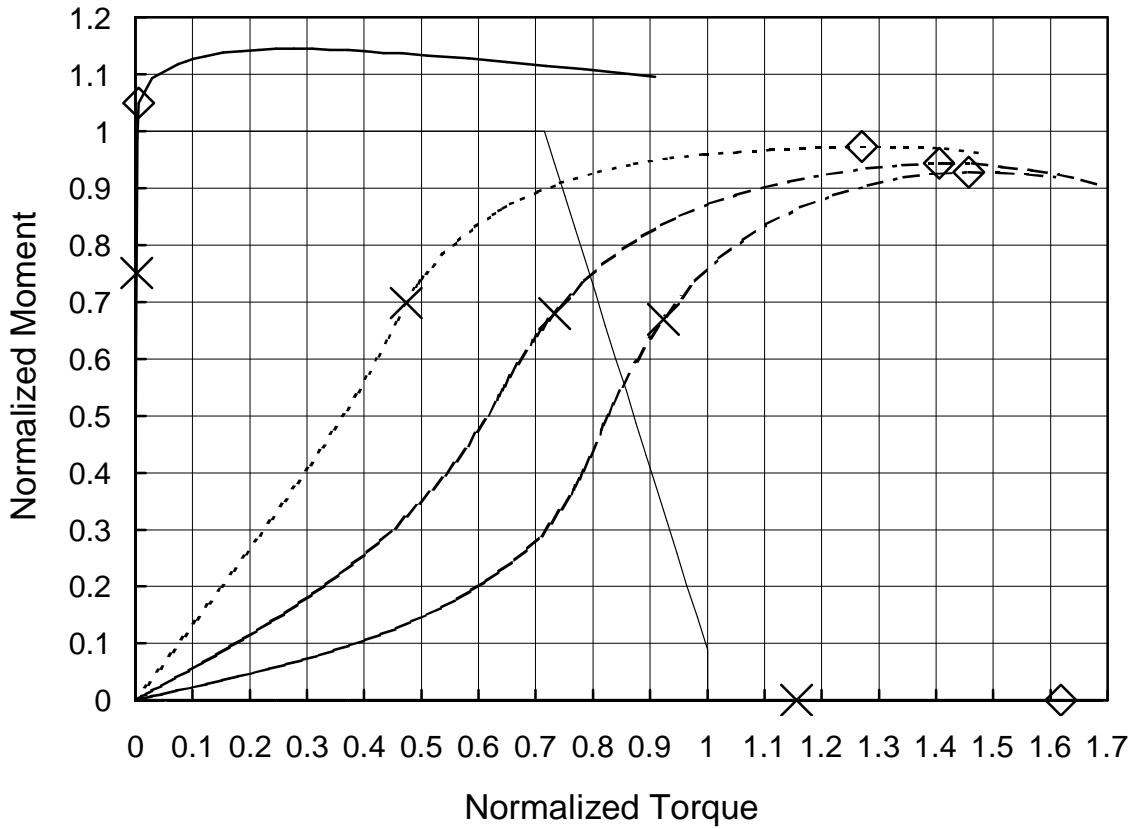
		E0	E1	E2	E3	E4
Service Load Point	Moment (kNm)	335.7	232.2	158.8	97.3	0.0
	Normalized Moment	0.73	0.51	0.35	0.21	0.00
	Torque (kNm)	0.15	6.52	9.78	13.94	14.13
	Normalized Torque	0.01	0.36	0.53	0.76	0.77
	Rotation (Deg)	1.1	11.9	17.1	24.0	23.3
	Maximum Deflection (mm)	38.93	31.58	24.87	20.75	2.84
	<i>L</i> / Deflection	198	244	310	371	2710
	Maximum Strain	0.0015	0.0032	0.0036	0.0046	0.0025
	Maximum Stress (MPa)	361	351	351	350	350
Ultimate Load Point	Moment (kNm)	470.0	325.1	222.3	136.3	0.0
	Normalized Moment	1.03	0.71	0.49	0.30	0.00
	Torque (kNm)	2.43	13.08	14.31	17.83	19.94
	Normalized Torque	0.13	0.71	0.78	0.97	1.09
	Rotation (Deg)	6.9	35.8	31.3	38.9	36.8
	Maximum Strain	0.0050	0.0402	0.0212	0.0241	0.0078
	Maximum Stress (MPa)	377	471	380	382	349
	FEPR Original	1.03	0.95	0.93	1.05	1.09
	FEPR Modified	1.03	1.43	1.27	1.27	1.09

Interaction Diagrams - Beam S6L2T1B2



		E0	E1	E2	E3	E4
Service Load Point	Moment (kNm)	406.7	304.6	168.6	131.2	0.0
	Normalized Moment	0.81	0.60	0.33	0.26	0.00
	Torque (kNm)	0.02	10.98	14.05	26.31	24.66
	Normalized Torque	0.00	0.35	0.45	0.85	0.79
	Rotation (Deg)	0.3	8.1	9.8	22.0	17.9
	Maximum Deflection (mm)	26.03	20.45	11.40	15.30	0.50
	$L / \text{Deflection}$	296	376	675	503	15500
	Maximum Strain	0.0014	0.0023	0.0020	0.0039	0.0023
	Maximum Stress (MPa)	340	350	350	357	350
Ultimate Load Point	Moment (kNm)	569.3	426.5	324.3	183.6	0.0
	Normalized Moment	1.13	0.85	0.64	0.36	0.00
	Torque (kNm)	0.61	22.02	30.58	34.31	34.52
	Normalized Torque	0.02	0.71	0.99	1.11	1.11
	Rotation (Deg)	1.2	25.0	35.3	37.5	37.8
	Maximum Strain	0.0025	0.0118	0.0161	0.0108	0.0065
	Maximum Stress (MPa)	350	375	402	403	378
	FEPR Original	1.13	1.21	1.34	1.28	1.11
	FEPR Modified	1.13	1.21	1.34	1.28	1.11

**Interaction Diagrams - Beam S6L2T1B3**



		E0	E1	E2	E3	E4
Service Load Point	Moment (kNm)	370.7	344.9	335.6	330.6	0.0
	Normalized Moment	0.75	0.70	0.68	0.67	0.00
	Torque (kNm)	0.03	7.92	12.25	15.45	19.34
	Normalized Torque	0.00	0.47	0.73	0.92	1.16
	Rotation (Deg)	0.6	38.8	59.4	75.4	97.6
	Maximum Deflection (mm)	167.00	168.57	189.14	213.37	4.02
	<i>L</i> / Deflection	46	46	41	36	1920
	Maximum Strain	0.0009	0.0022	0.0034	0.0050	0.0029
	Maximum Stress (MPa)	231	230	231	233	218
Ultimate Load Point	Moment (kNm)	518.8	480.4	466.2	458.6	0.0
	Normalized Moment	1.05	0.97	0.94	0.93	0.00
	Torque (kNm)	0.10	21.26	23.52	24.40	27.07
	Normalized Torque	0.01	1.27	1.41	1.46	1.62
	Rotation (Deg)	1.2	62.9	75.5	83.6	167
	Maximum Strain	0.0016	0.0131	0.0140	0.0145	0.0103
	Maximum Stress (MPa)	234	241	250	256	236
	FEPR Original	1.05	1.53	1.66	1.70	1.62
	FEPR Modified	1.05	1.53	1.66	1.70	1.62

## **APPENDIX C**

### Complementary Case Results

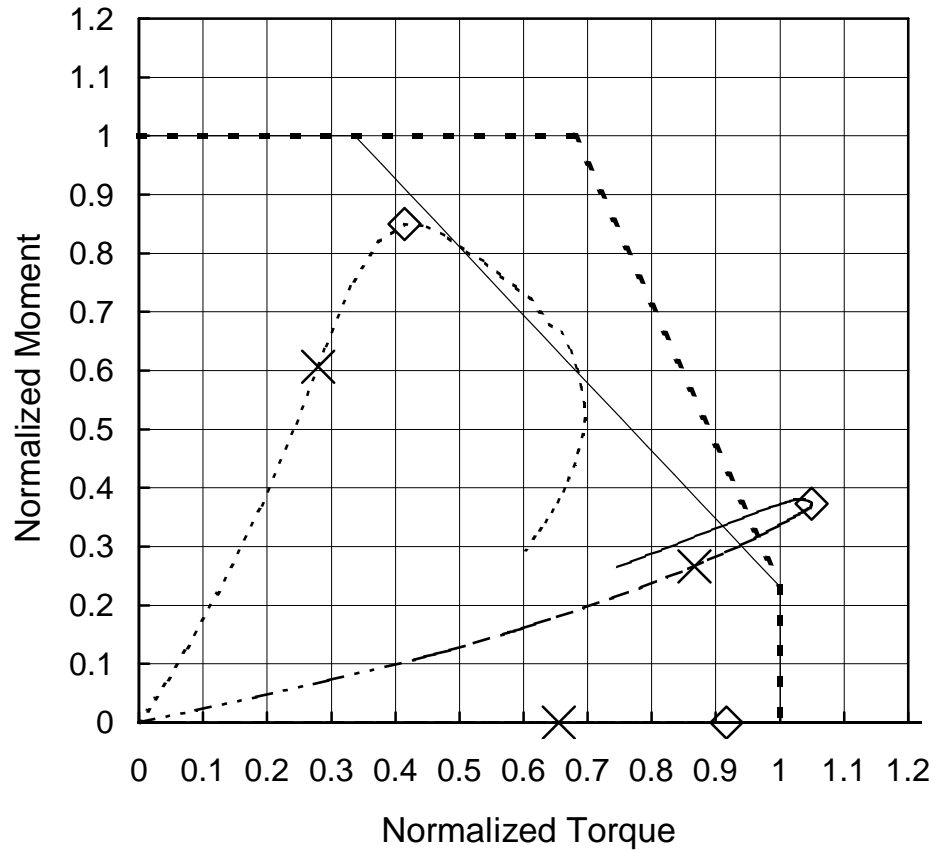
## APPENDIX C – COMPLEMENTARY CASE RESULTS

This appendix contains a complete presentation of the data describing the ultimate limit state and serviceability limit states (including moment, normalized moment, torque, normalized torque, deflection, rotation, maximum cross-sectional strain and stress, and Finite Element to Predicted Ratio (FEPR) values for both the original and modified interaction diagrams) as well as the resulting ultimate moment–torque interaction diagrams. The moment and torque values are normalized by dividing the moment and torque values by their respective resistances. This appendix includes the results of all of the beams analyzed as complementary cases discussed in Chapter 7.

### Legend:

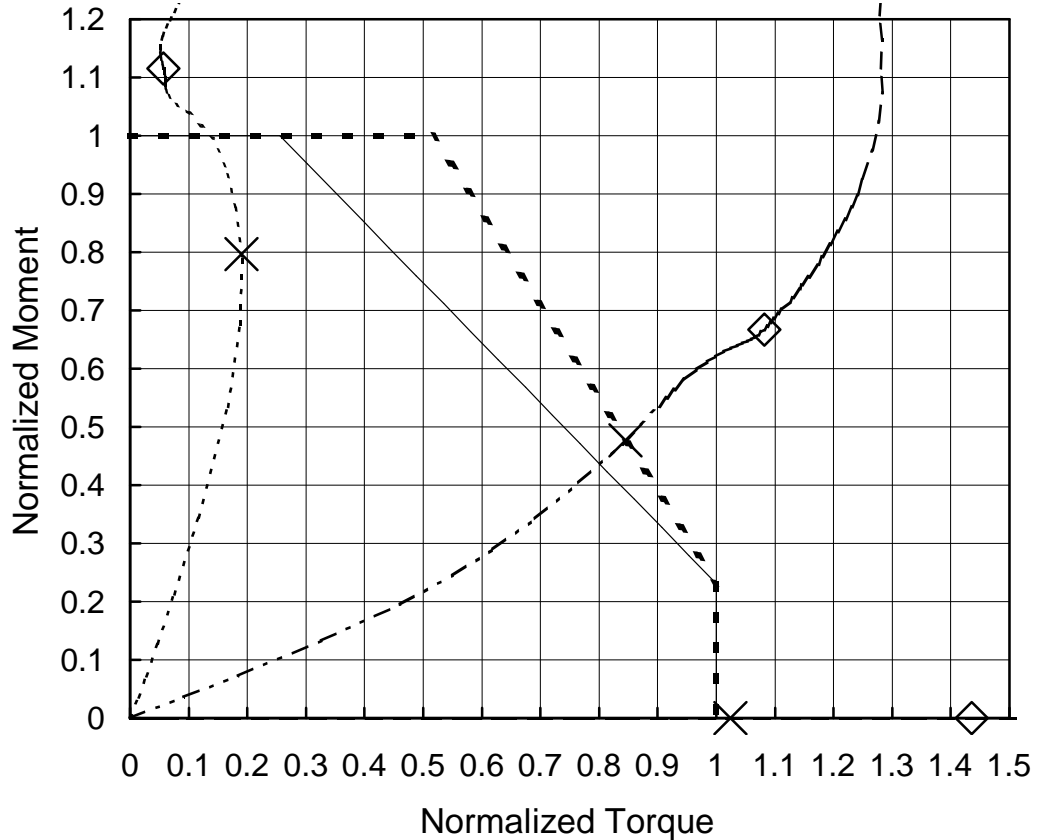
- E0 Beam (Pure moment case)
- x--x- E0.5 Beam (Half of minimum eccentricity case)
- E1 Beam (Minimum eccentricity case)
- E2 Beam (Medium eccentricity case)
- E3 Beam (Maximum eccentricity case)
- E4 Beam (Torsion only loading case)
- Modified Interaction Equation
- - - - Original Interaction Equation

**Interaction Diagrams - Beam SPL1T1B1**



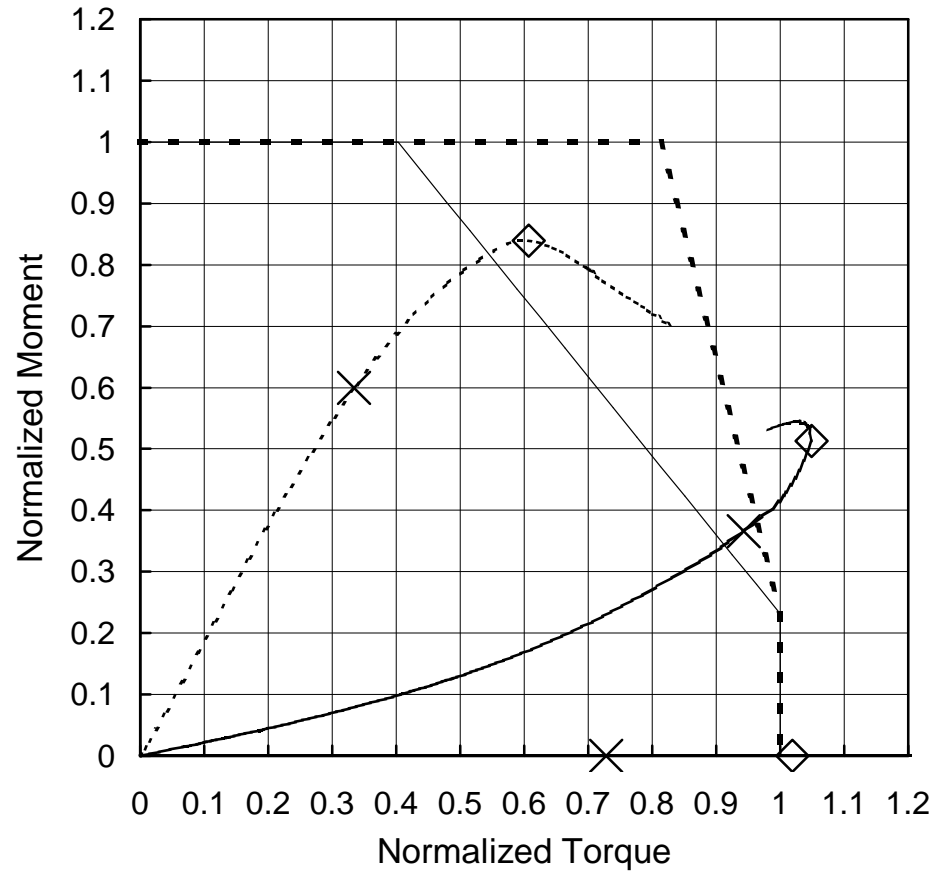
		E1	E3	E4
Service Load Point	Moment (kNm)	443.3	194.7	0.0
	Normalized Moment	0.61	0.27	0.00
	Torque (kNm)	8.00	24.77	18.72
	Normalized Torque	0.28	0.87	0.65
	Rotation (Deg)	15.5	42.4	37.6
	Maximum Deflection (mm)	14.62	-18.02	-28.80
	<i>L</i> / Deflection	406	330	206
	Maximum Strain	0.0068	0.0322	0.0340
	Maximum Stress (MPa)	380	432	445
Ultimate Load Point	Moment (kNm)	620.7	272.6	0.0
	Normalized Moment	0.85	0.37	0.00
	Torque (kNm)	11.84	30.00	26.20
	Normalized Torque	0.41	1.05	0.92
	Rotation (Deg)	24.2	63.4	58.1
	Maximum Strain	0.0129	0.0390	0.0520
	Maximum Stress (MPa)	431	462	447
	FEPR Original	0.85	1.18	0.92
	FEPR Modified	0.96	1.42	0.92

### Interaction Diagrams - Beam SPL1T1B2



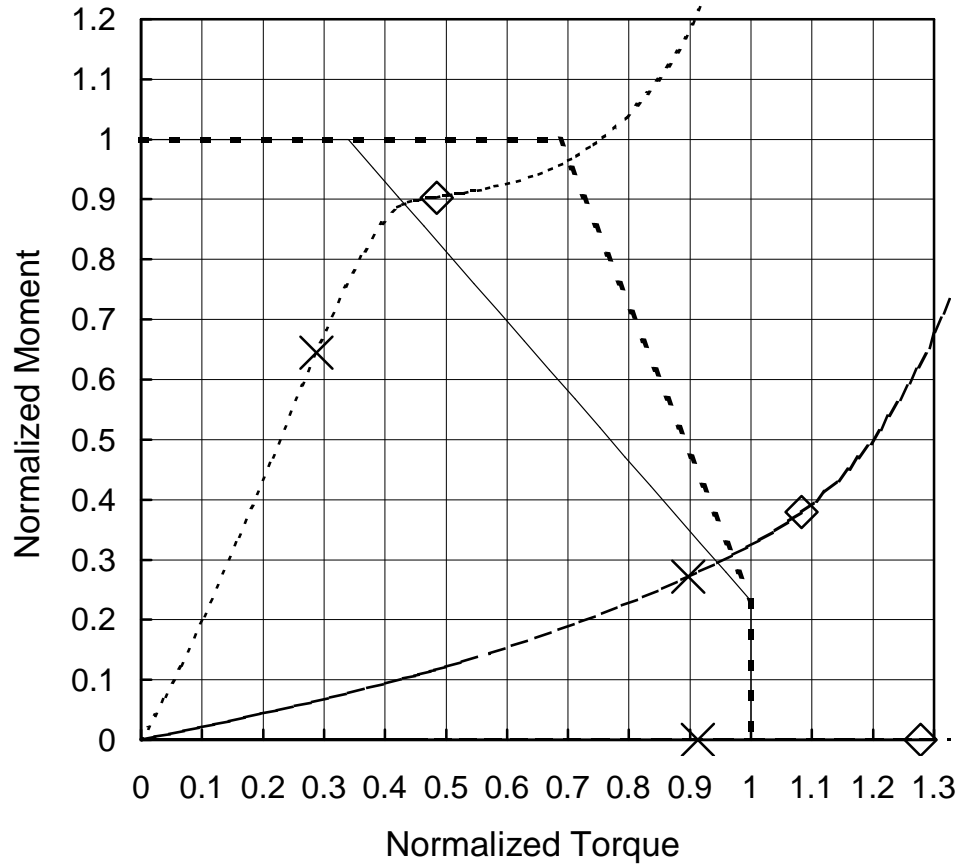
		E1	E3	E4
Service Load Point	Moment (kNm)	581.9	348.0	0.0
	Normalized Moment	0.80	0.48	0.00
	Torque (kNm)	7.17	31.83	38.62
	Normalized Torque	0.19	0.84	1.02
	Rotation (Deg)	6.3	28.4	28.2
	Maximum Deflection (mm)	14.10	5.82	-8.11
	$L / \text{Deflection}$	421	1020	733
	Maximum Strain	0.0016	0.0047	0.0037
	Maximum Stress (MPa)	378	393	379
Ultimate Load Point	Moment (kNm)	814.6	487.2	0.0
	Normalized Moment	1.12	0.67	0.00
	Torque (kNm)	2.14	40.76	54.10
	Normalized Torque	0.06	1.08	1.44
	Rotation (Deg)	12.9	53.1	38.4
	Maximum Strain	0.0110	0.0379	0.0076
	Maximum Stress (MPa)	386	463	383
	FEPR Original	1.12	1.33	1.44
	FEPR Modified	1.12	1.45	1.44

### Interaction Diagrams - Beam SPL2T1B1



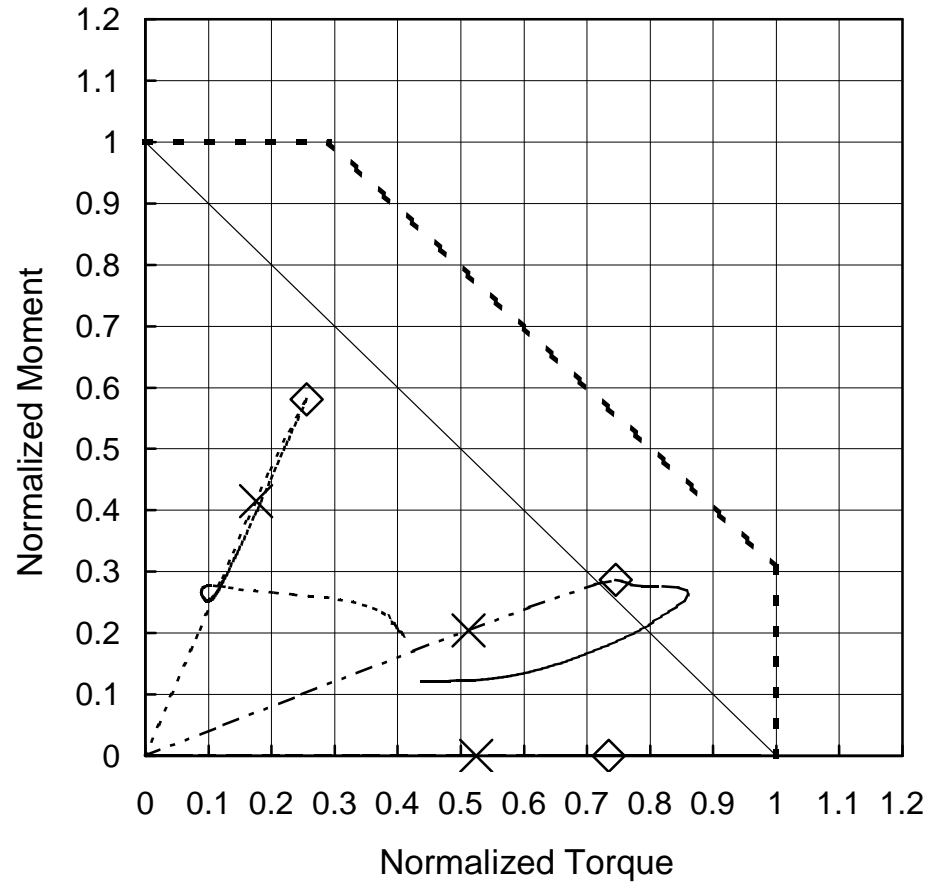
		E1	E3	E4
Service Load Point	Moment (kNm)	278.3	170.0	0.0
	Normalized Moment	0.60	0.37	0.00
	Torque (kNm)	7.99	22.54	17.40
	Normalized Torque	0.33	0.94	0.73
	Rotation (Deg)	28.0	78.1	74.0
	Maximum Deflection (mm)	27.64	-30.00	-140.4
	$L / \text{Deflection}$	441	407	87
	Maximum Strain	0.0017	0.0137	0.0269
	Maximum Stress (MPa)	349	423	442
Ultimate Load Point	Moment (kNm)	389.6	238.1	0.0
	Normalized Moment	0.84	0.51	0.00
	Torque (kNm)	14.52	25.08	24.36
	Normalized Torque	0.61	1.05	1.02
	Rotation (Deg)	45.7	88.4	99.8
	Maximum Strain	0.0060	0.0405	0.0454
	Maximum Stress (MPa)	415	493	446
	FEPR Original	0.84	1.19	1.02
	FEPR Modified	1.06	1.56	1.02

### Interaction Diagrams - Beam SPL2T1B2



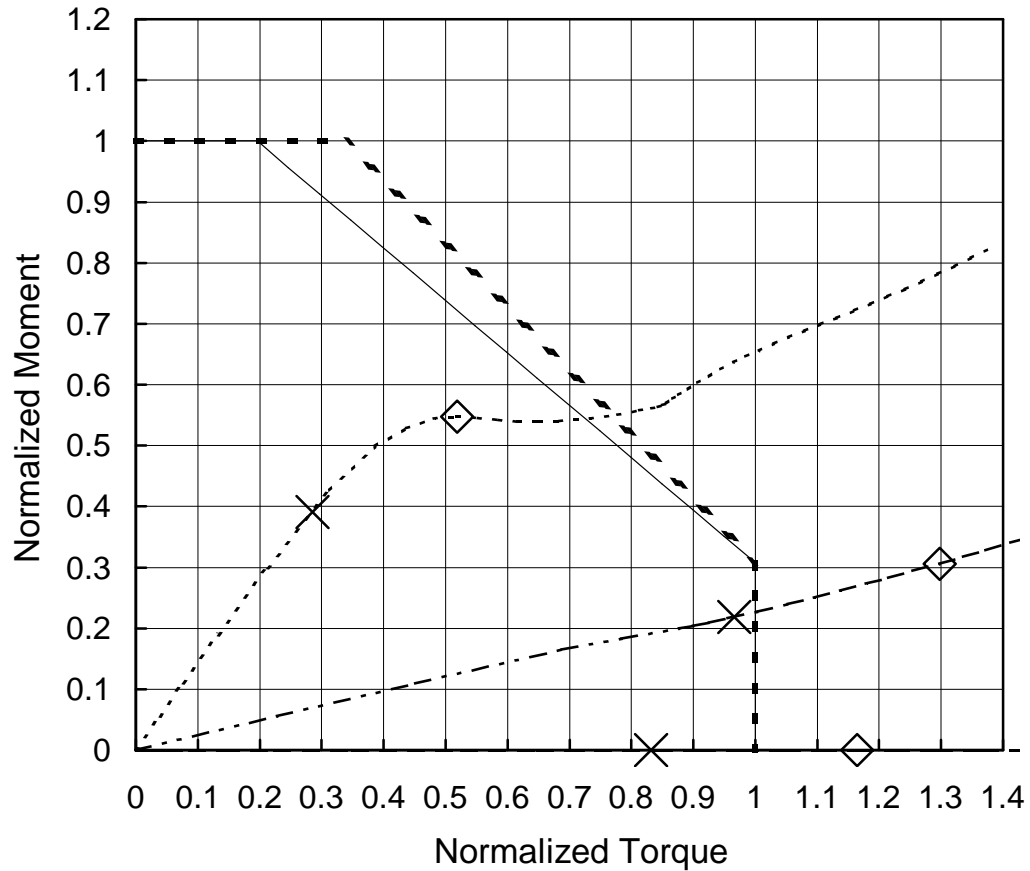
		E1	E3	E4
Service Load Point	Moment (kNm)	446.0	187.8	0.0
	Normalized Moment	0.64	0.27	0.00
	Torque (kNm)	8.15	25.44	25.88
	Normalized Torque	0.29	0.90	0.91
	Rotation (Deg)	20.1	55.9	53.9
	Maximum Deflection (mm)	33.09	1.00	-28.74
	$L / \text{Deflection}$	369	12200	424
	Maximum Strain	0.0019	0.0064	0.0036
	Maximum Stress (MPa)	381	381	379
Ultimate Load Point	Moment (kNm)	624.5	262.9	0.0
	Normalized Moment	0.90	0.38	0.00
	Torque (kNm)	13.75	30.70	36.23
	Normalized Torque	0.49	1.08	1.28
	Rotation (Deg)	36.7	69.1	69.9
	Maximum Strain	0.0091	0.0195	0.0076
	Maximum Stress (MPa)	384	395	383
	FEPR Original	0.90	1.15	1.28
	FEPR Modified	1.06	1.20	1.28

### Interaction Diagrams - Beam S7L1T1B1



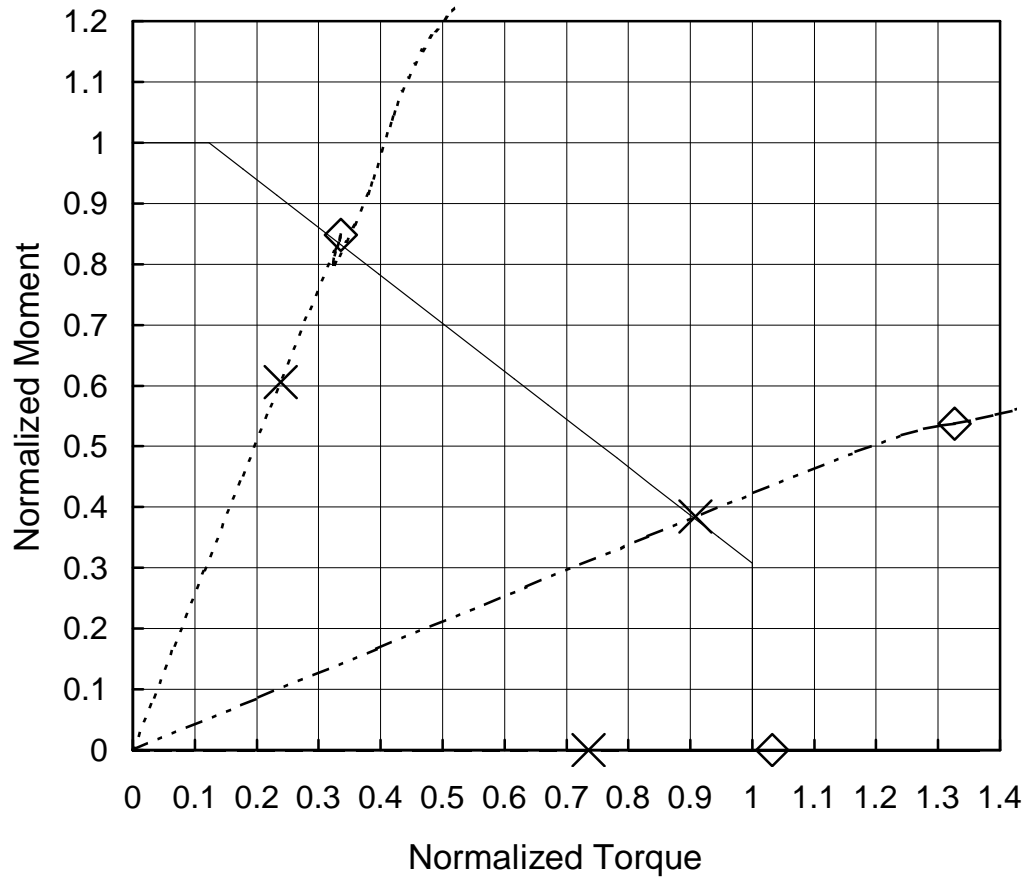
		E1	E3	E4
Service Load Point	Moment (kNm)	1359.5	670.4	0.0
	Normalized Moment	0.41	0.20	0.00
	Torque (kNm)	26.95	78.90	80.73
	Normalized Torque	0.18	0.51	0.52
	Rotation (Deg)	0.5	1.4	1.7
	Maximum Deflection (mm)	9.48	2.35	0.16
	$L / \text{Deflection}$	331	1340	19100
	Maximum Strain	0.0014	0.0027	0.0028
	Maximum Stress (MPa)	351	350	350
Ultimate Load Point	Moment (kNm)	1903.2	938.5	0.0
	Normalized Moment	0.58	0.29	0.00
	Torque (kNm)	39.33	114.79	113.11
	Normalized Torque	0.26	0.75	0.73
	Rotation (Deg)	1.0	2.9	5.7
	Maximum Strain	0.0028	0.0084	0.0138
	Maximum Stress (MPa)	351	350	391
	FEPR Original	0.70	0.79	0.74
	FEPR Modified	0.84	1.03	0.74

### Interaction Diagrams - Beam S7L3T1B2



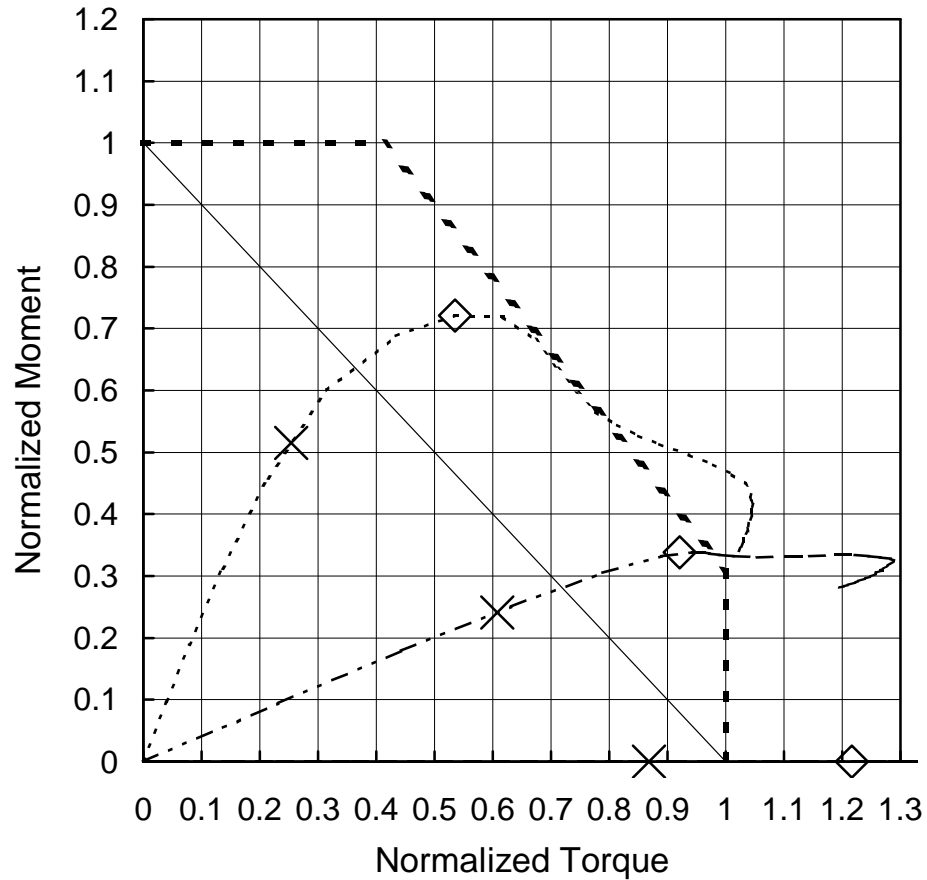
		E1	E3	E4
Service Load Point	Moment (kNm)	1175.4	656.8	0.0
	Normalized Moment	0.39	0.22	0.00
	Torque (kNm)	37.66	127.70	109.96
	Normalized Torque	0.28	0.97	0.83
	Rotation (Deg)	2.4	12.4	9.7
	Maximum Deflection (mm)	6.39	12.91	3.29
	<i>L</i> / Deflection	1230	607	2390
	Maximum Strain	0.0022	0.0093	0.0215
	Maximum Stress (MPa)	350	391	395
Ultimate Load Point	Moment (kNm)	1645.8	919.5	0.0
	Normalized Moment	0.55	0.31	0.00
	Torque (kNm)	68.52	171.55	153.93
	Normalized Torque	0.52	1.30	1.16
	Rotation (Deg)	6.0	22.6	16.5
	Maximum Strain	0.0067	0.0221	0.0290
	Maximum Stress (MPa)	350	397	408
	FEPR Original	0.80	1.20	1.17
	FEPR Modified	0.84	1.18	1.17

### Interaction Diagrams - Beam S8L1T1B2



		E1	E3	E4
Service Load Point	Moment (kNm)	3331.4	2112.6	0.0
	Normalized Moment	0.61	0.38	0.00
	Torque (kNm)	114.34	435.94	353.11
	Normalized Torque	0.24	0.91	0.74
	Rotation (Deg)	0.4	1.1	1.7
	Maximum Deflection (mm)	4.65	3.00	0.06
	<i>L</i> / Deflection	1120	1740	83000
	Maximum Strain	0.0012	0.0031	0.0027
	Maximum Stress (MPa)	326	354	353
Ultimate Load Point	Moment (kNm)	4663.9	2957.6	0.0
	Normalized Moment	0.85	0.54	0.00
	Torque (kNm)	161.28	636.56	495.19
	Normalized Torque	0.34	1.33	1.03
	Rotation (Deg)	0.7	3.0	4.7
	Maximum Strain	0.0021	0.0183	0.0280
	Maximum Stress (MPa)	350	392	401
	FEPR Original	1.01	1.39	1.03
	FEPR Modified	1.01	1.39	1.03

### Interaction Diagrams - Beam S8L3T1B1

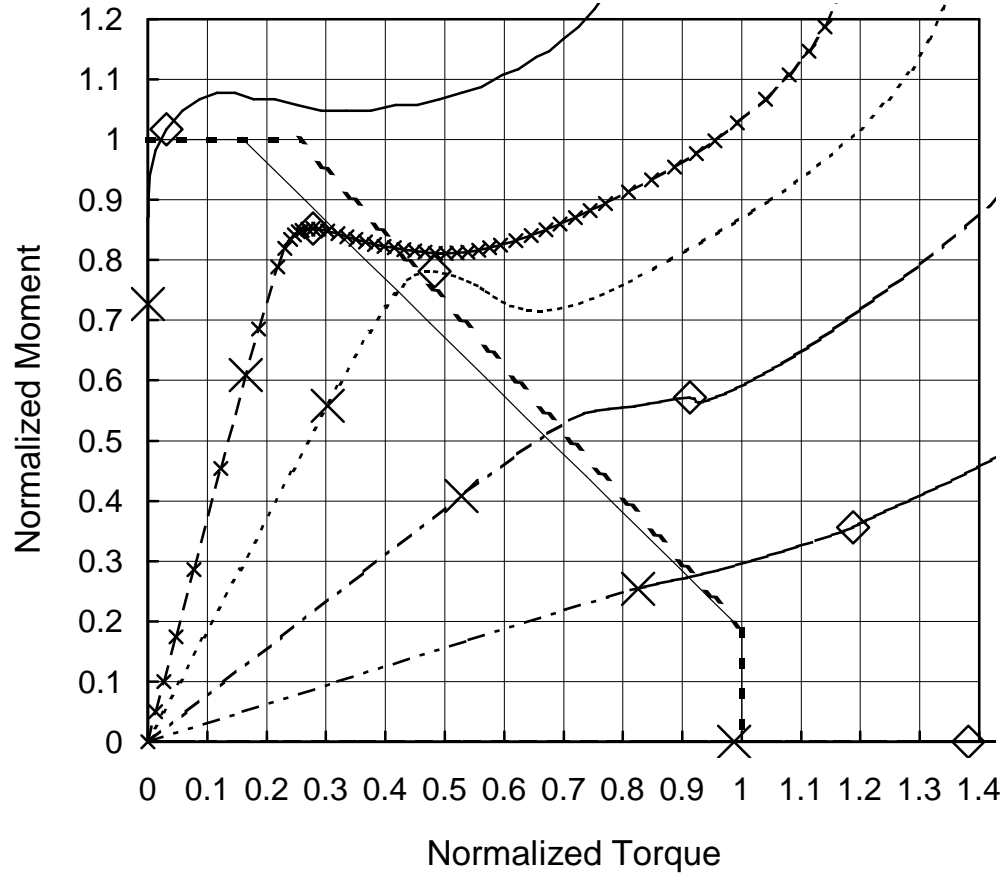


		E1	E3	E4
Service Load Point	Moment (kNm)	2511.9	1178.1	0.0
	Normalized Moment	0.51	0.24	0.00
	Torque (kNm)	36.17	86.55	123.67
	Normalized Torque	0.25	0.61	0.87
	Rotation (Deg)	2.9	6.3	8.8
	Maximum Deflection (mm)	12.74	8.66	2.45
	$L / \text{Deflection}$	1030	1510	5340
	Maximum Strain	0.0014	0.0021	0.0022
	Maximum Stress (MPa)	333	350	350
Ultimate Load Point	Moment (kNm)	3516.9	1649.4	0.0
	Normalized Moment	0.72	0.34	0.00
	Torque (kNm)	76.21	131.18	173.14
	Normalized Torque	0.54	0.92	1.22
	Rotation (Deg)	6.9	12.3	13.7
	Maximum Strain	0.0040	0.0100	0.0075
	Maximum Stress (MPa)	350	354	350
	FEPR Original	0.89	0.90	1.22
	FEPR Modified	1.26	1.26	1.22



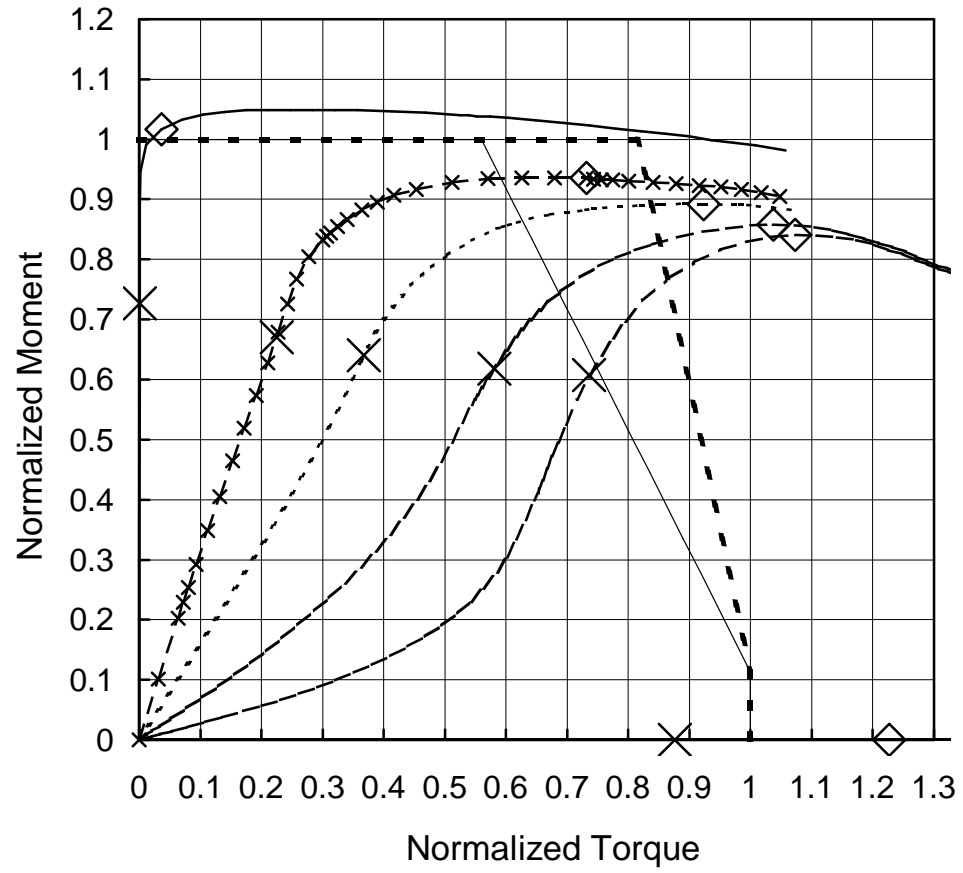
		E0	E0.5	E1	E2	E3	E4
Service Load Point	Moment (kNm)	50.4	44.3	40.3	35.6	17.2	0.0
	Normalized Moment	0.75	0.66	0.60	0.53	0.26	0.00
	Torque (kNm)	0.01	0.96	1.76	4.04	4.17	4.69
	Normalized Torque	0.00	0.15	0.27	0.62	0.64	0.72
	Rotation (Deg)	0.3	3.1	5.8	18.4	16.8	21.9
	Maximum Deflection (mm)	5.82	5.16	5.11	9.85	4.56	-0.04
	$L$ / Deflection	420	474	478	248	536	66100
	Maximum Strain	0.0013	0.0018	0.0022	0.0027	0.0025	0.0155
	Maximum Stress (MPa)	336	349	350	360	353	349
Ultimate Load Point	Moment (kNm)	70.6	62.1	56.4	49.9	24.1	0.0
	Normalized Moment	1.05	0.92	0.84	0.74	0.36	0.00
	Torque (kNm)	0.14	2.53	4.61	5.93	5.53	6.57
	Normalized Torque	0.02	0.39	0.71	0.92	0.85	1.01
	Rotation (Deg)	1.1	12.5	27.9	42.4	32.2	47.7
	Maximum Strain	0.0020	0.0026	0.0042	0.0050	0.0029	0.0299
	Maximum Stress (MPa)	350	353	377	385	372	416
	FEPR Original	1.05	0.82	1.07	1.21	0.96	1.02
	FEPR Modified	1.05	1.04	1.26	1.36	1.02	1.02

Interaction Diagrams - Beam S3L1T1B2



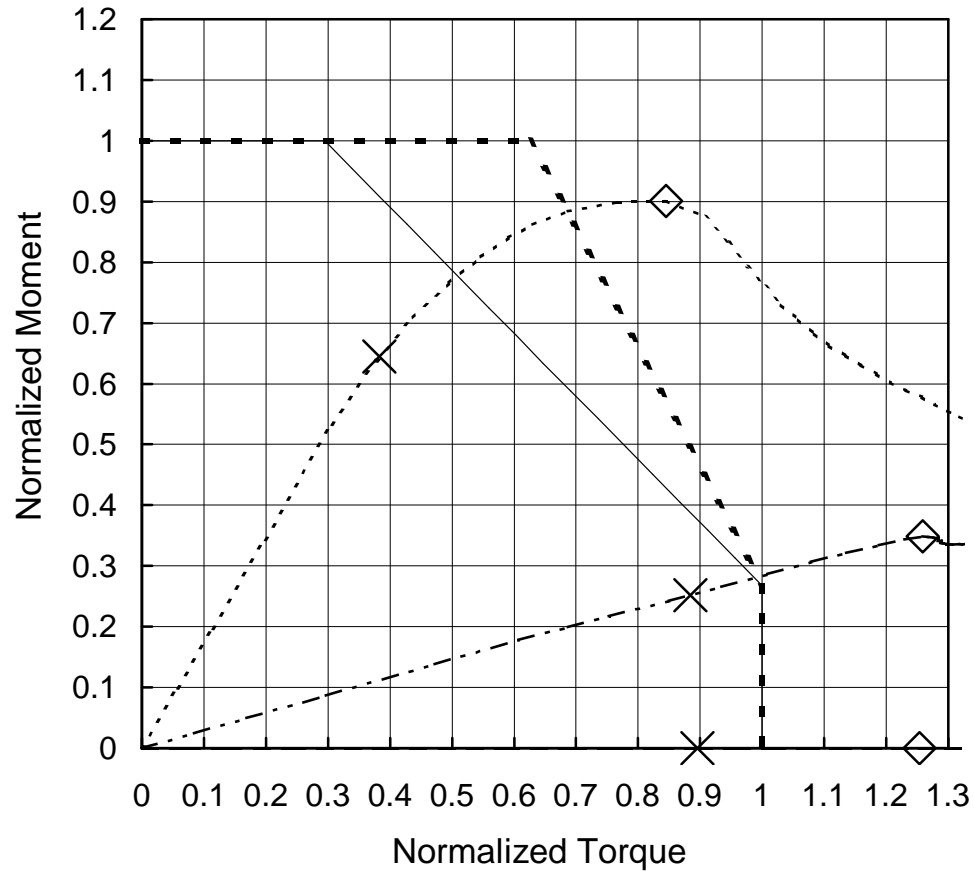
		E0	E0.5	E1	E2	E3	E4
Service Load Point	Moment (kNm)	679.3	568.7	521.4	381.6	237.8	0.0
	Normalized Moment	0.73	0.61	0.56	0.41	0.25	0.00
	Torque (kNm)	0.01	14.14	25.91	45.25	70.74	84.56
	Normalized Torque	0.00	0.17	0.30	0.53	0.83	0.99
	Rotation (Deg)	0.0	0.6	1.0	1.8	4.2	9.8
	Maximum Deflection (mm)	6.63	5.33	4.92	3.70	3.12	1.01
	$L$ / Deflection	500	622	674	897	1060	3300
	Maximum Strain	0.0014	0.0018	0.0024	0.0034	0.0085	0.0221
	Maximum Stress (MPa)	351	346	350	350	348	391
Ultimate Load Point	Moment (kNm)	951.0	796.2	730.0	534.2	332.9	0.0
	Normalized Moment	1.02	0.85	0.78	0.57	0.36	0.00
	Torque (kNm)	2.70	23.85	41.36	78.18	101.69	118.39
	Normalized Torque	0.03	0.28	0.48	0.91	1.19	1.38
	Rotation (Deg)	1.1	3.6	5.2	12.8	20.8	24.1
	Maximum Strain	0.0207	0.0124	0.0173	0.0330	0.0445	0.0424
	Maximum Stress (MPa)	404	399	396	433	448	447
	FEPR Original	1.02	0.91	1.03	1.23	1.29	1.38
	FEPR Modified	1.02	0.97	1.08	1.26	1.30	1.38

Interaction Diagrams - Beam S4L2T1B3



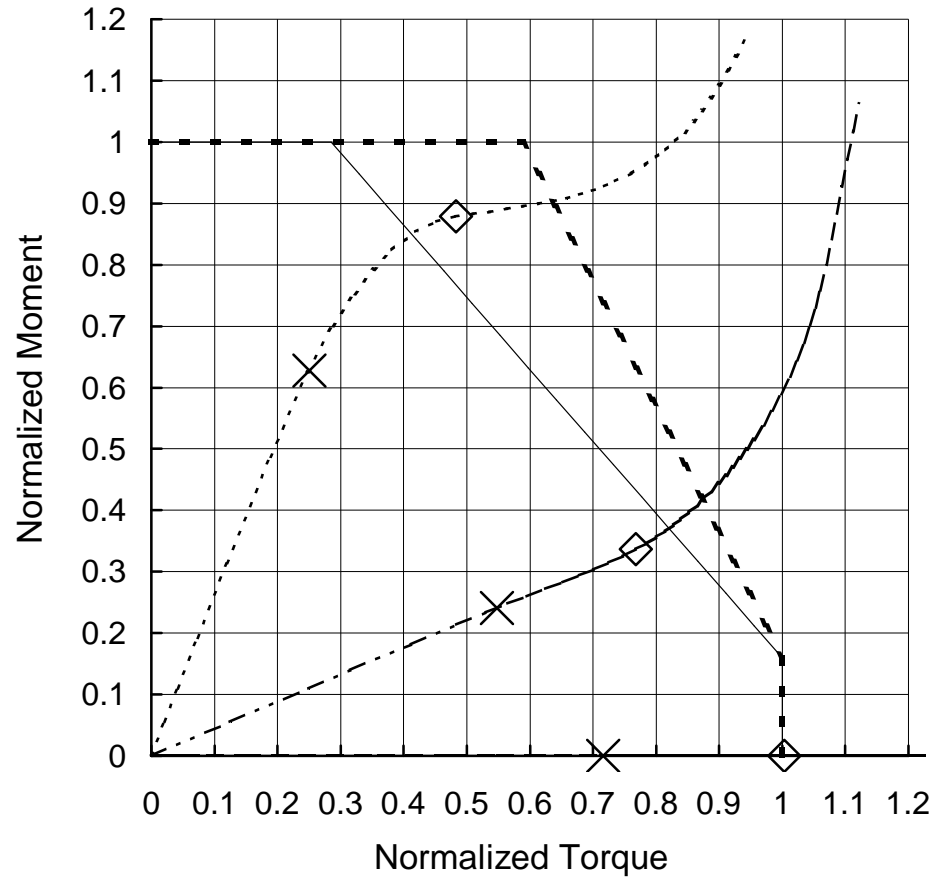
		E0	E0.5	E1	E2	E3	E4
Service Load Point	Moment (kNm)	142.7	131.6	125.8	121.4	119.2	0.0
	Normalized Moment	0.73	0.67	0.64	0.62	0.61	0.00
	Torque (kNm)	0.01	2.09	3.41	5.39	6.83	8.13
	Normalized Torque	0.00	0.22	0.37	0.58	0.74	0.88
	Rotation (Deg)	0.5	20.5	34.4	55.4	73.8	73.8
	Maximum Deflection (mm)	122.33	114.22	114.53	126.93	145.82	2.29
	<i>L</i> / Deflection	42	45	45	41	35	2260
	Maximum Strain	0.0010	0.0015	0.0033	0.0033	0.0051	0.0023
	Maximum Stress (MPa)	235	235	236	234	238	220
Ultimate Load Point	Moment (kNm)	199.7	183.6	175.2	168.4	165.1	0.0
	Normalized Moment	1.02	0.94	0.89	0.86	0.84	0.00
	Torque (kNm)	0.34	6.80	8.57	9.63	9.96	11.38
	Normalized Torque	0.04	0.73	0.92	1.04	1.07	1.23
	Rotation (Deg)	1.7	42.6	57.9	72.7	82.5	142
	Maximum Strain	0.0030	0.0109	0.0128	0.0139	0.0143	0.0093
	Maximum Stress (MPa)	238	243	243	246	249	232
	FEPR Original	1.02	0.91	1.08	1.19	1.22	1.23
	FEPR Modified	1.02	1.13	1.29	1.39	1.41	1.23

### Interaction Diagrams - Beam S9L1T1B3



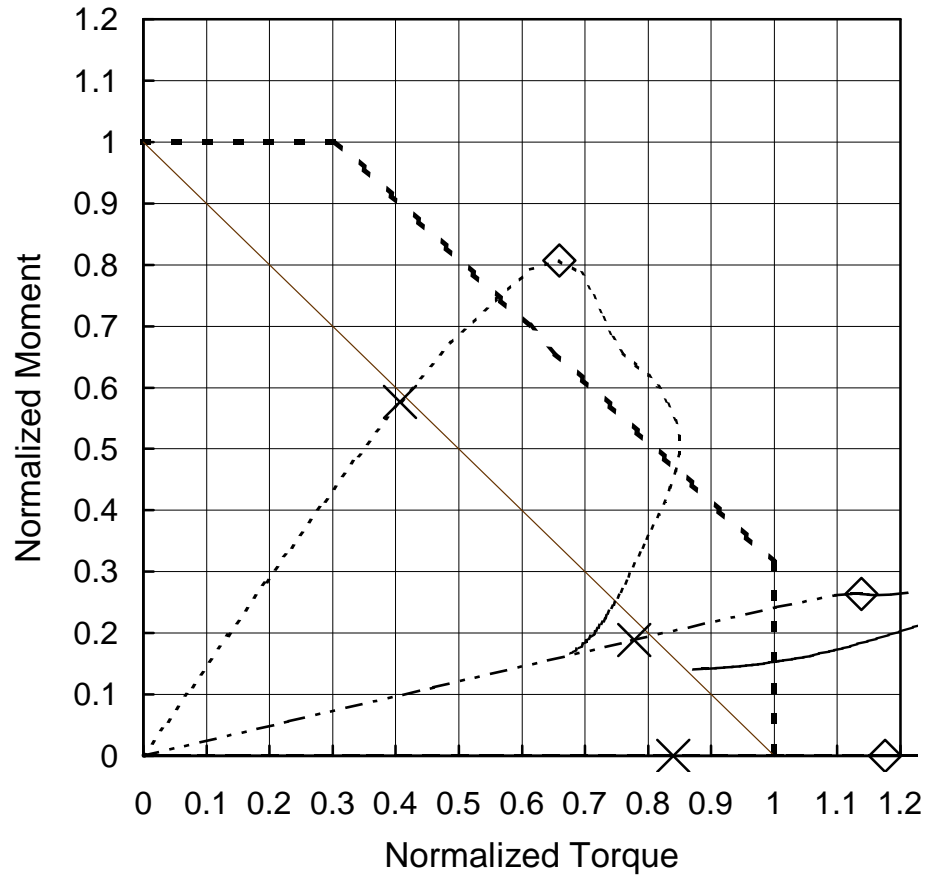
		E1	E3	E4
Service Load Point	Moment (kNm)	3833.9	1497.7	0.0
	Normalized Moment	0.64	0.25	0.00
	Torque (kNm)	131.56	303.84	307.74
	Normalized Torque	0.38	0.88	0.90
	Rotation (Deg)	4.1	12.2	13.1
	Maximum Deflection (mm)	14.27	8.95	0.58
	$L / \text{Deflection}$	235	375	5820
	Maximum Strain	0.0038	0.0103	0.0093
	Maximum Stress (MPa)	237	236	237
Ultimate Load Point	Moment (kNm)	5356.9	2073.0	0.0
	Normalized Moment	0.90	0.35	0.00
	Torque (kNm)	290.35	432.58	430.82
	Normalized Torque	0.85	1.26	1.25
	Rotation (Deg)	13.6	27.1	26.5
	Maximum Strain	0.0183	0.0178	0.0155
	Maximum Stress (MPa)	297	275	276
	FEPR Original	1.15	1.26	1.25
	FEPR Modified	1.36	1.27	1.25

### Interaction Diagrams - Beam S10L2T1B2



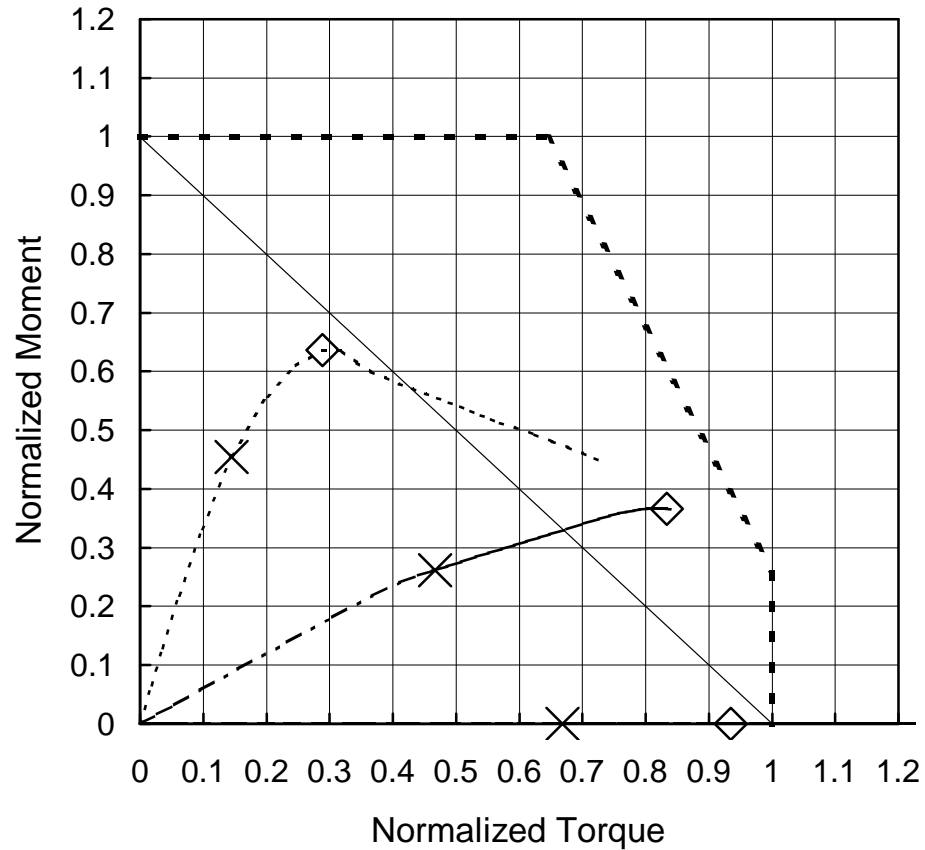
		E1	E3	E4
Service Load Point	Moment (kNm)	1306.4	500.1	0.0
	Normalized Moment	0.63	0.24	0.00
	Torque (kNm)	61.96	135.44	177.27
	Normalized Torque	0.25	0.55	0.72
	Rotation (Deg)	4.6	11.1	20.1
	Maximum Deflection (mm)	12.92	7.43	1.64
	<i>L</i> / Deflection	543	945	4280
	Maximum Strain	0.0032	0.0057	0.0073
	Maximum Stress (MPa)	350	370	402
Ultimate Load Point	Moment (kNm)	1829.0	700.1	0.0
	Normalized Moment	0.88	0.34	0.00
	Torque (kNm)	119.43	190.01	248.18
	Normalized Torque	0.48	0.77	1.00
	Rotation (Deg)	13.1	23.9	50.0
	Maximum Strain	0.0113	0.0120	0.0200
	Maximum Stress (MPa)	404	399	401
	FEPR Original	0.85	0.86	1.00
	FEPR Modified	1.08	0.92	1.00

### Interaction Diagrams - Beam S11L1T1B1



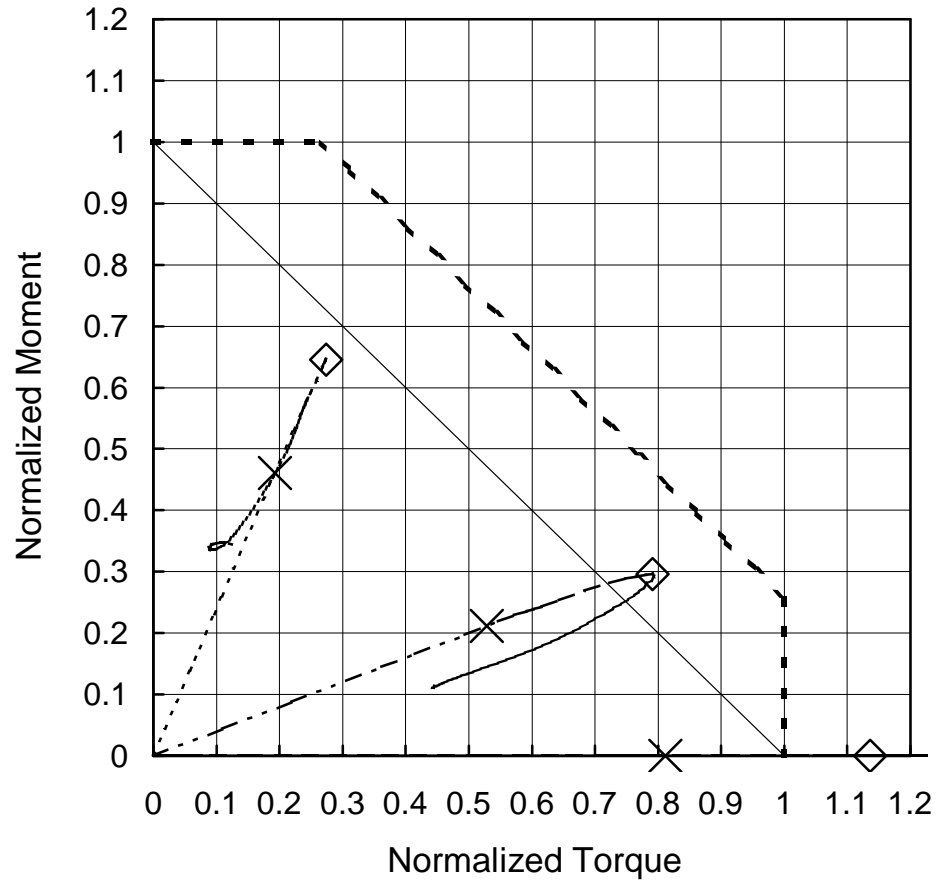
		E1	E3	E4
Service Load Point	Moment (kNm)	413.6	135.4	0.0
	Normalized Moment	0.58	0.19	0.00
	Torque (kNm)	10.38	19.85	21.43
	Normalized Torque	0.41	0.78	0.84
	Rotation (Deg)	0.9	1.6	1.7
	Maximum Deflection (mm)	5.64	0.98	0.06
	$L / \text{Deflection}$	409	2350	37800
	Maximum Strain	0.0023	0.0023	0.0020
	Maximum Stress (MPa)	350	350	350
Ultimate Load Point	Moment (kNm)	579.0	189.5	0.0
	Normalized Moment	0.81	0.26	0.00
	Torque (kNm)	16.82	29.05	30.00
	Normalized Torque	0.66	1.14	1.18
	Rotation (Deg)	2.8	3.7	3.5
	Maximum Strain	0.0077	0.0093	0.0079
	Maximum Stress (MPa)	350	363	358
	FEPR Original	1.14	1.13	1.18
	FEPR Modified	1.47	1.40	1.18

### Interaction Diagrams - Beam S2L3T1B1



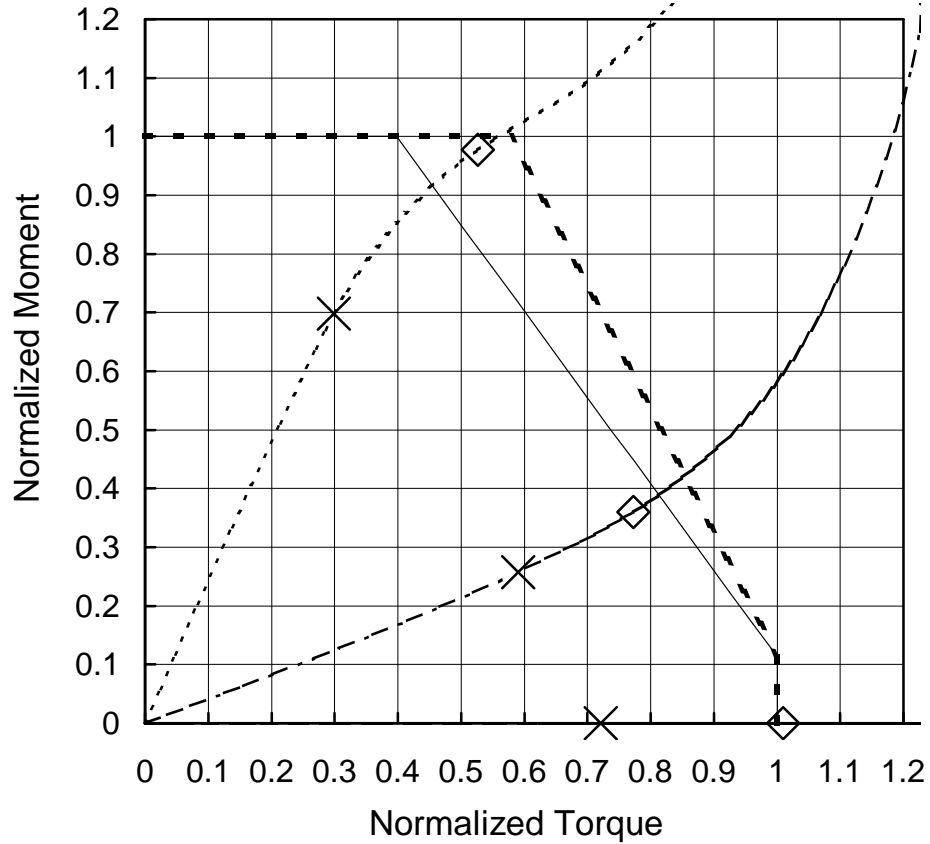
		E1	E3	E4
Service Load Point	Moment (kNm)	337.0	193.7	0.0
	Normalized Moment	0.45	0.26	0.00
	Torque (kNm)	7.87	25.44	36.42
	Normalized Torque	0.14	0.47	0.67
	Rotation (Deg)	4.2	15.3	21.8
	Maximum Deflection (mm)	7.79	16.49	9.49
	$L / \text{Deflection}$	745	352	611
	Maximum Strain	0.0019	0.0191	0.0233
	Maximum Stress (MPa)	350	368	376
Ultimate Load Point	Moment (kNm)	471.8	271.1	0.0
	Normalized Moment	0.64	0.37	0.00
	Torque (kNm)	15.73	45.43	50.99
	Normalized Torque	0.29	0.83	0.94
	Rotation (Deg)	9.4	46.2	35.8
	Maximum Strain	0.0068	0.0730	0.0323
	Maximum Stress (MPa)	363	461	431
	FEPR Original	0.70	0.87	0.94
	FEPR Modified	0.93	1.20	0.94

### Interaction Diagrams - Beam S2L4T1B1



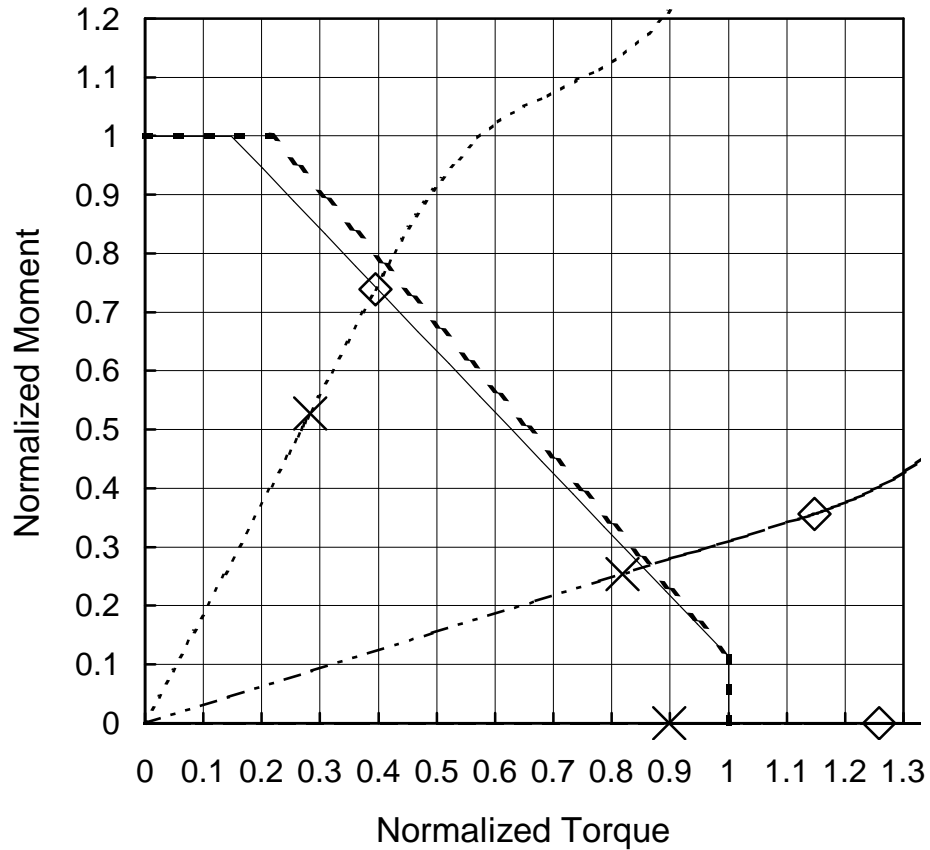
		E1	E3	E4
Service Load Point	Moment (kNm)	517.6	237.4	0.0
	Normalized Moment	0.46	0.21	0.00
	Torque (kNm)	25.37	69.68	106.96
	Normalized Torque	0.19	0.53	0.81
	Rotation (Deg)	0.3	0.9	3.3
	Maximum Deflection (mm)	10.85	1.96	0.27
	$L / \text{Deflection}$	107	593	4280
	Maximum Strain	0.0024	0.0061	0.0123
	Maximum Stress (MPa)	373	375	389
Ultimate Load Point	Moment (kNm)	724.7	332.3	0.0
	Normalized Moment	0.65	0.30	0.00
	Torque (kNm)	36.12	104.35	149.75
	Normalized Torque	0.27	0.79	1.14
	Rotation (Deg)	1.0	6.4	12.9
	Maximum Strain	0.0112	0.0929	0.0666
	Maximum Stress (MPa)	402	475	508
	FEPR Original	0.79	0.88	1.14
	FEPR Modified	0.92	1.09	1.14

### Interaction Diagrams - Beam S4L3T1B2



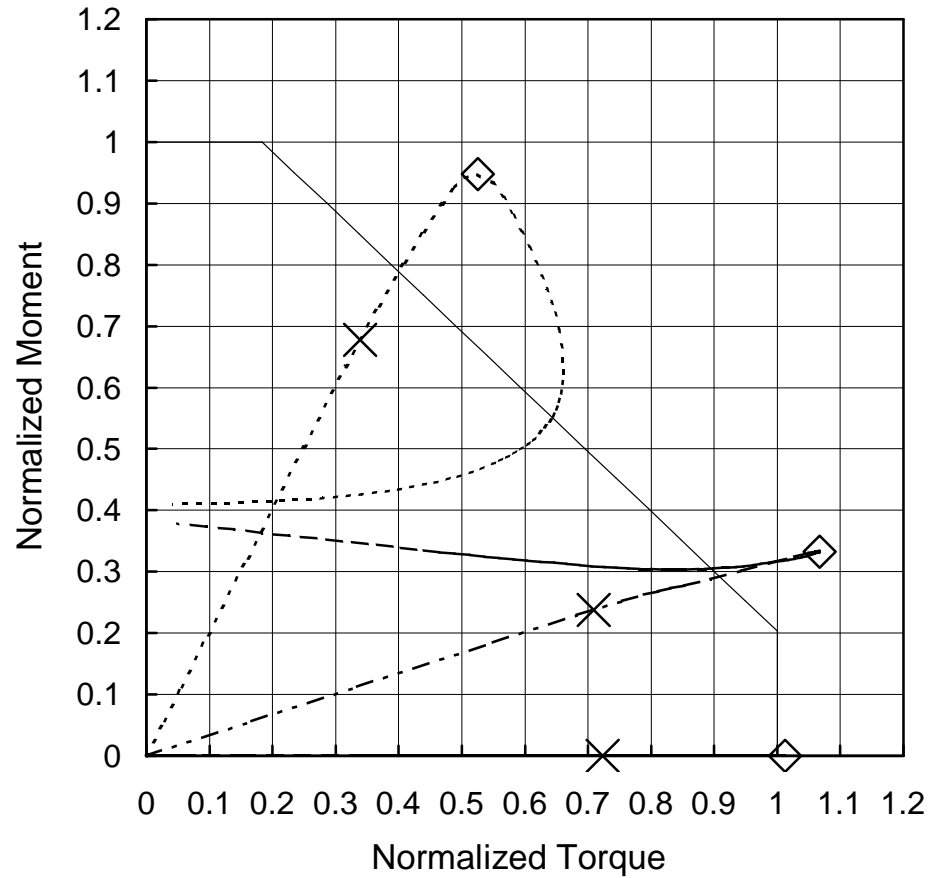
		E1	E3	E4
Service Load Point	Moment (kNm)	106.4	39.2	0.0
	Normalized Moment	0.70	0.26	0.00
	Torque (kNm)	3.90	7.70	9.42
	Normalized Torque	0.30	0.59	0.72
	Rotation (Deg)	11.6	22.3	28.5
	Maximum Deflection (mm)	20.36	9.39	0.54
	$L / \text{Deflection}$	317	688	12100
	Maximum Strain	0.0030	0.0031	0.0041
	Maximum Stress (MPa)	350	349	349
Ultimate Load Point	Moment (kNm)	148.9	54.9	0.0
	Normalized Moment	0.98	0.36	0.00
	Torque (kNm)	6.87	10.09	13.19
	Normalized Torque	0.53	0.77	1.01
	Rotation (Deg)	24.8	34.6	53.1
	Maximum Strain	0.0118	0.0114	0.0162
	Maximum Stress (MPa)	371	350	351
	FEPR Original	0.94	0.89	1.01
	FEPR Modified	1.10	0.93	1.01

### Interaction Diagrams - Beam S4L4T1B2



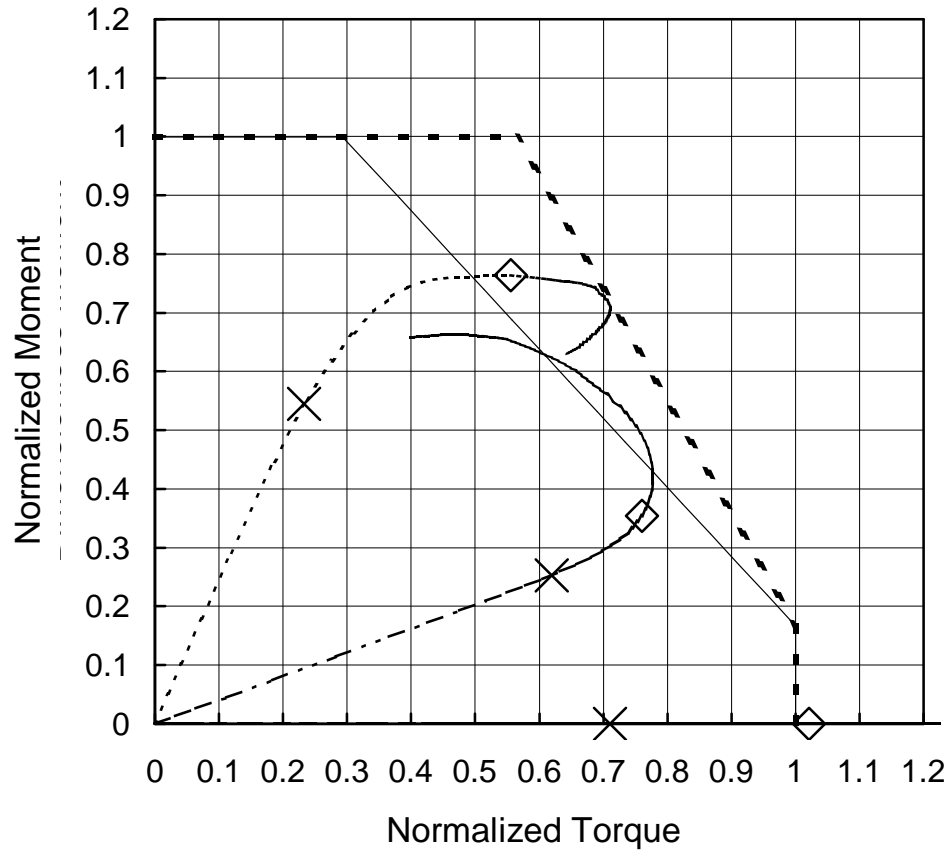
		E1	E3	E4
Service Load Point	Moment (kNm)	105.3	50.8	0.0
	Normalized Moment	0.53	0.25	0.00
	Torque (kNm)	9.91	28.67	31.49
	Normalized Torque	0.28	0.82	0.90
	Rotation (Deg)	0.5	1.9	2.3
	Maximum Deflection (mm)	9.95	1.31	0.02
	$L / \text{Deflection}$	130	986	68000
	Maximum Strain	0.0022	0.0051	0.0064
	Maximum Stress (MPa)	350	348	378
Ultimate Load Point	Moment (kNm)	147.5	71.1	0.0
	Normalized Moment	0.74	0.36	0.00
	Torque (kNm)	13.84	40.19	44.09
	Normalized Torque	0.39	1.15	1.26
	Rotation (Deg)	1.9	16.7	19.7
	Maximum Strain	0.0203	0.0457	0.0497
	Maximum Stress (MPa)	397	465	447
	FEPR Original	0.95	1.33	1.26
	FEPR Modified	1.00	1.34	1.26

### Interaction Diagrams - Beam S5L1T1B4



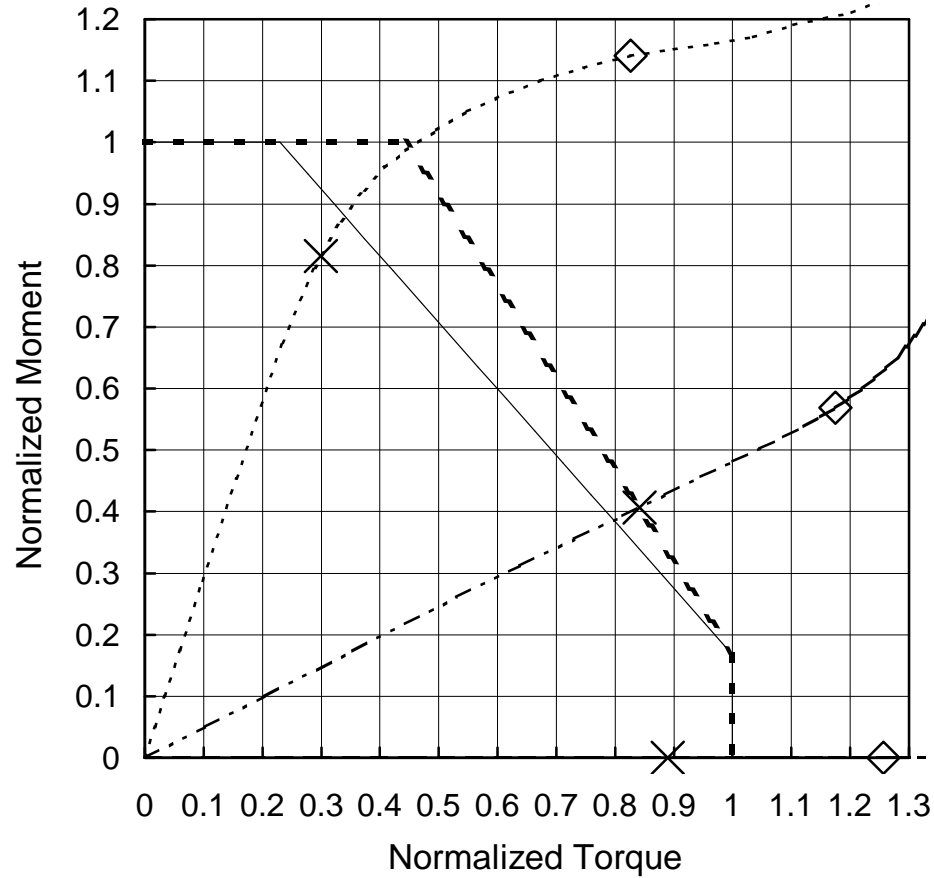
		E1	E3	E4
Service Load Point	Moment (kNm)	30.1	10.6	0.0
	Normalized Moment	0.68	0.24	0.00
	Torque (kNm)	1.26	2.64	2.69
	Normalized Torque	0.34	0.71	0.72
	Rotation (Deg)	1.1	2.5	1.1
	Maximum Deflection (mm)	1.42	0.56	-1.52
	<i>L</i> / Deflection	751	1900	-706
	Maximum Strain	0.0016	0.0020	0.0017
	Maximum Stress (MPa)	350	350	350
Ultimate Load Point	Moment (kNm)	42.1	14.8	0.0
	Normalized Moment	0.95	0.33	0.00
	Torque (kNm)	1.96	3.98	3.77
	Normalized Torque	0.53	1.07	1.01
	Rotation (Deg)	3.8	16.3	4.7
	Maximum Strain	0.0024	0.0200	0.0022
	Maximum Stress (MPa)	348	386	346
	FEPR Original	1.24	1.17	1.01
	FEPR Modified	1.24	1.17	1.01

### Interaction Diagrams - Beam S1L2T1B4



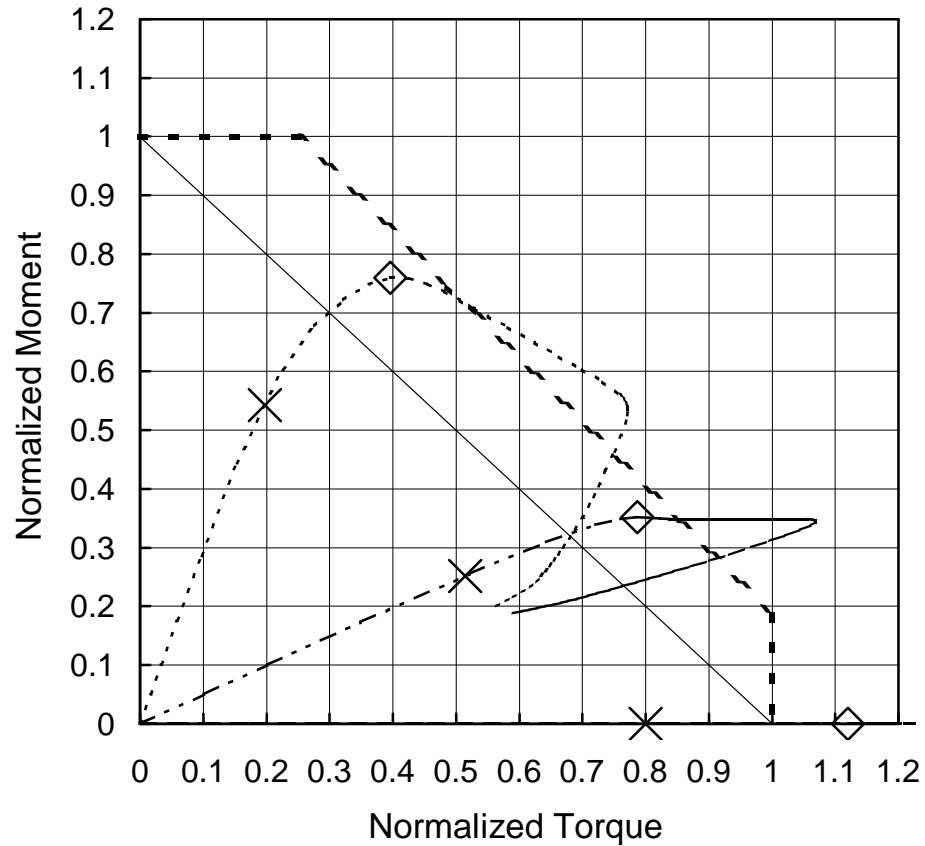
		E1	E3	E4
Service Load Point	Moment (kNm)	36.5	17.0	0.0
	Normalized Moment	0.55	0.25	0.00
	Torque (kNm)	1.45	3.86	4.42
	Normalized Torque	0.23	0.62	0.71
	Rotation (Deg)	6.4	22.8	34.1
	Maximum Deflection (mm)	5.03	7.70	-0.14
	$L / \text{Deflection}$	486	318	-17300
	Maximum Strain	0.0019	0.0025	0.0024
	Maximum Stress (MPa)	350	356	357
Ultimate Load Point	Moment (kNm)	51.1	23.7	0.0
	Normalized Moment	0.76	0.35	0.00
	Torque (kNm)	3.46	4.73	6.36
	Normalized Torque	0.56	0.76	1.02
	Rotation (Deg)	26.9	42.0	94.4
	Maximum Strain	0.0028	0.0029	0.0036
	Maximum Stress (MPa)	368	374	380
	FEPR Original	0.88	0.87	1.02
	FEPR Modified	1.05	0.93	1.02

### Interaction Diagrams - Beam S1L2T2B2



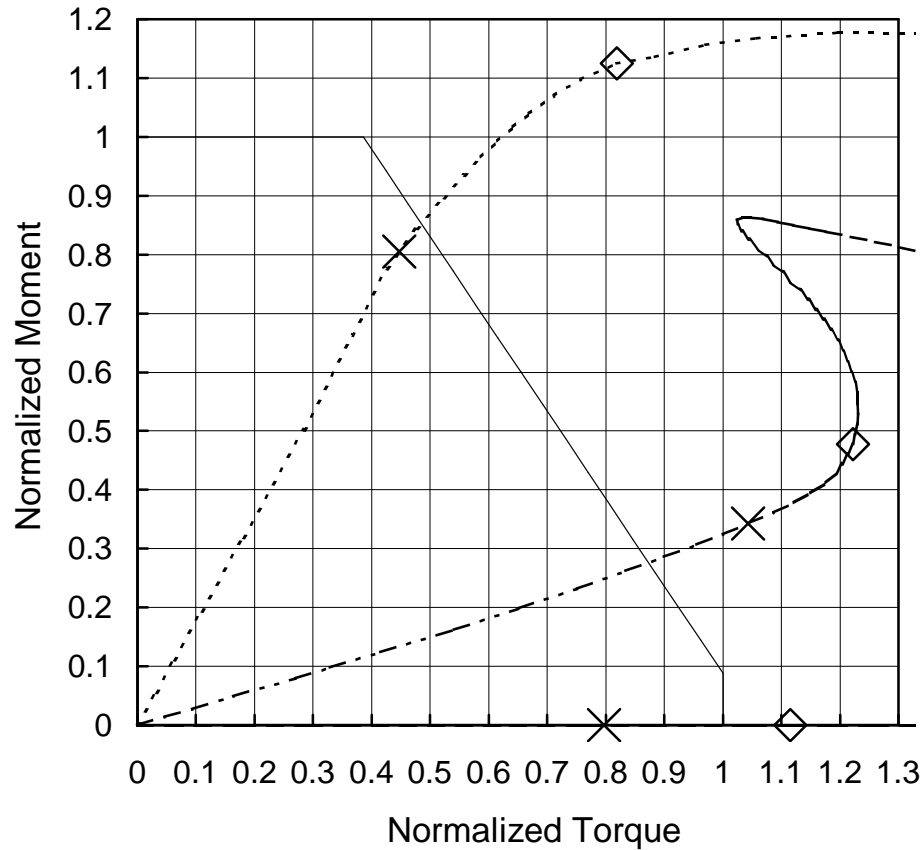
		E1	E3	E4
Service Load Point	Moment (kNm)	54.8	27.3	0.0
	Normalized Moment	0.81	0.41	0.00
	Torque (kNm)	2.38	6.69	7.07
	Normalized Torque	0.30	0.84	0.89
	Rotation (Deg)	4.6	14.6	15.3
	Maximum Deflection (mm)	5.58	4.73	0.27
	$L / \text{Deflection}$	439	516	9160
	Maximum Strain	0.0017	0.0028	0.0019
	Maximum Stress (MPa)	350	351	350
Ultimate Load Point	Moment (kNm)	76.7	38.3	0.0
	Normalized Moment	1.14	0.57	0.00
	Torque (kNm)	6.57	9.34	9.98
	Normalized Torque	0.83	1.18	1.26
	Rotation (Deg)	19.3	30.9	30.8
	Maximum Strain	0.0117	0.0077	0.0040
	Maximum Stress (MPa)	371	351	350
	FEPR Original	1.43	1.40	1.26
	FEPR Modified	1.63	1.47	1.26

### Interaction Diagrams - Beam S3L1T2B1



		E1	E3	E4
Service Load Point	Moment (kNm)	506.8	235.0	0.0
	Normalized Moment	0.54	0.25	0.00
	Torque (kNm)	16.87	44.05	68.54
	Normalized Torque	0.20	0.51	0.80
	Rotation (Deg)	1.6	3.8	6.3
	Maximum Deflection (mm)	7.28	3.74	0.34
	<i>L</i> / Deflection	455	885	9670
	Maximum Strain	0.0022	0.0027	0.0031
	Maximum Stress (MPa)	350	350	350
Ultimate Load Point	Moment (kNm)	709.5	329.1	0.0
	Normalized Moment	0.76	0.35	0.00
	Torque (kNm)	33.91	67.43	95.94
	Normalized Torque	0.40	0.79	1.12
	Rotation (Deg)	15.2	8.7	16.1
	Maximum Strain	0.0090	0.0124	0.0168
	Maximum Stress (MPa)	369	350	403
	FEPR Original	0.99	0.97	1.12
	FEPR Modified	1.16	1.14	1.12

## Interaction Diagrams - Beam S6L1T2B3



		E1	E3	E4
Service Load Point	Moment (kNm)	405.9	172.5	0.0
	Normalized Moment	0.81	0.34	0.00
	Torque (kNm)	13.88	32.37	24.73
	Normalized Torque	0.45	1.04	0.80
	Rotation (Deg)	11.7	29.1	17.0
	Maximum Deflection (mm)	42.11	24.52	0.30
	$L / \text{Deflection}$	91	157	12700
	Maximum Strain	0.0040	0.0088	0.0014
	Maximum Stress (MPa)	236	229	216
Ultimate Load Point	Moment (kNm)	567.0	240.8	0.0
	Normalized Moment	1.13	0.48	0.00
	Torque (kNm)	25.42	37.92	34.62
	Normalized Torque	0.82	1.22	1.12
	Rotation (Deg)	30.2	46.8	25.7
	Maximum Strain	0.0213	0.0166	0.0038
	Maximum Stress (MPa)	277	252	219
	FEPR Original	1.49	1.46	1.12
	FEPR Modified	1.49	1.46	1.12